MOLECULAR AND ELECTRONIC DYNAMICS IN VAN DER WAALS CLUSTER SPECTROSCOPY, HYDROGEN ABSTRACTION REACTIONS, AND INELASTIC COLLISIONS AT LIQUID SURFACES

by

Michael P. Ziemkiewicz

B. S., University of Pittsburgh, 1999

A thesis submitted to the
Faculty of the Graduate School of the
University of Colorado in partial fulfillment
of the requirement for the degree of
Doctor of Philosophy
Department of Physics
2012

This thesis entitled:

Molecular and Electronic Dynamics in Van Der Waals Cluster Spectroscopy, Hydrogen Abstraction Reactions, and Inelastic Collisions at Liquid Surfaces

written by Michael P. Ziemkiewicz

has been approved for the Department of Physics by

_____

Dr. David J. Nesbitt

_____

Dr. Jun Ye

Date_____

The final copy of this thesis has been examined by the signatories, and we
Find that both the content and the form meet acceptable presentation standards
Of scholarly work in the above mentioned discipline.

Ziemkiewicz, Michael P. (Ph.D. Physics)

Molecular and Electronic Dynamics in Van Der Waals Cluster Spectroscopy, Hydrogen Abstraction Reactions, and Inelastic Collisions at Liquid Surfaces

Thesis directed by Professor David J. Nesbitt

Quantum mechanical measurements are essential for an understanding of collision and reaction dynamics on the molecular scale. To this end, laser induced fluorescence (LIF) is used to probe rotational, vibrational, and electronic product state distributions following various chemical events. For example, LIF on the hydroxyl radical is employed to examine the propensity to populate different levels of OH following photolysis of H_2O molecules using a technique known as vibrationally mediated dissociation (VMD). VMD is also used as an indirect method for obtaining infrared spectra of water clusters (Ar-H_2O, H_2O-H_2O, and H_2-H_2O), weakly bound species which are produced in the cold (~ 5 K) environment of a slit supersonic expansion. Peaks are then assigned with the aid of high level theoretical calculations. LIF is also performed to study systems where reactive precursors produce OH/OD radicals ($F + D_2O \rightarrow DF + OD$ and $F + H_2O \rightarrow HF + OH$) as well as for nonreactive processes where ground state NO inelastically is scattered from liquid Ga metal or room temperature ionic liquid (RTIL) surfaces. In the reactive scattering experiments, careful examination of OH product spin-orbit branching provides an opportunity to quantify the degree of multiple surface behavior in these systems. Rotational-state-resolved scattering of nitric oxide from a molten metal provides an opportunity to directly observe thermal roughening of the liquid due to capillary wave excitations. Scattered NO electronic distributions, which are out of

thermal equilibrium with rotation, are quite sensitive to surface temperature, a possible consequence of interactions with electron-hole pairs during the collision. Finally, NO is scattered from room temperature ionic liquid (RTIL) samples where branching between the two possible scattered spin orbit states ($^2\Pi_{1/2}$ and $^2\Pi_{3/2}$) is found to be highly sensitive to surface heating and choice of ionic liquid. This may serve as a novel means for characterizing these surfaces, which are of technological interest due to their potential role as advanced solvents.

To Eva

Acknowledgments

My time as a graduate student at the University of Colorado has deeply impacted my life in ways that I cannot begin to sum up in a few short pages. From the countless adventures to be had in the mountains, to the fascinating , vibrant, and delightfully strange culture of the city of Boulder, this is truly a special place to live. At the same time, JILA and the University of Colorado have provided an ideal environment for learning and doing science. During my time here, I have encountered a great many talented and warm people who have helped me along in this journey.

I would like to start by thanking Peter Siska, who opened up my eyes to the wonderful and subtle ideas of chemical physics when I was an undergraduate at the University of Pittsburgh. When I came to Colorado, he suggested I talk to his friend, David Nesbitt, who would eventually become my graduate advisor. David has never ceased to amaze me with the clarity of his thinking, which often turns a complex problem into a solvable one. I would like to thank David for sharing this method of approaching the endless issues that come up during a scientific study. I would also like to thank David for always pushing me to analyze the data more deeply, to think more carefully about this work, and to learn more about why things work the way they do.

I would also like to thank the many dedicated faculty members from whom I have learned, and with whom I have worked and taught. I'd like to particularly thank Alan Knight, Leon Phillips, Ad van der Avoird, Shijie Jong, Kevin Stenson, and all the professors who taught my graduate classes. In addition, I owe a huge debt of gratitude to the postdocs with whom I have worked. Tanya Myers introduced me to my first

experiment with enthusiasm. Sergei Nizkorodov inspired me by showing how much can be done by hard work and dedication. Mike Wojcik and Christian Pluetzer were both invaluable partners in performing experiments, but more importantly their friendship was crucial for keeping my spirits up during that time. Rob Roscioli's pure love of science was simply infectious, and he has been a crucial source of advice on all things scientific. I also want to thank Mia Zutz for her enthusiasm for learning to run the experiment. It is comforting to know that the apparatus is in good hands and will go on to do amazing new things.

The Nesbitt group itself also deserves thanks because so many people in it have made this such a friendly and intellectually stimulating environment in which to work. Special thanks to the current and recent members who have managed to make life more pleasant while I've been finishing up my work. I owe a lot to my current office mates who always seem to have a quick answer to whatever question I ask, which has sped my progress considerably. At the same time they have managed to make this a fun place to work no matter what obstacles appeared. Andrej Grubisic has helped me considerably by always being available for a fascinating discussion on any complex issue. Chih-Hsuan Chang has impressed me with his extensive knowledge of spectroscopy, and Monika Grutter has provided invaluable help during my search for what I will do in the next step of my career. My days here have also been made brighter by Melanie Roberts's spirit, Grant Buckingham's sense of humour, and Dan Nelson's enthusiasm. I'd also like to thank Nick Dupuis and Larry Fiegland; our weekly trips to Starbucks gave me the perspective I needed to complete my studies. Thanks also go out to the rest of the current Nesbitt group: Andy Gisler, Tom Baker, Erik Homstrom, Kevin Early, and Mario

Vieweger, whose friendship I value greatly. Finally, I'd like to thank all the previous group members, of whom there are far too many to thank individually. However, special thanks go out to Brad Perkins, Erin Sharp-Williams, Alex Zolot, Oliver Monti, Erin Whitney, Julie Fiore, Erin Sharp, and Mike Deskevich, each of whom has helped me in a very significant way during this time.

None of these experiments could have been done without the efforts of the fantastic JILA staff. I owe so much of what I have learned and built in the instrument shop to the dedication of the people there, particularly Hans Green, Tracy Keep, Todd Ansicar, Blaine Horner, and Ariel Paul. Also, I owe a debt of gratitude to the electronics shop personnel, specifically Paul Beckingham, James Fung-A-Fat, and Terry Brown. I have also been helped greatly along the way by the efforts of the JILA and Physics administrators, particularly Agnieszka Lynch, Jeanne Nijhowne, and Maryly Dole.

I would also like to thank all of the wonderful people in Boulder who have made my life here so enjoyable. All of my friends and neighbors have helped me and enriched my life in so many ways. Thanks to all the people with whom I've skied and explored the Colorado mountains. Thanks for the good times at the Sloggi Dome. Thanks to the Boulder / Denver improv community, and thanks to the South Boulder sand volleyball crew.

I'd also like to thank my parents for all their support and kindness, and finally I'd like to thank Eva for being my constant companion through this adventure that we share together.

TABLE OF CONTENTS

Chapter I	**Introduction**	**1**
	References for Chapter I	19
Chapter II	**Experimental Apparatus**	**22**
2.1	Laser Induced Fluorescence (LIF) detection	22
2.2	Spectroscopy and Dynamics of H_2O-containing clusters	48
2.3	Crossed Jet Reactive Scattering	57
2.4	State-to-State Scattering at the Gas-Liquid Interface	64
	References for Chapter II	69
Chapter III	**Vibrationally-Mediated Dissociation Dynamics of H_2O in the $v_{OH} = 2$ polyad**	**70**
3.1	Introduction	70
3.2	Experimental Technique	74
3.3	Results and Analysis	78
3.4	Nascent OH Rotational Populations	84
3.5	Nascent OH Spin-Orbit and Lambda-Doublet Distributions	90
3.6	OH Vibrational Distributions	93
3.7	Summary / Conclusions	99
	References for Chapter III	100
Chapter IV	**Overtone Spectroscopy of H_2O Clusters in the $v_{OH} = 2$ Manifold: IR-UV Vibrationally Mediated Dissociation Studies**	**102**
4.1	Introduction	102
4.2	Experimental Technique	105
4.3	Spectroscopic Notation	106
4.4	Overview Spectrum	109
4.5	First Overtone ($v_{OH} = 2$) Spectra of H_2O Dimer	112
4.6	Overtone ($v_{OH} = 2$) Spectra of Ar-H_2O	119
4.7	Vibrational Predissociation Dynamics	124
4.8	Summary / Conclusions	131
	References for Chapter IV	132

Chapter V		**Overtone Vibrational Spectroscopy and Dynamics in H_2-H_2O Complexes: A Combined Theoretical and Experimental study**	**136**
	5.1	Introduction	136
	5.2	Theoretical Background	140
	5.3	Calculated Results	148
	5.4	Experimental Technique	152
	5.5	Results	156
	5.6	Discussion	166
	5.7	Summary / Conclusions	172
		References for Chapter V	174
Chapter VI		**Direct Evidence for Nonadiabatic Dynamics in Atom + Polyatom Reactions: Crossed-Jet Laser Studies of F + D_2O → DF + OD**	**179**
	6.1	Introduction	179
	6.2	Experimental Technique	184
	6.3	Results	188
	6.4	Discussion	192
	6.5	Summary / Conclusions	202
		References for Chapter VI	204
Chapter VII		**Non-Adiabatic Reactive Scattering in Atom + Triatom Systems: Nascent Rovibronic Distributions in F + H_2O → HF + OH**	**209**
	7.1	Introduction	209
	7.2	Experimental Technique	213
	7.3	Results	217
	7.4	Discussion	223
	7.5	Summary / Conclusions	232
		References for Chapter VII	233
Chapter VIII		**State-to-State Dynamics at the Gas-Liquid Metal Interface: Rotationally and Electronically Inelastic Scattering of NO[$^2\Pi_{1/2}$(0.5)] from Molten Gallium.**	**237**
	8.1	Introduction	237
	8.2	Experimental Technique	243
	8.3	Results	248
	8.4	Discussion	259

8.5	Summary / Conclusions	269
	References for Chapter VIII	270
Chapter IX	**Inelastic Scattering of Radicals at the Gas-Ionic Liquid Interface: Probing Surface Dynamics of BMIM-Cl, BMIM-BF_4, and BMIM-Tf_2N by Rovibronic Scattering of NO [$^2\Pi_{1/2}$(0.5)]**	**275**
9.1	Introduction	275
9.2	Experimental Technique	280
9.3	Results	285
9.4	Discussion	292
9.5	NO Rotational Excitation: Trapping Desorption and Impulsive Scattering	296
9.6	NO Spin-Orbit Excitation: Possible Mechanism(s) for Facile Spin Flip Dynamics	299
9.7	Summary / Conclusions	303
	References for Chapter IX	304
	Bibliography	**308**
Appendix A	**Circuit Diagrams**	**319**
A.1	PMT Switcher	319
A.2	Pulsed Discharge Source	321
Appendix B	**Data Analysis Software**	**323**
B.1	Labview Data Taking Program	323
B.2	Labview Frequency Calibration	381
B.3	LIF Spectrum Fitter	387
B.4	Double Exponential Fits	403

TABLES

3.1	Review of previous studies on H_2O photodissociation	73
3.2	Observed OH quantum state distributions after H_2O photolysis	82
4.1	Positions and assignments for Ar-H_2O and $(H_2O)_2$ transitions	112
4.2	Values for $(H_2O)_2$ fundamental stretching frequencies	113
5.1	H_2-H_2O ground state symmetry relations	143
5.2	Symmetry relations in H_2O-H_2O for H_2O in |02-)	145
5.3	Rovibrational selection rules in H_2O-H_2O	146
5.4	pH_2-pH_2O rovibrational levels	149
5.5	pH_2-oH_2O rovibrational levels	149
5.6	oH_2-pH_2O rovibrational levels	150
5.7	oH_2-oH_2O rovibrational levels	151
5.8	H_2-H_2O binding energy for each species	167
6.1	OD rotational and electronic distributions	192
7.1	Nascent OH quantum state distributions	220
8.1	Dependence of scattered rotational and electronic temperatures on surface heating in NO + Ga(*l*)	254
9.1	Two temperature fits for NO scattered from RTIL's	298

FIGURES

1.1	Scheme used to detect H_2O-containing clusters	5
1.2	F + H_2O energetics	10
1.3	Liquid scattering experiment	15
1.4	Ionic liquids used in these studies	17
2.1	LIF detection scheme	24
2.2	Spectroscopy of NO	25
2.3	Sample NO spectrum	27
2.4	YAG infrared laser	28
2.5	Dye laser overview	31
2.6	UV light generation by BBO frequency doubling	33
2.7	Baffles for scattered light mitigation	35
2.8	Schematic of the LIF imaging tube	37
2.9	PMT wiring scheme	38
2.10	Labview data taking program: front panel	42
2.11	Labview frequency calibrator: front panel	45
2.12	Tests on a room temperature NO distribution	47
2.13	Cleaning metal surfaces with Ar^+	50
2.14	Gas handling	52
2.15	Gas-liquid scattering apparatus	54
2.16	Vibrationally mediated photodissociation scheme	58
2.17	Tunable infrared generation using an OPO	60
2.18	Sample predissociation lifetime data	63
2.19	Crossed jet reactive scattering setup	65
3.1	Sample H_2O action spectrum	79
3.2	Sample LIF probe spectrum after H_2O photolysis	81
3.3	OH photolytic rotational distributions in v = 1 and v = 0	84
3.4	Effect of |02-) H_2O rotation on photolytically-generated OH product distributions	85
3.5	Oscillation of scattering distributions with J_{OH}	87
3.6	Effect of initial H_2O stretch vibration on OH rotational distribution	88
3.7	Effect of initial H_2O bend vibration on OH rotational distribution	89
3.8	Spin orbit branching after photolysis of H_2O |02-)	91
3.9	Λ-doublet ratios from H_2O |02-) and |01-2)	92
3.10	Ground and excited state electronic wavefunctions relevant to photolysis	97

4.1	H_2O clusters experimental approach	104
4.2	$(H_2O)_2$ energy level diagram	107
4.3	Ar-H_2O and H_2O energy levels	109
4.4	Overview vibrationally mediated photolysis spectrum	110
4.5	Predicted water dimer transition energies	114
4.6	Rotationally-resolved spectrum and simulation of the water dimer band at 7193 cm^{-1}	115
4.7	Rotationally-resolved spectrum and simulation of Ar-H_2O: $\|02-\rangle \Sigma(0_{00}) \leftarrow \|00+\rangle \Sigma(1_{01})$	122
4.8	Cluster predissociation lifetimes	125
4.9	Nascent OH quantum state distributions after cluster photolysis	128
4.10	OH photolysis distributions after Ar-H_2O predissociation	129
5.1	Infrared action spectroscopy scheme	154
5.2	Sample infrared spectrum: H_2O and H_2-H_2O	157
5.3	Calculated H_2-H_2O wavefunctions	158
5.4	H_2-H_2O: Comparison between experiment and theory	160
5.5	Rotational distribution of photolytically-generated OH	162
5.6	Direct measurement of H_2-H_2O predissociation lifetime	165
5.7	Energetic channels available for predissociation in oH_2-oH_2O and oH_2-pH_2O	169
6.1	Reaction energetics for F + D_2O - DF + OD	183
6.2	Experimental schematic: F + D_2O	185
6.3	Testing the data analysis procedure using a static 300 K H_2O cell	189
6.4	Sample OD LIF spectrum	190
6.5	OD product distributions	193
6.6	Boltzmann plots for product OD molecules	197
6.7	Spin orbit ratio as a function of N_{OD}	199
6.8	Two temperature fits to the OD rotational distribution	200
7.1	Reaction energetics for F + H_2O - HF + OH	213
7.2	Calculated collision energy distribution	216
7.3	Sample OH spectrum	218
7.4	OH product population distributions	221
7.5	Electronic branching ratios and average rotational energy	222
7.6	Nascent OH Boltzmann distributions	227
7.7	Comparison with F + D_2O results	231
8.1	Schematic for the liquid metal scattering experiment	244
8.2	Rotational characterization of the incident NO / H_2 beam	247

8.3	Rotational distributions for a static NO fill at 300 K	249
8.4	Sample distributions for inelastically scattered NO on liquid Ga	250
8.5	The effect of collision energy on the scattered rotational distribution	251
8.6	NO rotational distribution at high collision energy	252
8.7	The effect of surface temperature on scattered rotational energy	253
8.8	Correlation between electronic and rotational energy in scattered NO	255
8.9	The dependence of surface heating on scattered spin-orbit temperature	257
8.10	Comparison with NO scattered from other metallic surfaces	261
8.11	Efficiency for conversion of NO translational energy to rotation on several metals	266
9.1	Room temperature ionic liquids used in the experiment	280
9.2	Schematic for NO scattering from ionic liquids	281
9.3	NO curve of growth in the incident beam	283
9.4	Sample LIF spectrum for NO on BMIM-Tf_2N	286
9.5	Rotational Boltzmann plots for NO on BMIM-Tf_2N	289
9.6	Average rotational energies for NO on various RTIL's	290
9.7	NO electronic temperatures	293
9.8	Possible spin-flip mechanism	301
A.1	PMT switcher circuit	320
A.2	Pulsed discharge source	322

Chapter I: Introduction

Quantum mechanics is essential for understanding the dynamics of chemical reactions. Electrons which are bound to angstrom-scale atoms and molecules tend to experience a high degree of quantum confinement which results in ground state kinetic energy on the order of tens of eV and a sparse set of electronic levels accessible at typical thermal collision energies. Since so few of these states participate in a reactive collision, classical pictures of electronic motion break down. In this case, it is appropriate to identify the electronic state of a molecular system for some starting set of atomic positions and treat the effect of changing molecular configuration as either a time-independent or a time-dependent perturbation of the electronic energy level structure. Atoms, on the other hand, have masses thousands of times larger than that of an electron, so for spatial confinement to molecular length scales, they give rise to molecular motions characterized by much lower energy spacings. Vibrational states, for example, are separated by half of an eV or less while low-J rotational levels are characterized by energy scales on the order of hundredths or thousandths of an eV. Even though these values are small compared to many electronic spacings, they still are often significant compared to the kinetic energies of reacting molecules. For this reason, a complete quantum description of the internal molecular degrees of freedom is the ideal means for understanding the results of chemical reaction dynamics at their most fundamental.

In practice, for bimolecular reaction dynamics, this complete quantum description takes the form of state-to-state studies where one specifies collision energy as well as the

internal quantum state of each reactant. If one can subsequently measure the probability distribution to produce specific quantum states of the products as well as the probability to scatter with a particular product momentum, then a nearly full description of the reaction has been achieved, limited only by lack of knowledge of the impact parameter. In many chemical reactions, the complicated hierarchy of product energy scales (electronic, vibrational, rotational) results in a good deal of dynamical richness even for a relatively simple hydrogen abstraction reaction such as F (ground state) + H_2O (ground state) $\rightarrow$ HF (excited state) + OH (excited state).

In this case, the exothermic process provides energetic access to several vibrational modes of both the HF and OH products and will excite one of many available rotational levels of each diatomic molecule. Additionally, the existence of an unpaired electron in the OH product gives rise to four low lying product electronic levels[1] which all lie within 0.016 eV of each other. This complexity makes it difficult to perform a single experiment or theoretical treatment which is able to observe the probability to produce each product quantum state. Therefore, it is often necessary to collect information from many different types of experimental and theoretical studies in order to form a full picture of the nature of a particular chemical reaction.

A wide variety of experimental techniques have been developed for obtaining information on relevant degrees of freedom for various scattered products. For example, mass spectroscopic studies are used to determine the probability of creating a specific set of product molecules in a crossed beam reaction chamber, providing a product branching ratio,[2] the most fundamental observation to be made in any chemical reaction. By combining these experiments with angular[3] and time of flight measurements,[4] researchers

are further able to specify the probability distribution for a specific product channel to be characterized by a particular recoil speed and scattering angle. While such studies cover a very large amount of the product phase space, they remain insensitive to internal degrees of freedom which must be accessed by more specialized methods. Scattered vibrational distributions of closed shell products such as HF, for example, are often accessed with infrared (IR) techniques ranging from vibrational chemiluminescence detection[5] to spectroscopic techniques where infrared laser light is absorbed[6] by specific rovibrational transitions. These methods are often aided by the use of a multipass cavity to improve experimental sensitivity or by coupling into a ringdown cavity[7] so that time domain information can be used to further separate signal from background. On the other hand, for certain molecules such as the open shell species detected in this work (OH and NO), very specific ultraviolet laser techniques can be employed to detect them with high sensitivity due to a greatly reduced influence of incident laser photons on the nonresonant background. One such method which has long been used to detect NO is resonantly enhanced multiphoton ionization (REMPI).[8] In this scheme, multiple ultraviolet photons are used to state-specifically ionize a specific rovibronic quantum state of a specific molecule. When coupled with sophisticated ion optics, REMPI can further provide information on translational distributions, either by time of flight methods or by velocity map imaging (VMI).[9] However, despite its high sensitivity and the large amount of information obtained in a single experiment, it is nontrivial to extract quantitative population distributions from these types of studies. This is partly due to the multiphoton nature of the excitation and partly due to high sensitivity to the electronic energy level structure of the molecule under study. While careful work on REMPI in nitric oxide has

been able to surmount these problems to a high degree, the hydroxyl radical has proven far more difficult to treat by this technique. For this reason, for the studies presented herein, detection of OH and NO is done using laser induced fluorescence (LIF),[10] where absorption on rovibronic UV transitions is inferred when spontaneously emitted photons are detected with k-vectors and frequencies different from those in the incident excitation laser. When this UV laser is scanned over several rovibronic bands, a spectrum is produced which can be further analyzed to yield rotational, vibrational and electronic product distributions.

LIF techniques are employed here initially as a means to examine spectroscopy and dynamics for water-containing Van der Waals clusters. In these experiments, the weakly-bound species are prepared by cooling in a slit supersonic jet source to temperatures between 5 and 15 K which is sufficient to ensure a measureable amount of cluster formation. A variety of different water-containing complexes are examined, namely Ar-H_2O, H_2O-H_2O, and H_2-H_2O. In each case, a tunable infrared laser is used to excite the first stretch vibrational overtone of the H_2O moiety which renders it susceptible to photolysis by a subsequent 193 nm laser pulse. After the water molecule has broken apart, a third ultraviolet laser pulse is introduced in order to measure the resulting OH population distributions by LIF. Since the 193 nm light does not efficiently photolyze ground state water, fixing detection on a single OH level while tuning of the infrared excitation laser provides an indirect but sensitive scheme for measuring infrared spectra for these complexes, a technique known as action spectroscopy. The overall detection scheme is shown in figure 1.1. In addition to finding infrared absorption lines, however, this method can be used to observe dynamical process on two very different timescales.

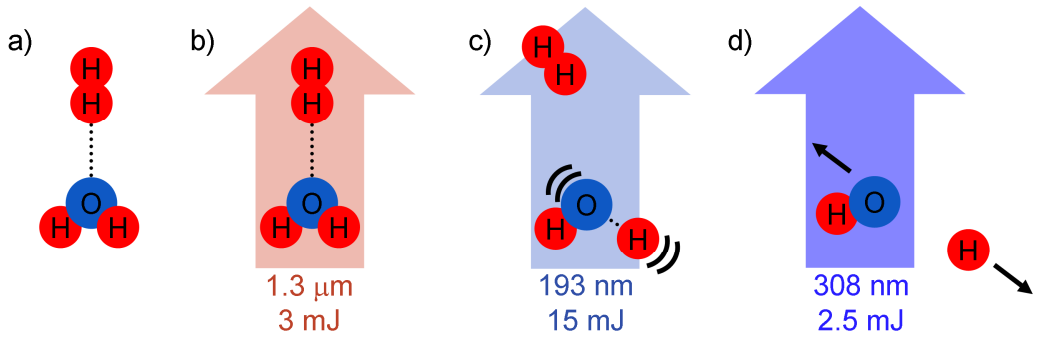

Figure 1.1 Scheme used to detect H_2 – H_2O clusters: a) Complexes are formed in a ~3 K slit supersonic jet. The potential energy minimum structure is shown here. b) An infrared laser pulse excites the $|02^-\rangle$ overtone stretch vibration of the H_2O moiety. c) The H_2O is photolyzed by a laser at 193 nm, a color which efficiently breaks apart vibrationally excited water while minimizing background from photolysis of the ground state. The time delay between the IR and photolysis lasers can be varied to probe predissociation of the metastable cluster state. d) OH photolysis products are detected by laser induced fluorescence following excitation by a tunable 308 nm pulse.

First of all, when the infrared laser is fixed on a specific cluster absorption line, one can scan the LIF laser in order to obtain OH distributions following a "half reaction" where photolysis from an initially bound configuration results in trajectories which lead to fully dissociated products. The resulting OH distributions are heavily influenced by the presence or absence of whichever molecule is complex-bound to its parent H_2O. For this reason, it is possible to directly measure predissociation timescales by varying the time delay between the nanosecond-wide infrared and photolysis laser pulses while both tunable lasers are parked on specific resonances. Photolysis of cluster-bound H_2O tends to create a rotationally colder OH distribution than photolysis of predissociated H_2O, likely due to the propensity to break apart into bend vibrationally excited water. Consequently, increasing the IR-photolysis time delay leads to an increase in the population of high-J OH states on the timescale of conversion of metastable H_2O vibrational excitation into intermolecular degrees of freedom.

In the case of H_2O bound to noble gas molecules, these predissociation events occur on a timescale of tens to hundreds of nanoseconds, which is very long compared to the femtosecond-scale vibrational period of the excited internal H_2O state. Additionally, the atom-molecule binding energies, on the order of 100 wavenumbers (cm^{-1}), are dwarfed by the 7600 cm^{-1} of vibrational energy in the overtone-excited water molecule. This provides an interesting opportunity to study the dynamics of a long-lived metastable state by comparing predissociation timescales and OH distributions, with very different dynamical signatures observed for excitation of various rovibrational states of H_2O clusters. Such distinguishability provides insight into the structure of the wavefunction for various excited vibrational levels of the atom-molecular clusters, which in turn assists in assigning the bands observed by action spectroscopy. This assignment, further confirmed by comparisons with theoretical results, represents the first identification of transitions in Ar-H_2O OH stretch overtone.

Methods for predicting infrared spectra are also employed for the more complicated systems H_2-H_2O and H_2O-H_2O. In these clusters, nuclear spin statistics dictate the existence of several different species since there is no pathway for cooling hydrogen atom nuclear spin on the time scale of the experiments. H_2 and H_2O will each be described by a statistical distribution of nuclear spin configurations, which due to fermion exchange symmetry, do not cool to the same rotational ground state. Infrared spectra and theoretical predictions are therefore used in tandem in order to decisively identify which particular ortho / para combinations are present at detectable levels in the supersonic expansion. The resulting infrared spectroscopy is of interest in both astrochemistry, where the H_2-H_2O interaction is expected to influence several critical

processes, and in high earth atmospheric contexts where $(H_2O)_2$ dimers may be present. For this reason, the dynamics of these species are also of interest. Predissociation of H_2O dimer in the $v_{OH} = 2$ polyad overtone manifold occurs on timescales faster than the resolution of this experiment (~ 8 ns), possibly indicating a structure exhibiting more rotational hindering of the internal H_2O motion than was seen for the water – noble gas studies. This rotational hindering may lead to better coupling between internal H_2O vibration and intermolecular stretching which results in a quicker predissociation process. The H_2-H_2O predissociation rate, on the other hand, is measurable but still faster than what was seen in Ar-H_2O, a likely indication of increased coupling between the metastable internal H_2O excitation, H_2 rotation, and vibrational excitation of the intermolecular stretch degree of freedom.

Critical to the theoretical ideas employed in the preceding discussion is a simplifying assumption which is fundamental to much of computational chemistry. This idea, known as the Born-Oppenheimer approximation,[11] is based on the fact that electronic excitation frequencies are often very fast compared to the timescale for motion of the atomic nuclei. To the extent that this assumption is correct, electronic dynamics can be treated as independent of the speed of nuclear motions, although still dependent on the actual positions of the nuclei. In other words, one can solve the Schrodinger equation for a range of different molecular configurations, producing a set of potential energy surfaces. Since Born-Oppenheimer dynamics are based on a separation between the timescales for electronic and nuclear motion, this approximation does not allow any way for a system to move from one electronic surface to another except in the localized cases of conical intersections[12] and coupling to an external radiation field. Instead, electrons

are expected to rearrange their configuration at fast enough speed that electronic degrees of freedom can be treated adiabatically. This would mean that a chemical reaction beginning in the ground electronic state of the reactants would need to terminate in the ground electronic state of the products. Conversely, electronically excited reactants would be expected to lead to products excited in whatever electronic level correlates with the starting configuration.

In gas phase reaction dynamics, the Born-Oppenheimer criteria are least certain near the transition state where adiabats (ϕ_1 and ϕ_2) may be coupled via $\left\langle \varphi_2 \left| \frac{d}{da} \right| \varphi_1 \right\rangle$ where motion along the dissociative coordinate, a, is sufficiently fast to lead to nuclear motion at high enough speeds to promote non-adiabatic dynamics. Most attempts to test the validity of the Born-Oppenheimer assumption have focused on comparing experimental product rotational and vibrational distributions with theoretical predictions made using the approximation.[13] In many cases, such as the simplest bimolecular reaction: $H + H_2 \rightarrow H_2 + H$ at collision energies below 1.5 eV, this program of study has yielded very good agreement,[14] raising confidence in the validity of the adiabatic approximation. However, this reaction may represent something of a special case since all electronic excitations require a good deal of energy, on the order of the atomic $^2P \leftarrow {}^2S$ transition for well-separated reagents, and still several eV at the transition state. In more typical chemical reactions, where the electronic structure is more complicated, there is debate about the role of nonadiabatic dynamics. This is especially true in the presence of smaller electronic splittings such as spin orbit, which are on the order of 120 cm^{-1} for NO and OH. In theses cases, the fundamental argument of the Born-Oppenheimer approximation breaks down since transitions between these levels are expected to occur on a timescale

which is no longer short compared to the rate of nuclear motion. Several previous experiments[6,15] have explored the degree of nonadiabatic nature in such systems with varied results, and at the same time, an array of theoretical methods have been developed for predicting the probability of hopping[16] from one electronic surface to another.

In order to shed further light on this question, a crossed molecular beam apparatus is employed for observing OH or OD product state distributions after one of these two reactions:

$$F + H_2O \rightarrow HF + OH \quad (1.1)$$

$$F + D_2O \rightarrow DF + OD. \quad (1.2)$$

This system proves to be an ideal testing ground for the role of nonadiabatic dynamics when coupled with theoretical predictions of the nature of the various electronic energy level surfaces in these systems. As shown in figure 1.2, the lowest two surfaces, which are separated by only a 120 cm^{-1} spin-orbit splitting in the exit channel, actually differ by 5000 cm^{-1} in their respective barriers to hydrogen abstraction reaction. By choosing a collision energy which is between the heights of the two transition states, it is possible to assign every spin-orbit-excited product molecule to the result of one or more surface hopping events in the exit channel. Reactively scattered OD is in fact found to be very likely to appear in its spin-orbit excited state, a result which points to the extensive occurrence of non-Born-Oppenheimer events during the course of this reaction. Isotopic substitution (reaction 1.2), results in substantially different rotational distributions but unchanged propensity for spin-flipping events. This can be used to further specify the location where the nonadiabatic dynamics occur. Since the exit channel dynamics clearly differ for the two systems, the insensitivity of spin-flip probability to isotopic

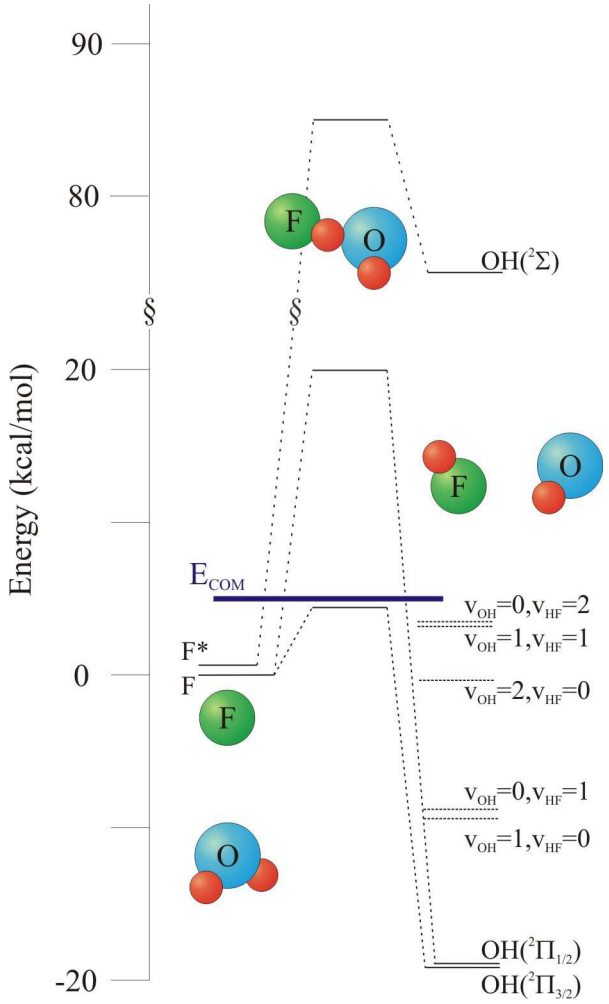

Figure 1.2 Energetics for the reaction F + $H_2O \rightarrow$ HF + OH($^2\Pi_{1/2, 3/2}$). Barriers are obtained from high level MRCI *ab initio* calculations.[17] Fluorine in its ground spin-orbit state can react adiabatically to produce OH($^2\Pi_{3/2}$) at our COM collision energies, but the higher barrier to adiabatically produce OH($^2\Pi_{1/2}$) is not accessible. Therefore, observation of spin-orbit excited product provides unambiguous evidence for nonadiabatic dynamics. Energetically accessible HF and OH vibrational states are also shown for the $^2\Pi_{3/2}$ ground electronic state.

substitution is likely a result of nonadiabatic dynamics occurring near the shared transition state rather than far out in the exit channel of the lowest electronic surfaces.

Even more direct evidence for the importance of nonadiabatic processes can be found in the field of gas-surface scattering dynamics. In particular, collisions of nitric oxide from single crystal (111) gold surfaces has been shown to be highly nonadiabatic by a number of theoretical[18] and experimental[19,20] methods. In a sense, the molecule-metal system represents the opposite of a problem tractable by the Born-Oppenheimer approximation, because electronic spacings near the Fermi energy are so close together that they can be treated as continuous. Therefore, when compared to this infinitesimal electronic level spacing, the NO vibrational structure is characterized by very large energy gaps, each of which is resonant with the energy needed to create a hot electron-hole pair excitation in the gold. Some experimental observations of these effects have taken the form of direct detection of the hot electrons or holes[20]. Conversely, these processes may be inferred by observation of very strong propensity for vibrational state changing[19] during collisions of NO with Au, a phenomenon which does not occur for scattering from insulating materials, which are characterized by a very low density of electronic states at the Fermi level.

Theoretical investigations into the mechanism behind these phenomena have focused on the high degree of charge transfer character when the open shell molecule NO is bound to a metal surface. In this picture, an electron jumps to the NO molecule upon approach to the surface, resulting in a configuration which is stabilized greatly by the attraction of the newly ionized NO^- to its image charge in the gold. This creates a free hole in the metal which is later joined by a free electron as the NO scatters and travels

away from the metal surface. Because the electron-hole pair (ehp) energy can take any one of a continuous set of values in the metal, there will always be such an electronic transition which is resonant with any molecular transition in the NO molecule. In contrast, insulating surfaces are characterized by a much lower probability for near resonance between molecular and condensed degrees of freedom, which therefore leads to the much lower probability to add or remove NO vibrational energy during a scattering event. Aside from explaining the observed nonadiabatic observations, however, this picture makes an interesting prediction about the probability for spin-orbit-changing collisions. In its ground state, NO contains a single unpaired Π electron which is presumably joined by a metal electron of the same spin but opposite projection of orbital angular momentum when the molecule picks up an electron from the metal to form a $^3\Sigma^-$ state on approach to the surface. As the molecule travels out the exit channel, an electron must be lost from this orbital, but the orbital angular momentum projection of the electron left behind may not be the same as that of the initially impinging NO. For this reason, spin-orbit-changing collisions may serve as a sensitive probe of the degree of charge transfer character for the system's wavefunction during approach to the surface, an idea which was earlier considered in analyzing spin-flip scattering of NO from Ag (111) surfaces.[21]

A good deal of work has been done on examining atomic and molecular scattering from various single crystal metal surfaces, although the vast majority of these studies did not specifically consider the probability for spin-orbit scattering events. Initially, much effort was focused on obtaining fundamental pictures of the effect of the metal-molecule potential on scattered rotational and translational distributions. For example, the hard

cube model[22] was created in order to quantify the degree to which a scattering event could be thought of as a collective impulsive collision with many atoms versus a collision with a single recoiling atomic partner. By observing the angular scattering distributions, it was straightforward to parameterize the problem as a two body collision where the mass of one of the participants was that of a calculable number of metal atoms (N). Larger values of N were observed for more stiffly bonded systems. Further investigation into higher order aspects of these distributions (such as translational rainbow scattering)[23] uncovered sensitivity to surface corrugation on the interatomic scale. Rotational distributions have also been extensively studied, leading to the discovery of interesting features such as rotational rainbows,[24] which arise from a singularity in the Jacobian which links an isotropic incident molecule angular distribution to the distribution of scattered rotational states. Additionally, detailed examination of the molecule-metal collisions results led to a picture where scattering may occur by at least two channels.[25] One of these channels, known as trapping-desorption (TD), is ascribed to events where the molecule is transiently adsorbed on the surface before being thermally ejected. The other, comprising all other scattering paths, may or may not be dominated by single bounce collisions where the event may be thought of as an impulsive scattering (IS) interaction as in the hard cube model.

In addition to the extensive literature on scattering from solid surfaces, there has also been a good deal of interest in interactions at the interface between liquid and gas phase species, particularly in recent years. While roughness at the solid-vacuum interface is somewhat static and mainly determined by the preparation history of the sample, liquid surfaces are constantly in higher amplitude motion as determined by the theory of

capillary waves[26]. For this reason, the roughness of a pure liquid surface is independent of preparation method and instead simply a reproducible function of the temperature of the sample. Heterogeneous liquids, such as salty solutions, for example, have an additional interesting phenomenon, namely the fact that the molecular composition of the interface may exhibit temperature dependence. Additionally, the surface concentration[27] of dilute species may be significantly enhanced or suppressed relative to that of the bulk due to thermodynamical driving forces based on surface tension, solvation energy, and entropy of mixing. In order to further explore this fascinating subject at the meeting ground between gas phase dynamics and condensed matter physics, an experiment (figure 1.3) has been built where nitric oxide molecules are scattered from a liquid surface in a temperature tunable crucible before being detected by LIF.

Collisions of NO with liquid gallium result in rotational distributions which can be fit to a two channel scattering process in agreement with the trapping desorption / impulsive scattering picture developed for the case of scattering from solid metal surfaces. Additionally, the average amount of energy transferred from initial translation to final rotation is found to depend strongly on incident collision energy, but weakly on the surface temperature. When compared with previous studies on NO scattering from single crystal surfaces, liquid gallium promotes rotational excitation much more effectively than does Ag(111), despite the fact that silver is characterized by an atomic mass which is 50% larger than that of the Ga atom. In fact, the degree of rotational excitation is on the order of that observed for collisions with Au(111) whose mass is almost three times larger than that of Ga. This effect is thought to be a consequence of the presence of small wavelength capillary waves which roughen the surface on the

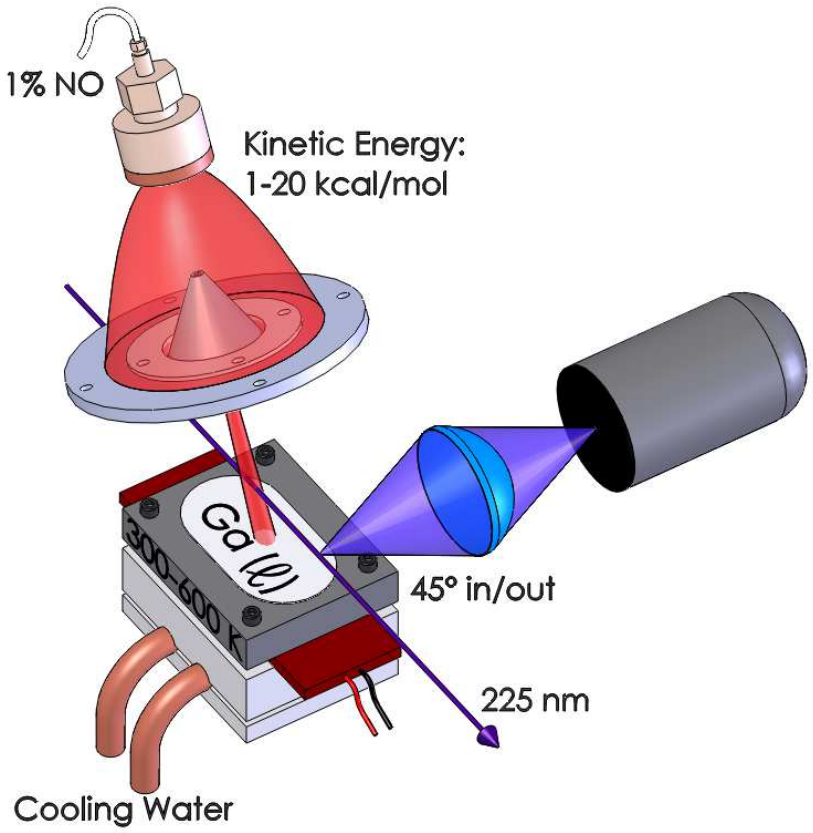

Figure 1.3 Schematic of the NO + liquid scattering experiment. Tunable energy NO molecules (E_{inc} = 1-20 kcal/mol) are generated in an Evan-Lavie valve, with the resulting supersonic jet skimmed before colliding with a molten Ga surface heated to between 313 and 600 K. Scattered molecules are detected by LIF, which probes a 5 mm section of the excitation laser beam. The apparatus has flexibility in excitation and detection geometry; however, the incident angle for the current experiments is fixed at 45(5)° with detection at the near specular angle.

length scale of interatomic spacings. Observations of the scattered electronic degrees of freedom show the presence of spin-orbit-changing collisions, similar to the effect seen for NO on Ag(111).[28] Furthermore, the electronic temperature characterizing the outgoing spin-orbit populations is shown to have a weak positive dependence on incident collision energy, a possible indication of the importance of non-Born-Oppenheimer dynamics in this system. Also, while the effect of surface temperature on the electronic degree of freedom is modest, it is stronger than that seen in rotation, a likely indication of very

different dynamical timescales for rotational versus electronic thermalization. This situation may provide confirmation for a picture where rotational excitation is governed by simple attractive and repulsive forces between surface and adsorbate, while electronic distributions provide insight into the multisurface nature of the scattering problem.

Further exploration of these phenomena is done by replacing the molten metal with a room temperature ionic liquid (RTIL). These novel materials (figure 1.4) are salts in that they are entirely composed of cations and anions. However, unlike sodium chloride, which melts at 1074 K, RTIL's are characterized by freezing points which are below 400 K and often well below room temperature. This property, along with generally low vapor pressure, makes these species very attractive as advanced reusable solvents[29] with the potential to reduce a good deal of waste in industrial processes. Because there are a variety of choices for anion (Tf_2N^-, BF_4^-, Cl^- for example) as well as a myriad of ways to functionalize the organic cation (1-butyl-3-methylimidazolium for example), the diversity of these species is tremendous. In principle, such a large set of choices allows for a good deal of tunability in the solvation properties of these liquids. For example, a RTIL could be chosen which dissolves reagents but not products for a specific reaction, allowing one to physically separate desirable chemical species while leaving the solvent ready for another production cycle. Recently, RTIL's have begun to show promise in a variety of disparate fields ranging from electrolytes[30] for batteries and capacitors to supported membranes for removing SO_2 and CO_2 during combustion processes.[31]

The NO scattering experiment is performed on a variety of RTIL surfaces for two reasons. First, it provides an opportunity to explore novel methods for characterizing the

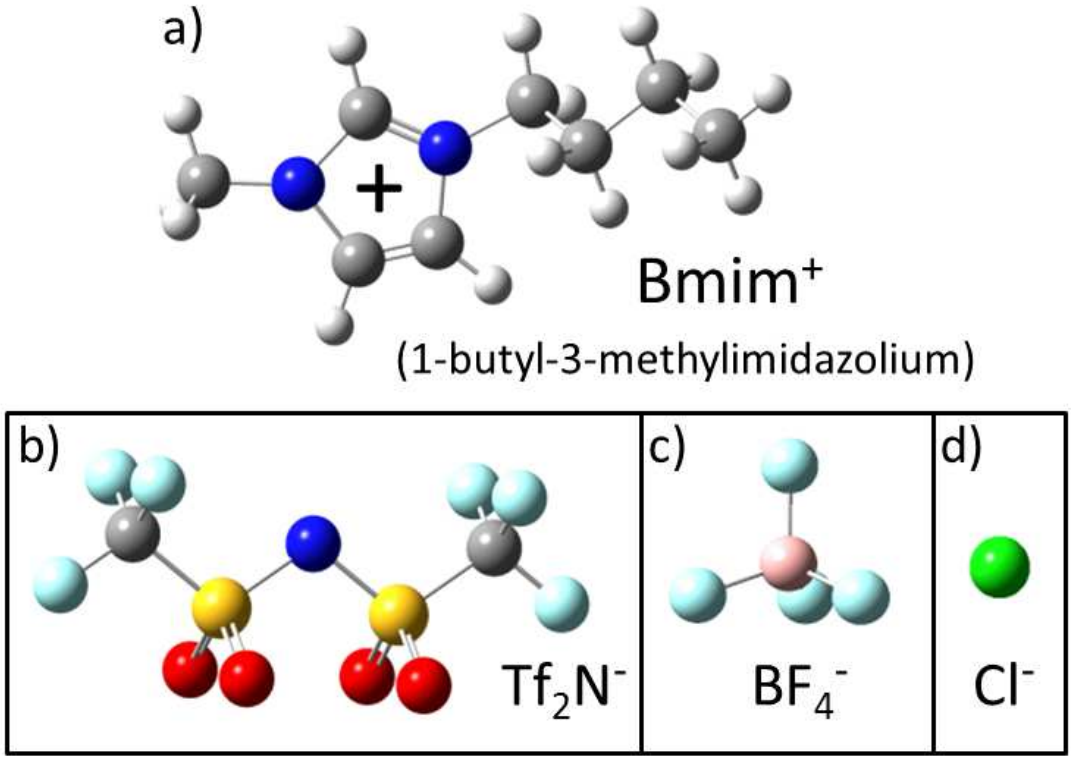

Figure 1.4 Room temperature ionic liquids (RTILs) used in this experiment. All consist of an organic cation (1-butyl-3-methylimidazolium) and one of three possible anionic species. In order of decreasing size they are: Bis(trifluormethanesulfonyl)imide (Tf_2N^-), BF_4^-, and chloride (Cl^-).

interfaces of these exciting new materials. Second, it is expected to provide further information on the role of charge transfer in the scattered electronic distributions as observed for NO on liquid metal surfaces. Unfortunately, the RTIL's cannot be heated as much as the molten metals due to vapor pressures that rapidly increase with temperature[32] and the possibility of thermal breakdown in the material.[33] Nevertheless, despite the modest (ΔT = 100 K) range of temperature examined, the effect of surface temperature on scattered spin-orbit temperature is quite strong for BMIM-Tf_2N when compared to the effect on scattering from liquid gallium. This surprising result may be due to charge

transfer between the RTIL anion species and the impinging NO molecule, with the temperature dependence possibly ascribable to an increased representation of anionic vs. cationic species on the surface is heated. Some confirmation of this picture is seen when the identity of the anion is changed, since smaller anions appear to lead to less charge transfer at elevated temperatures. It is possible that the larger anionic species are more likely to be pushed out to the top layers of the liquid surface, making them more available as collision partners for the NO molecule. Further exploration of this charge transfer picture is needed; a promising path of study may be observing the effect on spin-flipping probability as the cation functionalization is changed. In particular, lengthening the alkane chain from four carbons to twelve is expected from theoretical studies to result in a surface dominated by carbon chains and reduced in anion character. Therefore, such a surface would be expected to lead to greatly decreased probability for NO spin-flipping.

In summary, the body of work presented below represents a variety of chemical dynamics experiments, each of which has employed the technique of laser induced fluorescence to make inferences on the nature of a chemical processes. The studies range from spectroscopy and dynamics of weakly bound bimolecular water clusters to reactive scattering of fluorine with H_2O to inelastic scattering of NO from various liquid species. Throughout this exploration, attention has been paid to the interplay of electronic dynamics with the motion of heavy atomic nuclei. This has led to the examination of regimes with a good deal of variation in the role of nonadiabatic dynamics. In the cluster studies, spectra are found to be in excellent agreement with Born-Oppenheimer-based theoretical techniques. In $F + H_2O$, multisurface dynamics prove to be an inescapable factor in the nature of this reaction. Finally, in collisions of NO with metallic and ionic

liquid surfaces, nonadiabatic spin-flip events serve as a sensitive probe of the interaction of potential adsorbates with the surface.

References for Chapter I

1 J. A. Coxon, Can. J. Phys. **58** (7), 933 (1980).

2 P. Casavecchia, Rep. Prog. Phys. **63** (3), 355 (2000).

3 Y. T. Lee, J. D. Mcdonald, P. R. Lebreton, and D. R. Herschbach, J. Chem. Phys. **49** (5), 2447 (1968).

4 A. M. Schmoltner, P. M. Chu, and Y. T. Lee, The J. Chem. Phys. **91** (9), 5365 (1989).

5 J. C. Polanyi, Accounts Chem. Res. **5** (5), 161 (1972).

6 W. W. Harper, S. A. Nizkorodov, and D. J. Nesbitt, Chem. Phys. Lett. **335**, 381 (2001).

7 J. J. Scherer, J. B. Paul, A. O'Keefe, and R. J. Saykally, Chem. Rev. **97** (1), 25 (1997).

8 F. Dong, S. H. Lee, and K. Liu, J. Chem. Phys. **115** (3), 1197 (2001).

9 J. R. Roscioli and D. J. Nesbitt, Faraday Discuss. **150** (0).

10 R. N. Zare and P. J. Dagdigian, Science **185** (4153), 739 (1974).

11 M. Born and J. R. Oppenheimer, Ann. Phys. **84**, 457 (1927).

12 D. R. Yarkony, Accounts Chem. Res. **31** (8), 511 (1998).

13 M. H. Alexander, G. Capecchi, and H. J. Werner, Faraday Discuss. **127**, 59 (2004).

14 L. Schnieder, K. Seekamp-Rahn, J. Borkowski, E. Wrede, K. H. Welge, F. J. Aoiz, L. Baniares, M. J. D'Mello, V. J. Herrero, V. S. e. Rabanos, and R. E. Wyatt, Science **269** (5221), 207 (1995).

[15] F. Dong, S.-H. Lee, and K. Liu, J. Chem. Phys. **115**, 1197 (2001); J. W. Hepburn, K. Liu, R. G. MacDonald, F. J. Northrup, and J. C. Polanyi, J. Chem. Phys. **75**, 3353 (1981).

[16] J. C. Tully and R. K. Preston, The J. Chem. Phys. **55** (2), 562 (1971).

[17] M. P. Deskevich, D. J. Nesbitt, and H. J. Werner, J. Chem. Phys. **120** (16), 7281 (2004).

[18] N. Shenvi, S. Roy, P. Parandekar, and J. Tully, J. Chem. Phys. **125** (15) (2006).

[19] A. M. Wodtke, D. Matsiev, and D. J. Auerbach, Prog. Surf. Sci. **83** (3), 167 (2008).

[20] D. Krix, R. Nunthel, and H. Nienhaus, Phys. Rev. B **75** (7) (2007).

[21] M. H. Alexander, J. Chem. Phys. **80** (7), 3485 (1984).

[22] R. M. Logan and R. E. Stickney, J. Chem. Phys. **44** (1), 195 (1966); E. K. Grimmelmann, J. C. Tully, and M. J. Cardillo, J. Chem. Phys. **72** (2), 1039 (1980).

[23] T. Kondo, H. S. Kato, T. Yamada, S. Yamamoto, and M. Kawai, J. Chem. Phys. **122** (24) (2005).

[24] M. A. Hines and R. N. Zare, J. Chem. Phys. **98** (11), 9134 (1993).

[25] M. Manning, J. A. Morgan, D. J. Castro, and G. M. Nathanson, J. Chem. Phys. **119** (23), 12593 (2003).

[26] P. Leon F, Chem. Phys. Lett. **330**, 15 (2000).

[27] J. L. DeZwaan, S. M. Brastad, and G. M. Nathanson, J. Phys. Chem. C **112** (8), 3008 (2008).

[28] G. D. Kubiak, J. E. Hurst, H. G. Rennagel, G. M. McClelland, and R. N. Zare, J. Chem. Phys. **79** (10), 5163 (1983).

[29] M. J. Earle, J. M. S. S. Esperanca, M. A. Gilea, J. N. C. Lopes, L. P. N. Rebelo, J. W. Magee, K. R. Seddon, and J. A. Widegren, Nature **439** (7078), 831 (2006).

[30] J. L. Sudworth, J. Power Sources **100** (1-2), 149 (2001).

[31] Y.-Y. Jiang, Z. Zhou, Z. Jiao, L. Li, Y.-T. Wu, and Z.-B. Zhang, J. Phys. Chem. B **111** (19), 5058 (2007).

[32] J. M. S. S. Esperanca, L. J. N. Canongia, M. Tariq, L. M. N. B. F. Santos, J. W. Magee, and L. P. N. Rebelo, J. Chem. Eng. Data **55** (1), 3 (2010).

[33] L. P. N. Rebelo, J. N. C. Lopes, J. M. S. S. Esperanca, and E. Filipe, J. Phys. Chem. B **109** (13), 6040 (2005).

Chapter II: Experimental apparatus

2.1 Laser Induced Fluorescence (LIF) detection and analysis

In all of the studies presented in this dissertation, LIF spectroscopy is used to obtain quantum state distributions for NO or OH molecules which result from various dynamical processes. Since the line intensities of the LIF spectra are the main experimental result and are used to make inferences about the nature of the chemical dynamics under study, a good deal of effort must be expended in order to ensure that these results are both meaningful and reproducible. The detection scheme begins with a tunable ultraviolet (UV) laser which brings molecules to an excited electronic state ($^2\Sigma$ in the case of both NO and OH). Over the course of the spontaneous emission lifetime (~ 200 ns for NO and ~ 1 μs for OH), fluorescence photons are detected over a range of solid angle chosen to omit the incident laser beam. This separation between the directions of wavevectors for excitation versus signal photons results in a very high detection sensitivity (~ 10^4 molecules per cubic centimeter per quantum state). However, in order to achieve these levels of signal to noise, it is very important to reduce the number of incident photons which are able to find their way to the detector by reflections from various parts of the experimental apparatus. Since our photosensitive device is capable of observing a single photon and the incident beam may contain ~ 10^{12} photons, even very unlikely paths from laser to detector may result in unacceptably high nonresonant background. This is prevented by a variety of geometrical and optical techniques designed to limit the freedom for scattered photons to be recorded. Once

selected in this way, the fluorescence light encounters a photomultiplier tube (PMT) which converts them into an electrical signal. The resulting voltage is amplified and recorded over a range of UV excitation frequency, producing a spectrum which is then analyzed using a least squares fitting program in order to extract the population distribution from the areas below the different peaks. The raw populations are afterwards subjected to more analysis in order to understand the data in terms of various theoretical pictures.

Fig. 2.1 shows the general scheme for detecting NO or OH by LIF. Briefly, a UV laser excites from nonvibrating (v=0) levels in the electronic ground state ($^2\Pi$) up to the first excited doublet level ($^2\Sigma$). Due to the large difference in equilibrium bond length for the two electronic manifolds, fluorescence tends to be much redder than the excitation frequency since Franck-Condon overlaps are most efficient for $^2\Sigma(v = 0) \rightarrow {}^2\Pi(v \sim 5)$. For this reason, a Schott Glass UG11 absorption filter will effectively block scattered light from the probe laser while passing the majority (~ 60 %) of fluorescent light. This effect is not present in OH, meaning that $^2\Sigma(v = 0) \leftarrow {}^2\Pi(v = 0)$ excitation light can not be substantially reduced by filtering. Fig. 2.2 shows the basic energy level structure of NO in both the electronic ground ($^2\Pi$) and excited ($^2\Sigma$) states relevant for LIF detection. Each $^2\Pi(v)$ ground state is split into four electronic sublevels ($^2\Pi_{1/2}{}^e$, $^2\Pi_{1/2}{}^f$, $^2\Pi_{3/2}{}^e$, and $^2\Pi_{3/2}{}^f$), each of which can exist in a manifold of different N-O tumbling states as denoted by the total angular momentum, J. The spin-orbit ($^2\Pi_{3/2}$ vs. $^2\Pi_{1/2}$) splitting of 125 cm^{-1} in NO reflects the mean relative orientation of the spin projection along the internuclear axis (also called Σ) vs. the unpaired electron angular momentum projection (known as Λ). The much smaller lambda doublet ($^2\Pi^e$ vs. $^2\Pi^f$) splitting of 0.1 cm^{-1} for $^2\Pi_{1/2}(J = 10.5)$,

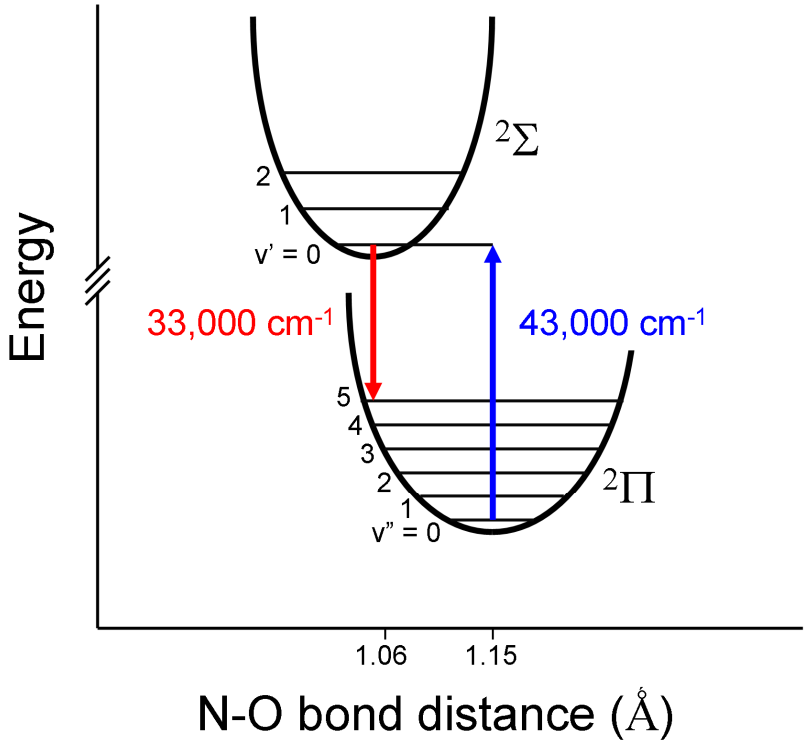

Figure 2.1 Electronic and vibrational levels involved in LIF detection of NO. Excitation is done on the transition $^2\Sigma(v = 0) \leftarrow {}^2\Pi(v = 0)$ with a tunable ultraviolet laser. When this is resonant with a transition from an occupied ground state, flourescentce preferentially involves relaxation vibrationally excited $^2\Pi$ levels due to more favorable Franck-Condon overlaps. For this reason, probe laser beam scatter can be largely removed using a UG11 low-pass optical filter.

on the other hand, arises from weak terms in the Hamiltonian sensitive to the relative direction of molecular tumbling angular momentum and internal angular momentum of the electron about the internuclear axis. These Λ-doublet levels are labeled *e* and *f* according to their inversion symmetry, i.e. an *e* state with angular momentum J has inversion symmetry of $(-1)^{J-1/2}$ while an *f* state would have $(-1)\times(-1)^{J-1/2}$. Note the need to remove the contribution of spin by adding (or equivalently subtracting) 1/2 from J in the exponent. The energy level structure of the $^2\Sigma$ upper state is simpler than that of

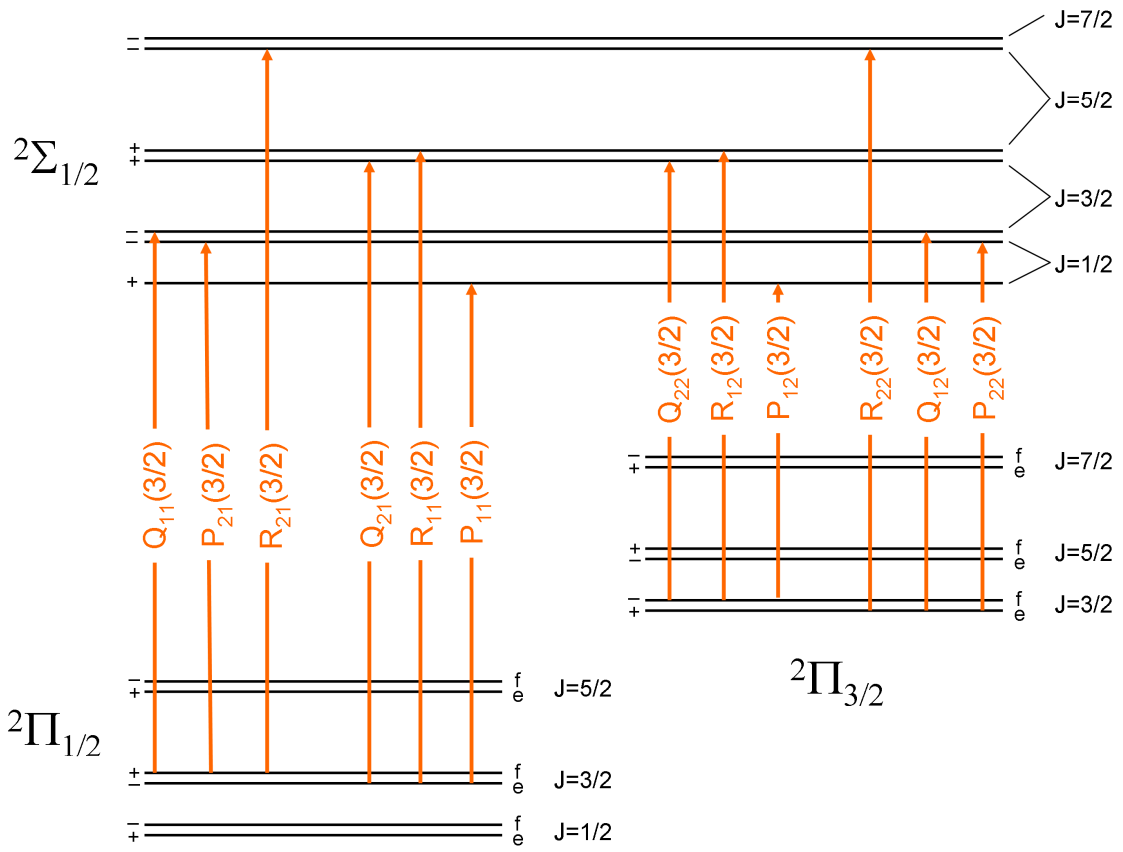

Figure 2.2 Absorption spectroscopy of NO ($^2\Sigma \leftarrow {}^2\Pi$). The 12 branches which originate from J = 3/2 levels are labeled to show which ground states they address. Each level is also labeled in terms of its parity in both (+/-) and (e/f) format.

the ground electronic state, but nevertheless, a similar naming convention is employed. However, due to the lack of any orbital angular momentum about the internuclear axis in a Σ state, the energy level structure is essentially that of a closed shell diatomic rotor with a small spin-rotation splitting built on top of each molecular tumbling state (labeled with approximate quantum number N). Also shown in Fig. 2.2 is the naming system for the various dipole-allowed transitions in this molecule, which appear as peaks in the LIF spectrum. Taking the transition $R_{11}(3/2)$ as an example, the "R" refers to the increase in J by one quantum from the $^2\Pi$ (J" = 3/2) state to the $^2\Sigma$ (J' = 5/2) level, while "P"

corresponds to transitions with J'=J"-1, and "Q" means that J'=J". The first and second subscripts refer to which spin-splitting level is addressed in $^2\Sigma$ and $^2\Pi$ respectively with "1" referring to the lower splitting state and "2" referring to the more energetic one in each case. Note, however, that "spin-splitting" in the $^2\Sigma$ level actually refers to the energy difference between each two levels with the same total angular momentum (J), which actually correspond to rotational energy differences in this species. Finally, the number in parenthesis is the total angular momentum in the $^2\Pi$ starting level. Each ground state rotational and electronic level is accessed by three transitions with the following correspondence between branch and electronic manifold probed:

$$^2\Pi^e_{1/2} \rightarrow P_{11}, R_{11}, Q_{21}$$
$$^2\Pi^f_{1/2} \rightarrow P_{21}, R_{21}, Q_{11}$$
$$^2\Pi^e_{3/2} \rightarrow P_{22}, R_{22}, Q_{12}$$
$$^2\Pi^f_{3/2} \rightarrow P_{12}, R_{12}, Q_{22}$$

Fig. 2.3 shows a sample NO LIF spectrum to give a rough idea of where the various branches appear in frequency. In this molecule, the following transitions are not resolvable within the 0.25 cm^{-1} frequency resolution of the dye laser, so together they each appear as one peak: Q_{11} & P_{21}, Q_{21} & R_{11}, Q_{22} & R_{12}, and P_{22} & Q_{12}. In OH, on the other hand, sufficient spin-rotation excitation exists in the $^2\Sigma$ manifold to separate these pairs, causing these peaks to separate beyond the laser linewidth.

The spin-orbit splitting in OH is ~ 120 cm^{-1}, similar to NO, but the ordering of the two levels is reversed, with $^2\Pi_{3/2}$ being the lower state of the hydroxyl radical. Additionally, unlike NO which remains in Hund's case A up to high J, OH rather quickly transitions to Hund's case B before J = 5, often resulting in a different naming convention for levels and transitions for this species. Because N, the tumbling angular

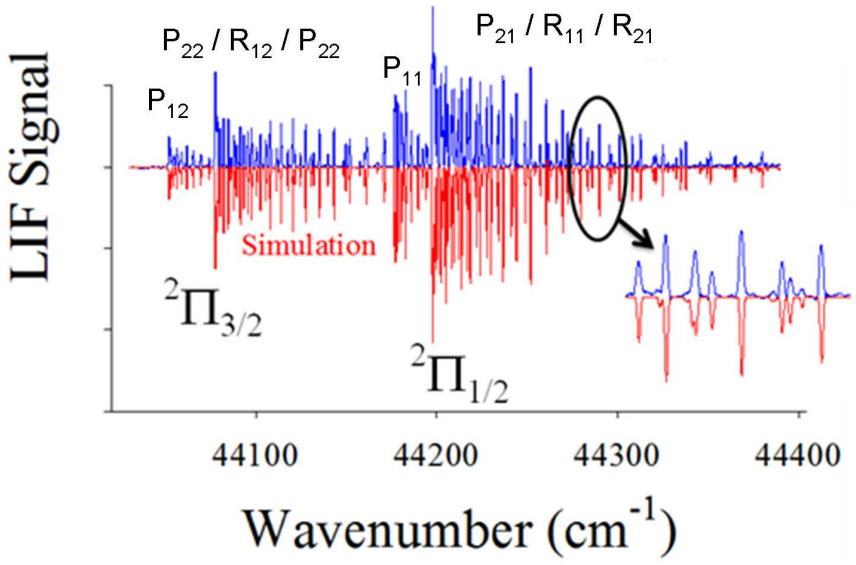

Figure 2.3 Sample LIF spectrum for NO scattered from liquid Ga. The branches corresponding to the four prominent bandheads are roughly labeled. Also shown is a blowup of a smaller section to show the average density of peaks. The negative-going red peaks show the best-fit simulation used to extract populations from the peak heights.

momentum of the molecule, becomes a useful quantum number in this limit, states are labeled, for example, as $^2\Pi_{1/2}(N = 1)$, where $N = J + 1/2$ for $^2\Pi_{1/2}$ and $N = J - 1/2$ for $^2\Pi_{3/2}$. Transitions are also now referenced to the lower N level, rather than the lower J, and the two subscripts in the transition symbol continue the convention of 1 referring to the ground (now $\Omega = 3/2$) spin-orbit level while 2 refers to the excited spin-orbit state ($\Omega = 1/2$) — note that the symbol $\Omega = \Lambda + \Sigma$ represents the total angular momentum about the internuclear axis. As an example, the transition $O_{21}(N = 2)$ corresponds to an excitation originating from $^2\Pi_{1/2}(N = 2)$ which changes N by +2 to N = 4 in the upper state. Note that, unlike in the case of closed shell molecules, this "o-branch" corresponds to a change in N by + 2, but total angular momentum J changes by only + 1. Therefore,

this is still an electric dipole allowed transition despite its strange naming scheme, and in fact, an s-branch can also be found in the OH excitation spectrum.

As a first step to produce spectra as shown in Fig. 2.3, ultraviolet laser light is created in a chain of devices starting with a Nd-YAG oscillator/amplifier which produces an ~ 8 ns pulse of green light at 532 nm. Fig. 2.4 shows the components of this device.

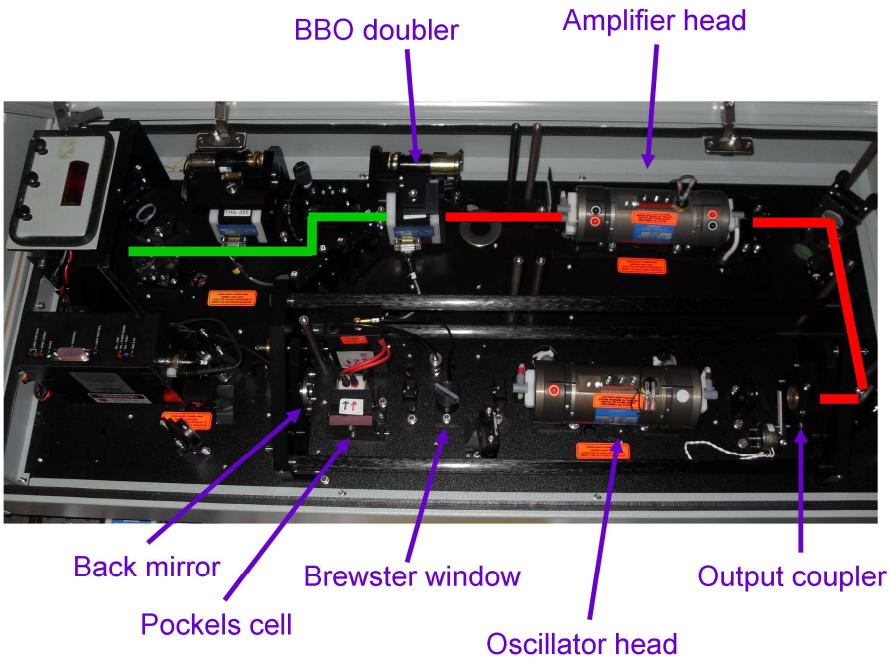

Figure 2.4 Internal workings of the YAG laser. In addition to some of the most important optical elements, the beam path of fundamental and doubled light are also shown.

The oscillator cavity, which is capable of producing 200 mJ of infrared (IR) light at 1064 nm, is bounded by two coated mirrors both of which sit in adjustable mounts. If a hotspot (as seen on a highly filtered CCD camera) forms in the output laser beam, a slight cavity alignment may be necessary. However, it is not advised to make more significant changes to the mirror angles unless lasing has been lost. If this is the case, shine a helium-neon (HeNe) laser through the center of the output coupler and all internal cavity

elements so that it strikes the centers of the back mirror. Irises should be mounted before and after the cavity to define a beam path. Adjust the back mirror to retroreflect the red beam through the first iris. Then, using a series of steering mirrors, send the HeNe into the cavity through the back mirror, through the same irises, and retroreflect from the output coupler. Now that the cavity is set, the output coupler must be translated so that the HeNe beam strikes it in its center (which can be identified by a series of faint concentric colored rings on the surface of the glass). Two set screws, on the side of the mount, should be used to move the mirror in plane until the red beam coincides with the colored rings. This entire process may need to be iterated several times to obtain a good alignment. The YAG active gain medium is a 15 cm long crystal rod with a diameter of 7.5 mm which sits in the middle of the cylindrical laser head. The head also contains a discharge flashlamp whose lifetime is somewhat limited and therefore must be replaced whenever laser power drops to unacceptably low levels. See the laser manual for information on how to replace the flashlamps. The manual also contains instructions on how to refresh the deionized water supply which cools the laser head, a task which must be carried out every few months. Before exiting the laser, the beam passes through a Nd-YAG amplifier crystal mounted in a similar head (but with two flashlamps) and a Beta barium borate (BBO) doubling crystal which produces 532 nm green light. The laser control box contains two buttons for adjusting the angle of this crystal to obtain maximum output power at 532 nm.

YAG laser timing, as well as all other synchronization in this experiment, is controlled by a Stanford Research Systems (SRS) digital delay generator (DDG), which presents rising edge triggers with delay specified by entering numbers in the front panel

for each of the four output channels. Each YAG laser requires two separate triggers to produce a laser pulse. The first activates the three flashlamps which bathe the crystals in light, leading to a population inversion. The second trigger controls a high voltage pulse in the Pockels cell, an electro-optical component in the oscillator beam path which "opens" the cavity. In short, the oscillator cavity contains a window oriented at Brewster's angle for 1064 nm, which results in lasing only for p-polarized light due to rejection of ~ 10% of s-polarized radiation on each pass. Normally, the combination of the Pockels cell and a 1/4-wave plate in the cavity results in a change from s to p polarization for each round trip in the cavity, meaning that lasing will not occur. However, when the Pockels cell is transiently activated, s and p components are no longer interconverted on a round trip, resulting in a cavity which is "open" for p-polarized light. Therefore, while the first DGG timing pulse creates a population inversion, the second pulse opens the cavity so that lasing can actually occur. Varying the delay between these two channels is one means of adjusting the 1064 nm output power as the opening of the cavity becomes more or less synchronized with the flashlamp firing. However, IR power can also be adjusted by simply turning down the flashlamp voltage as controlled by a dial on the laser power supply. This is the preferred method since lower voltages result in longer flashlamp lifetime, and furthermore, the flashlamp - Pockels cell delay can be directly accessed by a dial on the front of the power supply. Nevertheless, the design of the YAG laser electronics requires one rising edge flashlamp trigger and a second trigger for the Pockels cell. Furthermore, the latter trigger pulse must have negative polarity (i.e. held at +5 V when not triggering) and a short duration to avoid damage to the Marx bank, a set of transistors that then delivers the high voltage pulse to

the Pockels cell. The instruction manual contains information on how to arrange triggers to produce the necessary timing inputs for the YAG electronics.

The 532 nm beam is used to pump a dye laser filled with one of two dyes: DCM for detecting OH, or LDS 698 for detecting NO molecules. Best results for tuning over the entire $^2\Sigma(v = 0) \leftarrow {}^2\Pi(v = 0)$ bands are obtained at a (oscillator, amplifier) DCM concentration of ~ (3.6×10^{-4} M, 1.9×10^{-4} M) in methanol for OH detection and an LDS 698 concentration of ~ (3.0×10^{-4} M, 5.0×10^{-5} M) in methanol for NO. Fig. 2.5 shows the internal

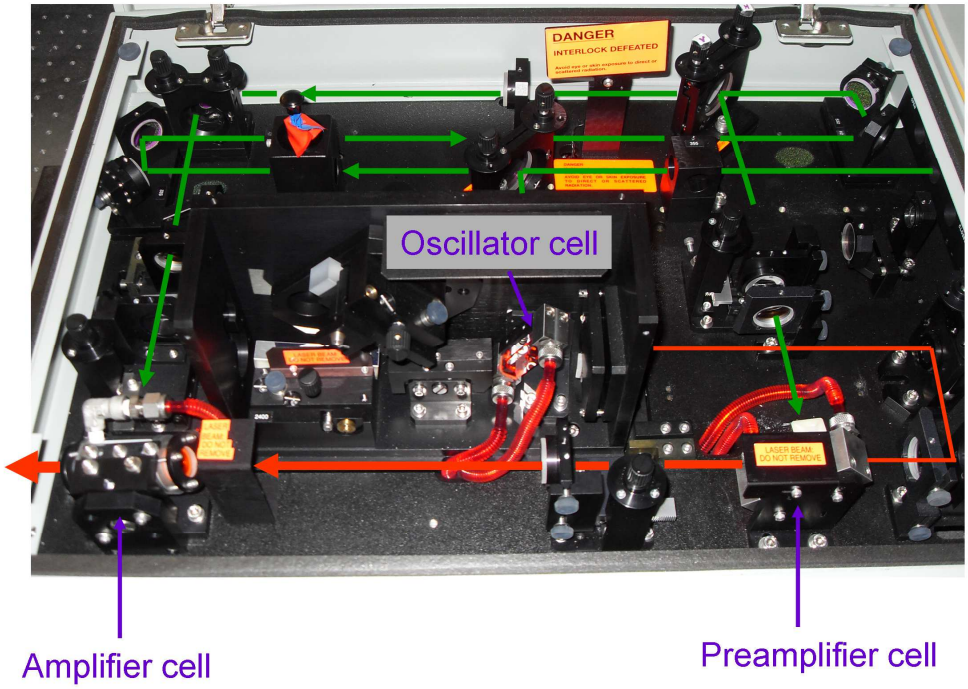

Figure 2.5 Photograph of the dye laser, which converts green laser light into a beam of lower energy photons. Paths are shown for both the 532 nm pump laser and the red output.

workings of this stage of light generation. A green beam from the previous YAG laser "side pumps" three liquid-containing dye cells, one of which is in the dye oscillator

cavity and two of which function as amplifier stages. The front mirror of the cavity is the edge a fully silvered mirror, from which output coupling achieved by having a small amount of radiation miss the it and travel through the amplification stages. Instead of a back mirror, the cavity is bounded on the other side by a diffraction grating which retroreflects a specific color of light depending on its angular position. The laser is managed by a dedicated DOS computer which is in turn controlled by Labview acquisition software on a modern computer (see appendix B.1). This tunable laser is able to cover both the $0 \leftarrow 0$ and $1 \leftarrow 1$ bands of the $^2\Sigma \leftarrow {}^2\Pi$ transitions[1] in both OH and NO. It converts 100 mJ of 532 nm light into 20 mJ at 616 nm when filled with DCM dye. The output energy varies by ~ 10% from pulse to pulse, the frequency resolution is about 0.25 cm^{-1}, and the polarization is vertical.

Visible red light from the dye laser is then passed through more BBO crystals, each of which resides in its own "autotracker" box (Fig. 2.6) featuring rotating stages for a crystal and a refractive compensator block as well as an active feedback system for maximizing production of UV laser light. Type II sum frequency generation (SFG) is employed, meaning that the output polarization is rotated by 90° from that of the input photons. A motor continuously adjusts the BBO angle for optimal SFG output energy, employing the principle that best phase matching is achieved when the input and output laser beams are coaxial. To this end, a small amount of output UV light is picked off, and sent through a series of color and neutral density filters before striking a split photodiode which is sensitive to changes in UV laser direction. At a fixed dye laser frequency, the BBO angular position is first chosen for maximum production of output UV light. Next, the position of the split photodiode must be adjusted so that equal

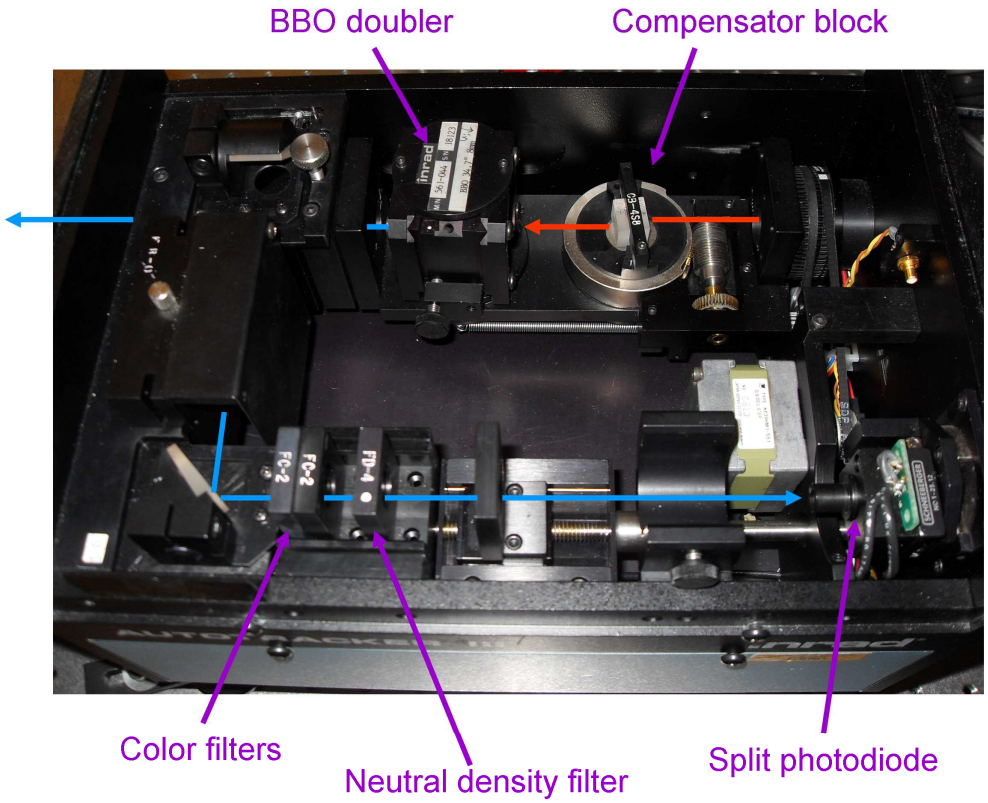

Figure 2.6 Elements of the autotracker, which doubles input visible light in a BBO crystal. A small amount of the output radiation is picked off and sent to a split photodiode which feeds back on the crystal position for maximum UV generation.

radiation lands on each side. Finally, putting the device in "auto" mode will allow it to continuously adjust the phasematching condition over the course of a spectral scan. In order to detect OH, only a single BBO stage is needed to double the ~ 616 nm dye laser output to produce a 308 nm tunable UV beam. To detect NO, two BBO stages are needed. The first converts some of the 690 nm incident beam into 345 nm light; next, the combination of fundamental and doubled radiation are both passed through a polarization

rotator to bring the 345 nm radiation back to the proper polarization. Finally, the two frequencies enter a second BBO crystal where sum frequency generation takes one photon from each beam to produce radiation at three times the frequency of the original light (230 nm). While these doubling and tripling stages do not broaden the output laser frequency distribution, they do tend to increase shot-to-shot energy noise due to the nonlinear nature of SFG. For example, for an input red beam of 20 mJ ± 10%, a typical doubled output energy would be ~ 2 mJ ± 20%, while a tripled beam would come out at 0.2 mJ ± 30%. The efficiency of UV light generation is sufficient for high sensitivity detection of these species, and in fact the flashlamp voltage often must be turned down to avoid saturation of the LIF transitions. For NO, a laser pulse of 5 μJ and a beam diameter of 2.5 mm was found to put the measurement in a safely non-saturating regime. The 30% pulse to pulse variation, on the other hand, represents a significant amount of on-peak noise, so it is important to record laser energy for each shot so that each data point can be normalized to this value. After passing through all necessary UV generation stages, the beam passes through a harmonic separator where two prisms mounted on a translatable stage shift the spatial positions of the various frequency components with respect to each other so that only the desired color is allowed to exit the device.

Since the resulting UV laser beam has poor spatial quality, a very small (~ 750 μm) portion is selected by placing an iris at the brightest part of the intensity distribution. This results in some diffraction which takes the form of a series of circular rings around the central bright spot which can be seen by fluorescence with the naked eye when a normal piece white paper is placed in the UV beam path. These diffracted photons cannot be allowed to enter the chamber because they come in at an off-axis angle, making

them more likely to scatter off of a surface inside the experiment. They are removed by sending the spatially-selected UV light down a long (2.7 m) path before it passes through a second aperture whose diameter is chosen to be large compared to the final beam size but small compared to the diameter of the brightest diffracted rings which do not pass on to the chamber. This beam path requires two turning mirrors as well as a periscope to raise the beam to the level of the chamber. In order to avoid scattered light contributions from multiple reflections from the two faces of a typical dichroic reflector, right angle fused silica prisms are employed instead. Ultraviolet light enters normally through one face, totally internally reflecting off the long face and leaving the reflected beam free of any ghosting. After being raised by a periscope, the UV beam enters the chamber through a thin (2 mm) calcium fluoride window which is tilted near Brewster's angle to minimize multiple reflections from its two planar surfaces which can be another source of stray photons inside the chamber. Once inside the vacuum, the beam passes through a series thin metal baffles (Fig. 2.7), four aluminum rings with increasing diameter ranging

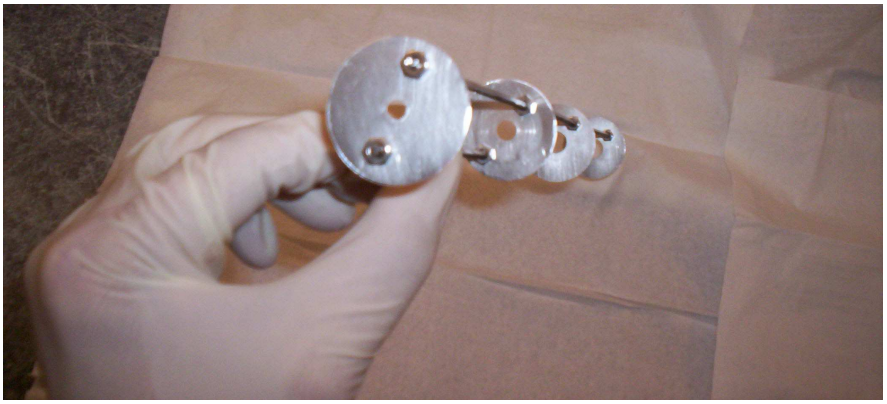

Figure 2.7 Aluminum baffles used to minimize scattered light produced as the ultraviolet laser beam enters the chamber. These stacked rings are slid into the 24" baffle arms on either side of the chamber.

from 5 mm to 11 mm. These apertures are chosen to be large compared to the 3 mm incident laser beam size but small enough to block light scattered from the entrance window. The beam then passes through the center of the cubical vacuum chamber, where it produces fluorescent light when resonant with a transition from a populated ground state of OH or NO. Afterwards, it again passes through an identical series of baffles with steadily decreasing size before passing through another fused silica Brewster window. After the exit window, the UV beam enters a solid state (J5) power meter which measures the energy of each laser pulse.

After NO or OH molecules are excited by the laser beam in the center of the vacuum chamber, fluorescence is collected by a pair of plano-convex fused silica lenses with diameter of 5 cm. These optics sit at the end of a welded stainless steel imaging tube (Fig. 2.8), and the first of them is pressed against an o-ring which forms a chamber seal. Therefore, there is no need for a window between the vacuum and the first collection optic, which results in reduced losses due to reflection from these surfaces. The two imaging lenses each are characterized by a focal length of 5 cm, and they are placed at a distance of 5 cm from the UV laser beam path, meaning that a 1 to 1 image is produced approximately 5 cm from the back of the second lens. A flat metal ring with inner diameter of 4 mm is placed in the imaging plane so that only a segment of the laser induced fluorescence is allowed to pass. This spatial filtering scheme serves to minimize

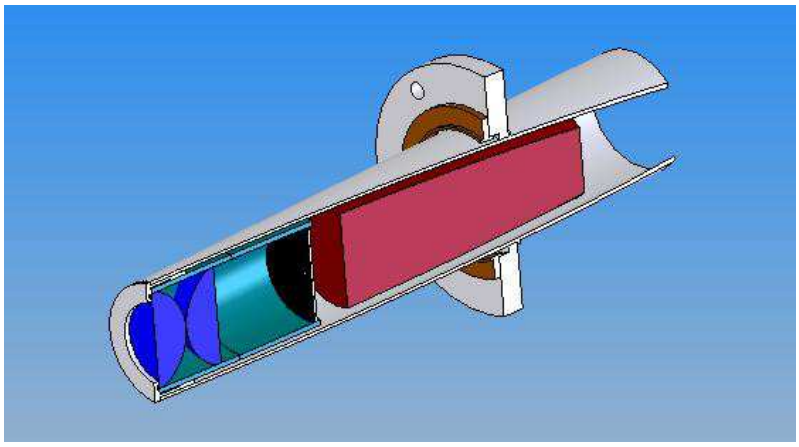

Figure 2.8 Schematic of the imaging tube. Fluorescence enters through a pair of plano-convex lenses (blue), the first of which must form a vacuum seal with an o-ring whose groove is machined into the endpiece. A second lens tube (aqua) contains a spatial filter (black) which limits the in-chamber detection region to a 4 mm segment of the UV excitation laser. Only light passing through this circular aperture is then allowed to reach the photomultiplier tube (red).

contributions from fluorescing NO molecules which are located far away from the collision geometry of interest. For example, in the absence of this mask, a very large and cold background signal is observed which occurs at the intersection of the incident supersonic molecular beam with the LIF laser beam. After the spatial filter, fluorescent light generally passes through a low pass glass filter chosen to further minimize background contributions from scattered photons in the chamber. This step is often not employed for detecting OH, but NO exhibits very favorable Franck-Condon overlaps for fluorescence from $^2\Sigma(v = 0)$ into a wide range of vibrationally excited ground state levels.

Fluorescent light is detected using a photomultiplier tube (PMT) which has been wired in the manufacturer-suggested configuration for maximum linearity (see Fig. 2.9) but is still capable of observing single photons striking its surface. In fact, the baseline noise from this device is so low that output noise is instead dominated by the arrival of the occasional stray photon on the detector. These background photons are inevitably

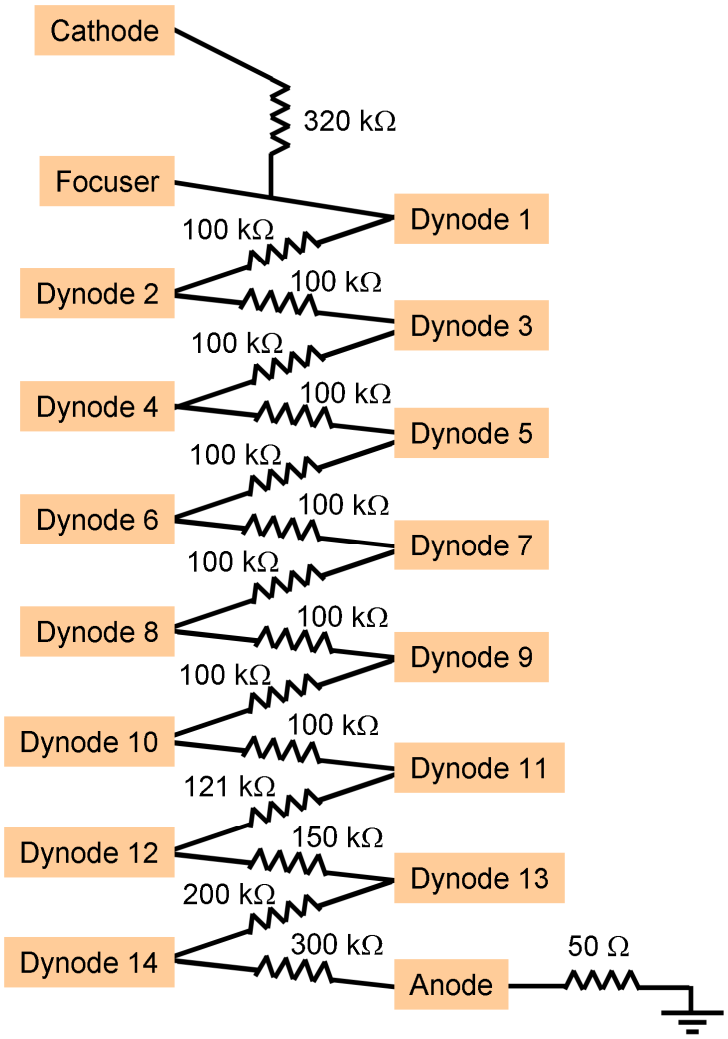

Figure 2.9 PMT wiring scheme. The resistor chain is chosen for maximum linearity to avoid saturation for large numbers of LIF photons per pulse. Current flows from the anode through a 50 Ω resistor over which signal voltage is measured.

related to direct scatter from the UV probe pulse or from fluorescence in, for example, the entrance and exit fused silica chamber windows, which is the reason that great effort is expended in reducing stray photons as discussed above. The PMT photocathode voltage is generally set somewhere between -2000 V and -1600 V relative to the anode stage where photocurrents are collected. Over this range of voltage, PMT sensitivity

varies by about a factor of 13, which is sometimes needed in order to avoid charge saturation in the final few dynodes in cases where OH or NO LIF signals are large. At -2000 V, the device (Electron Tubes model 9813QB) is characterized by a gain g = 2.2(9) x 10^7 electrons per detected photon and a quantum yield of approximately 30%. For studies on reactive scattering of F with H_2O, it is necessary to transiently turn off[2] the PMT while the discharge fluorine source is firing in order to avoid saturation by resulting photons. This was done with a home made high voltage switch (see appendix A.1) which transiently sets the relative voltage from the cathode to the first dynode to -200 V, which is sufficient to repel photoelectrons and thus avoid PMT saturation. The switch effectively turns off the PMT throughout the duration of a TTL positive pulse from a sum combination of two channels on the DDG. After the collection anode, the device is wired through a 50 Ω readout resistor to the ground of the high voltage power supply.

Therefore, a single collected photon produces a peak signal of $V_{peak} = \frac{geR}{\Delta t}$. Since the time response (Δt) is on the order of 3.5 ns for this device, peak signal is ~ 50 mV for a PMT cathode-anode bias of -2000 V. PMT signals can be related to NO or OH densities in the detected region by taking into account the major sources of reduction in collection efficiency, starting with the fact that the first imaging lens subtends a solid angle of Ω_{det} = 0.66 steradians. Taking into account the R ~ 5% reflections from the six glass surfaces encountered en route to the PMT, the 60% signal transmission through the UG11 filter, as well as the 30% PMT quantum yield and the capability to saturate the LIF transition of interest (saturation means that f_{ex} = 50% of molecules from a particular ground state will be excited by the pulse to a level with the same degeneracy), it is possible to predict the number of NO molecules from a particular ground state corresponding to a single

detected photon as $N_{\min} = \left(\frac{\Omega_{\det}}{4\pi} \times T_{filter} \times (1 - R_{glass})^6 \times QY_{\det} \times f_{ex} \right)^{-1} \approx 300$. Since the probed volume is on the order of 0.006 cm^3, this means that the fundamental detection sensitivity limit is ~ 5 x 10^4 molecules/cm^3/quantum state. For NO detection, stray photons arrive with a frequency on the order of 1 photon per 10 laser shots, meaning that this limiting level of sensitivity is readily achievable with minimal time averaging required. Due to the less favorable Franck-Condon overlaps in OH, the minimum detectable density is higher for this system by an order of magnitude. In either case, to preserve maximum sensitivity, it is important to avoid adding noise in subsequent amplification and data processing steps.

Signal level is obtained by measuring the voltage across the 50 Ω resistor on each shot of the 10 Hz UV laser beam. Voltages are next increased by a factor of 10 in a 20 dB preamplifier (1 GHz bandwidth) in order to swamp input voltage noise in the next stage where the fluorescence transient is captured with a boxcar integrator. The boxcar width is set at the radiative lifetime of the molecule (~ 200 ns for NO) and is timed to begin averaging on the order of 20 ns after the firing of the probe laser. The boxcar duration sets the bandwidth of the measurement to ~ 5 MHz and also provides a final, temporal, means of discriminating against scattered photons from the incident laser beam, resulting in a background level of typically less than one photon per pulse. Note that the output from the boxcar is equal to the average voltage during the detection window. Therefore, the 500 mV, 3.5 ns signal after the preamp corresponds to an output of ~ $500\,mV \frac{3.5\,ns}{200\,ns} = 9\,mV$. This signal is typically further boosted by a factor of 20 in a second amplifier which is built into the input of the boxcar integrator. Finally, this signal

enters an analog to digital converter which sends the digitized boxcar signal level to a data taking computer. Like all elements of the experiment, this digitization step is triggered at 10 Hz by a TTL pulse delivered from one channel of one of the SRS digital delay generators.

In fact, all experimental timing is ultimately controlled by a pair of Stanford Research Systems delay generators, one of which is triggered from the other master clock. In addition to specific devices which will be discussed separately for each experimental setup, the following items each require their own timing pulse: 1) the Nd-YAG flashlamps, 2) the Nd-YAG Q-switch which determines the time when the probe laser pulse fires, 3) the LIF boxcar integrator, 4) a boxcar integrator for the probe laser energy, and 5) the Labview control and readout program (Fig. 2.10 and appendix B.1). Upon receiving a timing pulse, the program records values for both LIF signal and probe laser energy which has its own preamplifier and boxcar integrator. On each laser shot, these values are stored in memory, and upon termination of the spectral scan, they are stored with a set of UV frequency values. These frequencies are calculated based on the assumption that the probe laser wavelength continuously advances at a rate which is determined in the Labview program and fed into the laser control computer at the beginning of the scan.

A typical scan proceeds as follows. Start by using the “go to” button to move the dye laser to the desired starting frequency. For the two channels of importance (LIF signal and Probe energy), enter the gain values selected with the boxcar amplifier stage into the appropriate boxes on the Labview program’s front panel. Next, press the button

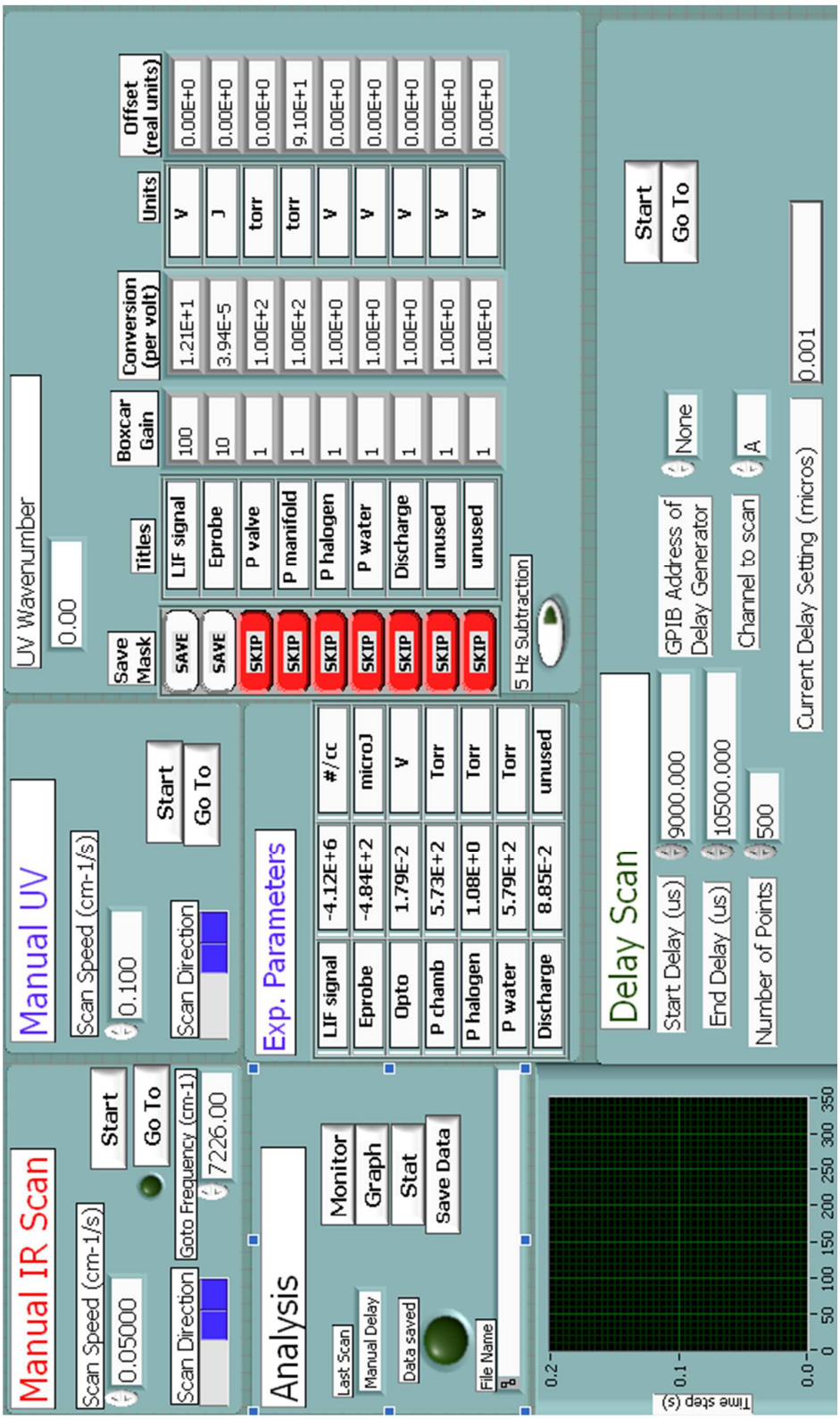

Figure 2.10 Front panel for the Labview data taking program. This virtual is capable of scanning the dye laser or the infrared OPO. It can also automatically vary laser timing.

called “Monitor”, which records data at 10 Hz with the probe laser frequency fixed. Press “stop” after a minute or two, and the program will report both the background and noise for both channels. Write these numbers down for later use. Incidentally, due to low frequency variation in boxcar output, it is necessary to perform this procedure at the beginning and ending of each spectral scan. Once the background has been obtained, choose the desired direction and velocity and press “Start” to initiate a manual UV spectrum. At 0.1 cm^{-1}/s, it takes about 2.5 hours to scan the entire $^2\Sigma(v = 0) \leftarrow {}^2\Pi(v = 0)$ NO band, and no other inputs are required of the user during this time. Once the scan is complete, hit “stop”, and an output file will automatically be generated in C:\spectra in a folder and file corresponding to the current date and time. Note that it is often useful to increase the PMT voltage for the last half of the spectrum, where the smaller peaks are less likely to saturate the PMT. This necessitates saving two separate scans (making sure to change the “LIF signal → Conversion” variable to reflect the change in PMT sensitivity) which can then be manually combined in a spreadsheet program such as Origin. One final note, the program is also capable of scanning in the time domain, where for example, the firing time of the pulsed jet source (which introduces NO into the chamber) can be varied with respect to the probe laser pulse to observe the gas arrival distribution in the time domain. These scans are done in the “Delay Scan” section by directly controlling the DGG timing on a shot to shot basis with time delays randomly selected between two user-specified limits in order to avoid systematic errors associated with low frequency drift in the system.

During a frequency scan, the actual laser light frequency tends to differ from this value by up to 0.2 cm^{-1} in a random manner over the course of a spectrum. It is likely that this error is caused by some lack of mechanical reproducibility in the scanning mechanism, but given that the output laser linewidth is only about 0.2 cm^{-1}, this frequency error is unacceptable. This is particularly true in the case of NO where a good frequency calibration is necessary in order to extract populations from the congested spectrum. Therefore, the frequencies must be calibrated in a second Labview program (Fig. 2.11 and appendix B.2) which performs a linear calibration to ensure proper line positions in a semi-automated manner. In short, the program displays a segment of the experimental spectrum along with a simulation at some user-defined temperature. Frequency shift and linear correction are automatically chosen via a least squares fit which must be accepted by the program user for each wavelength region, typically set to 50 cm^{-1} in width. The automatic calibration is generated by comparing the experimental spectrum with a thermal simulation based on a user-defined temperature. While the peak intensities are, of course, not expected to agree with the simulation, the program still does a reasonably good job of choosing a frequency offset and a linear correction term to correct the wavelength error. However, this does not always work, so it is sometimes necessary for the user to vary the limits of the fitted frequency region ("backwalk" and "step") until a visually satisfactory fit is obtained. Press "next segment" when a reasonable frequency calibration has been obtained. Upon pressing the “stop” button at the end of the scan, the output data will be saved as “C-*”, where “*” stands for the name of the input data file.

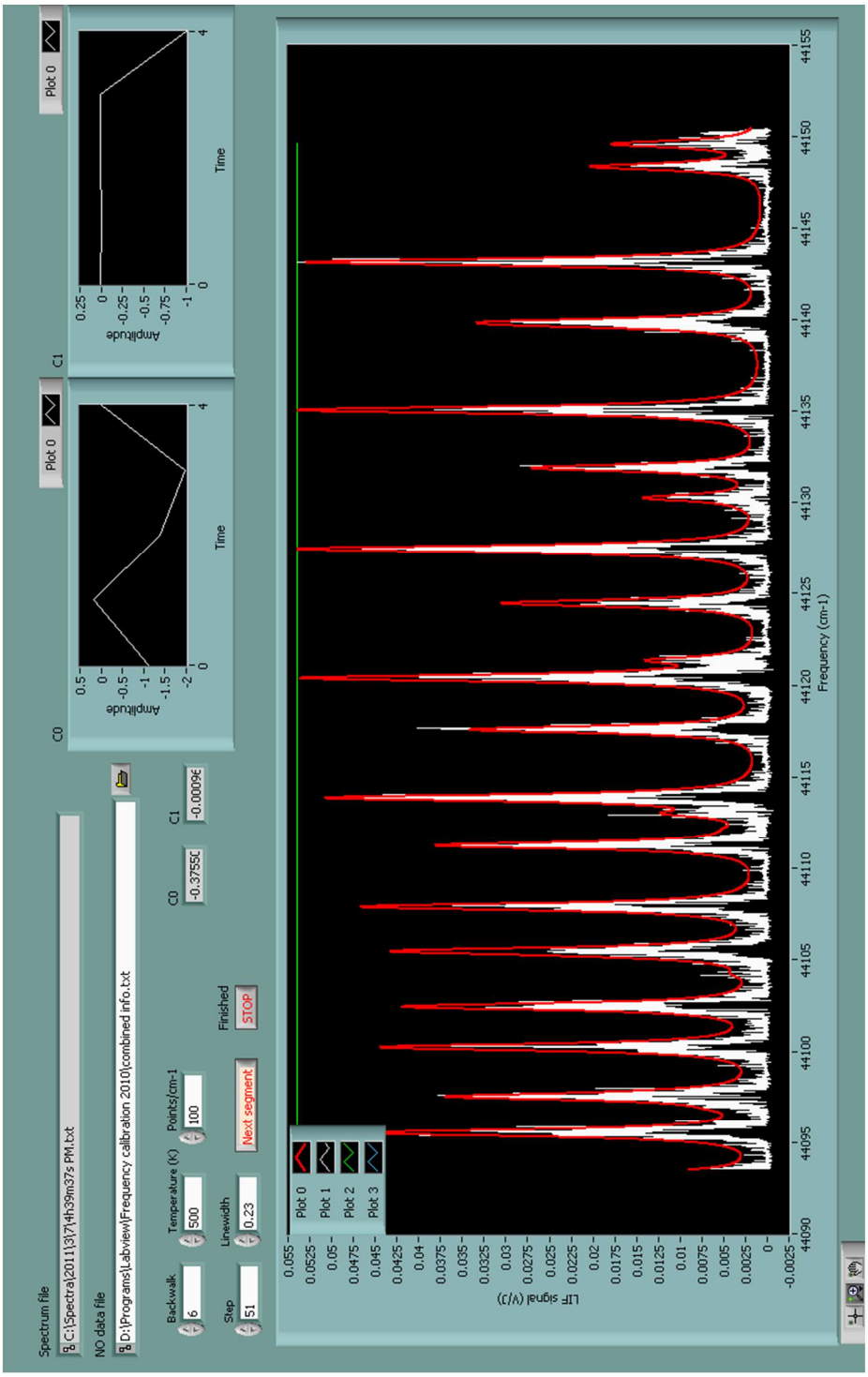

Figure 2.11 Front panel of the Labview frequency calibration program. The abscissa of the raw data (white) is shifted and scaled to obtain agreement with known line positions (shown as a thermal simulation in red).

Once calibrated, spectra are entered into a FORTRAN program called “LIFfits.f” (appendix B.3) which uses STARPAC[3] nonlinear least squares fitting to vary NO or OH populations until the experimental spectrum is reproduced as shown in Fig. 2.3. Extensive spectral overlap in both systems is mitigated by the fact that each quantum state is generally represented by several peaks in well separated areas of the spectrum. Therefore, low intensity lines in the uncluttered blue end, for example, are absolutely crucial for disentangling spectral information in the dense central portion, so it is very important to scan over a sufficiently wide range. This is especially true in OH, where the Hund's case B character of the molecule results in low intensity “O” and “S” branches far from the highest peaks.[4] The program outputs populations tabulated according to ground rotational level as well as electronic manifold of which there are four ($^2\Pi_{1/2}^e$, $^2\Pi_{1/2}^f$, $^2\Pi_{3/2}^e$, and $^2\Pi_{3/2}^f$) for both NO and OH (see Fig. 2.12). The accuracy of this rather involved analysis can be tested by firing the probe laser well after the supersonic jet so that radical populations are allowed to fully thermally equilibrate with the chamber walls. Fig. 2.12 shows a Boltzmann plot of such a study for NO. Not only is the rotational distribution characteristic of a room temperature sample, but the summed spin-orbit ratio also corresponds to a temperature of 300 K, showing that this degree of freedom has also reached thermal equilibrium and is properly handled by the data analysis procedure. The LIFfits.f program is controlled by an input file called “par.dat” whose inputs include the folder and name of the input file, the wavenumber range to be considered, the maximum J to include in the fit, the peak width, and the names of files containing information on transitions and energy levels.

Once an acceptable fit has been achieved, several output files are generated including mC* (showing the best fit model spectrum), pC* (with the quantum state populations extracted from the raw data), and prawC* (containing a Boltzmann analysis of the population distribution). The file pC* in turn serves as an input for another fortran

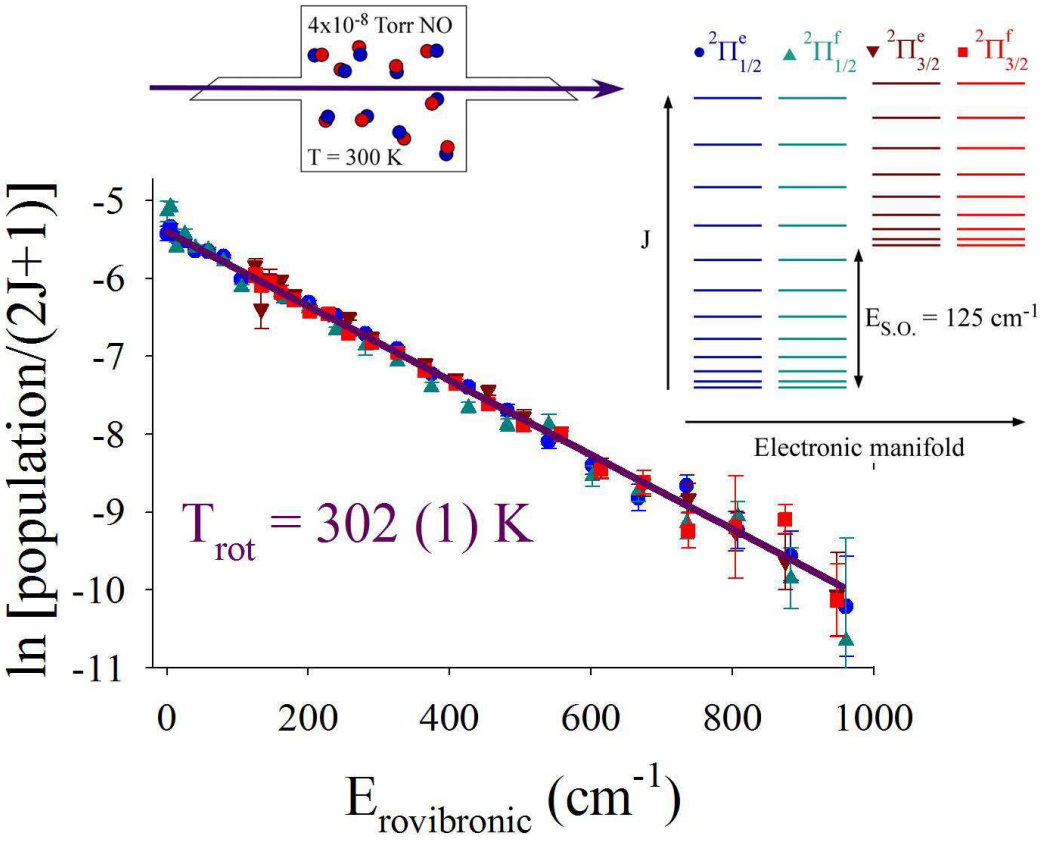

Figure 2.12 LIF analysis procedure applied to a 300 K static NO fill (4x10^{-8} Torr). When plotted on a Boltzmann axis, populations extracted from the spectrum agree well with the expected 300 K distribution. Inset: energy level diagram for NO($X^2\Pi_\Omega$) showing the spin-orbit splitting of $E_{Spin\text{-}Orbit.} \approx 125$ cm^{-1} and negligibly small energy difference between lambda doublet levels.

programs for further data analysis. "Double_Exp_fit.f" (appendix B.4), fits the raw data (population(J) for each electronic manifold) to a two temperature distribution according

to $P(J) = (2J+1)\left[\frac{\alpha}{Q_1}\exp(-\varepsilon_J / kT_1) + \frac{1-\alpha}{Q_2}\exp(-\varepsilon_J / kT_2)\right]$, where T_1 and T_2 are the temperatures of the two sub-populations and α is the branching between them. Q_1 and Q_2 are normalization factors for each sub-distribution. Yet another file called "par.dat" contains the name of the input file, the energy range to consider, guesses for the parameters T_1, T_2, & α, and Boolean variables which determine whether to float or fix these values in the fit.

2.2 State-to-State Scattering at the Gas-Liquid Interface

Several aspects of the nature of liquid surfaces are explored by observing inelastic collisions of ground state NO molecules to form excited rotational and spin-orbit states. LIF detection (section 2.1) is employed to determine the probability to populate various internal motions of the NO molecule after interaction with molten metals and room temperature ionic liquids (RTIL's). In addition to examining rotational excitation of the scattered NO, a good deal of effort is expended in obtaining reproducible electronic distributions showing the probability for incident ground spin-orbit state molecules to undergo a spin-orbit flip to scatter in the excited $^2\Pi_{3/2}$ manifold. These experiments are performed using a much improved LIF detection scheme compared to that used for examining clusters and gas phase reaction dynamics, but the basic principles are the same. For brevity, the LIF system described in section 2.1 is in fact the one used for these studies on scattering from liquids. These NO scattering studies are somewhat simpler due to the use of only a single laser and the lack of need for an electric discharge to produce reagents. However, considerable care must be taken to ensure purity and

cleanliness of these liquid surfaces so that, for example, the NO molecules are not inadvertently scattered from a gallium oxide surface rather than bare liquid gallium.

A turbomolecular pump is employed so that surfaces under study will not experience contamination from oil molecules. This device features a rated pumping speed of 1800 l/s for N_2 molecules and an 8" entrance. The turbomolecular device is backed by a E2M80 25 l/s foreline pump. Additionally, a residual gas analyzer is installed inside the chamber to observe, in real time, the constituents of the background gas. The vacuum-chamber system is able to reach a base pressure of ~ 3 x 10^{-8} Torr as measured on a Bayard-Alpert style ionization gauge. Further exmination of the composition of this background gas on the RGA reveals a proportion of more than 90 % of H_2O, and a molecular oxygen partial pressure of less than 10^{-9} Torr.

O_2 concentrations are of particular importance because liquid gallium surfaces are expected to form several monolayers of Ga_2O_3 in the presence of an oxidizing environment. The rate of this process has been measured, by sensitive x-ray reflectivity studies,[13] to occur on a timescale of several hours at 10^{-9} Torr O_2. This means that experiments can be carried out on a clean surface throughout the 2 hour scanning times in this study as long as the oxide layer has been removed prior to scanning. Removal is done with the use of a 2 keV Ar^+ sputtering source mounted 5 cm away and at 45° from the surface normal. Prior to each spectral scan, this device is run for 15 minutes, which is sufficient to completely clean the surface as observed by reduction in the total intensity of the scattered NO signal (Fig. 2.13). This effect of surface cleaning is thought to be a consequence of increased excitation of thermal capillary waves on the pure metal surface compared with the flatter oxidized interface. As this backfill Ar^+ source requires a

neutral Ar chamber pressure of 5 x 10^{-5} Torr, a lecture bottle of 99.995 % pure argon is introduced directly into the chamber through a needle valve followed by a small port in the side of the vacuum can.

Ar^+ cleaning is not possible on the RTIL surfaces because local heating vaporizes the material, resulting in a white coating on the nearby LIF imaging lens, which decreases overall detection sensitivity. However, these liquids will not form a floating oxide layer

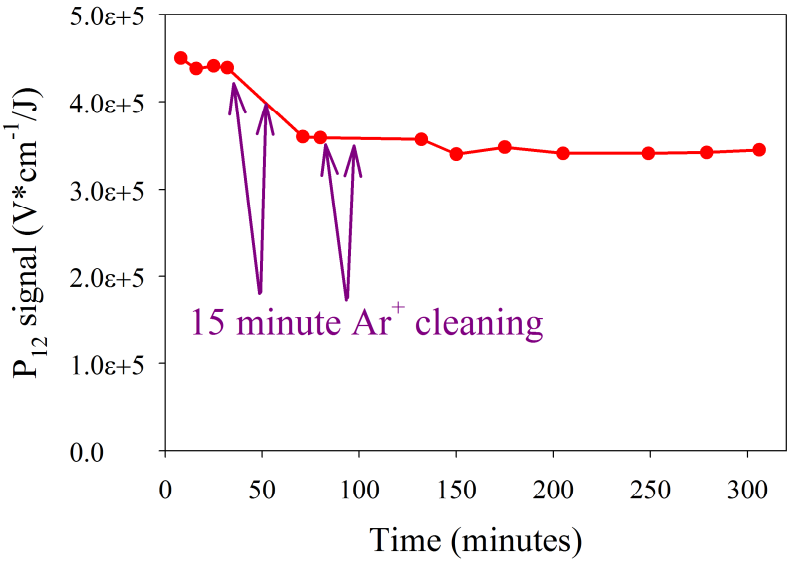

Figure 2.13 The effect of Ar^+ cleaning on NO + Ga LIF signal integrated over the P_{12} branch of NO. Cleaning decreases the overall amount of scattered NO, likely a result of increased roughening of the pure Ga surface relative to the flatter oxide.

in the presence of O_2 as was the case for liquid metals in the chamber. Also, due to their superior ability to dissolve H_2O, the dominant background species in the chamber, these liquids are not expected to form a water film on their surface at the background water pressures used in this experiment. For example, previous studies[14] on the effect of gas phase H_2O on surface properties of RTIL's found no measureable effect below partial

pressures of 10^{-4} Torr, a value which is 4 orders of magnitude greater than what is seen in the vacuum can. Nevertheless, cleanliness can be confirmed by periodically scraping and disposing of the surface every 5 minutes with a steel wire which can be fed through an UltraTorr fitting below the entrance baffle arm. When this is done, scattered NO distributions are in good agreement with those from an unscraped surface, indicating that these liquid surfaces are sufficiently clean. Before being placed in the crucible, ionic liquid samples, even BMIM-Cl, which is a solid at room temperature, must be degassed. Removal of dissolved gases is crucial because it eliminates H_2O contaminant, and it also avoids violent degassing in the experimental vacuum chamber, which can result in a liquid coating on the LIF collection lens. Removal of dissolved N_2 and O_2 is done in a round bottomed glass flask which is heated to 350 K (to additionally boil away dissolved H_2O) and agitated with a teflon-coated stir bar. The top of the flask is evacuated with a mechanical pump whose backstreaming oil is eliminated by pumping through a coil of ¼" copper tubing immersed in liquid nitrogen. Typically, liquids are degassed for 4 hours prior to being quickly transferred to the chamber.

For these studies, NO is seeded in a variety of nonreactive ballast gases in order to control the collision energy with which the molecules strike the surface. These gases include argon, neon, helium, and hydrogen, which give collision energies of 1.0, 2.7, 10, and 20 kcal/mol respectively. In each case, 50 Torr of NO gas is mixed with 5000 Torr of ballast in a 1 L stainless steel tank, resulting in a NO concentration of 1%. Mixing pressures are measured on a 10,000 Torr Baratron gauge to ensure accurate NO concentrations which are further confirmed by using the RGA to directly observe chamber NO and ballast concentration while the gas is pulsed through the valve. Before

use, the steel premix tanks are left untouched for at least 24 hours to allow full diffusive mixing of NO with the carrier gas. All gas handling is done in a welded stainless steel manifold featuring o-ring sealed VCO fittings and PTFE tubing connecting to gas cylinders, the premix cylinders, Baratrons, and the pulsed valve, as shown in figure 2.14. It is exceptionally important to ensure that this manifold is leak free because even a very small concentration of O_2 is capable of reacting with NO and reducing observed signal

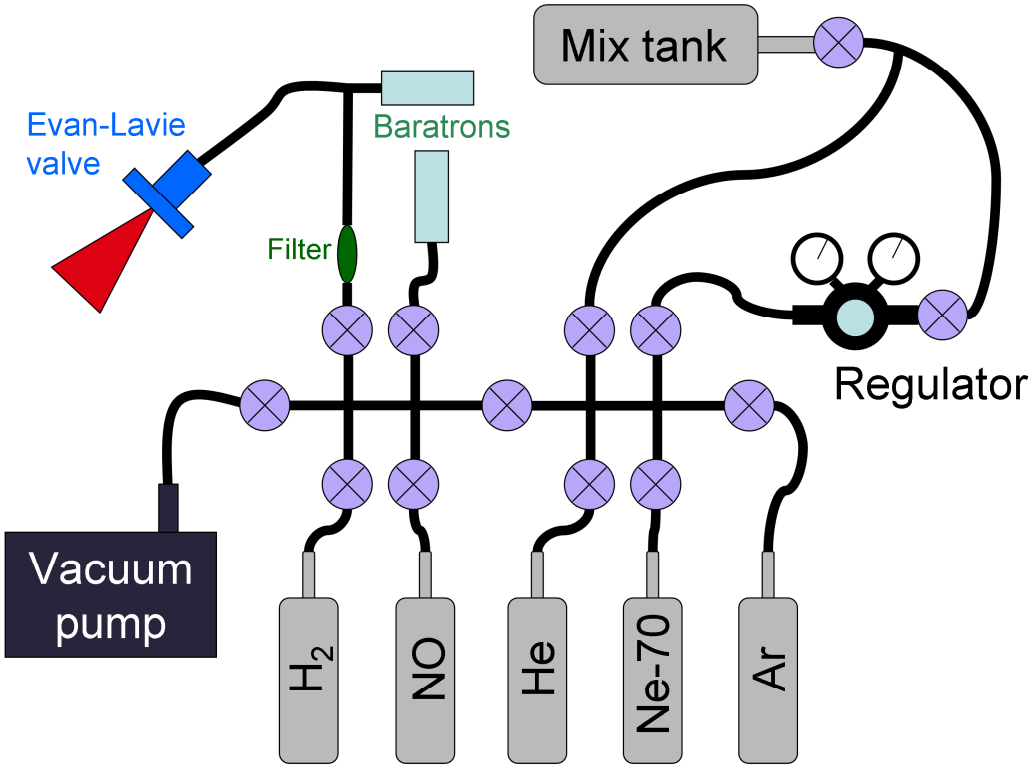

Figure 2.14 Manifold used for creating gas mixtures and delivering them to the pulsed valve inside the vacuum chamber. Violet circles represent ball valves for flow control. The manifold itself is welded stainless steel tubing with VCO fittings. All tubing is teflon.

levels. Therefore, anytime a change is made to the gas handling system, it is important to use a helium leak checker to ensure leak rates less than 10^{-6} standard cubic centimeters per minute (sccm).

After the premix cylinder, gas flows through a corrosion-resistant stainless steel and monel regulator which determines the backing pressure and is typically operated at its maximum value of 3000 Torr (absolute). Next, a metal mesh filter is encountered which is meant to remove any particulates that might clog the pulsed valve downstream. After the filter, the gas encounters another 10,000 Torr Baratron gauge which serves to accurately measure the backing pressure. Finally, gas flows into the pulsed valve, an Evan Lavie style device which accepts a 1/8" teflon tube through a small swagelok fitting. It is very important to realize that these small swagelok fittings do not require 1 and ¼ turns of initial tightening like normal swagelok nuts, but instead only need ¾ of a turn. These devices are designed to handle very high pressures, up to 76,000 Torr. Since this number is very high compared to the 3000 Torr backing pressure employed in this experiment, it is necessary to input relatively large values for "pulse time" into the control unit in order to ensure full valve opening. In practice, it has been found that a pulse time between 40 and 45 μs is sufficient for all carrier gases used here; larger values are not recommended since they tend to lead to a good deal of afterpulsing as seen when running a "Delay Scan" on the Labview control program (Fig. 2.10). The subsequent molecular beam travels 5.3 cm before passing through a 3 mm skimmer (Fig. 2.15) which collimates the molecular paths well enough to eliminate LIF background from the cold incident beam when looking at specular scattering a distance 1.6 cm above the surface. The pulsed valve is mounted on a rotatable 80/20 structure allowing access to a large

range of incident collision angles from at least 0° to 45° with respect to the surface normal. Additionally, the liquid surface can be translated in both dimensions in the scattering plane in order to control the detected angle over a similar range. In the studies presented below, incidence angles are fixed at 45° and specular detection is employed except for the special case where the incident beam itself is observed by removing the liquid surface completely and placing the detected point (fixed at the center of the chamber) directly in line with the molecular beam. When this is done, incident beam

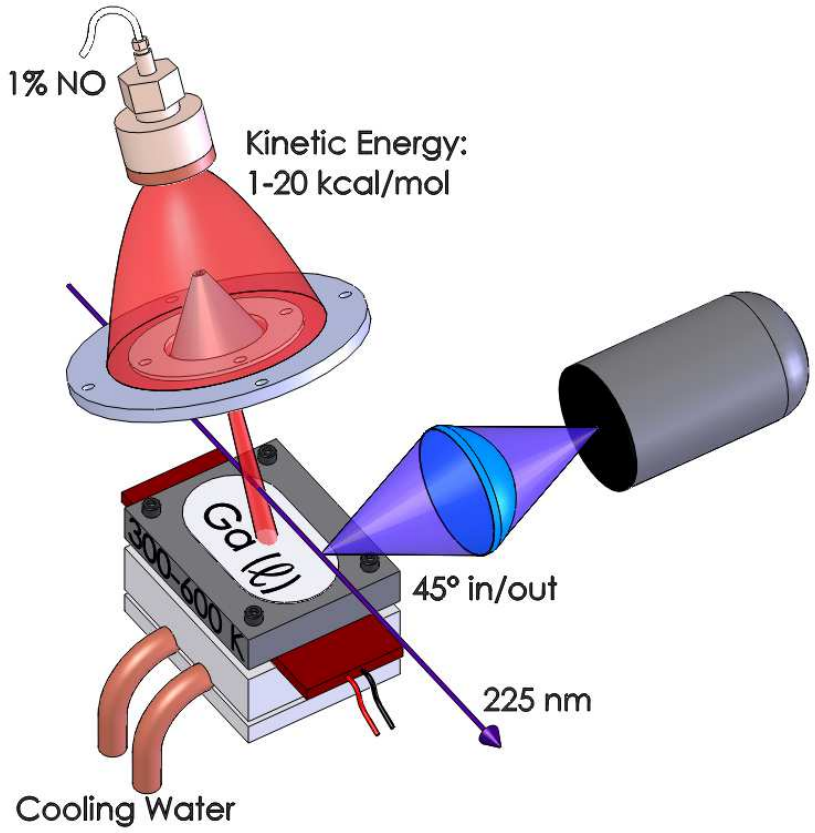

Figure 2.15 Gas-liquid scattering experimental apparatus. An mixture of NO in a seed gas flows out of an Evan Lavie valve and is collimated in a skimmer to form a small spot on the liquid surface. Specularly scattered molecules are detected using laser induced fluorescence. Also shown is the aluminum and stainless steel crucible assembly for heating, cooling, and containment of the molten sample.

temperatures are found to be exceptionally cold (often below 1 K), attesting to the high cooling power of this valve system.

The liquid surface is contained in a stainless steel crucible which is held near the center of the chamber and attached to the 80/20 mounting structure by four 4-40 threaded stainless steel standoffs with a length of 4 cm. This setup provides a good deal of thermal isolation between crucible and chamber which is expected to be characterized by on the order of 25 W of conductive heat loss when the crucible is heated to 1000 K. This is a result of the standard heat flow equation for heat flow power (P): $P = \kappa \Delta T \frac{A}{l}$. κ = 27.7 W/mK is the thermal conductivity of stainless steel at 1000 K, ΔT is the 700 K temperature difference across the standoffs, A = 8×10^{-5} m^2 is the total cross sectional area of the four 4-40 rods, and l = .04 m is the length of the standoffs. In fact, at these temperatures, this conductive loss is very small compared to the expected radiatave power of ~ 150 W. Note that thermally radiated power can be roughly estimated as $P_{rad} = \sigma A T^4$, where σ = 5.67×10^{-8} $W/m^2/K^4$ and A ~ 30 cm^2 is the crucible surface area. 285 K cooling water is flowed through a block of aluminum to which the stainless steel standoffs connect, ensuring that the chamber itself remains cool as the crucible is heated. As shown in Fig. 2.15, the crucible itself is a block of stainless steel with cavity dimensions of 4 cm x 2.4 cm x 0.25 cm (2.4 mL) — a previous version also exists with dimensions 4.4 cm x 2.4 cm x 0.5 cm. Two NiCr cartridge heaters are sandwiched between the bottom of the crucible and a lower plate each of which contains machined grooves for the cylindrical devices. These heaters, each of which is capable of delivering 500 W of power, can easily heat the crucible to 1000 K. However, higher temperatures cannot be achieved due to a rapid loss of mechanical stability of the NiCr wires which

eventually leads to an electrical spark as the wire breaks. 4-40 nuts on the standoff rods hold the whole device together and provide enough pressure to ensure good thermal contact between heaters and crucible. A small blind hole is drilled through the back of the crucible block, and threaded 4-40 set screws come in from the top and bottom of the resulting cavity. A type K thermocouple is inserted into the blind hole and secured by tightening the set screws, a scheme which provides a measurement of liquid temperature with an accuracy of 1 K, as confirmed with a thermocouple placed directly in the liquid under study or in an icewater bath.

In liquid metals at high temperature, the choice of crucible material is very important because of the possibility of amalgamation where metallic crucible atoms are dissolved into the liquid under study. This is particularly serious because of a phenomenon whereby a small bulk concentration of an unwanted species in a liquid metal can lead to a very high proportion of impurities on the surface[15] For gallium in steel, solvation of Fe in Ga is the most important interaction, and previous studies[16] show that the iron concentration will be below 1% at temperatures below 900 K. However, upon further heating, the Fe concentration rises rather rapidly, meaning that a steel crucible is not ideal for a very hot gallium sample. Many other potential materials such as aluminum also amalgamate well with Ga, and even carbon will be dissolved, ruling out the use of a graphite crucible. One promising alternative is to line the steel crucible with a layer of tungsten foil, which does not easily leave the solid phase to amalgamate with a nearby liquid metal at an interface[17].

2.3 Spectroscopy and Dynamics of H_2O-containing Clusters

A variety of water clusters were studied using a slit jet spectroscopy apparatus. The list of species consists of Ar-H_2O, H_2-H_2O, and H_2O-H_2O. With the exception of H_2O dimer[5], these complexes[6] are bound by tens to hundreds of cm^{-1}, meaning that samples must be cooled rather aggressively in order to ensure measureable cluster concentrations in the detection region. This is done by co-expanding on the order of 0.1 % H_2O in a gas of the desired atomic or molecular partner in a supersonic beam[7]. Gases are typically mixed by bubbling Ar, Ne, or H_2 through a reservoir of purified liquid water which is cooled in an ice bath to maintain a steady water vapor pressure of ~ 5 Torr. The richness of the water mixture is adjusted by varying the carrier gas pressure in the mixing cylinder, and the total backing pressure in the nozzle is dynamically varied with an in-line needle valve to control total gas flow and thus pressure behind the expansion. The expansion is produced by a home made pulsed supersonic slit jet source which has been discussed in detail elsewhere[8]. A pair of steel jaws typically limits the slit width to ~ 100 μm, and the length is held fixed at 5 cm. Because of the inherent propensity for three body collisions in a slit expansion as opposed to a pinhole, this is an ideal setup for generating water clusters by cold gas phase collisions. The resulting molecular beam expands into a 96 L cubical vacuum chamber evacuated by a 10” diffusion pump which is backed by a 25 l/s E2M80 mechanical pump. A liquid nitrogen cooled baffle is employed to limit the presence of backstreaming diffusion pump oil in the chamber. The resulting chamber pressure of ~ 10^{-6} Torr exhibits a mean free path ~ 70 m which is more

than sufficient to ensure an absence of collisions with background gases in the chamber before encountering the set of detection laser beams 2 cm downstream.

Gas phase clusters within the 5 cm path length of the molecular beam are detected by three-laser action spectroscopy[9] as shown schematically in Fig. 2.16. Briefly, each cluster first encounters a tunable infrared laser beam whose frequency is chosen to be near resonance[10] for two quanta of H_2O monomer vibrational excitation. Next comes a 193 nm photolysis pulse whose energy is appropriate to preferentially break apart vibrationally excited water molecules. Finally, resulting OH molecules are state-selectively detected by LIF with a 308 nm probe pulse as discussed in section 2.1. All three laser beams are spatially overlapped inside the chamber, and the fused silica

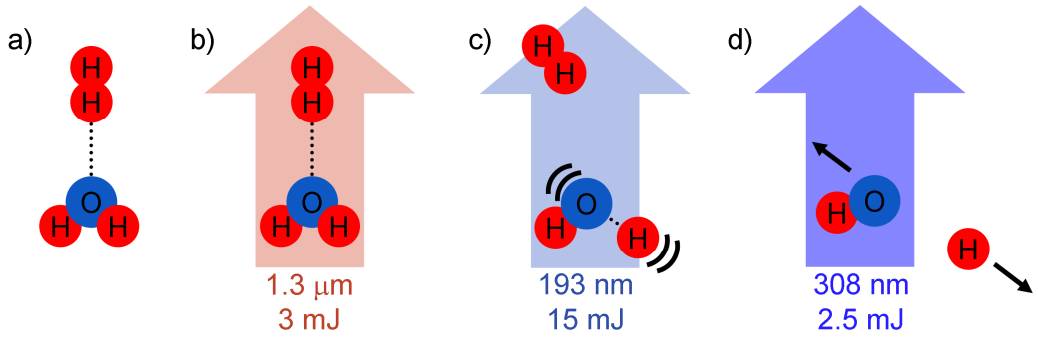

Figure 2.16 Scheme used to detect H_2 – H_2O clusters: a) Complexes are formed in a ~ 3 K slit supersonic jet. The potential energy minimum structure is shown here. b) An infrared laser pulse excites the $|02^-\rangle$ overtone stretch vibration of the H2O moiety. c) The H_2O is photolyzed by a laser at 193 nm, a color which efficiently breaks apart vibrationally excited water while minimizing background from photolysis of the ground state. The time delay between the IR and photolysis lasers can be varied to probe predissociation of the metastable cluster state. d) OH photolysis products are detected by laser induced fluorescence following excitation by a tunable 308 nm pulse.

Brewster windows must be replaced with calcium fluoride in order to minimize absorption of the 193 nm pulse. Due to the mm-scale diameter for these beams, OH

products are expected to fly out of the probed region on a microsecond timescale, meaning that the time delay between photolysis and probe lasers can safely be set to several tens of nanoseconds to allow the PMT to recover from the flash of scattered UV radiation from the excimer beam. Even though photolysis cross sections are at least an order of magnitude greater for vibrationally excited versus ground state water molecules, this still leaves a significant OH background which is observed even in the absence of any infrared laser light. Since these background radicals originate mostly from water monomers, they are not at all specific to the presence of cluster species and therefore must be removed from reported data. This is done by running the infrared laser at 5 Hz while all other experimental components are pulsed at 10 Hz. Then, the Labview data taking program automatically subtracts adjacent data points in order to obtain a background-free spectrum.

Infrared laser light is produced by a Laser Vision optical parametric oscillator (OPO) pumped by a Nd-YAG laser as shown in Fig. 2.17. 1064 nm laser light exits the YAG before entering the OPO where it is immediately doubled to make a 532 nm green beam. This beam enters a grating-containing oscillator cavity in which KTP crystals

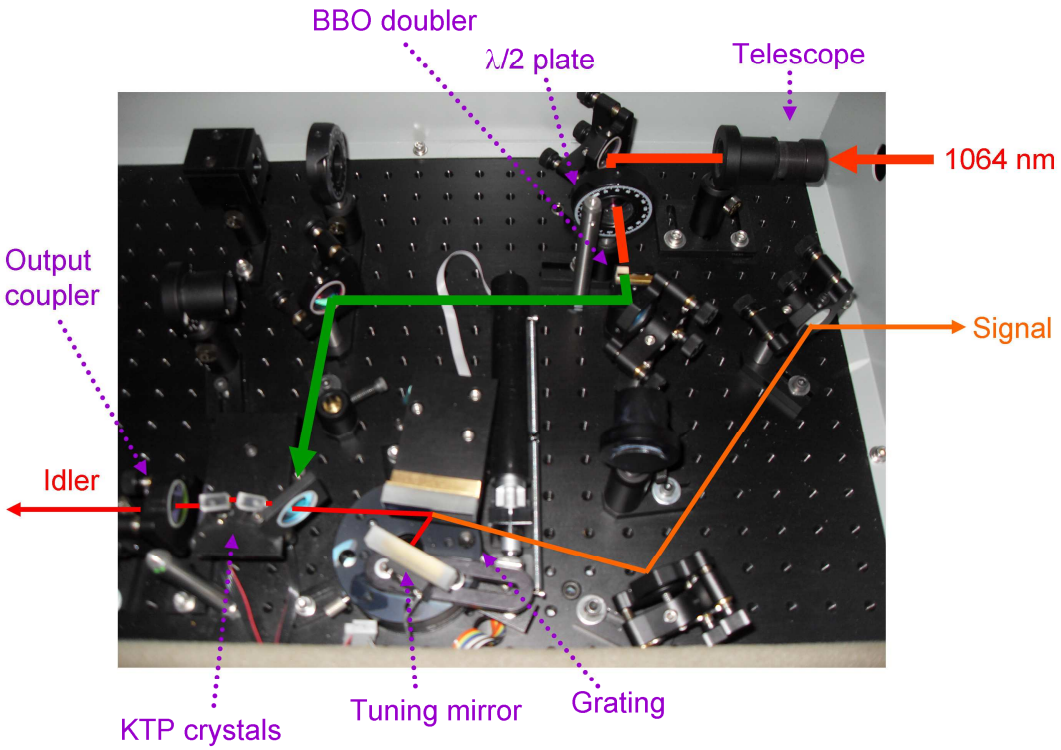

Figure 2.17 Optical parametric oscillator (OPO) laser used to produce tunable infrared light. A doubled YAG (532 nm) beam is introduced to a cavity where it is converted into an idler frequency (resonant with a cavity) and a signal beam (which is removed by specular reflection from the diffraction grating.

consume photons at 532 nm (pump) and output two photons (signal and idler) whose energies add up to that of the green pump photon. The grating and output coupler retroreflect the signal beam while the idler exits through the output coupler before leaving the laser. This system is equipped with an amplifier stage where the idler beam and some 1064 nm light is sent through four KTA crystals to produce more idler light by optical parametric amplification. However, at the wavelengths of interest for these studies (~ 1.4 μm), the amplifier stage tends to actually attenuate the idler, so it is physically removed from the beam path. The device is capable of producing about 15 mJ

of light at 1.4 μm, which is near the resonance for first harmonic excitation of the OH stretch in H_2O. Tuning is done on the accompanying computer which moves the grating and nonlinear crystal angles with stepper motors. The position of the grating ultimately controls the value of the output idler frequency, and the angular positions of the KTP crystals are chosen to ensure phase matching to produce maximum OPO power. The laser must be periodically recalibrated for maximum power by manually tuning through the desired frequency range while recording optimal (maximum idler power) positions for all crystals. This information is then fit to a third order polynomial and entered into the OPO controller software for velocity control of the stepper motors. Frequency calibration of this laser is done using a low pressure H_2O cell containing a microphone for acquiring optoacoustic spectra during each IR scan. While the peak intensities of such a scan are of limited use, the frequencies are compared with expected values in the HITRAN H_2O database.[10] Linear interpretation between such peaks results in an accurate frequency measurement compared to the 0.2 cm^{-1} linewidth of the laser radiation.

Photolysis at 193 nm is done with a Lambda Physik Lextra 50 excimer laser running on metastable argon fluoride. The laser head is filled with 65 mbar of 10% F_2 in He, 250 mbar of Ar, and 2700 mbar of "Ne-70" (70% Ne, 30% He), and the discharge voltage is typically set to 24 kV. Under these conditions, approximately 100 mJ of UV light is produced at the laser output, but due to significant losses from dichroic mirrors, focusing lenses, and travel through air, only about 10 mJ is actually focused to the inside of the chamber. Under normal operating conditions, the inside surface of the output coupler must be cleaned every few weeks due to the formation of a white residue which

seems to originate from the discharge source. To do this, the laser head must be emptied, purged, and opened. The caked-on white residue is removed by hard scrubbing with a fine abrasive powder such as Vienna chalk. Upon replacing the output coupler, the laser head must then be evacuated, repassivated, and refilled before use. Passivation is done by filling first with 2600 mbar of He and running at 16 kV and 15 Hz for 10 minutes. Next, the head is loaded with 100 mbar of 10% F_2 in He and 2000 mbar of He, and the discharge is run at 24 kV, 10 Hz for 15 minutes.

When both IR and probe lasers are fixed on particular transitions of an H_2O-containing cluster and OH respectively, the time delay between vibrational excitation and photolysis can be varied in order to obtain a predissociation spectrum. Given the approximately 8 ns time duration of these pulses, this procedure allows measurement of LIF signal versus time delay with a resolution of about 5 ns. Such a process can be used to discover the rate for predissociation of a cluster from a metastable initial state where ~ 7250 cm^{-1} of internal energy is present in the water monomer inside a cluster which is only bound by an energy on the order of 30 cm^{-1}. Photolysis of a free, predissociated water molecule leads to a very different OH distribution than does photolysis of H_2O bound in a cluster. Therefore, variation of IR-excimer time delay tends to show an exponential change in LIF intensity between that observed for photolysis of bound water and that of free H_2O, as shown in Fig. 2.18. For short-lived complexes, analysis of these

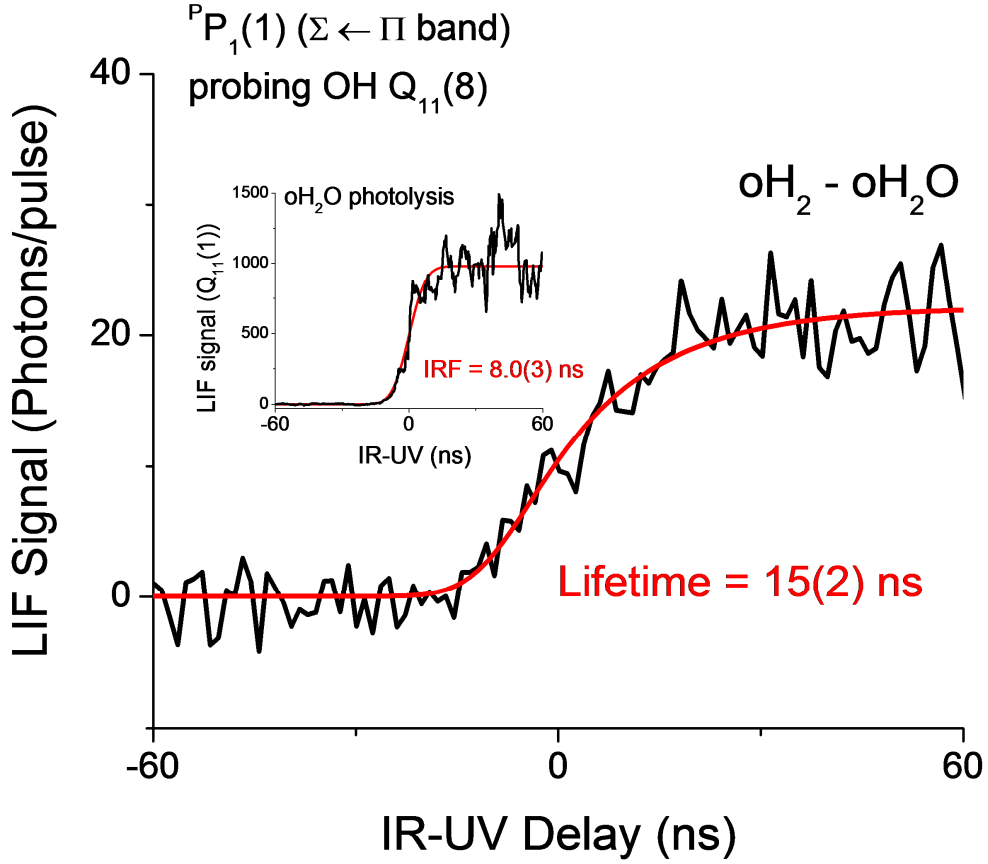

Figure 2.18 Direct observation of predissociation lifetime in oH_2-oH_2O. This is obtained by varying the time delay between the infrared excitation and the photolysis pulse while examining a specific cluster transition and a particular OH level. The measured lifetime of 15(2) ns is large compared to the instrument response function of 8 ns as determined by observing H_2O monomer lines (inset).

results is somewhat complicated by the finite temporal resolution associated with the nanosecond laser pulses in use. However, this can be mitigated by deconvoluting the observed signal from a Gaussian which is used to describe the overlap between the two beam. The following function is employed:

$$f(t) = S_0 + \left(\frac{S_f - S_0}{2}\right)\left\{1 + erf\left(\frac{t-t_0}{\sigma}\right) - e^{\sigma^2/4\tau^2} e^{-(t-t_0)/\tau}\left[1 - erf\left(\frac{\sigma}{2\tau} - \frac{t-t_0}{\sigma}\right)\right]\right\} \qquad (2.1)$$

where S_0 is the background signal level, which is seen when the photolysis laser fires before vibrational excitation, S_f is the signal after predissociation, and t_0 is the time delay resulting in a signal halfway between these extremes. σ is a parameter describing the instrument response function arising from the ~ 8 ns duration of both pulsed laser beams; it is found by looking at photolysis of water monomer, a system which does not predissociate. Finally, τ is the predissociation lifetime, which is extracted from the data by a least squares fit. Note that this fitting procedure is only appropriate in the case where the LIF laser is parked on a transition from an OH level whose production is enhanced after predissociation. In the clusters studied here, $N_{OH} = 8$ levels meet that criterion.

2.4 Crossed Jet Reactive Scattering

As shown schematically in Fig. 2.19, LIF detection of OH (or OD) molecules (see section 2.1) is also used as a method to observe the result of reactive scattering collisions between fluorine atoms and water molecules to produce HF + OH(D). In short, F_2 molecules, seeded in helium, are converted to F atoms in a pulsed discharge supersonic beam source. At the same time, a water-containing helium molecular beam is crossed with the fluorine one at 90° and 5 cm from each valve, leading to a collision energy of 6(2) kcal/mol. After

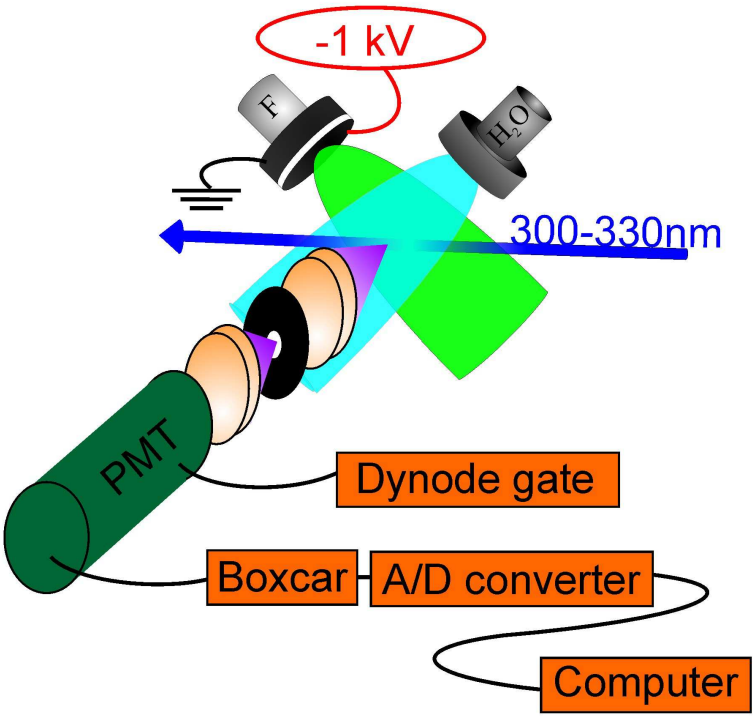

Figure 2.19 Reactions between F and H_2O are carried out in a crossed molecular beam experiment. F2 is converted into its atomic form with a -1 kV pulsed electrical discharge at the throat of the expansion. Product OH molecules are detected by laser induced fluorescence at the intersection of the two jets. Also shown is the dynode control which shuts off the PMT during the discharge pulse.

the fluorine atom has abstracted a hydrogen from the water molecule, OH is produced in some rotational and electronic state which is then detected by LIF. This experiment is carried out in the same 96 L cubical chamber as that used for water cluster studies. The vacuum system is also essentially the same as that used in the cluster experiments with typical base pressure of 10^{-6} Torr.

Molecular fluorine is purchased in cylinders where it is already mixed with He at a ratio of 10% F_2 to 90% He. This tank is connected to the stagnation region of a general valve with a stainless steel needle valve in between in order to adjust pressure by controlling flow. Choice of tubing is crucial since sintered teflon tends to trap H_2O

which degases and produces an OH background after the discharge. Extruded PTFE tubing was found to be much freer of background moisture. The backing pressure is typically set to 50 Torr ($1.6x10^{16}$ molecules/cm^3), and the valve is opened for approximately 1 ms. As the hydrogen-fluorine mix expands through a 400 μm oriface into the vacuum chamber, it travels through an electrical discharge driven by a transient high voltage pulse. This pulse is created by a home made push-pull circuit (appendix A.2) which supplies ~ 800 V and 200 mA through a 1 kΩ ballast resistor in line with the discharge gap. The electronics are wired as shown in Fig. 2.19 so that the cathode is formed by a pair of knife edges spaced to produce a miniature slit expansion with a spacing of ~ 1 mm. The body of the steel general valve forms the anode so that electrons flow upstream through the exiting gas, leading to a more stable discharge than can be obtained by wiring in the opposite direction with respect to gas flow. This is likely due to the relative ease cations to flow in the direction of gas motion while the negatively charged electrons flow upstream relative to the opposite situation where cations attempt to move against the direction of mass transport. In between cathode and anode lies a glass insulator with 1.5 mm thickness. These insulators can be produced by drilling a 1 mm hole through a microscope slide, but they must be periodically replaced because the discharge will slowly damage and blacken the edges of the hole.

Water-helium mixtures are produced in an ice-cooled bubbler similar to that used in the water cluster experiments in section 2.2. The resulting H_2O / He gas flows through a separate manifold and a needle valve before entering a piezoelectric actuated valve[11] with total backing pressure of 200 Torr ($6x10^{18}$ molecules/cm3). Care must be taken to avoid electrical breakdown to the piezoelectric drum since a single discharge event is

capable of ruining it. Therefore, it is important to always turn off the high voltage source when the valve is being pumped down. Internal metal surfaces are painted with Corona Dope high voltage insulation in order to further suppress breakdown through the water-containing backing gas. Experiments on F + D_2O are performed with the same setup after extensive passivation with respect to H → D exchange, where a D_2O-containing mixture is contained the valve and manifold over the course of several days. The degree of passivation can be immediately seen in the small OH / OD background which can be seen in the absence of flourine collision partners and originates from background H_2O / D_2O in the discharge.

Care is taken to ensure that single collision conditions are obtained so that each fluorine atom is likely to collide with at most one atom or molecule during its flight through the detected region of the experiment. At the same time, it is important to ensure that background gas pressures are low enough that there is a low probability for OH products to collide with anything before being interrogated by the probe laser beam. Both of these criteria are met by ensuring that gas pressures are sufficiently low in this crossed-beam experiment. For example, as the H_2O / He jet travels x = 5 cm from the stagnation region, its density drops from its stagnation region value of $n_0 = 6\text{x}10^{16}$ #/cm^3 (where "#" stands for "molecules") down to $n(x) \approx 0.24 n_0 \left(\frac{d}{x}\right)^2$. Given that d, the aperture diameter, is equal to ~ 500 μm for the jet source valve, a density of n(5 cm) ~ $1.4\text{x}10^{12}$ #/cc of mostly He atoms is expected in the collision region as potential targets for the incident F atoms. For a hard sphere collision cross section of $\sigma \sim 5\text{x}10^{-15}$ cm^2, the

fluorine collision probability is $P_{coll} \sim \sigma_{H.S.} n_{He/H_2O} l_{travel}$, which comes out to $P_{coll} \sim 4$ %, i.e. safely in the single-collision regime.

A collision of F seeded in He with H_2O also seeded in He at an angle of 90° is characterized by a center of mass kinetic energy (E_{COM}) of 6 kcal/mol. However, these unskimmed molecular beams collide with a rather wide range of E_{COM}, and therefore OH products from high E_{COM} geometries (i.e. places where the two molecules have more of a head on collision) feature some finite probability of arriving in the LIF detection region which lies at the 90° collision point between the centerlines of the two beams. To gain a higher order understanding of the range of collision geometries under consideration, Monte Carlo simulations[12] are employed in which incident beam angular distributions are modeled by $\cos^n(\theta)$ functions. From this analysis, the likelihood that an OH product is the result of a collision at a certain E_{COM} can be found from the probability for collision at a specific point in space times the probability that the resulting OH molecule will be found within the 0.16 cm^3 detection region at the time of laser pulse firing. Such an analysis depends on some assumptions about the angular distribution of reactively scattered OH molecules, but it was found to be insensitive over a rather large range of possibilities. For example, less than a 10% change in both the average and the standard deviation of the collision energy distribution is observed when the molecular frame scattering distribution is changed from isotropic to $\cos(\theta)$. On the basis of this Monte Carlo analysis, the effective collision energy is found to have an average of 6 kcal/mol with a standard deviation of 2 kcal/mol.

References for Chapter II

[1] J. Luque and D. R. Crosley, http://www.sri.com/psd/lifbase.

[2] D. J. Creasey, P. A. Halford-Maw, D. E. Heard, J. E. Spence, and B. J. Whitaker, Rev. Sci. Instrum.**69** (12), 4068 (1998).

[3] J. R. Donaldson and P. V. Tryon, edited by N. I. o. S. a. Technology (U. S. Department of Commerce, Center for Computing and Applied Mathematics, 1990), Vol. Internal Report NBSIR 86-3448; http://water.usgs.gov/software/OTIS/addl/starpac/nls.html.

[4] I. L. Chidsey and D. R. Crosley, J. Quant. Spectrosc. Ra. **23** (2), 187 (1980).

[5] M. W. Feyereisen, D. Feller, and D. A. Dixon, J. Phys. Chem. **100** (8), 2993 (1996).

[6] R. C. Cohen and R. J. Saykally, J. Chem. Phys. **98** (8), 6007 (1993); A. van der Avoird and D. J. Nesbitt, J. Chem. Phys. **134** (4), 044314 (2011).

[7] G. Scoles, *Atomic and Molecular Beam Methods*. (Oxford University Press, New York, 1988).

[8] C. M. Lovejoy and D. J. Nesbitt, Rev. Sci. Instrum.**58** (5), 807 (1987).

[9] D. F. Plusquellic, O. Votava, and D. J. Nesbitt, J. Chem. Phys. **101** (7), 6356 (1994).

[10] L. S. Rothman et al., J. Quant. Spectrosc. Ra. **60** (5), 665 (1998).

[11] D. Proch and T. Trickl, Rev. Sci. Instrum.**60** (4), 713 (1989).

[12] W. W. Harper, S. A. Nizkorodov, and D. J. Nesbitt, J. Chem. Phys. **116** (13), 5622 (2002).

[13] K. J. D. Schmeisser, D. M. Kolb, Le Vide-Les Couches Minces (Suppl.) **201**, 256 (1980).

[14] K. R. J. Lovelock, E. F. Smith, A. Deyko, I. J. Villar-Garcia, P. Licence, and R. G. Jones, Chem. Commun. (Cambridge, U. K.) (46), 4866 (2007).

[15] J. A. Morgan and G. M. Nathanson, J. Chem. Phys. **114** (5), 1958 (2001).

[16] H. Okamoto, J. Phase Equilib. **11** (6), 576 (1990).

[17] H. Okamoto and T. Massalski, J. Phase Equilib. **6** (2), 136 (1985).

Chapter III: Vibrationally-mediated dissociation dynamics of H_2O in the $v_{OH} = 2$ polyad

Published in *J. Chem. Phys.* **119**, 10158 (2003)

3.1 Introduction

Photofragmentation of H_2O in the first absorption band ($A^1B_1 \leftarrow X^1A_1$) has long represented a fundamental paradigm for direct dissociation on a single repulsive potential energy surface (PES).[1] In contrast to photodissociation in the second absorption band ($B^1B_2 \leftarrow X^1A_1$), which involves multiple product channels, conical intersections, and considerable excess internal energy in the OH fragment,[2] photoinduced bond-breaking via the A^1B_1 state is less complicated, in principle, permitting development of simple physical models of the dissociation event. For example, $A^1B_1 \leftarrow X^1A_1$ excitation produces little change in the HOH bend PES angular anisotropy, which largely accounts for the low degree of rotational angular momentum transferred to the nascent OH product.[3] The moderate levels of OH vibrational excitation observed can also be rationalized from a classical perspective by preferred initial motion on the upper potential surface along the symmetric stretch coordinate.[1,4]

However, when examined on a fully *state-to-state* basis, this rather simple picture for photodissociation of H_2O proves somewhat deceptive, and indeed becomes far richer and dynamically more interesting.[5-10] The first experiments on photodissociation dynamics of water from single ro-vibrational excited states were due to Andresen and co-workers.[6] Their pioneering experiments on state-selected $H_2O(J_{K_aK_c})$ in the v_{OH}=1 vibrational polyad revealed surprisingly strong oscillations in the OH fragment quantum state populations as a function of N_{OH} for a

single spin-orbit/Λ-doublet manifold. What made this observation particularly noteworthy was that these same oscillations vanished for photodissociation of rotationally equilibrated water, even when cooled into the lowest two nuclear spin states ($J_{K_aK_c}$ = 1_{01}, 0_{00}) at supersonic jet temperatures.[11] This oscillatory behavior has since been unambiguously verified in single rovibrational state photodissociaion studies of H_2O for higher OH stretching polyads for v_{OH} = 3-5.[5,7,9,10] Subsequent experimental and theoretical studies have demonstrated that these oscillations result from coupling between OH angular momentum states in the exit channel. Specifically, a Franck-Condon model projecting the initial HOH wave function into asymptotic OH states was developed by Balint-Kurti[12]. This has provided an excellent qualitative (and in some test cases, semi-quantitative) description of the nascent OH populations[8], clearly confirming the extreme sensitivity to the initial rotational and bending states of H_2O. Indeed, this analysis provided the necessary framework to explain how the presence of two $J_{K_aK_c}$ = 1_{01}, 0_{00} nuclear spin isomers in the early beam experiments of Andresen[11] had been sufficient to average out all oscillations in the observed OH rotational distributions.

From the perspective of vibrationally mediated control of photofragmentation dynamics, state-selection of H_2O via overtone excitation offers special advantages. As first elucidated by Lawton and Child, the OH stretch structure for H_2O can be best described by polyads, with each polyad containing v_{OH}+1 levels corresponding to v_{OH} quanta distributed between the two identical bonds. By virtue of anharmonic detuning effects that increase with v_{OH}, these quantum states can often be quite well described by a single symmetric or antisymmetric linear combination of pure "local mode" excitations (e.g. $|nm\rangle^{\pm} \approx 2^{-1/2}\{|n,m\rangle \pm |m,n\rangle\}$) with perturbative contributions from other nearby members of the same polyad (e.g., $\approx 2^{-1/2}\{|n\pm1,m\mp1\rangle \pm |m\mp1,n\pm1\rangle\}$). At least for higher polyad numbers (v_{OH} = 3,4,5), this has led to

the "spectator" paradigm, i.e. a strong propensity for cleavage of the OH bond with greater local mode vibrational excitation, with the surviving OH bond retaining its initial local mode excitation.[13] For example, elegant experiments in the Crim group demonstrated that 220-250 nm photodissociation of H_2O in $|04\rangle^-$ local mode state predominantly results in OH(v=0) fragments, whereas dissociation of the nearly isoenergetic $|13\rangle^-$ state produces mostly OH(v=1). Indeed, nearly 100% selective bond fission has been demonstrated in analogous HOD studies, for which the OH vs OD stretch local mode behavior is now essentially complete.[14] These studies have been extensively corroborated by exact QM dynamical calculations,[13] resulting in an impressive level of consensus between theory and experiment.[1] It remains an open question, however, what happens to this spectator paradigm at lower levels of polyad excitation, e.g. where a local mode description of the H_2O stretch vibrations might begin to break down. However, such studies require accessing multiple vibrational states with "tunable" spectator mode character, which do not exist for the lowest $v_{OH} = 0$ and $v_{OH} = 1$ polyads. It therefore proves particularly interesting to explore vibrationally mediated photodissociation in the v_{OH}=2 polyad, which permits access to the lowest OH stretching states (e.g. $|02\rangle^-$, $|02\rangle^+$, and $|11\rangle^+$) with *distinguishable* local mode quanta in the spectator bond.

The thrust of the present work is to explore state-selected photodissociation of H_2O in the v_{OH}=2 polyad, which allows several questions of dynamical interest to be addressed. First of all, as mentioned above, such studies can directly access several different intermediate levels, $|02\rangle^-$, $|02\rangle^+$, and $|11\rangle^+$, whereby photodissociation now has the option of either conserving (or destroying) vibrational excitation in the uncleaved OH bond. As a secondary motivation, photolysis of these vibrational states with 193 nm excitation ($E_{total} \approx 7.3$eV) samples regions on the upper PES quite energetically similar (see table 3.1) to those of Crim and co-workers[7] in the

H_2O state	$\lambda_{photolysis}$ (nm)	E_{excess} (cm^{-1})	OH in v=0	OH in v=1	Reference
$\|00\rangle^+$	193	10530	> 99.8	< 0.2	[16]
$\|00\rangle^+$	157	22410	50*	50*	[11]
$\|01\rangle^-$	193	14290	§		[6,8]
$\|01^-2\rangle$	193	17400	§		This work
$\|02\rangle^+$	193	17730	63(3)	37(3)	This work
$\|02\rangle^-$	193	17780	97.8(3)	2.2(3)	This work
$\|11\rangle^+$	193	17980	47(5)	53(5)	This work
$\|03\rangle^+$	248	9640	§		[10]
$\|03\rangle^-$	248	9660	> 99.5	< 0.5	[10]
$\|12\rangle^+$	248	9910	§		[10]
$\|12\rangle^-$	248	10070	> 98	< 2	[10]
$\|03^-1\rangle$	218.5	16640	> 90	< 10	[9]
$\|03^-2\rangle$	218.5	18140	> 90	< 10	[9]
$\|04\rangle^-$	282	8010	§		[5]
$\|04\rangle^-$	266	10140	> 98	< 2	[7]
$\|04\rangle^-$	239.5	14300	99(1)	1(1)	[7]
$\|04\rangle^-$	218.5	18320	91(3)	9(3)	[7,9]
$\|13\rangle^-$	239.5	14790	16(6)	84(7)	[7]
$\|13\rangle^-$	218.5	18800	6(5)	94(5)	[7]
$\|04^-2\rangle$	282	11000	> 98	< 2	[5]
$\|05\rangle^-$	282	11670	> 98	< 2	[5]

Table 3.1 Summary of vibrationally mediated photodissociation dynamics studies of H_2O in the first absorption band ($A^1B_1 \leftarrow X^1A_1$). The H_2O states are labeled using notation $|mn^{\pm}k\rangle$, where *m* and *n* are the number of quanta in the OH local mode stretches and *k* is the number of quanta in the bend (if any). Excess energy refers to the total excitation energy above D_0(H-OH) = 5.118 eV (41280 cm^{-1}). In some studies, H_2O is excited in the Franck-Condon forbidden region, i.e. substantially below the saddle point on the A^1B_1 PES, which is located some 16000 cm^{-1} above D_0. OH populations are normalized to the sum of OH(v=0) + OH(v=1).

classic $v_{OH} = 4$ studies of H_2O. As a result, one can further explore how photolysis dynamics depend on the initial wavefunction projection on the upper surface for comparable energies, specifically probing nascent OH product state distributions. Thirdly, as all three of these $v_{OH}=2$ overtone states are sufficiently bright for vibrationally mediated photogragmentation, the influence of wave function symmetry (*gerade* vs. *ungerade*) on the photodissociation dynamics can be directly tested. Finally, as a somewhat more practical consideration, these monomer photodissociation results provide essential background for interpreting vibrationally mediated spectroscopy and dynamics of water containing clusters currently under investigation.[15]

The organization of this paper is as follows. Key experimental details relevant to the present work are discussed in Sec II, followed in Sec III by quantum state resolved fragmentation results for H_2O excited to a series of $v_{OH}=2$ vibrational levels. These distributions are analyzed and discussed in Sec IV, and interpreted in the context of simple QM models for the fragmentation event. The major conclusions are summarized in Sec V.

3.2 Experimental Technique

The essential experimental approach has been described in previous studies from this laboratory,[10,16] and builds on powerful vibrationally-mediated dissociation methods pioneered by Andresen and Crim.[6,7,17] Water molecules are excited into specific rovibrational intermediate states with direct overtone pumping and then selectively photolyzed with 193 nm ultraviolet radiation. This excimer photolysis wavelength is close to optimal for Franck-Condon excitation of the outermost lobe of the wavefunction in the H_2O A←X absorption band, which therefore suppresses UV absorption by unexcited water molecules present in the expansion by several orders of magnitude. The translational, vibrational, and rotational states of OH fragments are

probed with laser induced fluorescence, providing information on the forces breaking the molecule apart during the photodissociation process. Experimental details relevant to the current study are briefly summarized below.

All experiments utilize a supersonic expansion of 1% of H_2O in a monoatomic carrier gas (He or Ar) at a total stagnation pressure of 50 Torr (1 Torr = 1.33322 mbar) through a pulsed slit valve (4 cm × 125 μm, 10 Hz, 500 μs pulse duration). Even under these mild supersonic expansion conditions, H_2O cools down almost entirely into the lowest rotational states allowed by the nuclear spin statistics, $J_{K_aK_c} = 0_{00}$ (para) and 1_{01} (ortho), in a 3:1 ratio. The jet-cooled molecules are intersected 2 cm downstream with an infrared laser beam (5 ns pulse duration, 0.25 cm^{-1} bandwidth), where the partial H_2O and total jet densities are 2×10^{13} #/cm^3 and 2×10^{15} #/cm^3, respectively. The IR laser can deliver up to 30 mJ/pulse to the jet region in a 5 mm^2 beam area. For a spectral pulse width of 0.25 cm^{-1}, this is sufficient to drive stronger v_{OH}=2 water overtone transitions nearly into saturation, resulting in vibrationally excited water densities approaching 10^{12} #/cm^3. The long path length nature and slower 1/r density drop off of the slit expansion permits laser excitation, photolysis and detection to occur efficiently over a much larger interaction region than would be accessible in a pinhole supersonic expansion geometry.

The IR laser (pump) pulse is followed in time by a counter-propagating ArF excimer laser (photolysis) pulse at 193 nm, delayed by approximately 20 ns from the pump. Typical photolysis laser energy in the intersection region is 1 mJ/pulse, with a 10 mm^2 cross section in the jet intersection area. Based on an estimated UV absorption cross-section of $\approx1.8\times10^{-21}$ cm^2/# [18] for ground state water molecules, a relative photodissociation probability of 2×10^{-5} is predicted for IR unexcited species. Empirically, we observe that for the strongest H_2O transitions in v_{OH}=2, the photodissociation signal is increased by 10^2–10^3 due to vibrationally-mediated enhancement

at 193 nm. Both the vibrationally-mediated and direct 193 nm photolysis signals scale linearly with the excimer laser power, indicating that multi-photon processes and saturation effects are of negligible importance for the photolysis laser.

Fluorescence from the OH fragments is detected on the $A^2\Sigma \leftarrow X^2\Pi$ v=1←0, 0←0 and 1←1 bands of OH. The probe radiation is produced by a frequency doubled dye laser (< 0.1 cm^{-1} bandwidth, Rhodamine 590) pumped by a frequency doubled Nd:YAG laser. The probe laser pulse (5 ns duration) is delayed by ≈ 20 ns from the photolysis pulse. To discriminate between vibrationally-mediated and direct 193 nm photolysis events, the pump laser is operated at half the repetition rate, with the laser off and on triggers subtracted to generate a background-free IR-induced signal. To minimize saturation effects, the UV probe laser power is maintained well below 25 μJ/pulse for v=0←0 /1←1 bands (< 90 μJ/pulse for the v=1←0 band) in an unfocused beam size of 30 mm^2 area that overfills both pump and photolysis beams. This results in partial saturation effects (< 20%) for the strongest OH lines, which are explicitly corrected by normalizing with respect to a reference spectrum of collisionally thermalized OH. The thermalized OH sample is obtained under identical probe laser conditions by photolyzing a flowing 1-2 Torr mixture of N_2O, CH_4 and Ar through the vacuum chamber. Delays of >500 μs between the photolysis and probe pulses translate into over 3000 hard-sphere collisions, which ensures complete thermalization. By way of contrast, densities and time delays selected for the actual photolysis studies correspond to fewer than 0.01 collisions of the nascent OH species.

The OH fluorescence is collected through an f/1 CaF_2 elliptical lens with a PMT positioned at right angles with respect to the supersonic expansion and collinear laser propagation axis. The pump and probe lasers propagate collinearly through the slit jet expansion, and are linearly polarized along the expansion axis. The OH fluorescence signal is sampled with

a boxcar integrator, with scattered light attenuated by a 295 nm long pass and UV band-pass (UG-5) filters positioned in front of the PMT. Overall photon collection efficiency is a few percent, typically yielding 10^4-10^5 signal photons per laser pulse with all three lasers present. Laser powers, gas pulse intensities, and reference photoacoustic spectra are stored for normalization, diagnostics, and frequency calibration purposes. The detection efficiency for OH is estimated from signal-to-noise resulting from 193 nm dissociation of H_2O. With the enhanced path length, density and collection volume due to the slit expansion, detection sensitivities below 5×10^5 OH molecules per quantum state are routinely obtained.

The relevant spectroscopy for the LIF detection of nascent OH product is as follows. Each ro-vibrational level of the ground electronic state of OH ($^2\Pi$) is split into two spin-orbit components, $F_1 \equiv {}^2\Pi_{3/2}$ and $F_2 \equiv {}^2\Pi_{1/2}$. Each spin-orbit level is further split into two closely-spaced Λ-doublets (A' and A''), which, in the high-J limit, can be correlated with the unpaired electron p-orbital lying in or perpendicular to the plane of rotation. The energy levels are labeled by ***J*** (total angular momentum), overall parity, ***N*** (total angular momentum excluding spin), symmetry with respect to the reflection through the plane of rotation ($A' \equiv \Pi^+$ and $A'' \equiv \Pi^-$), and additionally with spectroscopic *e/f* labels. For example, in this notation, ${}^2\Pi_{3/2}{}^+(5)$ refers to a state with $N = 5$ in F_{1e} manifold with A' reflection symmetry, with rotational branches of the $A^2\Sigma(v')\leftarrow X^2\Pi(v'')$ bands labeled using notation $\Delta N_{F'F''}(N'')$, e.g. $Q_{21}(3)$. To achieve high oversampling in the data set, all 12 rotational branches with the exception of S_{21} are used in the data analysis, with each spin-orbit and Λ-doublet level independently probed on at least two branches.

3.3 Results and Analysis

Figure 3.1 displays a sample action spectrum of jet-cooled H_2O between 7205 and 7310 cm^{-1}, obtained by tuning the probe laser to the top of the OH $Q_{11}(2)$ probe transition and scanning the IR pump laser frequency. All features in the spectrum result from vibrationally-mediated dissociation of quantum state-selected H_2O in the jet cooled expansion. The lines in this spectral range are therefore due to the transitions out of the lowest nuclear spin states ($J_{K_aK_c}$ = 0_{00} and 1_{01}) of H_2O, into rotational levels belonging to the $|02>^-$ ($\equiv\nu_1+\nu_3$ in normal mode representation) and $|02>^+$ ($\equiv 2\nu_1$) vibrational modes. Throughout this paper, we will be using the $|mn^{\pm}k>$ notation[9] for H_2O vibrational states, where m and n represent local mode stretching quanta,[19] and k (omitted for k = 0) represents the quanta in the HOH bend. The strongest band, $|02>^-$, is of A-type (i.e. $\Delta K_a = 0$, $\Delta K_c = \pm 1$) and can therefore access 0_{00}, 1_{01}, 2_{02} and 2_{20} rotational levels (the $2_{20}\leftarrow 1_{01}$ transition lies outside the frequency range shown in Fig. 3.1). The corresponding $|02>^+$ band is of B-type (i.e. $\Delta K_a = \pm 1$, $\Delta K_c = \pm 1$); it is an order of magnitude weaker and accesses a different subset of rotational levels: $1_{11}\leftarrow 0_{00}$, $2_{10}\leftarrow 1_{01}$, and $2_{12}\leftarrow 1_{01}$. Lines in the action spectrum labeled with asterisks are straightforwardly assigned to $|02>^-$ transitions from incompletely cooled H_2O 1_{10} rotational state (e.g., the transition at ≈7300 cm^{-1} is $2_{11}\leftarrow 1_{10}$). Such "hot" transitions can be purposely enhanced by less efficient rotational cooling in pure He diluent vs. Ar expansions. Approximately 300 cm^{-1} to the red of these $|02>^+$ and $|02>^-$ bands, another two weak groups of lines can be assigned to combination bands of symmetric and asymmetric stretch fundamentals with two quanta of bending excitation, $\nu_1+2\nu_2$ and $\nu_3+2\nu_2$ in normal mode notation, and referred to in local mode notation as $|01^-2>$ and $|01^+2>$. Finally, an extremely weak band (down in intensity by 400 compared to $|02>^-$) due to $|11>^+$ is observed at

around 7400 cm^{-1}, corresponding to the overtone of the asymmetric OH stretch ($2v_3$), but still accessible with quite respectable S/N ≈ 10 in the slit jet apparatus.

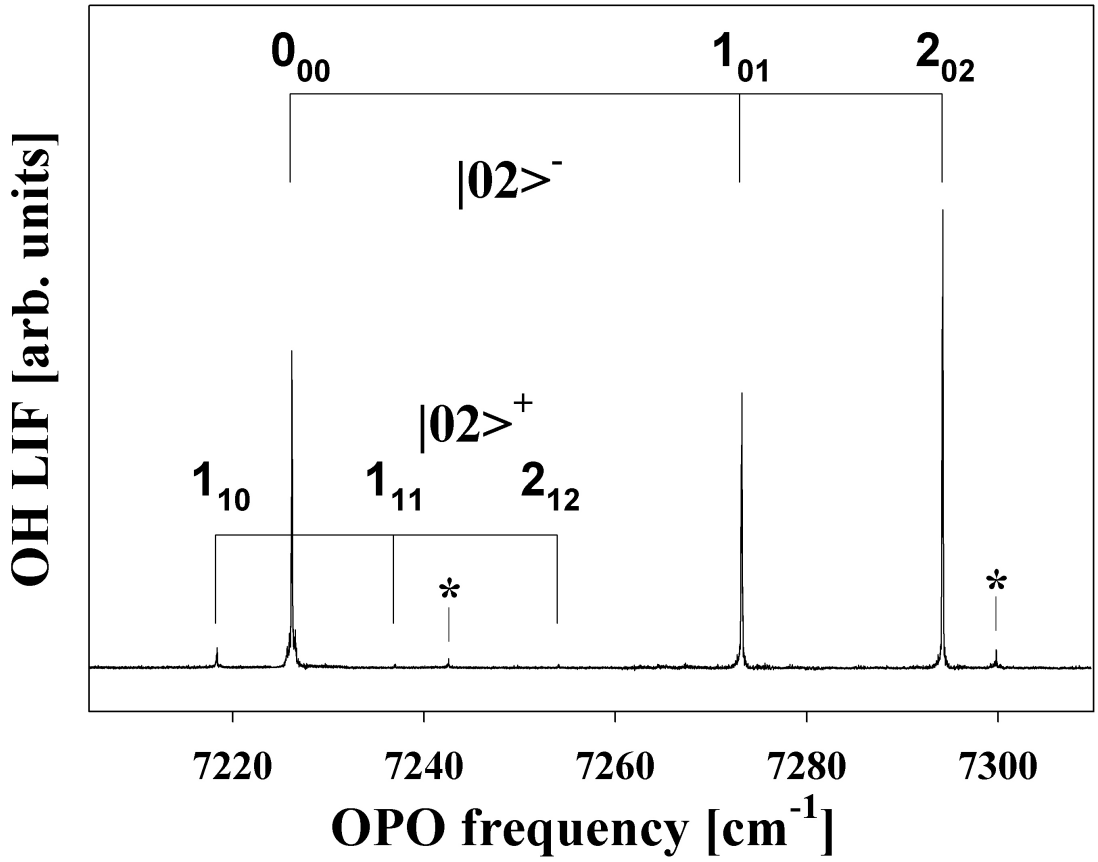

Figure 3.1 Sample action spectrum obtained by scanning the IR probe laser over H_2O absorption lines within the v_{OH}=2 vibrational manifold. The probe laser is fixed on the v=1←0 $Q_{11}(2)$ line of OH. Transitions from $J_{K_aK_c} = 0_{00}$ and 1_{01} states of H_2O into rotational levels of $|02>^-$ and $|02>^+$ vibrations are observed in the displayed spectral range. Transitions from incompletely cooled rotational levels of $|02>^-$ state (such as $J_{K_aK_c} = 1_{10}$) are marked with asterisks. The relative intensities of peaks in the action spectrum depend on: i) relative populations of H_2O states; ii) state-to-state infrared absorption cross-sections; iii) UV photolysis cross-sections; iv) photodissociation quantum yields of OH into the $^2\Pi_{3/2}^-(N=2)$ probe state.

Access to this broad range of intermediate states permits one to investigate photodissociation dynamics from a family of energetically similar but physically quite distinct vibrational intermediates. For example, one might expect photodissociation of H_2O via excited bending states ($\nu_2 > 0$) to produce hotter OH rotational excitation.[5,9] Similarly, the $|11>^+$ state has its OH stretch excitation more equally distributed between the two equivalent OH bonds; based on the spectator model, therefore, one might predict significantly more OH(v=1) vibrational excitation from $|11>^+$ photodissociation compared to either $|02>^+$ or $|02>^-$ states. These effects will be discussed in more detail below. In particular, we find both qualitative successes and failures of these spectator model predictions at such low polyad numbers.

By fixing the IR pump laser on a specific feature in the H_2O action spectrum and scanning the probe laser, a fluorescence excitation spectrum of the OH photofragments is obtained. Figure 3.2 shows sample portions of such spectra extending over the $R_{11}+R_{21}$ branches in the v=1←0 band of OH. Both branches probe the $^2\Pi_{3/2}{}^+(N)$ rotational manifold of OH. The top panel corresponds to photodissociation via the rotationless $|02>^-$ 0_{00} intermediate state. The lower two panels, $|02>^-$ 2_{02} and $|01^-2>$ 2_{02}, correspond to progressively increasing amounts of rotational and bending excitation, respectively. Note that the relative intensities of individual OH rotational transitions are quite different for these three intermediate states of H_2O. The $|01^-2>$ 2_{02} state of H_2O, which has both bending and rotational degrees excited, clearly results in the most energetic distribution. To verify that the populations are indeed nascent, the stagnation pressure and the photolysis-probe delay have been increased by more than an order of magnitude without affecting the relative intensities in the spectrum. This is fully consistent with only ≈ 1% probability of hard-sphere collisions between the OH photolysis fragment ($\upsilon_{OH} \approx 1.2\times10^5$ cm/s) and the carrier gas expected for the present experimental conditions.

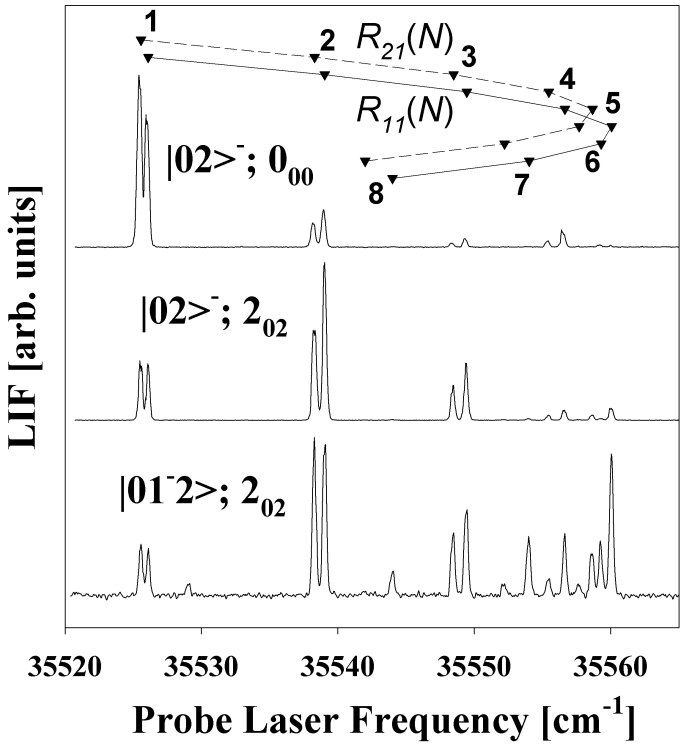

Figure 3.2 Sample $^2\Sigma(v=1)\leftarrow{}^2\Pi(v=0)$ LIF probe spectra of OH photofragments. Only the R_{11} and R_{21} branches are displayed, probing $^2\Pi_{3/2}{}^+(N)$ levels of OH. From top to bottom, the intermediate H_2O state systematically changes from a) $|02>^-$ with no rotation, b) $|02>^-$ with two quanta of rotation, and, finally, c) two quanta of both rotation and bending excitation. Note the increase in photofragment rotational excitation, due to projection of H_2O bending and rotational motion onto the asymptotic states of OH.

From probe scans extending over 11 branches characteristic of the OH $A^2\Sigma\leftarrow X^2\Pi$ vibrational bands (all possible branches except S_{21}), the relative populations of *all* rotational, spin-orbit, and Λ-doublet states of OH can be obtained for a given rovibrational intermediate state. Complete OH fluorescence excitation spectra have been recorded for strong $|02>^-$, $|02>^+$, and $|01^-2>$ intermediate vibrational levels of H_2O, for each of several rotational states accessible out of $J_{KaKc} = 0_{00}$, 1_{01}. Due to the 200 fold weaker[20] IR cross sections relative to $|02>^-$**,** only a limited set of populations in $^2\Pi_{3/2}{}^{\pm}$ OH manifolds have been examined for excitation into $|11>^+$ state. To enhance the statistics, each spectrum is collected 2-5 times and analyzed independently. Lines in all spectra are integrated and the resulting areas least-square fitted using OH populations

OH state	N	$\|02\rangle^-$ 0_{00}	$\|02\rangle^-$ 1_{01}	$\|02\rangle^-$ 2_{02}	$\|02\rangle^-$ 2_{20}	$\|02\rangle^+$ 1_{10}	$\|02\rangle^+$ 1_{11}	$\|02\rangle^+$ 2_{12}	$\|01^-2\rangle$ 0_{00}	$\|01^-2\rangle$ 1_{01}	$\|01^-2\rangle$ 2_{02}
$^2\Pi_{3/2}{}^+$	1	19.5(6)	11.2(2)	4.29(35)	12.8(16)	0.46(14)	6.93(28)	15.0(13)	6.66(31)	3.20(12)	1.47(29)
	2	2.82(15)	6.48(29)	9.0(5)	3.5(4)	12.7(9)	7.7(9)	2.45(10)	0.63(6)	2.13(26)	3.87(12)
	3	0.57(5)	1.13(33)	2.58(14)	9.6(11)	2.2(5)	2.26(8)	3.5(4)	0.35(4)	0.78(6)	1.76(3)
	4	0.88(9)	0.71(4)	0.61(4)	2.8(9)	0.71(9)	0.74(5)	1.03(14)	2.44(3)	1.17(4)	0.98(4)
	5	0.061(9)	0.27(3)	0.61(2)	0.19(5)	0.58(2)	0.48(2)	0.29(7)	0.32(4)	0.89(14)	2.15(33)
	6	0.12(3)	0.074(10)	0.072(2)	0.37(14)	0.08(2)	0.22(3)	0.28(3)	1.48(11)	0.61(2)	0.78(9)
	7	0.04(1)	0.069(8)	0.072(7)	0.15(8)	0.15(3)			0.64(8)	0.44(2)	0.77(6)
	8			0.032(5)	0.05(3)				0.15(3)	0.19(2)	0.48(2)
	9								0.16(5)		0.20(5)
	10								0.021(5)		0.20(2)
$^2\Pi_{3/2}{}^-$	1	2.01(19)	6.94(34)	12.6(9)	5.9(5)	21.3(19)	11.0(5)	2.4(6)	0.59(13)	3.03(8)	4.0(10)
	2	17.3(4)	11.4(1)	6.63(36)	15.4(3)	4.5(6)	9.7(17)	14.3(8)	5.6(7)	2.14(18)	0.95(6)
	3	11.0(4)	11.2(3)	10.6(6)	10.2(11)	10.7(23)	6.9(19)	6.4(5)	1.99(15)	1.98(3)	1.86(42)
	4	1.65(7)	3.84(17)	7.1(6)	4.3(1)	7.0(10)	6.4(13)	6.7(6)	1.65(16)	4.89(40)	6.6(7
	5	5.0(4)	4.64(18)	2.17(11)	5.9(4)	1.80(11)	2.52(6)	3.90(7)	17.7(13)	11.2(6)	4.19(8)
	6	0.30(2)	1.05(25)	1.80(25)	0.47(9)	0.81(28)	0.78(45)	0.46(6)	1.48(40)	8.30(8)	11.8(5)
	7	0.93(13)	0.73(4)	0.61(3)	0.74(2)	0.095(10)	0.78(4)	2.10(37)	10.5(13)	7.5(8)	5.17(20)
	8	0.34(3)	0.47(3)	0.62(3)	0.21(9)	0.77(17)	0.61(17)	0.19(10)	6.1(16)	6.69(43)	6.20(30)
	9	0.047(9)	0.061(5)	0.20(3)	0.07(2)	0.14(3)	0.32(9)	0.55(20)	0.78(5)	1.3(7	2.85(46)
	10	0.064(4)	0.041(5)	0.046(6)	0.047(8)			0.09(3)	1.23(9)	1.28(21)	0.35(8)
	11			0.035(5)							
$^2\Pi_{1/2}{}^-$	1	0.76(7)	3.23(23)	5.6(5)	0.77(14)	8.6(5)	7.2(19)	1.45(16)	0.18(6)	1.29(19)	1.85(36)
	2	10.7(8)	7.95(60)	3.94(20)	5.4(7)	1.92(24)	7.3(14)	10.6(21)	2.6(8)	1.46(2)	0.85(3)
	3	5.83(26)	7.71(12)	6.3(5)	3.80(15)	6.5(8)	5.8(5)	3.8(6)	0.89(20)	1.25(6)	1.32(1)
	4	1.18(4)	2.32(16)	5.0(5)	2.63(22)	4.01(30)	6.11(31)	4.2(6)	0.88(11)	4.26(39)	5.3(6)
	5	3.34(33)	3.00(12)	1.59(11)	2.6(4)	0.72(5)	1.51(36)	2.4(5)	9.7(12)	7.4(5)	2.1(8)
	6	0.60(7)	1.25(10)	2.42(6)	0.44(5)	2.1(5)	1.81(4)	0.98(11)	1.40(11)	6.6(5)	9.1(8)
	7	0.63(7)	0.55(2)	0.47(4)	0.44(5)	0.17(4)	0.60(8)	1.67(33)	9.3(27)	4.92(19)	3.83(4)
	8	0.31(8)	0.43(3)	0.58(5)	0.24(9)	0.54(29)	0.50(7)	0.20(4)	3.83(26)	4.9(20)	5.2(5)
	9	0.038(2)	0.065(3)	0.17(1)	0.068(5)	0.11(4)	0.23(5)	0.48(15)	0.39(7)	0.82(19)	3.1(9)
	10	0.037(4)	0.055(4)	0.042(7)	0.074(5)				1.6(6)	1.18(37)	0.48(2)
	11									0.25(8)	0.75(7)
	12										0.13(5)
$^2\Pi_{1/2}{}^+$	1	9.25(41)	6.1(4)	2.33(24)	3.35(19)	0.40(19)	3.28(5)	7.4(13)	4.3(8)	2.44(17)	1.2(7)
	2	1.45(14)	3.97(14)	7.5(7	1.52(11)	7.4(18)	5.08(20)	1.61(10)	0.39(3)	1.92(2)	2.30(24)
	3	1.44(21)	1.51(9)	2.11(29)	3.28(13)	1.30(26)	1.85(5)	3.4(12)	0.56(21)	0.40(11)	0.92(6)
	4	1.21(15)	1.02(8)	1.16(15)	2.03(26)	1.22(36)	0.79(6)	0.95(11)	1.11(4)	0.60(6)	0.66(19)
	5	0.18(2)	0.29(2)	0.75(5)	0.25(7)	0.71(16)	0.59(20)	0.52(13)	0.26(5)	0.68(5)	1.47(20)
	6	0.26(3)	0.25(1)	0.15(1)	0.32(4)	0.16(6)		0.38(9)	1.03(24)	0.70(4)	0.77(2)
	7	0.077(19)	0.095(6)	0.18(2)	0.12(1)	0.27(2)		0.11(5)	0.32(5)	0.60(7)	1.13(15)
	8	0.029(5)	0.0087(5)	0.058(11)	0.059(13)			0.10(5)	0.45(8)	0.48(8)	0.57(17)
	9			0.025(5)	0.04(1)				0.34(5)	0.22(2)	0.32(2)
	10			0.017(5)							0.073(6)

Table 3.2 Observed populations of OH rotational, spin-orbit, and lambda-doublet states produced in the vibrationally-mediated 193 nm photolysis of H_2O. The intermediate rovibrational states of H_2O are specified in the title row. The populations are normalized to 100% for each H_2O state. The 2σ uncertainties estimated from comparing populations obtained from independent data runs are given in parenthesis. The fractional uncertainties in the reported populations average to $\langle 2\sigma \rangle = 5\%$.

as adjustable parameters. The required individual rotational transition strengths are taken from Chidsey and Crosley database[21] and small saturation correction factors are explicitly determined

from the reference room-temperature OH spectra on a line-by-line basis. Since all populations are statistically quite overdetermined (each level is probed by up to 3 independent branches), the least-square fitting is extremely robust. Although accidental line overlaps do occur (e.g., $R_{22}(3)$ line is blended with the $Q_{11}(1)+Q_{21}(1)$ doublet in the v=1←0 band) , the low power and relatively high resolution of the probe laser reduce such overlaps to a minimum. The line widths in the recorded spectra are limited by the Doppler broadening with FWHM ≈ 0.3 cm^{-1}, i.e. consistent with the expected OH translational energy release. The fitted populations for OH(v=0) are summarized in Table 3.2, wherein the results and uncertainties are obtained as a weighted average of populations from several independent data runs. OH(v=1) populations are not listed because they were recorded only for a limited subset of states within $^2\Pi_{3/2}{}^{\pm}$ OH manifolds to verify that OH rotational and vibrational distributions are decoupled form each other (see below).

Of particular interest in this work is the fractional branching into OH(v=1) and OH(v=0) products as a function of H_2O rovibrational intermediate states, which are examined in a separate experiment by comparing repeated scans over the $Q_{11}(3)$ line, which probes the $^2\Pi_{3/2}{}^{-}(3)$ level in OH, for the v=1←1 and v=0←0 sub-bands, for a series of intermediate states and range of IR pump powers. Relative transition probabilities for these v=1←1 and v=0←0 sub-bands are taken from[21] Ref 21. This ratio could in principle be further corrected for fractional v=1 vs v=0 population in the initial $^2\Pi_{3/2}{}^{-}$ manifold level. In practice, however, the rotational, spin-orbit and lambda-doublet distributions appear to be strongly uncoupled from the OH(v) vibrational state, despite a clear sensitivity to different intermediate rotational states. For example, figure 3.3 shows a comparison between relative OH(v=1) and OH(v=0) populations in $^2\Pi_{3/2}{}^{\pm}$ manifolds resulting from UV photolysis of $|02>^+ 1_{10}$ and $|11>^+ 1_{10}$ states of H_2O. The lambda-doublet and rotational populations are the same within the experimental precision. Therefore, the nascent

vibrational populations of OH integrated over each manifold can be reliably estimated from comparison of a single rotational line in the $^2\Pi_{3/2}^-$ manifold for v=1←1 and v=0←0 OH transitions (as long as the same rotational state of H_2O is photolyzed). The results of these measurements are listed in table 3.1, put explicitly into context with OH(v=1)/OH(v=0) branching ratios obtained from all vibrationally mediated dissociation studies to date.

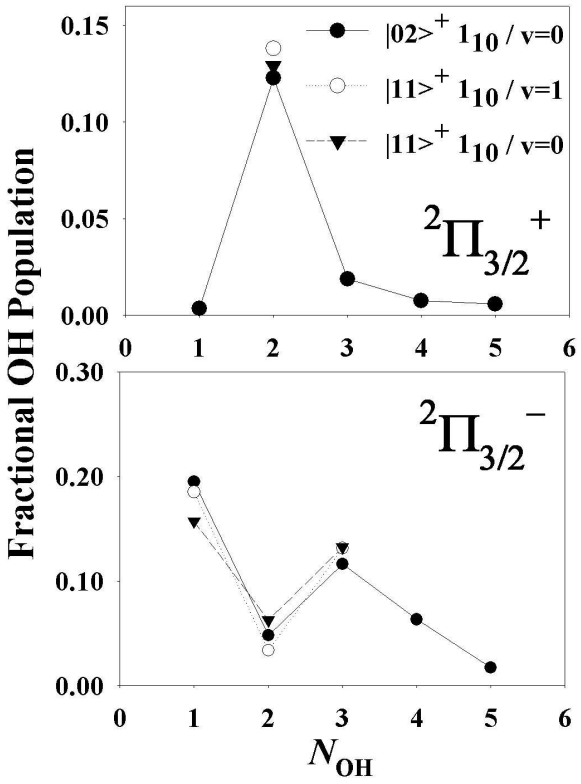

Figure 3.3 A subset of relative OH(v=1) and OH(v=0) populations in $^2\Pi_{3/2}^{\pm}$ manifolds resulting from UV photolysis of $|02>^+ 1_{10}$ and $|11>^+ 1_{10}$ states of H_2O. Strong similarities in the observed distributions support the assumption of decoupling between vibrational and rotational degrees of freedom in OH photofragments (this assumption is used to derive relative final vibrational populations of OH listed in table 3.1).

3.4 Nascent OH Rotational Populations

A particularly striking observation from previous vibrationally-mediated dissociation studies[6 5,7,9,10] has been the presence of strong oscillations in OH nascent populations as a

function of rotational state. Such oscillations in the nascent OH distributions are also quite evident in the present study of the v=2 polyad (table 3.2). By way of example, figure 3.4 displays experimental OH populations vs. *N* for each spin-orbit and Λ-doublet manifolds for

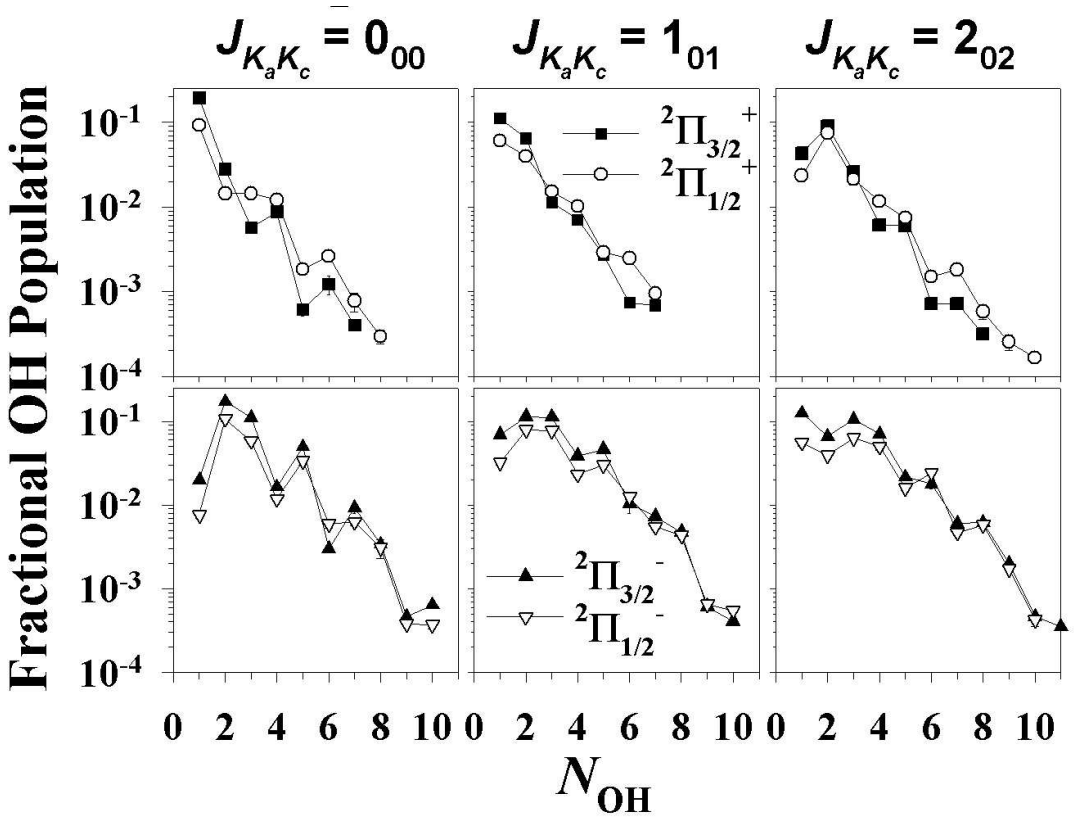

Figure 3.4 Effect of initial $H_2O(|02>^-)$ rotation on the observed OH distributions. The distributions are plotted as a function of *N* for each spin-orbit and Λ-doublet rotational manifolds. The oscillations of populations vs. *N* are pronounced even on the logarithmic scale of the figure. Notice that there is little difference in the populations of the two spin-orbit components ($^2\Pi_{1/2}$ vs. $^2\Pi_{3/2}$) but an appreciable difference between the *A′* and *A″* Λ-doublets. The rotational state of $H_2O(|02>^-)$ changes from 0_{00} to 1_{01} to 2_{02} from left to right, which has the effect of slightly increasing the average rotational energy of OH fragments.

photodissociation of $H_2O(|02>^-)$ in a series of intermediate rotational states, which indicate clear oscillations even on a logarithmic scale. Interestingly, these trends are remarkably similar for the two spin-orbit components ($^2\Pi_{1/2}$ and $^2\Pi_{3/2}$) for each lambda-doublet manifold, whereas appreciably larger differences are apparent between the *A′* vs. *A″* Λ-doublets. It is worth noting

that the population data for different spin-orbit manifolds are obtained from entirely independent rotational branches; the systematic agreement between $^2\Pi_{1/2}$ and $^2\Pi_{3/2}$ traces, therefore, provides additional support for the high S/N and reproducibility of our data.

The origin of these oscillations in OH population [1,3,5,8,10,12,22] has been thoroughly discussed, and arises from quantum mechanical interference between the various OH outgoing spin-orbit and lambda-doublet product channels. As a simple zeroth order prediction, this would suggest a much smoother distribution when summed over all interfering channels. This prediction is tested in figure 3.5, which displays OH photofragment distributions resulting from photodissociation of H_2O via $|02>^-$ $J_{KaKc} = 2_{02}$, nicely confirming the interference nature of the photodissociation process. Specifically, while populations within a given individual spin-orbit/Λ-doublet manifold (figure 3.5a) are highly nonmonotonic functions of J_{OH}, the sum over these manifolds (figure 3.5b) is much more consistent with a smooth rotational distribution, arising from largely complete cancellation between the Λ^+ and Λ^- doublets contributions. This behavior is echoed in distributions for each of the intermediate rotational states of water from this study, as can be verified from a detailed investigation of table 3.2.

The theoretical framework developed by Balint-Kurti, Schinke and others [1,3,5,8,10,12,22] to explain such trends is that the OH nascent state distribution reflects a Franck-Condon like projection of the intermediate state wavefunction on the upper potential surface, followed by wave packet evolution in the exit channel out toward asymptotic products. Based on this picture, one would expect a relatively strong dependence of OH(v) populations on H_2O intermediate vibrational state, and, conversely, OH rotational state populations relatively insensitive to intermediate state vibrations of the same local mode character. Striking support for the former assertion is evident in figure 3.6, which shows nascent populations for the $^2\Pi_{3/2}{}^{\pm}$ manifolds,

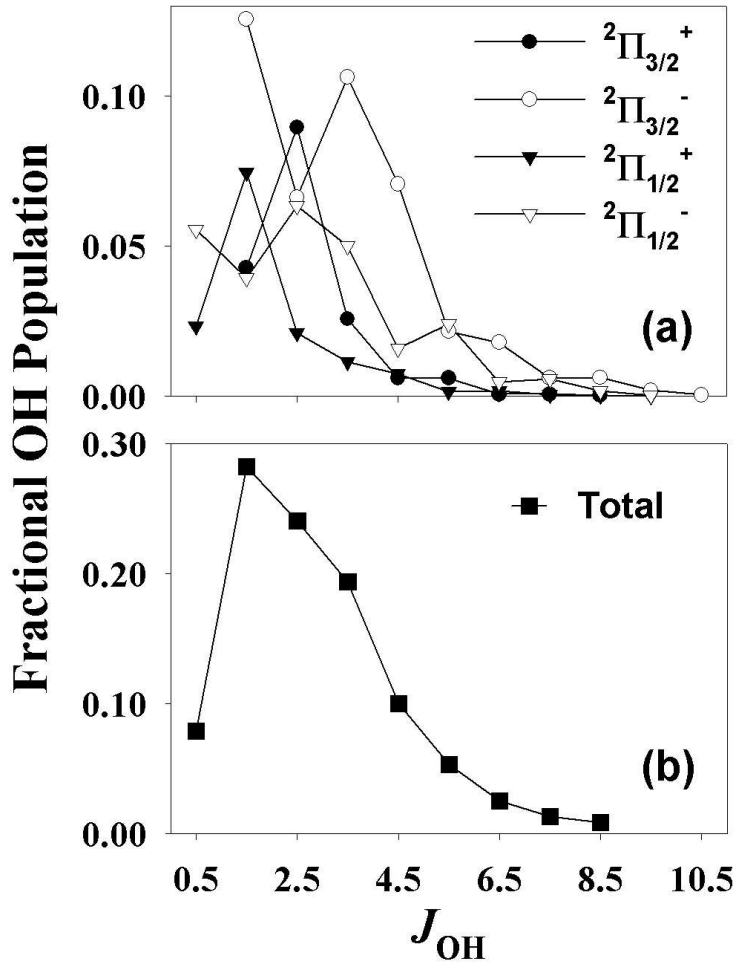

Figure 3.5 OH photofragment distributions resulting from photodissociation of $H_2O(|02>^-)$ in 2_{02} rotational state plotted as a function of J_{OH}. While the populations within the individual spin-orbit and Λ-doublet manifolds (top panel) strongly oscillate with J_{OH}, the *total* population (bottom panel) is much smoother reflecting the interference nature of the photodissociation.

obtained for a progression of increasingly OH stretch excited polyad states (e.g. $|0n>^-$, n=1-5) out of $J_{KaKc} = 0_{00}$. Although the excess energies for the H_2O states in figure 3.6 vary by more than a factor of two (table 3.1), the *N*-dependence of the distributions within a given spin-orbit and Λ-doublet manifold remains nearly identical. Photodissociation of H_2O from a series of vibrational states with non-zero angular momenta yields results that follow similar trends, although subtle differences between the OH distributions start to appear already at J=1.[10]

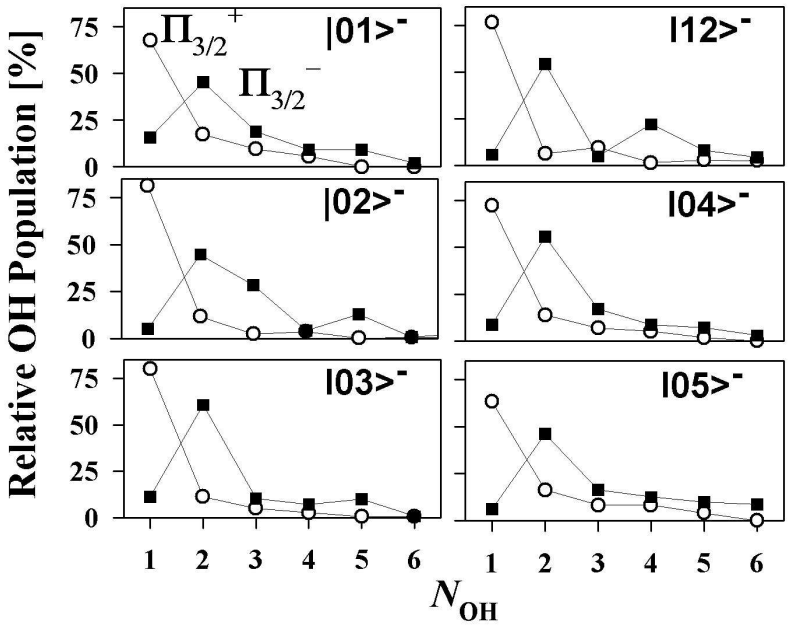

Figure 3.6 Populations of $^2\Pi_{3/2}^{+}$ (open circles) and $^2\Pi_{3/2}^{-}$ (filled squares) states of OH in photodissociation of different vibrational states (v_{OH} = 1 to 5) of H_2O in $J_{KaKc} = 0_{00}$. Although the photodissociation is probed at very different excess energies (see Table 3.1), the gross features of the rotational distributions are strikingly similar, due to the good separability of vibrational and rotational time-scales for the motion.

In the context of such a Franck-Condon picture, one would expect overall rotation of the H_2O prior to photodissociation to result in warmer OH rotational state distributions, as is indeed clearly evident in figure 3.4. Vibrational pre-excitation of HOH *bending* states would imply even stronger overlap on final OH rotation wave functions, and thus a Franck-Condon picture for photolysis would predict a much hotter rotational distribution. This prediction is directly confirmed in figure 3.7, which compares rotational populations resulting from the photolysis of H_2O in $|02>^-$ and $|01^-2>$ states, with the latter clearly resulting in a much more rotationally energetic OH distribution. However, in spite of large differences in populations, a more detailed inspection reveals clear similarities in the oscillatory structure. For example, the $^2\Pi^-$ distributions for $|02>^- 0_{00}$ and $|01^-2> 0_{00}$ intermediate states (figure 3.7, lower panels) exhibit local maxima (at N = 2, 5, 7) and minima (at N = 1, 4, 6, 9), despite quite clear differences in the overall smoother

trend. Such behavior is in fact consistent with a Franck-Condon picture, reflecting a separability of the rotational-bending wavefunction for the H_2O intermediate state. Specifically, the rotational wavefunction is responsible for the fast oscillations, while the bending wavefunction dictates the overall shape of the OH distribution.

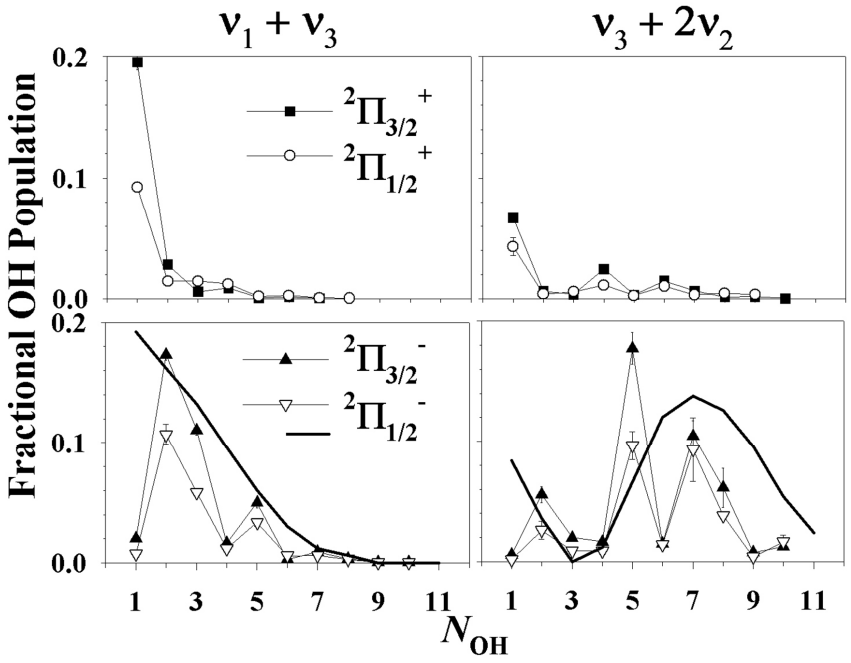

Figure 3.7 Effect of H_2O bending excitation on the OH rotational distribution. The distributions are plotted as a function of *N* for each spin-orbit and Λ-doublet rotational manifold. The panels on the left and right show data for $|02>^-$ and $|01^-2>$, respectively. Although the bending excitation of H_2O significantly increases the OH rotation, the non-monotonic structure on top of the distributions is quite similar. The solid curves in the bottom panels correspond to the Franck-Condon projections of the H_2O bending wavefuntions on the OH rotational states.[9]

More quantitatively, one can model this second contribution by projecting the HOH bending wavefunction onto the asymptotic OH rotational states.[1,5,9] This leads to a distribution proportional to $\sin^2\left(j\gamma_e + (-1)^k \frac{\pi}{4}\right)\phi_k^2\left(\frac{j}{\overline{m}\,\omega_{HOH}}\right)$, where ϕ_k is the HOH bending wavefunction for *k* quanta of excitation, *j* is the rotational angular momentum of OH fragment, γ_e is the

equilibrium bond angle in H_2O, ω_{HOH} is harmonic frequency for the bending motion, and $\overline{m}$ is the effective reduced mass for the bending motion.[9] figure 3.7 shows the non-oscillatory part of the Franck-Condon distribution for k=2 compared with the experimental data obtained for the $|01^{-}2>$ state of H_2O. The data are in excellent agreement with this simple model, especially in reproducing the slow nodal structure around N=3 and a secondary maximum at N=7.

3.5 Nascent OH Spin-Orbit and Lambda-Doublet Distributions

As shown above, spin-orbit and lambda-doublet states have already proven important in generating quantum interference effects between outgoing exit channels. However, they also provide additional dynamical information on the photolysis event. figure 3.8 shows the population ratio of the two spin-orbit components, $[^2\Pi_{3/2}(N)]/ [^2\Pi_{1/2}(N)]*N/(N+1)$, and its variation with N and Λ-doublet symmetry, where the $N/(N+1)$ coefficient includes the $2J+1$ space degeneracy. In the statistical regime, $[^2\Pi_{3/2}(N)]/ [^2\Pi_{1/2}(N)]*N/(N+1)$, should eventually reach unity for high N. Indeed, this statistical limit is what was observed in early 157 nm photolysis of room temperature H_2O[11] as well as 193 nm photolysis of H_2O in 0_{00} $|01>^{-}$ state.[6,8] However, as shown in figure 3.8, this is not in good agreement with the current 193 nm photolysis study of H_2O in the v=2 polyad, where sizable N-dependent deviations from unity are evident out at high rotational levels with high S/N. Supporting results were also observed in previous photodissociation studies of H_2O in the v_{OH}=3 polyad, which revealed sizable deviations from the statistical limit.[10] At the present time, there is no theoretical understanding for the predominance of $\Pi_{3/2}$ states in the asymmetric (A'') manifold and $\Pi_{1/2}$ states in the symmetric (A') manifold. In fact, the data might suggest a trend *away* from statistical behavior in

nascent spin orbit distributions as a function of H_2O polyad number, though this issue awaits more detailed theoretical investigation.

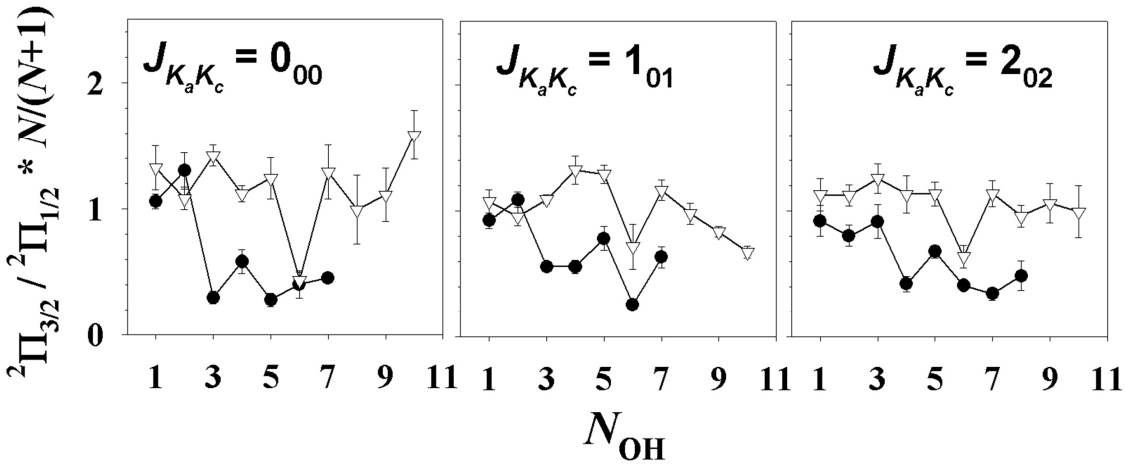

Figure 3.8 Relative populations of OH spin-orbit states in photodissociation of $H_2O(|02>^-)$. Triangles and filled circles represent the ratios $[^2\Pi_{3/2}(N)]/ [^2\Pi_{1/2}(N)]*N/(N+1)$ for A" and A' Λ-doublets, respectively. The $N/(N+1)$ multiplier accounts for the $2J+1$ space degeneracy; the high-temperature statistical limit would correspond to $N/(N+1) = 1$.

The Λ-doublet ratio of asymmetric (A'') to symmetric (A') OH product states has been of special dynamical interest. In the limit of zero spin-orbit interaction (which is valid for sufficiently high OH rotational levels), the electronic transition symmetry in H_2O should strongly favor production of A'' states of OH. A rapid increase in the [OH(A'')]/[OH(A')] ratio with N has indeed been observed in several previous studies of photodissociation of H_2O and its general shape is now reasonably well understood, at least in the absence of the parent rotation.[11,16] The Λ-doublet ratios from the present study for two intermediate vibrational states ($|02>^-$ and $|01^-2>$) and several rotational states of H_2O are shown in figure 3.9 (note the logarithmic axis). In interesting contrast to the OH rotational energy distribution, which strongly depends on the parent bending state, the [OH(A'')]/[OH(A')] ratio appears to be remarkably insensitive to the

vibrational state of H_2O. The magnitudes and phases of oscillations in this ratio are now very close agreement for $|02>^-$ and $|01^-2>$, as well as for all pairs of H_2O rotational states considered. This is again consistent with a simple Franck-Condon separability of bending and rotational wavefunctions; the bending wavefunction influences only the *N* dependent features of the OH distribution and not preferential formation of specific parity levels.

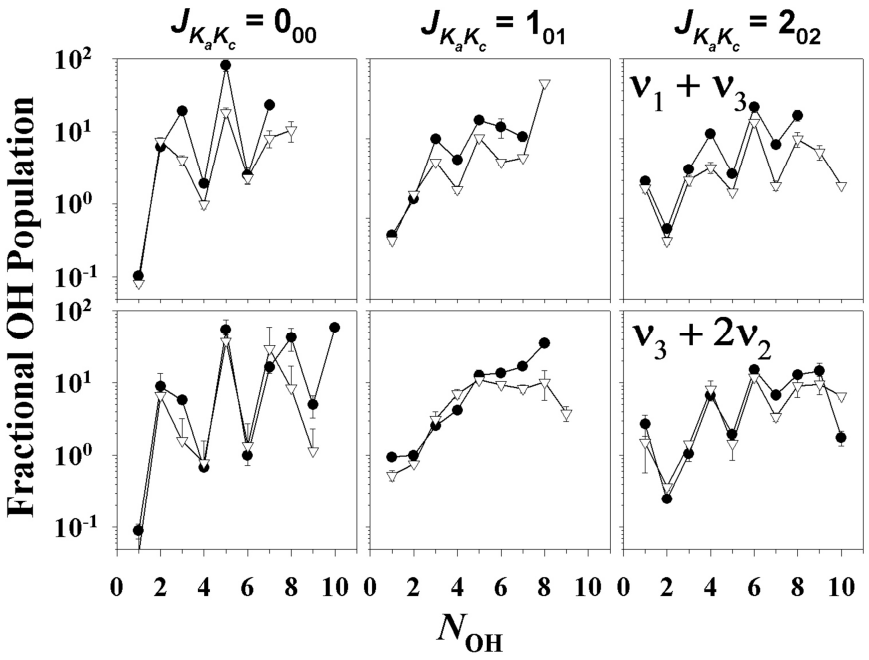

Figure 3.9 Relative populations of OH Λ-doublets in photodissociation of H_2O. The top three panels are for 0_{00}, 1_{01}, and 2_{02} rotational states of $H_2O(|02>^-)$ and the bottom panels are for the same rotational states of $H_2O(|01^-2>)$. Filled circles and open triangles represent $^2\Pi_{3/2}^-(N)$ / $^2\Pi_{3/2}^+(N)$ and $^2\Pi_{1/2}^-(N)$ / $^2\Pi_{1/2}^+(N)$, respectively. The ratios are quite similar for the two vibrational states but are sensitive to H_2O angular momentum .Faster water rotation results in a smaller difference between the positive and negative OH Λ-doublets.

As a final note, these results make for interesting comparison with previous 157 nm photolysis studies of room temperature H_2O.[11], which exhibit a surprising *absence* of any Λ-doublet inversion ratio. It has been previously argued that this "smearing out" of the Λ-doublet

population inversion for room temperature samples may be the result of orbital mixing caused preferentially by out-of-plane rotational motion of H_2O.[11,16] Indeed, the data in figure 3.9 shows clear Λ-doublet inversion for the series of $J_{K_aK_c} = 0_{00}$, 1_{01}, 2_{02} H_2O rotational states, which would correspond classically to increasing *in-plane* vs out-of-plane rotational versus motion. However, close examination of table 3.2 indicates that similar Λ-doublet inversion behavior is observed for photolysis from both 2_{02} and 2_{20} levels (i.e. the two classical extremes of in-plane and out-of-plane rotational motion), suggesting that such an orbital mixing effect is not important, at least for small angular momentum values.

3.6 OH Vibrational Distributions

A particularly relevant aspect of this study is the ability to investigate vibrational state symmetry effects on H_2O photodissociation dynamics, as well as the potential breakdown of the spectator model in vibrationally mediated photolysis events. First of all, as noted in Sec II, previous studies have focused on a subset of high overtone vibrations, specifically antisymmetric (i.e. *ungerade*) states and typically with strongly local mode character due to anharmonic limitations on vibrational overtone intensities. At the v_{OH}=2 overtone level, these anharmonic effects are less important, yielding sufficient oscillator strength for probing photolysis events from each member of the polyad, $|02>^+$, $|11>^+$, and $|02>^-$, including both *gerade* and *ungerade* states. Secondly, v_{OH}=2 is the lowest polyad with sufficient rearrangements of vibrational quanta to distinguish between cleaved and surviving bonds in the photolyzed H_2O. This offers a unique opportunity to test the spectator paradigm down at low levels of vibrational excitation. It is worth noting that predictive understanding of such effects at low vibrational quanta on chemical reaction dynamics is particularly relevant, for example, in thermal models of combustion

phenomena. Finally, despite the 50% weaker initial vibrational excitation in the H_2O intermediate state, 193 nm photolysis of these first overtone $|02>^+$, $|11>^+$, and $|02>^-$ levels sample comparable upper state energies as previous studies of $|04>^-$ and $|13>^-$ states by Vanderwal *et al.* [7] As a result, this allows the present study to focus selectively on the influence of symmetry and intramolecular nodal distribution on the photolysis dynamics.

Inspection of Table 3.1 reveals two important facts. The first observation is that photodissociation of *gerade* $|11>^+$ and $|02>^+$ states produces substantially more vibrational excitation in OH compared to that of the *ungerade* $|02>^-$ state. Specifically, one finds significant levels of vibrational excitation from both $|02>^+$ and $|11>^+$, with [OH(v=0)]:[OH(v=1)] = 0.63(3):0.37(3) and 0.47(5):0.53(5), respectively; these results are in clear contrast to nearly quantitative 98% yield of OH(v=0) from $|02>^-$. This observation is consistent with time-dependent wavepacket simulations,[23,24] which predict significant differences in the photodissociation dynamics of *ungerade* and *gerade* states of H_2O. Specifically, wavepackets prepared from *ungerade* states are predicted to evolve initially along the asymmetric stretch coordinate, whereas *gerade* state wavepackets have an appreciable initial component along the symmetric stretch. This difference shows up as a 19 fs recurrence in the wavepacket autocorrelation function, which is found for all *gerade* states but does not occur for *ungerade* ones.[24] Physically, displacement on the upper surface along the symmetric stretching coordinate corresponds to motion *perpendicular* to the minimum energy path. Such motion would predict enhanced vibrational excitation of the surviving OH bond, in good agreement with the current experimental observations.

A second, more subtle observation is that the OH vibrational distributions from $|11>^+$ and $|02>^-$ cannot be fully explained by adiabatic conservation of the vibrational nodal pattern in the

undissociated H_2O bond. Indeed, this is the essence of the simple spectator model, which worked so beautifully for photodissociation of the higher $|04\rangle^-$, $|13\rangle^-$, $|03\rangle^-$, and $|12\rangle^-$ states of H_2O.[1,7,10] Such a model assumes that the region of the excited PES sampled by the photolysis is characterized by weak interactions between the two OH bonds. Although the excess energies utilized in the current study fall in the expected range of validity of the spectator model,[24] the level of agreement with observed product OH vibrational excitation is clearly mixed. On one hand, the fractional yield of OH (v=1) from dissociation of $|11\rangle^+$ (53±5 %) is significantly higher than that from $|02\rangle^-$ (2±1 %), in qualitative agreement with expectation. However, there is only a minimal difference (≈1.4 fold) between [OH(v=1)]/ [OH(v=0)] product ratios resulting from photolysis of $|11\rangle^+$ and $|02\rangle^+$ states. This is in striking contrast with the $|13\rangle^-$ state behavior, which at 218.5 nm exhibited an order of magnitude more OH(v=1) than $|04\rangle^-$.[7] Even more to the point, there is an order of magnitude difference in OH(v=1,0) photolysis behavior between $|02\rangle^+$ and $|02\rangle^-$ states, which is in clear contradiction to predictions from the spectator model.

To help identify the physical origin of these discrepancies, we have explicitly calculated 2D wavefunctions for the bound and continuum OH (R_1, R_2) stretching states of H_2O. Specifically, the ground state wave functions are obtained from matrix diagonalization of a 2D distributed Gaussian basis set on the Sorbie-Murrell potential energy surface,[25] with the HOH bend angle fixed at 104.5 degrees and eigenvalues converged by successively increasing basis set size. Similarly, the excited state wave functions are obtained by matrix diagonalization on the Staemmler-Palma potential surface,[26] for a uniformly distributed grid of Gaussian basis functions over the Franck-Condon region and extending ($r_{max} \approx 10\ a_0$) out into the entrance (HO+H) and exit (H+OH) channels. Out at r_{max}, the upper state eigenfunctions approximate the behavior of true continuum wave functions, whose asymptotic OH(v) state can be readily identified by the

nodal pattern. Such a matrix procedure necessarily yields a discrete representation for the upper state; however, the state density is sufficiently high that adjacent energy eigenfunctions are nearly identical in the overlap region. This permits estimation of Franck-Condon factors appropriate to a finite bin of photolysis energy, and for wave functions correlating asymptotically with a specified OH(v).

The resulting lower state wave functions for $|02\rangle^+$ and $|02\rangle^-$ states of H_2O are shown in figure 3.10. Also shown are sample symmetric and antisymmetric upper state wave functions correlating asymptotically with OH(v=0) and OH(v=1), respectively. As anticipated, the upper state wavefunctions are confined to the saddle region on the upper PES energetically accessible via 193 nm excitation from v_{OH}=2; for the purposes of visualization, this area is enclosed in figure 3.10 by bold lines. From the Franck-Condon principle, the photodissociation dynamics will be dominated by wavefunction overlap in this classically accessible region.

Figure 3.10 offers a good zeroth order picture for interpreting the observed trends. Specifically, due to a strong *outward* shift of the wave function along the symmetric stretch direction, the two lobes of the upper state wave function correlating with OH(v=1) overlap well with the *outer* two lobes for the $|02\rangle^+$ state. Conversely, the upper state wave function correlating with OH(v=0) has only one lobe in the symmetric stretch direction, and furthermore, by virtue of lower asymptotic OH stretch energy, reaches further *inward* along the symmetric stretch coordinate. This moves the single upper state lobe over the oppositely signed lower state lobes of $|02\rangle^+$, yielding destructive interference of the Franck-Condon overlap. The result is a net *decrease* and *increase* in photolysis efficiency for formation of OH(v=0) and OH(v=1), respectively, as experimentally observed for the $|02\rangle^+$ lower state. The situation for the photolysis of $|02\rangle^-$ is precisely reversed, with the outer two lobes of the $|02\rangle^-$ wavefunction now

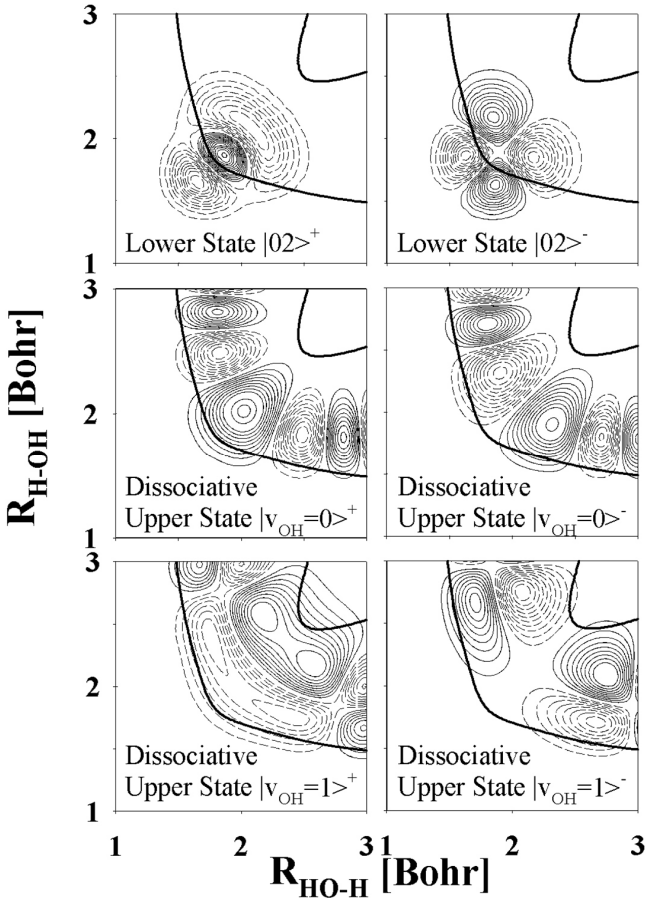

Figure 3.10 Ground state ($|02>^+$ and $|02>^-$) and excited state symmetric/antisymmetric wave functions correlating with OH(v=0,1) and accessed via excitation near 193 nm. Bold lines surround the energetically accessible Franck-Condon region for 193 nm excitation out of v_{OH}=2 H_2O states. Contours corresponding to positive and negative wavefunction values are shown in solid and dashed lines, respectively.

overlapping well with the upper state wavefunction correlating with OH(v=0). Additionally, $|02>^-$ overlap with the upper state wavefunction correlating with OH(v=1) is much less efficient, due both to a node in the asymmetric stretch direction and a larger displacement between lobe centers in the upper state. The net effect is now an *increase* and *decrease* in photolysis efficiency for formation of OH(v=0) and OH(v=1), respectively, again in good agreement with experimental observation for the $|02>^-$ lower state.

This qualitative picture suggests that the success of the spectator model at *higher* quanta of excitation arises from anharmonic elongation of the lower state eigenfunctions along the dissociation coordinate. Since both lower and upper state potential surfaces have overlapping wells in the spectator OH stretch, this leads to relatively tight (i.e. parallel) registry of the upper and lower wave functions on the way toward dissociation. The spectator model then follows immediately from an effective 1D Franck Condon overlap in these elongated geometries, which is therefore quasi-diagonal in vibrational quanta along the spectator bond. On the other hand, these elongation effects become less important for lower quanta of excitation, and particularly so for the pure symmetric stretch overtone, i.e. $|02\rangle^{+}$. In this regime, Franck-Condon factors depend in detail on the energy dependent shift in registry between the upper and lower state wave functions along the symmetric stretch coordinate, which, as evidenced in this work, can lead to dramatic deviations from simple spectator model predictions.

An alternative interpretation of such non-spectator model predictions arises from the degree of localization in the H_2O vibrational modes. According to the calculations of Lawton and Child,[27] the stretching vibrations in H_2O are represented with the local mode basis set, $\psi_{mn}^{(\pm)} = 2^{-1/2}\left[\chi_m(R_1)\chi_n(R_2) \pm \chi_n(R_1)\chi_m(R_2)\right]$, where $\chi_n(R)$ are Morse eigenfunctions for the individual OH bonds in H_2O. Most relevantly, Lawton and Child showed that the H_2O vibrational Hamiltonian can be highly diagonal in this $\psi_{mn}^{(\pm)}$ basis, at least for high vibrational levels. For example, H_2O states $|04\rangle^{-}$, $|13\rangle^{-}$, and $|02\rangle^{-}$ are heavily dominated by $\psi_{04}^{(-)}$ (94.9%), $\psi_{13}^{(-)}$ (94.7%), and $\psi_{02}^{(-)}$ (99.9 %), respectively (percent values in parenthesis represent the squares of the coefficients in front of the respective basis functions). In fact, the majority of *ungerade* H_2O vibrational states can be well described by just one local mode basis function with only minor contamination from other members of the basis. On the contrary, *gerade* states ($|02\rangle^{+}$

and $|11\rangle^{+}$), although still dominated by the respective local mode basis functions, tend to have much smaller degree of localization (79.7 % and 79.6 %, respectively).[27] The most important mixing terms have the form $\langle n \pm 1, m \mp 1 | H | n, m \rangle$ reflecting interactions between basis states differing by one vibrational quantum within the same polyad. Such increased coupling between the two bonds can therefore lead to one quantum changes in the vibrational state of the surviving OH bond. This is of course consistent with present observations that photolysis of $|02\rangle^{+}$ and $|11\rangle^{+}$ states, which each contain both $\psi_{02}^{(+)}$ and $\psi_{11}^{(+)}$ basis functions, produce more and less OH(v=1), respectively, than predicted from a pure spectator model. In view of this, it would be interesting to examine photodissociation dynamics of vibrational states such as $|22\rangle^{+}$ and $|13\rangle^{+}$, which are even more poorly described by the local mode picture. Based on the present analysis, one would predict photolysis to produce a significant spread in OH(v) levels, mirroring the broader local mode content of the initial wavefunction. Although such states cannot be accessed from the ground state via a direct overtone excitation, they may be populated by means of two photon-transitions as demonstrated[28] in Ref 28.

3.7 Summary / Conclusions

193 nm photodissociation dynamics of gas-phase H_2O molecules has been examined from selected rotational and vibrational quantum states within the v_{OH}=2 polyad. Rotational, spin-orbit, and lambda-doublet quantum state distributions of the OH photofragments can be well described in the framework of previous theoretical and experimental studies at both higher and lower polyad numbers. However, the OH vibrational distributions deviate considerably from conventional spectator model predictions, which are based on assuming adiabatic conservation of vibrational quanta in the surviving OH bond. Instead, the data suggest a somewhat more

restricted regime of applicability for the spectator model, specifically for vibrational states of H_2O at relatively high levels of local mode excitation. This breakdown of the spectator model is seen to be particularly strong for *gerade* states of the $v_{OH} = 2$ polyad such as $|11>^+$ and $|02>^+$, both of which yield comparable photolysis branching into OH(v=0) and OH(v=1). This is in good agreement with theoretical wavepacket studies and can be rationalized by higher initial momentum projection along the symmetric stretch coordinate for *gerade* state photolysis. This results in a greater departure from the minimum energy photolysis path and therefore enhanced vibrational excitation in the asympototic OH.

References for Chapter III

1 V. Engel et al., J. Phys. Chem. **96** (8), 3201 (1992).

2 S. A. Harich, D. W. H. Hwang, X. F. Yang, J. J. Lin, X. M. Yang, and R. N. Dixon, J. Chem. Phys. **113** (22), 10073 (2000).

3 R. Schinke, V. Engel, and V. Staemmler, J. Chem. Phys. **83** (9), 4522 (1985).

4 R. N. Dixon, Chem. Soc. Rev. **23** (6), 375 (1994).

5 M. Brouard, S. R. Langford, and D. E. Manolopoulos, J. Chem. Phys. **101** (9), 7458 (1994).

6 P. Andresen, V. Beushausen, D. Hausler, H. W. Lulf, and E. W. Rothe, J. Chem. Phys. **83** (3), 1429 (1985).

7 R. L. Vanderwal, J. L. Scott, and F. F. Crim, J. Chem. Phys. **94** (3), 1859 (1991).

8 R. Schinke, V. Engle, P. Andresen, D. Hausler, and G. G. Balintkurti, Phys. Rev. Lett. **55** (11), 1180 (1985).

9 R. Schinke, R. L. Vanderwal, J. L. Scott, and F. F. Crim, J. Chem. Phys. **94** (1), 283 (1991).

10 O. Votava, D. F. Plusquellic, and D. J. Nesbitt, J. Chem. Phys. **110**, 8564 (1999).

[11] P. Andresen, G. S. Ondrey, B. Titze, and E. W. Rothe, J. Chem. Phys. **80** (6), 2548 (1984).

[12] G. G. Balintkurti, J. Chem. Phys. **84** (8), 4443 (1986).

[13] R. L. Vanderwal, J. L. Scott, F. F. Crim, K. Weide, and R. Schinke, J. Chem. Phys. **94** (5), 3548 (1991).

[14] M. Brouard and S. R. Langford, J. Chem. Phys. **106** (15), 6354 (1997); I. Bar, Y. Cohen, D. David, T. Arusiparpar, S. Rosenwaks, and J. J. Valentini, J. Chem. Phys. **95** (5), 3341 (1991); R. L. Vanderwal, J. L. Scott, and F. F. Crim, J. Chem. Phys. **92** (1), 803 (1990); D. F. Plusquellic, O. Votava, and D. J. Nesbitt, J. Chem. Phys. **109**, 6631 (1998).

[15] S. A. Nizkorodov, M. Ziemkiewicz, D. J. Nesbitt, and A. E. W. Knight, J. Chem. Phys. **122**, 194316 (2005).

[16] D. F. Plusquellic, O. Votava, and D. J. Nesbitt, J. Chem. Phys. **107**, 6123 (1997).

[17] R. L. Vanderwal and F. F. Crim, J. Phys. Chem. **93** (14), 5331 (1989).

[18] C. A. Cantrell, A. Zimmer, and G. S. Tyndall, Geophys. Res. Lett. **24** (17), 2195 (1997).

[19] M. S. Child and L. Halonen, Adv. Chem. Phys. **57**, 1 (1984).

[20] R. A. Toth, Appl. Optics **33** (21), 4851 (1994).

[21] I. L. Chidsey and D. R. Crosley, J. Quant. Spectrosc. Radiat. Transf. **23**, 187 (1980).

[22] D. Hausler, P. Andresen, and R. Schinke, J. Chem. Phys. **87** (7), 3949 (1987).

[23] J. Z. Zhang and D. G. Imre, J. Chem. Phys. **90** (3), 1666 (1989).

[24] K. Weide, S. Hennig, and R. Schinke, J. Chem. Phys. **91** (12), 7630 (1989).

[25] K. S. Sorbie and J. N. Murrell, Mol. Phys. **29** (5), 1387 (1975).

[26] V. Staemmler and A. Palma, Chem. Phy. **93** (1), 63 (1985).

[27] R. T. Lawton and M. S. Child, Mol. Phys. **40** (4), 773 (1980).

[28] R. J. Barnes, A. F. Gross, and A. Sinha, J. Chem. Phys. **106** (3), 1284 (1997).

Chapter IV: Overtone spectroscopy of H_2O clusters in the $v_{OH} = 2$ manifold: IR-UV vibrationally mediated dissociation studies

Published in *Journal of Chemical Physics* **122**, 194316 (2005)

4.1 Introduction

Water dimer, $(H_2O)_2$, is arguably one of the most important binary complexes in nature. It has been intensively studied ever since its first spectroscopic observation in a solid nitrogen matrix[1] and in gas-phase.[2,3] The most significant spectroscopic studies of $(H_2O)_2$ include a comprehensive symmetry classification of its tunneling-rotational energy levels;[4] observation of low-resolution infrared[5] and coherent anti-Stokes Raman scattering[6] spectra of jet-cooled water complexes; observation of high resolution infrared[7-9], far-infrared,[10,11] and microwave[12,13] spectra of $(H_2O)_2$; determination of a reliable water pair potential;[14] and an elegant measurement of low-resolution infrared spectra of size-selected water clusters,[15] which resolved many discrepancies in previous spectroscopic assignment of $(H_2O)_2$ fundamental transitions.

In spite of the impressive roster of spectroscopic studies of $(H_2O)_2$ and larger water clusters, relatively little is known about their OH stretching overtones. Overtone excitations in $(H_2O)_2$ are especially interesting because of their potential effect on the dynamics of donor-acceptor switching and other hydrogen bond tunneling-interchange motions in the complex. There have been just a few theoretical studies of the positions and transition strengths of $(H_2O)_n$ overtone bands.[16-19] Matrix isolation vibrational spectra of H_2O polymers in the OH-overtone range have been reported only recently.[20,21] No gas-phase spectra of $(H_2O)_2$ overtone bands are presently available.

Additional interest in the overtone spectroscopy of $(H_2O)_2$ stems from the potential atmospheric importance of water clusters[22,23]. Atmospheric $(H_2O)_2$ influences the radiation balance of the planet,[22] homogeneous nucleation dynamics of aerosol formation,[24] and even rates and mechanisms of certain chemical reactions.[25] Overtone spectroscopy is a powerful potential tool for quantitative characterization of $(H_2O)_2$ column abundances in the atmosphere. Indeed, a weak band at 749.5 nm recently detected[26] in long-pass atmospheric spectra has been tentatively assigned to the bound OH ($v_{OH} = 4$) third overtone transition of $(H_2O)_2$ based on comparison with the existing theoretical predictions.[18,19] Lower order overtones of $(H_2O)_2$, such as $v_{OH}=2$ bands described here, may be more convenient for observational work on atmospheric $(H_2O)_2$ because of their less ambiguous spectroscopic assignments.

This manuscript examines $v_{OH}=2$ vibrational states of $(H_2O)_2$ using an approach of vibrationally mediated dissociation,[27-29] wherein selectively prepared ro-vibrational states of H_2O complexes are photolyzed and the resulting OH photofragments are detected with full quantum state resolution (figure 4.1). This method provides detailed information not only about overtone spectroscopy but also about molecular energy transfer dynamics in H_2O and its complexes. Specifically, this manuscript presents the first observation of the $v_{OH}=2$ overtones in $(H_2O)_2$ with partial rotational resolution and provides information about the dynamics of $(H_2O)_2$ predissociation at the $v_{OH}=2$ excitation energies (≈ 7000 cm^{-1}).

By way of contrast, the much simpler complex between Ar and H_2O provides a useful juxtaposition with $(H_2O)_2$.[29,30] Compared to the water dimer, Ar-H_2O has a substantially smaller potential energy well depth (140 cm^{-1} in Ar-H_2O vs. 1700 cm^{-1} in $(H_2O)_2$),[14,31] and considerably

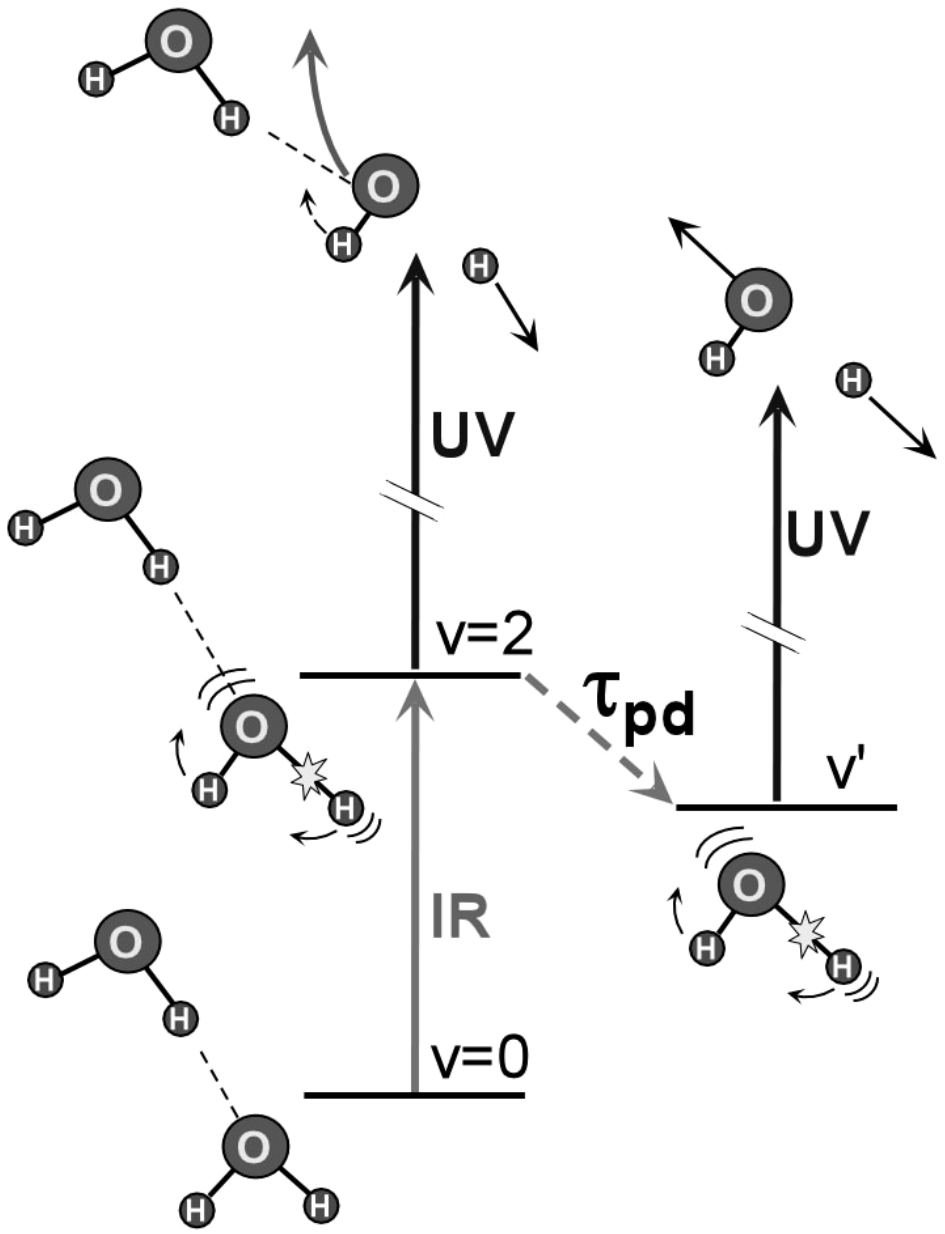

Figure 4.1 Experimental approach. Complexes are excited in v_{OH}=2 state followed by photodissociation of $H_2O(v_{OH}=2)$ directly inside the complexes with a UV laser pulse (left). Alternatively, the excited complexes first predissociate on time scale τ_{pd} generating H_2O molecules in a different vibrational state (v'), which are then photodissociated by the photolysis laser (right). In either case, the resulting OH fragments are detected in specific final quantum states by laser induced fluorescence.

weaker interactions between inter- and intra-molecular modes. This makes Ar-H_2O a convenient system for studying photodissociation dynamics of H_2O in the presence of a weakly perturbing rare gas "solvent" as opposed to the strongly hydrogen bonded interactions present in $(H_2O)_2$. Vibrationally mediated dissociation studies of Ar-H_2O in the v_{OH}=3 manifold have been reported,[29] however none in the first overtone region corresponding to the present study of H_2O dimer. To establish a suitable experimental perspective for the more complicated spectra of $(H_2O)_2$, therefore, this study also briefly considers vibrationally mediated spectroscopy and dynamics out of selected v_{OH}=2 vibrational states of Ar-H_2O.

4.2 Experimental Technique

Pertinent experimental information has been summarized in recent work dealing with the dynamics of vibrationally-mediated dissociation of H_2O monomer in the v_{OH}=2 polyad;[32] thus only the most relevant details are summarized here. Ar-H_2O and $(H_2O)_2$ complexes are produced in a supersonic expansion of 1% H_2O in 30% Ar / 70% He mixture through a pulsed slit valve (4 cm $\times$ 125 μm, 10 Hz, 0.5 ms). The best yields of Ar-H_2O and $(H_2O)_2$ complexes are achieved at a total stagnation pressure of 300 – 500 Torr, with the yield of dimer decreasing at higher pressures or at larger Ar fractions presumably because of preferential formation of larger clusters. The v_{OH}=2 overtone vibrations of jet-cooled molecules are excited with a tunable near-infrared pump laser (ν = 7100 cm^{-1} – 7300 cm^{-1}, up to 20-30 mJ/pulse, 0.2 cm^{-1} resolution, 5 ns pulse width). A counter-propagating ArF excimer photolysis laser pulse (193 nm, 5 mJ/pulse, 7 ns pulse width) follows after a variable time delay (0-1000 ns) with respect to the pump, dissociating a fraction of vibrationally exited water molecules (figure 4.1). Finally, a probe laser pulse (30 μJ/pulse, 0.1 cm^{-1}, 5 ns) excites the nascent OH on the off-diagonal $A^2\Sigma \leftarrow X^2\Pi$ v=1←0

band some 20 ns after the photolysis pulse, with the resulting OH fluorescence collected from the diagonal $A^2\Sigma \leftarrow X^2\Pi$ v=1←1 band at 310 nm. Both excitation and detection take place approximately 2 cm downstream from the expansion slit. To discriminate between i) vibrationally-mediated and ii) direct 193 nm photolysis of H_2O and its complexes, the near-infrared pump laser is operated at half the repetition rate, with the data from alternate laser shots subtracted to generate a background-free signal.

The resulting OH fluorescence signal is found to be linear in the 193 nm photolysis laser power, indicating that multiphoton photodissociation processes in the parent molecule are not relevant. The OH transitions are then probed in the weak saturation limit, and calibrated against fluorescence excitation spectra under fully thermalized conditions. On the other hand, the IR pump transitions can be saturated significantly, despite the decrease in absorption strength with successive overtone excitation. Indeed, for the strongest overtone transitions, it proves necessary to attenuate the pump laser power by as much as two orders of magnitude to avoid power-broadening of spectral lines beyond the specified laser resolution of 0.2 cm^{-1}. For optimal sensitivity, therefore, overview scans are taken under full near-IR pump laser power, with scans of individual overtone bands taken under reduced power conditions.

4.3 Spectroscopic Notation

We use $|mn\rangle^{\pm}$ local mode notation[33] for labeling OH stretching vibrations of free H_2O, Ar-H_2O, and the monomer proton acceptor subunit in $(H_2O)_2$, where *m* and *n* are the local mode stretching quanta.[34] In this notation, one can approximately correlate $\nu_1+\nu_3$ and $2\nu_1$ normal mode states of H_2O with $|02\rangle^-$ and $|02\rangle^+$ local mode states, respectively. For the proton-donor unit of $(H_2O)_2$, the states are labeled by specifying the number of local mode excitations in the bound-

OH and free-OH bonds.[18] For example, $|0>_f|1>_b$ designates the $v_{OH} = 1$ hydrogen-bonded OH stretch fundamental vibration of $(H_2O)_2$.

We use the notation of Ref. 8 for labeling rotational states of $(H_2O)_2$. Briefly, each rotational level of $(H_2O)_2$ is split into sextets by three internal motions: acceptor internal rotation, acceptor-donor interchange, and donor proton interchange (figure 4.2). Internal rotation of the

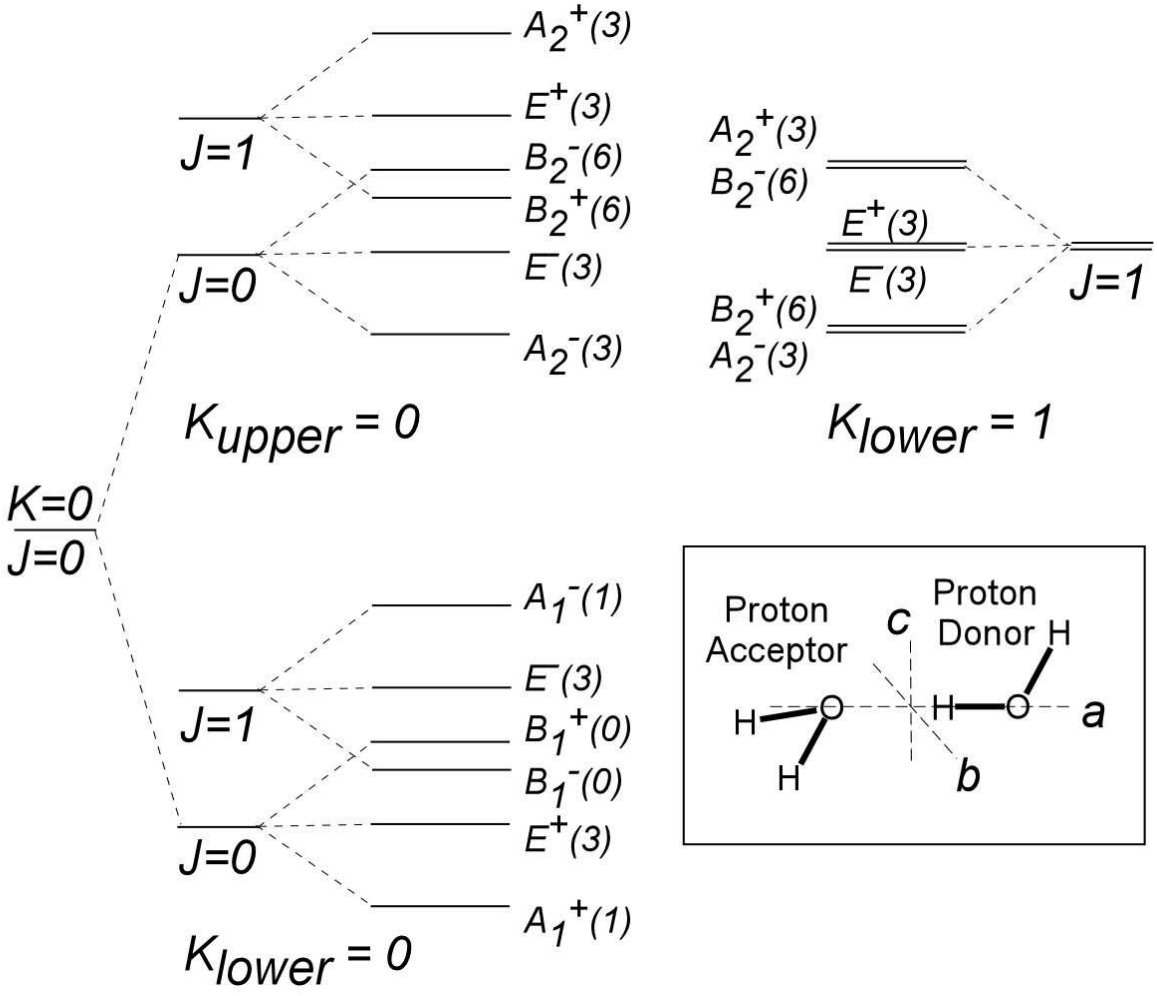

Figure 4.2 Schematic diagram of $(H_2O)_2$ energy levels (not to scale) and principle inertial axes for $(H_2O)_2$. Only *K* levels appreciably populated at jet temperatures are shown. Each *K* level is split into K_{lower} and K_{upper} components by proton acceptor internal rotation. Further splitting arises because of donor-acceptor interchange. For $K>0$, there is an additional doubling of all levels. The total symmetry including rotation (in permutation-inversion group isomorphic to D_{4h}) and nuclear weights for each level are given for a totally symmetric vibration of $(H_2O)_2$.

proton acceptor subunit is extremely facile, splitting each *J,K*-state into widely separated "upper" and "lower" *K*-manifolds (e.g. ≈ 10 cm^{-1} between $K=0_{lower}$ and $K=0_{upper}$), with acceptor-donor interchange and donor switching resulting in more modest additional splittings of each *K*-level into $A_{1,2}$, E, and $B_{1,2}$ sublevels (e.g., $A_2^-$and B_2^- are separated by ≈ 0.65 cm^{-1} in *J*=0, $K=0_{upper}$). Furthermore, all $K\neq0$ levels are split into doublets by conventional asymmetry considerations. The K_{lower} =1 and K_{upper} = 0 manifolds are close in energy due to the comparable tunneling and K_a=1 rotational pathways around the A-axis. Finally, $(H_2O)_2$ molecules under supersonic conditions cool down to the lowest levels within its 5 nuclear spin symmetry sub-groups (A_1, E, B_1, A_2, and B_2), with a fairly large spacing (10 cm^{-1}) between the A_1, E, B_1 and A_2, B_2 manifolds. To the extent that all internal motion in H_2O dimer is maximally cooled, one would quite simply expect comparable (≈ 7:9) populations in the K_{lower} = 0 vs. K_{upper} = 0/K_{lower} = 1 manifolds.

The energy levels of Ar-H_2O are much more simply represented in the framework of nearly freely rotating H_2O in the slightly anisotropic potential resulting from the Ar atom. Specifically, *ortho* and *para* nuclear spin designations are still good, and the energy levels of the complex can be conveniently labeled by quantum numbers of the free H_2O rotational states ($J_{K_aK_c}$) with which they correlate. Ar-H_2O levels are additionally characterized by the projection of the total angular momentum on the intermolecular axis, and by the number of quanta in the intermolecular stretching mode (ν_s) as explained in Refs. 35,36. Figure 4.3 displays a schematic diagram of the lowest energy levels of Ar-H_2O adopted from far-infrared and near-infrared studies[9,31,36,37] along with allowed transitions for $|02>^-$ band.

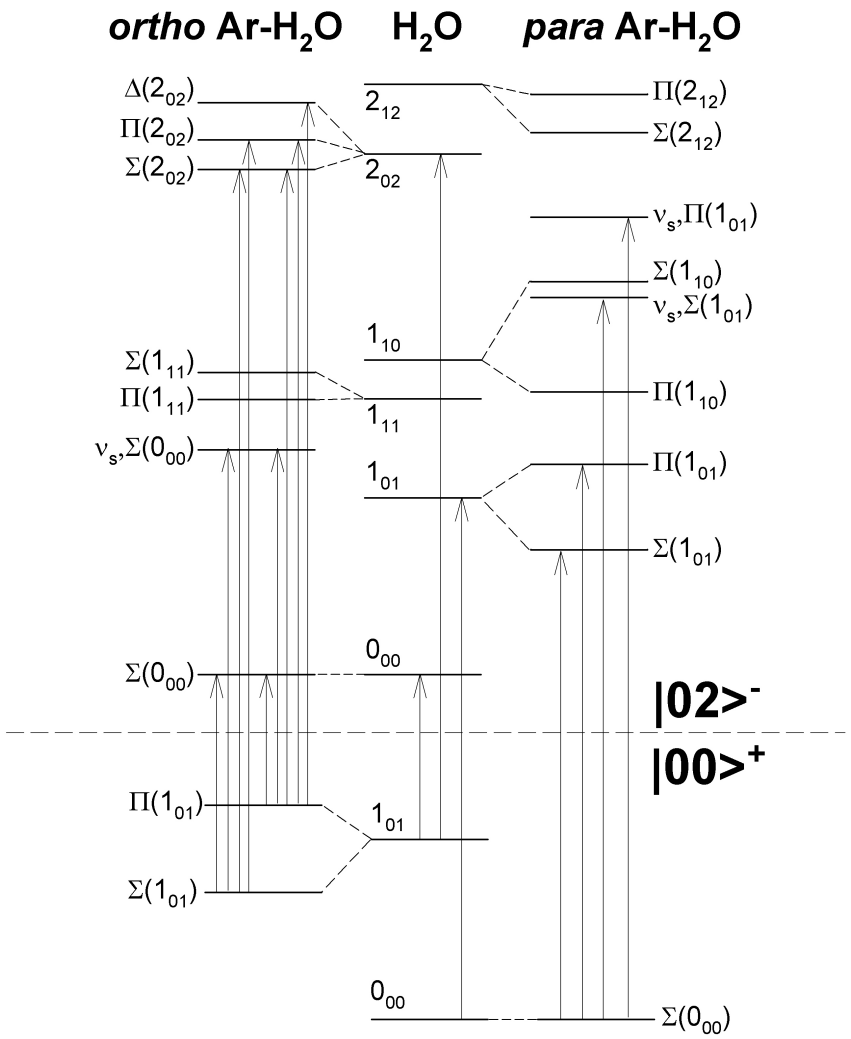

Figure 4.3 Correlation between the Ar-H_2O and H_2O energy levels. The grid of the Ar-H_2O levels is shifted with respect to that of H_2O by the binding energy of the complex. For $|02\rangle^-$ vibrational state, the *ortho* and *para* labels are interchanged compared to $|00\rangle^+$ on the account of the asymmetry of the vibration, with the $|02\rangle^- \leftarrow |00\rangle^+$ transitions following a-type selection rules: ΔK_a =even, ΔK_c = odd.

4.4 Overview Spectrum

Figure 4.4 shows an overview spectrum recorded under conditions optimized for the maximal yield of Ar-H_2O complexes. The spectrum is obtained by tuning the UV probe laser on

the $Q_{11}(8)$ line of the $A^2\Sigma \leftarrow X^2\Pi$ v=1←0 band, which probes the $^2\Pi_{3/2}^-(N=8)$ rotational state of OH(v=0), and then continuously scanning the near-infrared pump laser frequency over the characteristic first OH stretching overtone region. As will be elucidated below, the choice of a relatively high-*N* state of OH for detection (e.g., *N*=8 vs. *N*=1*)* is utilized to maximize action spectral intensities from complexes relative to those from H_2O monomer. In addition to a strong dependence on OH probe state, band intensities in the spectrum are also affected by time delay between the pump and photolysis laser pulses because vibrationally excited complexes can undergo intermolecular predissociation *before* H_2O molecules inside them are photolyzed (figure 4.1). Indeed, this will serve as a basis for direct measurement of vibrational predissociation lifetimes for Ar-H_2O and $(H_2O)_2$, as described later. The spectra in figure 4.4 are obtained with a pump-photolysis delay chosen to be 500 ns; this effectively ensures that all complexes predissociate prior to photolysis by the excimer laser pulse.

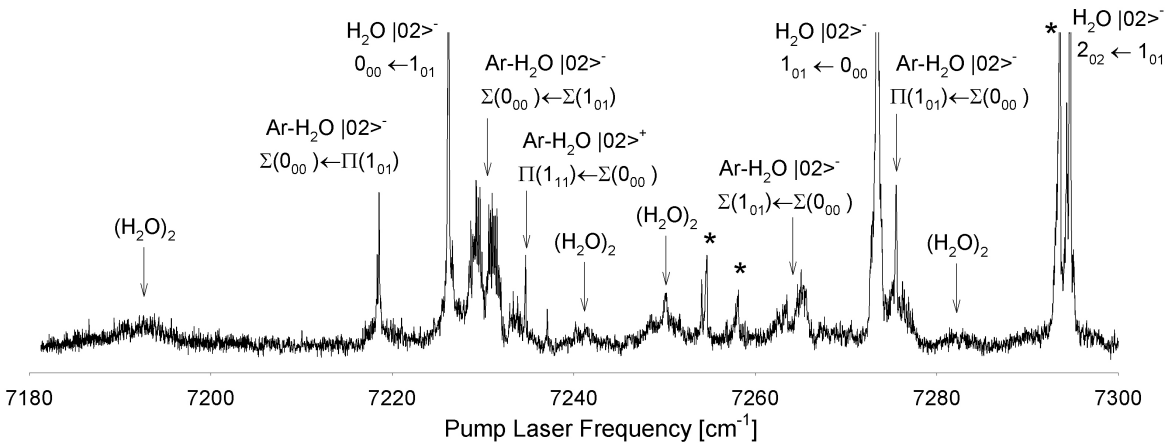

Figure 4.4 Survey action spectrum. The probe laser is tuned to the $^2\Pi_{3/2}^-(8)$ rotational state of OH(v=0), while the pump laser is scanned in frequency. The time delay between the IR pump and UV photolysis laser is sufficiently long to allow all vibrationally exited complexes to predissociate. Apart from a few easily identifiable H_2O monomer lines, all the structure in the spectrum is due to Ar-H_2O and $(H_2O)_2$. The bands labeled with asterisks almost certainly belong to Ar-H_2O but require further studies for definitive assignment.

As the first stage in the spectral assignment, only three rovibrational transitions of jet cooled H_2O appear in this spectral range and with appreciable intensity; these correspond to $J_{K_aK_c}$ = $1_{01}\leftarrow0_{00}$ (*para*) and $0_{00}\leftarrow1_{01}$ and $2_{02}\leftarrow1_{01}$ (*ortho*) transitions in the $|02>^-$ vibrational overtone band. A few H_2O monomer transitions into $|02>^+$ state also occur in this spectral range but are considerably weaker and indeed undetectable at the current S/N in figure 4.4. The remaining bands in the spectrum cannot be attributed to free H_2O lines and, therefore, must belong to complexes containing H_2O. Note that these bands are of comparable intensity to vibrationally mediated water monomer lines. This is not a reflection of water clustering efficiency, but rather that detection on high OH(*N*) states provides an enormous discrimination against water monomer, obviously present in much higher concentrations.

Many bands in the action spectrum are strongly correlated with fractional Ar content in the expansion mixture, suggesting complexes between H_2O and Ar (Table 4.1 and figure 4.4). Indeed, some of these bands display partially resolved rotational structure consistent with the Ar-H_2O binary complex. However, a significant number of bands in the spectrum remain even if Ar is completely replaced by He in the carrier gas mixture, although their signal intensities are reduced due to much smaller clustering efficiency in pure He jets. Since He-H_2O clustering is expected to be negligible under room temperature stagnation conditions, these can be assigned to overtone spectra of $(H_2O)_n$ complexes (table 4.1). To the best of our knowledge, this represents the first such overtone spectra for neutral H_2O clusters, specifically made possible by the enhanced sensitivity of vibrationally mediated photodissociation methods. Indeed, at least one of these bands (at 7193 cm^{-1}) even exhibits partially resolved *rotational* structure characteristic of H_2O dimer, to which we next direct our attention.

Positions [cm^{-1}]	Carrier	Band Shape	Assignment
7193 [a]	$(H_2O)_2$	∥	$\|02\rangle_a^+$ or $\|1\rangle_f\|1\rangle_b$
7218.45 [b]	Ar-H_2O	⊥	$\|02\rangle^- \Sigma(0_{00}) \leftarrow \Pi(1_{01})$
7230.05 [c]	Ar-H_2O	∥	$\|02\rangle^- \Sigma(0_{00}) \leftarrow \Sigma(1_{01})$
7240 [b]	$(H_2O)_2$	⊥ [d]	most likely $\|2\rangle_f\|0\rangle_b$
7249.8 [b]	$(H_2O)_2$	⊥ [d]	most likely $\|2\rangle_f\|0\rangle_b$
7263.7 [a]	Ar-H_2O	∥	$\|02\rangle^- \Sigma(1_{01}) \leftarrow \Sigma(0_{00})$
7275.0 [b]	Ar-H_2O	⊥	$\|02\rangle^- \Pi(1_{01}) \leftarrow \Sigma(0_{00})$
7282 [a]	$(H_2O)_2$	∥ [d]	

[a] approximate band center; [b] Q-branch position; [c] band origin from fitting; [d] poorly defined shape

Table 4.1 Positions and assignments of the observed overtone bands of Ar-H_2O and $(H_2O)_n$. Positions are accurate to within 0.2 cm^{-1}. Whereas Ar-H_2O assignments are relatively certain, $(H_2O)_2$ assignments should be considered speculative and a source of stimulation for further theoretical efforts.

4.5 First Overtone (v_{OH} = 2) Spectra of H_2O Dimer

Vibrational assignment of the OH stretching bands of $(H_2O)_2$ has historically proven to be a challenging task, even at the *fundamental* level. Indeed, the four OH stretching fundamentals have been re-assigned several times and only more or less definitively understood from recent cluster size-selective spectroscopic work of Huisken *et al.*[15] Table 4.2 summarizes the presently accepted assignments at the v_{OH}=1 level. With two quanta of OH stretching excitation, the overtone spectral region is certain to be significantly more complex; for example,

there are as many as ten different possibilities to distribute them among the four OH bonds in $(H_2O)_2$.

Mode	$K' \leftarrow K''$	Position [cm^{-1}]
$\|01\rangle_a^-$	$0_{lower} \leftarrow 1_{lower}$	3738.4
	$1_{upper} \leftarrow 0_{upper}$ & $1_{lower} \leftarrow 0_{lower}$	3753
	$2_{upper} \leftarrow 1_{lower}$	3777
$\|1\rangle_f\|0\rangle_b$	$0_{upper} \leftarrow 1_{lower}$ & $1_{lower} \leftarrow 0_{upper}$	3731.7
$\|01\rangle_a^+$	not observed	3633[a]
$\|0\rangle_f\|1\rangle_b$	$0_{upper} \leftarrow 1_{lower}$ & $1_{lower} \leftarrow 0_{upper}$	3601

Table 4.2 Currently accepted gas-phase positions of $(H_2O)_2$ stretching fundamentals. The positions are taken from Ref. 8 with $|01\rangle_a^+$ reassigned to $|0\rangle_f|1\rangle_b$ based on the results of Ref. 15. The $|01\rangle_a^+$ transition has only been observed in Ar matrices,[20] where it is quite weak. Calculations suggest that it should occur at around 3650 cm^{-1} in gas-phase.

Fortunately, theory predicts only a few of these combination states to be efficiently produced from the ground state of $(H_2O)_2$ via direct overtone pumping. Harmonically coupled anharmonic oscillator (HCAO) calculations by Kjaergaard and co-workers[18,19] predict that the strongest OH overtone transitions in $(H_2O)_2$ should be $|02\rangle_a^-$, $|2\rangle_f|0\rangle_b$, $|02\rangle_a^+$, and $|1\rangle_f|1\rangle_b$ (listed in the order of decreasing transition strengths), where "a", "f" and "b" refer to proton acceptor, free proton donor and bound proton donor OH stretches, respectively. Calculations by Chaban and Gerber done at CC-VSCF level[16] predict a somewhat different order of intensities: $|02\rangle_a^-$, $|1\rangle_f|1\rangle_b$, $|2\rangle_f|0\rangle_b$, $|02\rangle_a^+$, but both studies agree that these four transitions should dominate the v_{OH}=2 spectrum of $(H_2O)_2$. The strongest v_{OH}=2 bands in the cyclic water trimer spectrum are predicted to be of the type $|2\rangle_f|0\rangle_b$ by calculation of Ref. 18. Chaban and Gerber predict that

transitions of $|1\rangle_f|1\rangle_b$ and $|0\rangle_f|2\rangle_b$ types should be just as strong. Figure 4.5 shows simulated low-resolution spectra of $(H_2O)_2$ based on the prediction of Refs. 16,18,19. Despite a promising concurrence in general theoretical predictions for the overtone intensities, these studies fail to agree on the more detailed relative frequency ordering of the $(H_2O)_2$ bands, making spectroscopic assignment of the observed $(H_2O)_n$ overtones quite difficult. The most significant disagreement appears to exist for the relative frequencies of the $|1\rangle_f|1\rangle_b$ and $|2\rangle_f|0\rangle_b$ overtone bands in both the dimer and trimer species.

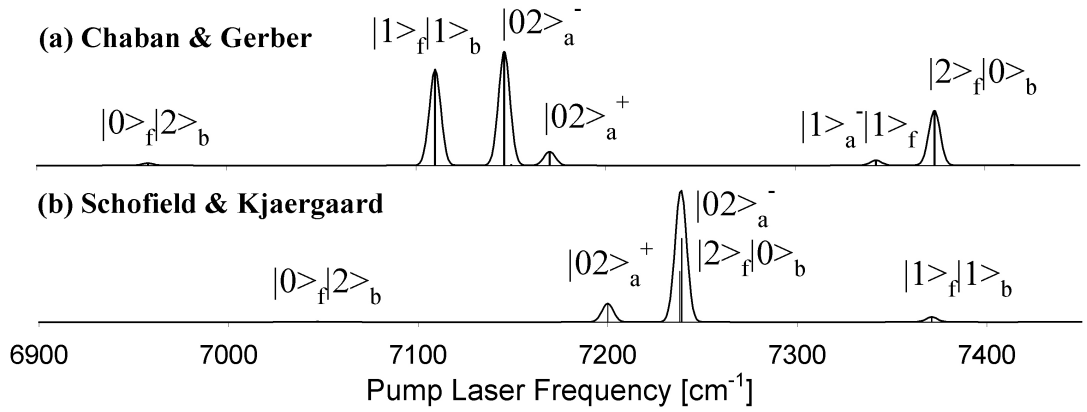

Figure 4.5 Predicted band positions and intensities of v_{OH}=2 bands of $(H_2O)_2$. (a) CC-VSCF calculation by Chaban and Gerber.[16] (b) HCAO calculation by Schofield and Kjaergaard.[19] For better representation of integrated band intensities, the transitions are convoluted over a Gaussian with HWHM=7 cm^{-1}.

The analysis of the $(H_2O)_n$ band centered at 7193 cm^{-1} may help shed some light on this issue. At higher sensitivity and lower IR pump powers to avoid saturation, this band clearly reveals a partially resolved rotational structure (see figure 4.6), with a characteristic spacing between adjacent lines of roughly ≈ 0.4 cm^{-1}. Though not fully resolved, this is nevertheless consistent with an a-type band for $(H_2O)_2$, which is known to have a near-prolate symmetric top

structure with B ≈ 0.2 cm^{-1}, [2,8,10,12] and is clearly inconsistent with any cluster larger than dimer. Simulations of this band profile using the fundamental spectroscopic constants for $(H_2O)_2$ quickly reveals it to be composed of at least two overlapping a-type transitions. Most relevantly to the above discussion, the profile can not be satisfactorily modeled with overlapping b-or c-type transitions, since such bands would be dominated by prominent Q-branch features not observed in the experimental spectrum.

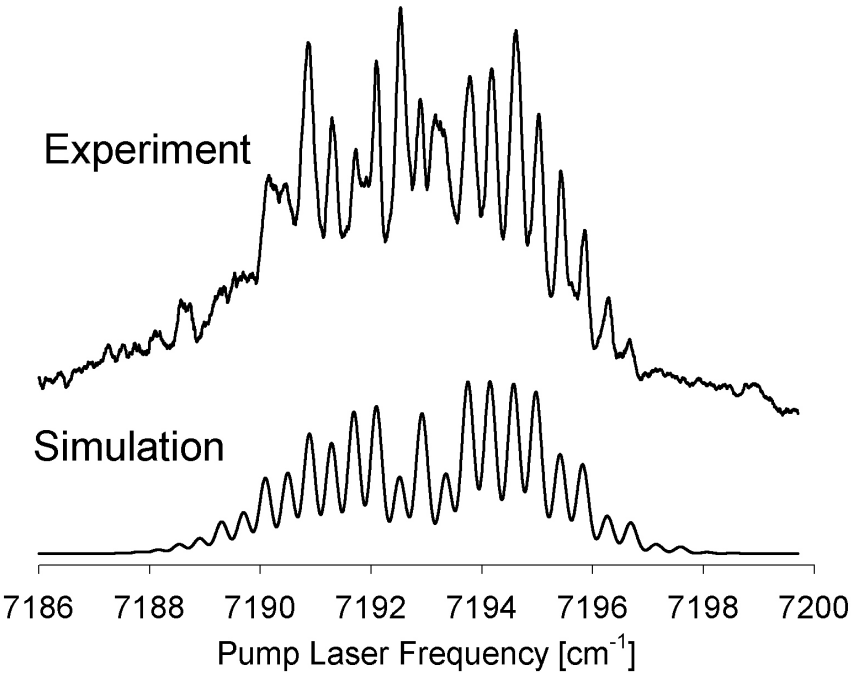

Figure 4.6 A slow scan over the $(H_2O)_2$ band at 7193 cm^{-1}. This band has a partially resolved rotational structure characteristic of a parallel transition in $(H_2O)_2$ complex. The band is simulated as a superposition of three *K=0←0* subbands with origins at 7192.5 cm^{-1} (B_2^- subband; odd J: even J = 3:6), 7191.3 cm^{-1} (E subband; no alternation), 7193.3 cm^{-1} (A_2^-subband; odd J:even J = 6:3). The band origins are not uniquely determined by the simulation, though a B ≈ 0.2 cm^{-1} rotational constant for water dimer is clearly consistent with the observed structure.

This lack of strong Q-branch transitions rules out assignment to the overtone vibration of the hydrogen bond acceptor, $|02>_a^-$, since this transition moment would be predominantly along the b-axis of $(H_2O)_2$. In support of this, Huang and Miller[8] only observe b-type transitions for the

corresponding $|01\rangle_a^-$ fundamental in H_2O dimer (see Tab. 2) Indeed, H_2O dimer exhibits considerable perpendicular structure in the $|01\rangle_a^-$ fundamental region due to i) $K=0_{lower} \leftarrow 1_{lower}$, ii) $K=1_{upper} \leftarrow 0_{upper}$/$K=1_{lower} \leftarrow 0_{lower}$ and iii) $K=2_{upper} \leftarrow 1_{lower}$ subbands, which are observed -18 cm^{-1}, -3 cm^{-1} and 22 cm^{-1} away from the $|01\rangle_a^-$ band origin, respectively. By way of contrast, we do not observe additional $(H_2O)_2$ features in this spectral region out to at least ±40 cm^{-1} away from the 7193 cm^{-1} band. In summary, both the 7193 cm^{-1} band shape as well as lack of $(H_2O)_2$ transitions in the vicinity make assignment to $|02\rangle_a^-$ unlikely.

In light of the a-type rotational contour, a more plausible assignment for the 7193 cm^{-1} band is the $|1\rangle_f|1\rangle_b$ vibration centered on the proton donor unit of $(H_2O)_2$. This vibrational motion promotes a dipole transition moment along the a-axis of $(H_2O)_2$, which is more consistent with the observed band profile. In addition, there is a strong similarity between the band observed here and the a-type transition profile from Huang and Miller[8], which has been assigned to $|0\rangle_f|1\rangle_b$[15], i.e. one quantum of the bound OH stretch. Furthermore, the $|1\rangle_f|1\rangle_b$ vibration is predicted to be the second strongest OH-stretching overtone in $(H_2O)_2$ by Chaban and Gerber,[16] and executes a motion which correlates with the strong $|02\rangle^-$ overtone in H_2O monomer. Also, the $|1\rangle_f|1\rangle_b$ vibrational prediction of 7110 cm^{-1} by Chaban and Gerber (see figure 4.5) is in relatively good agreement with experiment. We note that the $|02\rangle_a^+$ acceptor overtone is yet another possibility for achieving such a strong a-type transition moment, with predicted band origins (7170 cm^{-1} [16] and 7200 cm^{-1} [19]) in even closer agreement with experiment, although the predicted overtone intensities are relatively weak in both sets of theoretical calculations.[16,19] In this regard, however, it is worth remembering the "action" nature of these spectra, intensities of which rely on vibrationally mediated UV photolysis of the resulting predissociated complex. For example, excitation of the symmetric $|02\rangle_a^+$ could well predissociate preferentially into H_2O in

v_{OH}=1, which in turn photodissociates efficiently at 193 nm to yield OH. We will return to this point later in the discussion, but stress the importance of vibrational overtone *dynamics* in interpreting the spectra. Clearly a predictive understanding of overtone frequencies, intensities and dynamics in hydrogen bonded systems remains a challenging area for future progress, which the present work hopes to further stimulate.

With a suggested assignment of the 7193 cm^{-1} band structure to either $|1>_f|1>_b$ or $|02>_a^+$, we next address whether one can reproduce the observed rotational profile with known spectroscopic constants of $(H_2O)_2$. Any a-type transition in $(H_2O)_2$ can in principle exhibit complicated fine structure due to the presence of 5 uncoolable nuclear spin symmetry species, specifically three $K=1\leftarrow1_{lower}$ subbands (A_2^-, E^-, B_2^-); three $K=0\leftarrow0_{upper}$ subbands (A_2^-, E^-, B_2^-); and three $K=0\leftarrow0_{lower}$ subbands (A_1^+, E^+, B_1^+). (Note that the specified subband symmetries do not include rotational symmetries unlike the labels shown in figure 4.2). For example, all of these a-type subbands appear in close proximity to each other in far-infrared spectra of acceptor-wag vibration in $(H_2O)_2$ and $(D_2O)_2$.[10,38] In practice, the A_1^+ and B_1^+ subbands from $K=0_{lower}$ are weak because of low statistical weights (figure 4.2). The *E* subbands from $K=1_{lower}$ and $K=0_{upper}$ are also weak because these levels can relax all the way down to $K=0_{lower}$ under supersonic jet conditions. Finally, based on v_{OH}=1 fundamental transitions in $(H_2O)_2$,[8] the $K=1\leftarrow1$ bands are likely to be significantly broadened by predissociation. Therefore, the dominant a-type contributions to the rotational structure should come from i) $K=0\leftarrow0_{upper}$ $A_2^-$and B_2^- and ii) $K=0\leftarrow0_{lower}$ E^+ subbands.

The $K=0_{upper}$ states in the vibrationless $(H_2O)_2$ are well understood: the donor-acceptor interchange splitting between $K=0_{upper}$ $A_2^-$and B_2^- states is approximately 0.65 cm^{-1}.[10,12,39] Although this splitting is known to increase for some intermolecular modes of $(H_2O)_2$ that

encourage the donor-acceptor interchange,[10] excitation of the OH-stretching states is expected to reduce it significantly. For example, the interchange A_2^-/ B_2^- splitting is just 0.061 cm^{-1} in the $|01>_a^-$ $K=0_{lower}$ state.[8] Since $(H_2O)_2$ retains its plane of symmetry in both $|1>_f|1>_b$ and $|02>_a^+$ states, the origin difference of the $K=0 \leftarrow 0_{upper}$ $A_2^-$and B_2^- subbands should equal the *sum* of the $K=0$ A_2^-/ B_2^- interchange splittings between lower and upper vibrational states, i.e. on the order of 0.7-0.8 cm^{-1}. Indeed, at our modest resolution, a ≈ 0.8 cm^{-1} separation of the $A_2^-$and B_2^- subband origins would nicely, albeit fortuitously, explain the lack of intensity alternation in the spectrum (especially evident in the R-branch region), due to cancellation at low J of the predicted B_2^- J_{even}/J_{odd}=6/3 vs. A_2^- J_{even}/J_{odd}=3/6 nuclear spin statistical ratios.

In the interest of simplicity, therefore, we have modeled the observed transition profile as a combination of i) two $K=0 \leftarrow 0_{upper}$ $A_2^-$and B_2^- subbands, separated by ≈ 0.8 cm^{-1} and ii) one $K=0 \leftarrow 0_{lower}$ E^+ subband, with the relative location of the $K=0 \leftarrow 0_{lower}$ and $K=0 \leftarrow 0_{upper}$ subbands treated as an adjustable parameter. Each $(H_2O)_2$ subband is calculated as a near prolate symmetric top with rotational parameters taken from Ref. 8, with the result shown in figure 4.6. The simulation is consistent with a 7±3 K rotational temperature (same as for Ar-H_2O bands discussed below), and readily reproduces several salient features of the observed band, namely i) parallel structure, ii) absence of a band gap, and iii) no obvious intensity alternation. However, with the present instrumental resolution, the simulation is not very sensitive to the transition band origins, which thus remain poorly determined. Nevertheless, the rotational structure clearly confirms the carrier of the observed band to be $(H_2O)_2$, which we can tentatively assign to either the $|1>_f|1>_b$ or $|02>_a^+$ overtone vibration.

Inspection of the spectrum in figure 4.4 indicates the potential presence of several other $(H_2O)_n$ bands, the assignment of which requires identification or suppression of the much

stronger Ar-H_2O transitions. Since the water complexes predissociate much faster than the laser pulse duration (see below), the Ar-H_2O bands can be largely suppressed by recording the spectrum using very small IR pump-UV photolysis delays. This procedure reveals that the bands at 7240, 7250 and 7282 cm^{-1} can be ascribed to $(H_2O)_n$ complexes, which based on both theoretical predictions and matrix studies, most likely correspond to $|2>_f|0>_b$ transitions in water dimer (Table 1). Specifically, Perchard reported a strong band at 7236 cm^{-1} in argon matrix[20] and a corresponding band at 7220 cm^{-1} in nitrogen matrix,[21] which he assigned to $|2>_f|0>_b$ overtone of the proton donor unit as well. His assignments were recently corroborated by HCAO calculations.[19] CC-VSCF calculations of Chaban and Gerber place this band higher in frequency but also predict a large transition strength for $|2>_f|0>_b$.[16] The present gas phase studies provide some additional information; in particular, the 7240 and 7250 cm^{-1} bands appear perpendicular, which is consistent with $|2>_f|0>_b$ vibrational motion predominantly along the c-axis. The subband spacings and rotational contours are consistent with a $|2>_f|0>_b$ overtone band assignment, but based on theoretical predictions, it could in principle arise from the acceptor $|02>_a^-$ band. Further theoretical efforts in this overtone region would be extremely useful to settle these issues.

4.6 Overtone ($v_{OH} = 2$) Spectra of Ar-H_2O

The vibrationally mediated IR spectra in figure 4.4 are clearly dominated by transitions of Ar-H_2O van der Waals clusters, to which we now turn our attention. Indeed, a first question worth raising is why the spectra of such weakly-bound van der Waals complexes can be so *prominent* over the much more strongly bound $(H_2O)_n$ species, even though the latter are likely present in much higher concentrations. The answer almost certainly has to do with the vibrationally mediated nature of the action spectroscopy, which requires the IR photon to

enhance the subsequent 193 nm photodissociation of H_2O, either in the complex or its predissociated fragments. This enhancement, in turn, depends very sensitively on the number of quanta in OH stretch excitation in the H_2O subunit, as beautifully elucidated by Crim, Schinke and coworkers.[27,33,40] For an atom-polyatom species such as Ar-H_2O, predissociation at the first overtone level occurs on a relatively slow time scale (≈ 10-100 ns, depending on the specific internal rotor quantum state excited), which with 7 ns laser time resolution readily permits efficient photolysis of H_2O in the v_{OH}=2 manifold. Furthermore, Δv_{OH}=-1 predissociation of the weakly bound Ar-H_2O complex ($D_0 \approx 140$ cm^{-1})[31] most likely yields H_2O in a near resonant vibrational state with v_{OH}=1, and thus still exhibit the necessary photolysis enhancement. H_2O dimer, on the other hand, is more strongly bound ($D_0 \approx 1700$ cm^{-1}),[14] predissociates rapidly (vide infra), and has more channels with which to deposit the excess overtone energy. The net effect is a decreased efficiency for detecting H_2O dimer by first overtone vibrationally mediated photolysis, and explains preferential sensitivity to weakly bound species such as Ar-H_2O, H_2-H_2O, etc. Furthermore, this also rationalizes the absence in our spectra of clusters beyond $(H_2O)_2$, since predissociation is statistically less likely to deposit sufficient OH stretching internal energy in the H_2O fragments required for subsequent photofragmentation. Interestingly, this also bodes well for vibrationally mediated action spectroscopy of H_2O dimer and larger clusters in the *second* region overtone region, for which a significant gain in detection sensitivity would be predicted.

High resolution rovibrational spectroscopy of Ar-H_2O has been well studied at the ground state (v_{OH}=0) and first excited state (v_{OH}=1) levels of H_2O.[9,29,31,36,37,41], revealing a weakly anisotropic potential and states best described by H_2O quantum numbers in the free rotor limit. Under the jet-cooled conditions, one therefore expects to observe only transitions originating

from the lowest *para* $\Sigma(0_{00})$ and *ortho* $\Sigma(1_{01})$ states of the complex, with weaker transitions also possible from the incompletely cooled *ortho* $\Pi(1_{01})$ state (which lies 11.4 cm^{-1} above $\Sigma(1_{01})$). Transitions built upon the stronger $|02>^-$ band of H_2O monomer should dominate those derived from the weaker $|02>^+$ and $|11>^+$ overtone bands. Based on these expectations, and on analogy with spectra of Ar-H_2O in the $v_{OH}=1$[9,36] and $v_{OH}=3$ spectral ranges[29], it is relatively straightforward to assign many of the bands to Ar-H_2O (table 4.1).

As predicted, the most prominent Ar-H_2O bands correlate with the $|02>^- 0_{00}\leftarrow 1_{01}$ and $|02>^- 1_{01}\leftarrow 0_{00}$ lines of H_2O monomer, just as seen in the previously studied fundamental $|01>^-$ [9,36] and second overtone $|03>^-$ [29] studies (figure 4.4). Due to weak potential anisotropy contributions from the Ar atom, the 3-fold spatial degeneracy of the 1_{01} internal rotor state of H_2O splits into a Π and Σ components, yielding $\Sigma(0_{00})\leftarrow\Pi(1_{01})$ (7218.45 cm^{-1}) and $\Sigma(0_{00})\leftarrow\Sigma(1_{01})$ (7230.05 cm^{-1}) subbands "flanking" the $|02>^- 0_{00}\leftarrow 1_{01}$ monomer transition. As this lifting of spatial degeneracy by Ar also occurs in the $|02>^- 1_{01}$ upper state, one similarly predicts two Ar-H_2O bands surrounding the $|02>^- 1_{01}\leftarrow 0_{00}$ monomer line, as indeed observed at 7263.7 cm^{-1} ($\Sigma(1_{01})\leftarrow\Sigma(0_{00})$) and 7275.0 cm^{-1} (($\Pi(1_{01})\leftarrow\Sigma(0_{00})$). Further confirmation of these assignments can be obtained from the presence (or absence) of sharp central Q-branches in these bands, respectively, in agreement with the predicted perpendicular and parallel nature of the $\Sigma\leftarrow\Pi$ and $\Sigma\leftarrow\Sigma$ transition moments (see table 4.1).

Similar to what was previously demonstrated for H_2O dimer, the rotational constants of this van der Waals complex are sufficiently large to permit rotational analysis of favorable bands, providing unambiguous additional confirmation of the species as Ar-H_2O. For example, a higher resolution scan of the $\Sigma(0_{00})\leftarrow\Sigma(1_{01})$ band at 7230.05 cm^{-1} is shown in figure 4.7, which can be well modeled using known rotational constants of Ar-H_2O[9,37] and a typical rotational

temperature of 7 K. From the observed splitting between $|02>^{-}$ $\Sigma(0_{00})\leftarrow\Pi(1_{01})$ and $|02>^{-}$ $\Sigma(0_{00})\leftarrow\Sigma(1_{01})$ bands, we can derive the energy separation of 11.6±0.3 cm^{-1} between J=1 $\Pi(1_{01})$ to J=1 $\Sigma(1_{01})$ in $|00>^{+}$ state, in good agreement with the value of 11.333 cm^{-1} obtained from high-resolution study of Ar-H_2O fundamentals by Lascola and Nesbitt.[9] From the $|02>^{-}$ $\Sigma(1_{01})\leftarrow\Sigma(0_{00})$ and $|02>^{-}$ $\Pi(1_{01})\leftarrow\Sigma(0_{00})$ band positions, one can also infer the corresponding splitting in the upper $|02>^{-}$ state to be 11.3±0.3 cm^{-1}, i.e. consistent with only minor changes in the anisotropy of the Ar-H_2O intermolecular potential upon OH stretch excitation.

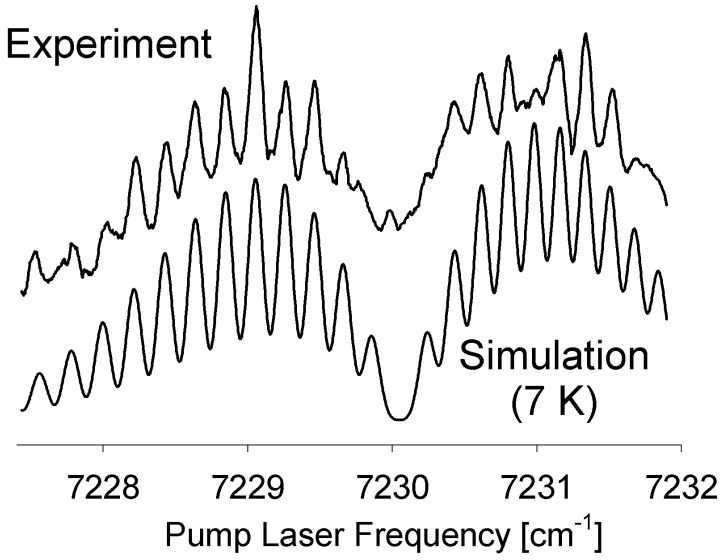

Figure 4.7 Sample scan over the Ar-H_2O $|02>^{-}\Sigma(0_{00}) \leftarrow |00>^{+}$ $\Sigma(1_{01})$ band. The profile is best described by a rotational temperature of 7 K, with a rotational line numbering certain to ±1 J.

The effect of the H_2O vibration on the Ar-H_2O potential well depth is similarly small as evidenced by a red-shift of only 2.9±0.3 cm^{-1} between the $|02>^{-}$ $\Sigma(0_{00}, J=0)\leftarrow |00>^{+}$ $\Sigma(0_{00}, J=0)$ band origins in free H_2O and in Ar-H_2O. The sign of the frequency shift is consistent with a

slightly stronger van der Waals bond in the $|02>^-$ state. The magnitude of the frequency shift is intermediate between that for the $|01>^-$ transition ($\Delta\nu$ = 1.32 cm^{-1})[9] and $|03>^-$ transition ($\Delta\nu$ = 3.06 cm^{-1})[29] indicating a systematic increase in the Ar-H_2O intermolecular bond strength with v_{OH}. This behavior is qualitatively consistent with observations on other atom-polyatom van der Waals complexes, such as Ar-HF.

The strong set of band(s) near 7293 cm^{-1} can also be assigned to Ar-H_2O complexes, which by proximity to the $|02>^-$ $2_{02}\leftarrow 1_{01}$ monomer transition at 7294.14 cm^{-1} probably arises from one or more projection components, Σ, Π, Δ, of the internal H_2O rotor subunit along the intermolecular axis. Detailed assignment of the much weaker band structures (for example, near 7234, 7254, 7258 cm^{-1}) is less certain. However, proximity to the $|02>^+$ $1_{11}\leftarrow 0_{00}$ and $|02>^+$ $2_{12}\leftarrow 1_{01}$ lines of water monomer clearly suggests that they are built on these transitions. What would make this dynamically interesting is that the $|02>^+$ overtone band in the monomer is extremely weak, i.e. the $|02>^+$ $1_{11}\leftarrow 0_{00}$ and $|02>^-$ $1_{01}\leftarrow 0_{00}$ line intensities differ by more than two orders of magnitude, yet the corresponding Ar-H_2O bands built on $|02>^+$ and $|02>^-$ vibrations have much more comparable intensities in action spectrum. In fact, this effect appears to be so strong for $|02>^+$ $1_{11}\leftarrow 0_{00}$ that we see in figure 4.4 vibrationally mediated photodissociation of the Ar-H_2O cluster but not of bare H_2O monomer. One can attribute this unusual intensity pattern to the difference in predissociation dynamics of Ar-H_2O from $|02>^+$ and $|02>^-$ states. Indeed, if the action spectrum is recorded using $^2\Pi_{3/2}^-(N=2)$ rotational state of OH instead of N=8, the intensity of Ar-H_2O $|02>^+$ bands relative to that of $|02>^-$ bands is substantially reduced, suggesting that predissociation of Ar-H_2O $|02>^+$ states results produces more rotational and bending excitation in the water monomer.[32] Experimental efforts to further elucidate these weaker band assignments

are currently being pursued, based on product state distributions and predissociation lifetimes, and will be presented elsewhere.

4.7 Vibrational Predissociation Dynamics

Vibrationally-mediated spectroscopy also permits one to *directly* measure predissociation lifetimes of complexes by monitoring the final photofragment (OH) as a function of the time delay between the near-infrared pump and UV photolysis lasers. The UV photodissociation of H_2O takes place on a femtosecond time scale, so the risetime for OH formation following the UV pulse can be completely neglected on the nanosecond timescale of our experiment. For typical laser pulse durations, molecular jet velocities of $\approx 10^5$ cm/s, and laser beam sizes of 1-3 mm, this technique can therefore straightforwardly access the time window between $\Delta t \approx 7$ and 1000 ns. The lower limit is determined by the finite pulse duration (5-7 ns), whereas the upper limit corresponds to the "flyout" time for excited molecules to exit the probe volume. The Ar-H_2O overtone states observed here conveniently result in predissociation within this time window.

By way of illustration, we consider the $|02\rangle^- \Sigma(0_{00}) \leftarrow \Sigma(1_{01})$ transition in Ar-H_2O (see figure 4.8). If the initially prepared Ar-H_2O complex $|02\rangle^- \Sigma(0_{00})$ photodissociates into *different* OH states than photolysis of the predissociated H_2O monomer distribution, the OH distributions will depend on the pump-photolysis delay. If photolysis occurs before predissociation, the OH distribution reflects break up of the Ar-H_2O cluster. At the other extreme, if photolysis occurs long after predissociation, the OH distributions reflect dynamics of the $H_2O(v')$ predissociation product. Signals probed on a single quantum state of OH reflect the superposition of both intra-cluster and predissociated cluster photolysis dynamics as function of time delay. Since Ar-H_2O predissociation tends to produce bend-excited H_2O (see below), which then photofragments to

form rotationally hotter OH distributions, one expects OH LIF signal to *increase* for high *N* and *decrease* for low *N* with pump-photolysis delay.

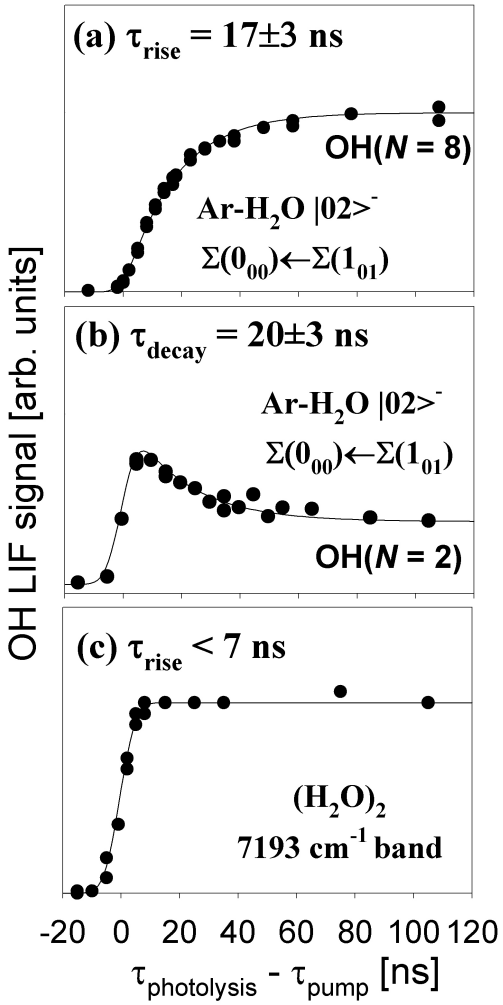

Figure 4.8 Predissociation lifetimes of Ar-H_2O and $(H_2O)_2$. The observed OH(*N*) signal comes from two independent channels: vibrationally-mediated photodissociation and predissociation followed by photodissociation (see figure 4.1). (a) Only the predissociation /photodissociation channel contributes to the rise of high-*N* states of OH in the Ar-H_2O case. (b) Vibrationally-mediated photodissociation is responsible for the rapid rise and the predissociation/photodissociation for the slower decay of the signal for low-*N* states of OH in the Ar-H_2O case. (c) Rapid predissociation of $(H_2O)_2$ followed by direct photolysis of the vibrationally excited H_2O predissociation fragments results in appearance of OH on a time scale of < 7 ns.

These trends are nicely verified in figure 4.8, which shows OH $^2\Pi_{3/2}^-$(N=8) and $^2\Pi_{3/2}^-$ (N=2) populations after the $|02\rangle^- \Sigma(0_{00})\leftarrow\Sigma(1_{01})$ overtone excitation of Ar-H_2O. The N=2 signal rises quickly at t = 0, as this state is produced in direct vibrationally-mediated dissociation of Ar-H_2O, but then decays to a constant level characteristic of the photolysis of the H_2O predissociation product. The N=8 signal starts out at zero because direct dissociation of Ar-H_2O in $|02\rangle^- \Sigma(0_{00})$ state does not produce such hot OH states, but it then rises to a steady level also determined by the H_2O predissociation product. Both sets of data can be least squares fit to an exponential rise or decay, clearly demonstrating that the complexes undergo predissociation on a 18±5 ns timescale. Note that this is essentially identical to the 16±5 ns predissociation lifetime for $|03\rangle^- \Sigma(0_{00})$ states[42], observed in a similar real time measurement. Also relevant in this regard are high resolution measurements on the $|01\rangle^- \Sigma(0_{00})$ state of Ar-H_2O, from which a lower limit of 16 ns is extracted from line-width studies.[9] At first this seems dynamically surprising; from Fermi's golden rule one might anticipate expect rapidly increasing predissociation rates with increasing internal energy. However, the vibrational density of states at these energies is still extremely sparse, and thus the predissociation dynamics in Ar-H_2O are likely to be highly non-statistical, resulting in long lifetimes sensitive to local resonances between the initial cluster and final H_2O distributions. In support of this picture, a more complete study currently underway of the other Ar-H_2O bands in the v_{OH}=2 region exhibit lifetimes that vary more or less erratically with vibration and internal rotor quantum state.

By way of comparison, figure 4.8c shows the corresponding time delay dependence for the 7193 cm^{-1} band of $(H_2O)_2$. In contrast to Ar-H_2O, the v_{OH}=2 excitation of $(H_2O)_2$ results in an instrumentally limited appearance of OH for all N. Indeed, this dynamical difference was exploited in the previous section to selectively discriminate in the action spectra between long

lived Ar-H_2O excitations from shorter lived $(H_2O)_2$ ones, and is consistent with a rapid predissociation of the complex on a time scale < 7 ns. The observations could also be explained by postulating a very long (> 1 μs) predissociation lifetime, but this scenario is highly unlikely in view of the rapid predissociation rates of $(H_2O)_2$ in the v_{OH}=1 manifold.[8]

For pump-photolysis time delays much shorter than the predissociation lifetime, these vibrationally mediated photolysis methods permit one to investigate intramolecular collision dynamics in a single size- and quantum state- selected cluster. For example, dissociation of free H_2O in $|02>^-$ states is known to result in rotationally cold OH (see figure 4.9) with the distribution peaked at N=1-3.[32] Indeed, the action spectrum (figure 4.4) would be dominated by free H_2O lines if a rotationally cold state of OH (e.g., N=2) were used in the probing step instead of N=8. With vibrationally mediated photolysis, one can measure the distribution of OH produced via dissociation of Ar-H_2O complexes via the $|02>^- \Sigma(0_{00}) \leftarrow \Sigma(1_{01})$ transition, and directly compare with photolysis of the "bare" internal rotor $|02>^- \Sigma(0_{00})$ excited H_2O monomer in the *absence* of the Ar atom. This data is summarized in figure 4.9 for each of the spin orbit and lambda doublet states, and reveals two interesting features. First of all, there are considerably higher populations in each electronic sublevel at high N, consistent with intracluster *rotational* excitation of the recoiling OH prior to exiting the cluster. Secondly, the strong oscillations in N for the various electronic sublevels (most apparent in the $^2\Pi_{3/2/1/2}^-$ manifolds) have much lower contrast ratios for the cluster vs. free monomer photodissociation processes. This implies less specificity in branching ratio into a given electronic manifold, which is consistent with partial scrambling of the nascent electronic state distributions, but this time reflecting *non-adiabatic* collisional dynamics inside the cluster. These results confirm those obtained on Ar-H_2O clusters in the second overtone region,[29] and which has been nicely

modeled by inelastic (rotational and electronic state changing) collisions between the recoiling OH and Ar atom within the complex.[29,30]

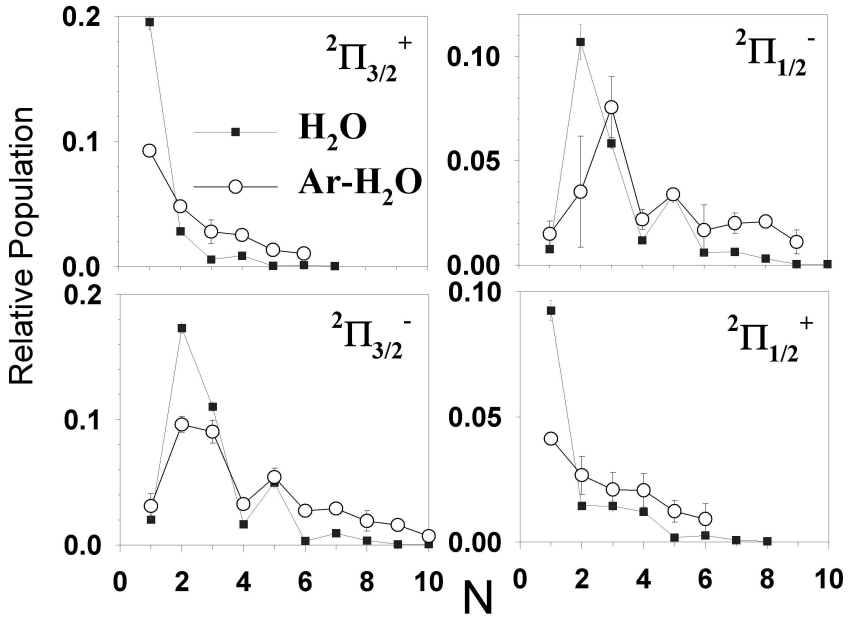

Figure 4.9 Quantum state distribution of all spin-orbit, lambda-doublet, and rotational OH states resulting from vibrationally-mediated dissociation of Ar-H_2O following excitation in the $|02>^-$ $\Sigma(0_{00})\leftarrow\Sigma(1_{01})$ band (filled squares). Compared to the results for $|02>^-$ $0_{00}\leftarrow1_{01}$ excitation in free H_2O (open circles), dissociation inside the complex produces slightly hotter and more statistical OH.

For pump-photolysis delays (200-500 ns) much longer than the vibrational predissociation lifetime (18 ± 5 ns), a completely different picture of the OH quantum state distributions emerges (see figure 4.10). By this time, all initially excited Ar-H_2O complexes ($|02>^-$ $\Sigma(0_{00})$) have predissociated, and the OH products are generated by UV photolysis from nascent H_2O(v') molecules. As clearly evident in figure 4.10 (shown for the $^2\Pi_{3/2}^-$ manifold), the OH distribution is now dramatically hotter, peaking at around N = 6. Interestingly, a qualitatively similar distribution is also seen for vibrationally mediated photolysis on the H_2O dimer bands, again showing a strong preference for highly rotationally excited OH, and suggesting a

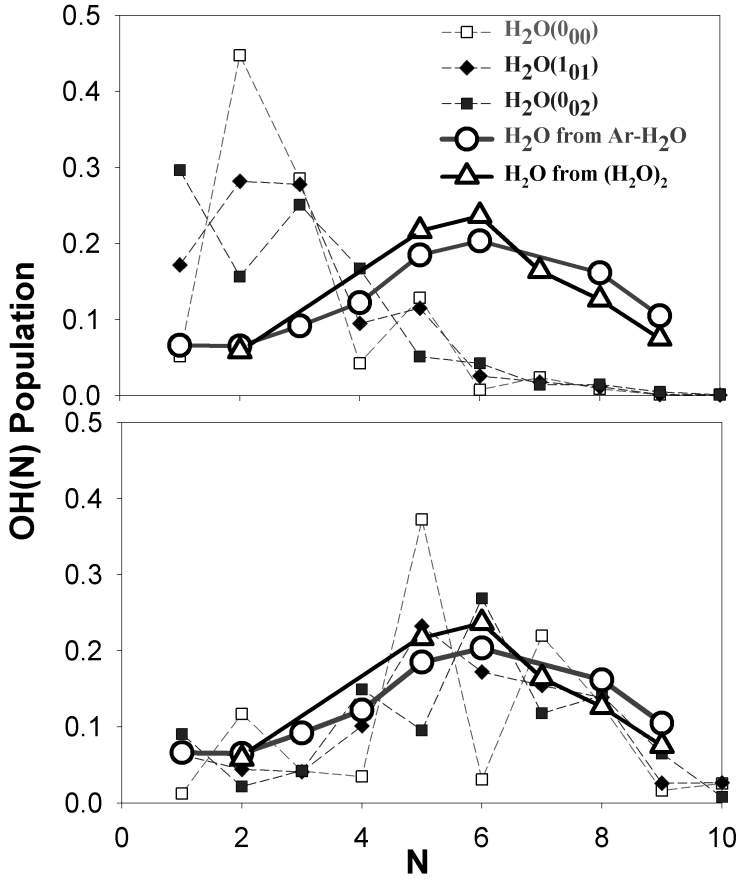

Figure 4.10 Rotational distribution of $^2\Pi_{3/2}^-(N)$ states of OH resulting from UV photolysis of H_2O(v') produced in predissociation of Ar-H_2O ($|02\rangle^- \Sigma(0_{00})$ state; large circles) and $(H_2O)_2$ (7193 cm^{-1} band; large triangles). Also shown are the corresponding OH state distributions resulting from direct photolysis of individual quantum states of free H_2O (J = 0, 1, 2) in $|02\rangle^-$ state (top panel) and $|01^-(2)\rangle$ state (bottom panel).[32] Explicit comparison suggests that $H_2O(v_{OH}=0,1; v_{bend}=2)$ is the dominant product of predissociation of Ar-H_2O and $(H_2O)_2$.

qualitatively similar predissociation pathway. Although our experiment does not probe these H_2O(v') distribution directly, we can nevertheless glean some insight into the nature of the states formed from the predissociation event by comparison with systematic vibrationally mediated photolysis studies of H_2O rotational and vibrational quantum states. Specifically, figure 4.10a displays 193 nm photolysis OH product state distributions ($^2\Pi_{3/2}^-$) from $J_{KaKc} = 0_{00}$, 1_{01} and 2_{02} rotational states of H_2O, each excited to the $|02\rangle^-$ overtone level. Consistent with similar results

by Crim and coworkers for $|04\rangle^-$ excited H_2O,[40] these results indicate a slight but systematic warming of the OH distributions with initial H_2O rotation. However, the shape of these distributions is qualitatively much colder than observed experimentally.

In marked contrast, figure 4.10b exhibits OH distributions from vibrationally mediated photolysis of H_2O for the same series of rotational levels, but now in $|01^-(2)\rangle$, i.e. a nearly isoenergetic combination state corresponding to i) OH stretch fundamental plus ii) two quanta of HOH bending excitation. These OH distributions are now substantially hotter, peaking at $N \approx 5$-6, and in qualitatively much more consistent with the Ar-H_2O dimer results. Although further experiments will be necessary to establish this definitively, the results plausibly suggest that vibrational predissociation of Ar-H_2O from $|02\rangle^- \Sigma(0_{00})$ has strong contributions from the near resonant V-V pathway:

$$\text{Ar-}H_2O(|02\rangle^- \Sigma(0_{00})) \rightarrow H_2O(v_{OH}=1; v_{bend}=2; J) + \text{Ar} \qquad \Delta E_{released} \approx 240 \text{ cm}^{-1} \quad (4)$$

which would then photofragment into the high-N OH distributions observed in figure 4.10. The smoothness of the resulting OH state distribution would also be consistent with several different J states produced in (4), since photolysis of single J states of H_2O generally result in much more structured OH quantum state distributions (for example, see figure 4.9-10). As a final comment, it is worth noting that the OH state distributions resulting from the photolysis of overtone excited $(H_2O)_2$ (i.e. 7193 cm^{-1} band) are remarkably similar to the above results for Ar-H_2O. This might again suggest substantial bending excitation in one or more of the HOH products. Due to the higher binding energy of $(H_2O)_2$ vs. Ar-H_2O ($D_0 \approx 1700$ cm^{-1} vs. 140 cm^{-1}), however, predissociation into same $H_2O(v_{OH}=1; v_{bend}=2; J)$ states is now not energetically possible. Nevertheless, several bend excited channels remain energetically open, such as formation of $H_2O(v_{OH}=0; v_{bend} \leq 3)$ and $H_2O(v_{OH}=1; v_{bend} \leq 1)$. Based on the requirement of vibraitonally

enhanced photodissociation cross section at 193 nm, the observed distributions plausibly arise from photolysis of $H_2O(v_{OH}=1; v_{bend}\leq 1, J)$. However, it is worth noting that since the action spectra derive both their sensitivity and specificity from strong vibrationally mediated skewing of the photodissociation cross sections, this need not be representative of the full distribution of predissociated H_2O. Nevertheless, these studies make simple predictions and highlight some interesting directions for further exploration with quantum state resolution in the ejected H_2O, as perhaps could be studied by IR photofragmentation recoil spectroscopy.[43]

4.8 Summary / Conclusions

The combination of slit jet expansions with i) IR pump vibrational excitation, ii) vibrationally selective excimer photolysis, followed by iii) state-resolved LIF probing of fragments, reveals itself as a powerful spectroscopic tool for extending traditional vibrationally-mediated photodissociation methods into the overtone region of the water clusters. Rich vibrational structure has been observed in vibrationally-mediated dissociation spectra of H_2O/Ar mixtures under supersonically cooled conditions in the vicinity of the first OH stretching overtones of H_2O. The observed resonances can be assigned to overtone transitions of Ar-H_2O and $(H_2O)_2$ based on their spectral structure and photodissociation dynamics, and in favorable cases, even permitting direct detection of resolved rotational structure. Indeed, this is the first reported gas phase spectra of H_2O dimer overtone in the gas phase, which reveals both agreement and disagreement with currently available theoretical models.

The use of time delayed IR pump and photolysis lasers allows direct observation of predissociation dynamics of H_2O complexes on the 10 ns -1 μs time scale, as demonstrated on $v_{OH}=2$ of Ar-H_2O clusters. For sufficiently long lived vibrational states, this method provides a

novel scheme for initiating photochemical events inside size and quantum state selected clusters. In conjunction with parallel studies of the isolated monomer, solvent effects on the photofragmentation dynamics of H_2O can be directly probed, by comparison with vibrationally-mediated photodissociation of the same free rotor state H_2O state in the absence of the perturbing Ar atom. Specifically, vibrationally-mediated dissociation of H_2O within Ar-H_2O complex clearly produces *hotter* rotational OH distributions, as well as promotes partial *non-adiabatic* energy transfer between $\Pi_{3/2,1/2}$ and lambda doublet electronic levels. A simple physical model for this would be intracluster collisions between the recoiling OH photofragment and Ar atom.[29,30] At a more challenging level, however, these data reflect the detailed photofragmentation dynamics of H_2O in the presence of a single solvent atom, yet with the considerable spectroscopic simplification of aligned, fully quantum state selected reagents, as well as the special intracluster advantage of well determined impact parameter and total angular momentum.

References for Chapter IV

1 M. Van Thiel, E. D. Becker, and G. C. Pimentel, J. Chem. Phys. **27**, 486 (1957).

2 T. R. Dyke and J. S. Muenter, J. Chem. Phys. **60** (7), 2929 (1974).

3 T. R. Dyke, K. M. Mack, and J. S. Muenter, J. Chem. Phys. **66** (2), 498 (1977).

4 T. R. Dyke, J. Chem. Phys. **66** (2), 492 (1977).

5 R. H. Page, J. G. Frey, Y. R. Shen, and Y. T. Lee, Chem. Phys. Lett. **106** (5), 373 (1984); M. F. Vernon, D. J. Krajnovich, H. S. Kwok, J. M. Lisy, Y. R. Shen, and Y. T. Lee, J. Chem. Phys. **77** (1), 47 (1982); D. F. Coker, R. E. Miller, and R. O. Watts, J. Chem. Phys. **82**, 3554 (1985).

6 S. Wuelfert, D. Herren, and S. Leutwyler, J. Chem. Phys. **86** (6), 3751 (1987).

[7] Z. S. Huang and R. E. Miller, J. Chem. Phys. **88**, 8008 (1988); J. B. Paul, R. A. Provencal, and R. J. Saykally, J. Phys. Chem. A **102**, 3279 (1998).

[8] Z. S. Huang and R. E. Miller, J. Chem. Phys. **91**, 6613 (1989).

[9] R. Lascola and D. J. Nesbitt, J. Chem. Phys. **95**, 791 7 (1991).

[10] L. B. Braly, K. Liu, M. G. Brown, F. N. Keutsch, R. S. Fellers, and R. J. Saykally, J. Chem. Phys. **112** (23), 10314 (2000).

[11] K. L. Busarow, R. C. Cohen, G. A. Blake, K. B. Laughlin, Y. T. Lee, and R. J. Saykally, J. Chem. Phys. **90**, 3937 (1989); R. C. Cohen and R. J. Saykally, J. Phys. Chem. **96** (3), 1024 (1992).

[12] L. H. Coudert and J. T. Hougen, J. Mol. Spectr. **139** (2), 259 (1990).

[13] G. T. Fraser, R. D. Suenram, and L. H. Coudert, J. Chem. Phys. **90** (11), 6077 (1989).

[14] R. S. Fellers, C. Leforestier, L. B. Braly, M. G. Brown, and R. J. Saykally, Science **284** (5416), 945 (1999).

[15] F. Huisken, M. Kaloudis, and A. Kulcke, J. Chem. Phys. **104** (1), 17 (1996).

[16] G. Chaban and R. Gerber, private communications (2002).

[17] H. C. W. Tso, D. J. W. Geldart, and P. Chylek, J. Chem. Phys. **108** (13), 5319 (1998).

[18] G. R. Low and H. G. Kjaergaard, J. Chem. Phys. **110** (18), 9104 (1999).

[19] D. P. Schofield and H. G. Kjaergaard, Phys. Chem. Chem. Phys. **5** (15), 3100 (2003).

[20] J. P. Perchard, Chem. Phys. **273** (2-3), 217 (2001).

[21] J. P. Perchard, Chem. Phys. **266** (1), 109 (2001).

[22] V. Vaida and J. E. Headrick, J. Phys. Chem. A **104** (23), 5401 (2000).

[23] G. T. Evans and V. Vaida, J. Chem. Phys. **113** (16), 6652 (2000); N. Goldman, R. S. Fellers, C. Leforestier, and R. J. Saykally, J. Phys. Chem. A **105** (3), 515 (2001).

[24] S. M. Kathmann, G. K. Schenter, and B. C. Garrett, J. Chem. Phys. **111** (10), 4688 (1999).

[25] C. E. Kolb, J. T. Jayne, D. R. Worsnop, M. J. Molina, R. F. Meads, and A. A. Viggiano, J. Am. Chem. Soc. **116** (22), 10314 (1994); A. B. Ryzhkov and P. A. Ariya, Chem. Phys. Lett. **367** (3,4), 423 (2002); P. M. Pawlowski, S. R. Okimoto, and F.-M. Tao, J. Phys.

Chem. A **107** (27), 5327 (2003); L. E. Christensen, M. Okumura, S. P. Sander, R. J. Salawitch, G. C. Toon, B. Sen, J. F. Blavier, and K. W. Jucks, Geophys. Res. Lett. **29** (9), 13/1 (2002).

[26] K. Pfeilsticker, A. Lotter, C. Peters, and H. Boesch, Science **300** (5628), 2078 (2003).

[27] R. L. Vanderwal, J. L. Scott, and F. F. Crim, J. Chem. Phys. **94** (3), 1859 (1991).

[28] R. L. Vanderwal and F. F. Crim, J. Phys. Chem. **93** (14), 5331 (1989); P. Andresen, V. Beushausen, D. Hausler, H. W. Lulf, and E. W. Rothe, J. Chem. Phys. **83** (3), 1429 (1985); D. F. Plusquellic, O. Votava, and D. J. Nesbitt, J. Chem. Phys. **101**, 6356 (1994).

[29] O. Votava, D. F. Plusquellic, T. L. Myers, and D. J. Nesbitt, J. Chem. Phys. **112**, 7449 (2000).

[30] K. M. Christoffel and J. M. Bowman, J. Chem. Phys. **104** (21), 8348 (1996).

[31] R. C. Cohen and R. J. Saykally, J. Chem. Phys. **98** (8), 6007 (1993).

[32] S. A. Nizkorodov, M. Ziemkiewicz, T. L. Myers, and D. J. Nesbitt, J. Chem. Phys. **119** (19), 10158 (2003).

[33] R. Schinke, R. L. Vanderwal, J. L. Scott, and F. F. Crim, J. Chem. Phys. **94** (1), 283 (1991).

[34] M. S. Child and L. Halonen, Adv. Chem. Phys. **57**, 1 (1984).

[35] R. C. Cohen and R. J. Saykally, Annu. Rev. Phys. Chem. **42**, 369 (1991).

[36] D. J. Nesbitt and R. Lascola, J. Chem. Phys. **97** (11), 8096 (1992).

[37] R. C. Cohen, K. L. Busarow, K. B. Laughlin, G. A. Blake, M. Havenith, Y. T. Lee, and R. J. Saykally, J. Chem. Phys. **89** (8), 4494 (1988).

[38] L. B. Braly, J. D. Cruzan, K. Liu, R. S. Fellers, and R. J. Saykally, J. Chem. Phys. **112** (23), 10293 (2000).

[39] L. H. Coudert, F. J. Lovas, R. D. Suenram, and J. T. Hougen, J. Chem. Phys. **87** (11), 6290 (1987).

[40] V. Engel, V. Staemmler, R. L. Vanderwal, F. F. Crim, R. J. Sension, B. Hudson, P. Andresen, S. Hennig, K. Weide, and R. Schinke, J. Phys. Chem. **96** (8), 3201 (1992).

[41] M. J. Weida and D. J. Nesbitt, J. Chem. Phys. **106** (8), 3078 (1997).

[42] O. Votava, University of Colorado, 1999.

[43] L. Oudejans and R. E. Miller, J. Chem. Phys. **113** (11), 4581 (2000); L. Oudejans and R. E. Miller, Annu. Rev. Phys. Chem. **52**, 607 (2001).

Chapter V: Overtone vibrational spectroscopy and dynamics in H_2-H_2O complexes: A combined theoretical and experimental study

5.1 Introduction

Intermolecular attraction can lead to formation of van der Waals complexes when a sample is cooled to low enough temperatures to stabilize clusters. Since formation of dimers (consisting of two molecular components) must be the first step in aggregation to larger clusters and ultimately condensation, such species warrant special theoretical and experimental attention. Additionally, complexation provides insight into condensed phase bonding between molecules in a variety of regimes.[2-4] In particular, bimolecular clusters encompass the wide range of noncovalent bonding interactions that can be accessed by the two molecular partners, ranging from pure van der Waals interactions[5] in Ar-Ar ($D_0 \approx 84$ cm^{-1}) to the significantly stronger hydrogen bonding interactions in water dimer[6] ($D_0 \approx 1103$ cm^{-1}). A striking feature of these weakly bound van der Waals systems is the propensity for each component to retain a significant fraction of monomeric character, for example, as noted in the typically perturbative shifting of infrared transition frequencies upon complexation.[7] Furthermore, weak coupling in the potential between dimer components can permit partial free internal rotation of the H_2O species in Ar-H_2O, leading to rotational spacings which are commonly shifted by only a few wavenumbers[8] from those of free H_2O.

As a result, bimolecular clusters have served as a focus of intense theoretical[9] and experimental[10] work over the years. These species are particularly attractive from a theoretical point of view, because there is often weak coupling between intramolecular

and intermolecular degrees of freedom. Thus, for a N atom cluster, the quite challenging and often intractable problem of performing *ab initio* and exact quantum nuclear dynamics calculations in full 3N – 6 internal coordinates can often be instead treated by reduced dimensionality schemes,[11] whereby intramolecular vibrations are assumed to be independent of the cluster formation. To a good approximation, this leads to a much simpler Hamiltonian described only by intermolecular coordinates, which are 5D for the specific complex of interest (i.e., H_2 -H_2O) and 6D at the very most. Though still challenging, it is now feasible to solve theoretically for eigenvalues and eigenfunctions of the complex, a process which is indeed often limited by the quality of ab initio potentials available in full or partial dimensionality.

In the rare cases where a high quality, full dimensional *ab initio* potential is available for the complex, one can hope to achieve an even higher level of rigor and benchmarking accuracy. Specifically, one can perform full quantum dynamical calculations for monomers in the dimer complex, and then extract an improved intermolecular dimer potential by averaging the *full D* potential over the intramolecular wavefunctions corresponding to a given pair of monomeric (electronic, vibrational) eigenstates. By repeating this procedure for both ground and vibrationally excited states of the complex, one can now make first principles predictions sufficiently accurate for benchmark comparison between theory and high resolution experimental spectroscopy.

The current work focuses on spectroscopy and dynamics of the H_2 -H_2O van der Waals dimer.[9,11-16] This weakly bound complex is of particular interest in the interstellar medium (ISM), due in part to predominance of atomic and molecular hydrogen in the universe.[17] Indeed, certain regions of the ISM depleted in deep ultraviolet radiation tend

to have appreciable concentrations of H_2 molecules rather than H atoms,[18] which can in fact trigger formation of higher molecular weight species.[19] In conjunction with appreciable concentrations of H_2O, this implies a relatively high probability for $H_2 + H_2O$ collisions, and even transient formation of H_2-H_2O clusters in the cold environment of interstellar clouds.

Beyond issues of transient van der Waals dimer formation, however, there is also substantial fundamental interest simply in inelastic scattering between H_2 and H_2O species,[20] for which the precise intermolecular potential energy surface plays a role of central importance. For example, the lowest rotational spacings in the para H_2 (358 cm^{-1}) and ortho H_2 (600 cm^{-1}) nuclear spin manifolds are greatly in excess of that of both para H_2O (37.1 cm^{-1}) and ortho H_2O (18.6 cm^{-1}), where the para/ortho (or p/o) designation refers to I = 0 vs I = 1 coupling of the H atom nuclear spins. Since H_2 is an extremely poor emitter, collisions between $H_2 + H_2O$ can provide an efficient means for transferring energy into H_2O rotation, which can be radiated away much more efficiently and thereby function as a "coolant" in interstellar clouds.[21,22] Such a decrease in total energy by radiation can lead to collapse of the cloud, initiating early stages of star formation.[17] Additionally, $H_2 + H_2O$ collisions are also thought to be responsible for formation of population inversions between H_2O energy levels. This has been invoked[23] to explain ubiquitous water maser radiation,[24] which has been observed from a variety of extra galactic,[25] galactic,[26] and interplanetary[17] objects. The H_2-H_2O dimer potential is also of pivotal interest in formation of H_2 from H atoms. In particular, considerable effort has been put into characterizing $H + H \rightarrow H_2$ reactions catalyzed by dust particles,[27-29] many of which are expected to be quite cold and coated by a water ice mantel.[19,30] As a result,

this requires recombination and desorption[31] of H_2 from the icy H_2O surface, the detailed interaction potential for which is necessary to characterize these important interstellar rate processes.

In addition to interstellar chemistry, the simple H_2-H_2O van der Waals dimer is of fundamental interest from a purely theoretical perspective. This complex has a small number of electrons (10), which facilitates high level ab initio efforts. It also contains only one non-hydrogenic atom which promotes convergence of dynamics calculations in multiple degrees of freedom. As a result this complex offers an unprecedented opportunity for a purely "first principles" test between experimental (i.e., high resolution spectroscopy) and theory (high level *ab initio*/dynamics calculations). Indeed, the small electron number has already stimulated the development of an *ab initio* potential energy surface[1] in full dimensionality (9D). This has been averaged over H_2 and H_2O intramolecular wavefunctions to provide a vibrationally adiabatic potential in the 5D subspace of intermolecular stretching and internal rotor coordinates, as first obtained by Valiron et al. in 2008 for H_2O and H_2 in their vibrational ground states. For the present studies, these calculations have been extended to the vibrationally excited overtone v_{OH} = 2 polyad of H_2O, in order to obtain accurate wavefunctions and energy levels relevant for detailed comparison to infrared overtone absorption spectroscopy.

The focus of this paper is two fold. First of all, we present a combination of *ab initio* and multidimensional dynamical calculations to obtain 5D intermolecular wavefunctions and energy levels for complexes of o/p-H_2(v=0) with both the ground o/p-H_2O ($|00^+\rangle$) and overtone excited states of o/p-H_2O ($|02^-\rangle$). These calculations are performed separately for each of the four spin symmetry species (i.e., oH_2-oH_2O, oH_2-

pH_2O, pH_2-oH_2O, and pH_2-pH_2O), which, in conjunction with a simple dipole moment function for $v_{OH} = 2$ excitation, are used to generate first principles infrared overtone absorption spectra for H_2-H_2O. As a second thrust of this paper, we describe and present results from a vibrationally mediated photodissociation (VMD) experiment, that permits us to indirectly but quite sensitively observe infrared absorption resonances in H_2-H_2O clusters by selective UV photolysis of vibrationally excited H_2O and laser induced fluorescence detection (LIF) of the resulting OH. With the aid of these high level predictions, we are able to identify and assign rotational progressions due to oH_2-oH_2O clusters in our experimental infrared spectrum. Additionally, the time delay between infrared and photolysis lasers as well as the transition of OH probed can be varied to gain further insight into the nature of predissociation dynamics in the complex.

5.2 Theoretical Background

A potential surface (PES) for H_2 -H_2O that includes all nine internal degrees of freedom has been calculated *ab initio* by Valiron *et al.*[1,32] with the use of the CCSD(T)-R12 method (coupled-cluster with singles, doubles, and perturbative triples, explicitly correlated). This PES is independent of nuclear mass and can be employed for any pair of water-hydrogen isotopologues. Several 5D "rigid-rotor" surfaces have been obtained, either by averaging the 9D potential over vibrational wavefunctions of H_2O and H_2 (or D_2)[1,13,32] or by fixing the internal geometry of the monomers at vibrationally averaged values, as done for[14,33,34] H_2-HDO, H_2-D_2O, and D_2-D_2O. In the case where both H_2O and H_2 are in their ground vibrational states, Valiron *et al*. have shown that the PES at the average vibrational ground state (VGS) geometry is in very good agreement with the

explicitly vibrationally averaged potential (VAP). The corresponding effects on scattering cross sections were examined by Scribano *et al.*[34], with the VGS and VAP potentials shown to provide very similar cross sections even at collision energies below 1 cm^{-1}. The high accuracy of these H_2-H_2O PES's has also been confirmed recently by a number of comparisons between theory and experiment including inelastic differential cross sections,[35] pressure broadening cross sections,[22,36] elastic integral cross sections,[14] and IR spectra of the complex.[11,13,37]

In the present work, we use two different vibrationally averaged 5D PES's with i) both H_2 and H_2O monomers in their ground vibrational state (as discussed in Valiron *et al.*[1]), and ii) ground state H_2 and H_2O in its doubly excited $|02^-)$ state, utilizing the wavefunction of Lori and Tennyson.[38,39] Both ground and excited state 5D potentials are expressed as a 149 term angular expansion,[1] with coupled spherical harmonics in polar angles for i) the center of mass vector $\boldsymbol{R}$ pointing from H_2O to H_2 and ii) the H_2 axis. These angles are defined with respect to a frame fixed to the H_2O monomer, with the *z* axis parallel to the C_2 symmetry axis and the *xz* plane parallel to the plane of the molecule. Note that these are not the same polar angles as the body-fixed (BF) angular coordinates used in the rovibrational level calculations, where the z axis of the BF frame is parallel to the vector $\boldsymbol{R}$. As shown elsewhere, however, one can analytically transform these angular functions into BF coordinates and directly use the R-dependent coefficients in the expansion of the potential to compute matrix elements of the Hamiltonian.

The global minimum corresponds to a planar geometry with C_{2v} symmetry, with a secondary, local minimum non-planar structure (see Fig. 2 and Fig. 1b in ref[11]). This global (local) minimum for *ground state* H_2-H_2O corresponds to a binding energy D_e =

235.14 cm^{-1} (199.40 cm^{-1}) and center-of-mass distance R_e of 5.82 a_0 (6.07 a_0)., with very small changes for H_2-H_2O with H_2O in its $|02^-)$ excited state (D_e = 235.66 cm^{-1}, R_e = 5.81 a_0 and D_e = 197.13 cm^{-1}, R_e = 6.15 a_0 for the global and local minima, respectively). Both of these geometries may be considered as hydrogen bonded: in the global minimum structure the H_2 monomer is the donor and H_2O the acceptor, in the local minimum structure H_2O is the donor and H_2 the acceptor. The $|02^-) \leftarrow |00^+)$ vibrational excitation needs to be accompanied by a rotational transition in order to make it dipole-allowed. Since this could either be internal (H_2O rotation) or intermolecular (tumbling of the cluster), the observed transitions are sensitive to the anisotropy of the intermolecular potential, and therefore to what extent the rotations of H_2O are hindered in the complex.

The method to compute the intermolecular rovibrational states on the 5D intermolecular potential surface is based on a general formalism[40] developed for weakly bound dimer molecular complexes with large amplitude internal motion such as ammonia[41-43] and water[40,44-47] dimer. For details on the Hamiltonian, body-fixed (BF) coordinates, etc., the reader is referred to previous work.[11] Rotational constants for H_2O (A_{gs} = 27.8806 cm^{-1}, B_{gs} = 14.52156 cm^{-1}, and C_{gs} = 9.2778 cm^{-1} for the ground state and A_{ex} = 25.9255 cm^{-1}, B_{ex} = 14.2100 cm^{-1}, and C_{ex} = 8.971415 cm^{-1} for the $|02^-)$ excited state) and H_2 (B_0 = 59.3398 cm^{-1}) are taken from experimental values,[48] with atomic masses of 1.007825 u for H and 15.994915 u for O. A discrete variable representation (DVR) grid in intermolecular distance contains 96 equidistant points between R = 4 to 26 a_0, contracted as before to form a radial basis of 20 functions.[11] The angular basis contains products of symmetric top Wigner D functions[49] and spherical harmonics for the

internal rotations of H_2O and H_2 , respectively, coupled with Wigner *D* functions for end-over-end rotation of the dimer and truncated at $j_{Amax} = 10$ for H_2O and $j_{Bmax} = 8$ for H_2.

The permutation-inversion (PI) or molecular symmetry group[50] $G_8 \equiv D_{2h}(M)$ of H_2-H_2O is generated by the permutation operation P_{12} interchanging the H nuclei in H_2O, a similar P_{34} operation that interchanges the H nuclei in H_2, and inversion E^*. Table 5.1 lists the resulting nuclear spin weights for the irreducible representations of G_8, as well as

irrep	j_B	H_2	k_A	H_2O	*weight*
A_1^+	even	p	even	p	1
A_1^-	even	p	even	p	1
A_2^+	even	p	odd	o	3
A_2^-	even	p	odd	o	3
B_1^+	odd	o	even	p	3
B_1^-	odd	o	even	p	3
B_2^+	odd	o	odd	o	9
B_2^-	odd	o	odd	o	9

Table 5.1: Symmetry relations in ground state $H_2 – H_2O$: irreducible representations of G_8, quantum numbers k_A and j_B relevant for symmetry, para/ortho (p/o) nature of the monomers, and nuclear spin statistical weights

quantum numbers k_A, which determine the para/ortho (p/o) nature of the H_2O states, and j_B , which determines whether the states belong to ortho or para H_2. The quantum number k_A is the projection of the H_2O angular momentum j_A on the C_2 symmetry axis of H_2O. Other (approximate) quantum numbers that help to understand the nature of the rovibrational states are m_A and m_B , the projections of the monomer angular momenta j_A

and j_B on the dimer axis $\boldsymbol{R}$, and the projection $K = m_A + m_B$ of the total angular momentum J on this axis. It is worth noting that the subscripts A, B refer to the two dimer subunits, and not, for example, to inertial axes of the H_2O internal rotor. Finally, we observe that the total angular momentum J and the parity $p = \pm 1$ under E^* are exact quantum numbers. In our analysis of the rovibrational states, we use the spectroscopic parity ε, which is related to the inversion parity by $p = \varepsilon(-1)^J$. With this notation, we also follow the convention of using the even/odd spectroscopic parity labels *e/f* to distinguish states with $K > 0$.[11]

The $|02^-\rangle$ vibrational state of H_2O is odd under P_{12} and belongs to the A_2^+ irrep of the symmetry group G_8 of the complex. The product of the $|02^-\rangle$ wavefunction of the H_2O monomer, the ground state of H_2, and the intermolecular rovibrational wavefunction must obey the usual relations, i.e., pH_2O corresponds to the $A_1^\pm$ and $B_1^\pm$ irreps, oH_2O corresponds to the $A_2^\pm$ and $B_2^\pm$ irreps, with *A/B* corresponding to pH_2/oH_2 and the parity $\pm$ referring to symmetry under inversion E^*. This yields the symmetry relations for the excited state wavefunctions shown in Table 5.2. The local H_2O coordinate frame is chosen with *z* and x axes along the *inertial* B (i.e. C_2) and A axes, with the molecule lying in the *xz* plane, by which para (ortho) H_2O wavefunctions can be identified by k_A = even (odd). The only nonzero component of the $|02^-\rangle \leftarrow |00^+\rangle$ transition dipole moment is the A-type component μ_x, which is invariant under all permutations, odd under inversion, and therefore has symmetry A_1^-. If we take the matrix element of μ_x between the ground state intramolecular wavefunction of A_1^+ symmetry and the $|02^-\rangle$ excited state wavefunction of A_2^+ symmetry, the resulting $|02^-\rangle \leftarrow |00^+\rangle$ transition dipole moment

irrep (total)	*irrep (intermolecular)*	j_B	H_2	k_A	H_2O
A_1^+	A_2^+	even	p	odd	p
A_1^-	A_2^-	even	p	odd	p
A_2^+	A_1^+	even	p	even	o
A_2^-	A_1^-	even	p	even	o
B_1^+	B_2^+	odd	o	odd	p
B_1^-	B_2^-	odd	o	odd	p
B_2^+	B_1^+	odd	o	even	o
B_2^-	B_1^-	odd	o	even	o

Table 5.2: Symmetry relations in H_2 – H_2O with H_2O in its excited |02-) state: irreducible representations of G8, intermolecular quantum numbers, and para/ortho (p/o) nature of the monomers.

function depends only on the intermolecular coordinates and has symmetry A_2^-. This leads to the selection rules for the intermolecular vibrational states given in Table 5.3.

The body-fixed (BF) basis in which the H_2-H_2O eigenstates are computed has been described previously,[11] and is a special case of the BF bases described by Eq. (16) of ref[51] and Eq. (16.24) of ref.[52] For the H_2 -H_2O basis, H_2O is treated as a rigid asymmetric top A, with H_2 as the specific case of a rigid symmetric top B with $k_B = 0$. The overall angular momentum J and its component M on the space-fixed (SF) z-axis are exact quantum numbers. The rovibrational wavefunctions $|i, J, M>$ of the complex, with i labeling the eigenstates of given J and M, are written as

$$|\, i, J, M\rangle = \sum_{n,I} |\, n, I; J, M\rangle c_{n,I}^{i,J,M} \qquad (2)$$

ground state irrep		*|02–) state irrep (intermolecular)*	*H_2*	*H_2O*
A_1^+	→	A_2^-	p	p
A_1^-	→	A_2^+	p	p
A_2^+	→	A_1^-	p	o
A_2^-	→	A_1^+	p	o
B_1^+	→	B_2^-	o	p
B_1^-	→	B_2^+	o	p
B_2^+	→	B_1^-	o	o
B_2^-	→	B_1^+	o	o

Table 5.3: Selection rules for the intermolecular rovibrational states involved in dipole transitions in H_2 – H_2O accompanying the (000) → |02-) transition in the H_2O monomer.

where *n* labels the radial basis functions and ***I*** denotes the set of internal angular quantum numbers [j_A, k_A, j_B, k_B, j_{AB}, K] in the BF basis. The coefficients $c_{n,I}^{i,J,M}$ are obtained by diagonalization of the dimer Hamiltonian in this basis. For calculating infrared transition intensities, one also needs the dipole moment operator (***μ***) as a function of intermolecular coordinates. In the same BF coordinates as the Hamiltonian, ***μ*** is given by Eqs. (35) to (38) of ref,[51] as well as Eqs. (16.14) to (16.17) of ref.[52] To obtain line strengths of $|02^-)$ ← $|00^+)$ transitions for the H_2 -H_2O complex, we consider ***μ*** as the 5D transition matrix element of the full 9D dipole function between ground state and $|02^-)$ excited state wavefunctions with respect to the 4 intramolecular coordinates.

The component matrix elements μ_m ($m = x,y,z$) of the dipole moment operator over the BF basis functions $|n,I;J,M>$ are given by Eq. (16.27) of ref.[52] We note, however, that

the correct phase factor $(-1)^{j_A'+j_B'+j_{AB}'+k_A'+k_B'+M'}$ should be $(-1)^{j_A+j_B+j_{AB}+k_A'+k_B'+L_A+L_B+L+M'}$. If we assume that the dipole moment function is determined purely by the (transition) dipole moment on H_2O monomer A, i.e., does not depend on intermolecular distance *R*, nor on the Euler angles of monomer B), the general formula can be simplified to:

$$\begin{aligned}
&\langle n', I'; J'M' | \mu_m | n, I; JM \rangle \\
&= (-1)^{j_{AB}+j_B+j_{AB}'+k_A'+M'+1} \delta_{n'n} \delta_{j_B' j_B} \delta_{k_B' k_B} \\
&\times [(2J'+1)(2J+1)(2j_A'+1)(2j_A+1)(2j_{AB}'+1)(2j_{AB}+1)]^{1/2} \\
&\times \begin{pmatrix} J' & 1 & J \\ -M' & m & M \end{pmatrix} \begin{Bmatrix} j_A & 1 & j_A' \\ j_{AB}' & j_B & j_{AB} \end{Bmatrix} \sum_k \begin{pmatrix} J' & 1 & J \\ -K' & k & K \end{pmatrix} \begin{pmatrix} j_{AB}' & 1 & j_{AB} \\ -K' & k & K \end{pmatrix} \\
&\times \sum_{K_A} \mu_{K_A} \begin{pmatrix} j_A' & 1 & j_A \\ -k_A' & K_A & k_A \end{pmatrix}
\end{aligned} \tag{10}$$

In Eq (10), $\mu_{K_A} \equiv Q_{K_A}^{(1)}$ are components of the (transition) dipole moment expressed in the local frame of monomer A, with 3-j and 6-j symbols designated by round and curly brackets, respectively.[49] In the local frame chosen on the H_2O monomer, the parallel (transition) dipole component with $K_A = 0$ is the $\mu_0 = \mu_z$ component and, since H_2O is a planar molecule and $\mu_y = 0$, the perpendicular components with $K_A = \pm 1$ are given by $\mu_{\pm 1} = \mp\mu_x/\sqrt{2}$, where choosing $\mu_x = 1$ is sufficient to obtain relative intensities. The transition dipole moment for a transition from state $|i, J, M\rangle$ to state $|i', J', M'\rangle$ is given by

$$d_m^{i,J,M \to i',J',M'} = \sum_{n',I';n,I} c_{n',I'}^{i',J',M'} c_{n,I}^{i,J,M} \langle n', I'; J'M' | \mu_m | n, I; JM \rangle \tag{11}$$

Since the molecules are randomly oriented in space and the energies of the states do not depend on the quantum number *M*, the transition line strength is obtained in the usual way by summing the square of the transition dipole moment over initial M′, averaging over final *M*, and using the sum relation

$$\sum_{M',M}\begin{pmatrix} J' & 1 & J \\ -M' & m & M \end{pmatrix}^2 = \frac{1}{3} \qquad (12)$$

The overall line strength is then given by $(d^{i,J\to i',J'})^2$, where $d^{i,J\to i',J'}$ is obtained from $d_m^{i,J,M\to i',J',M'}$ in Eqs. (10)-(11) by omitting the factor $\begin{pmatrix} J' & 1 & J \\ -M' & m & M \end{pmatrix}$.

5.3 Calculated Results

All bound rovibrational levels on the ground state intermolecular potential and all quasi-bound levels on the excited state potential have been calculated as a function of total angular momentum *J* and all four ortho/para combinations of H_2 and H_2O. The ground state levels for all four nuclear spin species have been reported previously in ref,[11] with the four sets of levels for the excited state potential listed in Tables 5.4-5.7. Information on the ground state Σ, Π, or Δ character (with approximate quantum numbers K = 0, 1, or 2) can also be found in ref,[11] which clearly demonstrates the lowest dimer states with pH_2 to have mostly Σ character (K = 0), whereas the corresponding lowest oH_2 states are always predominantly of Π character (K = 1). One important distinction between ground state and the vibrationally excited levels concerns the assignment to oH_2O vs. pH_2O species, which arises simply due to antisymmetry of the H_2O $|02^-\rangle$ wavefunction with respect to exchange of identical H atoms. As a result, the internal rotor rovibrational levels associated with the H_2O $|02^-\rangle$ excited vs. ground state potential surface of the complex have o and p labels interchanged.

Σ(K = 0)

Parity	*J = 0*	*J = 1*	*J = 2*	*J = 3*
e	-14.272	-13.5226 (90%)	-11.7442 (80%)	-8.7553 (73%)
e	20.9514	20.9433 (64%)	21.6149 (57%)	22.8614 (53%)
f	12.3387	14.0284 (96%)	17.3196 (91%)	22.0751 (85%)

Π(K = 1)

Parity	*J = 1*	*J = 2*	*J = 3*
e	-7.1213 (90%)	-3.4031 (80%)	1.7787 (73%)
e	4.2473	7.0008	11.1029
e	22.7788 (65%)		
f	-7.7672	-5.0476	-1.0071
f	3.8823 (96%)	5.976 (91%)	9.2156 (86%)
f	22.1423	23.2544	

Table 5.4: Rovibrational levels of symmetry $A_2^{\pm}$ of $pH_2 - pH_2O$ |02-) (in cm^{-1}). The energy of the dissociation limit to pH_2 and pH_2O |02-) is at 23.7994 cm^{-1}, so the dissociation energy D_0 = 38.07 cm^{-1}. In parentheses is the Σ or Π character, which is higher than 99% if not otherwise indicated. The parity e/f is the spectroscopic parity.

Σ(K = 0)

Parity	*J = 0*	*J = 1*	*J = 2*	*J = 3*
e	-34.5328	-33.1532	-30.4075	-26.3243
e	-2.9507	-2.2637 (95%)	-0.8188 (94%)	

Table 5.5: Rovibrational levels of symmetry $A_1^{\pm}$ of $pH_2 - oH_2O$ |02-) (in cm^{-1}). The dissociation energy D_0 = 34.53 cm^{-1}.

Σ(K = 0)

Parity	*J = 0*	*J = 1*	*J = 2*	*J = 3*
e	90.7607	92.3868 (98%)	95.5992 (95%)	100.3258 (91%)
e	112.8261	113.9473 (97%)	116.219 (93%)	119.6747 (89%)
e	135.8546	136.928 (95%)	138.8707 (90%)	141.5769 (65%)
e	139.7633	140.9057 (94%)		
f	96.2396	97.0102 (74%)	99.0267 (63%)	102.3673 (57%)
f	118.9932	120.3044 (97%)	122.9131 (90%)	126.8016 (79%)
f	126.7211	127.9918	130.523 (97%)	134.2767 (94%)
f	139.8353	140.7114 (91%)	142.3644 (73%)	

Π(K = 1)

Parity	*J = 1*	*J = 2*	*J = 3*
e	80.4069 (98%)	82.8192 (95%)	86.4685 (91%)
e	98.6498 (0%)	101.1751 (97%)	104.9825 (94%)
e	123.0357 (97%)	126.2302 (86%)	130.7134 (77%)
e	132.9728 (94%)	134.2682 (85%)	136.4236 (78%)
e	138.0829 (97%)	139.3161 (87%)	141.124 (57%)
f	80.6253	83.4491 (99%)	87.6636 (98%)
f	99.2279 (74%)	102.3898 (62%)	106.7318 (53%)
f	122.8846 (97%)	125.8496 (84%)	130.1521 (73%)
f	133.306	135.113 (98%)	137.7444 (94%)
f	137.9746 (92%)	138.9842 (78%)	140.6585 (71%)

Δ(K = 2)

Parity	*J = 2*	*J = 3*
e	109.2813 (98%)	113.3813 (95%)
e	123.8142 (92%)	127.735 (86%)
e	141.3118 (86%)	
f	109.3114 (97%)	113.5212 (92%)
f	123.8082 (89%)	127.7344 (77%)
f	141.2413 (83%)	

Table 5.6: Rovibrational levels of symmetry $B_2^{\pm}$ of $oH_2 - pH_2O$ |02-) (in cm^{-1}). The dissociation energy $D_0 = 62.07\ cm^{-1}$.

Σ(K = 0)

Parity	*J = 0*	*J = 1*	*J = 2*	*J = 3*
e	62.4181	63.8496	66.7038 (99%)	70.9616 (98%)
e	107.767	108.9822 (92%)	111.216 (83%)	114.0028 (53%)
e	113.136	114.2694 (98%)	116.6432 (86%)	
f	115.1	116.3106 (81%)		

Π(K = 1)

Parity	*J = 1*	*J = 2*	*J = 3*
e	79.3032	81.9811 (99%)	85.9748 (98%)
e	107.9309 (92%)	110.3614 (81%)	114.1719 (50%)
e	117.3353 (98%)		
f	79.3623	82.1564	86.3196
f	107.9024 (98%)	110.2522 (94%)	113.7747 (90%)
f	117.4753 (84%)	118.1563 (73%)	

Δ(K = 2)

Parity	*J = 2*	*J = 3*
e	116.046	
f	116.075	

Table 5.7: Rovibrational levels of symmetry $B_2^{\pm}$ of $oH_2 - oH_2O$ |02-) (in cm^{-1}). The dissociation energy $D_0 = 56.26\ cm^{-1}$.

It is also worth noting that levels on the excited state potential are more strongly bound (by up to 3 cm^{-1}) than those of the same symmetry on the ground state potential, despite only minor changes in the intermolecular surfaces. The predominant reason is that the H_2O rotational constants *decrease* in the excited $|02^-\rangle$ state, and thus the zero-point energy associated with the hindered internal rotations is lowered correspondingly.

The wavefunctions and formulae in Sec. IC.2 permit us to calculate line strengths for all the allowed $\Delta J = 0$ and ± 1 transitions between all bound levels with $J = 0 - 6$ on the ground and excited state potentials. Transitions with $\Delta J = \pm 1$ occur between ground and excited state levels of the same spectroscopic parity: $e \rightarrow e$ and $f \rightarrow f$; transitions with $\Delta J = 0$ require a change of spectroscopic parity: $e \rightarrow f$ and $f \rightarrow e$. The calculated line strengths and the Boltzmann factors for the ground state levels combine to yield detailed spectral simulations for each of the four ortho/para combinations of H_2-H_2O, which can then be used to assign and interpret the measured action spectra described below.

5.4 Experimental Technique

The experimental apparatus for obtaining the H_2-H_2O cluster overtone spectra has been described previously;[8,53] therefore, only a brief overview and details relevant to these specific studies will be necessary. Water-hydrogen gas mixtures are prepared by bubbling pure (99.99 %) H_2 through a sealed reservoir filled with purified (ρ = 10 MΩ*cm) and degassed water. The stainless steel reservoir is held at 0° C by immersing in an ice water bath in order to maintain a steady water vapor pressure[55] of 4.6 Torr. In addition, this “precooling” scheme ensures that all downstream components of the gas

delivery system are at a higher temperature than the liquid reservoir, thus ensuring an absence of condensation once the mixture has been formed. Water partial pressure is fixed by maintaining a constant H_2 gas pressure in the bubbler, with the pulsed jet stagnation pressure independentaly controlled by a needle valve immediately downstream. Total pressure inside the bubbler is monitored with a Baratron capacitance manometer and used to infer H_2/H_2O molar ratios. Typical values of 0.1 % water are found to optimize H_2-H_2O cluster formation, presumably because richer mixtures reduce dimer population in favor of larger complexes. A second Baratron monitors and stabilizes pressure in the jet source stagnation region at 550 torr, a value that again appears to lead to maximal OH signal production for H_2-H_2O.

The H_2/H_2O mixture is delivered to a home built slit jet source described extensively elsewhere. A 1 ms pulse duration and 100 ms spacing between valve firing events results in a 99 % reduction in average versus peak gas flow, allowing the chamber to be at ~ 10^{-5} Torr with a 4500 L/s diffusion pump backed by a 25 L/s mechanical pump. Action spectra of water monomer species that remain unclustered in the beam show no rotational excitation above the signal to noise level. This yields an upper limit of T_{rot} < 5.1 K for the jet temperature, which compares favorably with T_{rot} = 3.5 K temperatures predicted from modeling[56] the slit jet as an isentropic expansion. As a result, H_2O cools exclusively down into the two lowest nuclear spin states, which are not expected to interconvert on the expansion time scale. Due to the requirement of exchange symmetry for the two identical hydrogen atoms, the ortho and para populations conform to the expected nuclear spin ratio of 3:1 for $J_{KaKc} = 1_{01}$ and 0_{00} states, respectively. While not

observed directly, a similar 3:1 ratio is anticipated for ortho (J=1) and para (J = 0) H_2 in the supersonic expansion.

The three laser cluster detection scheme is shown in Fig. 5.1. Vibrational excitation of H_2O, either in the H_2-H_2O cluster or after predissociation, is achieved with

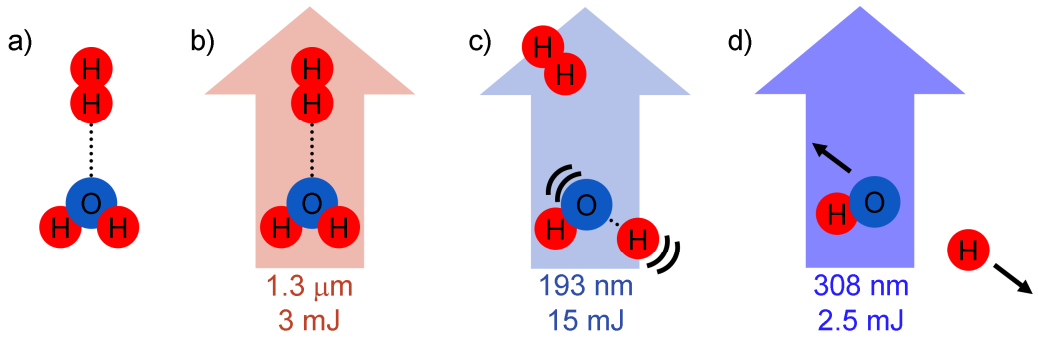

Figure 5.1 Scheme used to detect H_2 – H_2O clusters: a) Complexes are formed in a ~ 3 K slit supersonic jet. The potential energy minimum structure is shown here. b) An infrared laser pulse excites the $|02^-\rangle$ overtone stretch vibration of the H2O moiety. c) The H_2O is photolyzed by a laser at 193 nm, a color which efficiently breaks apart vibrationally excited water while minimizing background from photolysis of the ground state. The time delay between the IR and photolysis lasers can be varied to probe predissociation of the metastable cluster state. d) OH photolysis products are detected by laser induced fluorescence following excitation by a tunable 308 nm pulse.

an optical parametric oscillator (OPO) laser pumped by 600 mJ of 1064 nm light. The idler beam is extracted from the OPO cavity and directly sent into the vacuum chamber with 3 mJ/pulse energies and 0.2 cm^2 spot area. At these intensities, H_2O in the 1_{01} rotational state has only a 5 % probability[57] of absorbing an IR photon, resulting in a safely negligible ($< 3 \times 10^{-3}$) probability for multiple photon absoprtion. In order to probe the expected range of H_2-H_2O absorptions, the laser frequency is tuned from 7210 cm^{-1} to 7310 cm^{-1}, with a small IR pickoff sent through an optoacoustic cell filled with 5

Torr of H_2O. Doppler broadening of H_2O lines in such a cell ($\Delta\nu \approx 0.02$ cm^{-1}) is > 10-fold narrower than the OPO laser ($\Delta\nu \approx 0.25$ cm^{-1}), and thus provides convenient frequency axis calibration by linear interpolation between known frequencies in the sufficienly dense (~ 2 lines/cm^{-1}) room temperature water absorption spectrum.

A digital delay generator provides a variable waiting time between the OPO and 193 nm excimer laser and therefore probes predissociation dynamics on time scales ranging from ~ 5 ns to 1 μs. The 193 nm UV beam (15 mJ/pulse, ~ 0.5 cm^2 area) selectively photolyzes the vibrationally excited H_2O to make OH radicals, which are subsequently detected by a third LIF laser (303 nm - 310 nm, beam energy ~ 2.5 mJ), obtained from frequency tripling the output of a dye laser pumped by a frequency doubled YAG laser. All three beams enter/exit the chamber through CaF windows tilted at Brewster's angle in order to minimize reflections of the p-polarized probe radiation, which can lead to an appreciable background degrading LIF detection. Furthermore, the 2 mm LIF probe beam travels through 8 annular optical baffles with inner diameter of 1 cm to further minimize the amount of window scatter entering the chamber.

Fluorescence emission from electronically excited OH is collected by a fused silica lens (f = 5 cm) positioned 5 cm from the excitation region, passing through a fused silica chamber window and a Schott UG11 filter to effectively block scatter from the 193 nm photolysis pulse. The LIF photons are imaged onto a solar blind 14 stage photomultiplier tube (PMT) with a gain at 1700 V of ~ 5 x 10^6 electrons/photon, sending the subsequent electrical current through a 50 Ω load resistor, across which a voltage is amplified (x 20), collected by boxcar integration between 10 ns to 1 μs after the probe beam, thereby capturing the majority of fluorescence photons over the ~ 1 μs lifetime of

the electronically excited OH molecules. The PMT voltage is then averaged over the boxcar detection window before being sent through an A/D converter and then recorded using a Labview program which also controls scanning of the IR excitation laser or the UV probe beam. The probe laser energy is monitiored in real time with a diode power meter, with the final LIF signal scaled to eliminate pulse-to-pulse variation in the probe laser beam.

5.5 Results

As immediately evident in Fig. 5.2, the action spectrum obtained by scanning the infrared excitation laser is completely dominated by overtone $|02^-)$ transitions (i.e., (101) ← (000) in normal mode notation) of the H_2O *monomer*, which attests to the limited degree of clustering occuring in the predominantly H_2 supersonic jet. However, upon closer inspection, a closely spaced progression of smaller peaks are observed with intensity above the signal to noise limit, as shown in the blowups in Fig. 5.2. These transitions do not correspond to any nearby peaks from water monomer such as the $|02^+)$ ← |00> overtone symmetric stretch excitation (i.e., (200) ← (000) in normal mode notation), nor can they be assigned to overtone transitions in any H/D isotopomers of H_2O. Since H_2 monomers do not exhibit any absorption due to lack of an infrared transition dipole moment, the small peaks in Fig. 5.2 are almost certainly reflect hydrogen-water clusters in the jet.

The *ab initio*/vibrational dynamics calculations described in the first half of this paper play a critical role in confirming such an assignment. We start building intuition with body fixed (BF) eigenfunctions generated from the 5D H_2-H_2O potential surface for

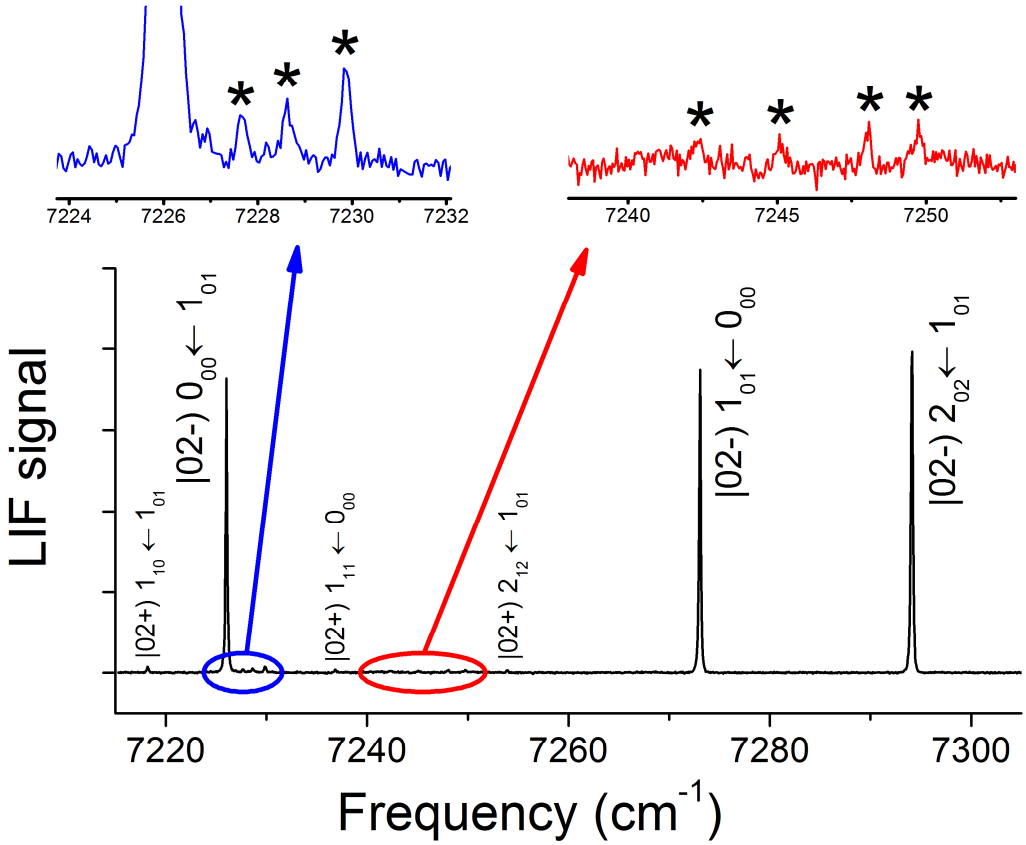

Figure 5.2 Action spectrum obtained by observing production of OH ($^2\Pi_{3/2}^e$, N=8) while varying the infrared excitation frequency at a fixed IR-photolysis time delay of 30 ns. The spectrum is dominated by water monomer transitions from the lowest rotational energy states in each nuclear spin manifold (ortho and para). Zooming in reveals two bands of smaller peaks which are likely due to H_2-H_2O clusters in the supersonically cooled beam. One band is near the free ortho H_2O transition $|02^-)$ 0_{00} ← 1_{01}, while the other sits at the rotationless band origin of the |02-) vibrational excitation.

the excited $|02^-)$ H_2O vibrational state. Specifically, Fig. 5.3 displays 2D slices through these eigenfunctions in the polar angles β_{H2O} and β_{H2}, for the lower Σ (upper panel) and first excited Π (lower panel) internal rotor states for oH_2-oH_2O complex. Note that both these states are built from the nominally "non-rotating" $j_{kakc} = 0_{00}$ internal rotor oH_2O state, so that the Σ vs Π projection comes prodominantly from angular momentum of the oH_2 subunit. In general, both wavefunctions are characterized by large amplitude

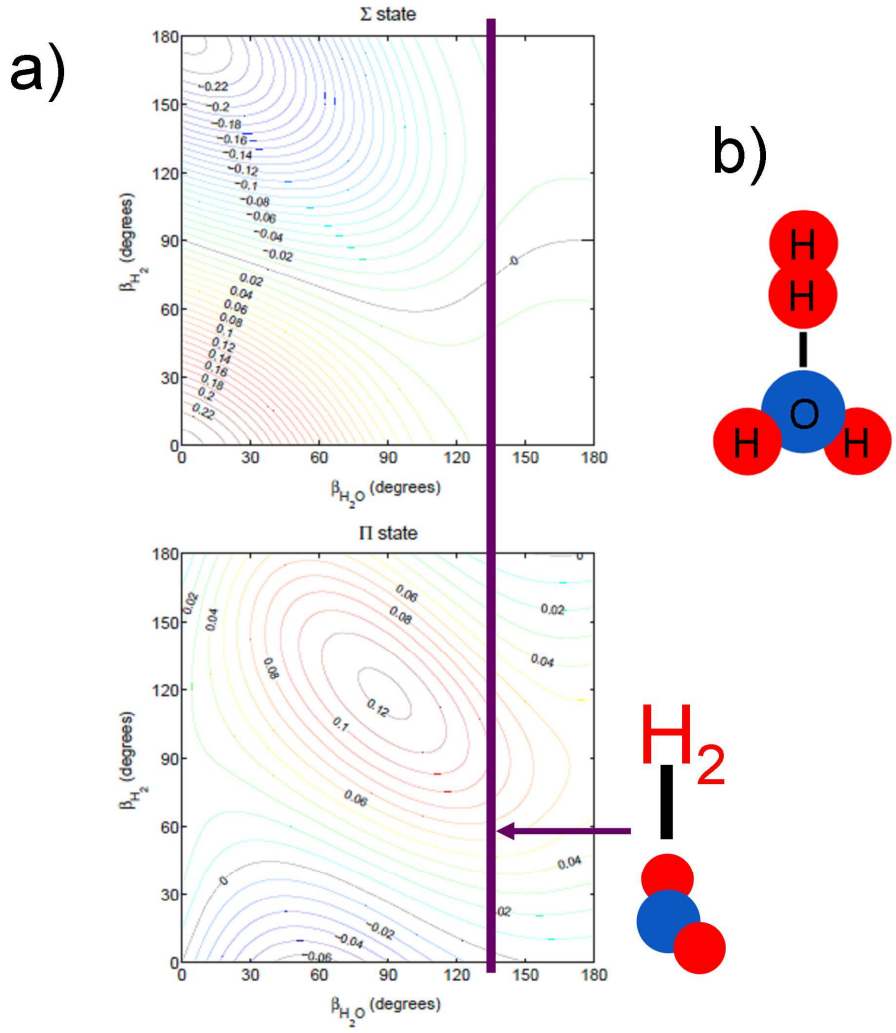

Figure 5.3 a) Cuts of the J = 1 wave functions of the Σ ground state and the lowest Π state of oH_2O –oH_2 for planar geometries. The angles β_{H_2O} and β_{H_2} are the polar angles of the H_2O symmetry axis and the H_2 bond axis in the BF dimer frame. The global minimum (b) in the potential for the planar hydrogen-bonded structure with H_2O as the acceptor corresponds to β_{H_2O} = 0° and β_{H_2} = 0° or 180°. The local minimum, where H_2O behaves as a hydrogen bond donor occurs at a non-planar structure which projects onto β_{H_2O} = 119° and β_{H_2} = 90°. The purple line corresponds to the range of planar geometries where the OH stretch aligns with the intermolecular axis. This range of geometries, which is expected to most efficiently couple internal |02-) H_2O vibrational motion into the dissociative intermolecular coordinate, is sampled extensively by the lowest Π state of the complex while it is much more unlikely in the lowest Σ state.

quantum motion and significant departure from the global minimum energy "hydrogen bond acceptor" structure for H_2O at $\beta_{H2O} = 0^o$ and $\beta_{H2} = 0^o$, 180^o, even sampling the higher minimum energy "hydrogen bond donor" structure at $\beta_{H2O} = 135^o$ and $\beta_{H2} = 90^o$. This confirms the zeroth order nature of H_2 and H_2O wavefunctions in the complex as that of nearly free internal rotors, with angular motion weakly coupled by the anisotropy in the potential energy surface. Thus, a more complete description of the states in Fig 5.3a for oH_2-oH_2O might be Σ $(1,0_{00})$ and Π $(1,0_{00})$, where the first and second terms in parenthesis refer to the quanta of H_2 and H_2O angular momenta.

Based on calculated energies and wavefunctions for all levels in both ground and internally vibrationally excited $|02^-)$ states, it is possible to predict an infrared spectrum of the complex from first principles. A small sample segment of this is shown in Fig 5.4a, where where observed lines are labeled using symmetric top notation as $^{\Delta K}\Delta J_{K''}(J'')$. For this simulation, the best fit to the data was obtained at a beam temperature of 3.8(3) K, a value achievable in the cold environment of a supersonic expansion and which agrees with the previously obtained upper limit of 5 K. Despite potential complications associated with action spectroscopy vs direct absorption spectroscopy based intensities, the degree of agreement observed between experiment and theory is extremely encouraging. In particular, this provides strong evidence for assignment of the peaks in the $0_{00} \leftarrow 1_{01}$ monomer region as coming from the corresponding Σ $(1, 0_{00}) \leftarrow \Pi$ $(1, 1_{01})$ free internal rotor transition in the oH_2-oH_2O complex, blueshifted by $\approx$ 4 cm-1 from the $0_{00} \leftarrow 1_{01}$ transition of the H_2O moiety at 7226 cm^{-1} due to presence of the $H_2(j=1)$.

In addition, a weaker second set of transitions is observed near the water monomer band origin [59,60] at $\nu_0 = 7249.823$ cm^{-1} (Fig. 5.4b), where again experiment and

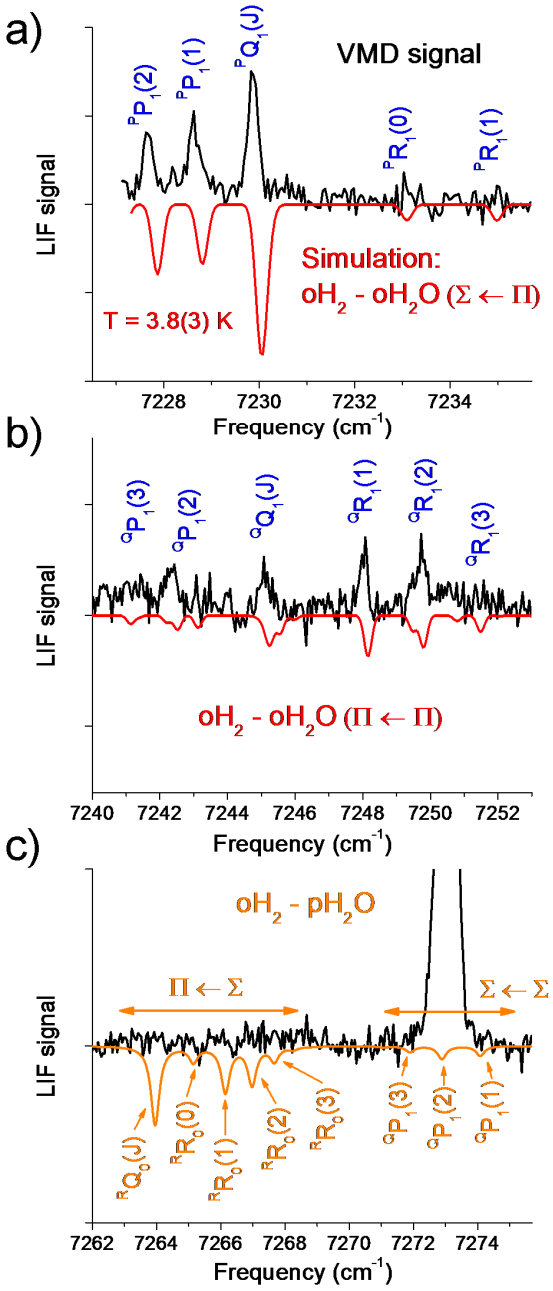

Figure 5.4 Theoretical calculations agree well with the experimental spectrum with a best fit temperature of 3.8(3) K. The excellent agreement between experiment and theory allows assignment of all observed peaks to oH_2O-oH_2 (as shown in red). Two bands are observed, a $\Sigma \leftarrow \Pi$ (a) and a $\Pi \leftarrow \Pi$ (b). Searches for the pH_2O - oH_2 species (c) do not reveal any transitions near the predicted peaks despite the fact that such transitions would be above the signal to noise limit were their magnitudes determined entirely by nuclear spin statistics. All lines are labeled in symmetric top notation according to $^{\Delta K}\Delta J_{K''}(J'')$.

theory agree reasonably well on the various infrared transitions, providing further support for assignment to the oH_2-oH_2O dimer species. Interestingly, there is no allowed transition for H_2O monomer in the band origin region, with appearance of spectral structure only made possible by angular anisotropy in the potential. Simply stated, this anisotropy makes angular momentum of the H_2O subunit an imperfect quantum number, and therefore generates oscillator strength on the nominally "forbidden" Q-branch monomer transitions corresponding to no change in water angular momentum. The presence of a Q-branch for the cluster and the expected cold temperature of the supersonic jet identify this as a progression in the Π $(1,0_{00}) \leftarrow \Pi$ $(1,1_{01})$ band, which probes a second, completely independent internal rotor state in the $|02^-)$ manifold. As will be discussed in more detail in Sec. IVB, this provides acess to photolysis and predissociation dynamics in two seperate metastable states of the oH_2-oH_2O cluster.

Finally, we see no evidence within our signal to noise limits for experimental action spectra corresponding to oH_2-pH_2O complexes. The relevant scan region is shown in Fig. 5.4c, which displays sample *ab initio*/dynamics predictions for the $\Pi(1,1_{01}) \leftarrow \Sigma(1,0_{00})$ and $\Sigma(1,1_{01}) \leftarrow \Sigma(1,0_{00})$ bands. Note that these band origins lie 9 cm^{-1} to the red and a few cm^{-1} to the blue, respectively, of the associated $1_{01} \leftarrow 0_{00}$ transition at 7273 cm^{-1} for the free pH_2O monomer. It is important to consider that these intensity predictions are based on incorporation of ortho/para H_2O nuclear spin states into the complexes in a 3:1 ratio, which may well be violated due to "chaperone" displacement effects in the slit jet expansion. As we shall see later, an even more intriguing dynamical possibility is that the upper state predissociation for both $\Pi(1,1_{01})$ and $\Sigma(1,1_{01})$ bands is selectively fast

enough for lifetime broadening to exceed the 0.5 cm^{-1} IR laser line width, and thereby greatly decrease the spectral signal to noise.

We can take these studies considerably further by exploring i) the product state distributions of the nascent OH photofragment, as well as ii) the predissociation time scale on which these distributions evolve. By way of example, Fig. 5.5 displays the

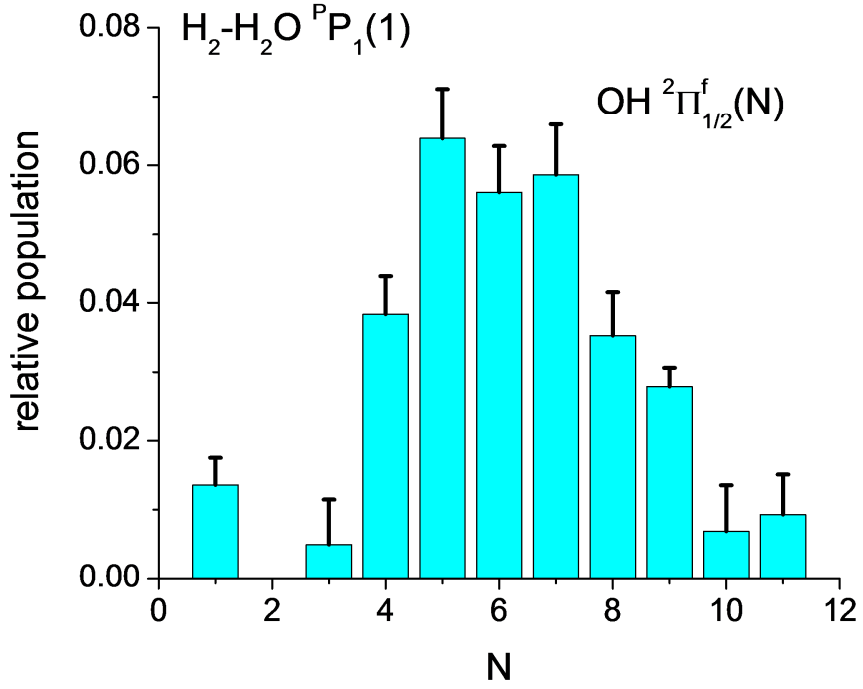

Figure 5.5 OH rotational distributions obtained with the infrared laser fixed on the $^{P}P_1(1)$ [$\Sigma \leftarrow \Pi$] transition of oH_2O-oH_2. The relatively hot rotational distribution is likely a result of photolysis in a bend vibrationally excited state of H_2O products of cluster predissociation.

nascent rotational state distribution in the $^{2}\Pi^{f}_{1/2}(N)$ OH manifold, subsequent to $^{p}P_1(1)$ infrared excitation of pH_2-oH_2O clusters in the Σ $(1, 0_{00}) \leftarrow \Pi$ $(1, 1_{01})$ band at an IR-photolysis delay of 30 ns. Interestingly, the rotational distribution is *quite hot*, peaking at an N-O tumbling angular momenta of N = 6. This is in sharp contrast with the extremely

cold rotational distributions observed in the absence of the H_2, for example, via coresponding overtone vibrationally mediated photolysis studies of oH_2O monomer out of the $|02^-)$ 0_{00} rotational state. Interstingly, however, this rotationally hot distribution from oH_2-oH_2O dimer is nearly identical to vibrationally mediated photolysis results[8] obtained for Ar-oH_2O and H_2O-H_2O. Clearly the presence of even weakly bound species such as H_2 can be responsible for qualitative changes in the resulting energy flow and photolysis dynamics of the excited H_2O subunit.

This point deserves further discussion. First of all, though OH(N = 6) corresponds to ≈ 850 cm^{-1} rotational energy, this is actually rather modest (< 5%) compared to the ≈ 17,860 cm^{-1} available after overtone IR excitation (≈ 7229 cm^{-1}), cluster dissociation (≈ 56 cm^{-1}), 193 nm photolysis (≈ 51,813 cm^{-1}) and H-OH bond breaking (≈ 41,128 cm^{-1}) events. Secondly, as discussed in more detail below, these scans are performed with the IR-photolysis time delay long compared to the predissociation lifetime of the complex, which means that photolysis is of the free H_2O monomer rather than an intact H_2-H_2O cluster. Thirdly, photojection of a light H atom species from rovibrationally cold H_2O on the A state surface is known to generate low rotational excitation in the resulting OH fragment. Therefore, the remarkable similarity of product OH distributions obtained from overtone vibrationally mediated photolysis of M-H_2O clusters for M = Ar, H_2O and H_2 is more likely an indication of qualitatively similar rovibrational excitation in the H_2O molecule *after* the predissociation event. Specifically, Ar-H_2O predissociation from the $|02^-)$ overtone state has previously been predicted to occur via near resonant energy transfer of one asymmetric stretch vibrational quantum into two quanta of the H-O-H bending mode. This would indeed be consistent with Fig.

5.5, as as excitation in the HOH bending coordinate is predicted from a Franck-Condon perspective to correlate with the much hotter OH rotation distributions observed. Finally, it is interesting to note that the OH rotational distributions observed from vibrational overtone mediated photolysis of each cluster species vary quite smoothly with N. This is in dramatic contrast with the high contrast, quantum interference oscillations observed for population vs. N in photolysis of $|02^-)$ H_2O from its lowest rotational state(s). As a simple physical picture, this might suggest either disruption of the quantum phase relationships between the outgoing H and OH fragments in the presence of a third body (i.e., H_2, Ar or H_2O), or simply a blurring of this interference structure due to rotational excitation of the bare H_2O monomer by predissociation prior to the photolysis event.

We can take this one step further by studies of predissociation dynamics in the time domain. As shown in Fig. 5.6, the observed OH (N = 8) population exhibits a slow sigmoidal increase with time delay between infrared ($|02^-)$ $^pP_1(1)$) cluster excitation and photolysis (193 nm) pulses. Since the photolysis process is essentially prompt, this provides an opportunity to make direct measurement of the predissociation timescale of the initial metastable cluster. Indeed, the inset in Fig. 5.6 shows the result of such a time delay scan for the corresponding H_2O monomer line. This yields an instrument response function (IRF) of 8.0(3) ns, which is entirely dominated by finite pump and photolysis laser beams, but significantly faster than experimental rise times observed for the cluster. For the $|02^-)$ Σ $(1,0_{00})$ J = 0 upper state of oH_2-oH_2O accessed by ($|02^-)$ $^pP_1(1)$ excitation at $\approx$ 7228.5 cm^{-1}, least squares deconvolution of signal and IRF yields a predissociation lifetime of 15(2) ns, i.e., in roughly 2-fold excess of the detection limit. However, these lifetimes might also be anticipated to depend sensitively on intermolecular orientation of

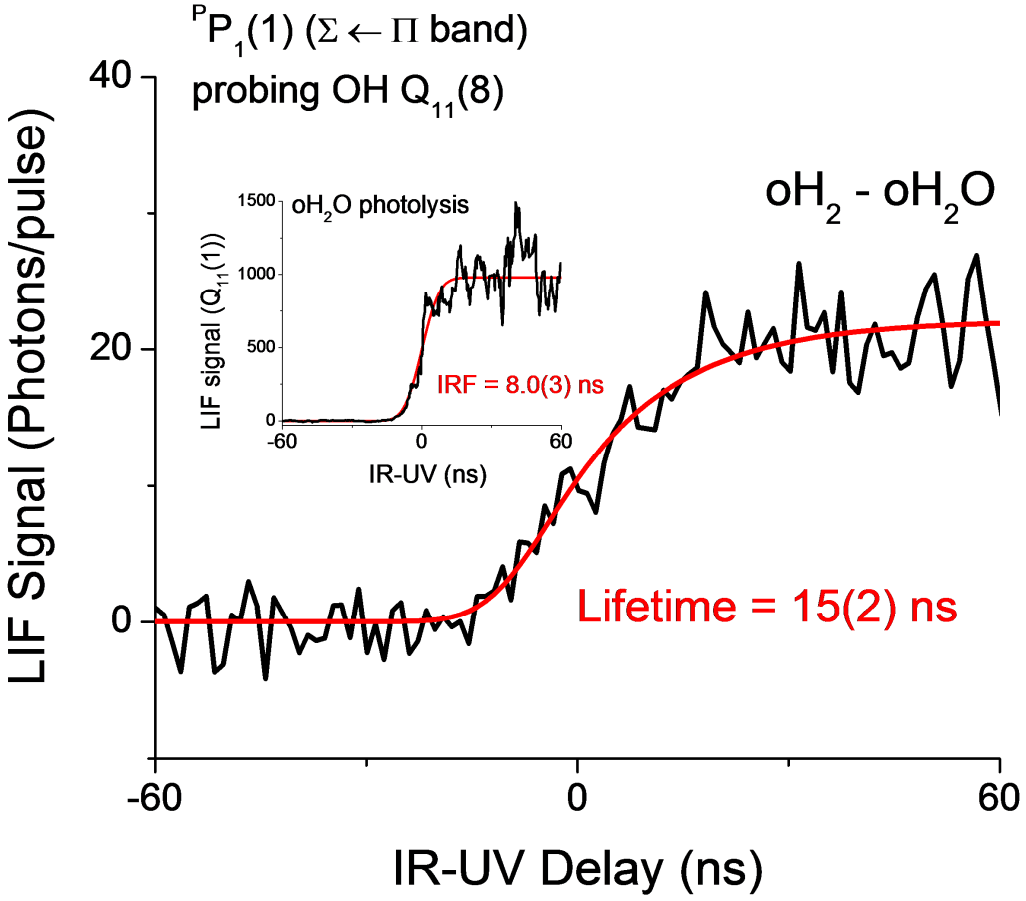

Figure 5.6 Direct observation of predissociation lifetime in oH_2-oH_2O. This is obtained by varying the time delay between the infrared excitation and the photolysis pulse while examining a specific cluster transition and a particular OH level. The measured lifetime of 15(2) ns is large compared to the instrument response function of 8 ns as determined by observing H_2O monomer lines (inset).

the H_2 and H_2O subunits. Indeed, by way of contrast, simular study of excitation to the corresponding |02-) Π state yields a predissociation lifetime of < 5(2) ns, i.e. indistinguishable from the IRF. Additional support for such a dynamical trend can be rationalized by inspection of the corresponding intermolecular wavefunctions for these excited states, as will be explored below,

5.6 Discussion

As one major goal of this work, we take the opportunity for a detailed comparison between quantum state resolved experimental spectra and first principles ab initio and dynamical theory. Indeed, consensus between experiment and theory is quite remarkable (see Fig. 5.4), with a sub-cm^{-1} level of agreement already 3 orders of magnitude smaller than the ≈ 235 cm^{-1} equilibrium 5D well depths for the (o/p)H_2-(o/p)H_2O potential surfaces. However, closer inspection of the least squares fits reveals that theoretical peak positions are slightly but systematically *blue shifted* (+0.195(7) cm^{-1})) relative to the experimental value. Note that our 5D theoretical framework does not allow intramolecular relaxation of either O-H or H-H bonds due to the presence of the other species in the cluster. Nevertheless, the global 9D minimum would be expected to reveal weak stretching of these coordinates due to hydrogen H atom and water oxygen attraction. This leads to a slight reduction in the oxygen atom confinement, resulting in lower energies for both ground $|00^+\rangle$ and excited $|02^-\rangle$ levels of the H_2O moiety. However, due to enhanced anharmonic sampling of the potential, one expects additional relaxation in the vibrationally excited state upper state, thus rationalizing a small but systematic ≈ 0.2 cm^{-1} blue shift between reduced dimensionality theory and "full D" experimental data.

A more fundamentally challenging issue arises when one considers the notable absence of any nuclear spin species other than oH_2-oH_2O in the observed spectrum. Due to the long spin flip thermalization time scales for this degree of freedom, the relative abundances of both [oH_2]/[pH_2] and [oH_2O]/[pH_2O] are expected to be very close to their spin-degeneracy ratios (3:1), as is indeed seen in the room temperature distribution in the

stagnation region of the pulsed jet source. Therefore, purely statistical arguments would predict relative 9:3:3:1 abundances for (oH_2-oH_2O):(oH_2-pH_2O):(pH_2-oH_2O):(pH_2-pH_2O), respectively. Fig. 5.4c shows sample results of such predictions for nuclear spin abundances fixed to the above ratios, with rotational distributions separately thermalized at 3.8 K. This dataset makes immediately clear that statistical ratios of both oH_2-pH_2O and pH_2-pH_2O would lead to populations well above the signal to noise limit yet not observable in the experimental spectrum.

A partial explanation can be found in the "chaparone effect" which is a consequence of the different binding energies of the various species (Table 5.8) and the 1000:1 abundance of H_2 vs. H_2O in the jet. In this model, pH_2-oH_2O and pH_2-pH_2O form early on in the supersonic jet, with subsequent collisions with oH_2 displacing the more weakly-bound pH_2 and systematically depleting the pH_2O vs oH_2O containing clusters. The reverse process, $pH_2 + oH_2\text{-}H_2O \rightarrow pH_2\text{-}H_2O + oH_2$, is suppressed by a $\Delta D_0 \approx 20$ cm^{-1} difference in binding energy for ortho vs. para H_2, which by detailed balance arguments plays a dramatic role at low jet temperatures. Indeed, in the high collision

Species	*Binding energy (cm^{-1})*
oH_2-oH_2O	59.04
oH_2-pH_2O	54.60
pH_2-oH_2O	37.63
pH_2-pH_2O	34.57

Table 5.8: Binding energy for H_2-H_2O for all four nuclear spin species.

regime, the number of pH_2 vs. oH_2 clusters at thermal equilibrium would be disfavored by a factor of $e^{-20/2.7} = 6 \times 10^{-4}$, i.e., sufficient to diminish signals well below the detection limit. Indeed, precedent for such differential binding affinities of ortho vs para H_2 has already been well established in previous high resolution IR studies of $(o/p)H_2$-HF and $(o/p)H_2$-HCl. Indeed, the most convincing comparison can be made with spectroscopic studies on exact same $(o/p)H_2$-(o/p) H_2O clusters in the fundamental HOH bend region, for which both pH_2-pH_2O and pH_2-oH_2O remained unobserved despite high signal to noise (> 20:1) on the corresponding oH_2-pH_2O and oH_2-oH_2O nuclear spin species.

However, this does not explain the absence of oH_2-pH_2O vs. oH_2-oH_2O clusters (see Fig. 5.4c), for which a differential binding energy of $\Delta D_0 \approx 5.5$ cm^{-1} would only predict a 4-5 fold reduction in population at thermal equilibrium. More importantly, the fractional concentrations of both oH_2O vs. pH_2O reagent are very minor components (< 0.1%) in the supersonic jet, resulting in vanishingly low collision rates for such processes to reach local thermal equilibrium. Indeed, the previous spectroscopic studies in the bend region noted above yielded high quality spectra of both oH_2-oH_2O and H_2-pH_2O clusters in the anticipated ≈ 3:1 ratio. Clearly some other phenomenon unique to $|02^-)$ excitation must be invoked to explain the *non-observance* of the oH_2-pH_2O species in the present studies.

Though this will require further experimental and theoretical efforts, one possibility worth exploring is rapid predissociation of oH_2-$pH_2O|02^-)$, which could broaden the IR transitions sufficiently to make them unobservable. Such broadening has in fact been observed[16] in our group via high resolution laser absorption for oH_2-pH_2O and oH_2-oH_2O clusters in the HOH bend fundamental region. However, while these

previous measurements reported predissociation lifetimes of 5.1(1) ns, 1000-fold faster values would be required to achieve ~ 1 cm^{-1} broadening of these transitions below the detection limit. Such 5 ps lifetimes would correspond to only ≈ 500 vibrations of the OH stretch in the H_2O molecule, a number strikingly small compared to the 1.6 x 10^6 vibrational periods observed for oH_2-oH_2O, as shown in Fig. 5.6.

However, some supporting evidence for this scenario can be found in Fig. 5.7, which summarizes cluster energy levels with respect to dissociated H_2 and H_2O

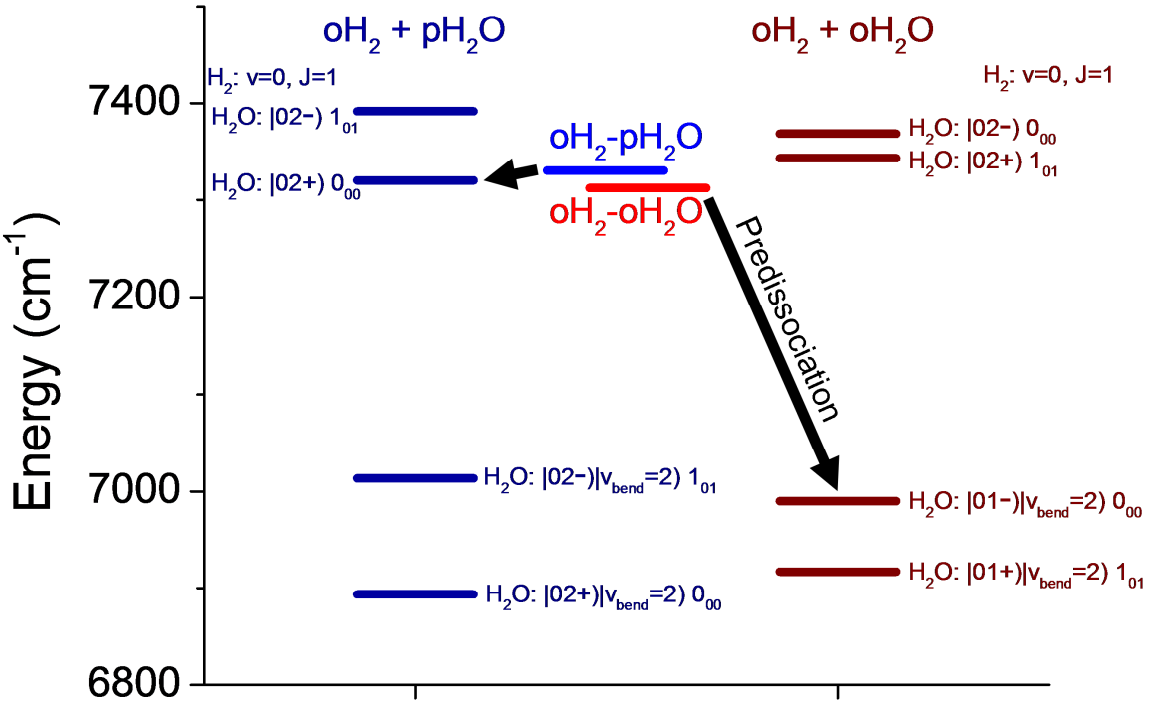

Figure 5.7 Energy levels for bound and free states of oH_2 + pH_2O (|02-)) and oH_2 + oH_2O (|02-)). All thermally-accessible levels of oH_2-pH_2O (a) lie within 30 cm^{-1} of the free molecules state H_2O |02+) + H_2 (v=0), likely leading to rapid predissociation due to the near resonance between the bound and unbound levels. In oH_2-oH_2O on the other hand, the vH_2O = |02+) level is not energetically open, meaning that the nearest available predissociation pathway is to the |01+)|vbend=2) level, which is 300 cm-1 away.

monomers in the appropriate nuclear spin states. Since predissociation pathways are typically most efficient when energy deposition into translation and rotation is minimized, such effects can be greatly accelerated by near resonances between accurately determined cluster vs. free molecule vibrational levels. As shown in Fig. 5.7, oH_2-pH_2O in the $|02^+)$ vibrational state is nearly resonant with (indeed, only 10 cm^{-1} higher than) predissociation into the $H_2(v=0,j=1) + H_2O|02^+)$ 000 asymptotic levels. In a simple physical picture, this predissociation event could be thought of corresponding to "intramolecular collisional readjustment" of the relative phases between the two local mode OH stretches in $|02^-)$ to generate the lower frequency |02+) vibration. By way of contrast, the oH_2-oH_2O cluster has no vibrationally asymptotic states closer than the $|01^+)|v_{bend}=2)$ level, which must be accompanied by simultaneously depositing ≈ 300 cm^{-1} into rotation and translation. From a Fermi Golden rule perspective, such highly nuclear spin species dependent densities of final states could be responsible for the requisite 1000-fold acceleration in predissociation rates out of the |02-) oH_2-pH_2O vs oH_2-oH_2O upper states.

In addition to such large differences in predissociation lifetimes for different nuclear spin states, it is worth briefly investigating reasons for the measurable differences in predissociation lifetimes for Π (<5(2) ns) and Σ (15(2) ns) upper states of oH_2 -oH_2O. Indeed, though covering a substantially different dynamic range, this discussion might also offer a useful basis of comparison with studies on rare gas complexes of Ar-oH_2O, where the $|02^-)$ $\Pi(1_{01})$ internal rotor state was also found to predissociate on a faster timescale of τ_{vp} ≈ 54(2) ns compared to $\Sigma(1_{01})$ which lasts for τ_{vp} ≈ 105(8) ns. Of particular relevance here is that we are comparing predissociation lifetimes for the *same*

nuclear spin and the *same* internal rotor state; thus the number and proximity of near resonant pathways is essentially identical. What is changing, however, is the relative projection of the internal rotor angular momenta between these two states from Π (K=1) to Σ (K=0) character. With the energetic playing field now approximately level, one very important aspect in influencing such predissociation rates will be the dynamical steric factor. By this we mean a probability for achieving geometries where transfer of the initial H_2O stretching vibration to intermolecular bond breaking would be expected to be most facile. For M-H_2O clusters, a reasonable case could be made that the propensity for either of the rapidly vibrating OH bonds to align with the intermolecular predissociation axis to represent a measure of such a coordinate.

With the intermolecular wavefunctions from first principles ab initio theory and dynamics, we can explore this further. Specifically, 2D body fixed angular wavefunction contour plots for the Σ ($1,0_{00}$) J=0 and Π ($1,0_{00}$) J = 1 levels of oH_2-oH_2O in the $|02^-)$ excited state manifold are shown in Fig. 5.3a, with the underlying monomer geometries shown for a number of representative points. Of particular relevance is the vertical dotted line in each contour at $\beta_{H2O} \approx 135^o$, which indicate the locus of all geometries with the OH bond pointing directly toward the H_2 monomer subunit. The wavefunction for the more slowly predissociating Σ state peaks far away from this line at the global minimum structure with H_2 as donor and H_2O as acceptor, for which both OH bonds of the H_2O monomer point away from H_2. By way of contrast, the wavefunction for the more rapidly predissociating Π state has its maximum amplitude much nearer to the alternative hydrogen-bonded structure, i.e., H_2 as acceptor and H_2O as donor, with the donor O–H bond pointing directly towards H_2. Clearly more theoretical work needs to be done to

elucidate this issue further. Nevertheless, this zero order analysis offers a simple and physically motivated picture for why $|02^-\rangle$ OH stretch excitation in M-H_2O complexes might be more effective in predissociation dynamics of Π vs. Σ internal rotor states.

As one final comment, such H_2-H_2O potential energy surfaces may have additional relevance toward understanding chemistry in the ISM. One of the most significant problems of interstellar importance is formation of molecular H_2 from H atoms on icy grain surfaces, for which a delicate balance must be struck to occur efficiently. At too high a temperature, the ice mantle will thermally desorb weakly bound H atoms before encountering other H atoms on the surface. On the other hand, at too low a temperature, the frequencies for activated hopping limit H atom encounter and Langmuir-Hinshelwood formation of H_2. In fact, careful studies on lab-grown porous amorphous solid water (ASW, the most likely form of surface ice) indicate a rapid drop off in H_2 formation efficiency outside a surface temperature window[61] between 11 K and 17 K. Interestingly, significant discrepancies exist between models based on laboratory rates vs. H_2 reformation rates observed in molecular clouds,[62] which may signal fundamental issues yet to be explored. It is our hope that such a benchmarked potential surface for the H_2-H_2O interaction may help provide a quantitative step toward a more first principles understanding of H atom recombination dynamics on icy grains.

5.7 Summary / Conclusions

A combined theoretical and experimental study has been carried out for weakly bound H_2-H_2O dimers. The theoretical calculations are based on a high level ab initio potential energy surface in full dimensionality, which has been reduced to a 5D surface in

intermolecular coordinates by suitable adiabatic averaging over the 4D intramolecular degrees of freedom for a specific H_2 and H_2O vibrational state. Eigenvalues and eigenfunctions of the intermolecular Hamiltonian are then obtained from high level dynamics calculations, which allow for large amplitude quantum motion in 5D. These calculations yield accurate predictions of both bound ground $|00^+\rangle$ and upper $|02^-\rangle$ state vibrational levels, which in conjunction with a dipole moment attached to the H_2O body frame, permit the direct absorption spectra of the H_2-H_2O clusters in the near IR region to be predicted for each of the four possible nuclear spin species: oH_2-oH_2O, oH_2-pH_2O, pH_2-oH_2O, pH_2-pH_2O. These predictions have been compared with experimental spectra of clusters obtained in a slit supersonic expansion and interrogated using a novel triple laser technique, based on i) IR laser absorption by the cluster in the first overtone region for H_2O, ii) 193 nm photolysis of the H_2O moiety, and iii) 308 nm laser induced fluorescence detection of the resulting OH radical.

Agreement for the oH_2-oH_2O nuclear spin species is quantitatively excellent, with the first principles theoretical spectrum uniformly blue shifted from experimental observation and consistent with a remarkably small 0.195(7) cm^{-1} residual differential error in the ground vs excited state H_2-H_2O dissociation energies. Two bands are observed for the oH_2-oH_2O species, a $\Sigma \leftarrow \Pi$ with a predissociation lifetime of 15(x) ns, and a $\Pi \leftarrow \Pi$, which predissociates on a < 5(2) ns time scale comparable to the experimental resolution. Based on the first principles eigenfunctions, we argue that these differences in predissociation rates are attributed to different propensities for intermolecular alignment of the OH bond along the intermolecular axis and thus different rates for intermolecular vibrational energy transfer into the cluster dissocation coordinate.

While observation and spectral assignment of the oH_2-oH_2O species is unambiguous, the other nuclear spin cluster modifications are not observed experimentally, despite quantitatively accurate predictions and high expected signal to noise presuming all nuclear spin species are populated statistically. We argue that this is a result of quantum mechanical, kinetic and dynamical considerations. From a quantum mechanical perspective, the pH_2-$(o/p)H_2O$ clusters are predicted to be more weakly bound by ≈ 20 cm^{-1} than the corresponding oH_2-$(o/p)H_2O$ species. This translates into a chaperone mechanism for collisional displacement of pH_2 by oH_2 to form the more stable oH_2-$(o/p)H_2O$ species, as noted in previous mid IR spectroscopic studies of HOH bend excited clusters. On the other hand, we attribute the surprising lack of observation of the remaining oH_2-pH_2O species to rapid predissociation arising from a near resonant channel ($\Delta E < 30$ cm^{-1}) to form $oH_2(j=1)$ + pH_2O $|02^+)$ (0_{00}). In summary, these studies represent a remarkable example of synergistic comparison between first principles ab initio/dynamical theory and detailed spectroscopic measurement, targeting a simple van der Waals/hydrogen bonded cluster that may play a crucial role in H_2 molecular formation in interstellar clouds.

References for Chapter V

1 P. Valiron, M. Wernli, A. Faure, L. Wiesenfeld, C. Rist, S. Kedzuch, and J. Noga, J. Chem. Phys. **129** (13), 134306 (2008).

2 R. C. Cohen and R. J. Saykally, J. Chem. Phys. **98** (8), 6007 (1993).

3 C. Chakravarty, D. C. Clary, A. D. Esposti, and H. J. Werner, J. Chem. Phys. **93** (5), 3367 (1990).

4 P. Soloveichik, B. A. Odonnell, M. I. Lester, J. S. Francisco, and A. B. McCoy, J. Phys. Chem. A **114** (3), 1529 (2009).

[5] K. Patkowski, G. Murdachaew, C.-M. Fou, and K. Szalewicz, Mol. Phys. **103** (15-16), 2031 (2005).

[6] M. W. Feyereisen, D. Feller, and D. A. Dixon, J. Phys. Chem. **100** (8), 2993 (1996).

[7] D. T. Anderson, M. Schuder, and D. J. Nesbitt, Chem. Phys. **239** (1-3), 253 (1998).

[8] S. A. Nizkorodov, M. Ziemkiewicz, D. J. Nesbitt, and A. E. W. Knight, J. Chem. Phys. **122** (19), 194316 (2005).

[9] V. Buch, J. Chem. Phys. **97** (1), 726 (1992).

[10] M. T. Berry, M. R. Brustein, and M. I. Lester, Chem. Phys. Lett. **153** (1), 17 (1988).

[11] A. van der Avoird and D. J. Nesbitt, J. Chem. Phys. **134** (4), 044314 (2011).

[12] T. Zeng, H. Li, R. J. Le Roy, and P.-N. Roy, J. Chem. Phys. **135** (9), 094304 (2011).

[13] A. van der Avoird, Y. Scribano, A. Faure, M. J. Weida, J. R. Fair, and D. J. Nesbitt, Chem. Phys. (in press) (2011).

[14] L. Belpassi, M. L. Reca, F. Tarantelli, L. F. Roncaratti, F. Pirani, D. Cappelletti, A. Faure, and Y. Scribano, J. Am. Chem. Soc. **132** (37), 13046 (2010).

[15] J. Sadlej, B. Rowland, J. P. Devlin, and V. Buch, J. Chem. Phys. **102** (12), 4804 (1995).

[16] M. J. Weida and D. J. Nesbitt, J. Chem. Phys. **110** (1), 156 (1999).

[17] A. Hanslmeier, *Water in the Universe*. (Springer, 2011).

[18] E. Habart, F. Boulanger, L. Verstraete, C. M. Walmsley, and G. P. des Forets, Astron. Astrophys. **414** (2), 531 (2004).

[19] F. Dulieu, L. Amiaud, E. Congiu, J. H. Fillion, E. Matar, A. Momeni, V. Pirronello, and J. L. Lemaire, Astron. Astrophys. **512** (2010).

[20] P. F. Zittel and D. E. Masturzo, J. Chem. Phys. **95** (11), 8005 (1991).

[21] D. A. Neufeld, S. Lepp, and G. J. Melnick, Astrophys. J. Suppl. S. **100** (1), 132 (1995).

[22] M. J. Dick, B. J. Drouin, and J. C. Pearson, Phys. Rev. A **81** (2), 022706 (2010).

[23] T. R. Phillips, S. Maluendes, and S. Green, Astrophys. J. Suppl. S. **107** (1), 467 (1996).

[24] J. Brand, R. Cesaroni, P. Caselli, M. Catarzi, C. Codella, G. Comoretto, G. P. Curioni, P. Curioni, S. Difranco, M. Felli, C. Giovanardi, L. Olmi, F. Palagi, F. Palla, D. Panella, G. Pareschi, E. Rossi, N. Speroni, and G. Tofani, Astron. Astrophys. Sup. **103** (3), 541 (1994).

[25] J. A. Braatz and N. E. Gugliucci, Astrophys. J. **678** (1), 96 (2008).

[26] M. Harwit and A. B. Edwin, Astrophys. J. Lett. **565** (2), L105 (2002).

[27] N. Watanabe, Y. Kimura, A. Kouchi, T. Chigai, T. Hama, and V. Pirronello, Astrophys. J. Lett. **714** (2), L233.

[28] A. M. Shaw, *Astrochemistry: Ffrom astronomy to astrobiology*. (John Wiley and sons, Ltd., West Sussex, England, 2006).

[29] S. M. Cazaux, P. Caselli, M. Walmsley, and A. G. G. M. Tielens, Proc. IAU **1** (Symposium S231), 325 (2005).

[30] L. Hornekaer, A. Baurichter, V. V. Petrunin, D. Field, and A. C. Luntz, Science **302** (5652), 1943 (2003).

[31] L. Hornekaer, A. Baurichter, V. V. Petrunin, A. C. Luntz, B. D. Kay, and A. Al-Halabi, J. Chem. Phys. **122** (12), 124701 (2005).

[32] A. Faure, P. Valiron, M. Wernli, L. Wiesenfeld, C. Rist, J. Noga, and J. Tennyson, J. Chem. Phys. **122** (22), 221102 (2005).

[33] L. Wiesenfeld, Y. Scribano, and A. Faure, Phys. Chem. Chem. Phys. (in press).

[34] Y. Scribano, A. Faure, and L. Wiesenfeld, J. Chem. Phys. **133** (23), 231105 (2010).

[35] C. H. Yang, G. Sarma, J. J. ter Meulen, D. H. Parker, G. C. McBane, L. Wiesenfeld, A. Faure, Y. Scribano, and N. Feautrier, J. Chem. Phys. **133** (13), 131103 (2010).

[36] L. Wiesenfeld and A. Faure, Phys. Rev. A **82** (4), 040702 (2010).

[37] X.-G. Wang and J. T. Carrington, J. Chem. Phys. **134** (4), 044313 (2011).

[38] S. V. Shirin, N. F. Zobov, R. I. Ovsyannikov, O. L. Polyansky, and J. Tennyson, J. Chem. Phys. **128** (22), 224306 (2008).

[39] L. Lori, private communication.

[40] G. C. Groenenboom, P. E. S. Wormer, A. van der Avoird, E. M. Mas, R. Bukowski, and K. Szalewicz, J. Chem. Phys. **113** (16), 6702 (2000).

[41] A. van der Avoird, P. E. S. Wormer, and R. Moszynski, Chem. Rev. **94** (7), 1931 (1994).

[42] J. W. I. van Bladel, A. van der Avoird, P. E. S. Wormer, and R. J. Saykally, J. Chem. Phys. **97** (7), 4750 (1992).

[43] E. H. T. Olthof, A. van der Avoird, and P. E. S. Wormer, J. Chem. Phys. **101** (10), 8430 (1994).

[44] R. Bukowski, K. Szalewicz, G. C. Groenenboom, and A. van der Avoird, Science **315** (5816), 1249 (2007).

[45] R. Bukowski, K. Szalewicz, G. C. Groenenboom, and A. van der Avoird, J. Chem. Phys. **128** (9), 094314 (2008).

[46] W. Cencek, K. Szalewicz, C. Leforestier, R. van Harrevelt, and A. van der Avoird, Phys. Chem. Chem. Phys. **10** (32), 4716 (2008).

[47] X. Huang, B. J. Braams, J. M. Bowman, R. E. A. Kelly, J. Tennyson, G. C. Groenenboom, and A. van der Avoird, J. Chem. Phys. **128** (3), 034312 (2008).

[48] R. A. Toth, Appl. Opt. **33** (21), 4851 (1994).

[49] D. M. Brink and G. R. Satchler, *Angular Momentum*, 3rd ed. (Clarendon, Oxford, 1993).

[50] P. R. Bunker and P. Jensen, *Molecular Symmetry and Spectroscopy*, 2nd ed. (NRC Research Press, Ottawa, 1998).

[51] J. W. I. Van Bladel, A. Van der Avoird, P. E. S. Wormer, and R. J. Saykally, J. Chem. Phys. **97** (7), 4750 (1992).

[52] W. Cencek, K. Szalewicz, C. Leforestier, R. van Harrevelt, and A. van der Avoird, Phys. Chem. Chem. Phys. **10** (32), 4716 (2008).

[53] S. A. Nizkorodov, M. Ziemkiewicz, T. L. Myers, and D. J. Nesbitt, J. Chem. Phys. **119** (19), 10158 (2003).

[54] J. A. Beswick and J. Jortner, Chem. Phys. Lett. **49** (1), 13 (1977).

[55] L. Haar, J. S. Gallagher, and G. S. Kell, *NBS/NRC Steam Tables*. (Hemisphere Pub. Corp., Washington, D.C., 1984).

[56] G. Scoles, *Atomic and Molecular Beam Methods*. (Oxford University Press, New York, 1988).

[57] L. S. Rothman, C. P. Rinsland, A. Goldman, S. T. Massie, D. P. Edwards, J. M. Flaud, A. Perrin, C. Camy-Peyret, V. Dana, J. Y. Mandin, J. Schroeder, A. McCann, R. R. Gamache, R. B. Wattson, K. Yoshino, K. V. Chance, K. W. Jucks, L. R. Brown, V. Nemtchinov, and P. Varanasi, Journal of Quantitative Spectroscopy and Radiative Transfer **60** (5), 665 (1998).

[58] M. A. A. Clyne, J. A. Coxon, and A. R. Woon Fat, J. Mol. Spectrosc. **46** (1), 146 (1973).

[59] J. Tennyson, N. F. Zobov, R. Williamson, O. L. Polyansky, and P. F. Bernath, J. Phys. Chem. Ref. Data **30** (3), 735 (2001).

[60] J. A. Fernley, S. Miller, and J. Tennyson, J. Mol. Spectrosc. **150** (2), 597 (1991).

[61] G. Vidali, J. E. Roser, L. Ling, E. Congiu, G. Manico, and V. Pirronello, Faraday Discuss. **133**, 125 (2006).

[62] D. Field, Astron. Astrophys. **362** (2), 774 (2000).

[63] M. Chehrouri, J. H. Fillion, H. Chaabouni, H. Mokrane, E. Congiu, F. Dulieu, E. Matar, X. Michaut, and J. L. Lemaire, Phys. Chem. Chem. Phys. **13** (6), 2172 (2011).

[64] R. Sliter, M. Gish, and A. F. Vilesov, J. Phys. Chem. A **115** (34), 9682 (2011).

[65] K. M. Menten, G. J. Melnick, T. G. Phillips, and D. A. Neufeld, Astrophys. J. **363** (2), L27 (1990).

[66] K. M. Menten, A. Lundgren, A. Belloche, S. Thorwirth, and M. J. Reid, Astron. Astrophys. **477** (1), 185 (2008).

[67] E. M. L. Humphreys, Proc. IAU **3** (Symposium S242), 471 (2007).

Chapter VI: Direct evidence for nonadiabatic dynamics in atom + polyatom reactions: crossed-jet laser studies of F + $D_2O \rightarrow$ DF + OD

Published in *J. Chem. Phys.* **123**, 224307 (2005)

6.1 Introduction

Though simple in principle, a detailed understanding of the elementary act of bond-breaking and bond-making remains one of the quintessential challenges of chemical reaction dynamics.[1-10] Considerable information for such bimolecular and unimolecular bond fission events has been gleaned from energy partitioning into product degrees of freedom, which has stimulated intense development of novel experimental methods with ever improving control of the initial reaction conditions[11] and detection of reaction products. Crossed molecular beams[12,13] and photolysis generation of radical precursors[9-11,14,15] have permitted greatly improved resolution of COM collision energies compared to previous bulk gas phase cell experiments. The use of "universal" mass spectroscopic methods[12,16] offers comparable detection sensitivity for nearly all products, which in turn allows branching ratios for reactions with multiple exit channels to be experimentally determined.[17] In order to obtain more detailed information about energy partitioning into product *internal* degrees of freedom, however, alternative product detection methods have proven quite powerful, including FTIR chemiluminescence,[2,18-20] high resolution infrared laser absorption,[21-24] resonantly enhanced multiphoton ionization (REMPI),[4,9,10,15,25-27] and laser-induced fluorescence (LIF).[28,29] Indeed, such early quantum state-resolved studies are responsible for the development of many of the classic paradigms for

chemical reaction dynamics such as the Polanyi rules for energy disposal and promotion of reactants over “early” and “late” barriers.[1,2,19,30]

Progress in such diversely challenging areas requires parallel advances and refinement in the underlying framework, fueled, as always, by a rigorous first principles comparison between experiment and theory.[5,31-34] Theoretical methods are now capable of calculating an impressive array of properties of reactive systems to remarkable accuracy. Single-surface *ab initio* calculations have been used to predict reaction barriers, resonance structures, and transition state geometries[35] for a wide variety of fundamental A + BC systems. On such surfaces, time-independent and/or time-dependent wave packet studies can be used to predict product branching ratios, angular and internal energy product distributions, and transition state resonance dynamics.[5,6,27,32,36] In systems where ground and excited state potentials can be calculated to sufficient accuracy, subtle but increasingly important factors controlling reaction dynamics, such as the presence of conical intersections[37] and nonadiabatic couplings between potential surfaces,[38] can be examined. However, calculation of multiple electronic surfaces at this level of computational accuracy requires more expensive multireference reference methods,[39,40] which, though now feasible for mapping out relatively light A+BC systems, are still quite hard to implement even for a “simple” 4 atom A+ BCD system.[33,41] Indeed, even with such surfaces available, reaction dynamics treating *nonadiabatic* multiple-excited state interactions proves extremely demanding, which for atom + polyatomic systems is likely to represent a benchmark theoretical challenge for the next decade.

This fundamental difficulty, both in (i) calculating multiple-coupled surfaces as well as (ii) performing exact quantum dynamics on such a manifold of surfaces, raises an interesting and yet still controversial question. Are such nonadiabatic complications qualitatively important in

typical open shell atom + diatom or atom + polyatom systems, or can one achieve sufficiently close approximation to the full dynamics by considering only wave packet propagation on the ground state surface? In unimolecular photolysis studies, the role of multiple electronic surfaces and nonadiabatic curve-crossing effects is well documented and indeed represents an essential guiding paradigm.[42,43] For bimolecular reaction dynamics with ground state reactants, however, there does not appear to be a general consensus as to whether nonadiabatic transitions *between* electronic surfaces play an ubiquitous or perhaps more rarified role, with debate going back to the early crossed beam scattering experiments and continuing to the present.[4,26,31,32,44] It is this issue, the importance of nonadiabatic dynamics in a simple bimolecular atom + polyatom reaction, which forms the specific focus of this paper.

A reaction is said to be nonadiabatic when couplings between potential energy surfaces are sufficiently large that the reaction dynamics are not confined to a single adiabatic surface. As adiabats are energy surfaces consistent with the Born-Oppenheimer approximation,[45] nonadiabatic effects can be traced to a coupling between electronic states by a nuclear velocity operator.[46] Nonadiabatic reactive-scattering events can be unambiguously identified when the asymptotic electronic state of the products does not correlate adiabatically with the electronic state of the reagents. Such experiments require an electronic state that is energetically accessible at typical collision energies, and, for that reason, studies of nonadiabatic dynamics have often focused on spin-orbit state changes in first row atoms and molecules. Indeed, nonadiabatic dynamics have been invoked to interpret reactivity of spin-orbit-excited halogen atoms in F^* + HBr, Br^* + H_2(v=1), F^* + H_2 and Cl^* + H_2 systems,[3,4,21-23,26,47] for which reaction only on the ground state adiabatic surface should be energetically accessible. However, the notion that these systems necessitate crossing between energy surfaces has been complicated by the indirect

nature of the observations as well as variable agreement with theoretical predictions.[7,31,32] Nonadiabatic transitions have clearly been invoked to explain electronically excited fragments in photolysis experiments.[42,48] Experiments on $H + N_2O \rightarrow OH + N_2$ [49] and $H + H_2O \rightarrow OH + H_2$ [29] as well as recent studies[9] of $HCl + CH_3 \rightarrow CH_4 + Cl$ have raised the possibility that ground state reagents react nonadiabatically to produce electronically spin-orbit-excited state products. However, there is a paucity of information on systems where multiple electronic surfaces and adiabatic barrier heights are sufficiently well determined to conclusively demonstrate the presence of nonadiabatic surface-hopping events in elementary atom + polyatomic chemical reactions.

In the present work, we report a study of the $F + D_2O \rightarrow DF + OD$ abstraction reaction (figure 6.1), exploiting the combination of (i) pulsed discharges and crossed molecular beam control of collision energy, (ii) laser-induced fluorescence on the final OD product quantum state distributions, and (iii) high level *ab initio* calculations to characterize the nonadiabatic dynamics. The choice of this system stems from theoretical potential surface studies for the $F + H_2O$ system developed in our group, for which energetics, reaction paths, and barrier heights for the lowest several adiabatic states have been calculated using dynamically weighted multiconfiguration self consistent field calculations followed by multireference configuration interaction (MRCI)[40] and extrapolation to the complete basis set (CBS) limit.[33] The relevant stationary points and adiabatic correlations from this study are briefly summarized in figure 6.1. Simply stated, the three-fold p-hole degeneracy in F is lifted by the presence of D_2O into three Born Oppenheimer surfaces, two of which asymptotically correlate with the ground $F(^2P_{3/2})$ spin orbit state. The lower of these two surfaces arising from ground state $F(^2P_{3/2})$ adiabatically correlates with the *ground* spin orbit state of $OD(^2\Pi_{3/2})$ over a barrier of ≤ 4 kcal/mol, while the higher of these two correlates with

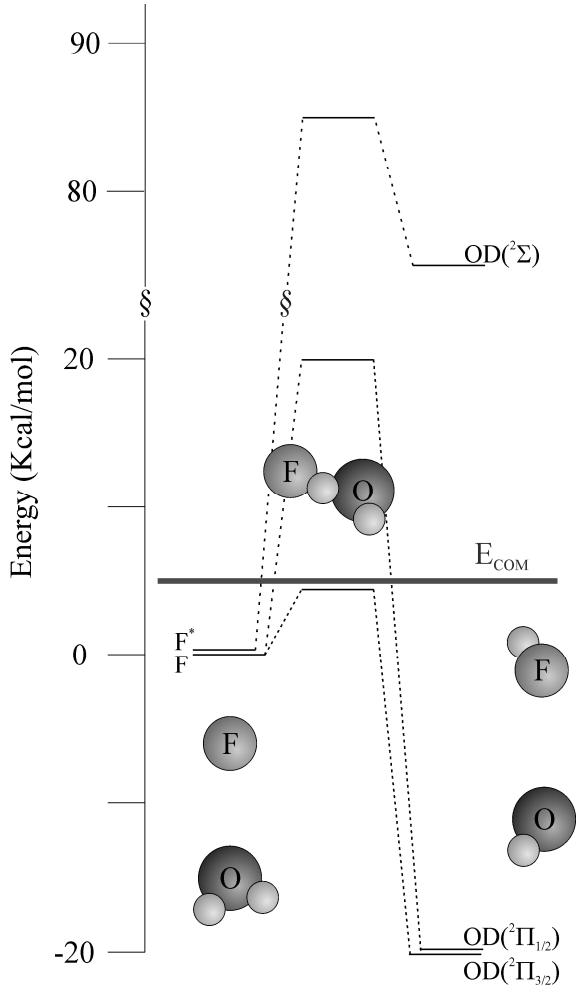

Figure 6.1 Calculated transition state energies (from dynamically weighted MCSCF + MRCI calculations, AVTZ basis) for the F + $D_2O \rightarrow$ DF + OD reaction. In the present study, E_{COM} = 5(1) kcal/mol is sufficient to surmount the ground state barrier ($\Delta E \approx 4$ kcal/mol) to form OD ($^2\Pi_{3/2}$) but insufficient to cross the second higher energy transition state ($\Delta E \approx 25$ kcal/mol), which adiabatically correlates with OD ($^2\Pi_{1/2}$). Therefore, any observed OD ($^2\Pi_{1/2}$) product must arise from nonadiabatic surface-hopping events.

the low-lying spin-orbit excited state of OD($^2\Pi_{1/2}$) over a barrier of ≈ 25 kcal/mol. Indeed, a third surface arising from spin orbit excited $F^*(^2P_{1/2})$ correlates over an even higher barrier (≈ 85 kcal/mol) to form electronically excited OD($^2\Sigma_{1/2}$) in the product channel, which is energetically

closed asymptotically and can be neglected from consideration. For sufficiently chosen experimental center-of-mass collision energies (e.g., E_{com} = 5(1) kcal/mol), only reactive passage over this lowest (≤ 4 kcal/mol) barrier is energetically accessible, which in an adiabatic limit can only correlate with the OD($^2\Pi_{3/2}$) ground spin orbit state. Any product formation in the spin orbit-excited OD ($^2\Pi_{1/2}$) manifold therefore immediately signals the presence of nonadiabatic surface-hopping dynamics in the post transition state region. Furthermore, detailed analysis of the OD rovibronic product state distributions can be used to gain additional insight into the magnitude of nonadiabatic coupling between these surfaces.

The organization of this paper is as follows. Section II provides a brief experimental description of the reactive-scattering apparatus, based on intersection of two low density supersonic jets and laser-induced fluorescence detection. In Sec. III, product state distributions of the OD molecule are reported, which most importantly indicate a minor, but nevertheless quite substantial (32%), formation into the nonadiabatic channel. These results are discussed in Sec. V.

6.2 Experimental Technique

The reactive-scattering studies are based on intersecting a pulsed supersonic jet discharge source of atomic radicals with a second expansion of jet-cooled reagents under sufficiently low densities to ensure single collision conditions and with the nascent product flux probed with full quantum state resolution. The approach is similar to the previous crossed jet studies in our group based on direct IR laser absorption, with the important sensitivity enhancement of laser-induced fluorescence (LIF) for product state detection.

A schematic of the experimental apparatus, which is based on a 60 L chamber with a base pressure < $1x10^{-6}$ Torr, maintained by a 10-inch diffusion pump backed by a 2-stage mechanical

pump, is shown in figure 6.2. A reagent gas pulse consisting of 2% D_2O doped in He enters the chamber through a fast piezoelectric pulsed valve ($\Delta t \approx 500$ μs) with 350 μm diameter pinhole

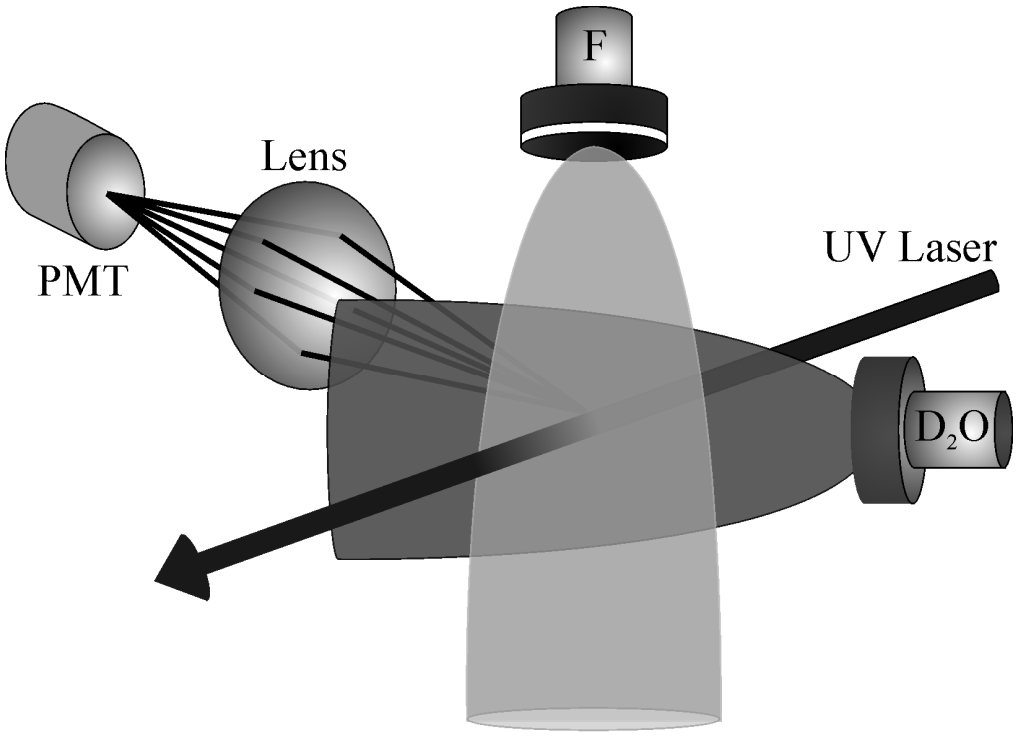

Figure 6.2 Experimental schematic. Fluorine radicals are produced by a discharge struck across a mixture of 10% F_2 and 90% He. D_2O molecules are introduced with a Helium buffer of 2% D_2O, 98% He. In the region of colliding reagent molecules, densities are chosen to ensure single-collision conditions, with the nascent OD products probed via LIF.

and total stagnation pressure of 200 Torr.[50] The corresponding jet of reactive F atoms is introduced to the vacuum chamber via a pulsed solenoid discharge valve (1 mm diameter orifice, $\Delta t \approx 1$ ms) with 50 Torr of 10% F_2 in He in the stagnation region. The F atoms are formed by a fast 100 mA discharge pulse ($\Delta t \approx 200$ μs) struck between a cathode disk 2 mm downstream of the orifice and the stainless steel valve body, as described in detail elsewhere.[22] The radicals produced by this discharge then expand through 300 μm x 5 mm slit jaws formed in the cathode

and intersect in the low density region with the expansion of jet-cooled D_2O molecules. Though not measured here directly for D_2O, experience from previous studies with such expansion geometries[22] suggests rotational temperatures low enough to cool molecules down into the lowest allowed asymmetric rotor states, 1_{01} and 0_{00}, with statistical weights of 2:4, respectively, due to nuclear spin statistics. Both valves are pulsed at 10 Hz for a duty cycle of 0.5–1%, which results in a 2×10^{-5} Torr background pressure and a mean free path of $\lambda \approx 120$ m under standard operating conditions. This is many orders of magnitude larger than the chamber dimensions. To ensure single collision conditions, both valves are placed 5 cm from the jet intersection region, resulting in total densities of $\sim 2 \times 10^{13}$ molecules/cm^3 for each pulsed valve at the intersection of the centerlines.[51] This yields D_2O concentrations in the intersection region of $\sim 2 \times 10^{11}$ molecules/cm^3, with F atom concentrations of comparable magnitude. Based on simple hard sphere cross section estimates, the reaction probability per F atom traversing a 2.5 cm intersection region path length is $\approx 5 \times 10^{-5}$, with < 1% probability of product molecules suffering a collision prior to detection. Under these beam conditions, the mean reagent velocities from direct time-of-flight measurement are $\approx 1.7(x) \times 10^5$ m/s for D_2O and $\approx 1.3(x) \times 10^5$ m/s for F, yielding a center-of-mass collision energy of $E_{com} = 5(1)$ kcal/mol. The 20% uncertainty in this collision energy is dominated by an angular spread of the two unskimmed beams and the subsequent variation in collision angle.[23] However, this uncertainty is small (< 5%) compared to the net energy release for the reaction. $F + D_2O \rightarrow DF + OD$ is the only neutral reaction channel accessible at these collision energies.[52] Furthermore, any reactions with trace F^- anions from the discharge source with D_2O are endoergic by at least 19 kcal/mol and can be eliminated from consideration.[52]

Quantum-state-resolved OD products are detected using laser-induced fluorescence (LIF) on the $A^2\Sigma \leftarrow X^2\prod$ electronic band near 300 nm. The UV light is generated by frequency doubling the DCM dye output from a 532 nm Nd:YAG laser, tuning through the v=0←0 (306 nm) and v=1←1 (320 nm) transitions of OD. Due to trace impurities (most likely H_2O) in the gas lines leading to the F atom discharge, there is also a weak and very cold OH background concentration ($\approx 1 \times 10^7$ molecules/cm^3) in the interaction region. While these concentrations are far too small to contribute any additional reactive scattering signal, they are easily detectable as background with LIF. As a result, we have chosen to examine the deuterated rather than protonated reaction and detect the nascent OD product, which therefore avoids any background problems. Radiation from the discharge and probe laser scatter are prevented from being seen on the PMT by switching the first dynode to high voltage for the duration of these sources of background UV radiation.[53]

From the known LIF transition intensities, one can determine the rovibrational quantum state number density for each of the four spin orbit and lambda doublet sublevels of the OD product ($^2\Pi^{\pm}_{3/2}$, $^2\prod^{\pm}_{1/2}$). Populations in two spin orbit states are readily resolved in the A-X band, with the much more closely spaced lambda doublet states isolated via probing on Q vs P/R branch transitions. However, there is significant overlap of different N state transitions in the Q_{11} and Q_{22} bandheads; this leads to strong parameter correlation and has historically made it challenging to determine populations in the $^2\prod^{-}_{1/2}$ manifold. These issues are further augmented by operating in a partially saturated LIF regime, which is experimentally necessary for maximizing radical detection sensitivity. To circumvent these problems, we fit all lines in the LIF spectrum simultaneously,[54] with OD populations in each quantum state treated as parameters in a least-squares analysis. Frequencies are obtained from the program LIFBASE,[55] with known

optical transition strengths included in the fit in order to account for partial saturation of the OD signals, as well as the minor peaks due to OH background from the discharge. To further break correlation effects, nascent OD quantum state populations for N values in the Q_{11} and Q_{22} bandheads are additionally probed on the slightly weaker O_{12} and the S_{21} branches. As a result, all branches in the OD spectral data are included on equal footing, which results in a redundant oversampling and remarkably robust fitting of the nascent OD populations.

To verify that our analysis method is quantitatively reliable, we have applied identical fitting procedures to OH spectra taken in the identical vacuum chamber geometry but now simply obtained via 193 nm UV excimer laser photolysis of H_2O to form H + OH. Under these buffer gas conditions, the OH radicals experience many hundreds of collisions prior to subsequent LIF detection and thus should reflect complete thermalization with the 298 K vacuum chamber. Sample data from such a fitting procedure are illustrated by means of a standard Boltzmann plot in figure. 6.3, which shows a remarkably good fit consistent with a room temperature, collision-dominated pressure regime. Our estimate of population uncertainties from such a redundant line fitting procedure is typically ± 10%, as confirmed by the comparable levels of scatter observed in results taken over multiple days of experimentation.

6.3 Results

A sample LIF scan over the full set of $^2\Sigma$ (v=0) ← $^2\Pi$ (v=0) sub-bands for nascent OD product is shown in figure 6.4(a), along with the simulation obtained from the least-squares fit. A blowup of a smaller spectral region is also shown in figure 6.4(b), illustrating the high level of signal-to-noise (S/N ≈ 250:1) as well as the quality of the least-squares-fitting procedure. The voltage response of the PMT has been calibrated in a single photon-counting regime, which

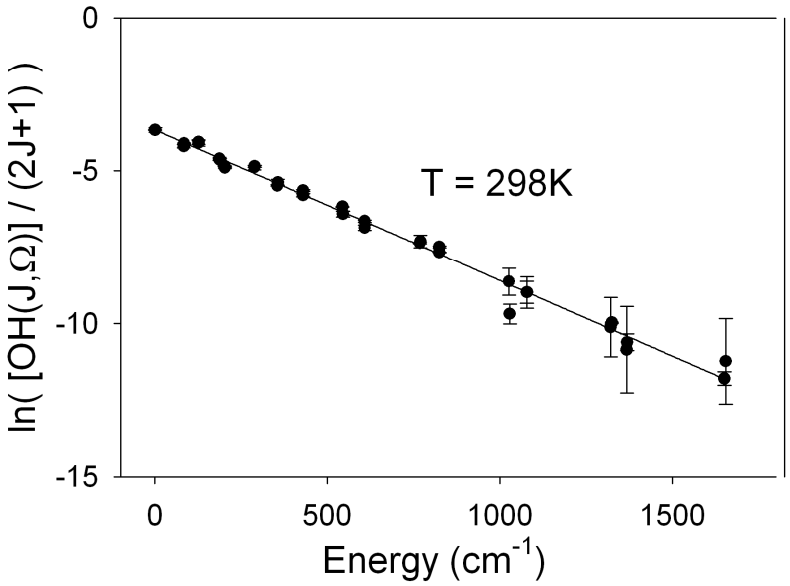

Figure 6.3 Tests of the OD population extraction procedure. OH molecules formed in the vacuum chamber by photolysis of static H_2O vapor are given sufficient time to reach thermal equilibrium (300 K) and analyzed by the same methods used for OD product characterization from $F + D_2O \rightarrow DF + OD$.

allows the experimental intensities to be reported directly in terms of detected photons per laser pulse. From the x20 expansion of the off peak LIF noise in figure 6.4(b), this corresponds to an rms fluctuation of ≈ 10 photons/pulse. The LIF signals are also normalized to probe laser power in the analysis process, which corrects for day-to-day variations in the laser intensities. figure 6.4(b) also shows the typical magnitude of reactive OD vs background OH signals, indicating that the background OH is not a significant problem. The OD signals disappear entirely when the discharge is struck across pure He instead of F_2/He, ensuring that these signals arise purely from reactive scattering with F atoms and not due to electronically excited He with D_2O.

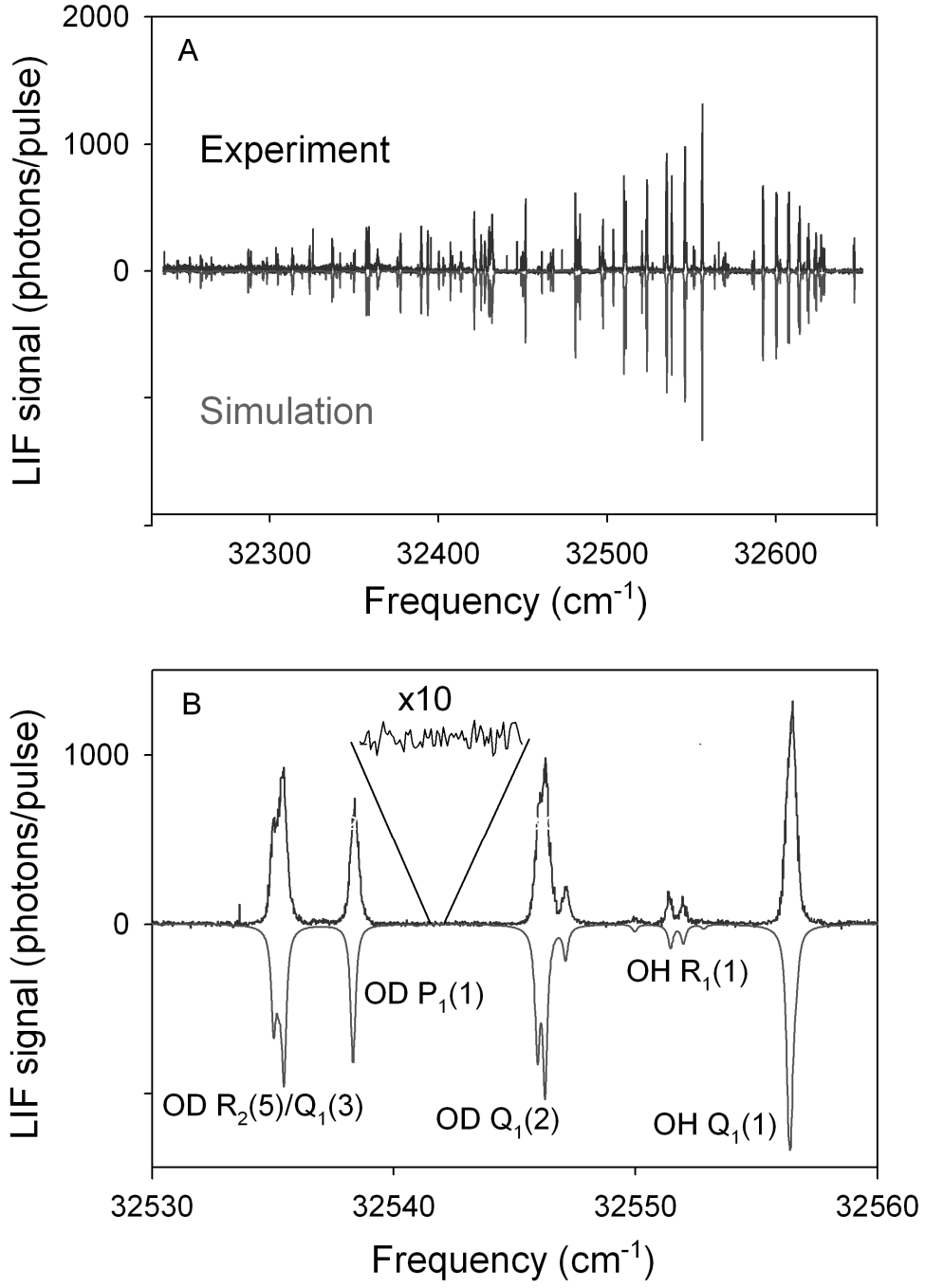

Figure 6.4 Sample scan of OD transitions in the $^2\Sigma(v=0) \leftarrow {}^2\Pi(v=0)$ rovibronic manifold. In (a), raw data is shown with the result of a nonlinear least-squares fit. (b) presents an expanded view of assigned OD and background OH transitions in a small spectral region, displaying a typical signal-to-noise ratio near ≈ 250:1.

A cursory scan of the LIF data reveals several interesting dynamical issues, which will be addressed further in Sec. IV. For the moment, however, we note that for $E_{com} \approx 5(1)$ kcal/mol and $\Delta E = 18.1$ kcal/mol exothermicity, there is $\Delta E \approx 23$ kcal/mol energy for distribution into the nascent OD and DF products, i.e., energetically sufficient to form the OD in v = 0,1,2,3. However, no peaks are discernable when the laser is scanned over the $^2\Sigma$ (v=1) $\leftarrow$ $^2\prod$ (v=1) band, despite respectably high S/N on the strongest transitions in the corresponding $^2\Sigma$ (v=0) $\leftarrow$ $^2\prod$ (v=0) band. Specifically, based on observed signal strengths for transitions from v=0, the magnitude of our noise, and the relative oscillator strengths for $^2\Sigma$ (v=1) $\leftarrow$ $^2\Pi$ (v=1) vs $^2\Sigma$ (v=0) $\leftarrow$ $^2\Pi$ (v=0) bands, we can quantify an upper limit of < 0.8% for the vibrational branching into v=1 vs v=0, with no evidence for any significant population of any higher vibrational states. As the product OD fragment corresponds to the unbroken bond in D_2O, this is qualitatively consistent with a simple spectator bond picture for this H abstraction reaction.[56]

With higher vibrational states excluded from further consideration, the nascent v=0 populations from these spectra are obtained by least-squares-fitting transitions from all lower state populations for OD(v, N) in each of the two spin orbit and lambda doublet electronic states ($^2\Pi_{3/2,1/2}^{\pm}$). Transitions from P_1,P_2,P_{12} and R_1,R_2,R_{21} branches in each of the spin orbit states are recorded, with all four Q_1,Q_2,Q_{12},Q_{21} branches included both to permit the +/- lambda doublet flux to be determined and the O_{12}, S_{12} branches to break population parameter correlation with N states overlapping in the Q branch bandhead regions. The fractional populations (without density to flux corrections) for OD(v=0) in each of the four electronic submanifolds are summarized in table 6.1.

N	$^2\Pi^+_{3/2}$	$^2\Pi^-_{3/2}$	$^2\Pi^+_{1/2}$	$^2\Pi^-_{1/2}$
1	5.9(1)	5.7(2)	1.5(1)	1.4(1)
2	5.9(3)	6.4(1)	1.9(1)	2.0(2)
3	5.6(4)	5.5(2)	2.3(2)	2.4(2)
4	4.6(4)	4.6(4)	2.7(3)	2.1(1)
5	3.7(4)	3.5(4)	1.6(7)	1.7(2)
6	2.7(2)	2.6(2)	1.5(1)	1.6(1)
7	1.7(3)	1.4(1)	1.4(3)	0.97(2)
8	1.4(4)	1.0(1)	1.1(2)	0.7(1)
9	1.0(1)	0.7(1)	0.7(2)	0.7(4)
10	0.9(1)	0.8(2)	0.5(1)	0.3(2)
11	0.4(3)	0.4(1)	0.3(1)	0.8(3)
12	0.3(4)	0.3(1)	0.3(1)	0.2(2)
13	0.6(1)	0.3(1)	0.2(2)	0.3(2)
14	0.1(1)	0.2(1)	0.03(3)	0.2(1)
15	0.07(9)	0.1(1)	0.2(1)	0.1(1)

Table 6.1 Rotational distributions of the OD product in each of its four energetically accessible electronic states. Uncertainties are estimated from repeated scans under the same reaction conditions. State-to-state variations in these uncertainties are typically dominated by the degree of spectral overlap in the probe region.

6.4 Discussion

The nascent rotational/electronic distributions for the OD(v=0) fragments are presented in figure 6.5 The results have been grouped according to spin-orbit state of the product OD, with the ground $^2\Pi_{3/2}$ and excited $^2\Pi_{1/2}$ states represented in the upper and lower panels, respectively. Error bars reflect variation in the least-squares-fit values sampled from analysis of multiple sets

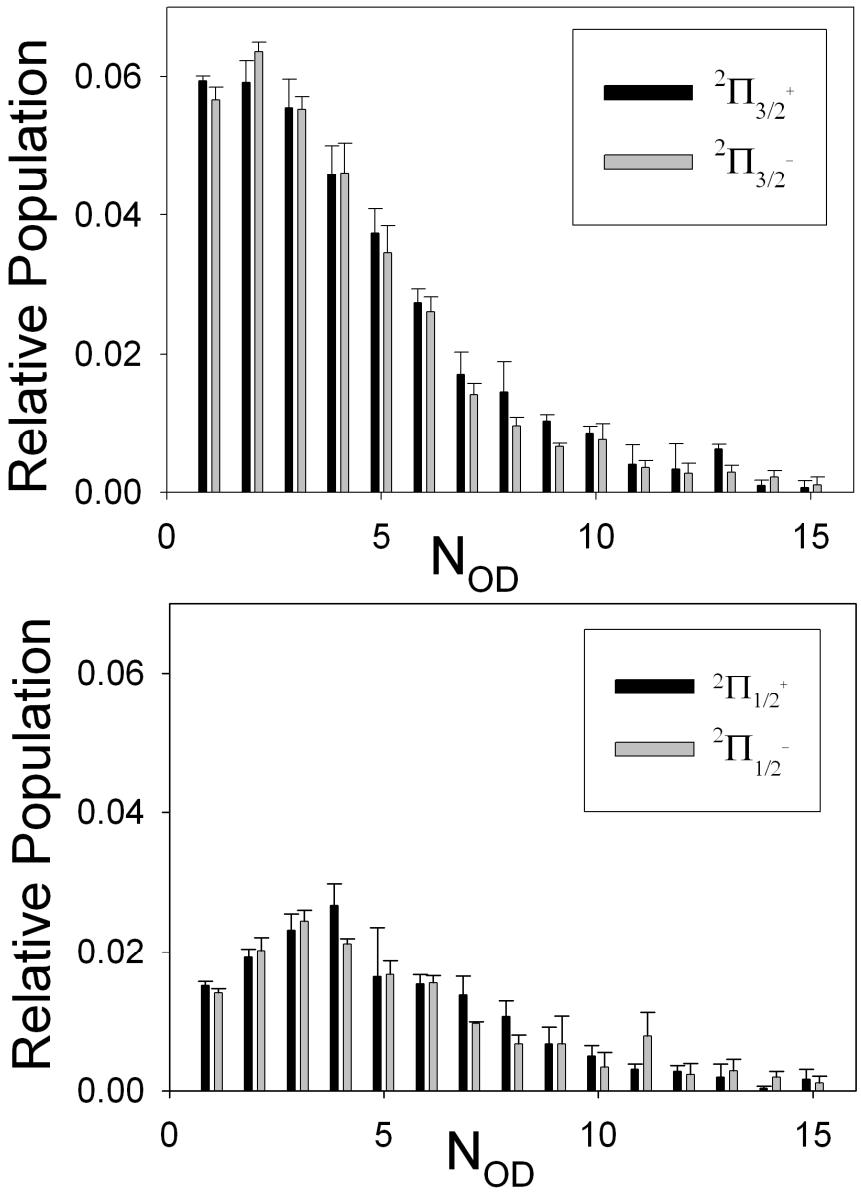

Figure 6.5 Product distributions from the F + $D_2O \rightarrow$ DF + OD reaction at $E_{COM} \approx 5(1)$ kcal/mol. Rotational distributions are in the (a) $^2\Pi_{3/2}(N)$ and the (b) spin-orbit-excited $^2\Pi_{1/2}(N)$ manifold of states. Nascent populations (uncorrected for density to flux effects) are shown for the two lambda-doublet levels of OD.

of spectral data. Several comments are worth noting. First of all, the rotational distributions vary quite smoothly as functions of J, for both spin orbit states and lambda doublet manifolds. This is

in contrast to the rapid oscillations in rotational N and spin orbit state population that are seen from UV photolysis studies of quantum-state-selected water in the A state,[57] which could be nearly quantitatively explained in terms of a Franck-Condon-like expansion of the ground state wavefunction in asymptotic OH rotor states. However, the contrast in these rapid oscillations effectively vanished for photolysis of room temperature H_2O distribution. Indeed, these rapid oscillations largely disappeared even for photolysis of a 3:1 superposition of jet-cooled 1_{01} and 0_{00} states in a supersonic expansion. Thus, although high contrast structure in the product quantum state distributions might in principle exist for "half reactions" initiated in a cluster with well-defined initial states, total J, etc., the absence of such structure due to averaging over impact parameter and a mixture of 1_{01}, 0_{00} reactant states is probably not surprising.

Substantially more surprising, on the other hand, is the presence of a significant fraction of the nascent OD population generated in the *excited* ($^2\Pi_{1/2}$) spin-orbit state. Summing over both lambda doublet states, the fraction of OD($^2\Pi_{1/2}$) formed is 32(1)%, i.e., nearly 1/3 of the total. This is surprising considering the correlation diagram in figure 6.1, which indicates that the adiabatic barrier (from high level MRCI calculations) for forming the spin orbit excited state is > 20 kcal/mol, i.e., well above the $E_{com} \approx 5(1)$ kcal/mole available to the system in these collisions. The presence of OD($^2\Pi_{1/2}$) population therefore immediately implies a significant probability ($P \approx 1/3$) for nonadiabatic surface hopping taking place during the course of this reaction. From the correlations in figure 6.1, we can state that such nonadiabatic interactions must be occurring *after* the transition state region, since all OD product formation must result from crossings over the lowest and only barrier accessible at these collision energies. Note that this does not rule out additional surface-hopping dynamics (e.g., between F($^2P_{3/2}$) and F*($^2P_{1/2}$) surfaces, or between the F($^2P_{3/2}$) surfaces) in the entrance channel, which may also be taking

place. The presence of electronically excited OD($^2\Pi_{1/2}$) in the nascent products is clearly inconsistent with F + D_2O reaction dynamics occurring purely on a single ground state adiabatic surface. Thus, detailed quantum modeling of even such relatively "simple" benchmark open shell atom + polyatom reaction systems is likely to be more complex than previously suspected and, in any event, will require explicit consideration of nonadiabatic dynamics with multiple surfaces.

One possibility is that nonadiabatic coupling between the OD($^2\Pi_{3/2}$) and $^2\Pi_{1/2}$ electronic manifolds is taking place far away from the transition state region and well into the asymptotic channel. Indeed, such exit channel effects have been proposed by way of explanation for the finite formation of both ground state and spin orbit-excited OH radical from H + H_2O reactions.[29] This does not account for the significant fraction of OD($^2\Pi_{1/2}$) product observed in the present system, for the following reasons. First, if the significant conversion to 1/3 OD($^2\Pi_{1/2}$) and 2/3 OD($^2\Pi_{3/2}$) were correctly ascribed to nonadiabatic coupling far out in the exit channel, then detailed balancing considerations would demand similarly high propensities for inelastic spin orbit energy transfer in the reverse direction. Indeed, significant formation of OD($^2\Pi_{1/2}$) from such a half collision event would imply near hard sphere efficiencies for spin orbit-changing collisions. This is in contrast with experimentally observed collision efficiencies on the order of 5% or lower,[58] at least for collision energies that cannot provide access to regions near the transition state.

Secondly, the reaction path and 1600 points sampling for the F + H_2O surface have been determined using high level multireference methods (CASSCF + MRCI + Q/AVTZ basis set), with inclusion of spin orbit terms and nonadiabatic coupling for the electronic wave functions.[33,59,60] This also permits explicit calculation of derivative-coupling matrix elements along the F + H_2O reaction path, which demonstrate a strong peaking of nonadiabatic

interactions in the post transition region, dropping off rapidly into the exit channel region.[60] The presence of such localized nonadiabatic coupling in the near transition state region but far from asymptotic energies is consistent with relatively inefficient spin orbit energy transfer in the reverse direction under thermal conditions. Interestingly, this coupling would also suggest a substantial increase in spin orbit energy transfer efficiency at appreciably higher center-of-mass collision energy, a prediction which could indeed be tested experimentally in DF + OD open shell inelastic-scattering studies.

By way of further elucidation of the reaction dynamics, nascent OD populations are plotted in a Boltzmann format in figure 6.6, where the horizontal axis reflects the internal rotational energy above the minimum for each spin orbit state. Note that both distributions extend out to internal energies in excess of 2500 cm^{-1}. Plots for both spin orbit states indicate a slight upward curvature away from a linear Boltzmann fit but with slopes below and above E_{int} = 500 cm^{-1} consistent with effective internal temperature of $T_{int} \approx$ 280 K and 800 K, respectively. This curvature in the Boltzmann plot at low J might suggest the presence of collisional relaxation in the crossed jet geometry, with the lower J states more easily relaxed due to smaller OD energy spacings. This would be inconsistent, however, with measured densities in the jet intersection region, which reflect operating conditions intentionally selected for < 1% probability for secondary collisions. To test explicitly for this possibility, we have performed measurements as a function of jet intersection density, monitoring nascent OD ($^2\Pi_{3/2}$) populations in high (i.e., N=10) vs low (i.e., N=1) rotational states. The $P_{N=10}/P_{N=1}$ ratios from these tests prove insensitive to threefold variations in jet intersection densities around the experimental conditions utilized for all reported measurements herein. Thus, the curvature in these Boltzmann plots is real, possibly

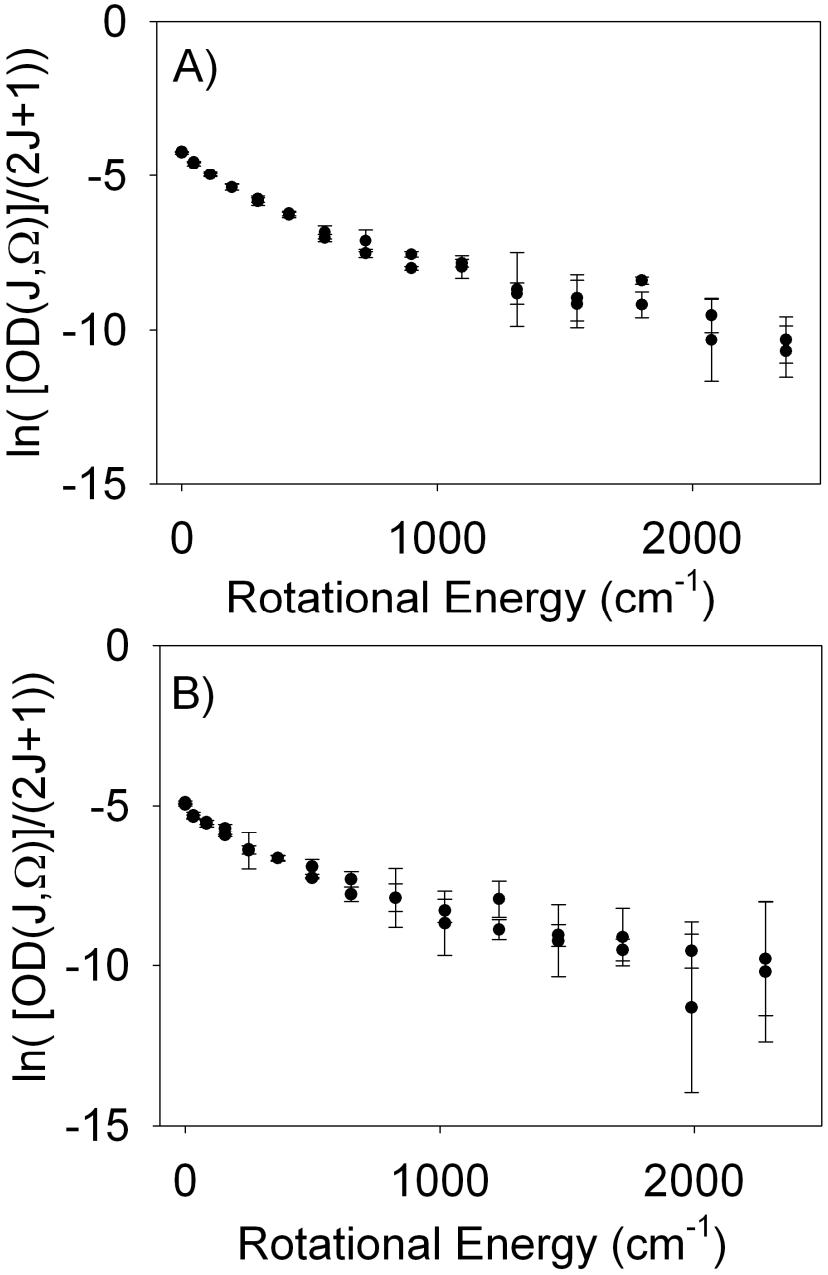

Figure 6.6 Boltzmann plots for OD in each spin-orbit manifold. The similarities in the plots are consistent with nonadiabatic mixing close in to the transition state region, before net torques presumably unique to a given adiabatic surface have been exerted on the OD fragment.

reflecting correlations between OD and DF(v) for different vibrational states of the DF coproduct.

The populations in table 6.1 can be used to yield the average energy funneled into each of the spin orbit manifolds. The average rotational energies (i.e., with respect to N =1 for that spin orbit state) are 0.82(1) kcal/mol and 1.06(1) kcal/mol, respectively, for the $^2\Pi_{3/2}(N)$ and $^2\Pi_{1/2}(N)$ manifolds. As mentioned in Sec. III, the nascent OD population is formed essentially entirely in the ground vibrational state. Therefore, the total rovibronic energy deposited into the OD fragment, $<E_{rovibronic}> \approx 1.01(1)$ kcal/mol), represents only a small fraction of the ≈ 23(1) kcal/mol of energy available in the center-of-mass frame. This provides further support for the simple picture of OD as a "spectator" bond in this reaction and implies that > 95% of the energy is deposited into center-of-mass translational recoil or rovibrational degrees of freedom of the DF fragment. Although no information is currently available for the DF(v,J) product states, the HF(v,J) distributions from crossed jet studies on the corresponding F + H_2O system have been recently investigated via direct IR laser absorption methods and will be reported elsewhere.[61] As predicted from Polanyi rules, the newly formed HF bond is found to be rovibrationally excited up to v=2 and with substantial energy release into translational recoil, as monitored by high resolution IR laser Dopplerimetry.[24,61]

The presence of spin-orbit-excited OD clearly indicates the presence of nonadiabatic dynamics in the F + D_2O reaction. The spin orbit branching fraction, η, as a function of end-over-end rotational quantum number N is shown in figure 6.7, where the ratios have been correctly scaled by (N+1)/N for their respective J degeneracies. This ratio η reflects the degree of nonadiabaticity in the reaction: In the limit of a completely statistical distribution of energy into the two electronic sublevels, η ≈ 1, whereas for a completely adiabatic reaction dynamics, η should be ≈ 0. The experimental results plotted in figure 6.7 indicate average values around $<\eta> \approx 0.6$, i.e., that the F + D_2O reaction behaves appreciably but not entirely in the nonadiabatic

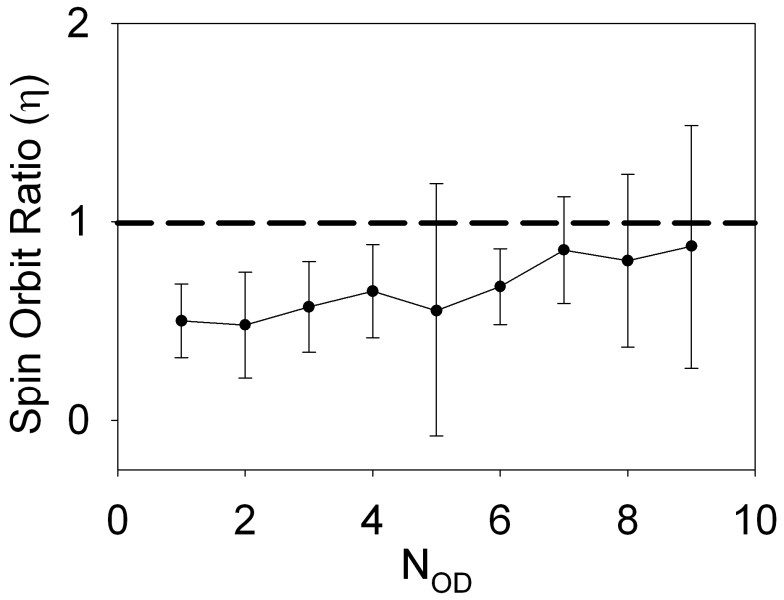

Figure 6.7 Degeneracy-weighted spin-orbit ratio (η) as a function of N. In the statistical limit (dotted line), η = 1, and in the limit of no production of electronically excited OD product, η = 0. The average value of <η> = 0.6 implies significant nonadiabatic mixing taking place in this system but not enough to achieve a completely statistical distribution of electronic excitation.

regime. This analysis is qualitatively similar to the results seen in studies of H + H_2O by Brouard *et al.*,[29] where partial thermalization of the spin orbit electronic manifold was attributed to strong nonadiabatic coupling in the exit channel. Although the important nonadiabatic contributions for the F + D_2O system appear to be much closer in towards the transition state region,[33,60] there is now clearly evidence in both of these systems for the need to consider the reaction dynamics on multiple electronic surfaces.

As a final comment, we can take this picture of partial nonadiabatic "thermalization" of the spin orbit manifolds one step further. Specifically, we return to our Boltzmann analysis of the nascent OD populations but now where both spin orbit states are plotted together on the same scale (averaged over lambda doublets) and referenced to the same zero of energy. The results

(shown in figure 6.8) immediately reveal two points worth noting. First, the population data for both spin orbit states appear to lie on a *common* curve, as if they were formed and had partially

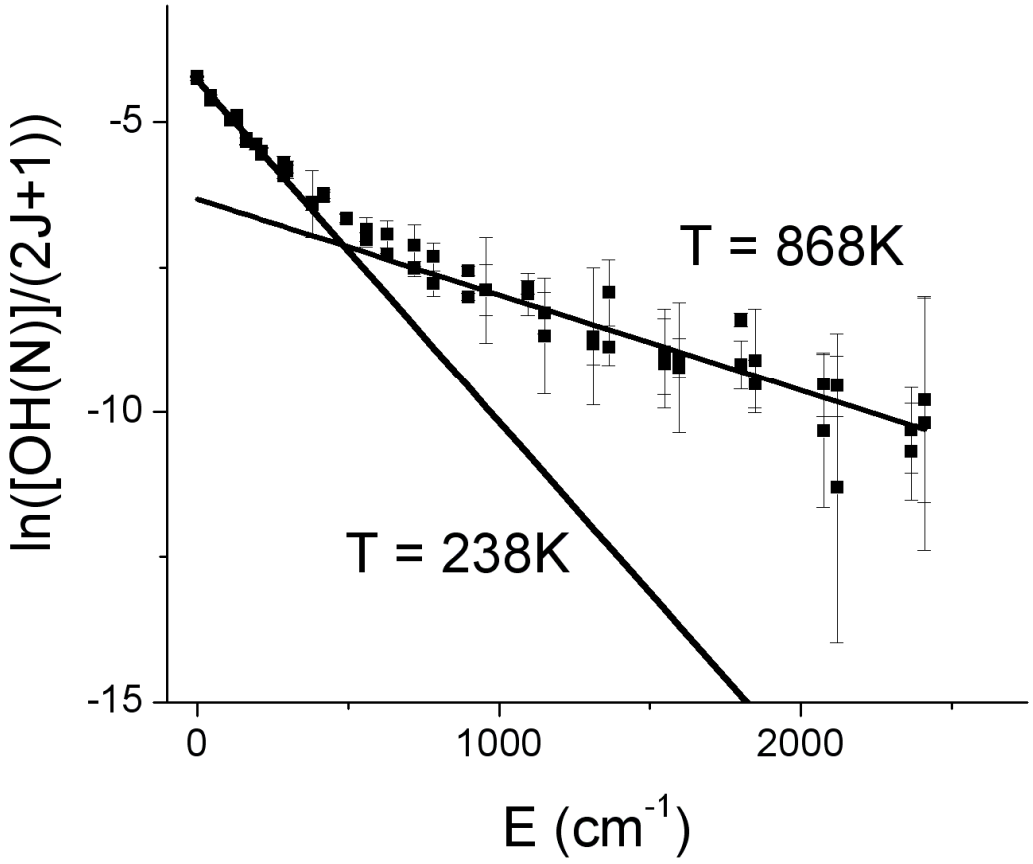

Figure 6.8 Boltzmann plot of the nascent OD rovibronic distribution, fit by a two-temperature model as a function of total (spin orbit + rotational) energy. For E > 500 cm^{-1}, the distribution has a characteristic temperature of 868 K, with a decidedly colder 238 K temperature at lower energies. This striking two-temperature behavior may reflect microscopic branching into vibrational (v=2,3) states of the DF co-product.

equilibrated with respect to a common zero of energy. Considering that these two spin orbit states correlate in the adiabatic limit with two different transition states, this degree of populational "consensus" is quite striking and unexpected. By way of physical example, such results would be consistent with extensive nonadiabatic mixing of the OD electronic states prior

to (or possibly simultaneous with) energy release into the rovibrational degrees of freedom. On the other hand, it seems much less probable that such similar rotational distributions would be consistent with surface-hopping dynamics localized primarily far into the exit channel region, i.e., after the integrated torques presumably unique to a given adiabatic surface had already been exerted on the OD fragment. In any event, these results clearly provide even more dramatic indications of strong coupling between the two potential energy surfaces in the post transition state region. A more detailed interpretation of this universal curve behavior would certainly require further theoretical efforts with multisurface quantum wave packet dynamics for atom + triatom systems, toward which we hope this data provides additional motivation.

The second observation is that the Boltzmann plot is significantly curved for both spin orbit states and can be quite well represented by a two-temperature fit, with $T_{low} \approx 238(6)$ K and $T_{high} \approx 868(95)$ K. There is no *a priori* reason to expect the quantum state distributions to reflect any temperature, though nearly linear Boltzmann plots have been seen for many nominally direct F atom abstraction reactions.[1,2,20,21,24,62] However, such Boltzmann-like behavior can be rationalized from a purely statistical perspective, based on microcanonical phase space arguments for a fixed amount of energy to be distributed into the observed product.[63] In particular, this is most likely to be valid for systems where distributions in the observed product states drop off far below the energetic upper limit, and thus in effect represent a limited statistical sampling of a much larger microcanonical heat bath. This is certainly the case for the F + D_2O system, where the average internal excitation of the OD, $\langle E_{int} \rangle \approx 1.01$ kcal/mol, is only ≈ 5% of the total energy available. Indeed, following this line of reasoning, it is interesting to speculate that the curvature in the Boltzmann plot might reflect nascent vibrational distributions in the DF coproduct. For example, DF coproduct formed in the highest accessible $v_{DF} = 2$ state would

sequester ≈ 19 kcal/mol in vibration, i.e., a significant fraction of the available 23 kcal/mol. This would greatly reduce the amount of energy that can be distributed into the OD product, resulting in a lower internal temperature. Based on Polanyi rule predictions of preferential population into highest v_{DF} states, the two regions of curvature in the Boltzmann plot may in fact correspond to formation of DF in v_{DF} = 1 and 2, respectively. Due to the different vibrational level spacings in HF vs DF, such a simple dynamical picture would obviously make interesting predictions for the corresponding OH product state distributions from F + H_2O reactions. These experiments are currently underway and should make for fascinating comparison with the present study, as well as providing isotope effects for nonadiabatic branching dynamics into the different spin orbit manifolds.

6.5 Summary / Conclusions

F + $D_2O \rightarrow$ DF + OD($^2\Pi_{3/2,1/2}$) reactions have been studied at E_{com} = 5(1) kcal/mol under single collision conditions in low density crossed supersonic jets, monitored by LIF probing of OD products with rovibrational, spin orbit, and lambda doublet resolution. The low rotational excitation and complete lack of vibrational excitation of the OD molecules is consistent with a spectator bond picture of the chemical reaction, whereby most of the energy appears in the newly formed bond. Most of the product is electronically formed in the ground OD($^2\Pi_{3/2}$) spin orbit state, which correlates adiabatically with a reaction over a low transition state barrier (≈ 5 kcal/mol). More notable, however, is the significant presence of OD product formed in the *excited* OD($^2\Pi_{1/2}$) spin orbit state, despite the fact that this product correlates adiabatically with reaction over a much higher barrier (≈ 25 kcal/mol), which is energetically inaccessible at our center-of-mass collision energy. This provides unambiguous evidence for strong nonadiabatic

interactions between the lowest two electronic surfaces and highlights the important role of surface-hopping dynamics in this prototypical atom + triatomic reaction system.

Also quite remarkably, the rotational product state distributions for the two spin orbit states, when referenced to a common zero of energy, can be well represented on a single nonlinear Boltzmann plot. This would suggest that the relevant region of nonadiabatic coupling occurs prior to or concurrent with the release of exothermicity into rotational degrees of freedom of the recoiling product. This is also consistent with high level multiple potential surface calculations,[60] which predict nonadiabatic coupling matrix elements between the lowest two surfaces to peak strongly in the "bond-making" region closely following the transition state, where maximum energy release is also occurring. Furthermore, curvature in this common Boltzmann plot is indicative of two (or possibly more) effective rotational temperatures in the nascent OD distributions, which may reflect a combination of phase space and/or dynamical constraints due to branching in the corresponding DF vibrational manifolds. These studies clearly indicate the richness of key dynamical issues raised in even such relatively simple open shell atom + triatomic reaction systems and highlight the urgent need for additional theoretical and experimental efforts in order to further elucidate the underlying nonadiabatic chemistry at the quantum state-to-state level. Though extremely challenging, such a level of understanding will undoubtedly require the significant advancement of theoretical tools for quantum reactive scattering both (i) on multiple electronic surfaces and (ii) in higher dimensionality degrees of freedom beyond the atom + diatom paradigm. It is our hope that quantum state resolved scattering results in simple but tractable atom + triatom systems provide the necessary additional incentive to the furtherance of such theoretical efforts.

References for Chapter VI

[1] J. C. Polanyi, Faraday Discuss. (55), 389 (1973).

[2] J. C. Polanyi, Acc. Chem. Res. 5 (5), 161 (1972).

[3] J. W. Hepburn, K. Liu, R. G. Macdonald, F. J. Northrup, and J. C. Polanyi, J. Chem. Phys. 75 (7), 3353 (1981); S. H. Lee and K. P. Liu, J. Chem. Phys. 111 (14), 6253 (1999).

[4] F. Dong, S. H. Lee, and K. Liu, J. Chem. Phys. 115 (3), 1197 (2001); S. H. Lee, L. H. Lai, K. P. Liu, and H. Chang, J. Chem. Phys. 110 (17), 8229 (1999).

[5] R. T. Skodje, D. Skouteris, D. E. Manolopoulos, S. H. Lee, F. Dong, and K. Liu, J. Chem. Phys. 112 (10), 4536 (2000).

[6] S. H. Lee, F. Dong, and K. Liu, Faraday Discuss. 127, 49 (2004).

[7] Y. R. Tzeng and M. H. Alexander, J. Chem. Phys. 121 (12), 5812 (2004).

[8] D. M. Neumark, A. M. Wodtke, G. N. Robinson, C. C. Hayden, K. Shobatake, R. K. Sparks, T. P. Schafer, and Y. T. Lee, J. Chem. Phys. 82 (7), 3067 (1985).

[9] B. Retail, J. K. Pearce, C. Murray, and A. J. Orr-Ewing, J. Chem. Phys. 122 (10) (2005).

[10] C. Murray and A. J. Orr-Ewing, Int. Rev. Phys. Chem. 23 (3), 435 (2004).

[11] S. Yoon, S. Henton, A. N. Zivkovic, and F. F. Crim, J. Chem. Phys. 116, 10744 (2002).

[12] Y. T. Lee, J. D. McDonald, and P. R. LeBreton, J. Chem. Phys. 49, 2447 (1968).

[13] R. J. Gordon, Y. T. Lee, and D. R. Herschbach, J. Chem. Phys. 54 (6), 2393 (1971).

[14] J. M. Parson and Y. T. Lee, J. Chem. Phys. 56, 4658 (1971); A. Sinha, J. D. Thoemke, and F. F. Crim, J. Chem. Phys. 96, 372 (1992).

[15] W. R. Simpson, T. P. Rakitzis, S. A. Kandel, A. J. Orr-Ewing, and R. N. Zare, J. Chem. Phys. 103 (17), 7313 (1995).

[16] X. Yang, J. Lin, Y. T. Lee, D. A. Blank, A. G. Suits, and A. M. Wodtke, Rev. Sci. Instrum. 68 (9), 3317 (1997); N. Balucani, D. Skouteris, L. Cartechini, G. Capozza, E. Segoloni, P. Casavecchia, M. H. Alexander, G. Capecchi, and H. J. Werner, Phys. Rev. Lett. 91 (1) (2003).

[17] J. Shu, J. J. LIn, Y. T. Lee, and X. Yang, Journal of the American Chemical Society 123, 322 (2001); P. Casavecchia, Rep. Prog. Phys. 63 (3), 355 (2000); M. Alagia, N. Balucani,

L. Cartechini, P. Casavecchia, E. H. van Kleef, G. G. Volpi, F. J. Aoiz, L. Banares, D. W. Schwenke, T. C. Allison, S. L. Mielke, and D. G. Truhlar, Science 273 (5281), 1519 (1996).

[18] N. I. Butkovskaya and D. W. Setser, J. Phys. Chem. 100, 4853 (1996); B. S. Agrawalla and D. W. Setser, J. Phys. Chem. 90 (11), 2450 (1986).

[19] D. S. Perry, J. C. Polanyi, and C. W. Wilson, Chem. Phys. 3 (3), 317 (1974).

[20] D. H. Maylotte, K. B. Woodall, and J. C. Polanyi, J. Chem. Phys. 57 (4), 1547 (1972); D. J. Bogan and D. W. Setser, J. Chem. Phys. 64 (2), 586 (1976).

[21] W. W. Harper, S. A. Nizkorodov, and D. J. Nesbitt, Chem. Phys. Lett. 335, 381 (2001).

[22] W. B. Chapman, B. W. Blackmon, S. Nizkorodov, and D. J. Nesbitt, J. Chem. Phys. 111, 8404 (1998).

[23] S. A. Nizkorodov, W. W. Harper, W. B. Chapman, B. W. Blackmon, and D. J. Nesbitt, J. Chem. Phys. 111, 8404 (1999).

[24] E. S. Whitney, A. M. Zolot, A. B. McCoy, J. S. Francisco, and D. J. Nesbitt, J. Chem. Phys. 122 (12) (2005).

[25] G. Sha, D. Proch, and K. L. Kompa, J. Chem. Phys. 87, 2742 (1987).

[26] J. G. Zhou, J. J. Lin, B. L. Zhang, and K. P. Liu, J. Phys. Chem. A 108 (39), 7832 (2004).

[27] K. Liu, R. T. Skodje, and D. E. Manolopoulos, Phys. Chem. Chem. Phys. (4), 27 (2002).

[28] R. N. Zare and P. J. Dagdigian, Science 185 (4153), 739 (1974); P. J. Dagdigian and M. L. Campbell, Chem. Rev. 87 (1), 1 (1987).

[29] M. Brouard, I. Burak, S. Marinakis, L. R. Lago, P. Tampkins, and C. Vallance, J. Chem. Phys. 121, 10426 (2004).

[30] J. C. Polanyi and K. B. Woodall, J. Chem. Phys. 57 (4), 1574 (1972); J. C. Polanyi and J. J. Sloan, J. Chem. Phys. 57 (11), 4988 (1972).

[31] M. H. Alexander, H. J. Werner, and D. E. Manolopoulos, J. Chem. Phys. 109 (14), 5710 (1998); M. H. Alexander, D. E. Manolopoulos, and H. J. Werner, J. Chem. Phys. 113 (24), 11084 (2000); M. H. Alexander, G. Capecchi, and H. J. Werner, Science 296 (5568), 715 (2002); M. H. Alexander, G. Capecchi, and H. J. Werner, Faraday Discuss. 127, 59 (2004); N. Balucani, D. Skouteris, G. Capozza, E. Segoloni, P. Casavecchia, M. H. Alexander, G. Capecchi, and H. J. Werner, Phys. Chem. Chem. Phys. 6 (21), 5007 (2004).

[32] Y. R. Tzeng and M. H. Alexander, J. Chem. Phys. 121 (11), 5183 (2004).

[33] M. P. Deskevich, D. J. Nesbitt, and H. J. Werner, J. Chem. Phys. 120 (16), 7281 (2004).

[34] K. Stark and H. J. Werner, J. Chem. Phys. 104 (17), 6515 (1996); F. Fernandez-Alonso and R. N. Zare, Annu. Rev. Phys. Chem. 53, 67 (2002).

[35] K. Morokuma and R. E. Davis, J. Am. Chem. Soc. 94, 1060 (1971); J. M. Bowman and G. C. Schatz, Annu. Rev. Phys. Chem. 46, 169 (1995); Y. Zhang, Q. S. Li, and S. Zhang, J. Mol. Struct. 682, 163 (2004); D. M. Grant, P. J. Wilson, D. J. Tozer, and S. C. Althorpe, Chem. Phys. Lett. 375, 162 (2003); G. Ochoa and D. C. Clary, J. Phys. Chem. A. 102, 9631 (1998); G. Wu, G. C. Schatz, G. Lendvay, D.-C. Fang, and L. B. Harding, J. Chem. Phys. 113, 3150 (2000).

[36] D. Troya, G. Lendvay, M. Gonzalez, and G. C. Schatz, Chem. Phys. Lett. 343, 420 (2001); C. L. Russell and D. E. Manolopoulos, J. Chem. Phys. 110, 177 (1999); S. D. Chao and R. T. Skodje, J. Chem. Phys. 119, 1462 (2002).

[37] D. R. Yarkony, Reviews of Modern Physics 68 (4), 985 (1996); D. R. Yarkony, Acc. Chem. Res. 31 (8), 511 (1998); D. R. Yarkony, J. Phys. Chem. A 105 (26), 6277 (2001); D. R. Yarkony, J. Phys. Chem. 100 (48), 18612 (1996); M. Dallos, H. Lischka, R. Shepard, D. Yarkony, and P. Szalay, J. Chem. Phys. 120, 7330 (2004); J. C. Juanes-Marcos and S. C. Althorpe, Chem. Phys. Lett. 381, 743 (2003).

[38] L. D. Landau, Phys. Z. Sowjetunion 2, 46 (1932); C. Zener, Proc. R. Soc. London A137, 696 (1932); H. R. Mayne, J. C. Polanyi, and J. C. Tully, J. Chem. Phys. 82, 161 (1984); Y.-R. Tzeng and M. H. Alexander, J. Chem. Phys. 121, 5812 (2004); A. E. Orel, D. P. Ali, and W. H. Miller, Chem. Phys. Lett. 79 (1), 137 (1981).

[39] H. J. Werner and P. J. Knowles, J. Chem. Phys. 82 (11), 5053 (1985).

[40] H. J. Werner and P. J. Knowles, J. Chem. Phys. 89 (9), 5803 (1988); P. J. Knowles and H. J. Werner, Chem. Phys. Lett. 145 (6), 514 (1988).

[41] D. H. Zhang and J. Z. H. Zhang, J. Chem. Phys. 99 (7), 5615 (1993); D. H. Zhang and J. Z. H. Zhang, J. Chem. Phys. 101 (5), 3671 (1994).

[42] P. W. Kash and L. J. Butler, J. Chem. Phys. 96, 8923 (1992).

[43] K. Q. Lao, M. D. Person, P. Xayariboun, and L. J. Butler, J. Chem. Phys. 92 (2), 823 (1990); M. D. Person, P. W. Kash, and L. J. Butler, J. Chem. Phys. 97 (1), 355 (1992).

[44] F. T. Smith, Phys. Rev. 179, 111 (1969).

[45] M. Born and J. R. Oppenheimer, Ann. Phys. 84, 457 (1927).

[46] H. Nakamura, *Nonadiabatic transition: concepts, basic theories and applications*. (World Scientific, River Edge, N.J., 2002).

[47] D. J. Nesbitt and S. R. Leone, J. Chem. Phys. 73 (12), 6182 (1980).

[48] T. L. Myers, N. R. Forde, B. Hu, D. C. Kitchen, and L. J. Butler, J. Chem. Phys. 107, 5361 (1997).

[49] M. Brouard, I. Burak, S. D. Gatenby, and G. A. J. Markillie, Chem. Phys. Lett. 287, 682 (1998).

[50] D. Proch and T. Trickl, Rev. Sci. Instrum. 60, 713 (1989).

[51] G. Scoles, *Atomic and molecular beam methods*. (Oxford University Press, New York, N. Y., 1988).

[52] D. R. Stull and H. Prophet, *JANAF Thermochemical Tables*, 2nd Edition ed. (National Standards Reference Data Series, 1971).

[53] D. J. Creasey, P. A. Halford-Mawm, D. E. Heard, J. E. Spence, and B. J. Whitaker, Rev. Sci. Instrum. 69, 4068 (1998).

[54] J. R. Donaldson and P. V. Tryon, Report No. NBSIR 86-3448, 1990.

[55] J. Luque and D. R. Crosley, Report No. MP 96-001, 1996.

[56] A. Sinha, M. C. Hsiao, and F. F. Crim, J. Chem. Phys. 94, 4928 (1990).

[57] S. A. Nizkorodov, M. Ziemkiewicz, T. L. Myers, and D. J. Nesbitt, J. Chem. Phys. 119, 10158 (2003).

[58] R. Cireasa, M. C. van Beek, A. Moise, and J. J. ter Meulen, J. Chem. Phys. 122 (2005).

[59] R. D. Amos, A. Bernhardsson, A. Berning, P. Celani, D. L. Cooper, M. J. O. Deegan, A. J. Dobbyn, F. Eckert, C. Hampel, G. Hetzer, P. J. Knowles, T. Korona, R. Lindh, A. W. Lloyd, S. J. McNicholas, F. R. Manby, W. Meyer, M. E. Mura, A. Nicklass, P. Palmieri, R. Pitzer, G. Rauhut, M. Schutz, U. Schumann, H. Stoll, A. J. Stone, R. Tarroni, T. Thorsteinsson, and H. J. Werner, MOLPRO, a package of ab initio programs designed by H. J. Werner and P. J. Knowles, version 2002.1 (Birmingham, UK, 2002).

[60] M. P. Deskevich and D. J. Nesbitt, (work in progress).

[61] A. Zolot and D. J. Nesbitt, (work in progress).

[62] K. G. Anlauf, J. C. Polanyi, K. B. Woodall, Macdonal.Rg, and D. S. Horne, J. Chem. Phys. 57 (4), 1561 (1972); H. W. Chang and D. W. Setser, J. Chem. Phys. 58 (6), 2298 (1973); M. A. Wickramaaratchi, D. W. Setser, H. Hildebrandt, B. Korbitzer, and H. Heydtmann, Chem. Phys. 94 (1-2), 109 (1985).

[63] R. D. Levine, *Molecular reaction dynamics and chemical reactivity*. (Oxford University Press, New York, 1987).

Chapter VII: Non-Adiabatic Reactive Scattering in Atom + Triatom Systems: Nascent Rovibronic Distributions in F + $H_2O \rightarrow$ HF + OH

Published in *J. Chem. Phys.* **131**, 054309 (2009)

7.1 Introduction

While experimentally challenging, the study of chemical reactions with control of initial reagent quantum state and full characterization of product states provides the ideal environment for studying chemistry at its most fundamental level.[1] Such state-to-state studies provide a critical meeting ground between experimental and theoretical chemistry, where quantum calculations can be directly compared with observations.[2] The specification of reagent states by photolytic generation,[3] supersonic jet cooling,[4,5] electrostatic state selection,[6,7] and infrared vibrational excitation[2,8] have provided extensive control of both internal and kinetic energy distributions for a multitude of bimolecular reagents. At the same time, a host of methods has been developed for carrying out state-specific characterization of the reaction products. The chemical identity and angular scattering distributions of product fragments can be detected by "universal" mass spectroscopic methods,[4,9] while vibrational product distributions can be characterized by techniques such as Fourier transform infrared (FTIR) chemiluminescence detection.[10] However, additional quantum state sensitive techniques are often required to reveal more detailed nascent product distributions, particularly for the ground vibrational state[11-14].

State-to-state reaction studies are uniquely suited for exploring detailed dynamics of chemical reactions.[15-17] In particular, nonadiabatic dynamics, i.e., intermolecular interactions taking place on more than one electronic energy surface, have long been known to be a crucial aspect of atom-atom scattering[18] and photolysis,[19] but their role in polyatomic reaction dynamics

remains poorly characterized. This is due in part to the greatly increased complexity of polyatomic systems, the subsequent computational cost of theoretically treating multisurface dynamics, and the growing importance of conical intersections[20] in such problems. The notion that a reaction occurs on a single electronic surface remains the dominant zeroth order paradigm in chemical physics. However, this situation has been slowly changing, as nonadiabatic reaction dynamics in benchmark triatomic systems have recently received considerable experimental and theoretical attention. Much of this effort has involved quantitative predictions and observations for hydrogen atom abstraction by *spin-orbit excited* halogen atoms in $F(^2P_{3/2})/ F^*(^2P_{1/2}) + H_2$ and $Cl(^2P_{3/2})/Cl^*(^2P_{1/2}) + H_2$ systems,[3,9,14,16,21] a phenomenon which could only occur by nonadiabatic exchange of energy between electronic and nuclear degrees of freedom. Unfortunately, intrinsic difficulties in performing experiments with spin-orbit selected reagents, and the absence of electronically excited surfaces near the transition state in this particular system, have left the wider role of nonadiabatic dynamics still a controversial question. Recently, a growing body of evidence has drawn attention to bimolecular reaction systems whose energetics require nonadiabatic dynamics to occur after the transition state barrier,[22] allowing the difficult problem of reagent quantum state selection to be unambiguously decoupled from experimental observation of nonadiabatic effects. While such measurements leave little doubt whether nonadiabatic transitions play a role in chemical reactions, there is still considerable debate about whether or not such dynamics represent a more generic aspect of systems with more than one energetically accessible electronic surface. Furthermore, there has been long standing interest[23-25] in whether the observed nonadiabatic phenomena occur near the transition state, where they could be ascribed to nuclear velocity coupling, or far out in the

product channel, where nonadiabatic dynamics are dominated by angular momentum recoupling effects.

We previously performed studies of the $F + D_2O \rightarrow DF + OD$ system, which unambiguously identified the presence of nonadiabatic surface hopping in the reaction dynamics.[22] Specifically, guided by dynamically weighted multiconfiguration calculations extrapolated to the complete basis set limit,[26] the center of mass (COM) collision energy was chosen to be in excess of the barrier for reaction via the ground electronic surface (correlating with $OD(^2\Pi_{3/2})$ in its ground spin-orbit state), but well below the barrier for the first excited surface (which correlates with spin-orbit excited $OD(^2\Pi_{1/2})$ products). Far out in the exit channel, the energy difference between these surfaces is very small compared to the available energy. Therefore, this reaction provided an opportunity to directly study nonadiabatic transitions by observing spin-orbit excited OD species. The resulting product state distribution was found to be 32(1)% : 68(1)% excited vs. ground state $OD(^2\Pi_{1/2})$, indicating that nonadiabatic processes play a significant role. The product electronic branching ratio unambiguously indicates that this system exhibits nonadiabatic behavior. However, it does not by itself provide explicit information about where these transitions take place on the electronic energy surface.

Further information can be obtained by observing the products of the isotopically substituted reaction $F + H_2O \rightarrow HF + OH$. Such isotopologue systems share the same set of Born Oppenheimer electronic surfaces, but can exhibit different reaction dynamics for branching into product states.[2,11,27,28] These differences in product state rovibrational distributions can naturally arise, for example, from different energy level spacings and/or nuclear masses responding differently to torques and forces in bond breaking and exothermic energy release. However, since nonadiabatic transitions arise fundamentally as a result of electronic surfaces

being coupled by nuclear velocity terms in the full Hamiltonian,[29] a D/H substitution furthermore offers a non-perturbative controlled modification of the corresponding electronic reaction dynamics. As a result, a study of isotopic effects on product state distributions can shed additional light on the nature of the nonadiabatic process and the underlying potential surface topology.

In this work, we present a study of the $F + H_2O \rightarrow HF + OH$ abstraction reaction at 6(2) kcal/mol COM collision energy. Figure 7.1 shows reagent [$F(^2P_{3/2})$, $F^*(^2P_{1/2}) + H_2O(^1A_2)$] and product [$OH(^2\Pi_{3/2})$, $OH(^2\Pi_{1/2}) + HF(^1\Sigma)$] vibronic states along with the theoretically calculated barriers for the lowest three electronic surfaces. Also shown is the energetically closed product channel on the first excited electronic surface, which adiabatically correlates with $F^*(^2P_{1/2}) + H_2O(^1A_2)$ reagents. Similar to the previously studied $F + D_2O$ reaction, the barrier height and collision energetics are such that formation of spin-orbit *excited* $OH(^2\Pi_{1/2})$ products necessarily requires nonadiabatic transitions to take place. Thus the appearance of spin-orbit excited OH product is an indication of hopping between Born-Oppenheimer surfaces, with the detailed rovibronic state distributions offering additional insight into the nature of the non-adiabatic events.

The organization of this paper is as follows. Sec. 7.2 provides a brief description of the experimental apparatus, focusing on additional modifications required to minimize and correct for background OH in the discharge radical source. Product state distributions are presented in Sec. 7.3, with data discussion and analysis of isotopic differences in Sec. 7.4. Conclusions of the paper are summarized in Sec. 7.5.

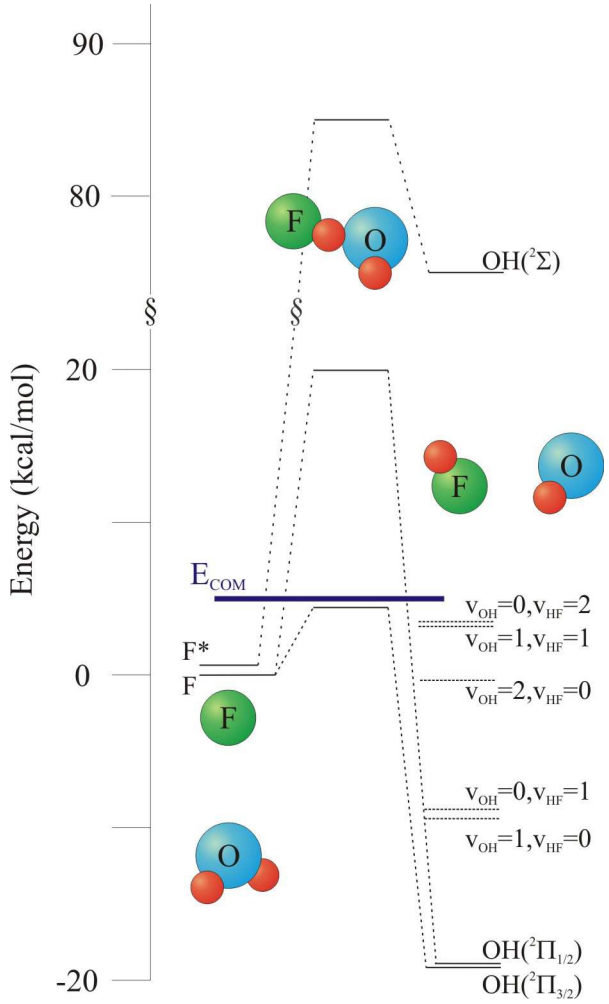

Figure 7.1 Energetics for the reaction F + $H_2O \rightarrow$ HF + OH($^2\Pi_{1/2, 3/2}$). Barriers are obtained from high level MRCI *ab initio* calculations.[26] Fluorine in its ground spin-orbit state can react adiabatically to produce OH($^2\Pi_{3/2}$) at our COM collision energies, but the higher barrier to adiabatically produce OH($^2\Pi_{1/2}$) is not accessible. Therefore, observation of spin-orbit excited product provides unambiguous evidence for nonadiabatic dynamics. Energetically accessible HF and OH vibrational states are also shown for the $^2\Pi_{3/2}$ ground electronic state.

7.2 Experimental Technique

The present F + H_2O measurements were carried out in the laser induced fluorescence (LIF) apparatus[22] used previously. Reactions occur at the intersection of two supersonic jets[30] in

a 60 L chamber which is kept below $1x10^{-6}$ Torr by a 10 inch diffusion pump with a liquid nitrogen trap and backed by a 26 liters/sec mechanical roughing pump. Tunable narrow band light (300 nm - 320 nm, $\Delta\nu = 0.3$ cm^{-1}) from a frequency doubled, 532 nm Nd:YAG pumped dye laser is used to probe OH product state distributions by laser excitation on the $A^2\Sigma(v=0) \leftarrow X^2\Pi_{\Omega=3/2,1/2}(v=0)$ and $A^2\Sigma(v=1) \leftarrow X^2\Pi_{\Omega=3/2,1/2}(v=1)$ band system, with the subsequent fluorescence 1:1 imaged[31] via two pairs of 10 cm focal length lenses and an aperture (5 mm) onto a 5.1 cm^2 area photomultiplier tube (PMT). This spatial filtering detection scheme selectively probes a 0.02 cm^3 volume, reducing scattered light on the PMT and restricting data collection to the center of the jet intersection region where the collision energies are optimally characterized. Fluorine atoms are produced 7 cm from the probe volume by a 200 mA discharge at the orifice (0.20 mm^2) of a pulsed valve, with 50 Torr backing pressure of 10% F_2/He gas and an estimated 10% dissociation efficiency of F_2. A 2% mixture of water seeded in He is expanded from a second valve 7 cm upstream of the probe laser. Particular care is taken to avoid contamination of fluorine lines by moisture. However, some trace H_2O contaminant is unavoidably present in the discharge and produces a weak jet-cooled OH background detectable at our levels of sensitivity. To eliminate these contributions, we pulse our H_2O jet at 5 Hz, with the F source, the discharge and probe laser pulsing at 10 Hz. Subtraction of signals with and without the H_2O jet allows us to remove the contribution due to background OH, which due to supersonic cooling is present only in its lowest rotational states. Even for these lowest OH levels, the discharge-introduced background is still a factor of 5 lower in OH density than the true reactive signal, and thus interferes minimally with extraction and analysis of the nascent distributions.

Reactions occur with a range of collision energies whose distribution is determined by the angle between the two jet sources, the angular spread in each beam and the size of the LIF collection volume at the jet intersection region. We estimate this collision energy distribution with the aid of a Monte Carlo simulation similar to that used in previous reactive scattering experiments probed by IR absorption.[32] In short, the simulation averages over random points where the two gas jets overlap and samples product recoil directions modeled by a given differential scattering distribution in the COM frame. A distribution of COM collision energies is obtained by weighting each product-yielding trajectory by i) the probability a collision occurs at a given point, ii) the probability of yielding energy and momentum conserving products that recoil into the laser detection region, and iii) the time spent moving through the probe volume. Extensive statistical sampling ($\approx 10^9$ trajectories) ensures convergence in both the average and variance of the energy distributions. Figure 7.2 shows the resulting kinetic energy distribution with $\langle E_{COM} \rangle$ = 6(2) kcal/mol, where 2 kcal/mol is the half width at half max. Due to angular divergence in the unskimmed crossed jets, there is considerable geometric averaging of the two collision partners, leading to a Monte Carlo analysis which is insensitive to the model for product angular recoil distribution. For example, the average and standard deviation of the predicted kinetic energy distributions vary by less than 5% for quite different [e.g., isotropic vs $\cos^2(\theta)$] choices. For simplicity, we proceed using an isotropic distribution of COM product recoil directions.

One additional piece of information that can be gleaned from our Monte Carlo simulation is the probability of detecting OH products from collisions occurring at various positions with respect to the probed region. The result is a strongly peaked function with more than 90% of all reactions taking place within 2 cm of the probe laser, 1-2 orders of magnitude smaller than the

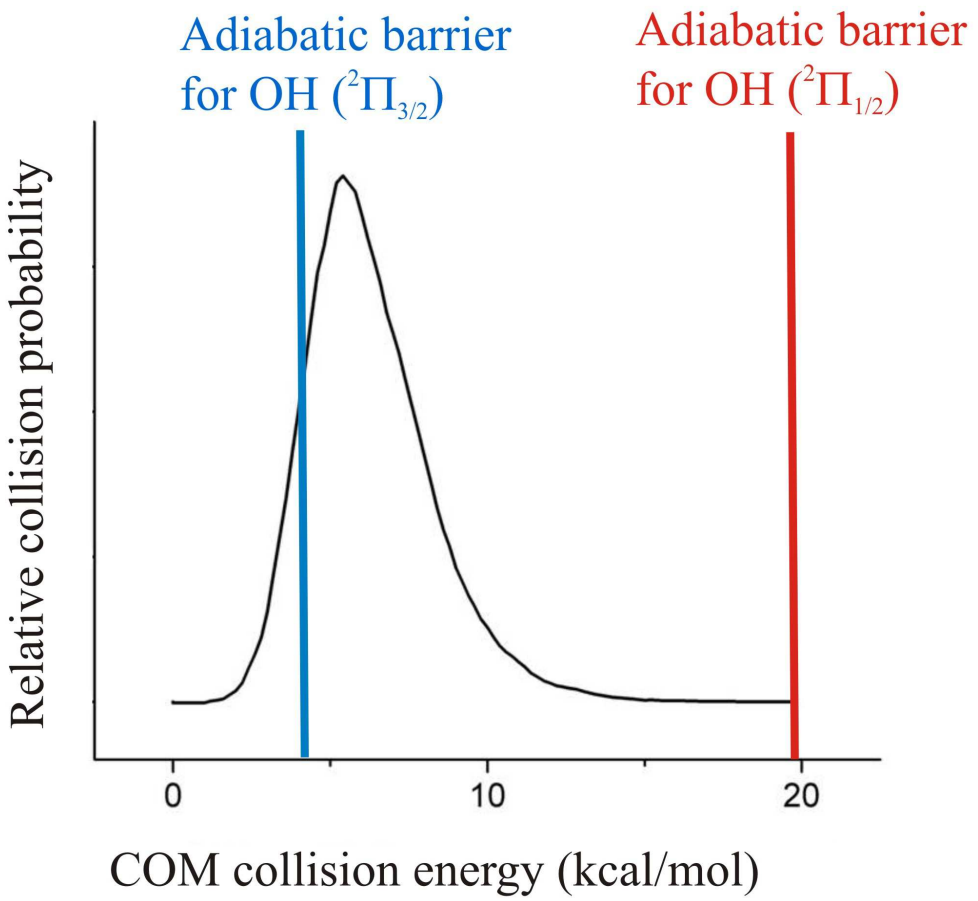

Figure 7.2 Results of a Monte Carlo simulation used to predict COM collision energy distributions in the crossed-jet reactive scattering experiment. The simulation yields a well-defined COM collision energy distribution sufficient to energetically access the barrier to produce OH in its electronic ground state. Collisions with sufficient energy to access the adiabatic barrier to produce spin-orbit excited OH($^2\Pi_{1/2}$) are vanishingly rare.

mean free path in the probe region. We further confirm the single collision nature of the scattered flux by systematic studies as a function of backing pressure, which show no change in the OH experimental distributions with increasing jet density. This, coupled with the <1% collision

probability for H_2O molecules traveling through the second F/F_2/He jet, permits both formation and detection of nascent OH products in the single collision regime.

High-speed, high-voltage switching[33] on the first dynode is exploited to prevent saturation of the PMT by light from the F atom discharge source. Specifically, the voltage of the first dynode and focusing assembly is switched from -2000V to -1800V in 30 ns, a full 10μs after the pulsed discharge is complete and yet in advance of the F atoms and/or OH products reaching the probe region. The 10 ns probe laser is then fired 30 μs after the discharge pulse, ensuring steady state conditions for F atom reaction with H_2O and OH recoil into the detection volume. The photoelectrons are amplified by $8.2x10^6$ in the PMT and sampled in a boxcar integrator (500 ns window) as a function of probe laser frequency. The laser is then scanned over the $^2\Sigma(v=0) \leftarrow {}^2\Pi(v=0)$ and $^2\Sigma(v=1) \leftarrow {}^2\Pi(v=1)$ vibronic bands of OH (≈ 31,250 to 33,300 cm^{-1}), in order to determine the complete OH(v=0,1) rovibronic distribution of product states. A sample spectrum, along with a least squares fit to extract populations (described below), is shown in figure 7.3, where each data point reflects a single (H_2O on-off) pair of laser pulses. Signal-to-noise on transitions from the most populated OH levels is ~600:1, which based on our estimated product densities corresponds to a detection sensitivity of $\sim 1x10^4$ OH radicals per cm^3 per quantum state.

7.3 Results

Nascent populations are obtained from least squares fitting the measured rovibrationally resolved band contours to the well-characterized OH A ← X spectrum.[34] For the v = 0-0 band, populations are obtained from known line strengths by varying OH densities in each of the 120 observed rotational/electronic states to find the best fit to the spectral contour. This method

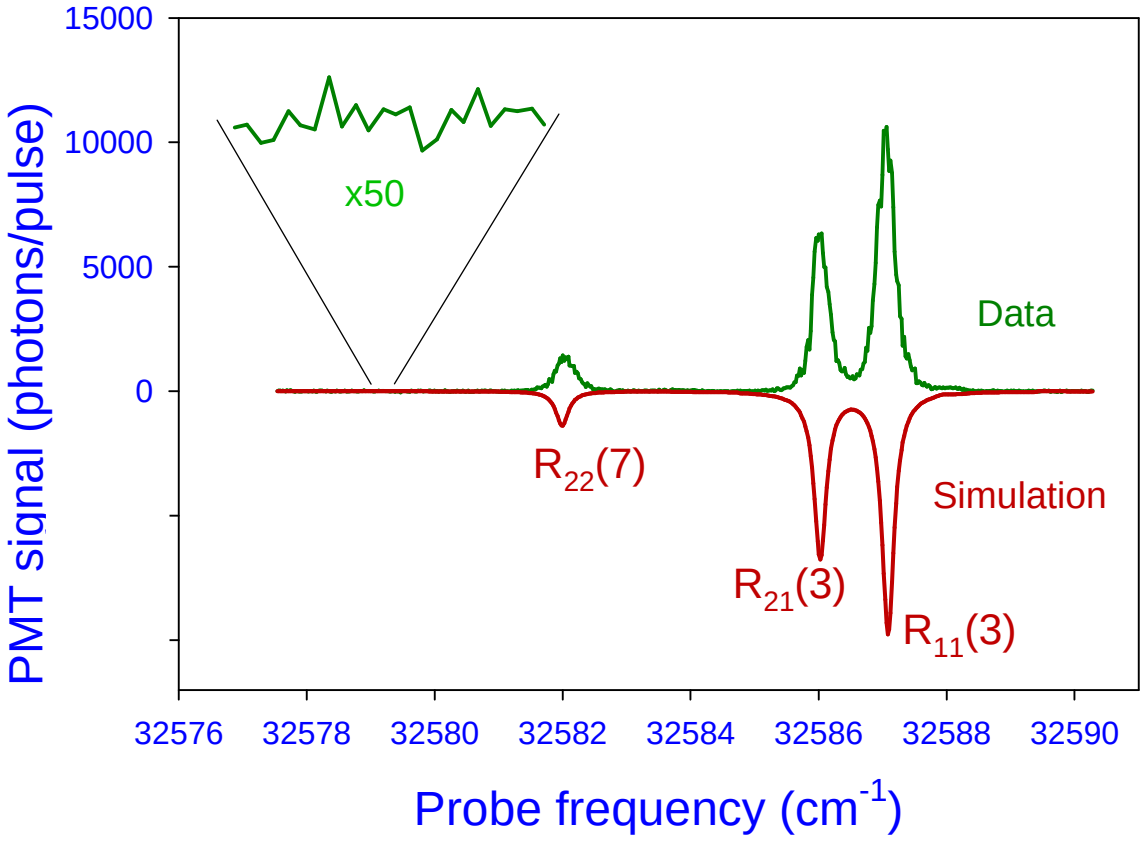

Figure 7.3 Sample data from a LIF scan over the OH product, yielding signal to noise ratios of 600:1 on the strongest lines. The $^2\Sigma$ (v=0) ← $^2\Pi$ (v=0) band is used to obtain OH(v=0) populations reported herein, while the lack of measurable signal in the $^2\Sigma$ (v=1) ← $^2\Pi$ (v=1) band sets an upper limit of ≤ 0.4% for vibrationally excited OH. Also shown is the corresponding segment of the simulated spectrum used to extract OH population densities from least squares fitting to the full rovibronic band.

exploits the fact that each OH rovibronic state is typically probed via 3 or more spectral lines independently. To take maximum advantage of this spectral redundancy, our scans include the largely uncongested O and S branches, which compensates for the extensive spectral congestion found near the Q branch band heads. Partial saturation of the probe transitions is taken into account by Einstein B coefficients and measured pulse energies, as described in detail

previously.[22] Specifically, this leaves only a single parameter accounting for probe laser beam size, which is fit simultaneously with the desired OH populations over the entire spectrum. The effectiveness of this saturation treatment can be immediately seen by examining fits to "satellite" (i.e., $F_{2(1)} \leftarrow F_{1(2)}$ spin-orbit manifold changing) transitions. These peaks probe the same lower state as main branch (i.e, $F_{1(2)} \leftarrow F_{1(2)}$ spin-orbit manifold conserving) transitions, but due to greatly reduced oscillator strengths, are less prone to saturation. Excellent agreement between fit and data (e.g., for both $R_{21}(3)$ and $R_{11}(3)$ in figure 7.3) is observed for every well-separated main/satellite pair, providing further confirmation of an effective treatment of saturation effects. To improve statistics and test for day-to-day drift effects, five independent scans are obtained over the full spectrum. The resulting state-resolved populations are then averaged to yield reported values as well as to obtain estimates of the underlying statistical uncertainty. Scans over the $^2\Sigma(v=1) \leftarrow {}^2\Pi(v=1)$ band region reveal no observable lines within signal to noise. This translates into an upper limit for [OH(v=1)]/[OH(v=0)] of $\leq 0.004(1)$, which would be consistent with the non-reacting OH bond behaving as a "spectator" mode.[35] Extracted rotational, spin-orbit and lambda doublet populations for the OH(v=0) manifold are listed in table 7.1 and summarized visually in figures. 7.4a,b.

The results warrant several comments. First of all, as seen in the $F + D_2O$ studies, substantial OH population is observed in both the ground $^2\Pi_{3/2}(N)$ and electronically excited $^2\Pi_{1/2}(N)$ spin-orbit manifolds. This provides unambiguous evidence for nonadiabatic surface hopping behavior, since the transition state barrier correlating adiabatically with electronically excited OH $^2\Pi_{1/2}(N)$ is inaccessible by more than 15-20 kcal/mol at the current 6(2) kcal/mol collision energy. Secondly, summing over rotational and lambda doublet levels yields OH spin-orbit branching ratios of 69(1)% and 31(1)% into $^2\Pi_{3/2}(N)$ and $^2\Pi_{1/2}(N)$, respectively. This

N	$OH(^2\Pi_{3/2}^+)$	$OH(^2\Pi_{3/2}^-)$	$OH(^2\Pi_{1/2}^+)$	$OH(^2\Pi_{1/2}^-)$
1	.0822(9)	.0874(78)	.0277(18)	.0231(34)
2	.0794(5)	.0772(16)	.0312(13)	.0321(17)
3	.0677(9)	.0583(14)	.0321(12)	.0316(34)
4	.0474(8)	.0406(44)	.0269(14)	.0164(7)
5	.0321(2)	.0248(18)	.0187(9)	.0140(5)
6	.0185(2)	.0111(19)	.0124(1)	.0094(2)
7	.0116(12)	.0074(3)	.0083(6)	.0059(9)
8	.0079(7)	.0067(1)	.0057(4)	.0040(1)
9	.0053(1)	.0046(4)	.0041(4)	.0023(1)
10	.0052(1)	.0030(2)	.0026(2)	.0019(1)
11	.0031(1)	.0019(2)	.0012(2)	.0013(1)
12	.0008(4)	-.0002(2)	.0006(1)	.0006(1)

Table 7.1 Fractional nascent rotational, spin-orbit and lambda doublet OH populations produced from $F + H_2O \rightarrow OH(^2\Pi) + HF$ reactions at E_{com} = 6(2) kcal/mol.

is remarkably close (within error bars) to the 68(1)% to 32(1)% values noted previously for the $F+D_2O$ system, as illustrated more quantitatively for each of the spin-orbit, and lambda doublet components in figure 7.5a. However, it is important to stress that this does not imply isotopic insensitivity to the full rovibronic product state distributions for these two systems, as can be readily seen on closer comparison of the OH vs OD data. That such differences exist is not surprising; for example, one would expect lower N states populated due to significantly (≈ 2-fold) larger OH vs OD rotational constants. Less obvious, however, is that these differences survive after integrating over populations, i.e., in the total rotational *energy* released into OD vs OH spin-orbit states. For example, figure 7.5b) displays the mean end-over-end tumbling energy (with respect to the lowest state in each manifold) for the four electronic sublevels, which indicate a *hotter* rotational distribution for OH vs. OD formation dynamics. We return to this point in the discussion, but note for the moment that such isotopic behavior (i.e., nearly identical

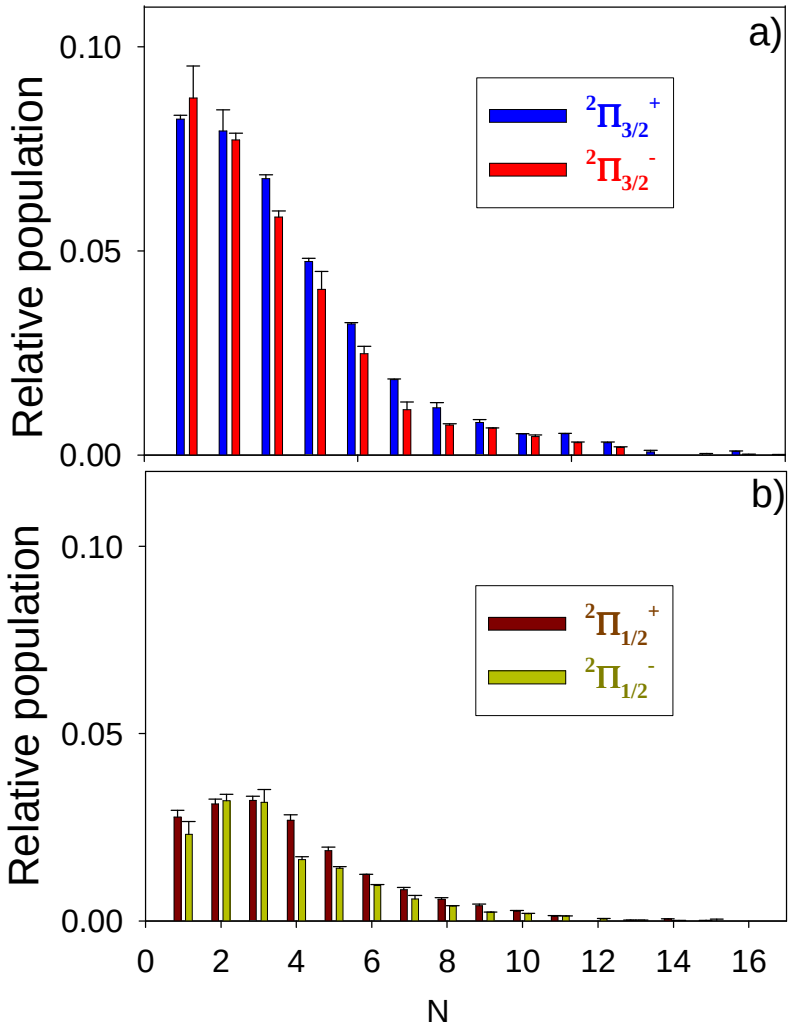

Figure 7.4 Rotational/electronic state distributions for the OH product. Figure 7.4a) shows the relative populations for the ground spin-orbit state which is adiabatically accessible at our COM collision energy. Figure 7.4b) shows results for the electronically-excited spin-orbit manifold, which is only populated as a result of nonadiabatic transitions. The superscripts "+" and "-" refer respectively to the upper and lower levels resulting from lambda doubling in each spin-orbit state.

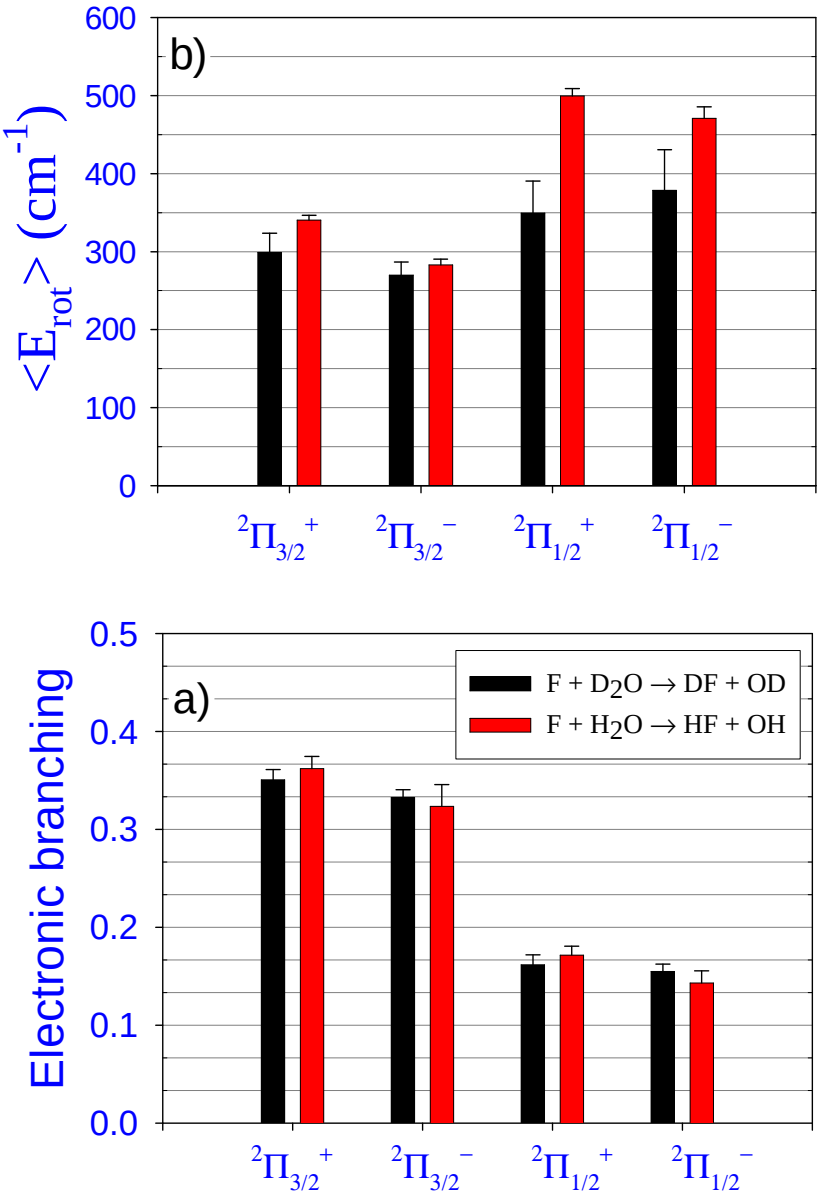

Figure 7.5 a) Electronic branching into the four manifolds of OH radical, obtained by summing over rotational states. Results from our previous experiments on F + D_2O → DF + OD are included for comparison.[22] Within error bars, electronic branching is identical for the two systems, b) Average rotational energy in each electronic manifold shows distinguishable results for OH vs OD, with the OH product being warmer.

spin-orbit branching ratios yet different partitioning of energy into rotation) would be consistent with non-adiabatic surface hopping events occurring *before* predominant energy release into the OD and OH products has taken place.

7.4 Discussion

We start by summarizing the relevant experimental observations. 1) Rotational, spin-orbit, and lambda doublet product state distributions from both F+ H_2O and F+D_2O reactions have been obtained under single collision conditions. 2) Each isotopic system reveals significant branching of the product OH/OD into spin-orbit *excited* ($^2\Pi_{1/2}$) states, which requires non-adiabatic hopping between Born-Oppenheimer electronic surfaces after passage over the lowest energy transition state. 3) Summed over rotational levels, the spin-orbit and lambda doublet product distributions from both F + H_2O and F + D_2O reactions are experimentally indistinguishable. 4) The end-over-end tumbling distributions for OH/OD are different, with larger average rotational energies appearing in the OH vs. OD fragments.

We first consider if these OH and OD distributions conform to “statistical” expectations. This is a word used broadly in description of nascent product states and deserves some clarification. In the present context, we mean statistical with respect to spin-orbit electronic excitation, which is to say the states would be populated (in the high temperature limit) in proportion to their total (2J+1) degeneracy, i.e., 2N+2 and 2N for the $^2\Pi_{3/2}$ and $^2\Pi_{1/2}$ manifolds, respectively. (Here N represents the resultant of end-over-end tumbling and electronic orbital angular momentum and is J-1/2 and J+1/2 for $^2\Pi_{3/2}$ (F1) and $^2\Pi_{1/2}$ (F2) manifolds, respectively. Several groups predict and have observed such “statistical” spin-orbit distributions for the molecular radical fragment from highly nonadiabatic reactive bimolecular scattering events, such

as the reaction[36] $O(^1D_2) + H_2 \rightarrow OH(^2\Pi_\Omega) + H(^2S_{1/2})$, which primarily proceeds via insertion into a long lived complex. By way of contrast, inspection of table 7.1 quickly reveals that the ratio $OH(^2\Pi_{3/2})/OH(^2\Pi_{1/2})$ is not 2N/(2N+2), but is in fact larger by a factor of 1.6-1.8, i.e., exhibiting a clear propensity for ground vs excited spin-orbit state formation. So in terms of electronic excitation, $F+H_2O$ and $F+D_2O$ yield nearly identical but clearly *non-statistical* distributions of spin-orbit states in the OH and OD product

The photolysis literature provides some basis for expectations. For example, statistical spin-orbit branching is often *not* observed in diatomic photodissociation processes, such as HCl + $h\nu \rightarrow Cl(^2P_j) + H(^2S_{1/2})$. Instead of being determined solely by a 2J+1 (4:2 for ^2P_J atomic states) degeneracy factor, the $Cl(^2P_{3/2})/Cl^*(^2P_{1/2})$ branching ratios are clearly non-statistical,[13,28] as well as sensitive to variation in photolysis wavelength[37] and H/D isotopic labeling[11] of the precursor. This arises in part from the high symmetry of the diatomic, whereby the orbital electronic angular momentum projection along the internuclear axis is *unquenched* (i.e. conserved) throughout the excited state recoil. As a result, unpaired electron spin remains strongly coupled to orbital angular momentum in the body fixed molecular axis.

Considerably non-statistical spin-orbit dynamics is also observed in photolysis experiments probing diatomic products from polyatomic precursors, including $OH(^2\Pi_\Omega) + H(^2S_{1/2})$ product formation from VUV photolysis of H_2O.[38] Indeed, H_2O photolysis arguably represents the most thoroughly studied polyatomic system from both experimental and theoretical perspectives,[39] with spectacularly detailed levels of agreement between fully quantum state-to-state resolved prediction and observation. Here, due to the lack of collinear symmetry (or equivalently, the presence of angular anisotropy in the electronic potential), orbital angular momentum is fully *quenched* in the H_2O electronically excited $A(^1B_1)$ state, and develops as the

fragments separate. Thus, electron spin is largely uncoupled from the body frame initially, and yet couples to the OH($^2\Pi_\Omega$) product frame (particularly at low N) as the recoil proceeds and orbital angular momentum projection becomes a good quantum number. In the case of H_2O A($^1B_1$) state photolysis, this recoil process (and therefore the transition from uncoupled to coupled orbital and electron spin angular momenta) is thought to be extremely fast, implying strongly *diabatic* behavior. In this limit,[17] spin-orbit, lambda doublet and even rotational distributions can be remarkably well predicted from a sudden, Franck-Condon like *projection* of H_2O rovibronic wavefunction onto the OH radical product, as elegantly demonstrated in ground breaking studies by Schinke and Balint Kurti.[24,39,40] It is worth noting that such a model requires no *a priori* knowledge of where on the potential surface such non-adiabatic interactions occur, only that the recoil process occur sufficiently rapidly with respect to the asymptotic spin-orbit precession rate.

In contrast to unimolecular photolysis dynamics, bimolecular reaction phenomena, such as the F + H_2O reaction of interest, involve additional averaging over impact parameter and orbital angular momentum. This makes the influence of non-adiabatic coupling on final OH spin-orbit, lambda doublet and rotational distributions substantially more challenging to predict and interpret. Based on the COM collision energetics and finite branching into the spin-orbit excited state, we know that reactive collisions must be sampling regions of the potential surface with significant non-adiabatic coupling. What remains an open question of importance is in what region or regions of the potential such non-adiabatic surface hopping phenomena might be taking place.

There appear to be differing schools of thought on this subject. The first is that surface hopping occurs far out in the exit channel, where the electronic surfaces correlating

asymptotically with OH($^2\Pi_{3/2}$) and ($^2\Pi_{1/2}$) spin-orbit states are closely spaced.[17] In this model, energy release into nuclear degrees of freedom (e.g, rotation, vibration) occurs early in the post transition state region, followed by evolution into final electronic (e.g, spin-orbit and lambda doublet) states due to angular momentum recoupling in the exit region. Such a model, for example, has been used to help interpret the near statistical distributions of spin-orbit states observed in insertion reactions such as O(^{1}D) + H_2, which proceed via a long lived intermediate.[36] The second view arises from the fact that barriers to bimolecular chemical reactions often arise from strongly avoided crossings of diabatic potential curves, and therefore imply the presence of strong non-adiabatic coupling dynamics near the transition state region.[41] This clearly appears to be the case for the F + H_2O reaction, as identified by Deskevich et al in high level dynamically weighted multireference configuration interaction (DW-MRCI) calculations.[26] These calculations predict significant stabilization and curve crossing interactions from ion pair states (e.g., F^- + H_2O^+ and OH^- + HF^+) due to the anomalously large electronegativities of F and OH in the reagent and product channels, respectively. From this second perspective, the regions on the potential surface of i) strong coupling by the nuclear momentum operator and ii) rovibrational energy release into products would effectively *overlap*, with corresponding dynamical impact on formation of final rovibrational and electronic product state distributions.

In light of this comparison, important insight into the surface hopping mechanics of this reaction is shown in figure 7.6, which displays degeneracy-weighted populations of OH on a logarithmic scale for each electronic manifold. If the abscissae are taken to be total angular momentum exclusive of spin, i.e. N_{OH} (figure 7.6a), clearly displaced curves are observed for formation into each of the $^2\Pi_{3/2}$ and $^2\Pi_{1/2}$ spin-orbit manifolds. This is quantitatively consistent

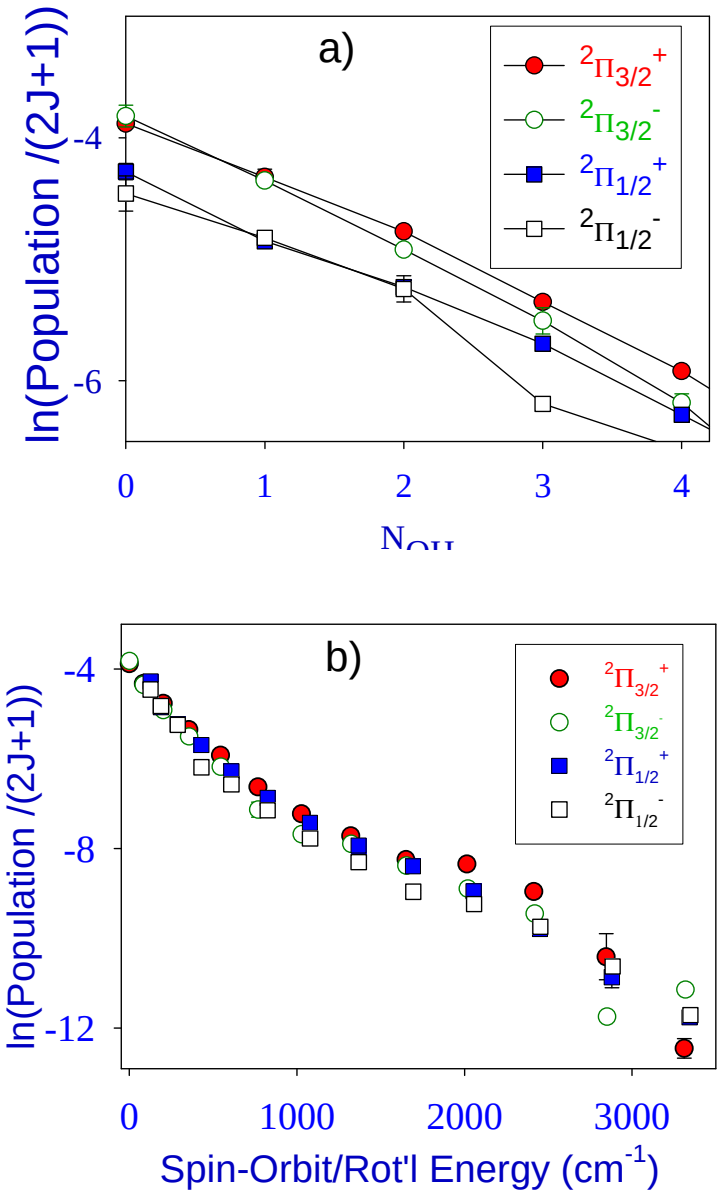

Figure 7.6 a) OH population analysis into each spin-orbit state as a function of end-over-end tumbling angular momentum, indicating a *non-statistical* branching into spin-orbit states at each $N_{OH.}$ b) Boltzmann plot of OH populations vs *total* internal energy, which lie on a single curve independent of asymptotic branching into spin-orbit, lambda doublet and end-over tumbling degrees of freedom.

with the observation made previously that the OH product spin-orbit distributions are formed non-statistically, with a degeneracy weighted ratio, $OH(^2\Pi_{3/2})/OH(^2\Pi_{1/2})*(N+1)/N$ of order 1.6-1.8. However, figure 7.6b displays the results if the abscissae are simply chosen as E_{OH}, i.e., the *total internal energy* of the OH product due to end-over-end tumbling, spin-orbit, and lambda doublet contributions. Quite remarkably, the set of rovibronic product state populations for each spin-orbit and lambda doublet component now lie on a single smooth curve. This is a surprising result which implies that each product OH state population is determined purely by *total* energy and degeneracy, *independent* of how this energy is *partitioned asymptotically* between electronic and nuclear degrees of freedom. Though additional theoretical effort will be required to confirm such a picture, the experimental data are strongly suggestive of the second scenario described above, whereby non-adiabatic surface hopping occurs in the immediate post transition state region of the potential, simultaneous with intermolecular forces and torques mediating energy release into rovibrational degrees of freedom.

Previous studies provide some additional guidance with respect to this interpretation. While this work represents the first study of $F + H_2O$ with LIF detection of the OH product, there have been several reports[8,25,27] of the chemically analogous (though endoergic) family of reactions $X + H_2O \rightarrow XH + OH$ where X = H, Cl, Br, or I. For example, LIF measurements of the $H + H_2O \rightarrow OH + H_2$ reaction also reveal[27] product OH spin-orbit distributions which were not fully statistical. A complement to these reactive studies can be found in a series of experimental[42] and theoretical[43] examinations of *nonreactive*, but electronically and rotationally inelastic collisions between OH and H_2. These studies have shown a strong propensity to conserve the OH spin-orbit state, despite clearly having enough energy for intimate access to

long range "asymptotic exit channel" regions of potential surface. Similar studies show that rotationally inelastic collisions between OH and XH where X = Cl, Br, and I, tend to preserve rather than scramble OH spin-orbit states,[7,44] despite, in some cases, having sufficient collision energy to surmount the transition state. These results indicate insufficient collisional interaction for statistical scrambling of spin-orbit populations at long range on the $X + H_2O \rightarrow HX + OH$ surface, and provide further support for the importance of non-adiabatic coupling in the immediate post transition state region.

We note that this does not imply a complete absence of non-adiabatic exit channel interactions for systems such as $F + H_2O$, but only that there is strong evidence for additional if not predominant contributions to surface hopping dynamics in the immediate post transition state region. Though clearly challenging, it would be most interesting to explore this prediction further from dynamical wavepacket calculations on the full set of non-adiabatically coupled electronic surfaces. Indeed, an interesting and potentially simpler system for exploration would be the atom + diatom reaction, $F(^2P_{3/2,1/2}) + HCl \rightarrow HF + Cl(^2P_{3/2,1/2})$, for which spin-orbit energy levels in the entrance and exit channels necessarily lead to non-adiabatic avoided crossings and seams of conical intersections in both the entrance and exit channels. Toward this end, we have been developing high level ab initio potential surfaces for both $F + H_2O$ and F + HCl chemical reaction systems.[26,45] These are based on dynamically weighted multireference configuration interaction methods and non-adiabatic coupling matrix element calculations, which in conjunction with full S-matrix and/or wavepacket calculations should eventually prove useful in further exploring the role of non-adiabatic coupling and detailed comparison with quantum state-resolved reactive scattering experiments.

As a final note, we compare results for F+H_2O and F+ D_2O reaction systems in a Boltzmann plot in figure 7.7, where the populations are scaled by the 2J+1 degeneracies and plotted against the total end-over-end tumbling, spin-orbit and lambda doublet energy of the OH or OD product. Both reaction systems reveal the same behavior independent of isotope, i.e. the data as a function of internal energy lie on common curves. This implies that the probability of forming a given final state depends on the *total* internal energy and is insensitive to partitioning between spin-orbit vs. end-over-end tumbling contributions. However, the OH and OD population distributions themselves are quite different, for example, with higher rotational energy release into the OH vs. OD product. Such isotopomer-specific behavior would again be consistent with the proposed interpretation of non-adiabatic surface hopping dynamics occurring prior to complete energy release into the product, i.e. predominantly in the immediate post transition state region.

Interestingly, the Boltzmann plots display two regions of approximately linear (i.e. "temperature-like") behavior, with a clear kink near ≈ 780 cm^{-1} and ≈ 470 cm^{-1} for F+H_2O and F+ D_2O reaction systems, respectively. Such dual-temperature Boltzmann behavior would be consistent with microscopic branching in the reaction dynamics, as has been seen, for example, in both reactive and inelastic scattering at the gas-liquid interface.[46] Based on a $\Delta E \approx 24(2)$ reaction exothermicity and 11.3 and 22.1 kcal/mol vibrational energies of HF(v=2,1), it is tempting to ascribe this break in the OH distributions (780 cm^{-1} ≈ 2.2 kcal/mol) to the energetic opening of the HF(v=2) co-product channel. Indeed, independent experiments in our group[47] have used direct IR laser absorption methods to study the nascent HF(v,J) rovibrational distributions from F + H_2O, which reveal small but finite fractional population into HF(v=2), more specifically with a 0.046(6):0.75(2):0.21(6) ratio observed for v_{HF} = 2:1:0. As these IR laser

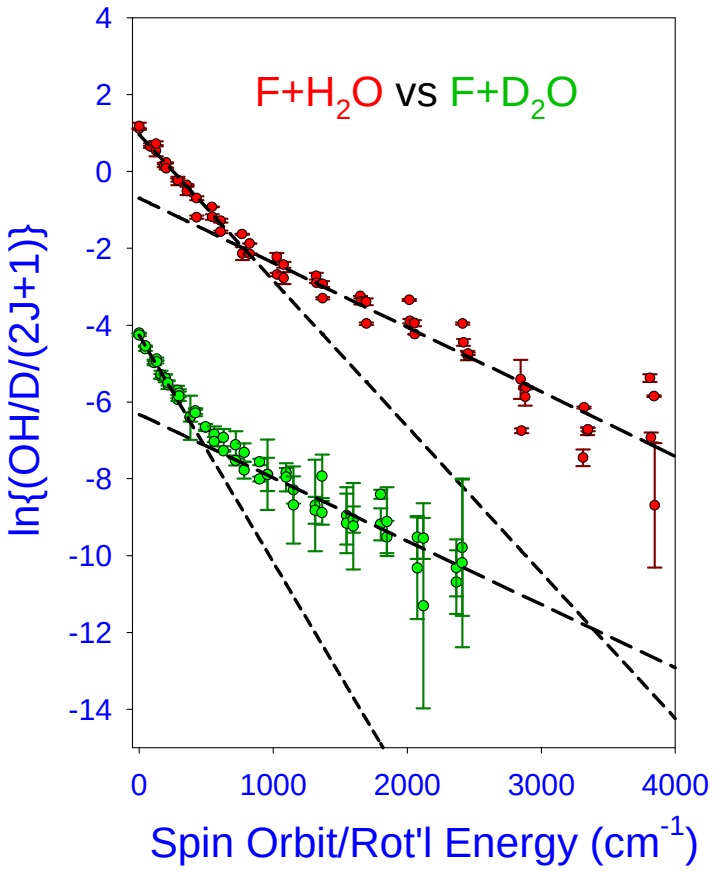

Figure 7.7 Boltzmann plots as a function of total (spin-orbit plus rotational) internal energy for a) F + H_2O and b) F + D_2O reactive scattering. The data indicate a striking equivalence between spin-orbit, lambda doublet and end-over tumbling energy, consistent with non-adiabatic surface hopping occurring predominantly in regions of the potential surface prior to energy release into the OH and OD products. Note the "dual temperature" behavior evident in both plots, with a kink at ≈ 780 cm^{-1} (2.2 kcal/mol) and ≈ 470 cm^{-1} (1.34 kcal/mol) for OH (OD). The short (long) dashed lines correspond to reciprocal slopes of 307 cm^{-1} (595 cm^{-1}) and 170 cm^{-1} (606 cm^{-1}) for F + H_2O and F + D_2O reaction systems, respectively.

studies were performed at somewhat lower collision energies (E_{COM} = 5(1) kcal/mol), the HF(v=2) channel is marginally closed, which could explain a larger fractional contribution into the HF(v=2) manifold under the ≈ 1 kcal/mol higher energy scattering conditions of the present work. The isotopic availability of the F+D_2O data offers one way to test such a hypothesis. A similar analysis predicts the DF(v=3) vs. DF(v=2) channels at E_{COM} = 6(2) kcal/mol to be endothermic and exothermic by ≈ 0.9 kcal/mol and 6.9 kcal/mol, respectively, neither of which is

consistent with the F + D_2O knee experimentally observed at 470 cm^{-1} ≈ 1.34 kcal/mol. One must conclude that the presence of such a striking, "dual-temperature" signature in the Boltzmann populations is not so simply ascribed to vibrational energy partitioning in the HF(v) and DF(v) co-products. Nevertheless, such a comparison underscores the value of quantum state-resolved reactive scattering studies on isotopically substituted systems, which we hope will stimulate further theoretical efforts toward a deeper understanding of the underlying dynamics.

7.5 Summary / Conclusions

We have measured nascant OH rotational/electronic distributions from the reaction F + $H_2O \rightarrow$ HF + OH at E_{COM} = 6(2) kcal/mol, with comparison made to earlier experiments in the isotopically substituted F + $D_2O \rightarrow$ DF + OD reaction. In both isotopologues, the observation of finite spin-orbit excited OH($^2\Pi_{1/2}$) and OD($^2\Pi_{1/2}$) provides direct evidence for nonadiabatic dynamics taking place in this reaction. A detailed analysis of the rotational/electronic distribution shows that the electronic spin-orbit branching ratio into $^2\Pi_{3/2}$ and $^2\Pi_{1/2}$ states is non-statistical and essentially identical for both protonated and deuterated systems. Most importantly, the final asymptotic product state distributions appear to be quite strikingly governed by *total* rotational/electronic energy, i.e., independent of the nuclear (rovibrational) vs. electronic (spin-orbit/lambda doublet) nature of the excitation. Furthermore, this surprising trend is confirmed in both F + H_2O and F + D_2O reaction systems. Though this does not rule out the possibility of *additional* non-adiabatic interactions at longer range, this is strongly suggestive of i) non-adiabatic surface hopping and ii) rovibrational energy release dynamics taking place in a similar post-transition state region of the full potential.

References for Chapter VII

[1] R. D. Levine, R. B. Bernstein, and R. D. Levine, *Molecular reaction dynamics and chemical reactivity*. (Oxford University Press, New York, 1987).

[2] R. L. Vanderwal, J. L. Scott, F. F. Crim, K. Weide, and R. Schinke, J. Chem. Phys. **94** (5), 3548 (1991).

[3] F. Dong, S. H. Lee, and K. Liu, J. Chem. Phys. **115** (3), 1197 (2001).

[4] K. P. Liu, J. Chem. Phys. **125** (13), 132307 (2006); X. Yang, J. Lin, Y. T. Lee, D. A. Blank, A. G. Suits, and A. M. Wodtke, Rev. Sci. Instrum. **68** (9), 3317 (1997); N. Balucani, D. Skouteris, L. Cartechini, G. Capozza, E. Segoloni, P. Casavecchia, M. H. Alexander, G. Capecchi, and H. J. Werner, Phys. Rev. Lett. **91** (1), 013201 (2003).

[5] Y. T. Lee, J. D. Mcdonald, P. R. Lebreton, and D. R. Herschbach, Rev. Sci. Instrum. **40** (11), 1402 (1969); Y. T. Lee, J. D. Mcdonald, P. R. Lebreton, and D. R. Herschbach, J. Chem. Phys. **49** (5), 2447 (1968); R. J. Gordon, Y. T. Lee, and Herschba.Dr, J. Chem. Phys. **54** (6), 2393 (1971).

[6] K. Schreel and J. J. ter Meulen, J. Chem. Phys. **105** (11), 4522 (1996).

[7] R. Cireasa, M. C. van Beek, A. Moise, and J. J. ter Meulen, J. Chem. Phys. **122** (7), 074319 (2005).

[8] A. Sinha, M. C. Hsiao, and F. F. Crim, J. Chem. Phys. **94** (7), 4928 (1991); A. Sinha, J. D. Thoemke, and F. F. Crim, J. Chem. Phys. **96** (1), 372 (1992); M. J. Bronikowski, W. R. Simpson, and R. N. Zare, J. Phys. Chem. **97** (10), 2204 (1993).

[9] D. M. Neumark, A. M. Wodtke, G. N. Robinson, C. C. Hayden, and Y. T. Lee, J. Chem. Phys. **82** (7), 3045 (1985); M. Faubel, L. Rusin, S. Schlemmer, F. Sondermann, U. Tappe, and J. P. Toennies, J. Chem. Phys. **101** (3), 2106 (1994).

[10] N. I. Butkovskaya and D. W. Setser, J. Phys. Chem. **100** (12), 4853 (1996); D. S. Perry, J. C. Polanyi, and C. W. Wilson, Chemical Physics **3** (3), 317 (1974); B. S. Agrawalla and D. W. Setser, J. Phys. Chem. **90** (11), 2450 (1986); D. J. Bogan and D. W. Setser, J. Chem. Phys. **64** (2), 586 (1976).

[11] D. Ascenzi, P. M. Regan, and A. J. Orr-Ewing, Chem. Phys. Lett. **310** (5-6), 477 (1999).

[12] C. Murray and A. J. Orr-Ewing, Int. Rev. Phys. Chem. **23** (3), 435 (2004); B. Retail, S. J. Greaves, J. K. Pearce, R. A. Rose, and A. J. Orr-Ewing, Phys. Chem. Chem. Phys. **9** (25), 3261 (2007); M. N. R. Ashfold, N. H. Nahler, A. J. Orr-Ewing, O. P. J. Vieuxmaire, R. L. Toomes, T. N. Kitsopoulos, I. A. Garcia, D. A. Chestakov, S. M. Wu, and D. H. Parker, Phys. Chem. Chem. Phys. **8** (1), 26 (2006); B. D. Leskiw, M. H. Kim, G. E. Hall, and A. G. Suits, Rev. Sci. Instrum. **76** (10), 104101 (2005); W. W. Harper, S. A. Nizkorodov, and D. J. Nesbitt, Chem. Phys. Lett. **335** (5-6), 381 (2001).

[13] J. Zhang, M. Dulligan, and C. Wittig, J. Chem. Phys. **107** (5), 1403 (1997).

[14] L. Che, Z. F. Ren, X. G. Wang, W. R. Dong, D. X. Dai, X. Y. Wang, D. H. Zhang, X. M. Yang, L. S. Sheng, G. L. Li, H. J. Werner, F. Lique, and M. H. Alexander, Science **317** (5841), 1061 (2007); W. B. Chapman, B. W. Blackmon, S. Nizkorodov, and D. J. Nesbitt, J. Chem. Phys. **109** (21), 9306 (1998); S. A. Nizkorodov, W. W. Harper, W. B. Chapman, B. W. Blackmon, and D. J. Nesbitt, J. Chem. Phys. **111** (18), 8404 (1999).

[15] M. H. Alexander, H. J. Werner, and D. E. Manolopoulos, J. Chem. Phys. **109** (14), 5710 (1998); P. J. Dagdigian and M. L. Campbell, Chem. Rev. **87** (1), 1 (1987).

[16] M. H. Alexander, D. E. Manolopoulos, and H. J. Werner, J. Chem. Phys. **113** (24), 11084 (2000).

[17] S. J. Singer, K. F. Freed, and Y. B. Band, Adv. Chem. Phys. **61**, 1 (1985).

[18] C. J. Williams and K. F. Freed, J. Phys. B **20** (21), 5737 (1987); J. Callaway and A. F. Dugan, Physical Review **163** (1), 26 (1967).

[19] H. L. Berghout, S. S. Brown, R. Delgado, and F. F. Crim, J. Chem. Phys. **109** (6), 2257 (1998); M. D. Person, P. W. Kash, and L. J. Butler, J. Chem. Phys. **94** (4), 2557 (1991); Y. Liu and L. J. Butler, J. Chem. Phys. **121** (22), 11016 (2004).

[20] D. R. Yarkony, Acc. Chem. Res. **31** (8), 511 (1998); D. R. Yarkony, Reviews of Modern Physics **68** (4), 985 (1996); J. C. Juanes-Marcos and S. C. Althorpe, Chem. Phys. Lett. **381** (5-6), 743 (2003); M. S. Schuurman and D. R. Yarkony, J. Chem. Phys. **126** (4), 044104 (2007); M. Dallos, H. Lischka, R. Shepard, D. R. Yarkony, and P. G. Szalay, J. Chem. Phys. **120** (16), 7330 (2004).

[21] M. H. Alexander, G. Capecchi, and H. J. Werner, Faraday Discussions **127**, 59 (2004); M. H. Alexander, G. Capecchi, and H. J. Werner, Science **296** (5568), 715 (2002); B. F. Parsons and D. W. Chandler, J. Chem. Phys. **122** (17), 174306 (2005); Y. Zhang, T. X. Xie, K. L. Han, and J. Z. H. Zhang, J. Chem. Phys. **124** (13), 134301 (2006); X. G. Wang, W. R. Dong, C. L. Xiao, L. Che, Z. F. Ren, D. X. Dai, X. Y. Wang, P. Casavecchia, X. M. Yang, B. Jiang, D. Q. Xie, Z. G. Sun, S. Y. Lee, D. H. Zhang, H. J. Werner, and M. H. Alexander, Science **322** (5901), 573 (2008).

[22] M. Ziemkiewicz, M. Wojcik, and D. J. Nesbitt, J. Chem. Phys. **123** (22), 224307 (2005).

[23] Y. B. Band, K. F. Freed, S. J. Singer, and C. J. Williams, J. Phys. Chem. **91** (21), 5402 (1987).

[24] G. G. Balint-Kurti, J. Chem. Phys. **84**, 4443 (1986).

[25] M. J. Bronikowski, W. R. Simpson, and R. N. Zare, J. Phys. Chem. **97** (10), 2194 (1993).

[26] M. P. Deskevich, D. J. Nesbitt, and H. J. Werner, J. Chem. Phys. **120** (16), 7281 (2004).

[27] M. Brouard, I. Burak, S. Marinakis, L. R. Lago, P. Tampkins, and C. Vallance, J. Chem. Phys. **121** (21), 10426 (2004).

[28] B. M. Cheng, C. Y. Chung, M. Bahou, Y. P. Lee, and L. C. Lee, J. Chem. Phys. **117** (9), 4293 (2002).

[29] H. Nakamura, *Nonadiabatic transition: concepts, basic theories and applications*. (World Scientific, River Edge, N.J., 2002).

[30] G. Scoles, *Atomic and molecular beam methods*. (Oxford University Press, New York, 1988).

[31] M. D. Bradke and R. A. Loomis, J. Chem. Phys. **118** (16), 7233 (2003).

[32] W. W. Harper, S. A. Nizkorodov, and D. J. Nesbitt, J. Chem. Phys. **116** (13), 5622 (2002).

[33] D. J. Creasey, P. A. Halford-Maw, D. E. Heard, J. E. Spence, and B. J. Whitaker, Rev. Sci. Instrum. **69** (12), 4068 (1998).

[34] J. Luque and D. R. Crosley, Report No. MP 96-001 (1996); J. Luque and D. R. Crosley, J. Chem. Phys. **109** (2), 439 (1998); J. A. Coxon, Can. J. Phys. **58** (7), 933 (1980).

[35] J. M. Pfeiffer, E. Woods, R. B. Metz, and F. F. Crim, J. Chem. Phys. **113** (18), 7982 (2000).

[36] M. H. Alexander, E. J. Rackham, and D. E. Manolopoulos, J. Chem. Phys. **121** (11), 5221 (2004).

[37] H. M. Lambert, P. J. Dagdigian, and M. H. Alexander, J. Chem. Phys. **108** (11), 4460 (1998).

[38] S. A. Nizkorodov, M. Ziemkiewicz, T. L. Myers, and D. J. Nesbitt, J. Chem. Phys. **119** (19), 10158 (2003).

[39] V. Engel, V. Staemmler, R. L. Vanderwal, F. F. Crim, R. J. Sension, B. Hudson, P. Andresen, S. Hennig, K. Weide, and R. Schinke, J. Phys. Chem. **96** (8), 3201 (1992).

[40] R. Schinke, V. Engle, P. Andresen, D. Hausler, and G. G. Balint-Kurti, Phys. Rev. Lett. **55** (11), 1180 (1985).

[41] L. J. Butler, Annu. Rev. Phys. Chem. **49**, 125 (1998).

[42] P. Andresen, D. Hausler, and H. W. Lulf, J. Chem. Phys. **81** (1), 571 (1984); P. Andresen, N. Aristov, V. Beushausen, D. Hausler, and H. W. Lulf, J. Chem. Phys. **95** (8), 5763 (1991).

[43] E. Kochanski and D. R. Flower, Chemical Physics **57** (1-2), 217 (1981); R. Schinke and P. Andresen, J. Chem. Phys. **81** (12), 5644 (1984).

[44] A. Moise, D. H. Parker, and J. J. ter Meulen, J. Chem. Phys. **126** (12), 124302 (2007).

[45] M. P. Deskevich, M. Y. Hayes, K. Takahashi, R. T. Skodje, and D. J. Nesbitt, J. Chem. Phys. **124** (22) (2006).

[46] B. G. Perkins and D. J. Nesbitt, J. Phys. Chem. A **112** (39), 9324 (2008); A. M. Zolot, P. J. Dagdigian, and D. J. Nesbitt, J. Chem. Phys. **129** (19), 194705 (2008).

[47] A. M. Zolot and D. J. Nesbitt, J. Chem. Phys. **129** (18), 184305 (2008).

Chapter VIII: State-to-state dynamics at the gas-liquid metal interface: Rotationally and electronically inelastic scattering of NO[$^2\Pi_{1/2}$(0.5)] from molten gallium.

Published in *J. Chem. Phys.* **134,** 234703 (2011)

8.1 Introduction

Fundamental studies of collisions between gas-phase molecules and condensed-phase surfaces are crucial for developing a more complete understanding of catalyst-mediated chemistry.[1] Of particular importance are inelastic scattering processes, whereby translational energy in the incident gas phase projectile is transferred into other degrees of freedom; if enough energy is removed from translation, molecules will stick to the surface[2], allowing further heterogeneous chemical process to occur. This loss of translational energy may form phonon excitations,[3] which ultimately arise from surface atom recoil after impulsive scattering events. In addition to direct translational energy transfer to the surface, however, molecules offer a whole plethora of channels involving *intramolecular* excitation. For example, when small molecules collide impulsively with solid surfaces, rotational excitation is especially facile.[4] Energetically accessible vibrational levels can also be excited during a collision,[5-7] although such processes can depend strongly on the electronic structure of the condensed phase material.[8] For example, electron hole pairs (ehp) can be nonadiabatically created during the scattering process,[9] which represents a particularly important pathway for molecular vibrational excitation and de-excitation due to the small density of phonon states at energies typical of stretching frequencies.[10-12] Finally, low-lying electronic energy levels such as spin-orbit excitations of open shell species represent yet another repository for energy transfer out of the incident translational degree of

freedom.[13] The variety of energy pathways, present in even simple open shell molecule surface scattering events, results in a rich dynamical system from both an experimental and a theoretical point of view.

Experimentally, the interplay between surface and projectile can be examined in a variety of ways. For example, high energy electron hole pair (ehp) excitations in the surface can be directly observed in chemicurrents surmounting a Schottky barrier[14] or by electron emission from a low work function metal.[12] In addition, molecule-surface binding strength can be examined by temperature programmed desorption studies (TPD),[15] which give an overall picture of the various well depths for molecular trapping. These direct binding measurements are supplemented by a wide range of studies probing molecules which do not remain on the surface on the microsecond timescale, but instead scatter inelastically. Mass spectrometry techniques have proven very fruitful in interrogating angularly resolved velocity distributions.[16-18] Due to energy conservation, these results can be immediately analyzed in terms of transfer of collisional motion to internal modes of both the surface and the scattered molecule, but without the ability to precisely determine which states have been excited in those two channels. To interrogate internal quantum state resolved distributions of scattered species, a variety of laser-based techniques have been employed. These techniques include laser induced fluorescence (LIF) for open shell species,[19-22] resonance enhanced multiphoton ionization (REMPI),[23-25] and direct IR absorption spectroscopy.[6,7,26] Such spectroscopic methods are capable of providing a nearly complete description of the electronic, rotational, and vibrational state of the scattered molecule, which have provided critical information about the molecular scattering dynamics.

A variety of theoretical methods are required in order to gain insights into the results of these experiments. Early studies of inelastic scattering of noble gases from solid metal surfaces

have been successfully analyzed in terms of an impulsive event between the impinging atom and a “hard cube” of the surface, with an effective mass of a few surface atoms.[27] Implicit in this picture is a loss of atomic corrugation in a "flat" gas-surface potential due to the presence of delocalized conduction electrons.[20] The resulting lack of momentum transfer in the plane for such a flat potential surface results in $\frac{1}{2}Mv_{\parallel}^2$ being a constant of the motion; though not a vector quantity, this is often referred to as conservation of "parallel energy”. Consequently, the dynamics prove to be more a function of the “normal energy", $E_n = \frac{1}{2}Mv_{\perp}^2$, rather than the total collision energy. Since surface corrugation is determined by the classical turning point of impinging atoms, the metal surface potential begins to look rougher as collision energy is increased. To treat such effects, this hard cube treatment was extended to a “washboard model” by Tully and coworkers, where conservation of parallel momentum continues to be assumed, but now “parallel” is defined with respect to local surface corrugation rather than the global surface normal.[28] In general, the net effect of such corrugation is a broadening of the angular distributions, but with the regularity of a single crystal surface capable of producing rainbow scattering phenomena arising from a classical singularity characteristic of an impulsive scattering event,.[29]

With the advent of diatomic scattering studies[19,20,30,31] focusing on NO, N_2, and CO, new internal degrees of freedom became available for exploration, with particular emphasis on rotational excitation of scattered molecules. For interactions with a relatively shallow and flat molecule-metal potential surface such as NO + Ag(111), the principle of parallel momentum conservation continues to hold.[20] For these systems, the extent of rotational excitation increases with collision energy, but the scattered distributions were found to be independent of parallel

momentum in the incident projectile, consistent with impulsive scattering (IS) dynamics. Furthermore, rotational rainbow behavior has also been observed at high collision energy in these systems.[30,32] By way of contrast, for the NO + Pt(111) scattering system,[16] rotational distributions were found to be largely independent of incident energy, a possible manifestation of a strongly attractive well between surface and adsorbate. This insensitivity to incident beam parameters indicated the existence of a true trapping-desorption (TD) channel characterized by complete thermal accommodation with the surface. The fact that collision dynamics can occur in such different regimes points to the importance of considering both the attractive (trapping) and repulsive (impulsive) parts of the molecule-surface interaction, as each appears to be capable of influencing scattered distributions. NO on metals has proven to be an especially interesting candidate for examining the relative importance of attractive vs. repulsive effects. Since the N-end is much more strongly attracted to the metal surface,[33] slowly approaching NO molecules can be highly sensitive to the anisotropy of the attractive potential on approach. Several studies have examined the effect of strong static fields which orient one end or the other towards the surface prior to scattering,[34] while others have focused on varying the depth of the binding well.[24]

In addition to studies of single crystal metal surfaces, the field of inelastic scattering from condensed phases has been extended to a wide variety of interfaces. These systems include passivated solid metal surfaces,[35] graphite,[36] salts,[37] organic monolayers,[13] and liquids.[38] In particular, the study of scattering from liquids has yielded fascinating phenomena, such as the prospect for monitoring long term loss of species (i.e., "solvation") into the bulk.[39] Several experiments have involved scattering from liquid polymers,[6] which tend to be characterized by comparable probabilities of both TD and IS trajectories. The resulting bimodal distributions

have been measured in both translational[40] and rotational[6] product state distributions, with the ratio of IS to TD character being particularly sensitive to (and therefore serving as one metric of) the surface "hardness". Interpretation of these liquid polymer studies has been enhanced by measurements on organic self assembled monolayers[41] (SAM) which approximate liquid behavior while being much more amenable to detailed numerical trajectory simulations.[42,43] While such simulations do correctly predict the experimentally observed "dual-temperature" thermal and hyperthermal Boltzmann behavior with remarkably quantitative accuracy, even nominally pure IS scattering events appear to be dominated by molecules interacting collisionally with the surface two or more times before being ejected back into the gas phase.[43]

To extend liquid scattering measurements beyond polymer surfaces, some research has also been done on ionic salt solutions,[39] ionic liquids,[26,44] and molten metals.[17,45 18,46,47] Of particular interest to the present work, many liquid metals exhibit very high surface tension and therefore a high degree of flatness in the gas-surface potential.[17,48] Additionally, some are characterized by vanishingly small vapor pressure, even at temperatures well above their melting points. Furthermore, liquid surfaces are free of static defect sites such as steps and terraces,[49] which eliminates experimental complications due to surface inhomogeneity. Instead, local roughness is governed by surface capillary waves, whose distribution of amplitude versus spatial frequency is controlled by surface tension and temperature. Interestingly, this means that the roughness of these molten metals can be experimentally and reversibly tuned simply by varying the temperature of the bulk liquid. Capillary waves of the highest spatial frequency correspond to oscillating of single atoms in and out of the surface. In Ga near its melting point (303 K), for example, this motion is expected to introduce rms fluctuations on the order of 0.1 Å along the surface normal.[17,50] While 0.1 Å is extremely small for a typical insulator liquid surface, this

fluctuation is actually quite large when compared to a single crystal metal surface, which can be smoother by two orders of magnitude for specific choices of scattering molecule and collision energy.[20]

Despite this high level of relevance, very few studies have examined scattering from molten metal surfaces, and none have examined state-resolved distributions of inelastically scattered molecules. A series of experiments by Nathanson and coworkers examined velocity distributions due to scattering of noble gas atoms from liquid metals,[17,18] revealing behavior intermediate between that of solid metals and liquid polymers. Unlike scattering from polymers, bimodal (TD/IS) translational energy distributions were not found to be the norm for these systems. Instead, the results could vary between overwhelmingly IS scattering, overwhelmingly TD scattering, or some intermediate trapping probability, by choice of incident atom and collision energy. However, compared to solid metals, the angular distributions of the scattered species from liquid metal interfaces were found to be considerably more diffuse, which was attributed to the increased surface roughness. Compared with solid surfaces of comparable atomic mass, the liquid metals permit more efficient transfer of incident collision energy into surface phonons, which again could be attributed to an increase in surface roughness.

To further explore the properties of scattering from a liquid metal surface, we have performed a series of experiments probing the full internal state distribution of NO after scattering from molten Ga. This represents the first fully rovibronically-resolved study of molecular scattering from a liquid metal surface, significantly building on and extending time-of-flight inert gas scattering efforts in the Nathanson group as well as early low resolution I_2 fluorescence studies by McCaffery and coworkers.[45,47] Such quantum state resolved investigation of molecular scattering provides a novel opportunity to probe the effect of dynamical roughening

by capillary waves on internal degrees of freedom. In addition, a detailed comparison between rotational distributions obtained for NO from molten metals vs. various single crystal surfaces offers the opportunity to identify properties unique to liquid metal scattering dynamics. At the same time, a close analysis of scattered spin-orbit distributions may allow some insight into nonadiabatic electronic dynamics during the scattering process.[10] In order to survey these previously unexamined aspects of molecule-surface interactions, we use laser induced fluorescence (LIF) techniques to probe rotational, vibrational, and spin-orbit distributions for NO molecules specularly scattered from a liquid gallium surface.

The organization of the rest of this paper is as follows. Section II describes details of a new experimental apparatus used to measure state-resolved scattering from liquid metal surfaces. Section III presents first results from this apparatus, specifically quantum state distributions for ground state NO scattered from liquid Ga, where rotational and electronic distributions are studied as a function of incident energy (E_{inc} = 1.0 - 20 kcal/mol) and surface temperature (T_S = 313K - 580K). Section IV compares the current results to previous studies on NO scattering from various single-crystal metal surfaces as well as studies on scattering of noble gases from molten metals, with conclusions and directions for further effort summarized in section V.

8.2 Experimental Technique

The apparatus is based on supersonic molecular beam scattering of NO reverse seeded in buffer gas from a liquid Ga surface, with the nascent rovibronic quantum state distributions monitored by laser induced fluorescence (LIF) on the γ-band region of NO. The experiment (Figure 8.1) is carried out in a cubical 96 L vacuum chamber with a base pressure of 1.5×10^{-8} torr, which is maintained by a 1500 L/s turbomolecular pump. Background O_2 levels are

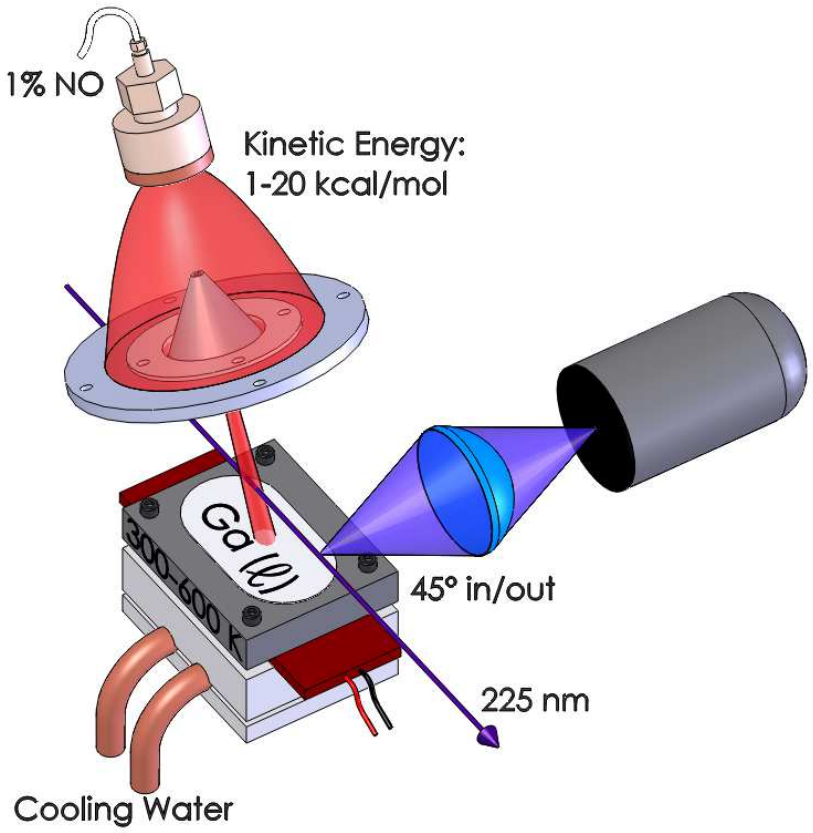

Figure 8.1 Schematic of the liquid metal scattering experiment. Tunable energy NO molecules (E_{inc} = 1-20 kcal/mol) are generated in an Evan-Lavie valve, with the resulting supersonic jet skimmed before colliding with a molten Ga surface heated to between 313 and 600 K. Scattered molecules are detected by confocal LIF, which probes a 5 mm section of the excitation laser beam. The apparatus has flexibility in excitation and detection geometry; however, the incident angle for the current experiments is fixed at 45(5)° with detection at the near specular angle.

monitored with a residual gas analyzer, which reveal partial pressures < $1x10^{-9}$ torr. At these pressures and from previous x-ray scattering data, oxidation of the Ga surface after Ar^+ sputtering is not expected to occur on the 2 hour timescale of a typical experiment.[51] Liquid Ga (99.9999% pure) is held in a stainless steel crucible (4.4 cm x 2.4 cm x 0.5 cm) whose temperature is varied by a resistive heater. The liquid Ga temperature is measured with a type K thermocouple mounted in the crucible, with maximum temperatures currently limited to 600 K by the choice of resistive heater. By way of confirmation, a second comparison thermocouple

inserted directly into the Ga liquid itself is found to agree within 1° C with the crucible mounted one. Ga vapor pressure is vanishingly small even at the highest temperature investigated in this study (580 K), which results in no observable change in the ~ 10^{-8} torr chamber pressure upon surface heating. While these measurements are all taken at temperatures above the 303 K melting point of Ga, the metal is readily observed to form a supercooled liquid state far below the freezing temperature, further attesting to the high purity of the sample.

Prior to each wavelength data scan, the surface is systematically cleaned with a beam of 2 keV Ar^+ ions at 10 μA for 20 minutes. Application of the Ar^+ sputtering beam to a Ga(l) sample freshly introduced into the vacuum results in a systematic 10% *decrease* in the scattered flux of NO molecules into the 45^0 specular detection region. This decrease saturates with a time constant of a few minutes of cleaning and does not recover in vacuum over several days, which we attribute to sputtering removal of a thin surface oxide layer. Indeed, when exposed to atmospheric pressures of O_2, liquid Ga is known to form a 5 Å film of Ga_2O_3, as has been seen in x-ray scattering studies.[51] This oxidized surface is expected to be less flexible than pure Ga(l), which is freer to undergo capillary wave motion. Thus, the decrease in specular scattering observed with Ar^+ cleaning appears to be a result of dynamical roughening of the surface upon removal of the oxide layer. Since NO is known to oxidize Ga less effectively than O_2, dosage from the incident beam is not expected to react with the surface on the timescale of this experiment.[52] Furthermore, comparisons of specularly scattered fluxes before and after each LIF scan show no indication of degradation in surface cleanliness nor change in the reported rovibronic distributions. In order to establish further confidence in our surface protocol, however, the molten Ga surface undergoes 20 minute Ar^+ sputtering routine immediately prior to each and every data run.

NO (99.5% pure) is mixed in a variety of gases at a concentration of 1% NO / 99% buffer. By seeding in Ar, Ne-70 (70% Ne, 30% He), He, and H_2 buffer gas, the incident beam kinetic energy can be varied from 1 to 20 kcal/mol.[53] The supersonic jet is produced by an Evan-Lavie pulsed jet source[54] with a backing pressure of 4000 torr and an opening time ~ 40 μs. Under these conditions, the incident beam is very cold (see figure 8.2), with incident beam temperatures ranging from 1 to 3 K depending on the specific seed gas used. Thus, the majority of incident NO molecules are cooled down into the two (λ-doubled) lowest quantum states $\{ {}^2\Pi^e_{1/2}(J=1/2) \text{ and } {}^2\Pi^f_{1/2}(J=1/2) \}$. At our experimental sensitivity, no spin-orbit-excited $\{ {}^2\Pi_{3/2} \}$ states at 120 cm^{-1} higher energy are detectable in the incident beam, which translates into an electronically excited fraction of less than 6.6×10^{-4}. The supersonic jet is collimated by a 3 mm skimmer 5.3 cm downstream from the valve orifice; after traveling another 8.6 cm, the molecular beam strikes the liquid Ga at 45° to the surface normal. While LIF detection is performed at a nominal 45° specular angle for the current experiment, the valve, sputtering source, and crucible are all mounted on a rotatable and translatable structure. This flexibility in support structure is designed to allow both incident and scattering angles to be varied in future studies.

Scattered molecules are detected by LIF at wavelengths near 225 nm to access the γ-bands ($A^2\Sigma \leftarrow X^2\Pi_{1/2,3/2}$) of NO.[55] The laser beam is obtained by tripling the output of a YAG-pumped dye laser operating with LDS-698 and characterized by a linewidth of 0.4 cm^{-1}. Spatial apertures are used to reduce the beam size to approximately 3.5 mm inside the chamber, with the pulse energy kept below 5 μJ to avoid saturation of the LIF transitions. Laser light enters and exits the chamber via fused silica Brewster windows mounted on 43 cm baffle arms. Inside the baffle arms, window scatter is blocked by four annular discs with inner diameter ranging from

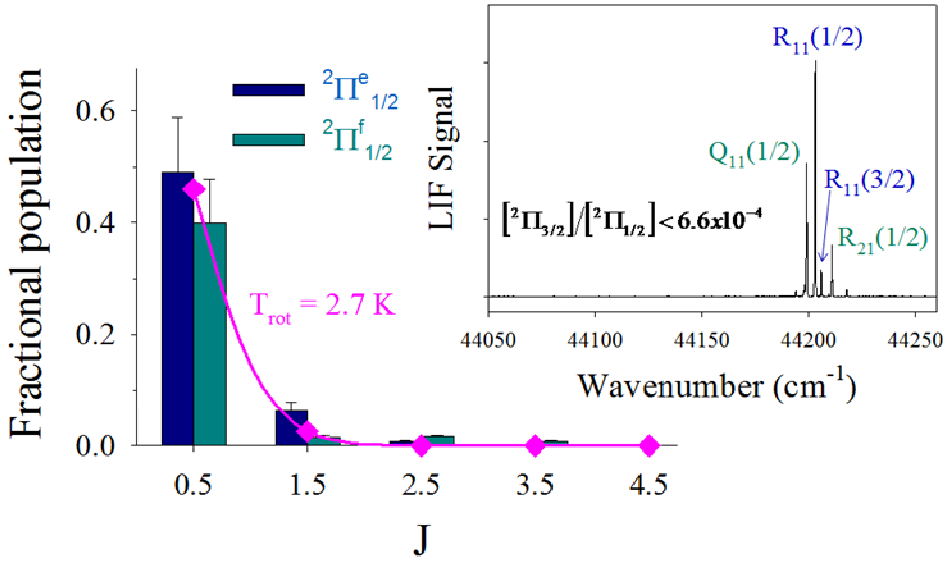

Figure 8.2 Populations and sample LIF spectrum (inset) of NO molecules in the incident molecular beam. An Evan-Lavie valve is backed with 4000 torr of 1% NO in Ar, producing a supersonic beam which can be parametrized by a rotational temperature of ≈ 3(1) K. At this temperature, the majority of molecules are in their rotational and spin-orbit ground state, $^2\Pi_{1/2}$(J = 0.5).

0.46 cm near the window to 1.1 cm at the entrance to the scattering chamber. The laser passes 1.6 cm above and parallel to the Ga surface in the scattering plane, with the fluorescence collected by 1:1 confocal imaging through a 4 mm circular mask. The measured fluorescence therefore originates from a well defined volume whose length is determined by the pinhole and whose depth/height corresponds to the UV laser beam diameter. The imaged volume is positioned to interrogate specular (45°) scattering from the surface, while successfully blocking any fluorescence signal from the cold incident molecular beam. After passing through a UG5 filter (which absorbs laser beam scatter), fluorescence from vibrationally off-diagonal transitions is imaged on a 5.1 cm diameter solar-blind photomultiplier tube (PMT). To maximize collection efficiency, the entire optical system, including the PMT, is placed in a 6.4 cm invaginated tube extending into the vacuum chamber. The necessary vacuum seal is formed by the first plano-

convex imaging lens at the end of the imaging tube, followed by a second lens, the pinhole, and the PMT.

Fluorescence signals are electronically gated and normalized to laser energy on a shot-to-shot basis. Due to the congested nature of this spectrum, analysis is performed by directly fitting ground state populations in a STARPAC least squares fit program.[56] Transition line strengths from the LIFBase database[57] are used, with laser pulse energies low enough to operate in a fully unsaturated regime. We extract populations for the four electronic sub-levels $\{ {}^2\Pi^e_{1/2}(J)$, ${}^2\Pi^f_{1/2}(J)$, ${}^2\Pi^e_{3/2}(J)$, ${}^2\Pi^f_{3/2}(J)\}$ up to a maximum J value of 50.5, at which point the photon signals begin to be comparable to background photon noise levels. Figure 8.3 shows the results of the analysis when applied to a static fill of NO in thermal equilibrium with the room temperature chamber walls. The observed populations in a Boltzmann plot (see figure 8.3) agree quantitatively with the expected room temperature 300 K distribution, which further confirms the reliability of our line fitting and population extraction protocol.

8.3 Results

By way of first test results, an LIF spectrum is obtained by scattering NO at E_{inc} = 1.0(3) kcal/mol from a Ga surface at T_S = 313 K (figure 8.4). Also shown in figure 8.4 is a small piece of the simulation obtained from the least squares fit procedure to find ground state ($^2\Pi_{1/2}$) populations. Note the substantial presence of electronically inelastic scattering to produce molecules in the spin-orbit excited $^2\Pi_{3/2}$ manifolds, despite the fact that these levels are vanishingly populated in the incident beam. Extracted populations from all four electronic state manifolds form a straight line when plotted on a Boltzmann axis vs. rotational energy, indicating

a quasi-thermal distribution which can be adequately represented at these low collision energies by a single effective "temperature". In fact, for a series of $^2\Pi^e_{1/2}(J)$ distributions taken at

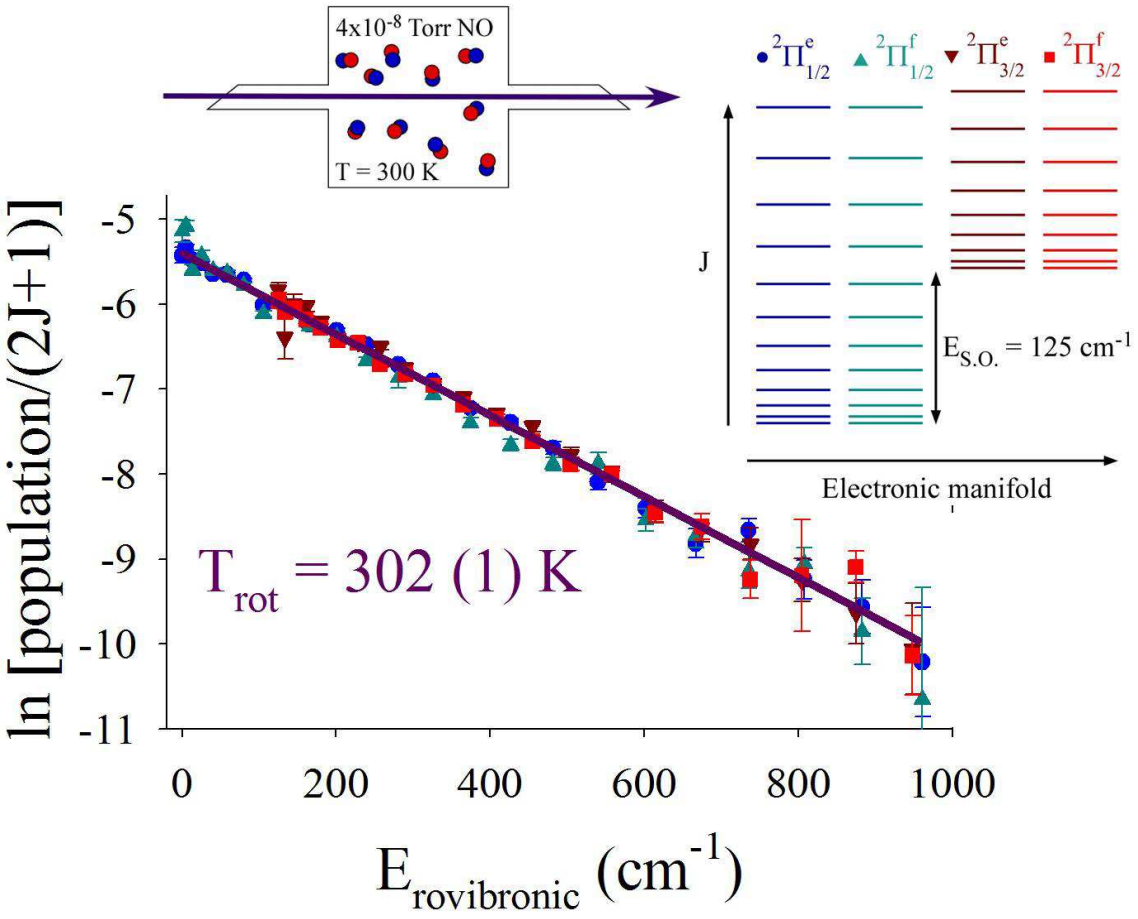

Figure 8.3 LIF analysis procedure applied to a 300 K static NO fill ($4x10^{-8}$ torr). When plotted on a Boltzmann axis, populations extracted from the spectrum agree well with the expected 300 K distribution. Inset: energy level diagram for NO($X^2\Pi_\Omega$) showing the spin-orbit splitting of $E_{Spin\text{-}Orbit.} \approx 125$ cm^{-1} and negligibly small energy difference between lambda doublet levels.

increasing values of E_{inc} (see figure 8.5), Boltzmann plots continue to be approximately linear out to at least $E_{rot} \approx 1000$ cm^{-1}, with a strong warming trend clearly visible as a function of collision energy. Indeed, at the lower incident energies (E_{inc} = 1.0 and 2.7 kcal/mol), the plots are

described by single exponential behavior up to the signal to noise limit, which would imply accurate characterization by a single rotational temperature. At higher collision energies (E_{inc} = 10 and 20 kcal/mol), however, the slopes appear to flatten out at rotational energies above 1000

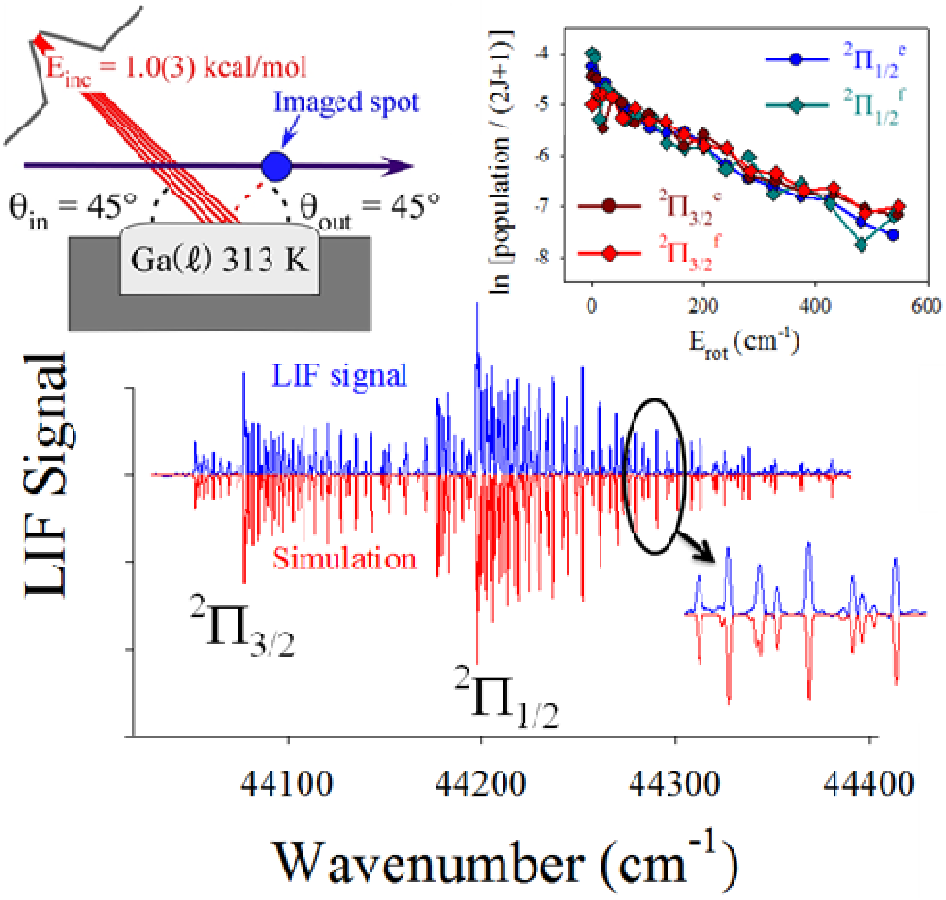

Figure 8.4 LIF spectrum of specularly scattered NO taken at E_{inc} = 1.0(3) kcal/mol, T_S = 313 K, θ_{inc} = 45°. Also shown is the least squares simulation used to extract populations, with a small sample region near 44300 cm^{-1} blown up to indicate the quality of the fit. The inset above shows populations plotted on a Boltzmann axis vs. rotational energy of the scattered molecule.

cm^{-1}, as shown in Fig. 8.6. This could be interpreted in a number of ways, e.g., i) microscopic branching between trapping-desorption (TD) and impulsive scattering (IS) components or ii) rotational rainbow contributions to the dynamics at higher rotational excitation. Though the

physical origin for this curvature at high-J is remains to be determined, the net effect on the *average* rotational energy transfer is negligibly small. In the interest of consistency, therefore, we prefer to report $\langle E_{rot} \rangle$ or $\langle E_{rot} \rangle / k_B$ as a simple one parameter metric of the distributions rather than the more model dependent slopes fitted from a Boltzmann plot.

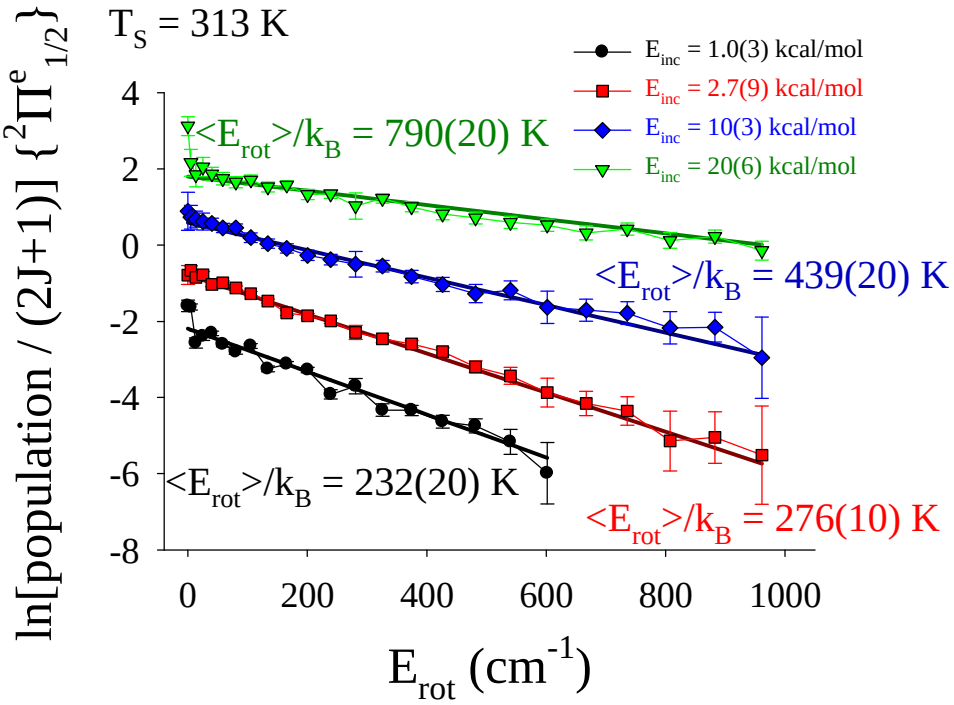

Figure 8.5 Boltzmann plots for the ${}^2\Pi^e_{1/2}(J)$ manifold, taken over a 20 fold range of incident collision energies. Data shown ($E_{rot} \leq 1000$ cm^{-1}) can be reasonably well parametrized by a single effective temperature, which can be alternatively estimated from $\langle E_{rot} \rangle / k_B$. Note that the effective temperature $\langle E_{rot} \rangle / k_B$ for scattered NO obtained is $< T_S$ at the lowest E_{inc}, with values increasing substantially with collision energy. Distributions have been displaced along the ordinate for visual clarity.

As the surface is heated, the effect on $\langle E_{rot} \rangle / k_B$ is a weak but approximately linear increase with surface temperature, as shown in figure 8.7 where the dashed line represents the results expected for fully equilibrated TD events. By way of contrast, the scattered rotational

energy increases quickly with incident energy at all surface temperatures. Furthermore, at the two lowest energies (E_{inc} = 1.0 and 2.7 kcal/mol), the rotational distributions are sub-thermal, i.e. $\langle E_{rot} \rangle / k_B < T_S$. Interestingly, the results at these two collision energies are clearly distinguishable, meaning that these sub-thermally scattered molecules have not "forgotten" their

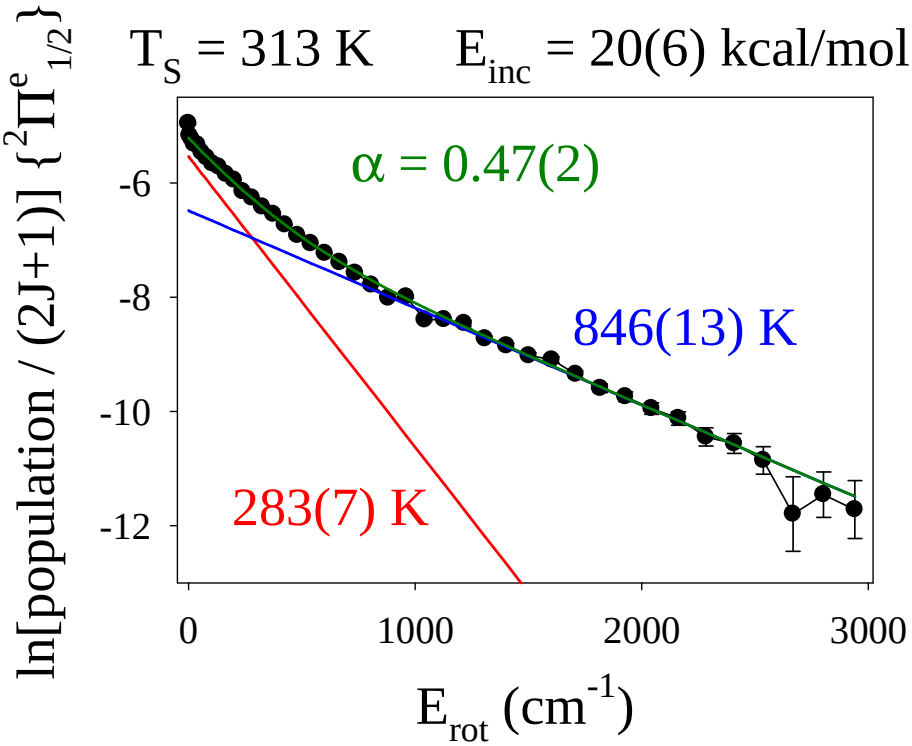

Figure 8.6 NO rotational distributions in the $^2\Pi^e_{1/2}$ manifold at high incident energy and over a wider range of rotational energies ($E_{rot} \leq 3000$ cm^{-1}). Data shown for $^2\Pi^e_{1/2}$ at T_S = 313 K and E_{inc} = 20(6) kcal/mol. The Boltzmann distribution at high-J is also surprisingly linear, suggesting the validity of a two temperature modeling of the data. Fitted parameters are shown on the plot, with low-temperature component of 283(7) K, high temperature component at 846(13) K, and branching ratio for specular scattering = 0.47(2).

incident kinetic energy, and thus can not at least be entirely ascribed to a trapping-desorption (TD) scattering process. Slopes are fitted to the data in figure 8.7 to obtain $\frac{\partial \langle E_{rot} \rangle}{k_B \partial T_S}$ as a function

of E_{inc}, with the results tabulated in the first column of table 8.1. Simply stated, this slope represents a unitless measure of the efficiency of conversion of surface energy into rotational energy at a given incident kinetic energy. It is notable that $\frac{\partial \langle E_{rot} \rangle}{k_B \partial T_S}$ *increases* with higher values of E_{inc}, despite a simple zeroth-order expectation that the importance of surface temperature

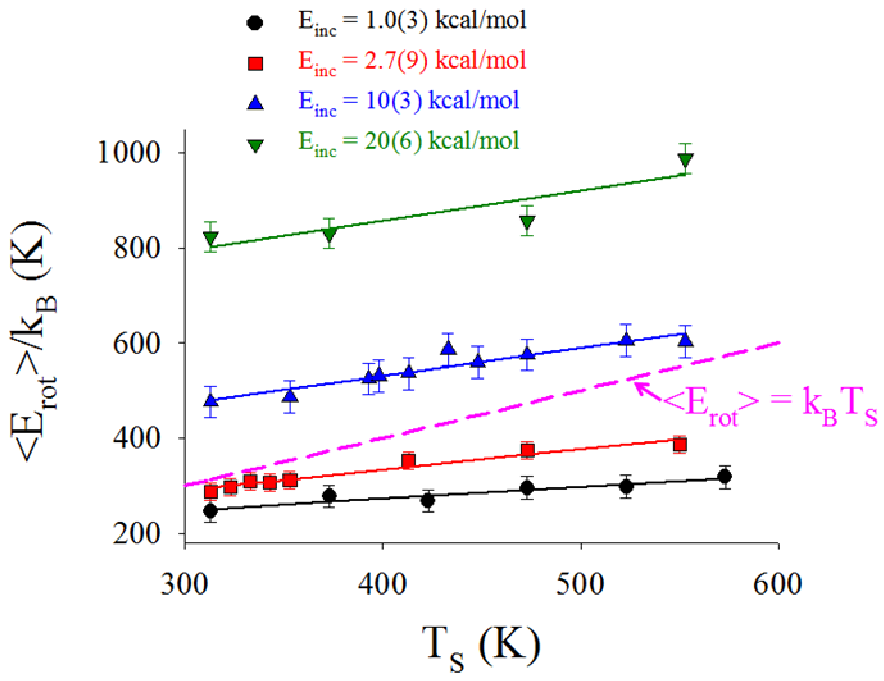

Figure 8.7 Dependence of average rotational energy on E_{inc} and T_S. Here, rotational energy has been averaged over the four electronic substates of NO. Scattered rotational energy depends strongly on E_{inc} and weakly on T_S. The dashed line represents complete rotational accommodation with the surface, such as might be expected for pure trapping desorption (TD) behavior with no dynamical effects resulting from exit channel barriers. Note that the experimental results are in clear disagreement with such a prediction with values both below and above k_BT_S as well as strongly dependent on E_{inc}. Note also the consistent increase in $\langle E_{rot} \rangle / k_B$ at all E_{inc} with T_S, which could be consistent with a model of rotational excitation enhanced by surface capillary wave roughening at the Ga(l) interface.

might *decrease* as it becomes overshadowed by larger incident kinetic energies. This suggests instead that, as the NO molecules penetrate deeper into the repulsive part of the NO-surface potential, they become more sensitive to thermal surface capillary wave motion of the Ga atoms.

In addition to information about the rotational degree of freedom, the spectrum contains distributions among the four electronic states energetically accessible in this experiment. First of all, the λ-doublet (e/f) level populations in the high J limit reflect the relative propensity for the unfilled p orbital lying i) in, or ii) perpendicular to, the end-over-end plane of rotation. These

E_{inc} *(kcal/mol)*	$\partial<E_{rot}>/k_B\partial T_s$	$\partial T_{elec}/\partial T_s$
1.0(3)	0.3(1)	0.2(1)
2.7(9)	0.4(1)	0.4(1)
10(3)	0.6(1)	1.0(2)
20(6)	0.6(2)	1.6(2)

Table 8.1 Rate of increase of scattered rotational and electronic temperature with surface heating. Interestingly, the slopes for surface temperature induced rotational excitation are in respectable qualitative agreement with predictions of ≈ 0.5 from the simple Bowman-Gossage "rotational cooling" model for desorption from rotor states bound to the surface. The corresponding slopes representing the dependence of spin-orbit excitation on surface temperature are both i) much lower at low E_{inc} and yet ii) appear to displays a much greater sensitivity as the incident collision energy is increased.

(e/f) populations agree to within experimental error bars at each value of total angular momentum J, which implies an absence of large intramolecular orbital alignment effects in the scattered flux. However, as seen in figure 8.8, there appears to be a small but clear correlation between spin-orbit excitation and rotational energy, with the rotational temperatures slightly

higher for the excited ($^2\Pi_{3/2}$) vs ground ($^2\Pi_{1/2}$) electronic state. While this is a relatively modest effect (10%-15%), it is consistently reiterated at each of the values of T_S and E_{inc}.

We can probe the electronic degree of freedom somewhat more quantitatively by analyzing the NO population distributions in terms of an approximate "electronic temperature". This can be obtained from the following expression:

$$\frac{[^2\Pi_{3/2}]}{[^2\Pi_{1/2}]} = e^{-\varepsilon_{SO}/k_B T_{elec}}, \qquad (8.1)$$

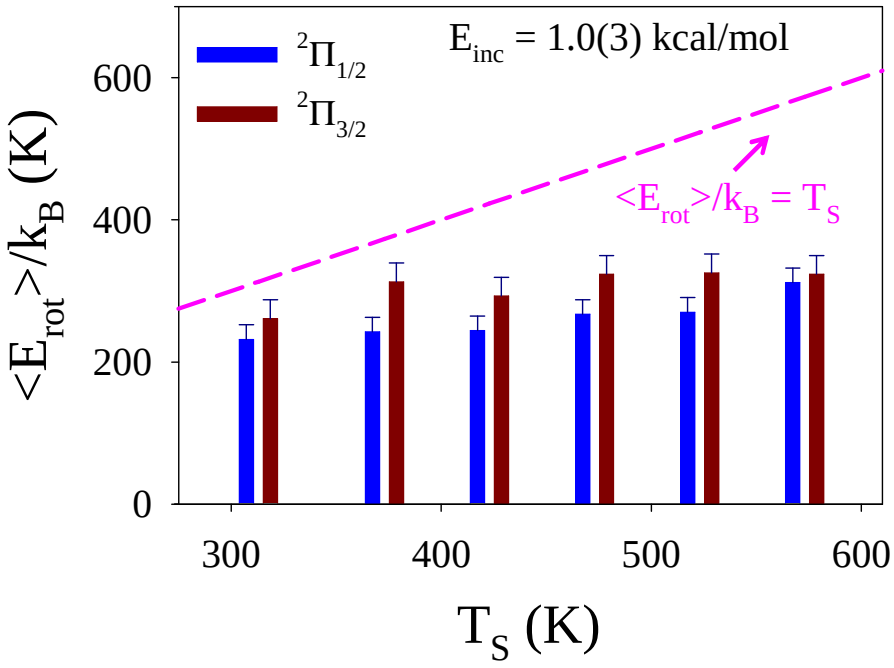

Figure 8.8 Correlation between electronic and rotational energy in the scattered products. Spin-orbit-excited ($^2\Pi_{3/2}$) molecules appear to be consistently scattered with slightly more rotational energy than the ground state ($^2\Pi_{1/2}$) species. Note, however, that the rotational temperatures for both electronic states at low incident energy (E_{inc} = 1.0(3) kcal/mol) are substantially below thermal trapping desorption (TD) predictions.

where $\left[^2\Pi_\Omega\right]$ represents the summed population of all λ-doublet and rotational levels with spin-orbit character Ω. This expression is based on the simplifying assumption that the spin-orbit splitting (ε_{SO}) is only weakly dependent on rotational state, thereby justifying the extraction of a rotationally averaged electronic temperature in a Hund's case (a) picture. Of course, this is only rigorously valid for low end-over-end rotational quantum number (N), since at sufficiently high N, the NO angular momenta become better described by a Hund's case (b) coupling scheme. However, Hund's case (a) provides an adequate first order description of angular momentum coupling up to where the adjacent rotational spacing becomes comparable to the spin orbit splitting. For $B \approx 1.7$ cm^{-1} and $\varepsilon_{SO} \approx 125$ cm^{-1}, this occurs at $N \approx 35$, i.e., at rotational energies > 2000 cm^{-1} and corresponding to population signals already near the background noise limit. For the purposes of an electronic temperature estimate, therefore, we can thus approximate ε_{SO} to be ≈125 cm^{-1} and independent of N. Figure 8.9 summarizes the resulting electronic temperatures and variation with T_S and E_{inc}. While somewhat noisier than the $\langle E_{rot}\rangle/k_B$ measurements in figure 8.7, the trends are unambiguous, revealing a clear sensitivity in the scattered electronic temperature to the temperature of the surface as well as the incident collision energy. In agreement with what was observed for rotational excitation, the electronic temperature is again systematically *colder* than the surface temperature (dashed line) at the lowest collision energies, but *increases* dramatically to values *in excess* of the surface temperature at the highest collision energies. This can be further quantified in terms of the unitless slope of scattered average rotational energy per increase in surface temperature (as reported in table 8.1). This again shows a modest but quite clear increase in electronic excitation with surface heating, as well as a very strong increase in this level of excitation with incident collision energy. Interestingly, a closer comparison between figures 8.7 and 8.9 as well as table 8.1 reveals substantial differences

between the surface temperature dependence for rotational vs. electronic degrees of freedom. In particular, the average electronic energy in the scattered NO flux is both i) colder and yet ii) more responsive to T_S than the corresponding rotational degree of freedom. While the very presence of spin-orbit excited products indicates some source of non-adiabatic coupling, its sensitivity to surface temperature is intriguing as well. This effect, along with the fact that electronic temperatures are somewhat close to that of the surface, combine to rule out a simple picture for "statistical" 4:2 population of NO($^2\Pi_{3/2}$) vs. NO($^2\Pi_{1/2}$) upon leaving the surface. In fact, these results may point to the importance of interaction with surface electron-hole pairs during the collision event, as will be discussed in more detail in section IV.

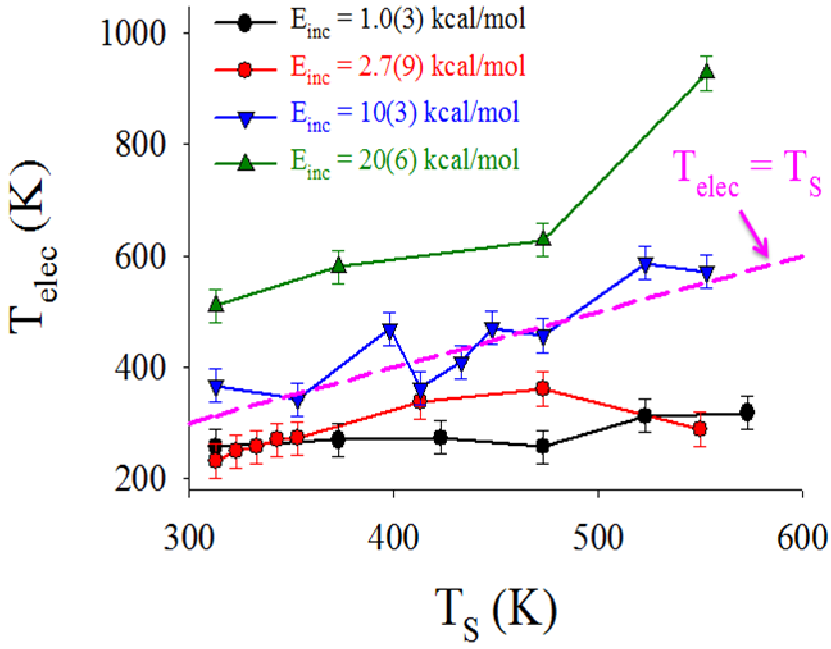

Figure 8.9 Electronic (spin-orbit) temperatures as a function of surface temperature and incident translational kinetic energy. Note the systematic increase in T_{elec} with surface temperature (T_S) as well as a rise with incident energy (E_{inc}). Compared to the rotational temperature behavior shown in figure 8.7 and table 8.1, the spin orbit temperatures are both i) significantly colder and ii) more sensitive to surface heating at the higher collision energies.

The quantum state resolved data also provides access to information on NO (v > 0), and therefore the role of vibrationally inelastic excitation in the gas-liquid metal scattering event. Indeed, the sensitivity of the LIF method is sufficiently high to detect trace fractional amounts ($5x10^{-5}$) of rotationally cold NO(v = 1) in the incident beam immediately downstream from the expansion orifice. This amount closely matches the populations expected due to thermal population of this state in the room temperature stagnation region, which is then inefficiently cooled and therefore frozen out in the supersonic expansion. However, despite this high sensitivity, we do not see any vibrationally inelastic collisions in the NO flux that eventually scatters from the Ga(l) surface over the current range of temperatures. This is not a matter of insufficient incident energy; we still observe strong LIF signals out of rotational levels as high as 3000 cm^{-1}, i.e., well above the fundamental NO vibrational spacing of ≈ 1904 cm^{-1}. More quantitatively, if we assume a NO(v = 1) rotational temperature similar to or cooler than that of NO(v = 0), we can place an upper limit of $2.6x10^{-4}$ on the vibrational branching to produce vibrationally excited v = 1 molecules on scattering from the Ga surface. Such a low probability of collisionally excited states is typical for insulating liquids, where the probability for vibrational excitation would be expected to be small due to the large energetic mismatch between surface phonon spacing and NO vibrational spacing.[10] However, this is somewhat more surprising for a conducting liquid metal, where thermally populated electron hole pair states could in principle provide an alternative pathway for resonant excitation of NO(v=1). The fact that we see so little vibrational excitation suggests that there is an insufficient density of thermally populated ehp excitations even at the highest temperatures currently studied (≈ 580 K). If the limitation is indeed ehp excitation density, this would predict an exponential sensitivity to increasing temperature. We are therefore presently modifying the crucible design to achieve

temperatures up to 1200K, which from simple Boltzmann predictions should permit access to an order of magnitude higher density in ehp states resonant with the 1904 cm^{-1} NO (v=1) vibration at the liquid Ga interface.

8.4 Discussion

For low internal energies in the scattered NO (i.e., < 1000 cm^{-1}), the rotational distributions are well-described by a single effective temperature. Furthermore, for low incident energies (i.e., 1.0 and 2.7 kcal/mol), where the NO is anticipated to have a sufficiently long residence time to lose all memory of the initial gas-liquid collision event, the rotational temperatures in the desorbing flux are systematically *colder* than that of the Ga(l) surface. Such a "rotational cooling" behavior has in fact been observed for NO scattered from many solid surfaces, both metallic and non-metallic.[20,24] This can be alternately viewed in terms of detailed balance[2] considerations to indicate sticking probabilities under equilibrium conditions which decrease strongly with rotational energy of the incident molecules.[21] The quasi-thermal and cold rotational distributions obtained in the current study at these low energies can therefore be tentatively ascribed to predominantly TD scattering, but with barrier dynamics in the exit channel for desorption resulting in a systematic lowering of the average rotational energies, as discussed in more detail below. We again stress that such a simple TD description of the collision dynamics is clearly not completely correct, since the characteristic rotational temperature varies with incident collision energy over the entire range studied, even revealing small but statistical differences at the lowest E_{inc} = 1.0 kcal/mol (T_{rot} = 232(20) K) vs. E_{inc} = 2.7 kcal/mol (T_{rot} = 276(10) K). This suggests that additional inherent averaging must be involved, possibly in the distribution of residence times and/or number of surface interactions as a function

of energy before desorption into the vacuum. Both further measurements and theoretical treatments will be required in order to better understand how such rotationally cool yet quasi-thermal behavior is achieved in the scattering dynamics.

The fact that the scattered rotational distribution at low E_{inc} are well characterized by temperatures *colder* than T_S differs qualitatively from observations of the rotational dynamics of CO_2 collisions with insulating liquids such as perfluorinated polyether (PFPE).[43] In these previous studies, similarly low energy collisions (E_{inc} = 1.1(3) kcal/mol) resulted in scattered rotational distributions in essentially perfect quantitative agreement with T_S over a range of temperatures and completely consistent with a TD dominated process and a J state independent sticking coefficient. In contrast, the sub-thermal and incident-energy-dependent rotational distributions obtained in the current study of NO on Ga(l) cannot be explained by a purely TD channel with sticking coefficients independent of incident rotational state. Overall, the qualitative features of the NO rotational distributions from Ga(l) appear to have more in common with scattering from single crystal solid metals than with previous measurements from insulating liquids.

These trends are examined more closely in figures 8.10a and 8.10b, which show a collection of experimentally measured rotational temperatures for NO scattering from a range of single crystal metal surfaces. Results from the current Ga study are also plotted together with the literature values, with $<E_{rot}>/k_B$ taken as an approximate measure of rotational temperature. The fact that these studies were done at a variety of i) surface temperatures and ii) experimental collision geometries poses a minor problem for quantitative comparisons between the different systems. Fortunately, experiments have revealed only a weak dependence of T_{rot} on T_S for all these systems, as well as an insensitivity of T_{rot} to detection angle. Thus, for the purposes of the

present comparison, variation in both surface temperature and detection angle is neglected, with $<E_{rot}>/k_B$ vs. E_{inc} plotted in figure 8.10a for a range of NO-metal scattering systems. Incident scattering angle, on the other hand, has been shown to have a significant effect on scattered NO rotational distributions, and so should also be taken into account. One common way to do this would be by assuming conservation of the NO translational momentum parallel to the surface. While the extreme smoothness of single-crystal metallic surfaces does justify such an assumption in many cases,[19] the corresponding validity for liquid metal surfaces remains as yet untested. Nevertheless, figure 8.10b shows the same dataset as in figure 8.10a, but with conservation of

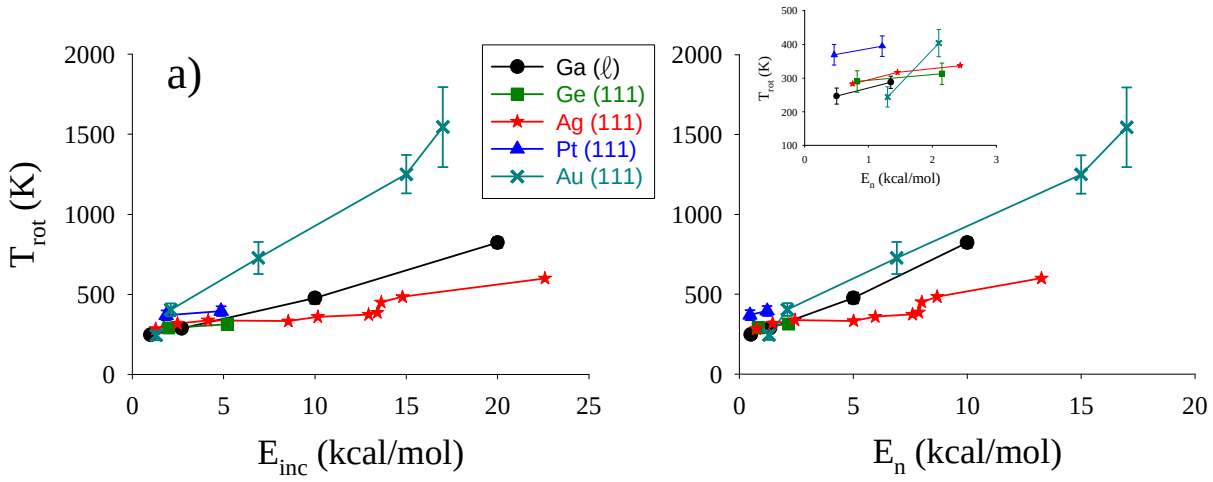

Figure 8.10 Comparison of the dependence of scattered rotational temperature with incident kinetic energy for NO scattering from various single crystal metals as well as the current Ga(l) results. (a). Experimental conditions are as follows: (Ga(l), T_S = 313 K, θ_{inc} = 45°), (Ge(oxidized), T_S = 346 K, θ_{inc} = 50°),[21] (Ag(111), T_S = 650 K, θ_{inc} = 40°),[19] (Pt(111), T_S = 412 K, θ_{inc} = 60°),[16] (Au(111), T_S = 298 K, θ_{inc} = 0°).[25] b) Same dataset as in a), but after normal energy scaling ($E_n = E_{inc}\cos^2\Theta_{inc}$). It is interesting to note that Ga(l), despite having the smallest atomic mass of all species considered, appears to promote rotational excitation as well as Au, the heaviest atom shown. The inset shows a blowup at low collision energies where all surfaces appear to exhibit similar propensities for NO rotational excitation.

parallel momentum assumed, which means that only a fraction of the incident energy (i.e. the "normal energy" component, $E_n \equiv E_{inc}\cos^2\theta_{inc}$) is available for rotational excitation. The abscissae in figures 8.10a and 8.10b therefore reflect plots based on these two simple limiting cases, with the more correct dynamical picture most likely somewhere in between. Broadly stated, the behaviors fall into two categories, with i) Au(111) being the most efficient and ii) the other single crystal metals being significantly less efficient at rotational excitation of the NO, while the results for Ga(l) lie between these two limits.

The first thing to note is that at the lowest collision energies (E_{inc} and E_n < 3 kcal/mol), the T_{rot} values approach what is clearly a nonzero intercept (see the inset in figure 8.10b). Physically, in the limit of zero incident energy, $<E_{rot}>$ should reflect ideal TD scattering, i.e., where the adsorbed species has become equilibrated with the surface before thermally desorbing into the vacuum. Interestingly, this limiting behavior for all single crystal metal surfaces suggests a NO rotational temperature for TD scattering which is *colder* than T_S, in agreement with the behavior noted above for Ga(l). Indeed, all metals, including Ga(l), have very similar intercepts below T_S, in spite of large differences in atomic masses, crystal lattice parameters, and surface temperatures. This consistency with respect to variation in surface temperature is at first somewhat surprising, since pure TD scattering reflects a thermally driven process. However, the scattered rotational temperatures (for example, NO + Ga(l) data in figure 8.9), depend only relatively weakly on surface temperature, so might not be expected to influence TD rotational dynamics to a large degree.

Somewhat more surprising is the apparent lack of sensitivity to the NO surface binding energy, a value which varies widely between, for example, NO + Ag (~0.27 eV) and NO + Ge (~1.5 eV). This peculiar unimportance of molecule-surface binding energy has been previously

discussed by Bowman and Gossage[58], based a simple model picture where physisorbed molecules are assumed to rotate freely in the surface plane prior to desorption. Model prediction of the nascent rotational distributions further requires that molecules desorb with minimal translational momentum, i.e. adsorbed species escape by transferring just enough energy from rotation into translation in order to overcome the well binding them to the surface. While equilibrium desorption events out of a barrierless potential well are expected to be characterized by velocities distributed over a thermal range, these non-zero translational energy distributions are not expected to strongly affect the rotational dynamics as long as the energy of binding is large compared to $k_B T_S$ at the surface temperatures under consideration. Based on these two assumptions, Bowman and Gossage derived the following probability for rotational distributions upon desorption from a potential well with binding energy Δ: $P_j = \frac{1}{Q}\sqrt{(2j+1)^2 + \frac{4\Delta}{B}}e^{-Bj(j+1)/kT_S}$, where B is the rotational constant of the diatomic (1.7 cm^{-1} for NO) and Q is the total partition function. The limiting cases yield the expected rotational degeneracies (i.e. $g_j = (2j+1)$ and 2) corresponding to i) free rotation vs. ii) rotation constrained to a plane for i) weak ($4\Delta/B << (2j+1)^2$) vs. ii) strong ($4\Delta/B >> (2j+1)^2$) binding energy, respectfully.

While the above distribution is not strictly thermal, it does yield a relatively straight Boltzmann plot over the range of rotational states. The corresponding temperatures obtained by fitting these distributions is indeed lower than that of the surface, as experimentally observed. The average rotational energy predicted by this distribution can be evaluated from $< E_{rot} > = \frac{1}{Q}\sum_{j=0}^{\infty} Bj(j+1)\sqrt{(2j+1)^2 + \frac{4\Delta}{B}}e^{-Bj(j+1)/kT_S}$. In the high temperature limit (B/kT <<1) and for $\Delta = 0$, this expression can be directly summed to yield $< E_{rot} > = kT_S$, as expected.

In the more physically motivated limit of $\frac{4\Delta}{B} \rangle\rangle (2j+1)^2$, the expression simplifies to $< E_{rot} > \rightarrow \frac{\sum_{j=0}^{\infty} Bj(j+1)e^{-Bj(j+1)/kT_S}}{\sum_{j=0}^{\infty} e^{-Bj(j+1)/kT_S}}$, which for B/kT <<1 can be summed analytically to yield

$< E_{rot} > = 0.5kT_S$ i.e., half of the equilibrium thermal limit and independent of the depth of the adsorption well. The NO - Ga(l) binding energy has not been experimentally measured, but even for a rough estimate of 0.5 eV - 1 eV, these conditions are satisfied out to j + 1/2 ≈ N ≈ 60, i.e. well beyond the maximum in the values observed experimentally.

This model accounts for many of the qualitative features of gas-surface scattering measurements. In particular, it predicts quasithermal rotational distributions characterized by temperatures below that of the surface. In addition, it correctly predicts a lack of sensitivity to molecule-surface binding energy for TD scattering, providing a plausible explanation of the common intercepts observed for scattering of NO from various single crystal and molten liquid metal surfaces in figure 8.10. Comparison at a more quantitative level is likely to be complicated by the fact that measured values of $<E_{rot}>$ contain contributions from both TD and IS scattering, while the model only considers the TD channel. Nevertheless, for $\frac{4\Delta}{B} \rangle\rangle (2j+1)^2$ the model predicts an effective rotational temperature on the order of $<E_{rot}>/k_B \approx T_S/2$. By way of example, for the present NO + Ga(l) data at 423 K, B = 1.7 cm^{-1}, and Δ = 0.5 eV the model predicts $<E_{rot}>/k_B$ = 218 K, which compares favorably with the experimentally measured value of 268(24) K for scattering at 1.0 kcal/mol. Furthermore, the model also makes explicit prediction of the dependence of this rotational temperature on the surface temperature. In the high

temperature limit, this should be $\partial \langle E_{rot} \rangle / k \, \partial T_S \approx 0.5$, which given the simplicity of the model is in reasonable qualitative agreement with the range of slopes observed in figure 8.7 for a series of incident collision energies and reported in table 8.1.

As E_{inc} is increased, IS scattering becomes non-negligible and differences begin to emerge for scattering of NO from various metal surfaces. In a "hard cube" model, the efficiency of rotational excitation for impulsive scattering depends on the total mass of surface atoms recoiling as the collision partner. In the limit of isolated atom recoil, therefore, one would expect impulsive rotational excitation to be more efficient for heavier atoms. Indeed, the data in figure 8.10 for Au (197 amu) vs. Ag (108 amu) follow this trend nicely. The results for Ga(l) (70 amu), however, clearly deviate from this expected trend. In fact, though significantly less massive, Ga(l) appears to excite rotations more efficiently than Ag(111), and nearly as efficiently as Au(111). Figure 8.11 shows the same data for Au, Ag, and Ga, but with the ordinate replaced by fraction of total incident energy ending up in NO rotation, which shows that the same order of rotational excitation efficiency (i.e Ag < Ga ≈ Au) is maintained. Furthermore, the fractional efficiencies for all three metals decrease with increasing normal energy and appear to reach an asymptotic value characteristic of fully impulsive scattering dynamics.

It is worth considering what is responsible for this enhanced rotational excitation propensity. Liquid Ga is known to exhibit a large degree of stratification over several monolayers at the vacuum interface[50,59], so it is possible that stiff interfacial bonding could be enough to overcome the substantial difference in mass between Au and Ga atoms, resulting in more efficient rotational excitation. However, a more likely possibility is that the capillary wave excitations in the liquid lead to surface corrugation effects which invalidate normal energy scaling ideas implicit in figure 8.10b. In fact, thermal roughening of Ga by such capillary waves

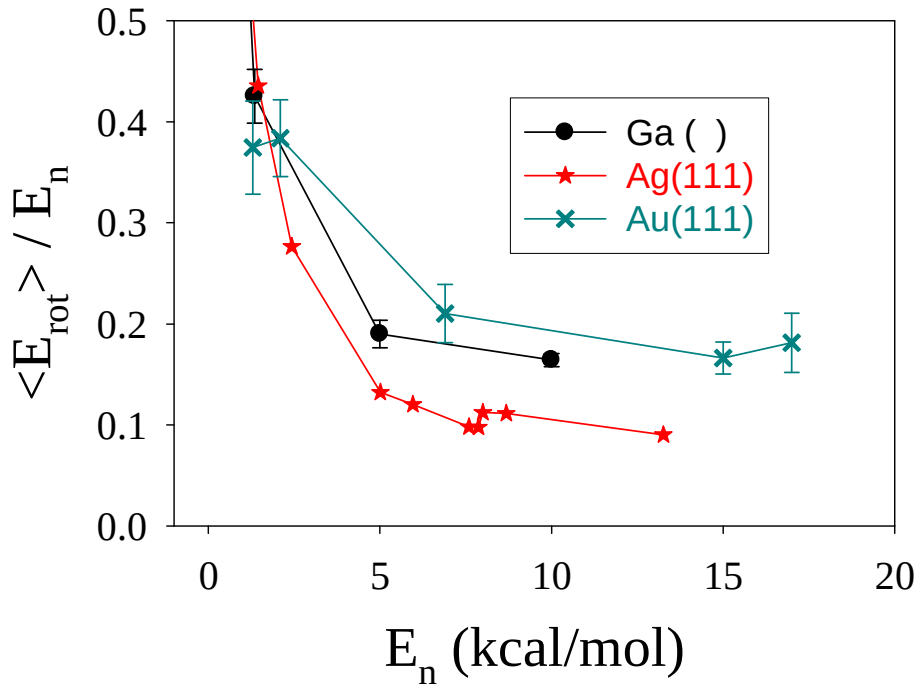

Figure 8.11 Fraction of incident energy appearing in rotational excitation as a function of normal energy. Asymptotic behavior at large values of E_n is indicative of an impulsive scattering process. The limiting value for fraction of incident energy going to rotation is a measure of effective surface mass when the hard cube model is applicable. The fact that Ga(l) is more effective at exciting rotations than heavier atoms such as Ag(111) suggests a deviation from conventional "normal energy scaling" ideas at liquid metal surfaces. This increased excitation efficiency may reflect increased dynamical corrugation due to surface capillary wave behavior at the gas-molten metal interface.

was invoked by Nathanson and co-workers to explain the much broader distribution of scattering angles for noble gases on liquid gallium compared to solid Ru(0001) of similar mass.[17] Yet another possibility would be surface puckering[60] as the liquid Ga surface relaxes via the radical-surface attraction upon NO approach. Since atomic mobility is higher in the liquid phase, this could permit enhanced transient deformation of the surface during the collision, in effect resulting in additional dynamical surface roughening on the timescale of a scattering event.

Previous experiments on state-resolved collisions of CO_2 from insulating liquids[6,7,26] have been successfully characterized by a simple TD/IS model, with the TD flux in complete thermal equilibrium with surface temperature. The presence of rotational distributions with temperatures lower than T_S suggests more involved surface dynamics for liquid metal scattering and therefore is potentially challenging to the TD/IS paradigm. At higher collision energies, however, the rotational distributions do exhibit non-linear behavior on a Boltzmann plot (see figure 8.6). In analogy with previous analysis of scattering from insulating liquids, we employ a dual temperature model to fit the emerging NO populations to

$$P(J) = (2J+1)\left[\frac{\alpha}{Q_1}\exp(-\varepsilon_J / kT_1) + \frac{1-\alpha}{Q_2}\exp(-\varepsilon_J / kT_2)\right]$$ for each electronic spin orbit

manifold, where T_i are the temperatures, Q_i the corresponding partition functions, and α the fraction of NO molecules scattering into the low vs high temperature channel. The resulting fit to $^2\Pi^e_{1/2}$ (T_S = 313 K, E_{inc} = 20 kcal/mol) is shown in figure 8.6. Once again, we see that the lower temperature component is even colder than T_S, i.e., consistent with single temperature fits performed at lower collision energies. Nevertheless, it is important to emphasize that this two temperature model contains an implicit assumption that the scattering dynamics occur via two channels, each of which can be characterized by a rotational temperature. Further experimental studies are required to explore the validity of this assumption, particularly since the high temperature component could actually be a manifestation of a rotational rainbow. Therefore, at the moment, it is too early to speculate on the origin of the peculiar form of the rotational Boltzmann plot even though the strikingly linear behavior at high J seems to indicate the existence of some sort of interesting dynamics akin to that observed in CO_2 scattering from liquids.

As a final comment, we consider spin orbit electronic excitation of NO in the liquid Ga surface scattering event, with the data summarized in figure 8.9. The trends are qualitatively the same as for rotational excitation, i.e., temperatures lower than T_S at low collision energies, increasing with E_{inc} and quasi-linearly with surface temperature. However, closer comparison of figure 8.9 with figure 8.7 also indicate significant differences, with i) spin orbit excitation indicating a 2-fold greater sensitivity to surface heating and ii) lower overall efficiency for electronic vs rotational excitation with collision energy. The greater sensitivity of electronic vs rotational degrees of freedom to surface temperature is particularly surprising since, while surface phonons should easily exchange energy with rotational degrees of freedom, non-adiabatic transitions are required to populate spin-orbit excited states.

Such differences in the electronic vs. rotational dynamics may signal different mechanisms for spin-orbit vs. rotational excitation during the scattering event. One intriguing possibility is that the spin orbit excitation could be mediated by electron transfer hopping interactions with the metal surface, as suggested by Tully and coworkers for NO + Au(111).[9,61] In this model, the NO reaches a critical distance from the surface where it is energetically favorable for an electron to jump non-adiabatically from the metal to the diatomic, forming a transient NO^- anion and a positively charged hole in the metal. Since the electron affinity of NO is quite small[62] (0.026 eV), energetic stabilization of the transient state is largely due to Coulombic attraction between the NO^- and a corresponding image charge below the surface. The NO^- anion then collides and recoils from the surface, resulting in a second nonadiabatic electron transfer back to the metal, which could provide a novel mechanism for non-equilibrium spin orbit state excitation. Indeed, the dependence of the electron affinity on NO intermolecular coordinate has been shown by Wodtke, Auerbach and coworkers[8] to lead to very efficient

nonadiabatic coupling between vibrational and electronic degrees of freedom in NO + Au(*s*) scattering processes. Whether such a treatment can adequately rationalize incident energy and surface temperature dependence of spin orbit excitation of NO scattering from liquid metals remains an outstanding challenge to further high level theoretical efforts, which we hope the present NO + Ga(l) data may serve to stimulate.

8.5 Summary / Conclusions

First quantum state-resolved measurements of NO scattering from liquid gallium have been obtained by the combination of skimmed supersonic molecular beam sources and laser induced fluorescence detection. Rotational distributions are well described by a simple Boltzmann distribution over the 0-1000 cm^{-1} range. However, the scattered rotational temperature deviates significantly from that of the surface, and in fact is systematically colder than T_S at the lowest collision energies (E_{inc} = 1.0(3) kcal/mol). Average rotational energy depends weakly on surface temperature and strongly on incident kinetic energy, with a slight increase in sensitivity to T_S as incident kinetic energy increased. Comparison with single-crystal scattering studies shows that liquid gallium promotes rotational excitation more efficiently than heavier species such as Ag(111) and almost as efficiently as Au(111). This suggests a substantial dynamical difference between scattering from liquids vs. solids, possibly due to intrinsic thermal roughening of the liquid surface by capillary waves. The NO spin-orbit degree of freedom is analyzed in terms of an electronic temperature, which is sensitive to incident kinetic energy and the temperature of the gallium surface. Differences between electronic and rotational excitation behavior are noted which may signal contributions due to transient electron transfer from the surface and/or interactions with electron hole pairs during the collision. At

high collision energies and high internal energy of scattered products, additional curvature is observed on a Boltzmann plot, possibly indicative of either a rotational rainbow or a dual-channel TD/IS scattering process. This phenomenon requires further study; in particular, variation of scattering geometry should provide information on whether the high angular momentum channel results from a rotational rainbow similar to scattering from single crystal metals, or an IS channel which would be less likely to be observed at non-specular angles. Furthermore, measurements done at higher surface temperature will be required to further elucidate the role of electron hole pairs in the scattering dynamics. In particular, the emergence of vibrationally inelastic NO fundamental (v=1) and overtone (v=2) scattering from a hot Ga(l) surface should provide an excellent target for further experimental and theoretical efforts.[10,12]

References for Chapter VIII

1 G. A. Somorjai, *Introduction to surface chemistry and catalysis*. (Wiley, New York, 1994).

2 J. C. Tully, Surf. Sci. **299** (1-3), 667 (1994).

3 R. Schinke and R. B. Gerber, J. Chem. Phys. **82** (3), 1567 (1985).

4 G. O. Sitz, E. Hasselbrink, and B. I. Lundqvist, *Handbook of Surface Science, Vol. 3: Dynamics*. (Elsevier, Amsterdam, 2008).

5 E. K. Watts, J. L. W. Siders, and G. O. Sitz, Surf. Sci. **374** (1-3), 191 (1997).

6 B. G. Perkins and D. J. Nesbitt, J. Phys. Chem. B **110** (34), 17126 (2006).

7 B. G. Perkins and D. J. Nesbitt, J. Phys. Chem. A **111** (31), 7420 (2007).

[8] Y. H. Huang, C. T. Rettner, D. J. Auerbach, and A. M. Wodtke, Science **290** (5489), 111 (2000).

[9] N. Shenvi, S. Roy, P. Parandekar, and J. Tully, J. Chem. Phys. **125** (15) (2006).

[10] A. M. Wodtke, D. Matsiev, and D. J. Auerbach, Prog. Surf. Sci. **83** (3), 167 (2008).

[11] Q. Ran, D. Matsiev, D. J. Auerbach, and A. M. Wodtke, Phys. Rev. Lett. **98** (23) (2007); Q. Ran, D. Matsiev, D. J. Auerbach, and A. M. Wodtke, Nucl. Instrum. Methods Phys. Res. Sect. B-Beam Interact. Mater. Atoms **258** (1), 1 (2007); R. Cooper, I. Rahinov, Z. S. Li, D. Matsiev, D. J. Auerbach, and A. M. Wodtke, Chem. Sci. **1** (1), 55 (2010).

[12] J. D. White, J. Chen, D. Matsiev, D. J. Auerbach, and A. M. Wodtke, Nature **433** (7025), 503 (2005).

[13] S. R. Cohen, R. Naaman, and G. G. Balint-Kurti, Chem. Phys. Lett. **152** (2-3), 269 (1988).

[14] D. Krix, R. Nunthel, and H. Nienhaus, Phys. Rev. B **75** (7) (2007).

[15] H. J. Borg, J. Reijerse, R. A. Vansanten, and J. W. Niemantsverdriet, J. Chem. Phys. **101** (11), 10052 (1994).

[16] J. Segner, H. Robota, W. Vielhaber, G. Ertl, F. Frenkel, J. Hager, W. Krieger, and H. Walther, Surf. Sci. **131** (2-3), 273 (1983).

[17] M. Manning, J. A. Morgan, D. J. Castro, and G. M. Nathanson, J. Chem. Phys. **119** (23), 12593 (2003).

[18] J. A. Morgan and G. M. Nathanson, J. Chem. Phys. **114** (5), 1958 (2001); W. R. Ronk, D. V. Kowalski, M. Manning, and G. M. Nathanson, J. Chem. Phys. **105** (10), 4397 (1996).

[19] A. W. Kleyn, A. C. Luntz, and D. J. Auerbach, Phys. Rev. Lett. **47** (16), 1169 (1981).

[20] G. D. Kubiak, J. E. Hurst, H. G. Rennagel, G. M. McClelland, and R. N. Zare, J. Chem. Phys. **79** (10), 5163 (1983).

[21] A. Modl, H. Robota, J. Segner, W. Vielhaber, M. C. Lin, and G. Ertl, J. Chem. Phys. **83** (9), 4800 (1985).

[22] P. A. J. Bagot, C. Waring, M. L. Costen, and K. G. McKendrick, J. Phys. Chem. C **112** (29), 10868 (2008).

[23] J. S. Hayden and G. J. Diebold, J. Chem. Phys. **77** (9), 4767 (1982).

[24] E. Kolodney, D. Baugh, P. S. Powers, H. Reisler, and C. Wittig, Chem. Phys. Lett. **145** (3), 177 (1988).

[25] A. M. Wodtke, Y. H. Huang, and D. J. Auerbach, Chem. Phys. Lett. **414** (1-3), 138 (2005).

[26] J. R. Roscioli and D. J. Nesbitt, J. Phys. Chem. Lett. **1** (4), 674 (2010).

[27] R. M. Logan and R. E. Stickney, J. Chem. Phys. **44** (1), 195 (1966); E. K. Grimmelmann, J. C. Tully, and M. J. Cardillo, J. Chem. Phys. **72** (2), 1039 (1980).

[28] J. C. Tully, J. Chem. Phys. **92** (1), 680 (1990).

[29] T. Kondo, H. S. Kato, T. Yamada, S. Yamamoto, and M. Kawai, J. Chem. Phys. **122** (24) (2005).

[30] M. A. Hines and R. N. Zare, J. Chem. Phys. **98** (11), 9134 (1993).

[31] T. F. Hanisco, C. Yan, and A. C. Kummel, J. Chem. Phys. **97** (2), 1484 (1992); K. R. Lykke and B. D. Kay, J. Chem. Phys. **90** (12), 7602 (1989).

[32] J. L. W. Siders and G. O. Sitz, J. Chem. Phys. **101** (7), 6264 (1994); A. Modl, T. Gritsch, F. Budde, T. J. Chuang, and G. Ertl, Phys. Rev. Lett. **57** (3), 384 (1986).

[33] J. E. Smedley, G. C. Corey, and M. H. Alexander, J. Chem. Phys. **87** (5), 3218 (1987).

[34] E. W. Kuipers, M. G. Tenner, A. W. Kleyn, and S. Stolte, Phys. Rev. Lett. **62** (18), 2152 (1989); B. Berenbak, B. Riedmuller, S. Stolte, and A. W. Kleyn, Chem. Phys. **301** (2-3), 309 (2004).

[35] B. Berenbak, B. Riedmuller, C. T. Rettner, D. J. Auerback, S. Stolte, and A. W. Kleyn, Physchemcomm **16** (15), 1 (2001); T. F. Hanisco and A. C. Kummel, J. Chem. Phys. **99** (9), 7076 (1993).

[36] F. Frenkel, J. Hager, W. Krieger, H. Walther, G. Ertl, J. Segner, and W. Vielhaber, Chem. Phys. Lett. **90** (3), 225 (1982).

[37] H. Zacharias, M. M. T. Loy, and P. A. Roland, Phys. Rev. Lett. **49** (24), 1790 (1982); A. M. Wodtke, Y. H. Huang, and D. J. Auerbach, J. Chem. Phys. **118** (17), 8033 (2003).

[38] G. M. Nathanson, P. Davidovits, D. R. Worsnop, and C. E. Kolb, J. Phys. Chem. **100** (31), 13007 (1996).

[39] J. L. DeZwaan, S. M. Brastad, and G. M. Nathanson, J. Phys. Chem. C **112** (8), 3008 (2008).

[40] M. E. Saecker, S. T. Govoni, D. V. Kowalski, M. E. King, and G. M. Nathanson, Science **252** (5011), 1421 (1991); B. G. Perkins, T. Haber, and D. J. Nesbitt, J. Phys. Chem. B **109** (34), 16396 (2005).

[41] S. F. Shuler, G. M. Davis, and J. R. Morris, J. Chem. Phys. **116** (21), 9147 (2002).

[42] U. Tasic and D. Troya, Physical Chemistry Chem. Phys. **10** (37), 5776 (2008).

[43] B. G. Perkins and D. J. Nesbitt, J. Phys. Chem. B **112** (2), 507 (2008).

[44] D. J. Castro, S. M. Dragulin, M. Manning, and G. M. Nathanson, J. Chem. Phys. **125** (14) (2006).

[45] A. J. Kenyon, A. J. McCaffery, C. M. Quintella, and M. D. Zidan, J. Am. Chem. Soc. - Fraday Trans. **89** (21), 3877 (1993).

[46] A. Muis and J. R. Manson, J. Chem. Phys. **111** (2), 730 (1999).

[47] A. J. Kenyon, A. J. McCaffery, C. M. Quintella, and M. D. Zidan, Chem. Phys. Lett. **190** (1-2), 55 (1992).

[48] B. B. Alchagirov and A. G. Mozgovoi, High Temp. **43** (5), 791 (2005).

[49] W. Pierro and H. J. Castejon, Surf. Sci. **602** (22), 3515 (2008).

[50] M. J. Regan, E. H. Kawamoto, S. Lee, P. S. Pershan, N. Maskil, M. Deutsch, O. M. Magnussen, B. M. Ocko, and L. E. Berman, Phys. Rev. Lett. **75** (13), 2498 (1995).

[51] M. J. Regan, H. Tostmann, P. S. Pershan, O. M. Magnussen, E. DiMasi, B. M. Ocko, and M. Deutsch, Phys. Rev. B **55** (16), 10786 (1997).

[52] D. Schmeisser and K. Jacobi, Surf. Sci. **108** (2), 421 (1981).

[53] G. Scoles, *Atomic and Molecular Beam Methods*. (Oxford University Press, New York, 1988).

[54] M. Hillenkamp, S. Keinan, and U. Even, J. Chem. Phys. **118** (19), 8699 (2003).

[55] P. H. Paul, J. Quant. Spectrosc. Ra. **57** (5), 581 (1997).

[56] M. Ziemkiewicz, M. Wojcik, and D. J. Nesbitt, J. Chem. Phys. **123** (22) (2005); M. Ziemkiewicz and D. J. Nesbitt, J. Chem. Phys. **131** (5) (2009).

[57] J. Luque and D. R. Crosley, http://www.sri.com/psd/lifbase.

[58] J. M. Bowman and J. L. Gossage, Chem. Phys. Lett. **96** (4), 481 (1983).

[59] M. S. Zhao, D. S. Chekmarev, Z. H. Cai, and S. A. Rice, Phys. Rev. E **56** (6), 7033 (1997).

[60] X. W. Sha and B. Jackson, Surf. Sci. **496** (3), 318 (2002).

[61] N. Shenvi, S. Roy, and J. C. Tully, Science **326** (5954), 829 (2009).

62 C. A. Arrington, T. H. Dunning, and D. E. Woon, J. Phys. Chem. A **111** (44), 11185 (2007).

Chapter IX: Inelastic scattering of radicals at the gas-ionic liquid interface: Probing surface dynamics of BMIM-Cl, BMIM-BF_4, and BMIM-Tf_2N by rovibronic scattering of NO [$^2\Pi_{1/2}(0.5)$]

In review in *J. Phys. Chem. C*

9.1 Introduction

Room temperature ionic liquids (RTILs) are novel materials characterized by strong Coulombic interactions and high cation/anion densities and yet with melting points below 100 °C, a combination of properties which has led to a great deal of interest[1,2]. This contrasts with typical inorganic salts such as sodium chloride and sodium hydroxide whose much higher melting points (1074 K and 591 K respectively)[3] can limit the range of industrial applications for these species. Interestingly, however, even given such physical limitations, molten inorganic salts still prove useful in advanced power sources, due to three orders of magnitude higher electrical conductivity when compared to a conventional battery electrolyte material[4]. In particular, the resulting gains in peak power delivery and energy storage density have stimulated the development of specialized batteries for use in high temperature environments. Clearly, RTILs offer the potential of both simplifying and extending such high power energy storage devices down to the ambient temperature regime[5], which represents one of many exciting applications responsible for stimulating considerable research efforts into these novel liquids.

Early synthesis of room temperature molten salts[6] such as ethylammonium nitrate[1] was achieved as early as 1914. However, the first examples of this class of material suffered from instability due to atmospheric moisture, which severely limited their utility. Furthermore, these materials presented an additional challenge in that they often required a mixture of several

different types of ionic species[7]. For example, the system 1-ethylpyridinium Bromide mixed with aluminum chloride can take the form of an ionic liquid, but only inside a very specific window of molar stochiometry[1]. Both of these difficulties were overcome by the development of second generation ionic liquids based on a single anionic species coupled with a functionalized cationic imidazole ring with an alkyl chain. For example, 1-butyl-3-methylimidazolium$^+$ [$BMIM^+$] and bis(trifluoromethylsulfonyl) imide$^-$ [Tf_2N^-] represent a prototypical RTIL system which has been the focus of much experimental and theoretical interest. This material exhibits a melting temperature[8] of 271 K, a simple composition, resistance to breakdown by atmospheric water, and a low vapor pressure. All of these properties combine to make a very attractive ionic liquid material for a wide variety of applications.

In particular, the low vapor pressure brings up the possibility of using these liquids as "green solvents," i.e. reaction media which may be reused because they are left behind after products are removed by distillation[9]. This application is further enhanced by the inherent structural diversity[10] exhibited by RTIL's. Even for a single cationic moiety such as $BMIM^+$, an enormous range of different RTILs can be created simply by using different anionic partners such as Cl^-, BF_4^-, PF_6^-, and Tf_2N^-, to name a few. Additionally, systematic variation of the alkyl groups (R) on the methylimidazolium cation also yields new RTILs, which again permits important modification of the molten salt properties. The combination of just these two parameters in solvent design results in a substantial number of different possible species to explore. Furthermore, appropriate choice of the cation/anoin pair allows considerable freedom to modify solvent properties such as reagent/product solubility, catalyst solubility[11], and temperature operating range. Indeed, it has even been shown that the choice of anion with $BMIM^+$ can influence branching reaction pathways when several channels are available[12].

A further consequence of tunable solubility is the possibility of employing these materials in supported ionic liquid membranes for SO_2 and CO_2 sequestration during combustion reactions[13]. Again, the diversity of ionic liquid species allows for variation of the relative solubility for N_2, CH_4, CO_2, and SO_2, ideally chosen such that the latter two species are preferentially dissolved and removed from the combustion chamber. However, equilibrium solubility does not entirely determine the efficiency for gas phase sequestration by these liquid species. Indeed, the gas phase molecule must first be captured by the surface before passing through the interfacial region, a complex process which can be characterized by propensities very different from those which govern bulk dissolution. For example, when a solute molecule approaches the interface, there is some probability that it will inelastically scatter back into the gas phase and some probability that it will be transiently bound to the surface. In the latter case, there is a further rate process for a surface-trapped species to be absorbed into the bulk to become a fully solvated molecule. The magnitude and efficiency of these absorption events are presumably related to the time spent in the surface-trapped state, and in competition with processes ejecting the adsorbate back into the gas phase. As an important corollary, a predictive understanding of solvation dynamics for gas phase species will require detailed knowledge of both i) the structure of the ionic liquid interface as well as ii) the transient interaction of gas phase molecules at these surfaces under equilibrium and non-equilibrium collision conditions.

Theoretical molecular dynamics studies[14-16] have explored many issues concerning the surface structure of RTIL's. One particularly interesting aspect of these systems concerns the relative abundance of cations vs. anions in the interfacial region. Similar to studies on ions solvated in water and glycerol,[17] it has been shown that a range of subtle thermodynamic considerations can result in surface ion concentrations which are very different from those seen

in the bulk. Since the $BMIM^+$ ion consists of a hydrophobic alkane chain and a hydrophilic positively charged imidazole ring, one anticipates a marbled texture of the liquid and stratification at the surface, with layers of alkane chains separated by anion concentration surrounding the cationic ring. Increasing the length of the alkane chain is predicted to lead to a surface progressively more and more dominated by alkyl groups. Theoretical studies[15] on the surface structure of BMIM-Tf_2N suggest a further complexity in that a submonolayer region of cation-anion islands is expected to result in a low density interface compared to the more closely-packed structure below. The existence of such structure, which represents a break from the overall stratification into hydrophobic and hydrophilic layers, may have additional interesting effects on the chemical activity of adsorbate molecules at this interface.

Several different experimental techniques have also been employed to characterize the structure of the liquid-gas interface. For example, direct sampling of macroscopic surface properties can be obtained through Langmuir Blodget trough measurement of surface tension[18]. Angle-resolved x-ray photoelectron spectroscopy[19,20] (ARXPS), provides information about the atomic species which are preferentially represented in the top several monolayers. Surface sum frequency generation[21] (SFG) uses an infrared absorption followed by visible or UV anti-Stokes Raman scattering to probe for the presence of various vibrational modes in the interfacial region. When combined with polarization analysis, this technique can be used to observe the average alignment of various chemical bonds as well. There has been particular interest in understanding the relative concentration of various species on the surface, specifically i) the anion, ii) the imidazole cation ring, and iii) the alkane chain. It appears that for alkane chain lengths with fewer than 4 carbons, there is a tendency for all species to be present at the surface. As the chain length is increased past 4, on the other hand, the interface becomes increasingly dominated by

the alkyl group[22]. For this reason, BMIM-Tf_2N represents an interesting system balanced between two different physical regimes, making it a particularly attractive RTIL candidate for further detailed studies.

In addition to the optical and x-ray techniques discussed above, atomic and molecular scattering techniques provide sensitivity to chemical, as opposed to physical, aspects of surface structure, allowing another line of attack on addressing some of the issues raised above. One such method involves the use of reactive scattering[23] where, for example, the interfacial presence of various types of CH bonds are probed by reactions with $O(^3P)$ to make OH products[24] which can be state-selectively detected by laser induced fluorescence (LIF). Complimentary information has also been obtained by inelastic rather than reactive scattering. For example, jet-cooled CO_2 molecules have been scattered from a variety of RTIL species[25], whose state-to-state scattering probabilities provide exquisitely surface sensitive information reporting exclusively on composition of the topmost liquid monolayer. In the present study, we extend this method considerably in both detection sensitivity and internal degrees of freedom probed, specifically reporting on inelastic scattering of open shell NO radical species from a range of ionic liquid species shown in figure 9.1. Sensitive examination of rovibrational distributions in the scattered flux by laser induced fluorescence provides information about both surface roughness and the probability for transient adsorption at the interface. Of particular importance, the existence of low-lying spin orbit electronic states for such an open shell NO projectile offers novel insights into electronically inelastic and thus non-adiabatic collision dynamics at the gas-liquid interface.

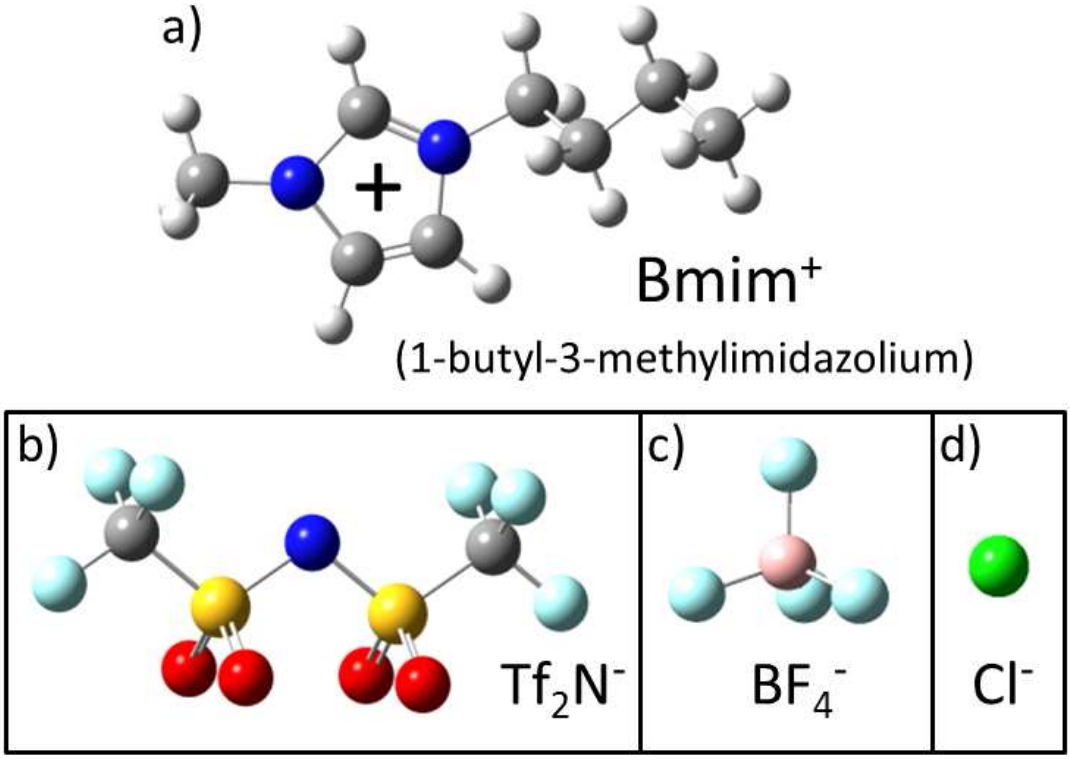

Figure 9.1 Room temperature ionic liquids (RTILs) used in this experiment. All consist of an organic cation (1-butyl-3-methylimidazolium) and one of three possible anionic species. In order of decreasing size, Bis(trifluormethanesulfonyl)imide (Tf_2N^-), BF_4^-, and chloride (Cl^-).

9.2 Experimental technique

Much of the experimental apparatus is similar to that previously described in some detail for collision studies on NO + molten gallium[26]. Hence, we present only a brief summary of the technique with emphasis on differences from the previous liquid metal experimental setup. Jet-cooled NO molecules from a skimmed supersonic expansion are allowed to collide at 45° with respect to the surface normal as shown in figure 9.2. Elastically and inelastically-scattered molecules are then detected at a 45° specular angle to obtain information on both the structure of the ionic liquid surface and the nature of the molecule-liquid interaction. Scattering events take

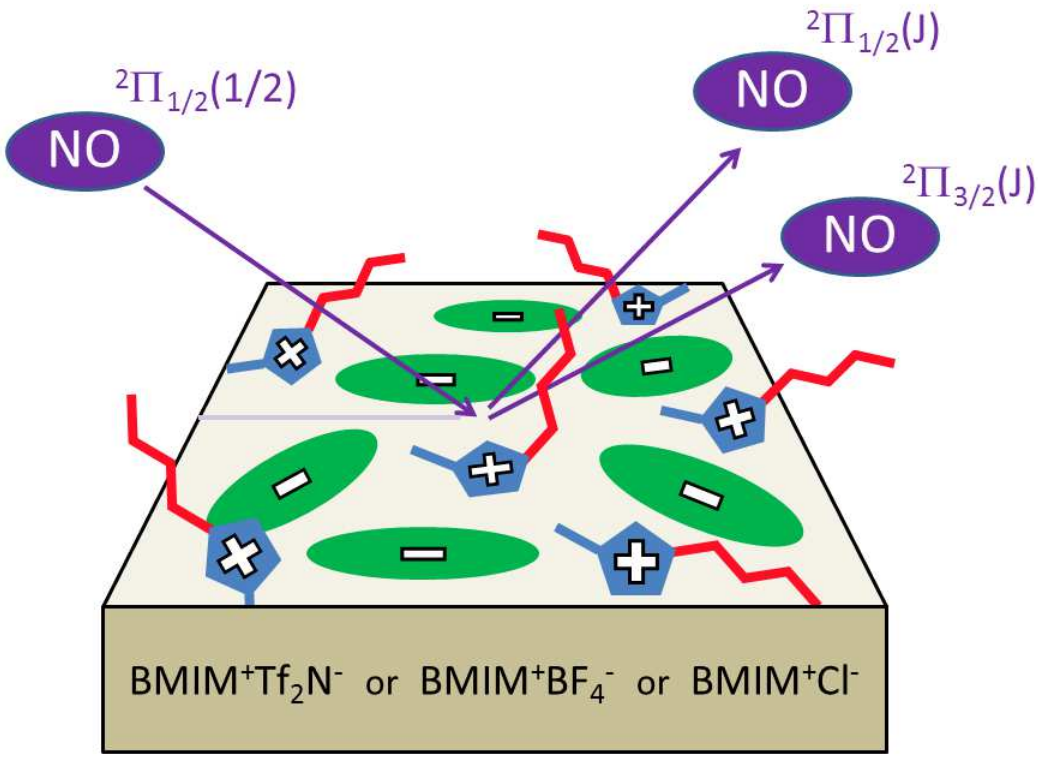

Figure 9.2 Experimental schematic. Jet-cooled NO molecules strike the liquid surface at 45° from the surface normal and detected at 45°. At typical beam temperatures ~ 1 K, the incident NO is overwhelmingly in the lowest rotational and spin-orbit ground state (with both lambda-doublet levels equally populated), thus permitting a nearly state-to-state description of the collision dynamics for this system. For a specific cation-anion pair, three chemically seperate entities may be present on the surface, i) the anion, ii) the cationic immidazolium ring and iii) its hydrophobic butyl side chain.

place in a cubical 96 L aluminum and steel chamber where a 1500 L/s turbomolecular pump maintains a base pressure ~ 1 x 10^{-8} torr. Ambient H_2O accounts for more than 90 % of this background gas as measured on a residual gas analyzer. However, H_2O at 10^{-8} Torr is expected to have no effect on interfacial properties, since the vast majority of any trapped H_2O is expected to reside in the bulk rather than near the surface layer[27]. This is supported by previous SFG

experiments, which have found that measurable surface reconfiguration requires ambient H_2O pressures near 10^{-4} Torr, i.e., well above the levels present in our experimental apparatus.

NO beams are introduced via a pulsed Even-Lavie supersonic valve[28] with 3000 Torr backing pressure, orifice diameter of 100 μm, and 40 μs pulse width. The resulting molecular beam is skimmed through a 3 mm orifice which is 5.3 cm downstream before travelling another 8.6 cm and colliding with the liquid surface. 1% NO is seeded in either H_2 or Ne-70 (30% He, 70% NO) buffer gas in order to achieve a collision energy of 20(6) kcal/mol or 2.7(9) kcal/mol respectively. These beams result in very efficient cooling of the NO to temperatures near or below 1 K, which results in the vast majority (> 99%) of molecules residing in their lowest two (λ-doublet) quantum states before impacting the surface. The incident NO molecules are in essentially a single rotational (N = 0) and spin-orbit state ($^2\Pi_{1/2}$), therefore offering insight into state-to-state collision processes. At such low temperatures, it is conceivable that clustering could be occurring in the beam, despite a low dimerization energy (~ 4 kcal/mol)[29] for clustering for this species. However, to eliminate this possibility, curves of growth (figure 9.3) as a function of stagnation pressure in the incident beam are obtained by adjusting the LIF experimental geometry so the incident NO is directly detected. Signal levels vary linearly with NO fractional concentration over nearly an order of magnitude change (0.25% to 2%), which supports negligible clustering under the 1% NO beam conditions employed in the reported studies. Figure 9.3 also shows an incident beam spectrum in which all significant peaks come from the two nearly degenerate e/f parity ground states associated with $^2\Pi_{1/2}(J=1/2)$.[30]

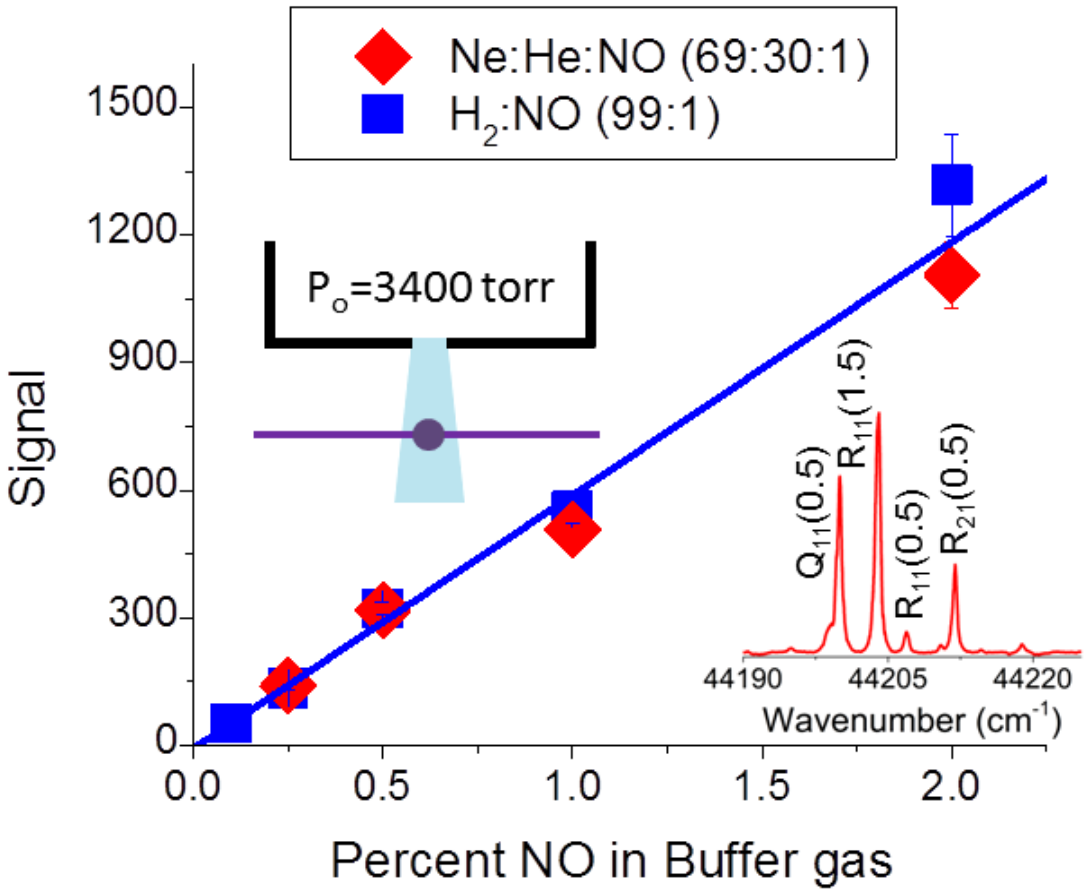

Figure 9.3 Curve of growth for NO in the incident beam as a function of fractional concentration in the stagnation region when reverse seeded in H_2 or a mixture of He and Ne. The linear growth with NO fraction indicates an absence of clustering in the jet. The inset shows a sample spectrum of the cooled molecular distribution, which is dominated by transitions originating from one of the two lowest states ($^2\Pi_{1/2}{}^e[J = ½]$, $^2\Pi_{1/2}{}^f[J = ½]$). Small peaks corresponding to one quantum of rotational excitation are used to measure beam temperature, which is typically on the order of 1 K.

The ionic liquid surface is held in a stainless steel crucible with dimensions of 4.4 cm × 2.4 cm × 0.5 cm, i.e., large compared with the 1 cm × 1.4 cm spot where the molecular beam strikes the surface. Furthermore, the crucible has *in vacuo* heating capabilities with which to

examine temperature-dependant properties of the RTIL sample. Indeed, elevated temperatures are particularly essential for BMIM-Cl, since this RTIL has a melting point near 340 K. Before placement in the crucible, dissolved gases are removed from each ionic liquid by stirring in a glass flask while pumping for several hours through a liquid nitrogen trap. The sample is held at 360 K to drive off dissolved H_2O. In the experimental vacuum chamber, the ionic liquids are characterized by vapor pressure < 10^{-8} torr as measured on a Bayard-Alpert ionization gauge, as expected from previous high precision measurements of vapor pressure for these species[31]. However, due to high latent heats of vaporization, RTILs exhibit a steep increase in vapor pressure with temperature.[32] This limits the experimental temperature range to approximately ΔT = 100 K for BMIM-Tf_2N and BMIM-BF_4 (varied from 293 to 400 K) while BMIM-Cl, which melts at 360 K, is only heated over a ΔT = 40 K range. In all cases, this range is well below the onset of thermal decomposition[7,31,33], as confirmed by the observation that heated RTIL vapor at these temperatures is dominated by single cation/anion pairs rather than organic fragments[34].

After colliding with the surface, inelastically-scattered NO products are state-selectively detected by laser induced fluorescence (LIF) on the γ-bands ($A^2\Sigma \leftarrow X^2\Pi_{1/2,3/2}$). Incident laser light is produced by frequency tripling the output of a dye laser operating with LDS 698. The resulting UV light is tuned from approximately 222 nm to 227 nm which covers both the ($v = 0 \leftarrow 0$) and ($v = 1 \leftarrow 1$) bands for this electronic transition. A series of apertures are used to select a region of uniform intensity from the UV output while minimizing the presence of diffracted photons in the chamber. This results in a 3 mm beam whose energy is kept below 5 μJ per pulse to avoid the saturating the LIF transition. Fluorescence is collected through a 5 cm diameter fused silica plano-convex lens which is mounted inside a stainless steel imaging tube invaginated into the chamber. This lens is O-ring sealed directly to the end of the imaging tube, so it

therefore serves both as a vacuum window as well as the first stage of a confocal imaging setup. A 4 mm segment of the cylindrical LIF region is then imaged through a circular mask onto a photomultiplier tube whose subsequent electronic signals are gated and recorded with an analog to digital converter. This confocal detection scheme limits the observation region to molecules scattered at the near specular angle (45°±10°). Though we are somewhat restricted in our normal cleaning procedures (e.g., Ar^+ sputtering) by chemical decomposition of the ionic liquid material, the RTIL surface is periodically scraped clean by a steel wire every 5 minutes over the course of a data scan. Further support for maintenance of sufficient RTIL surface cleanliness is found in the consistency of scattered NO quantum state distributions as a function of scan time and day.

9.3 Results

Figure **9.**4a displays a sample LIF spectrum taken for NO scattered from BMIM-Tf_2N at E_{inc} = 20(6) kcal/mol (H_2 carrier gas), where the surface temperature is 313 K and the incident beam characterized by a rotational temperature (T_{rot}) below 1 K. The large number of transitions indicates that substantial energy is transferred from incident translation to scattered rotational degrees of freedom. Measurable population is seen in states as high as J = 45, which corresponds to roughly 10 kcal/mol of rotational energy. Interestingly, this ability of the gas-RTIL interface to efficiently excite rotational states contrasts dramatically with the complete lack of vibrational excitation of NO(v=0), despite the fact that NO(v=1) corresponds to only ~ 6 kcal/mol. This result is similar to what was seen previously for NO scattering from molten gallium, and likely reflects a mismatch between the timescale for NO vibration and phonon modes in the liquid. The spin-orbit degree of freedom, on the other hand, is readily excited by gas-surface collisions, as evidenced by the appreciable spectral intensity in the $^2\Sigma(v=0) \leftarrow$

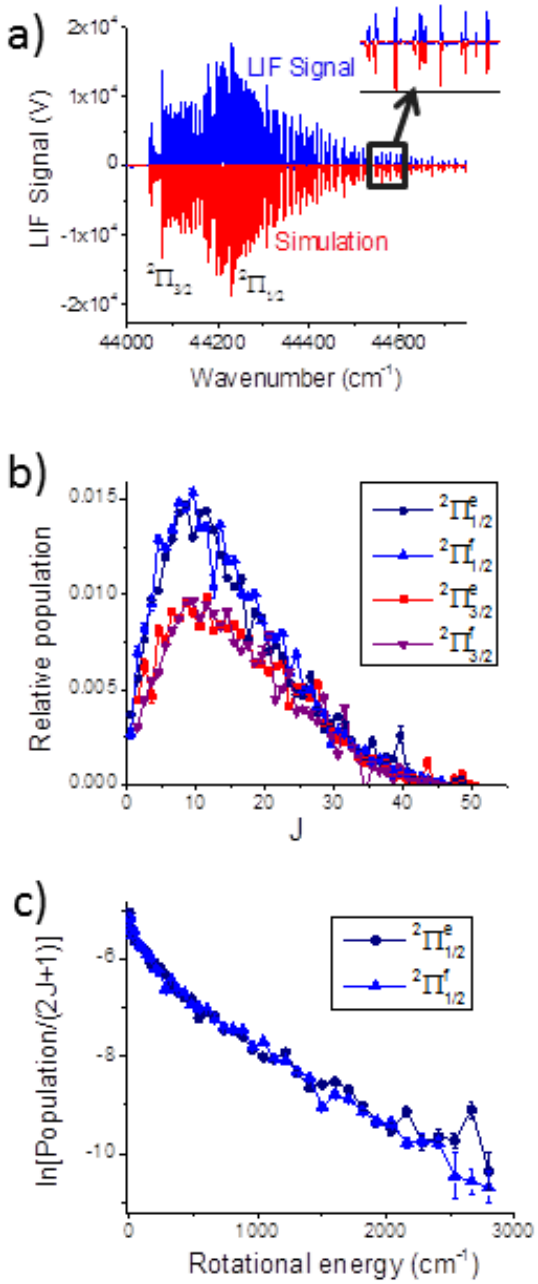

Figure 9.4 a) Sample LIF spectrum for NO scattered from BMIM-Tf_2N at 20 (6) kcal/mol and T_S = 313 K. Populations are extracted with a least squares fit (shown in red), with each state occupancy allowed to vary independantly. b) Sample fit results reveal a propensity to populate the electronically-excited $^2\Pi_{3/2}$ state, which requires a non-adiabatic mechanism for changing spin-orbit manifolds. c) A Boltzmann plot reveals substantial curvature, indicating the influence of both trapping desorption (TD) and direct impulsive scattering (IS) events at these higher collision energies.

$^2\Pi_{3/2}$(v=0) subband Indeed, since essentially all of the *incident* molecules are in the *ground spin orbit state* ($^2\Pi_{1/2}$), the existence of *electronically-excited products* ($^2\Pi_{3/2}$) in the scattered flux necessarily indicates the presence of *nonadiabatic dynamics* in the collision process.

With a laser linewidth of ≈ 0.4 cm^{-1}, the spectrum exhibits predominantly resolved rotational and electronic structure. Quantum state populations are extracted by least squares fitting[30] the spectra, adjusting populations of each NO spin orbit/lambda doublet (($^2\Pi^{e/f}_{1/2}$) and ($^2\Pi^{e/f}_{3/2}$)) and rotational level ($J \leq 50$).[35] Figure 9.4b shows the resulting quantum state population distributions. Despite some spectral congestion, the data nevertheless demonstrate a quite acceptably low degree of correlation in the least squares fit. Specifically, correlation is largely broken by the presence of multiple peaks arising from the same lower state in the fit, meaning that accidental overlap in one part of the spectrum can automatically be disentangled by stand-alone peaks elsewhere. Populations are tabulated according to total angular momentum (J), spin-orbit level (1/2 or 3/2), and λ-doubling state (e or f). For a given J and spin-orbit value, λ-doubling populations are experimentally found to be indistinguishable, which indicates a negligible correlation between NO i) end-over-end tumbling and ii) electronic angular momenta as the molecule recoils from the surface.[36] Rotational and spin-orbit populations, on the other hand, both show significant variation in population as a function of quantum state. This is readily apparent, for example, in the propensity to maintain the incident spin orbit state (i.e., $^2\Pi_{1/2}$) versus the lower probability of an electron spin flip event to yield $^2\Pi_{3/2}$ products.

Further insight into the rotational excitation dynamics can be obtained from Boltzmann plots of logarithmic populations scaled by 2J+1 degeneracy (i.e., Pop/(2J+1)) vs. the NO rotational energy. In this representation, a purely thermal distribution corresponds to a straight line with a slope of -1/kT, which has been unambiguously confirmed by analyzing the static

quantum state distributions for fully equilibrated 300 K NO at low pressure (1 x10^{-6} Torr). As can be seen in Fig. 4c, the scattered NO molecules (E_{inc} = 20(6) kcal/mol) are rather poorly characterized by a truly "thermal" distribution because the rotational levels do not form a straight line on the Boltzmann plot. However, for internal energies greater than 1000 cm^{-1}, a straight line is obtained, raising the possibility that the scattered populations may be treated as the sum of two components, at least one of which is thermal. This may be a consequence of multiple channels for scattering, leading to a low temperature distribution which is thermalized with the surface and a high temperature distribution which is not. Seeding NO in Ne-70 reduces the collision energy to 2.7(9) kcal/mol and gives a very different final rotational distribution (figure 9.5a). Instead of being multimodal, this Boltzmann plot forms a straight line whose temperature, in the case of spin-orbit-preserving collisions to make $^2\Pi_{1/2}$, is that of the surface and increases as the sample is heated. This picture is further confirmed by changing the liquid temperature and observing the proportional increase in scattered rotational temperature. Interestingly, the spin-orbit-changing collisions result in a slightly hotter rotational distribution even for these very low incident energies.

Because of the multistate nature of these distributions, it is often useful to report average rotational temperature divided by Boltzmann's constant (i.e., $T_{rot} \equiv \langle E_{rot} \rangle / k_B$) as a way of quickly comparing scattering distributions under different experimental conditions. Figures 9.6a and 9.6b show the results of such an analysis at a surface temperature of 353 K. At low collision energy, thermalization with the surface is observed for scattered NO molecules which maintain their incoming spin-orbit state throughout the course of the collision event. However, molecules scattered into the excited $^2\Pi_{3/2}$ levels appear to be slightly hotter than would be expected for full

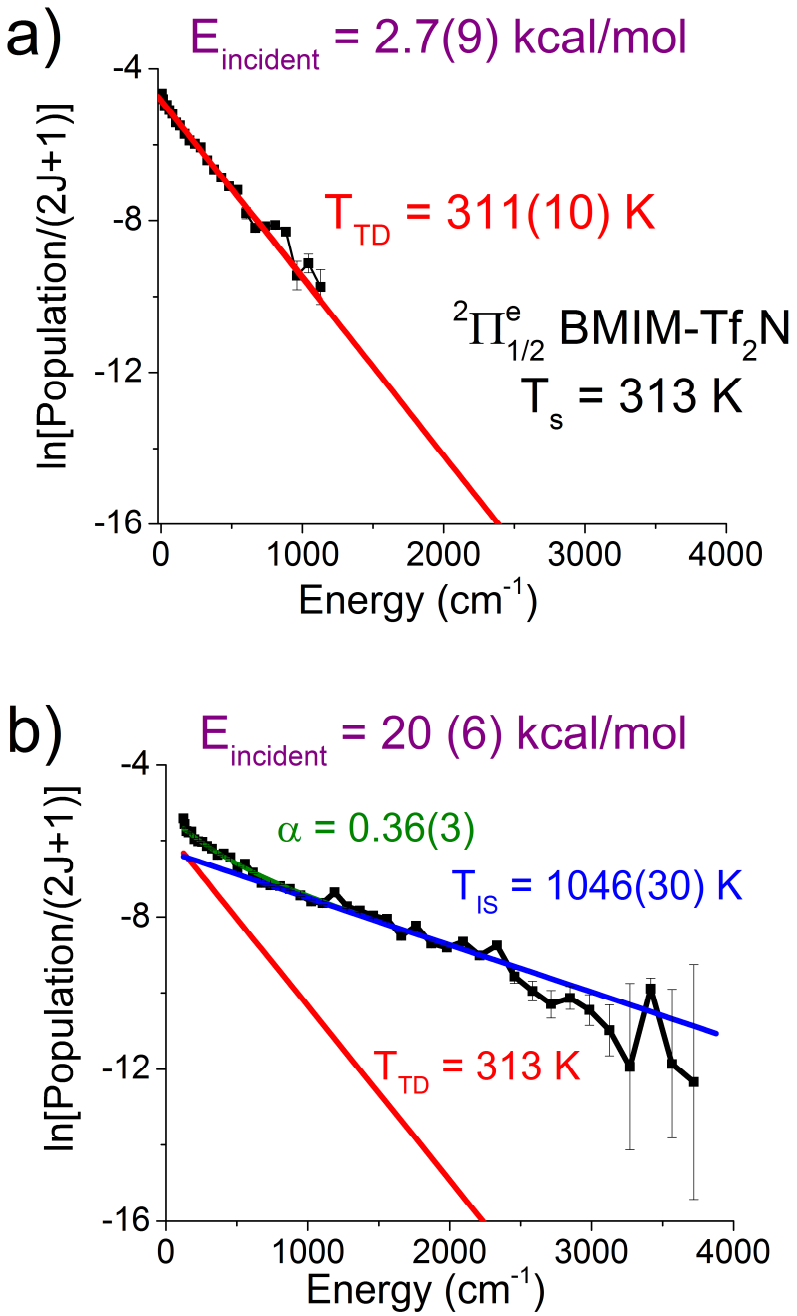

Figure 9.5 a) At a low collision energy of 2.7(9) kcal/mol and in the $^2\Pi_{1/2}{}^e$ manifold, the scattered distribution follows a straight line on a Boltzmann plot, indicating efficient thermalization with the surface. b) This suggests interpretation of the high energy (20(6) kcal/mol) data as two scattering distributions characterized by TD and IS temperatures. The lower component is fixed at the surface temperature (T_S) in accordance with a trapping desorption (TD) picture where a fraction α of the incident NO flux is thermally accomodated on the surface.

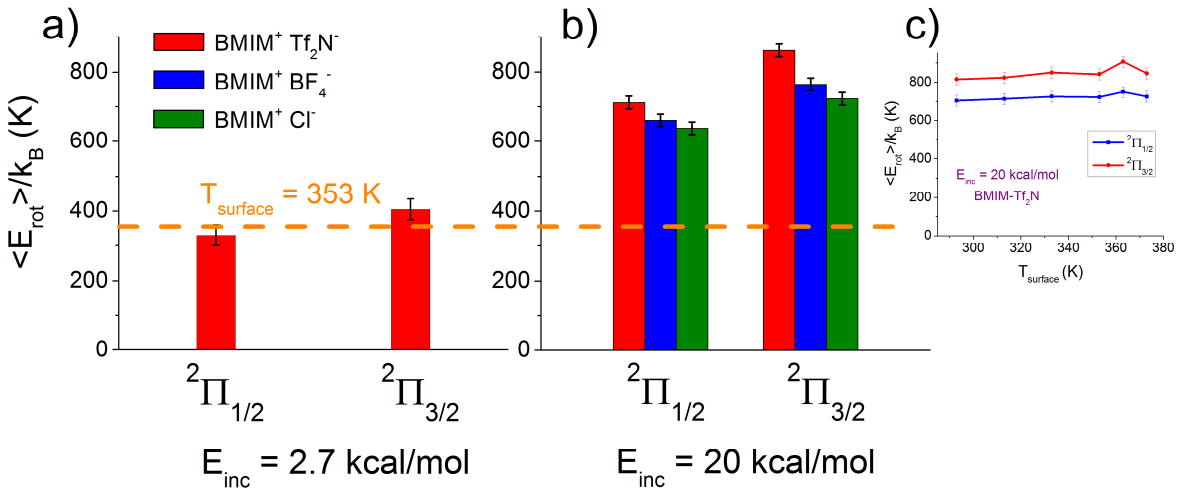

Figure 9.6 Sample average rotational energies scaled to k_B for each spin-orbit manifold. a) At low E_{inc} (2.7 kcal/mole), NO in the spin-orbit ground state ($^2\Pi_{1/2}$) appear fully accomodated to the surface temperature, with spin-orbit-changing collisions weakly correlated with increased rotational excitation. b) At high E_{inc} (20 kcal/mol), a clear trend is seen whereby rotational excitation decreases systematically with smaller anionic species, in addition to a positive correlation between electronic and rotational excitation. c) Furthermore, the scattered rotational excitation also at high E_{inc} is dominated by IS events and largely independent of T_S, a possible indication of scattering dynamics governed by intrinsic RTIL surface roughness.

thermalization with the BMIM-Tf_2N surface, which suggests the presence of two different dynamical channels leading to the two scattered spin-orbit states.

At the higher collision energy of 20(6) kcal/mol, the average rotational energy is now substantially warmed compared to the surface temperature, a consequence of the presence of a hot scattered component of the distribution. Again, the phenomenon of spin-orbit-flipping appears to be correlated with a higher degree of rotational excitation for each liquid surface under study. Additionally, a modest but clear trend is observed as the ionic liquid identity is varied. In general, increasing the size of the anion leads to an increase in degree of rotational excitation in the scattered NO. Over the 100 K temperature range accessible in this experiment, there is no measurable change in average rotational energy (figure 9.6c). In contrast, previous

experiments on NO scattering from liquid gallium did result in an *increase* in scattered rotational temperature, thought to be a result of thermal surface roughening by capillary waves. That the effect is not seen here may be related to the larger inherent roughness of these complicated surfaces, even at low surface temperature, but it is also certainly related to the much smaller temperature range available in these ionic liquid studies (100 K vs. 300 K).

In addition to examining the rotational degree of freedom, this LIF experiment also measures overall probabilities for non-adiabatic scattering into each of the two spin-orbit states available. For consistency, this probability is also reported as a temperature which describes the relative sum total population observed in each spin-orbit state.

$$\frac{[^2\Pi_{3/2}]}{[^2\Pi_{1/2}]} = e^{-\varepsilon_{SO}/k_B T_{elec}} \qquad \varepsilon_{SO} = 125\ cm^{-1} \tag{9.1}$$

For the purposes of the present analysis, the spin-orbit splitting is taken to be independent of rotational level J. While this represents an approximation at sufficiently high J, it works quite well in the Hund's case A limit appropriate for describing the majority of NO rotational levels studied here. Indeed, we can rigorously test this assumption with a low pressure static NO fill at 300 K; this yields a two point electronic "temperature" of $T_{elec} \approx 298(2)$ K and provides additional confirmation of our least squares fit methods for reporting spin orbit excited $^2\Pi_{3/2}$: $^2\Pi_{1/2}$ branching ratios.

Figure 9.7 summarizes the observed T_{elec} values over a range of temperatures and ionic liquid identities, which exhibits some rather striking trends. 1) First of all, there is clear evidence for *nonequilibrium dynamical behavior* in the scattered NO flux, specifically, with all T_{elec} values significantly *higher than* the RTIL surface temperature (T_S). This is most evident in the

RTIL with the bulkiest anion (i.e., BMIM-Tf_2N), which exhibits as much as a *2 fold larger* electronic vs surface temperature. This immediately indicates that whatever non-adiabatic process is responsible for spin orbit changing dynamics in the colliding NO can not simply be one equilibrating electronic and surface degrees of freedom. 2) Secondly, there is a strong dependence in T_{elec} to the *surface temperature itself*. In BMIM-Tf_2N, for example, there is a linear variation of ΔT_{elec} = 200K for a ΔT_S = 80K change in T_S (i.e., $\partial T_{elec}/ \partial T_S = 2.5$) with clear sensitivity to T_S for BMIM-BF_4 and BMIM-Cl as well. 3) Thirdly, and perhaps most remarkably, there is a clear dependence of the NO spin orbit excitation efficiency on the nature of the RTIL itself. Specifically, the RTIL with the "bulkiest" anion, Tf_2N^-, reveals the highest propensity for NO spin-orbit energy transfer for all surface temperatures, with a progressively reduced trend for RTILs such as BMIM-BF_4 and BMIM-Cl with smaller and more "compact" anion moieties. Though a more dynamical explanation of this spin orbit flip enhancement will clearly require further discussion (vide infra), this observation alone provides unambiguous confirmation for the presence of interfacial anions in RTILs, at least for imidazolium cation rings with relatively short alkyl chain lengths such as $BMIM^+$. Such a dependence on anion "footprint" is in excellent agreement with previous theoretical and experimental studies of CO2 scattering from a similar series of gas-RTIL interfaces.[25,37]

9.4 Discussion

As noted above, previous studies on these RTIL systems have been used to make inferences about the relative propensities of the various molecular components in the interfacial region. Due to the flexible nature of the alkyl chain, the $BMIM^+$ $Anion^-$ system can be conceptually deconstructed into three different entities: i) a positively charged imidazolium ring,

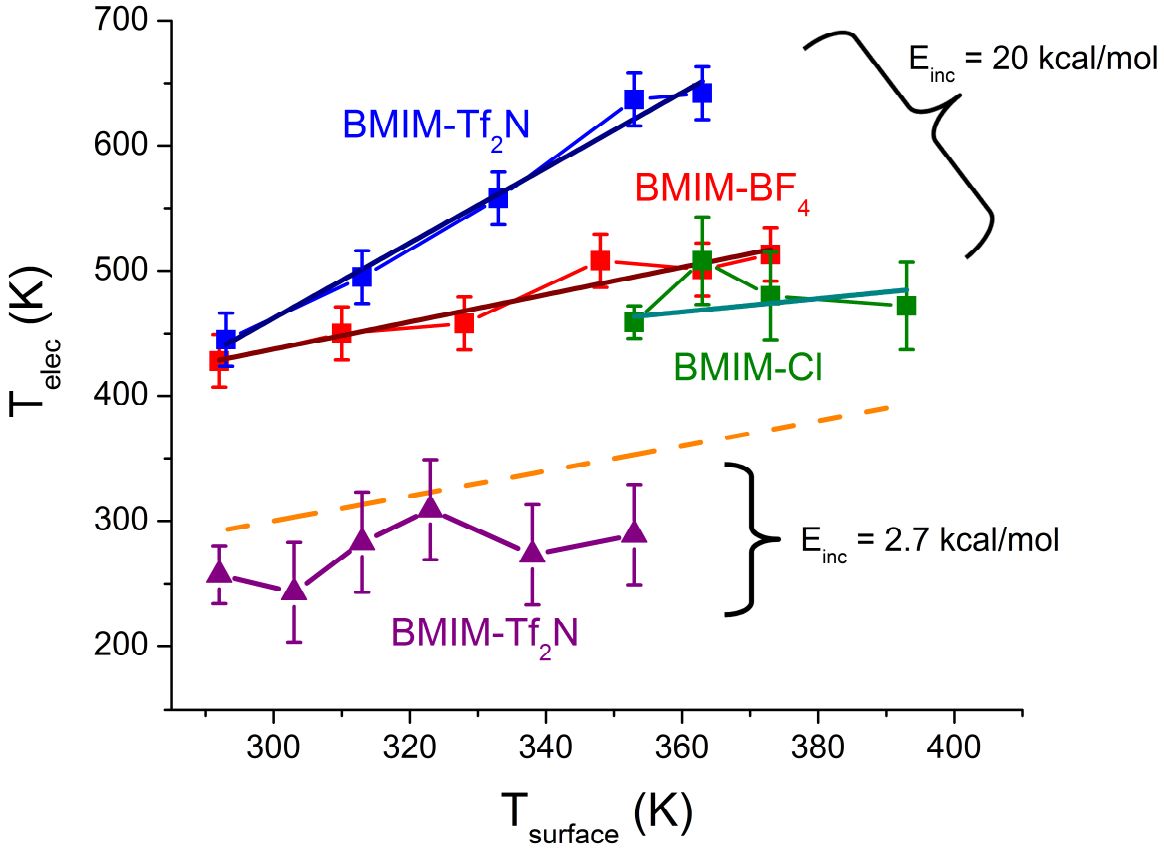

Figure 9.7 NO electronic temperatures, T_{elec}, computed from the populations in each spin-orbit manifold, which reveal a systematic increase with surface temperature as well as striking sensitivity to counteranion. Therefore, scattered NO electronic temperature appears to be a probe of surface structure in ionic liquids. For comparison, the electronic temperature is measured for scattering at 2.7 kcal/mol on BMIM-Tf_2N. This results in comparable surface and electronic temperatures, consistent with low speed collisions leading to thermalized trapping-desorption dynamics in the electronic degree of freedom.

ii) a hydrophobic butyl chain, and iii) a negatively charged anion. Much theoretical and experimental work has been focused on identifying the relative concentration of these species on the surface. Due to the atom-specific nature of angle resolved x-ray photoemission spectroscopy (ARXPS), studies using this method can be used to identify the presence of each RTIL component. In fact, such experiments have identified all three of these moieties in the near

surface region[20], in excellent agreement with theoretical predictions by Schatz and coworkers[16] and Voth and coworkers[15]. Unfortunately, the high energy electrons detected by ARXPS are capable of escaping from tens of monolayers below the surface, which reduces substantially the degree of specificity to the top most interfacial layer. While this problem can be mitigated by measuring differential changes in scattering direction at very wide angle detection geometries[38], there is still no guarantee that the atomic species observed are exclusively representative of the very top layer of liquid molecules. Similarly, recoil kinetic energy spectroscopy has been used to measure inelastic scattering of ~ 2 keV rare gas ions (Ar^+ and Ne^+) at the interface, which travel with enough speed to scatter impulsively from specific atoms on the surface. These studies also reveal scattered kinetic energy distributions characteristic of a nearly equivalent mix of cationic and anionic species at the surface[39], but again the depth of surface probed can not be rigorously confined to the topmost monolayer.

These issues were partially addressed through the use of sum frequency generation[40] (SFG) methods, which are surface sensitive by virtue of the fact that this nonlinear optical process can only occur in a non-centrosymmetric environment typical of the gas-liquid interface. This lack of centrosymmetry is indeed highly surface specific, over a depth to which the interface ceases to significantly influence local ordering of the liquid molecules. Specifically, SFG polarization studies by Rivero-Rubero and Baldelli on $BMIM^+$ with a variety of counteranions have been used to obtain information on alignment of the various species near the surface. These results have been interpreted as supporting a picture where the alkyl chain has a tendency to align parallel with the surface normal, pushing the CH_3 group out into the vacuum.[41] C-H stretches on the imidazole ring, on the other hand, were found to preferentially lie in the plane of the surface. This would imply an interfacial structure where the hydrophobic alkane

chain is expelled into the vacuum while the hydrophilic cation ring lies below accompanied by counter anions, and would possibly suggest that the surface of the liquid is dominated by alkane chains. Such a picture has also been forwarded in the interpretation of surface tension measurements by Law and Watson in these RTIL systems, which again suggest a tendency for cations to orient with alkyl chains pointing out into the vacuum while imidazole rings are submerged beneath the surface[18]. Additionally, these studies show a reduction in both surface excess entropy and energy with decreasing anion size, indicating disruption of the ordered alkyl chains pointing into the vacuum by surface anions.

The current results from NO + RTIL collisional scattering, which should be exclusively sensitive to composition of the very topmost layer of the liquid, strongly support and confirm the above expectations that anions are present at the surface. This is immediately clear from the fact that choice of RTIL counteranion has a strong and measurable effect on both the rotational and spin orbit electronic distributions of the scattered NO products. Furthermore, a clear trend is observed where larger and heavier anions lead to more efficient transformation of incident collision energy into rotational excitation of the scattered molecules. Such a result is consistent with the picture that anions occupy surface sites, possibly by displacement of alkane chain moieties. Indeed, in previous experiments on CO_2 scattering from liquid polymers such as squalane and perfluoroploy ether[42] the squalane system exhibits a relatively "soft" surface dominated by light, flexible hydrocarbon chains, compared to a somewhat "harder" surface in PFPE, dominated by more massive, stiff fluorocarbon chains. On the softer surfaces, more of the incident collision energy was found to flow into the liquid as heat, leaving less probability to redistribute the incident kinetic energy into translational and rotational degrees of freedom in the scattered molecule. A similar dynamic may be at work in the present studies on scattering NO

from ionic liquids. Specifically, NO scattering from "soft" flexibile alkane chains would be expected to yield a higher trapping desorption probability and thus lower internal levels of excitation. In contrast, however, stiffer and/or more massive groups at the gas-RTIL interface would permit more of the incident collision energy in the scattered flux. Since the anionic species are composed of heavier atoms with stiffer structures than the alkane chains, it would be reasonable to expect collisions with anions at the surface could lead to higher scattered internal excitation of the NO.

9.5 NO Rotational Excitation: Trapping Desorption and Impulsive Scattering

These simple expectations can be explored in greater detail by examination of the scattered NO rotational distributions. As a first example, we consider the NO distributions for scattering at low incident energy (E_{inc} = 2.7(9) kcal/mol, Fig. 5a). At these energies, the NO has the maximum time for interaction with the surface molecules, which would promote so called "trapping-desorption" (TD) events and thus thermal equilibration of NO at the liquid interface. Provided there is no quantum state dependence to the accommodation coefficient, simple detailed balance considerations rigorously predict that the quantum states desorbing from the liquid must remain in equilibrium with the surface temperature.[43] This is clearly supported by the spin orbit elastic scattered NO($^2\Pi_{1/2}$) distributions in Fig. 5a, which can be well characterized by a Boltzmann plot with the characteristic temperature (T_S = 313K) of the surface. It should be noted that these rotational distributions are quite different than those obtained for low energy collisions of NO from molten metals such as liquid Ga, where the scattered rotational temperatures were observed to be significantly *lower* than T_S. This behavior was interpreted as arising from "rotational cooling" on desorption, which from detailed balance principles implies

the presence of an anisotropic barrier that favors preferential "sticking" of the lower rotationally excited NO quantum states in the adsorption channel. One explanation of this much more straightforward behavior for NO is simply the absence of quantum state dependent sticking coefficients on RTIL surfaces, which in turn would result in no rotational cooling effects upon desorption.

The quantum state distributions at low energy contrast significantly with the high incident energy behavior for NO + BMIM-Tf_2N shown in Fig. 5b (E_{inc} = 20(6) kcal/mol). These Boltzmann plots now exhibit a clear *upward curvature*, inconsistent with Boltzmann predictions for a *single* rotational temperature. In light of the above discussion of trapping-desorption events, this lack of a single temperature description of the resulting flux is not at all surprising. For such high energy collisions, insufficient time exists for complete energy transfer/accommodation to/from the liquid interface to establish equilibrium behavior. In addition to a TD pathway, this gives rise to so-called "impulsive scattering" (IS) events, where the "memory" of the incident collision dynamics has not been fully obscured prior to ejection from the interface back into the vacuum. These rotational quantum state distributions have been found to be remarkably well characterized by an empirical *two-temperature* Boltzmann distribution (T_{TD} and T_{IS}), as represented by the red and blue lines in Fig. 5b. In such a least squares fit, large correlations exist between the branching ratio (α) and temperature (T_{TD}) of the thermalized flux component, particularly for conditions of low sticking coefficients, i.e., $\alpha << 1$. We therefore assume that TD events are well characterized by the surface temperature and constrain $T_{TD} = T_S$, as supported by analysis of the low energy scattering results shown above under conditions with $\alpha \approx 1$. Such fits yield $T_{IS} \approx 960(30)$ K, i.e. > 3-fold higher than the surface temperature and indicating a relatively facile conversion of incident energy into rotational excitation of the NO, as well as a rather low

fraction of thermal accommodation (α = 0.31(3)) with the liquid. Interestingly, high energy collisions of NO with BMIM-BF_4 and BMIM-Cl RTIL systems yield similarly hot IS rotational distributions, but with systematically increasing accommodation coefficient with decreasing anion bulk as shown in table I. This would be consistent with the trends both for i) the explicit presence of anions at the gas-RTIL interface as well as ii) decreased trapping-desorption and thermal accommodation for a more bulky anion collision partner such as Tf_2N^-.

RTIL	α	T_{high} *(K)*
$BMIM^+ Tf_2N^-$	0.22 (5)	1009(80)
$BMIM^+ BF_4^-$	0.32 (5)	1132(80)
$BMIM^+ Cl^-$	0.42 (5)	1021(80)

Table 9.1 Parameters derived from the two-temperature fits shown in figure 5b). T_{TD} is fixed at the surface temperature (353 K), and both T_{IS} and α are allowed to float in a least squares fit. T_{IS} does not vary appreciably from system to system, possibly due to a uniform surface roughness in all cases. On the other hand, α, the fraction thermalizing with the liquid, nearly doubles with reduction in anion size. This would be consistent, for example, with an increased surface "hardness" and collision mass for bulkier anions.

It is worth stressing that such a record of IS events does not represent a single dynamical pathway but instead clearly a broad continuum of possible outcomes, with no simple *a priori* expectations for the resulting distributions. It is therefore surprising that these IS populations can be so adequately fit to a Boltzmann distribution at a hyperthermal temperature. We have posited from trajectory calculations that this surprising and simplistic temperature-like T_{IS} behavior may arise from multiple scattering interactions at the gas-liquid interface, which could begin to reflect a more microcanonical sampling of the collision event. Indeed, we anticipate that at sufficient

level of detail and signal to noise, such a temperature-like description of the IS pathways certainly must fail. What is noteworthy and even remarkable is that this picture does not appear to fail easily, even for population of rotational states with > 50% of the incident collisional energy of the projectile.

Analysis of the IS scattering channel and accommodation coefficients for all three RTIL systems are summarized in Table I. The temperature characterizing the IS component appears to be relatively insensitive to choice of anion, but α, the probability for a scattering event to occur by surface trapping, decreases rapidly as the anion choice is varied. This result is again consistent with a picture where small anions give rise to a soft surface dominated by alkane chains while large anions are more likely to be represented in the top monolayer. This higher proportion of stiff, heavy anions could have the result of hardening the surface overall, leading to less probability for transferring sufficient incident energy to cause surface trapping. The insensitivity of T_{high} to choice of anion is a somewhat curious result, because one might expect a heavier anionic collision partner to also excite rotational excitation more efficiently. Such an effect could indeed be occurring at levels which are below the signal to noise limit of the present experiment, but it is nevertheless surprising that the temperature of this impulsively scattered channel is less sensitive than the branching into the channel itself.

9.6 NO Spin-Orbit Excitation: Possible Mechanism(s) for Facile Spin Flip Dynamics

We return to the intriguing behavior with respect to spin orbit electronic excitation of the open shell NO projectile. Preferential scattering from the ground spin orbit state NO($^2\Pi_{1/2}$) into either NO($^2\Pi_{1/2}$) or NO($^2\Pi_{3/2}$) spin-orbit levels is clearly quite sensitive to the surface structure, as nicely demonstrated in Fig. 7. Not only is there a noticeable dependence on anion type, but

surface heating also has a robustly systematic influence on branching into spin orbit electronic states. This dependence of the spin orbit excitation dynamics on choice of counteranion serves as another indication of the presence of negatively charged species at the top monolayer of the interface, since the length scale for molecule-surface electronic interactions is expected to be on the order of a few angstroms[44]. Spin-orbit flipping has been seen in collisions of NO with a Ag(111) surface[45], a result which was suggested to be due to partial charge transfer character in the NO-Ag wavefunction. Electron exchange between gas and condensed phases can lead to the nonadiabatic flipping of spin-orbit state, which is necessary for changing an incoming NO($^2\Pi_{1/2}$) into an outgoing NO($^2\Pi_{3/2}$) molecule. This picture is suggested by the work of Tully and coworkers[46] who invoke charge transfer dynamics in order to understand the significant role of nonadiabatic processes in the interactions of NO with Au(111).

Figure 9.8 provides a pictorial illustration of such a potential mechanism in which an electron is transferred from an anion site to the incident NO ($^2\Pi_{1/2}$) radical to form NO^- ($^3\Sigma^-$), a process which may be stabilized by binding of the newly formed anion to its image charge within the electrically conducting RTIL. As the NO molecule leaves the surface an electron jumps back, originating from either of the two possible directions of molecular rotation with respect to the electron spin projection along the internuclear axis. Therefore, this is a possible pathway for producing scattered NO in a different spin-orbit state than that which it possessed in the input channel. Since electron capture by NO is much more energetically favorable than electron donation, such charge transfer dynamics are expected to be more sensitive to interactions with the anion rather than with the cationic ring or the neutral alkane chain. The large increase in spin-orbit excitation with surface temperature may therefore be the result of increased anion representation on the surface as it is heated.

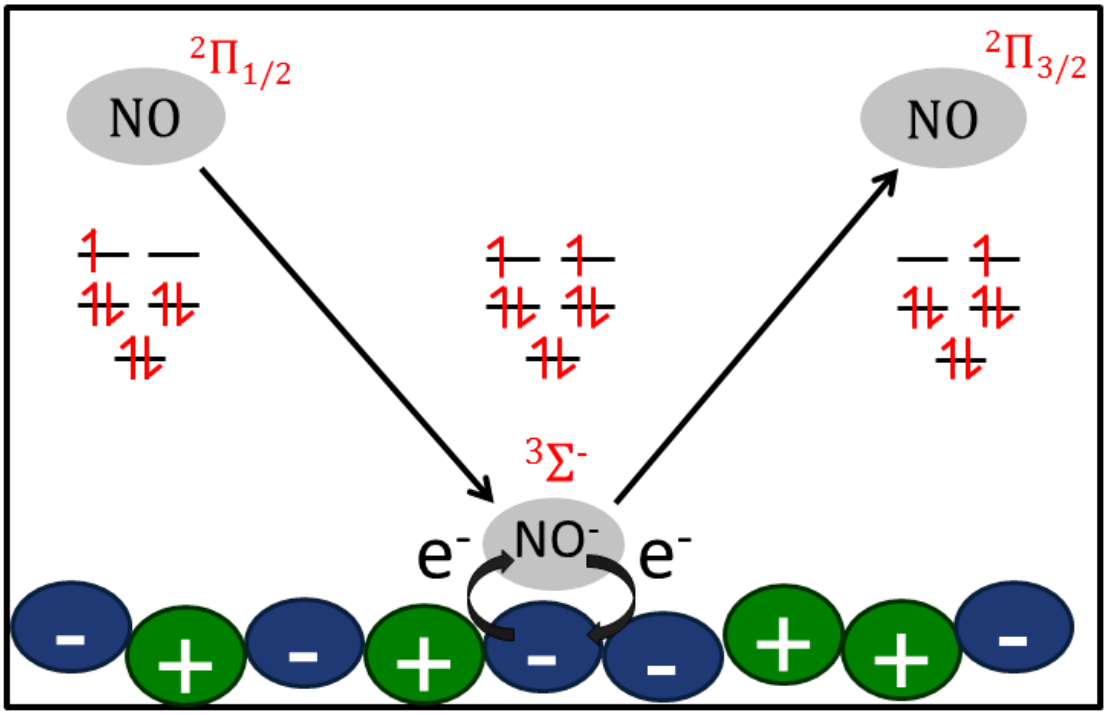

Figure 8 Possible spin-orbit-flipping mechanism for promoting electronic excitation in NO [$^2\Pi_{3/2}$]. Partial charge transfer character in the diatomic-surface wavefunction upon close approach will lead to some amplitude for surface anion electron transfer into the LUMO, resulting transiently in NO^- [$^3\Sigma^-$]. The electron hopping back to the donating anion as the NO recoils can leave the neutral species in either spin-orbit state. This could explain the sensitivity to both identity and coverage by surface anions.

If this picture is correct, one interpretation of the data would be that increased scattered NO electronic temperature is indicative of increased charge transfer character of the NO – surface electronic wavefunction upon close approach. Furthermore, in the case of ionic liquid surfaces, it is possible that this increased probability for charge transfer may be a consequence of increased anionic representation at the surface as, for example, surface temperature is increased. It is certainly plausible that, for example, a chloride anion with a gas phase ionization potential[3]

(i.e., Cl electron affinity) of 3.61 eV would be much more likely to give up an electron than the butyl chain whose ionization potential could be approximated by the gas phase IP of butane (10.53 eV). However, this picture becomes somewhat more complex when one considers the likely variation in adiabatic ionization energies as the anion is changed. BF_4^-, for example, is theoretically predicted[47] to have an IP near 6.75 eV, while for Tf_2N^-, to our knowledge, there is no experimental measurement nor theoretical prediction for the IP. Even though the chloride ion is the only species for which the IP can be thought of as being experimentally known, it is still likely that a good deal of variation exists in this value among these different species. It is interesting then that the physical size of the ion appears to have such a clear correlation with scattered NO electronic temperature while the anion IP may be anticorrelated or uncorrelated. This may be related to the well-demonstrated propensities for larger, more polarizable ions to preferentially reside at the surface in salty solutions[17], a phenonemon which could also be at work in the surface dynamics of the room temperature ionic liquids in the current study.

As a parting comment, the above is clearly only one of several putative possibilities for explaining such novel gas-liquid interfacial spin orbit excitation dynamics. For example, another plausible mechanism for facile flipping of the electron spin could invoke strong interactions between the unpaired Π orbital electron and the RTIL surface, which could uncouple the two lambda doublet levels by lifting the degeneracy of the $\Pi_{x,y}$ molecular orbitals and thus total energies for the free NO molecule. This would result in differential rates of phase change for the two newly non-degenerate levels, effectively quenching the electronic orbital angular momentum for approach with NO parallel to the surface. Therefore, as originally suggested by Alexander[48] to explain the high probability for spin-orbit flipping in NO + Ag(111) scattering, spin-orbit flipping propensities should be sensitive to the difference in energy between the two lowest

electronic surfaces for the NO + surface potential. However, these two physical pictures may not be entirely inconsistent; for example, Alexander suggests that charge transfer character for the electronic wavefunction may be responsible for the anisotropy splitting of the electronic wavefunction for NO + Ag. In any case, the purpose of this discussion is not to establish a definitive mechanism, but rather to present intriguing data for spin orbit propensities for NO + RTIL collisions and highlight the relevant issues for further investigation. For example, the reason for the positive correlation between spin-orbit and rotational excitation is at present unknown, although it could be related to similar effects seen on solid[45] and liquid[26] metal surfaces which has been previously ascribed to different binding wells for the two electronic species. Clearly more experimental and theoretical work will be necessary to establish a firm basis for interpreting the underlying spin orbit dynamics for such intriguing open shell collisions at the gas-room temperature ionic liquid interface.

9.7 Summary / Conclusions

Ground state NO molecules have been inelastically scattered from a series of room temperature ionic liquids at both high (20 kcal/mol) and low (2.7 kcal/mol) collision energies. Final average rotational energies are found to increase with the mass of the anion for several different liquids which all share the same cation: BMIM-Cl, BMIM-BF_4, and BMIM-Tf_2N. An increase in scattered collision energy with anion size serves as direct evidence for the presence of anionic species on the surface of these materials. Upon closer inspection, rotational distributions can be fit to a two temperature model in which the cooler component is thermalized with the surface, presumably due to transient adsorption followed by thermal ejection. While the temperature of the hotter component is rather insensitive to the specific ionic liquid examined,

the branching between the two channels depends strongly on this choice. Specifically, scattering into the hotter channel becomes less dominant as the size of the anion is decreased, possibly pointing to a greater representation of "soft" hydrocarbon chains in this case. This picture is further supported by examination of the scattered electronic (spin-orbit) degree of freedom, where, at elevated surface temperatures, the probability for spin-orbit-flipping also increases with anion size, again a possible indication of increased representation at the surface for larger anionic species. The mechanism for *nonadiabatic* spin-orbit-changing interactions is discussed in terms of a picture where partial charge transfer character may mediate a spin-orbit-flip event upon close approach of the NO molecule to the ionic liquid surface, particularly in the vicinity of an anion.

References for Chapter IX

1 N. V. Plechkova and K. R. Seddon, Chem. Soc. Rev. **37** (1), 123 (2008).

2 C. A. Angell, N. Byrne, and J. P. Belieres, Acc. Chem. Res. **40** (11), 1228 (2007); E. W. Castner, Jr., C. J. Margulis, M. Maroncelli, and J. F. Wishart, Annu. Rev. Phys. Chem. **62**, 85 (2011).

3 *CRC Handbook of Chemistry and Physics*, 92nd ed. (Chemical Rubber Company, Cleveland, 2011).

4 J. L. Sudworth, J. Power Sources **100** (1-2), 149 (2001).

5 E. Frackowiak, G. Lota, and J. Pernak, Appl. Phys. Lett. **86** (16), 164104/1 (2005).

6 J. S. Wilkes, Green Chem. **4** (2), 73 (2002).

7 M. Freemantle, Chem. Eng. News **76** (13), 32 (1998).

8 C. P. Fredlake, J. M. Crosthwaite, D. G. Hert, S. N. V. K. Aki, and J. F. Brennecke, J. Chem. Eng. Data **49** (4), 954 (2004).

9 M. J. Earle, J. M. S. S. Esperanca, M. A. Gilea, J. N. C. Lopes, L. P. N. Rebelo, J. W. Magee, K. R. Seddon, and J. A. Widegren, Nature **439** (7078), 831 (2006).

[10] P. Wasserscheid and W. Keim, Angew. Chem., Int. Ed. **39** (21), 3772 (2000).

[11] N. Jain, A. Kumar, and S. M. S. Chauhan, Tetrahedron Lett. **46** (15), 2599 (2005).

[12] M. J. Earle, S. P. Katdare, and K. R. Seddon, Org. Lett. **6** (5), 707 (2004).

[13] Y.-Y. Jiang, Z. Zhou, Z. Jiao, L. Li, Y.-T. Wu, and Z.-B. Zhang, J. Phys. Chem. B **111** (19), 5058 (2007); J. E. Bara, T. K. Carlisle, C. J. Gabriel, D. Camper, A. Finotello, D. L. Gin, and R. D. Noble, Ind. Eng. Chem. Res. **48** (6), 2739 (2009).

[14] Y. Wang and G. A. Voth, J. Am. Chem. Soc. **127** (35), 12192 (2005).

[15] T. Yan, S. Li, W. Jiang, X. Gao, B. Xiang, and G. A. Voth, J. Phys. Chem. B **110** (4), 1800 (2006).

[16] S. Yockel and G. C. Schatz, J. Phys. Chem. B **114** (45), 14241 (2010).

[17] J. L. DeZwaan, S. M. Brastad, and G. M. Nathanson, J. Phys. Chem. C **112** (8), 3008 (2008).

[18] G. Law and P. R. Watson, Langmuir **17** (20), 6138 (2001).

[19] V. Lockett, R. Sedev, C. Bassell, and J. Ralston, Phys. Chem. Chem. Phys. **10** (9), 1330 (2008).

[20] C. Kolbeck, T. Cremer, K. R. J. Lovelock, N. Paape, P. S. Schulz, P. Wasserscheid, F. Maier, and H. P. Steinrueck, J. Phys. Chem. B **113** (25), 8682 (2009).

[21] S. Baldelli, J. Phys. Chem. B **107** (25), 6148 (2003).

[22] T. Iimori, T. Iwahashi, K. Kanai, K. Seki, J. Sung, D. Kim, H.-O. Hamaguchi, and Y. Ouchi, J. Phys. Chem. B **111** (18), 4860 (2007).

[23] D. J. Garton, T. K. Minton, M. Alagia, N. Balucani, P. Casavecchia, and V. G. Gualberto, Faraday Discuss. **108** (Dynamics of Electronically Excited States in Gaseous, Cluster and Condensed Media, 1997), 387 (1998).

[24] C. Waring, P. A. J. Bagot, J. M. Slattery, M. L. Costen, and K. G. McKendrick, J. Phys. Chem. A **114** (14), 4896 (2009).

[25] J. R. Roscioli and D. J. Nesbitt, J. Phys. Chem. Lett. **1** (4), 674 (2010).

[26] M. P. Ziemkiewicz, J. R. Roscioli, and D. J. Nesbitt, J. Chem. Phys. **134** (23), 234703/1 (2011).

[27] K. R. J. Lovelock, E. F. Smith, A. Deyko, I. J. Villar-Garcia, P. Licence, and R. G. Jones, Chem. Comm. **46**, 4866 (2007).

[28] U. Even, J. Jortner, D. Noy, N. Lavie, and C. Cossart-Magos, J. Chem. Phys. **112** (18), 8068 (2000).

[29] S. G. Kukolich, J. Am. Chem. Soc. **104** (17), 4715 (1982).

[30] J. R. Donaldson and P. V. Tryon, User's Guide to STARPAC (U. S. Department of Commerce, Center for Computing and Applied Mathematics, Gaithersburg, 1990).

[31] J. M. S. S. Esperanca, L. J. N. Canongia, M. Tariq, L. M. N. B. F. Santos, J. W. Magee, and L. P. N. Rebelo, J. Chem. Eng. Data **55** (1), 3 (2010).

[32] M. Bier and S. Dietrich, arXiv.org, e-Print Arch., Condens. Matter, 1 (2010).

[33] L. P. N. Rebelo, J. N. C. Lopes, J. M. S. S. Esperanca, and E. Filipe, J. Phys. Chem. B **109** (13), 6040 (2005).

[34] R. Ludwig and U. Kragl, Angew. Chem., Int. Ed. **46** (35), 6582 (2007); J. P. Armstrong, C. Hurst, R. G. Jones, P. Licence, K. R. J. Lovelock, C. J. Satterley, and I. J. Villar-Garcia, Phys. Chem. Chem. Phys. **9** (8), 982 (2007).

[35] M. Ziemkiewicz and D. J. Nesbitt, J. Chem. Phys. **131** (5) (2009).

[36] P. Andresen, G. S. Ondrey, B. Titze, and E. W. Rothe, The J. Chem. Phys. **80** (6), 2548 (1984).

[37] J. R. Roscioli and D. J. Nesbitt, The J. Phys. Chem. A **115** (34), 9764.

[38] K. R. J. Lovelock, C. Kolbeck, T. Cremer, N. Paape, P. S. Schulz, P. Wasserscheid, F. Maier, and H. P. Steinrueck, J. Phys. Chem. B **113** (9), 2854 (2009).

[39] T. J. Gannon, G. Law, P. R. Watson, A. J. Carmichael, and K. R. Seddon, Langmuir **15** (24), 8429 (1999).

[40] S. Rivera-Rubero and S. Baldelli, J. Am. Chem. Soc. **126** (38), 11788 (2004).

[41] S. Rivera-Rubero and S. Baldelli, J. Phys. Chem. B **110** (10), 4756 (2006).

[42] B. G. Perkins, T. Haber, and D. J. Nesbitt, J. Phys. Chem. B **109** (34), 16396 (2005); B. G. Perkins and D. J. Nesbitt, J. Phys. Chem. B **112** (2), 507 (2008).

[43] J. I. Steinfeld, J. S. Francisco, and W. L. Hase, *Chemical Kinetics and Dynamics*, 2nd ed. (Prentice-Hall, Inc., Upper Saddle River, 1999).

[44] E. A. Gislason and J. G. Sachs, J. Chem. Phys. **62** (7), 2678 (1975).

[45] G. D. Kubiak, J. E. Hurst, H. G. Rennagel, G. M. McClelland, and R. N. Zare, J. Chem. Phys. **79** (10), 5163 (1983).

[46] N. Shenvi, S. Roy, P. Parandekar, and J. Tully, J. Chem. Phys. **125** (15) (2006); N. Shenvi, S. Roy, and J. C. Tully, Science **326** (5954), 829 (2009).

[47] G. L. Gutsev, P. Jena, and R. J. Bartlett, Chem. Phys. Lett. **292** (3), 289 (1998).

[48] M. H. Alexander, J. Chem. Phys. **80** (7), 3485 (1984).

Bibliography

CRC Handbook of Chemistry and Physics, 2011).

Alchagirov, B. B. and A. G. Mozgovoi, High Temp. **43**, 791 (2005).

Alexander, M. H., J. Chem. Phys. **80**, 3485 (1984).

Anderson, D. T., et al., Chem. Phys. **239**, 253 (1998).

Andresen, P., et al., J. Chem. Phys. **80**, 2548 (1984).

Angell, C. A., et al., Acc. Chem. Res. **40**, 1228 (2007).

Aoiz, F. J., et al., J. Chem. Phys. **119**, 5860 (2003).

Armstrong, J. P., et al., Phys. Chem. Chem. Phys. **9**, 982 (2007).

Arrington, C. A., et al., J. Phys. Chem. A **111**, 11185 (2007).

Backus, E. H. G., et al., J. Phys. Chem. B **111**, 6141 (2007).

Bagot, P. A. J., et al., J. Phys. Chem. C **112**, 10868 (2008).

Baldelli, S., J. Phys. Chem. B **107**, 6148 (2003).

Bara, J. E., et al., Ind. Eng. Chem. Res. **48**, 2739 (2009).

Belpassi, L., et al., J. Am. Chem. Soc. **132**, 13046 (2010).

Berenbak, B., et al., Surf. Sci. **414**, 271 (1998).

Berenbak, B., et al., Physchemcomm **16**, 1 (2001).

Berenbak, B., et al., Chem. Phys. **301**, 309 (2004).

Berry, M. T., et al., Chem. Phys. Lett. **153**, 17 (1988).

Beswick, J. A. and J. Jortner, Chem. Phys. Lett. **49**, 13 (1977).

Bier, M. and S. Dietrich, Mol. Phys. **108**, 211 (2010).

Bisson, R., et al., J. Phys. Chem. A **111**, 12679 (2007).

Borg, H. J., et al., J. Chem. Phys. **101**, 10052 (1994).

Bowman, J. M. and J. L. Gossage, Chem. Phys. Lett. **96**, 481 (1983).

Braatz, J. A. and N. A. Gugliucci, Astrophys. J. **678**, 96 (2008).

Brand, J., et al., Astron. Astrophys. Suppl. Ser. **103**, 541 (1994).

Buch, V., J. Chem. Phys. **97**, 726 (1992).

Buch, V. and J. P. Devlin, J. Chem. Phys. **94**, 4091 (1991).

Candel, S., Proc. Comb. Inst. **29**, 1 (2002).

Casassa, M. P., et al., Faraday Discuss. Chem. Soc. **82**, 251 (1986).

Casassa, M. P., et al., J. Chem. Phys. **89**, 1966 (1988).

Castner, E. W., Jr., et al., Annu. Rev. Phys. Chem. **62**, 85 (2011).

Castro, D. J., et al., J. Chem. Phys. **125** (2006).

Cazaux, S. M., et al., Proc. IAU **1**, 325 (2005).

Cencek, W., et al., Phys. Chem. Chem. Phys. **10**, 4716 (2008).

Chakravarty, C., et al., J. Chem. Phys. **93**, 3367 (1990).

Chehrouri, M., et al., Phys. Chem. Chem. Phys. **13**, 2172 (2011).

Child, M. S., Acc. Chem. Res. **18**, 45 (1985).

Clyne, M. A. A., et al., J. Mol. Spec. **46**, 146 (1973).

Cohen, R. C. and R. J. Saykally, J. Chem. Phys. **98**, 6007 (1993).

Cohen, S. R., et al., Chem. Phys. Lett. **152**, 269 (1988).

Crim, F. F., Proc. Nat. Acad. Sci USA **105**, 12654 (2008).

D. Schmeisser, K. J., D. M. Kolb, Le Vide-Les Couches Minces (Suppl.) **201**, 256 (1980).

DeZwaan, J. L., et al., J. Phys. Chem. C **112**, 3008 (2008).

Dick, M. J., et al., Phys. Rev. A **81**, 022706 (2010).

Donaldson, J. R. and P. V. Tryon, edited by Technology, N. I. o. S. a. (U. S. Department of Commerce, Center for Computing and Applied Mamatics, 1990), Vol. Internal Report NBSIR 86-3448.

Dulieu, F., et al., Astron. Astrophys. **512** (2010).

Earle, M. J., et al., Nature **439**, 831 (2006).

Earle, M. J., et al., Org. Lett. **6**, 707 (2004).

Esperanca, J. M. S. S., et al., J. Chem. Eng. Data **55**, 3 (2010).

Even, U., et al., J. Chem. Phys. **112**, 8068 (2000).

Fernley, J. A., et al., J. Mol. Spec. **150**, 597 (1991).

Feyereisen, M. W., et al., J. Phys. Chem. **100**, 2993 (1996).

Field, D., Astron. Astrophys. **362**, 774 (2000).

Fink, U., et al., J. Mol. Spec. **18**, 384 (1965).

Frackowiak, E., et al., Appl. Phys. Lett. **86**, 164104/1 (2005).

Fredlake, C. P., et al., J. Chem. Eng. Data **49**, 954 (2004).

Freemantle, M., Chem. Eng. News **76**, 32 (1998).

Frenkel, F., et al., Chem. Phys. Lett. **90**, 225 (1982).

Gannon, T. J., et al., Langmuir **15**, 8429 (1999).

Garton, D. J., et al., Faraday Discuss. **108**, 387 (1998).

Geltenbort, P., et al., Tech. Phys. Lett. **35**, 700 (2009).

Gergen, B., et al., Science **294**, 2521 (2001).

Gislason, E. A. and J. G. Sachs, J. Chem. Phys. **62**, 2678 (1975).

Grimmelmann, E. K., et al., J. Chem. Phys. **72**, 1039 (1980).

Gutsev, G. L., et al., Chem. Phys. Lett. **292**, 289 (1998).

Haar, L., et al., *NBS/NRC Steam Tables* (Hemisphere Pub. Corp., Washington, D.C., 1984).

Habart, E., et al., Astron. Astrophys. **414**, 531 (2004).

Hanisco, T. F. and A. C. Kummel, J. Chem. Phys. **99**, 7076 (1993).

Hanisco, T. F., et al., J. Chem. Phys. **97**, 1484 (1992).

Hanslmeier, A., *Water in Universe* (Springer, 2011).

Hayden, J. S. and G. J. Diebold, J. Chem. Phys. **77**, 4767 (1982).

Hellman, A., et al., Phys. Rev. B **71** (2005).

Hillenkamp, M., et al., J. Chem. Phys. **118**, 8699 (2003).

Hines, M. A. and R. N. Zare, J. Chem. Phys. **98**, 9134 (1993).

Hodges, M. P., et al., J. Chem. Phys. **117**, 7169 (2002).

Hornek, et al., Proc. IAU **1**, 337 (2005).

Hornekaer, L., et al., Science **302**, 1943 (2003).

Hornekaer, L., et al., J. Chem. Phys. **122**, 124701 (2005).

Huang, Y. H., et al., Science **290**, 111 (2000).

Humphreys, E. M. L., Proc. IAU **3**, 471 (2007).

Humphreys, E. M. L., et al., Astrophys. J. Letters **634**, L133 (2005).

Huneycutt, A. J., et al., J. Chem. Phys. **118**, 1221 (2003).

Iimori, T., et al., J. Phys. Chem. B **111**, 4860 (2007).

Jacobs, D. C., et al., J. Chem. Phys. **91**, 3182 (1989).

Jain, N., et al., Tetrahedron Lett. **46**, 2599 (2005).

Jiang, Y.-Y., et al., J. Phys. Chem. B **111**, 5058 (2007).

Juaristi, J. I., et al., Phys. Rev. Lett. **100** (2008).

Jucks, K. W. and R. E. Miller, J. Chem. Phys. **87**, 5629 (1987).

Kenyon, A. J., et al., J. Chem. Soc. Faraday Trans. **89**, 3877 (1993).

Kimman, J., et al., Phys. Rev. Lett. **57**, 2053 (1986).

Kisiel, Z., et al., J. Phys. Chem. A **104**, 6970 (2000).

Kleyn, A. W., et al., Phys. Rev. Lett. **47**, 1169 (1981).

Kohn, A., et al., Chem-Eur. J. **11**, 5575 (2005).

Kolbeck, C., et al., J. Phys. Chem. B **113**, 8682 (2009).

Kolodney, E., et al., Chem. Phys. Lett. **145**, 177 (1988).

Komrowski, A. J., et al., J. Chem. Phys. **117**, 8185 (2002).

Kondo, T., et al., J. Chem. Phys. **122** (2005).

Krix, D., et al., Phys. Rev. B **75** (2007).

Kubiak, G. D., et al., J. Chem. Phys. **79**, 5163 (1983).

Kuipers, E. W., et al., Phys. Rev. Lett. **62**, 2152 (1989).

Kukolich, S. G., J. Am. Chem. Soc. **104**, 4715 (1982).

Kwok, S., *Physics and Chemistry of Interstellar Medium* (University Science Books, 2007).

Law, G. and P. R. Watson, Langmuir **17**, 6138 (2001).

Levchenko, S. V., et al., J Chem Phys **125**, 084301 (2006).

Lockett, V., et al., Phys. Chem. Chem. Phys. **10**, 1330 (2008).

Logan, R. M. and R. E. Stickney, J. Chem. Phys. **44**, 195 (1966).

Lovelock, K. R. J., et al., Chemphyschem **10**, 337 (2009).

Lovelock, K. R. J., et al., Phys Chem Chem Phys **12**, 8893 (2010).

Lovelock, K. R. J., et al., J. Phys. Chem. B **113**, 2854 (2009).

Lovelock, K. R. J., et al., Chem. Commun. (Cambridge, U. K.), 4866 (2007).

Ludwig, R. and U. Kragl, Angew. Chem., Int. Ed. **46**, 6582 (2007).

Luntz, A. C., et al., J. Chem. Phys. **76**, 737 (1982).

Luque, J. and D. R. Crosley, http://www.sri.com/psd/lifbase.

Lykke, K. R. and B. D. Kay, J. Chem. Phys. **90**, 7602 (1989).

Manning, M., et al., J. Chem. Phys. **119**, 12593 (2003).

Martin, H. and A. B. Edwin, Astrophys. J. Lett. **565**, L105 (2002).

McKellar, A. R. W., Faraday Discuss. **73**, 89 (1982).

Menten, K. M., et al., Astron. Astrophys. **477**, 185 (2008).

Menten, K. M., et al., Astrophys. J. **363**, L27 (1990).

Miller, S. M., et al., Mol. Phys. **83**, 405 (1994).

Modl, A., et al., Phys. Rev. Lett. **57**, 384 (1986).

Modl, A., et al., J. Chem. Phys. **83**, 4800 (1985).

Morgan, J. A. and G. M. Nathanson, J. Chem. Phys. **114**, 1958 (2001).

Muis, A. and J. R. Manson, J. Chem. Phys. **111**, 730 (1999).

Naoki Watanabe and Yuki Kimura and Akira Kouchi and Takeshi Chigai and Tetsuya Hama and Valerio, P., Astrophys. J. Letters **714**, L233 (2010).

Nathanson, G. M., et al., J. Phys. Chem. **100**, 13007 (1996).

Neufeld, D. A., et al., Astrophys. J. Suppl. Ser. **100**, 132 (1995).

Nizkorodov, S. A., et al., J. Chem. Phys. **119**, 10158 (2003).

Nizkorodov, S. A., et al., J. Chem. Phys. **122**, 194316 (2005).

Patkowski, K., et al., Mol. Phys. **103**, 2031 (2005).

Paul, P. H., J. Qaunt. Spectrosc. Ra. **57**, 581 (1997).

Perkins, B. G., et al., J. Phys. Chem. B **109**, 16396 (2005).

Perkins, B. G. and D. J. Nesbitt, J. Phys. Chem. B **110**, 17126 (2006).

Perkins, B. G. and D. J. Nesbitt, J. Phys. Chem. A **111**, 7420 (2007).

Perkins, B. G. and D. J. Nesbitt, J. Phys. Chem. B **112**, 507 (2008).

Petek, H., et al., Science **288**, 1402 (2000).

Phillips, T. R., et al., Astrophys. J. Suppl. Ser. **107**, 467 (1996).

Pierro, W. and H. J. Castejon, Surf. Sci. **602**, 3515 (2008).

Plechkova, N. V. and K. R. Seddon, Chem. Soc. Rev. **37**, 123 (2008).

Rebelo, L. P. N., et al., J. Phys. Chem. B **109**, 6040 (2005).

Regan, M. J., et al., Phys. Rev. Lett. **75**, 2498 (1995).

Regan, M. J., et al., Phys. Rev. B **55**, 10786 (1997).

Rettner, C. T., et al., J. Vac. Soc. A **5**, 508 (1987).

Rivera-Rubero, S. and S. Baldelli, J. Am. Chem. Soc. **126**, 11788 (2004).

Rivera-Rubero, S. and S. Baldelli, J. Phys. Chem. B **110**, 4756 (2006).

Rogers, R. D. and G. A. Voth, Acc. Chem. Res. **40**, 1077 (2007).

Ronk, W. R., et al., J. Chem. Phys. **105**, 4397 (1996).

Roscioli, J. R. and D. J. Nesbitt, J. Phys. Chem. Lett. **1**, 674 (2010).

Roscioli, J. R. and D. J. Nesbitt, J. Phys. Chem. A **115**, 9764 (2011).

Rosenthal, D., et al., Astron. Astrophys. **356**, 705 (2000).

Rothman, L. S., et al., J. Quant Spectrosc. Ra. **60**, 665 (1998).

Rowland, B., et al., J. Chem. Phys. **95**, 1378 (1991).

Sadlej, J., et al., J. Chem. Phys. **102**, 4804 (1995).

Saecker, M. E., et al., Science **252**, 1421 (1991).

Schinke, R. and R. B. Gerber, J. Chem. Phys. **82**, 1567 (1985).

Schmeisser, D. and K. Jacobi, Surf. Sci. **108**, 421 (1981).

Schmid, M. P., et al., Rev. Sci. Instrum. **74**, 4110 (2003).

Schwartz, R. L., et al., Chem. Phys. Lett. **273**, 18 (1997).

Schwenke, D. W., et al., J. Chem. Phys. **94**, 2986 (1991).

Scoles, G., *Atomic and Molecular Beam Methods* (Oxford University Press, New York, 1988).

Segner, J., et al., Surf. Sci. **131**, 273 (1983).

Sha, X. W. and B. Jackson, Surf. Sci. **496**, 318 (2002).

Shaw, A. M., *Astrochemistry: from astronomy to astrobiology* (John Wiley and sons, ltd., West Sussex, England, 2006).

Shenvi, N., et al., J. Chem. Phys. **125** (2006).

Shenvi, N., et al., Science **326**, 829 (2009).

Shuler, S. F., et al., J. Chem. Phys. **116**, 9147 (2002).

Siders, J. L. W. and G. O. Sitz, J. Chem. Phys. **101**, 6264 (1994).

Sitz, G. O., et al., *Handbook of Surf. Sci., Vol. 3: Dynamics* (Elsevier, Amsterdam, 2008).

Sliter, R., et al., J. Phys. Chem. A **115**, 9682 (2011).

Smedley, J. E., et al., J. Chem. Phys. **87**, 3218 (1987).

Soloveichik, P., et al., J. Phys. Chem. A **114**, 1529 (2009).

Somorjai, G. A., *Introduction to surface chemistry and catalysis* (Wiley, New York, 1994).

Staib, P. G., J. Va. Sci. B **29**, 03C125/1 (2011).

Steinfeld, J. I., et al., *Chemical Kinetics and Dynamics* (Prentice-Hall, Inc., Upper Saddle River, New Jersey, 1999).

Sudworth, J. L., J. Power Sourc. **100**, 149 (2001).

Suma, K., et al., Science **311**, 1278 (2006).

Tasic, U. and D. Troya, Phys. Chem. Chem. Phys. **10**, 5776 (2008).

Tennyson, J., et al., J. Phys. Chem. Ref. Data **30**, 735 (2001).

Toth, R. A., Appl. Optics **33**, 4851 (1994).

Tully, J. C., J. Chem. Phys. **92**, 680 (1990).

Tully, J. C., Surf. Sci. **299**, 667 (1994).

Valiron, P., et al., J. Chem. Phys. **129**, 134306 (2008).

Van Bladel, J. W. I., et al., J. Chem. Phys. **97**, 4750 (1992).

van der Avoird, A. and D. J. Nesbitt, J. Chem. Phys. **134**, 044314 (2011).

van der Avoird, A., et al., Chem. Phys. (2011).

Vidali, G., et al., Faraday Discuss. **133**, 125 (2006).

Wang, Y. and G. A. Voth, J. Am. Chem. Soc. **127**, 12192 (2005).

Waring, C., et al., J. Phys. Chem. A **114**, 4896 (2009).

Wasserscheid, P. and W. Keim, Angew. Chem., Int. Ed. **39**, 3772 (2000).

Watanabe, N., et al., Astrophys. J. Lett. **714**, L233.

Watts, E. K., et al., Surf. Sci. **374**, 191 (1997).

Weida, M. J. and D. J. Nesbitt, J. Chem. Phys. **110**, 156 (1999).

White, J. D., et al., Nature **433**, 503 (2005).

Wilkes, J. S., Green Chem. **4**, 73 (2002).

Wiskerke, A. E., et al., Faraday Discuss. **96**, 297 (1993).

Wodtke, A. M., et al., J. Chem. Phys. **118**, 8033 (2003).

Wodtke, A. M., et al., Chem. Phys. Lett. **414**, 138 (2005).

Wodtke, A. M., et al., Prog. Surf. Sci. **83**, 167 (2008).

Wodtke, A. M., et al., Chem. Phys. Lett. **413**, 326 (2005).

Yan, T., et al., J. Phys. Chem. B **110**, 1800 (2006).

Yeo, G. A. and T. A. Ford, Spectrochimica Acta Part A: Molecular Spectroscopy **47**, 485 (1991).

Yockel, S. and G. C. Schatz, J. Phys. Chem. B **114**, 14241 (2010).

Zacharias, H., et al., Phys. Rev. Lett. **49**, 1790 (1982).

Zaitsau, D. H., et al., J. Phys. Chem. A **110**, 7303 (2006).

Zecho, T., et al., J. Chem. Phys. **117**, 8486 (2002).

Zeng, T., et al., J. Chem. Phys. **135**, 094304 (2011).

Zhang, X. and S. P. Sander, J. Phys. Chem. A **115**, 9854 (2011).

Zhao, J., et al., Phys. Rev. B **78** (2008).

Zhao, M. S., et al., Phys. Rev. E **56**, 7033 (1997).

Ziemkiewicz, M. and D. J. Nesbitt, J. Chem. Phys. **131** (2009).

Ziemkiewicz, M., et al., J. Chem. Phys. **123** (2005).

Ziemkiewicz, M. P., et al., J. Chem. Phys. **134**, 234703/1 (2011).

Zittel, P. F. and D. E. Masturzo, J. Chem. Phys. **95**, 8005 (1991).

Appendix A: Circuit Diagrams

A.1 PMT Switcher

The photomultiplier tube is a very sensitive detector of fluorescence photons. For this reason, it is necessary to use every means possible to reduce the amount of unwanted light impinging on the device. This is especially important in the F + H_2O experiments where the electrical discharge across the He / F_2 mixture produces an intense flash of radiation. When this much light strikes the PMT, it temporarily reduces its sensitivity over a timescale of many microseconds, meaning that it renders the device inoperable when it is needed to observe LIF signal.

We overcome this difficulty by transiently switching off the PMT using the circuit shown in figure A.1. Briefly, an external voltage divider (not shown) is used to select the appropriate first dynode voltage for normal PMT operation. This voltage is sent into the PMT switcher, and most of the time it is the output voltage produced by the box. However, upon receiving a TTL trigger pulse, the PMT switcher will instead deliver the normal output voltage minus 200 V to the first dynode. This results in electric fields pushing photogenerated electrons back towards the PMT cathode, leading to a reduction in sensitivity of 2 to 3 orders of magnitude during the entire duration of the trigger pulse.

In addition to removing background from the discharge, the device can also, in principle, be used to block UV probe laser beam scatter to some extent, thus eliminating afterpulsing underneath the detection boxcar integrator. However, in practice the sensitivity of the PMT fluctuates somewhat while the voltage is turned back on, rendering this box somewhat less appropriate for this situation.

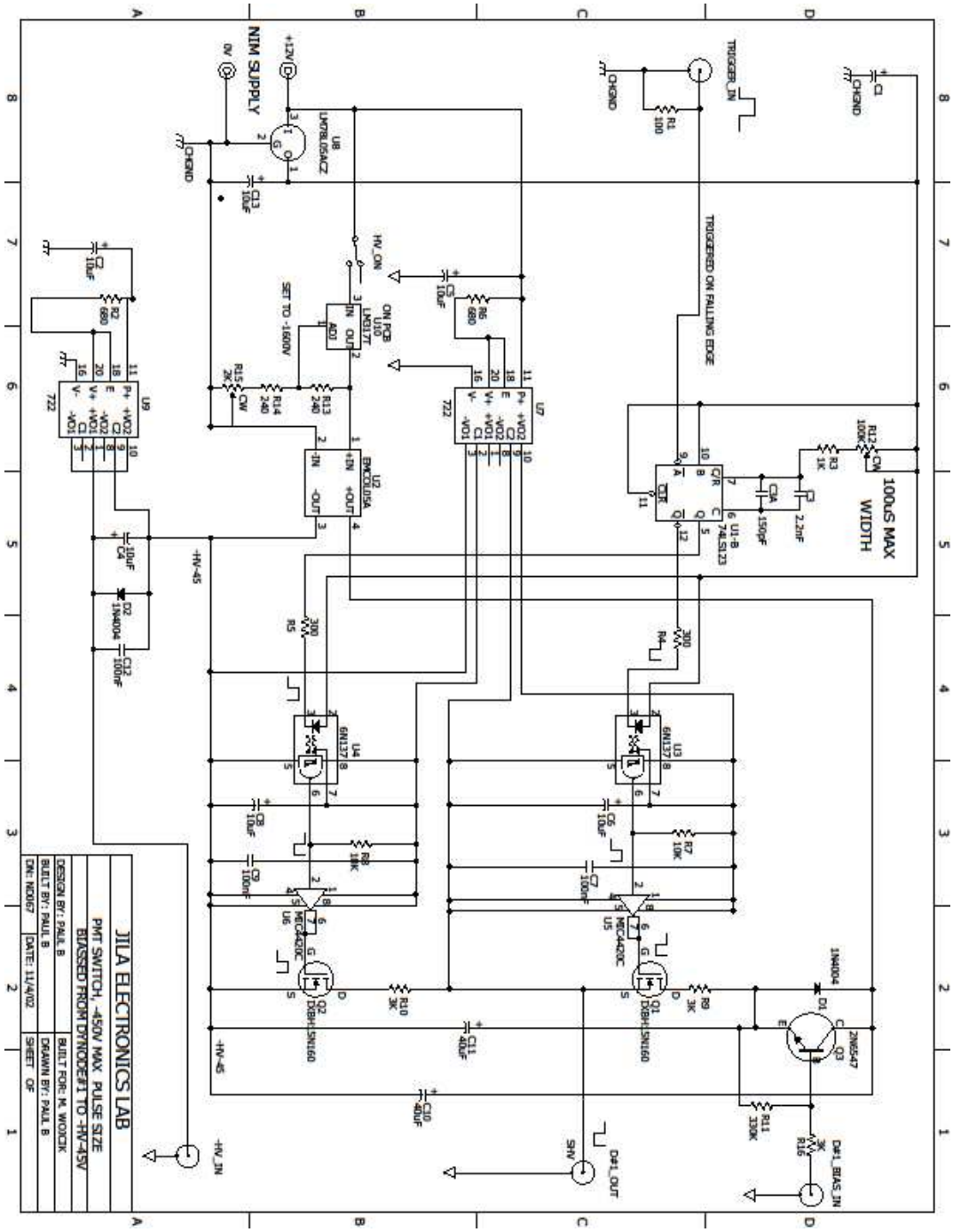

Figure A.1 The push-pull circuit which transiently turns off the PMT by placing its first dynode at several hundred volts below the photocathode. This repels photoelectrons, thus reducing the gain by two orders of magnitude to avoid PMT saturation while the fluorine discharge is running. The output is floated relative to ground in order to allow the device to switch less than the full - 2000 V on the photocathode.

A.2 Pulsed Discharge Source

Fluorine atoms are produced when a beam of 10% molecular fluorine in helium is passed through an electrical discharge at the throat of a supersonic pinhole expansion. The electronics responsible for this are very similar to those which control the PMT switcher, but 8 υF in high voltage capacitors are needed to store the substantial charge needed to deliver 200 mA of current at 800 V through the gas pulse over a period of several tens of μs. Before entering the knife edge jaws at the pulsed valve output, discharge current is made to pass through a 1 kΩ ballast resistor. The ballast serves to reduce instabilities during the critical period right after the voltage is switched on and a steady state current has not yet been established through the gas.. It is important to ensure that the current returns back to this electronic box and that it be shielded and physically separated as much as possible from all signal electronics. Otherwise, RF radiation from the pulsed discharge source may write a substantial amount of noise on the PMT output.

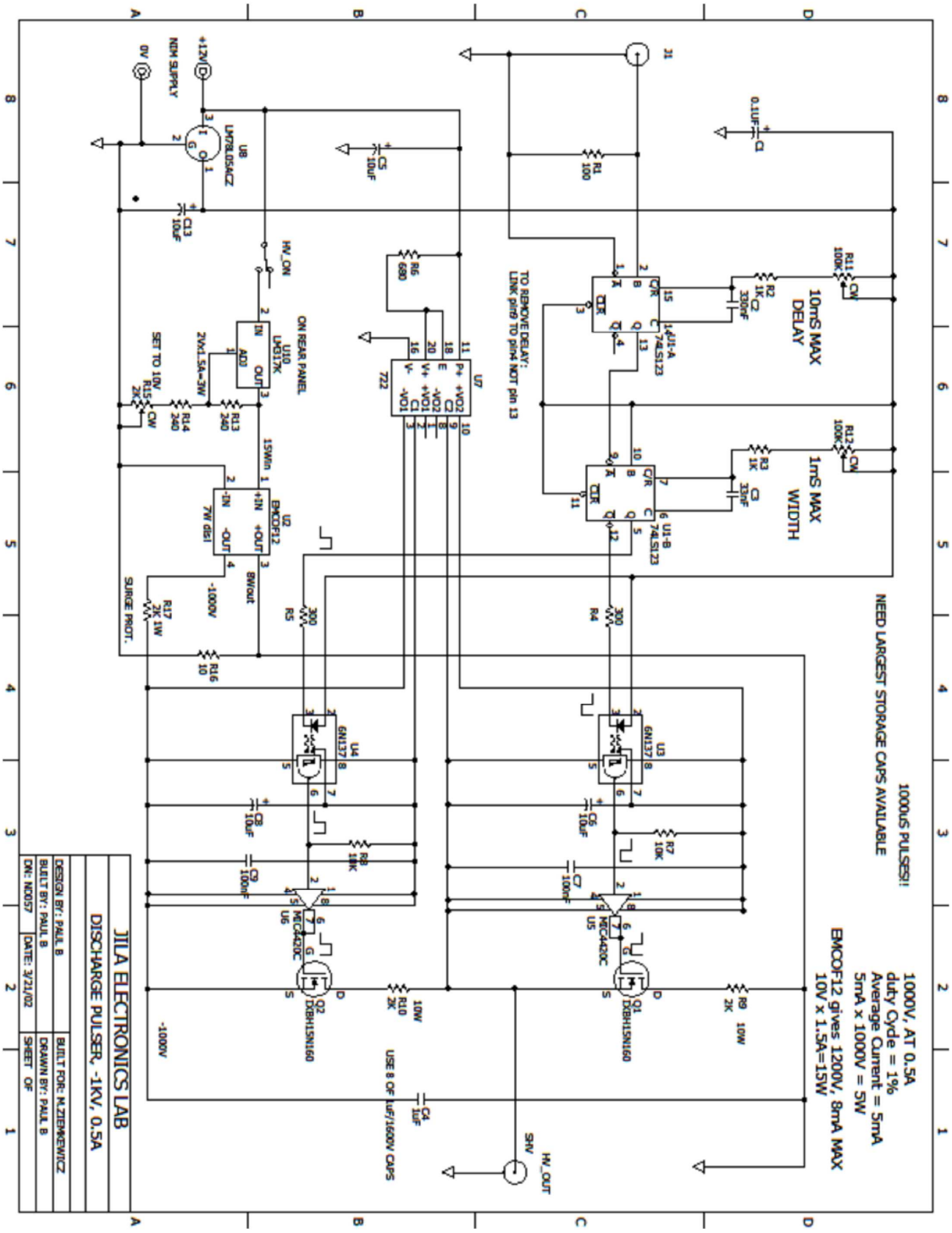

Figure A.2 A second push-pull circuit which supplies current to maintain a 200 mA, 800 V discharge for converting F_2 molecules to F atoms. This circuit is of similar design to that shown in A.1, but its storage capacitors are much larger (8 μF, 1600 V)

Appendix B: Data Analysis Software

B.1 Labview Data Taking Program

This program is able to take IR spectra by scanning the OPO, UV spectra by scanning the dye laser, or time delay spectra by addressing the digital delay generators. In some places, arrows have been used to show other frames in sequences and case structures.

Labview data taking program

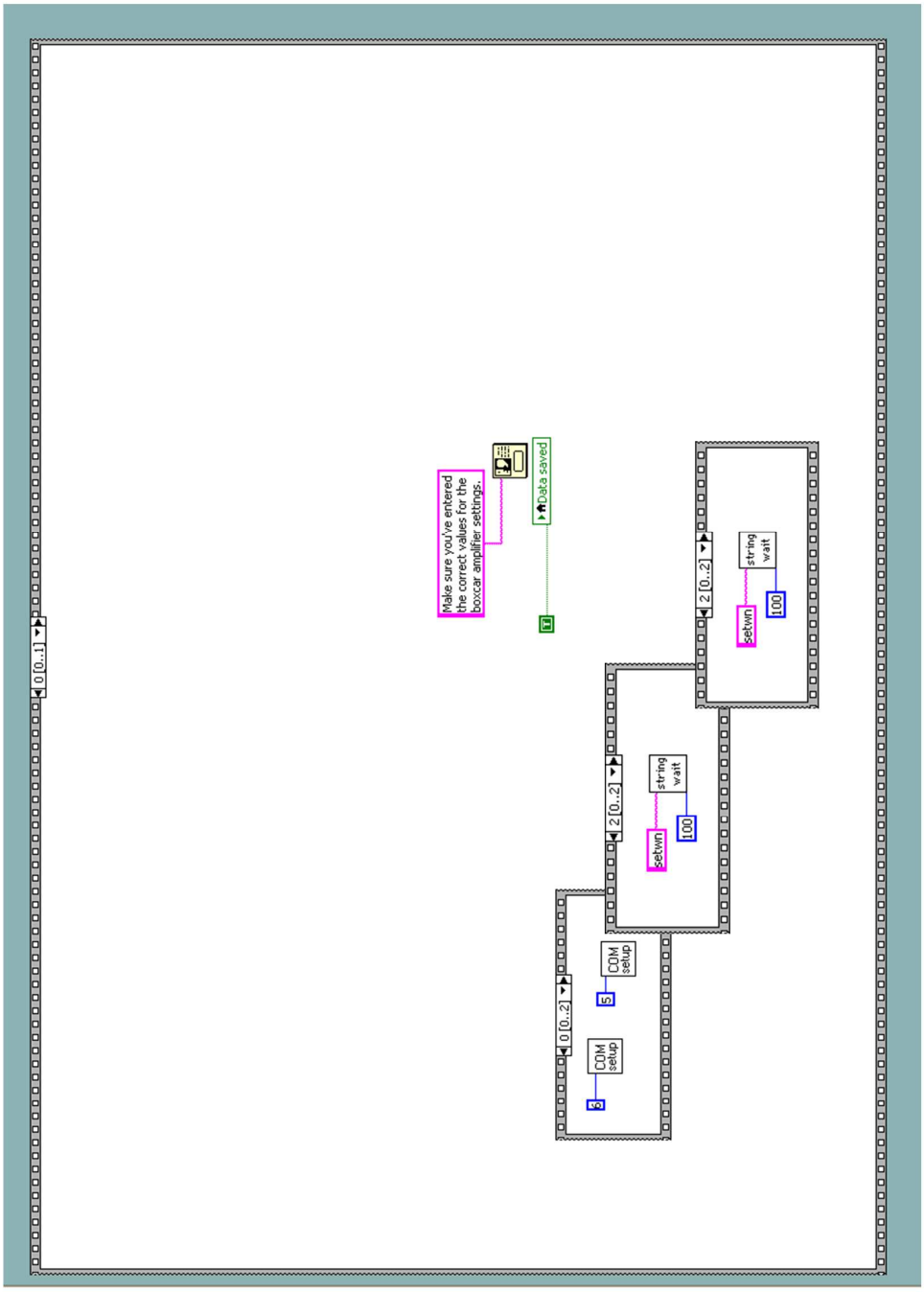

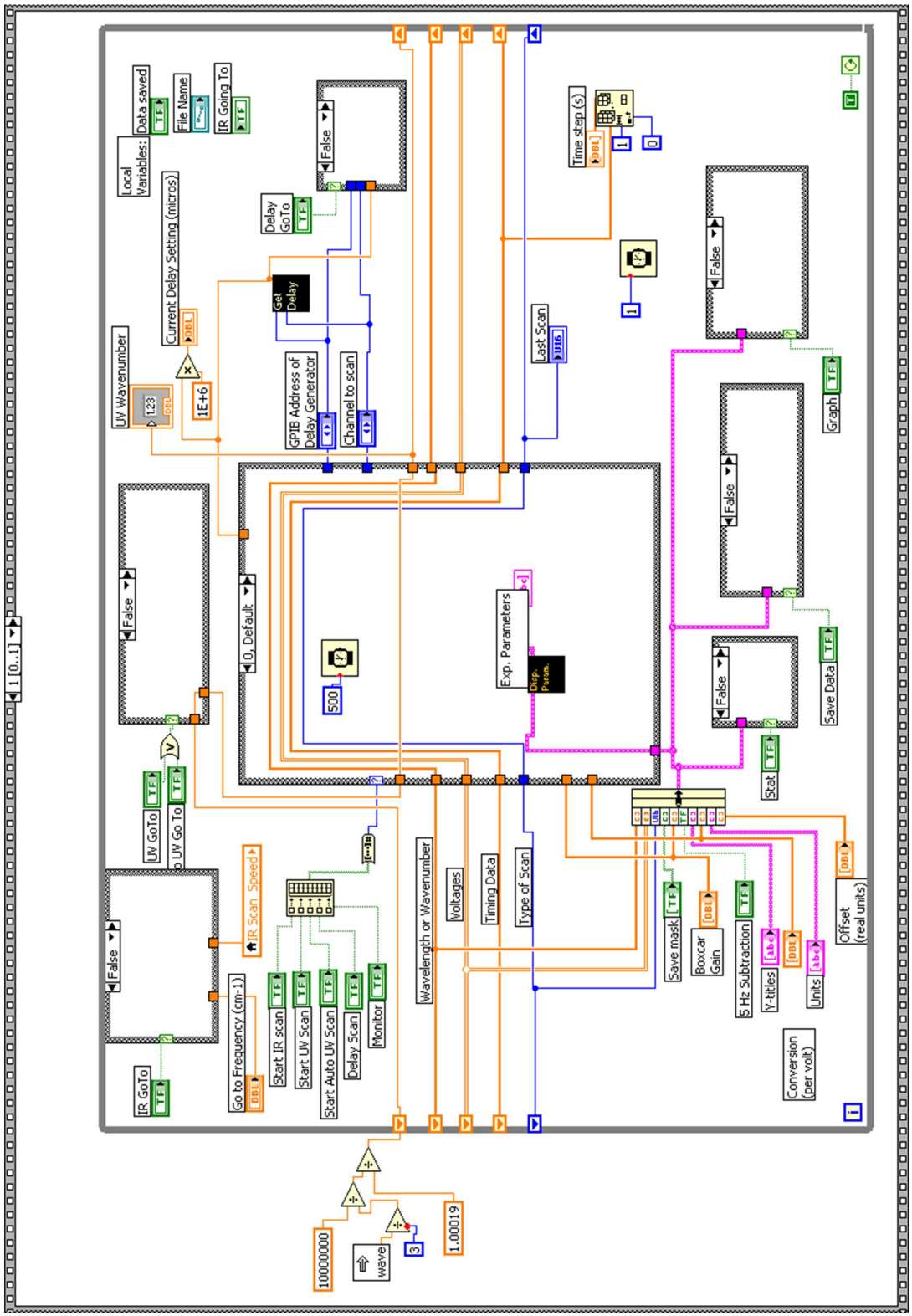
1 [0..1]
Local Variables:
Data saved
File Name
IR Going To
Current Delay Setting (micros)
UV Wavenumber
1E+6
Set Delay
Delay GoTo
False
GPIB Address of Delay Generator
Channel to scan
Time step (s)
Last Scan
0, Default
500
Exp. Parameters
Disp Param.
Graph
Save Data
Stat
UV GoTo
UV Go To
IR Scan Speed
IR GoTo
Go to Frequency (cm-1)
Start IR scan
Start UV Scan
Start Auto UV Scan
Delay Scan
Monitor
Wavelength or Wavenumber
Voltages
Timing Data
Type of Scan
Save mask
Boxcar Gain
5 Hz Subtraction
Y-titles
Units
Offset (real units)
Conversion (per volt)
10000000
wave
3
1.00019

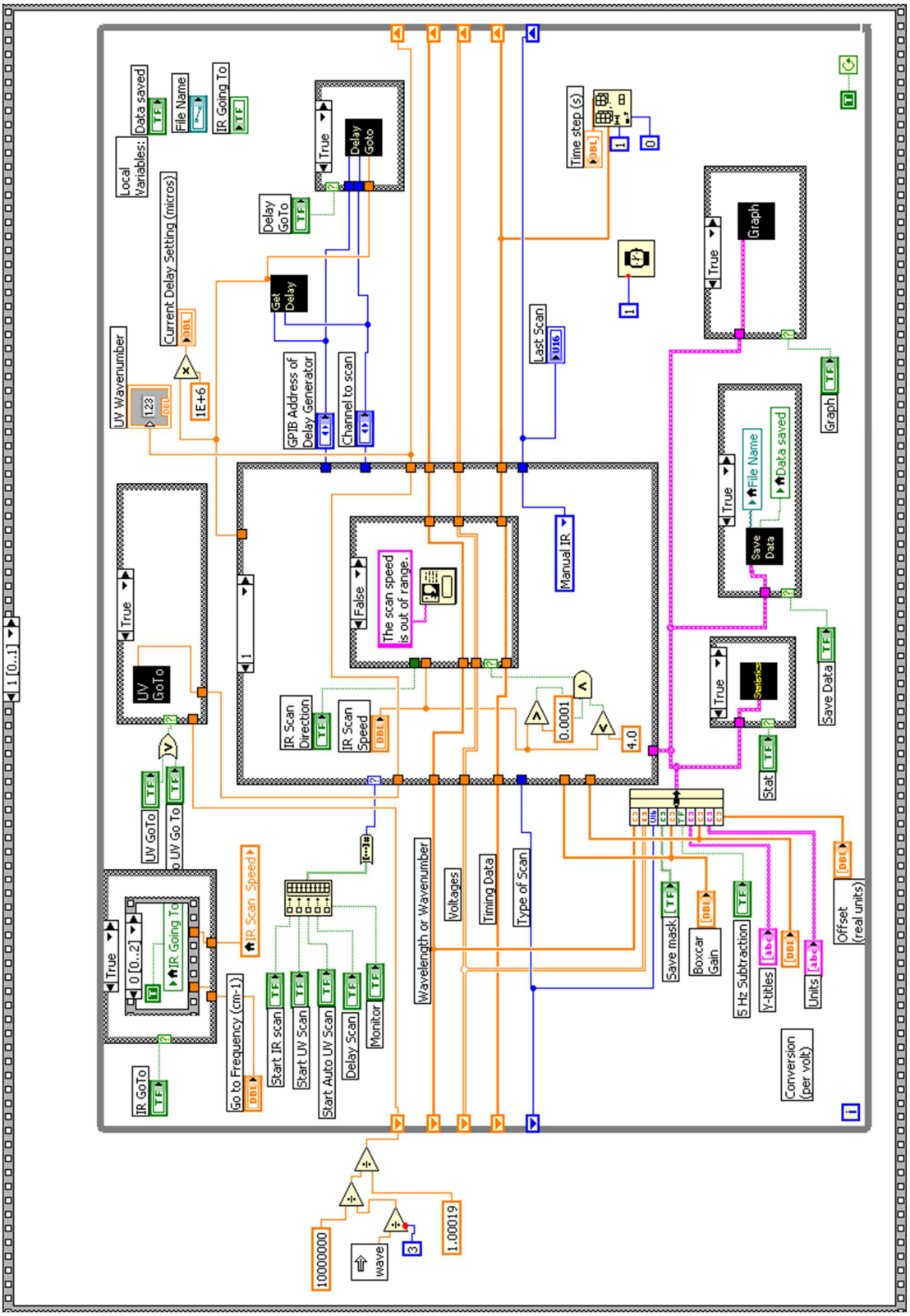
Local Variables:
Data saved
File Name
IR Going To
Current Delay Setting (micros)
UV Wavenumber
1E+6
Get Delay
Delay GoTo
Delay Goto
GPIB Address of Delay Generator
Channel to scan
Last Scan
Time step (s)
Graph
Save Data
UV GoTo
UV Go To
IR Going To
IR Scan Speed
IR Scan Direction
IR Scan Speed
The scan speed is out of range.
Manual IR
0.0001
4.0
IR GoTo
Go to Frequency (cm-1)
Start IR scan
Start UV Scan
Start Auto UV Scan
Delay Scan
Monitor
Wavelength or Wavenumber
Voltages
Timing Data
Type of Scan
Save mask
Boxcar Gain
5 Hz Subtraction
Y-titles
Units
Offset (real units)
Conversion (per volt)
Stat
10000000
wave
3
1.00019

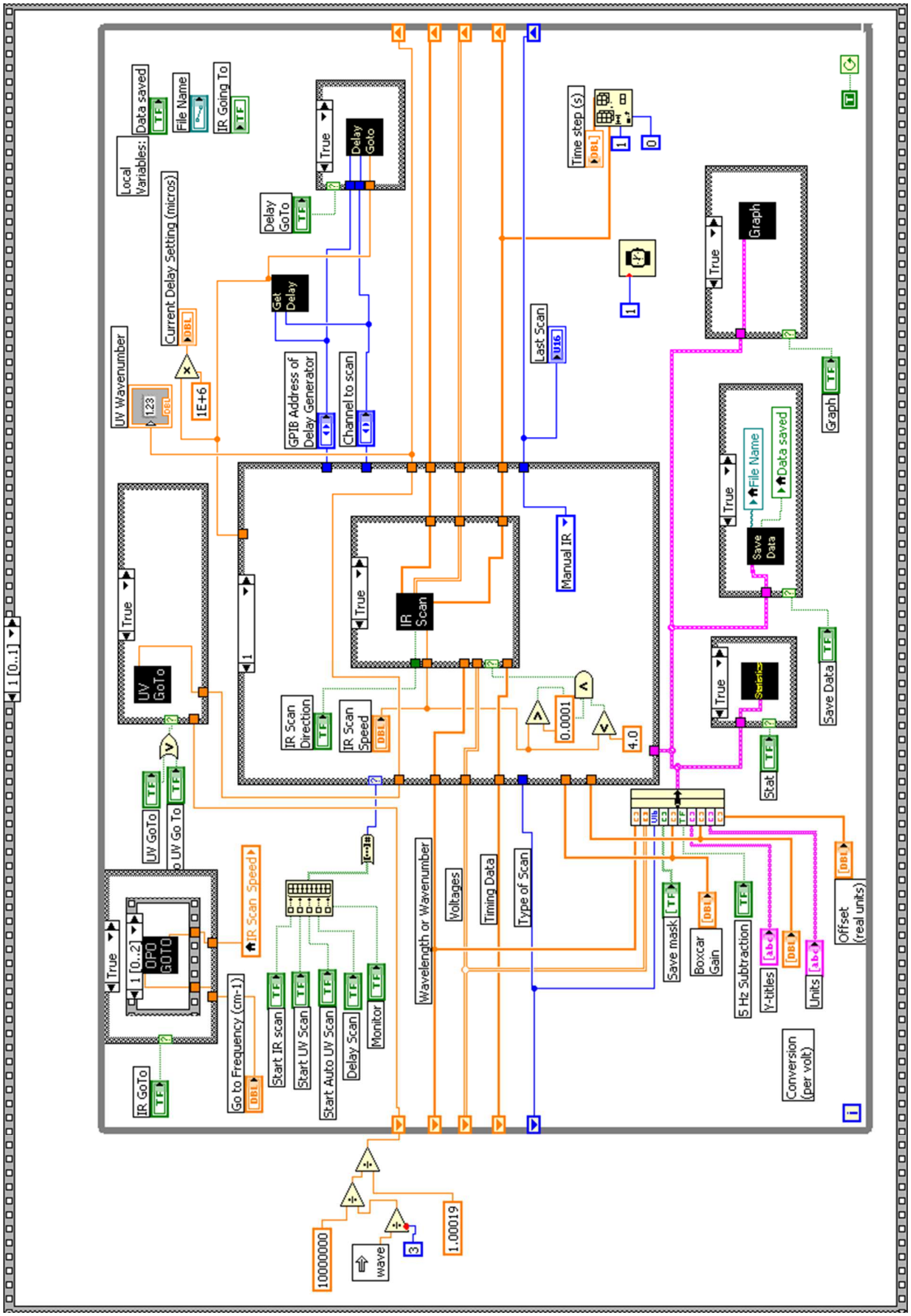
Local Variables:
Data saved
File Name
IR Going To
Current Delay Setting (microns)
1E+6
UV Wavenumber
Get Delay
Delay GoTo
Delay Goto
GPIB Address of Delay Generator
Channel to scan
Last Scan
Time step (s)
Manual IR
IR Scan
IR Scan Direction
IR Scan Speed
0.0001
4.0
UV GoTo
UV GoTo
Go To UV Go To
IR Scan Speed
OPO GOTO
IR GoTo
Go to Frequency (cm-1)
Start IR scan
Start UV Scan
Start Auto UV Scan
Delay Scan
Monitor
Wavelength or Wavenumber
Voltages
Timing Data
Type of Scan
Graph
Save Data
Stat
Save mask
Boxcar Gain
5 Hz Subtraction
Y-titles
Units
Offset (real units)
Conversion (per volt)
10000000
wave
1.00019

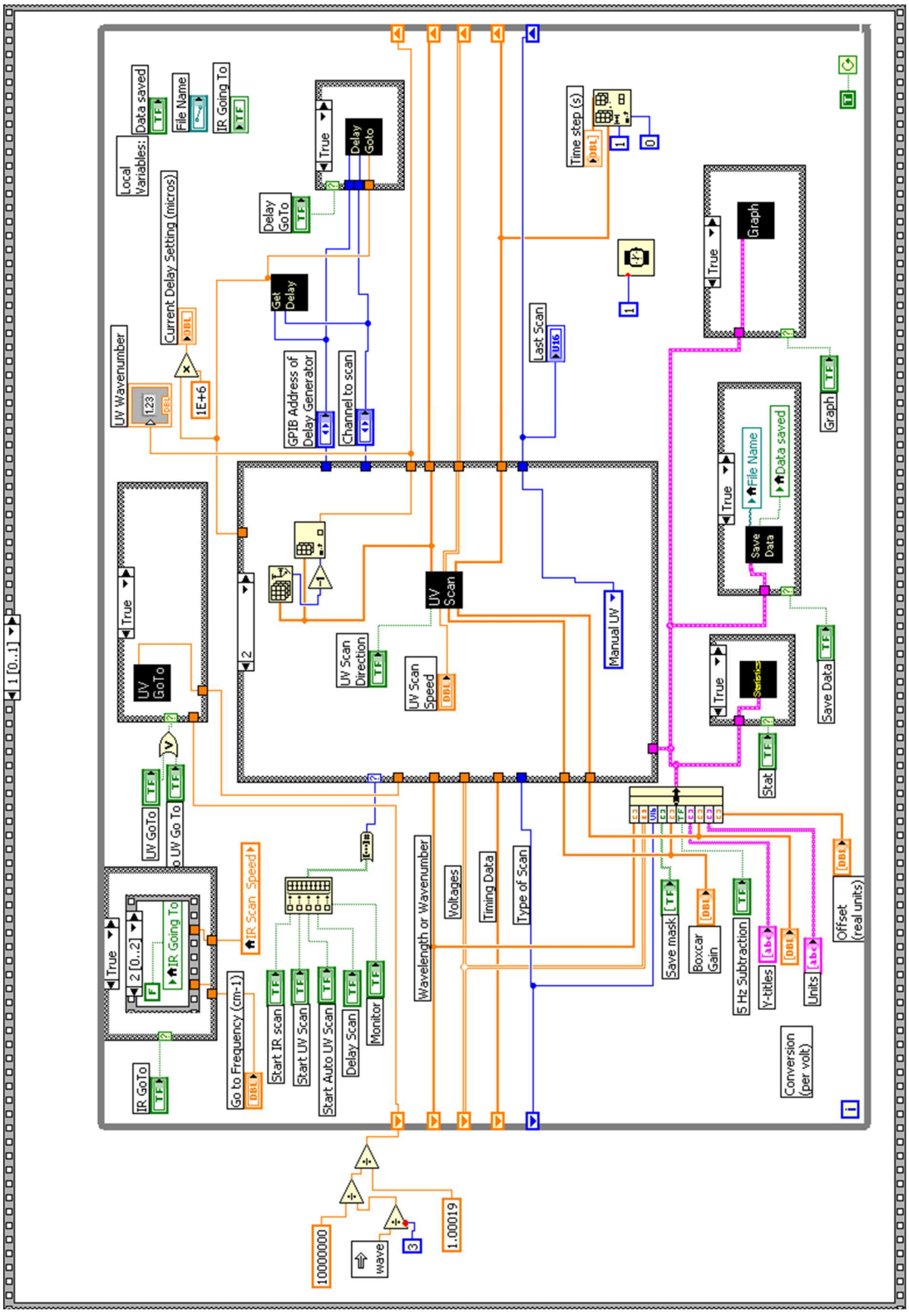
Local Variables:
Data saved
File Name
IR Going To
Current Delay Setting (micros)
UV Wavenumber
1E+6
Delay GoTo
Get Delay
GPIB Address of Delay Generator
Channel to scan
Time step (s)
Last Scan
Graph
Save Data
UV GoTo
UV Scan
UV Scan Direction
UV Scan Speed
Manual UV
Statistics
Stat
IR Scan Speed
IR GoTo
Go to Frequency (cm-1)
Start IR scan
Start UV Scan
Start Auto UV Scan
Delay Scan
Monitor
Wavelength or Wavenumber
Voltages
Timing Data
Type of Scan
Save mask
Boxcar Gain
5 Hz Subtraction
Y-titles
Units
Offset (real units)
Conversion (per volt)
10000000
wave
1.00019

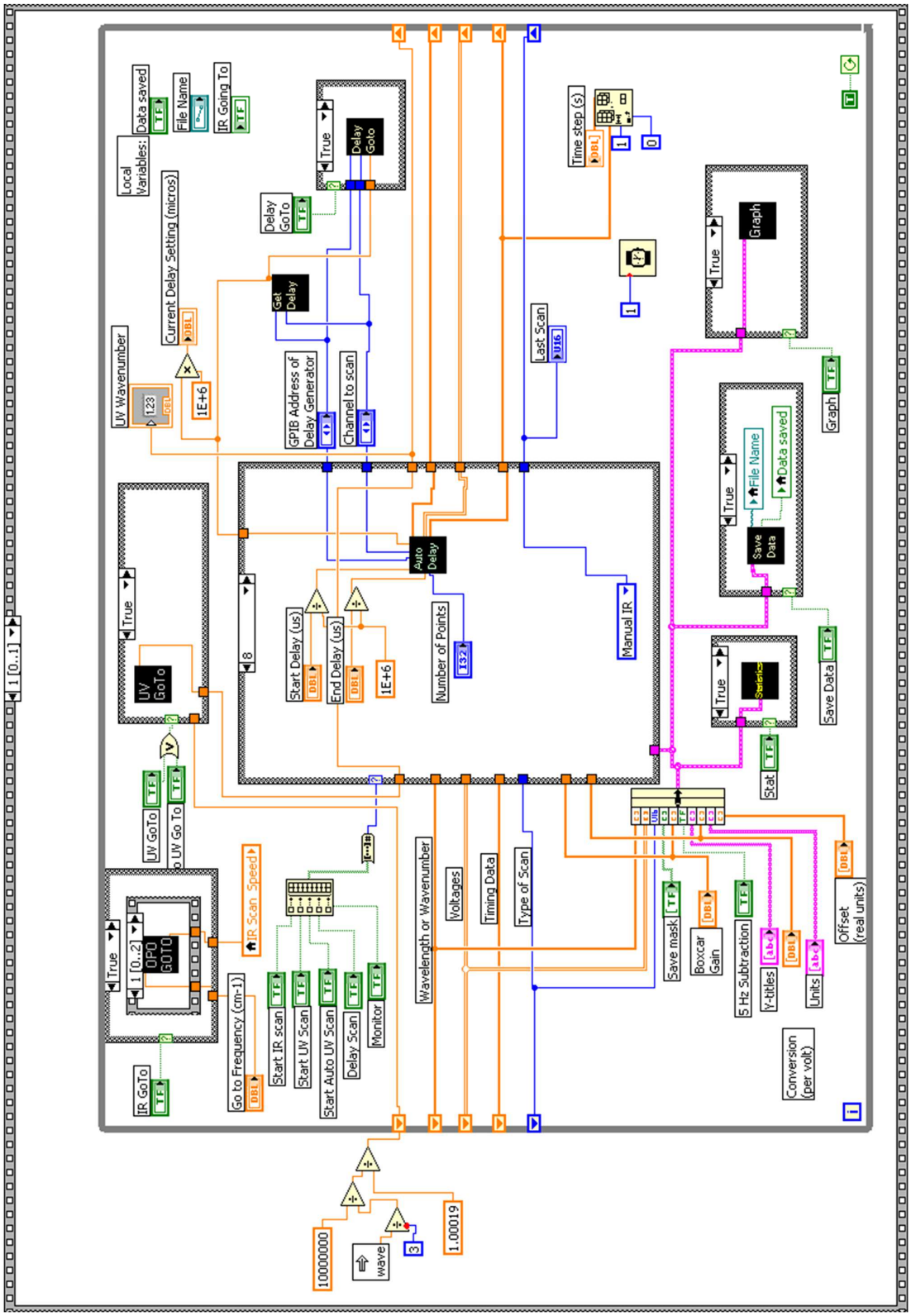
1 [0..1]
Local Variables:
Data saved
File Name
IR Going To
Current Delay Setting (micros)
1E+6
UV Wavenumber
Get Delay
Delay GoTo
True
Delay Goto
GPIB Address of Delay Generator
Channel to scan
Auto Delay
Start Delay (us)
End Delay (us)
Number of Points
Manual IR
Last Scan
Time step (s)
Graph
Save Data
Statistics
Stat
UV GoTo
UV Go To
IR Scan Speed
OPO GOTO
IR GoTo
Go to Frequency (cm-1)
Start IR scan
Start UW Scan
Start Auto UW Scan
Delay Scan
Monitor
Wavelength or Wavenumber
Voltages
Timing Data
Type of Scan
Save mask
Boxcar Gain
5 Hz Subtraction
Y-titles
Units
Offset (real units)
Conversion (per volt)
10000000
wave
3
1.00019

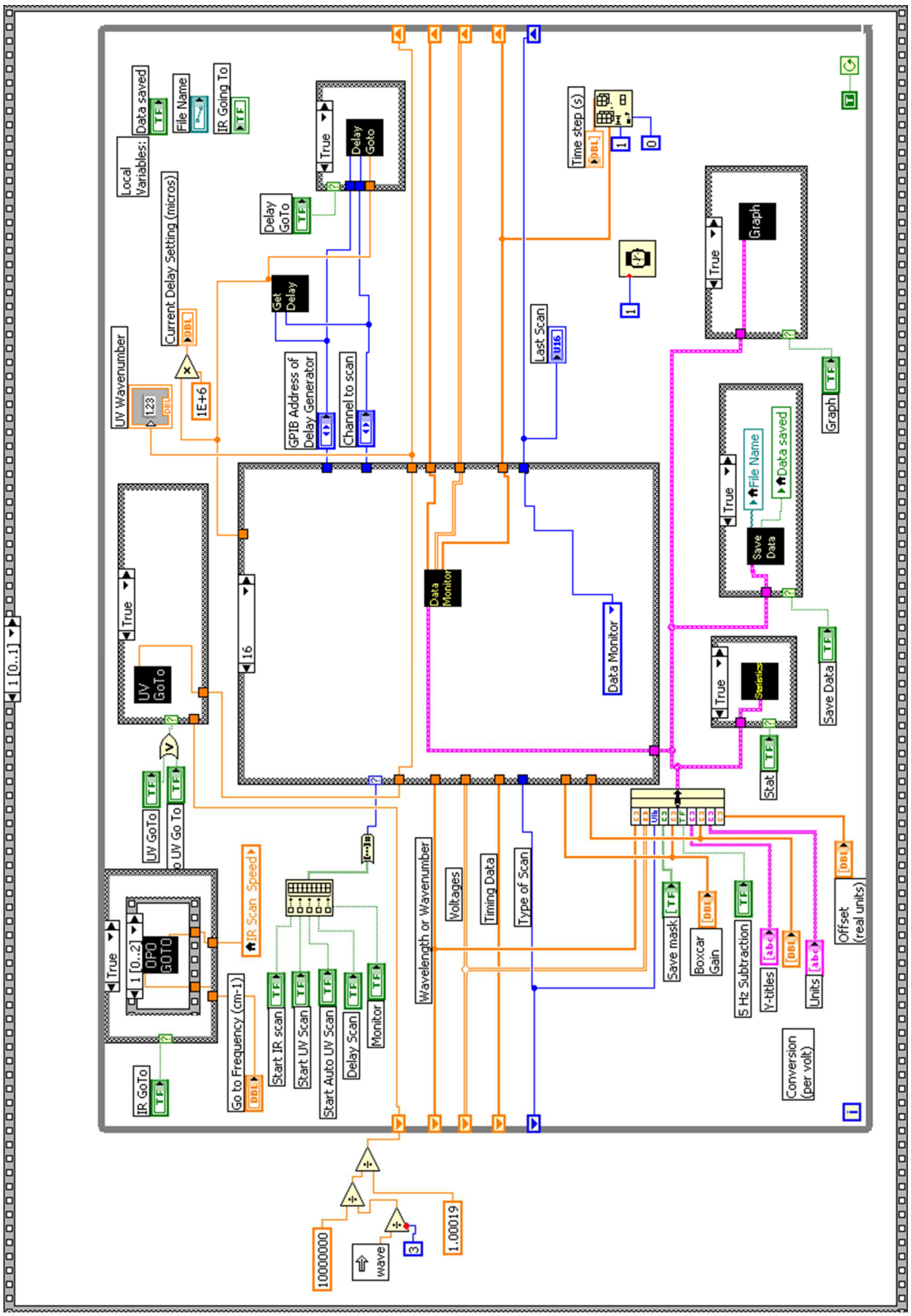
1 [0..1]
Local Variables:
Data saved
File Name
IR Going To
Current Delay Setting (micros)
1E+6
UV Wavenumber
Delay GoTo
Delay Goto
Get Delay
GPIB Address of Delay Generator
Channel to scan
Time step (s)
Last Scan
Graph
Save Data
Data Monitor
UV GoTo
IR GoTo
IR Scan Speed
Go to Frequency (cm-1)
Start IR scan
Start UV Scan
Start Auto UV Scan
Delay Scan
Monitor
Wavelength or Wavenumber
Voltages
Timing Data
Type of Scan
Save mask
Boxcar Gain
5 Hz Subtraction
Y-titles
Units
Offset (real units)
Conversion (per volt)
Stat
16
OPO GOTO
10000000
wave
1.00019

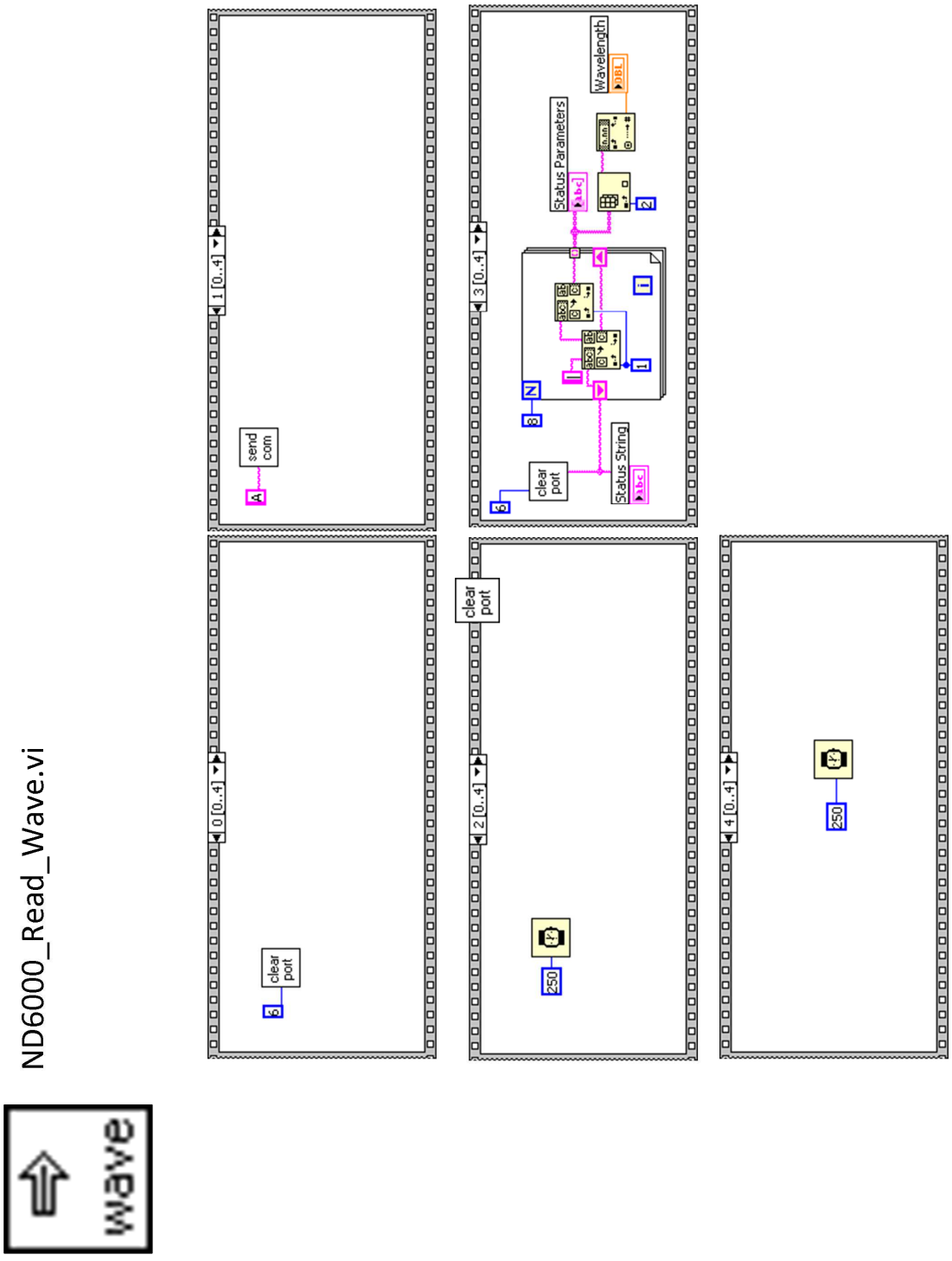
ND6000_Read_Wave.vi
wave
0 [0..4]
clear port
1 [0..4]
send com
2 [0..4]
clear port
250
3 [0..4]
clear port
Status String
Status Parameters
Wavelength
4 [0..4]
250

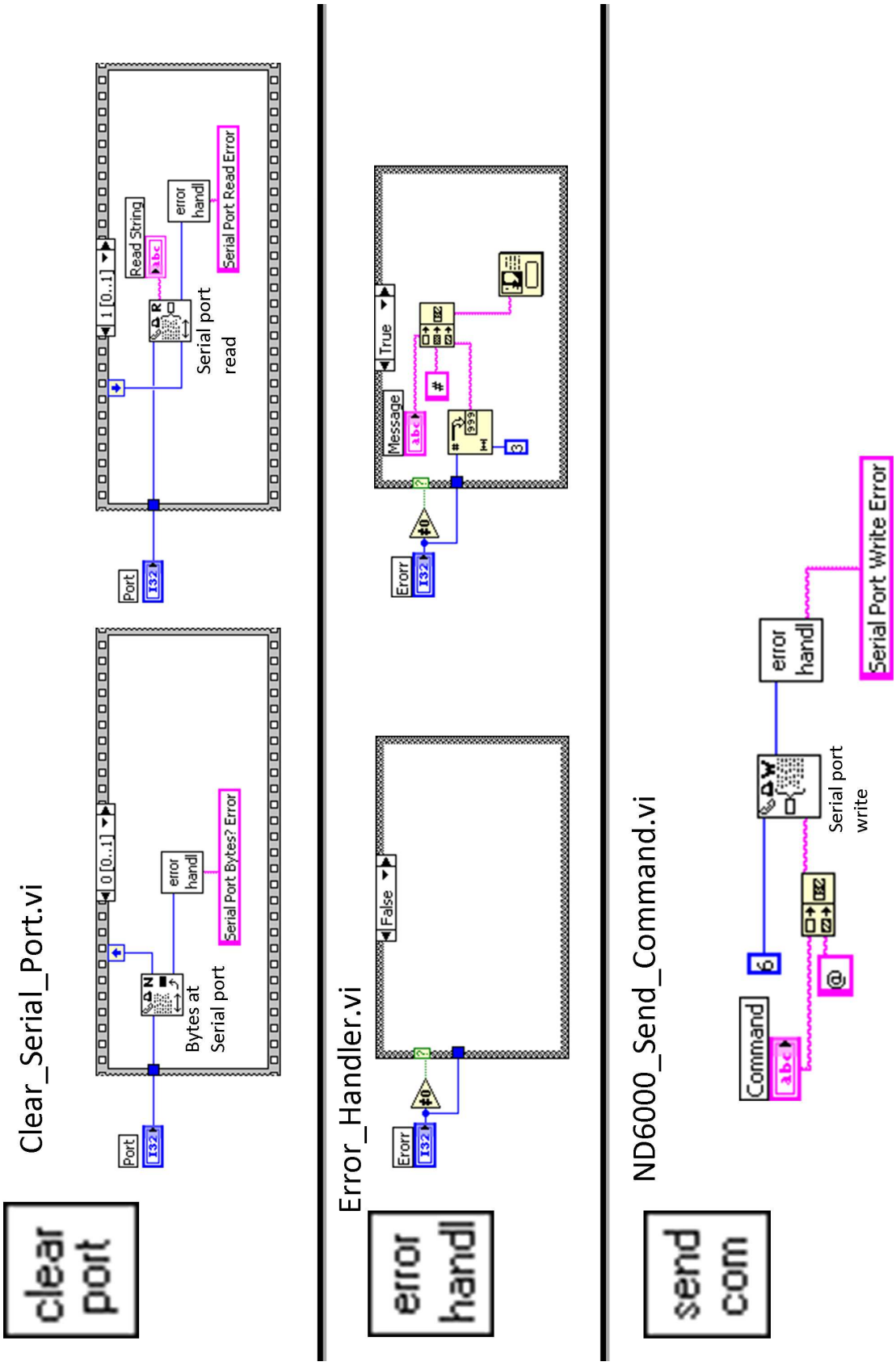
clear port
Clear_Serial_Port.vi
Port
I32
0 [0..1]
Bytes at Serial port
error handl
Serial Port Bytes? Error
1 [0..1]
Serial port read
Read String
error handl
Serial Port Read Error
error handl
Error_Handler.vi
Erorr
I32
False
True
Message
send com
ND6000_Send_Command.vi
Command
Serial port write
error handl
Serial Port Write Error

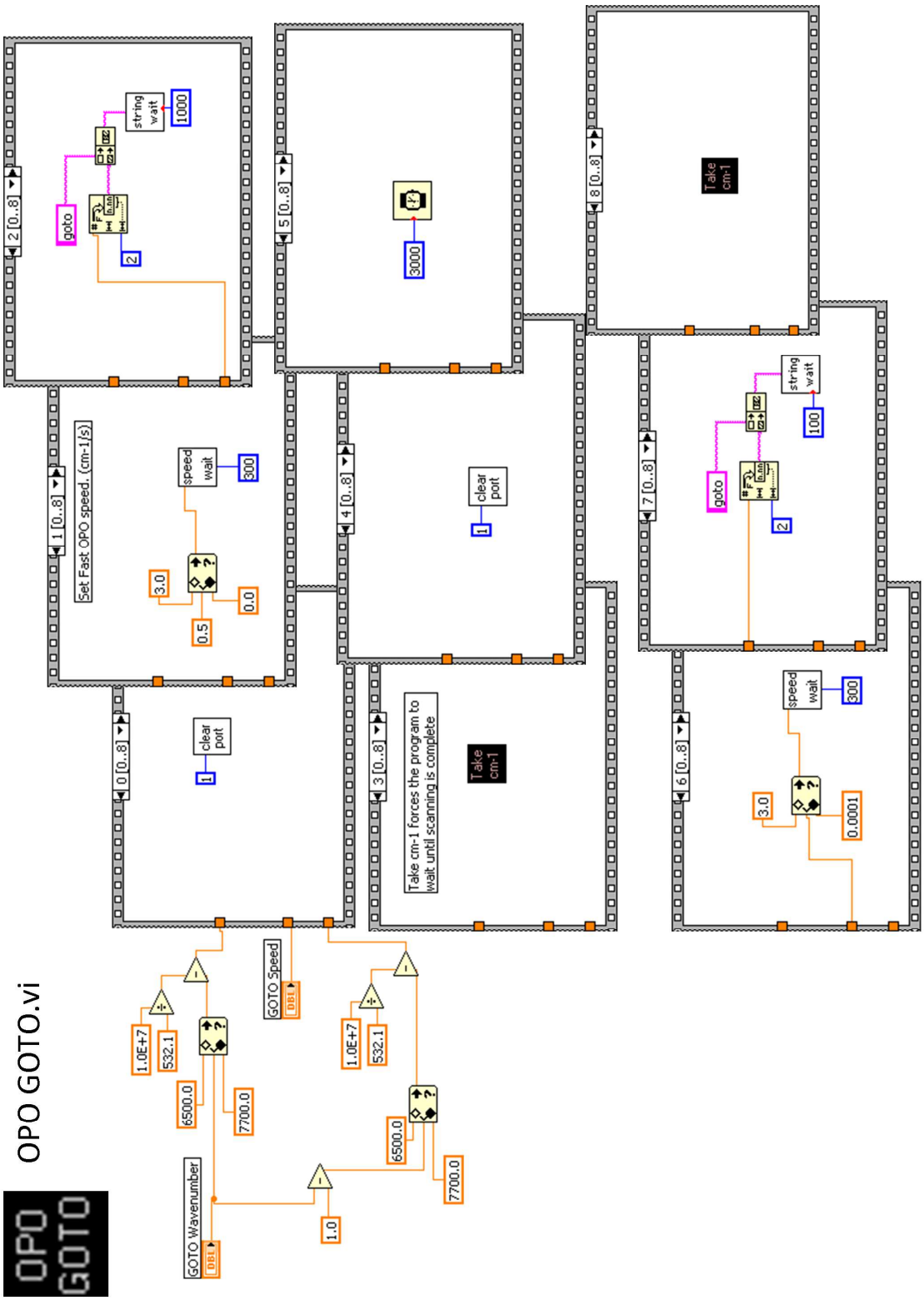
OPO GOTO.vi
OPO GOTO
GOTO Wavenumber
GOTO Speed
1.0E+7
532.1
6500.0
7700.0
1.0
0 [0..8]
clear port
1 [0..8]
Set Fast OPO speed. (cm-1/s)
speed wait
300
3.0
0.5
0.0
2 [0..8]
goto
string wait
1000
2
3 [0..8]
Take cm-1 forces the program to wait until scanning is complete
Take cm-1
4 [0..8]
clear port
1
5 [0..8]
3000
6 [0..8]
speed wait
300
3.0
0.0001
7 [0..8]
goto
string wait
100
2
8 [0..8]
Take cm-1

speed
wait

LV_Set_Speed.vi

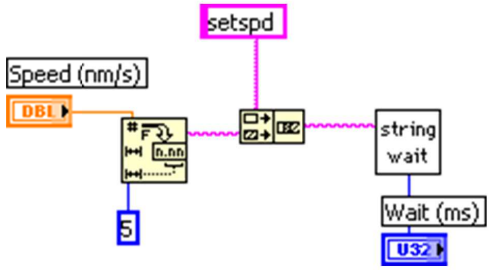

---

string
wait

LV_Write_String.vi

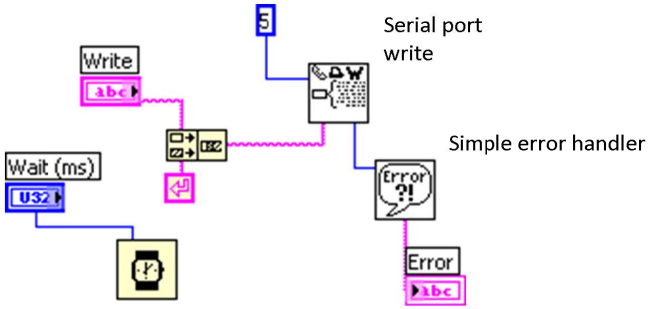

Take
cm-1

OPO get wavenumber.vi

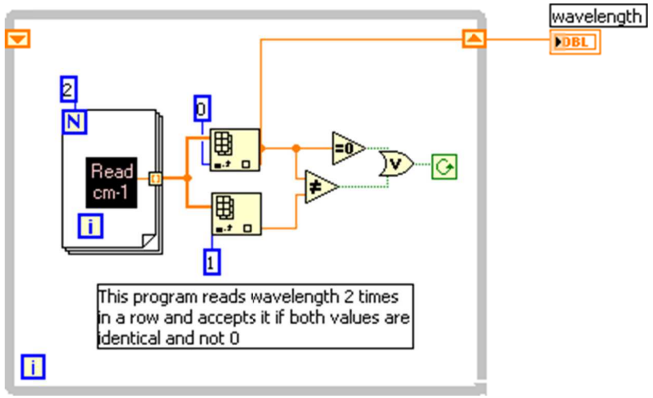

Read MIR wavenumber.vi

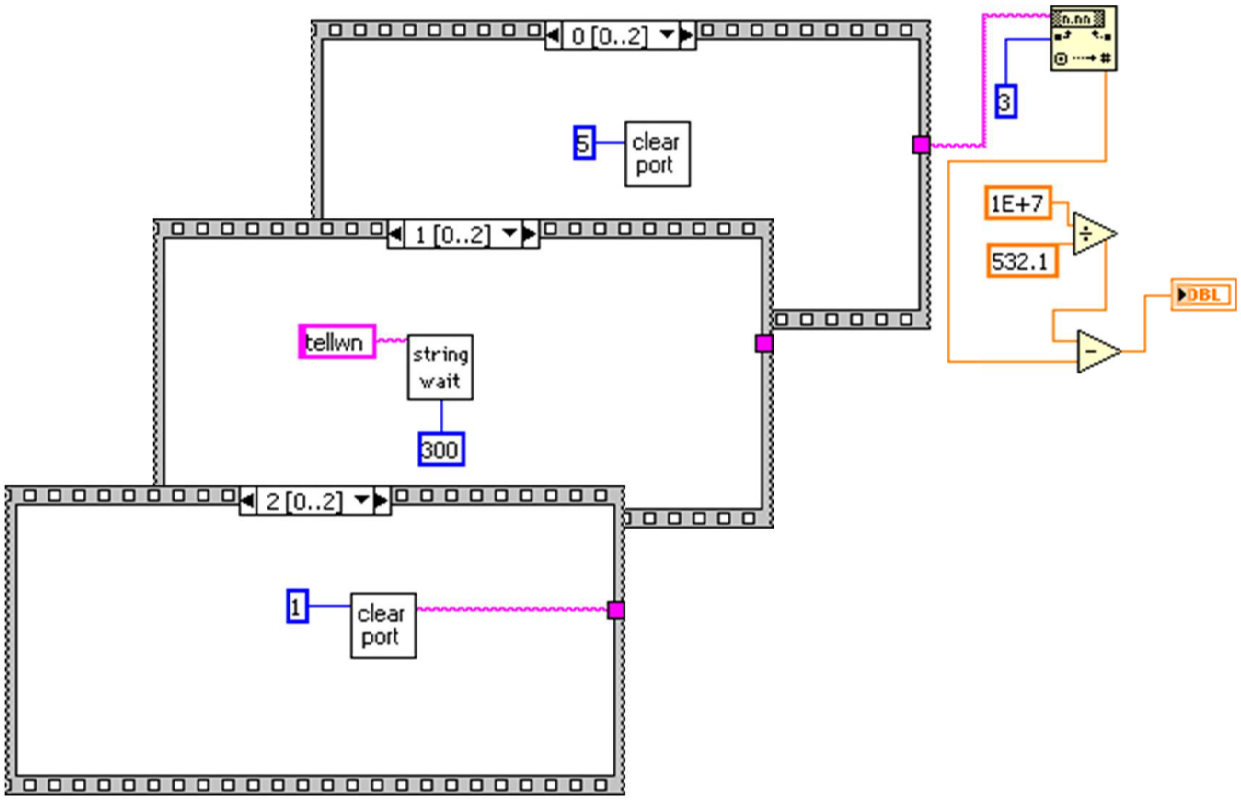

UV GoTo

UV Go To.vi

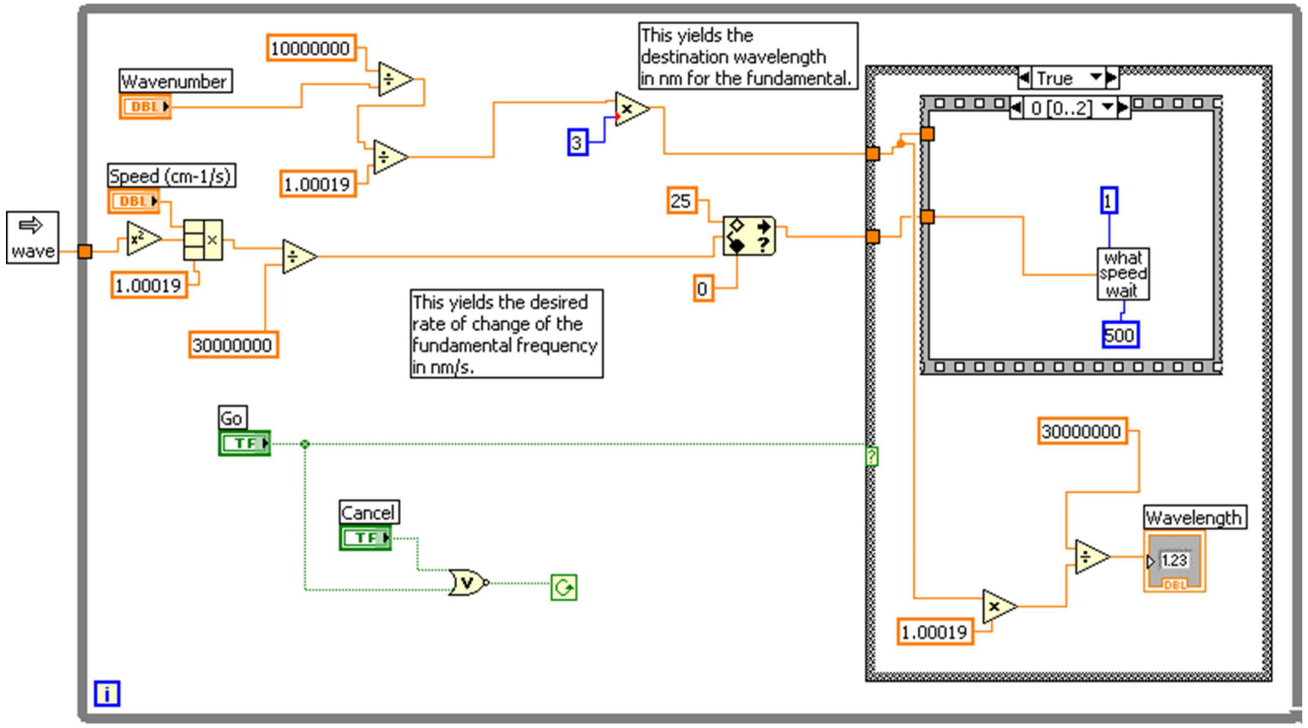

Other cases:

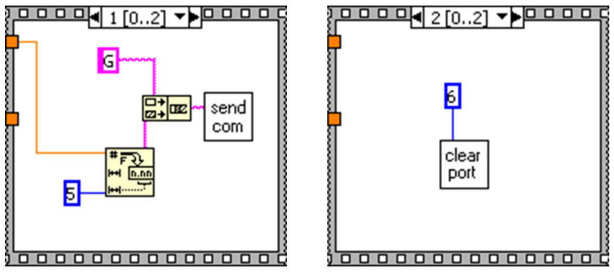

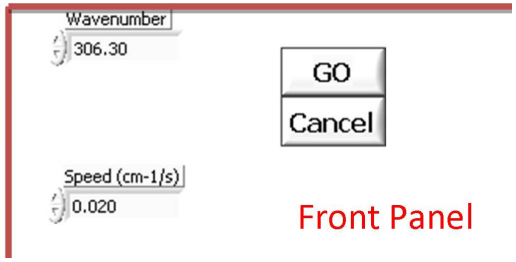

Front Panel

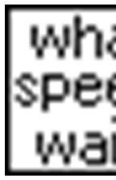

ND6000_Set_Speed.vi

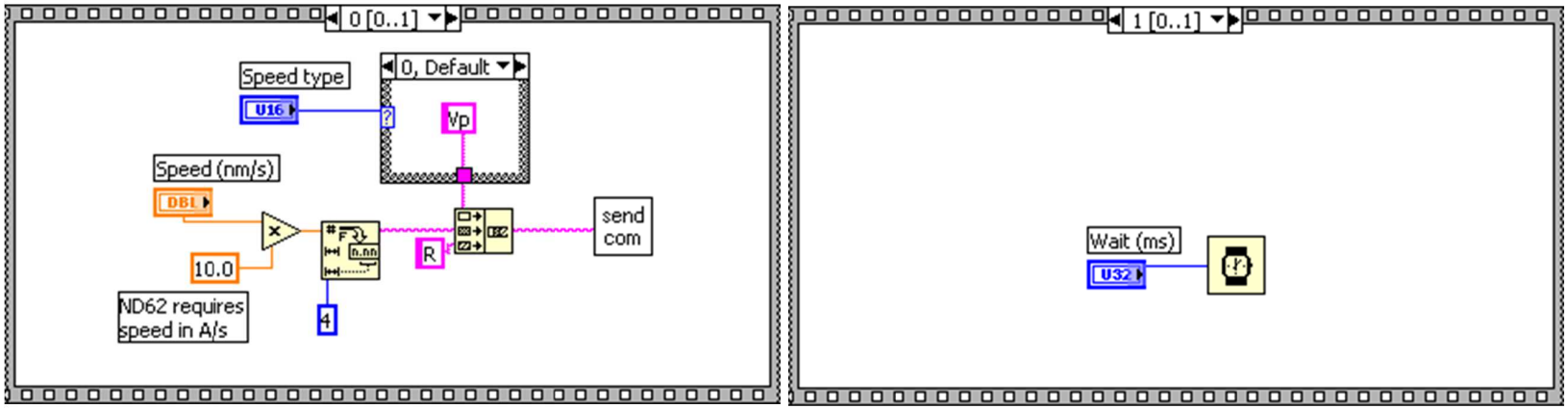

Other cases:

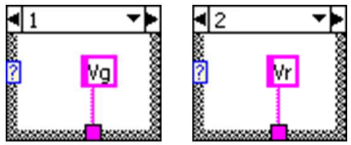

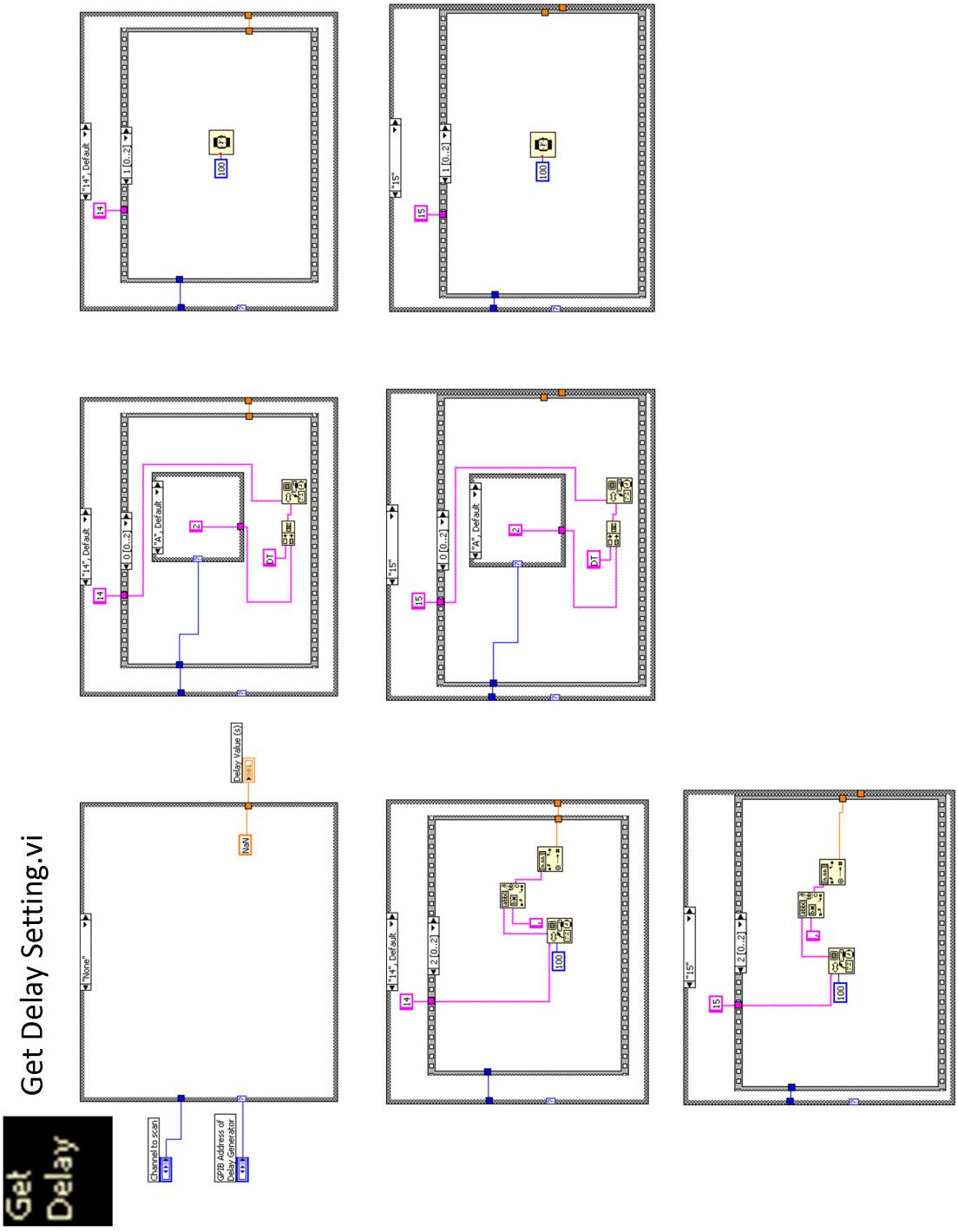
Get Delay Setting.vi
Get Delay
Channel to scan
GPIB Address of Delay Generator
Delay Value (s)
"None"
"14", Default
"15"
"A", Default
0..2
100
dT

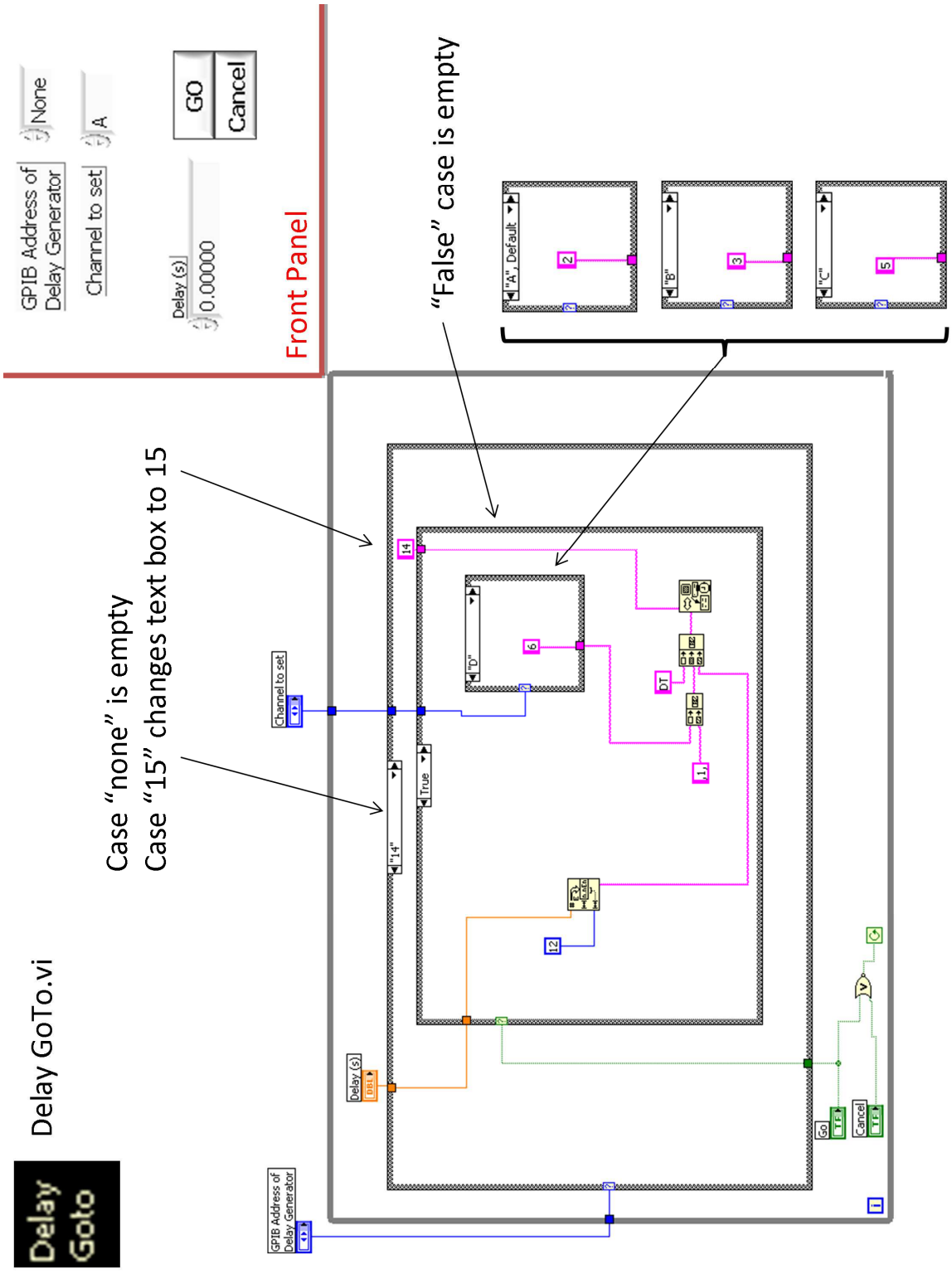
Delay Goto
Delay GoTo.vi
Case "none" is empty
Case "15" changes text box to 15
"False" case is empty
Front Panel
GPIB Address of Delay Generator
None
Channel to set
A
Delay (s)
0.00000
GO
Cancel
"A", Default
"B"
"C"
"D"
"14"
True
Channel to set
Delay (s)
GPIB Address of Delay Generator
DT
Go
Cancel

Display parameters.vi

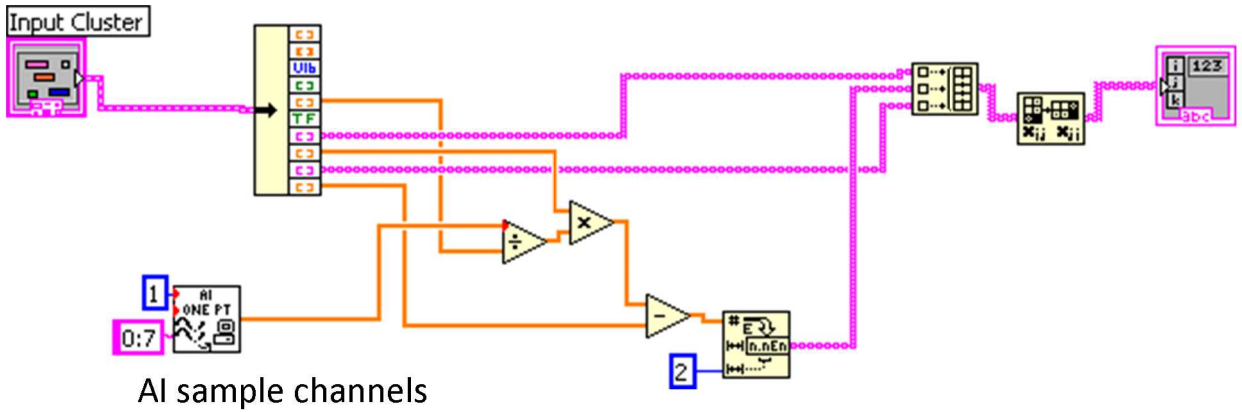

AI sample channels
vi for the A/D card

IR Scan

Better IR scan.vi

Front panel

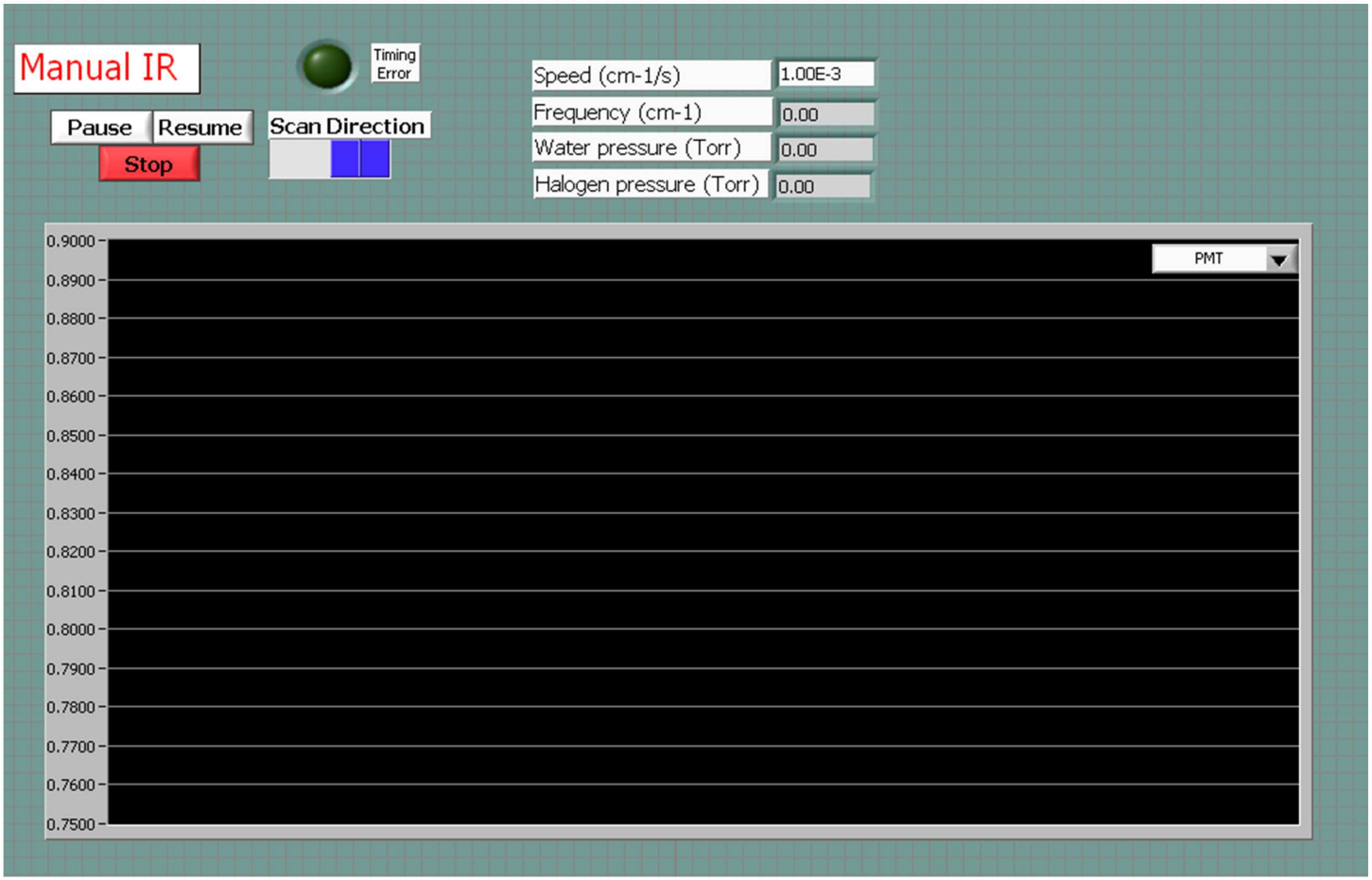

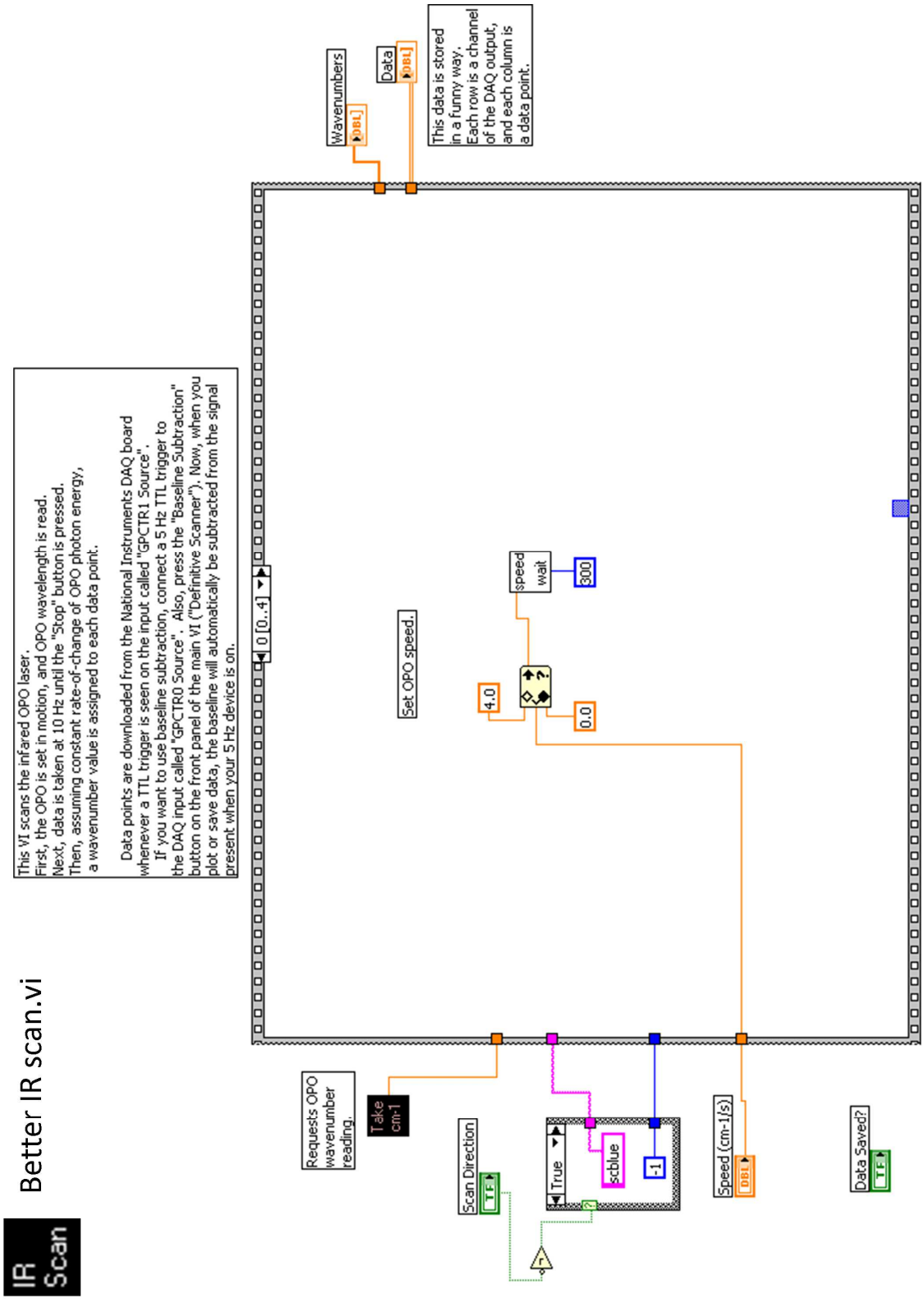
IR Scan
Better IR scan.vi
This VI scans the infared OPO laser.
First, the OPO is set in motion, and OPO wavelength is read.
Next, data is taken at 10 Hz until the "Stop" button is pressed.
Then, assuming constant rate-of-change of OPO photon energy,
a wavenumber value is assigned to each data point.
Data points are downloaded from the National Instruments DAQ board whenever a TTL trigger is seen on the input called "GPCTR1 Source".
If you want to use baseline subtraction, connect a 5 Hz TTL trigger to the DAQ input called "GPCTR0 Source". Also, press the "Baseline Subtraction" button on the front panel of the main VI ("Definitive Scanner"). Now, when you plot or save data, the baseline will automatically be subtracted from the signal present when your 5 Hz device is on.
Wavenumbers
Data
This data is stored in a funny way. Each row is a channel of the DAQ output, and each column is a data point.
0 [0..4]
Set OPO speed.
speed
wait
300
4.0
0.0
Requests OPO wavenumber reading.
Take cm-1
Scan Direction
TF
True
scblue
-1
Speed (cm-1/s)
DBL
Data Saved?
TF

IR Scan ... continued

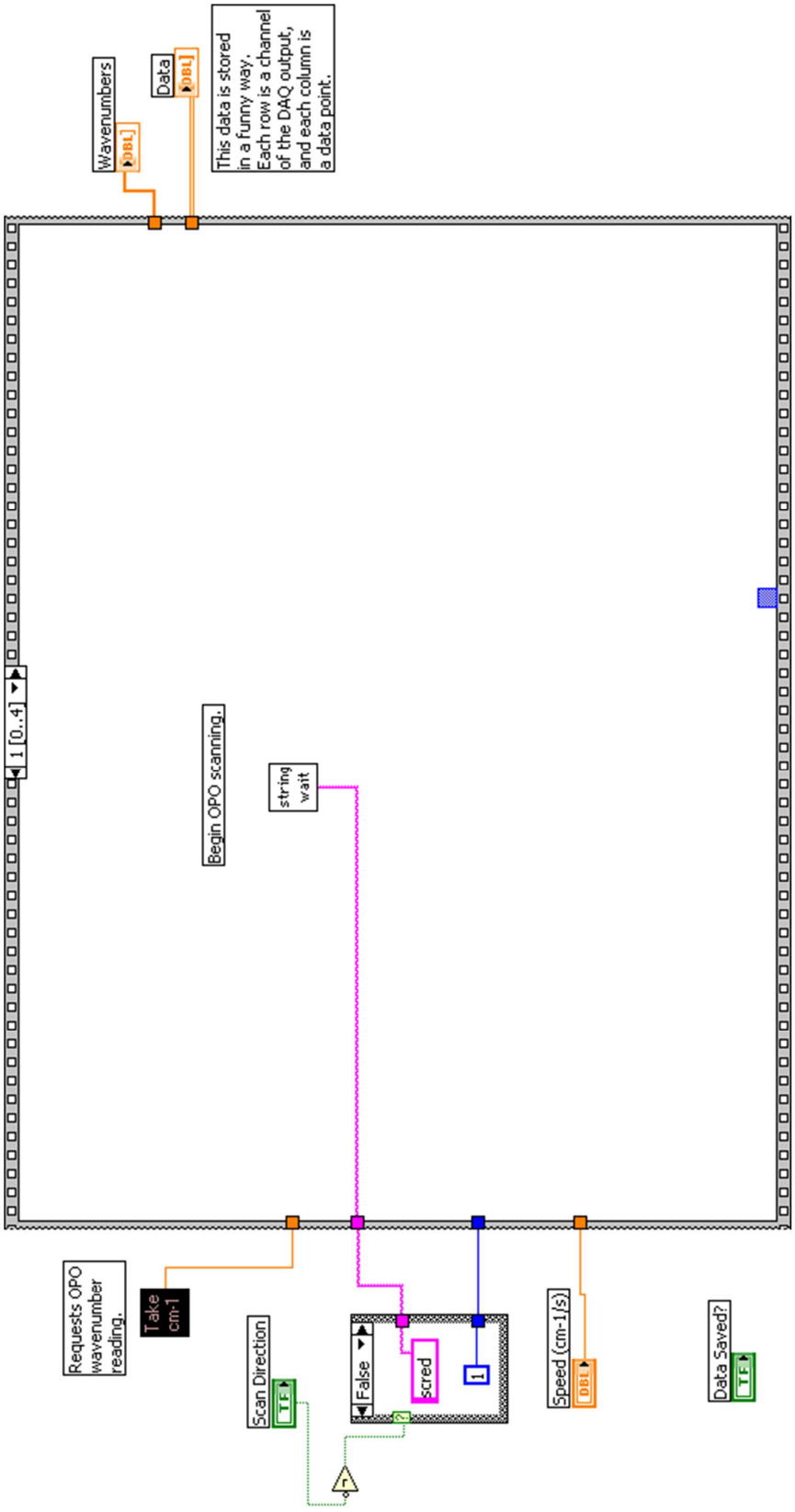

IR Scan

... continued

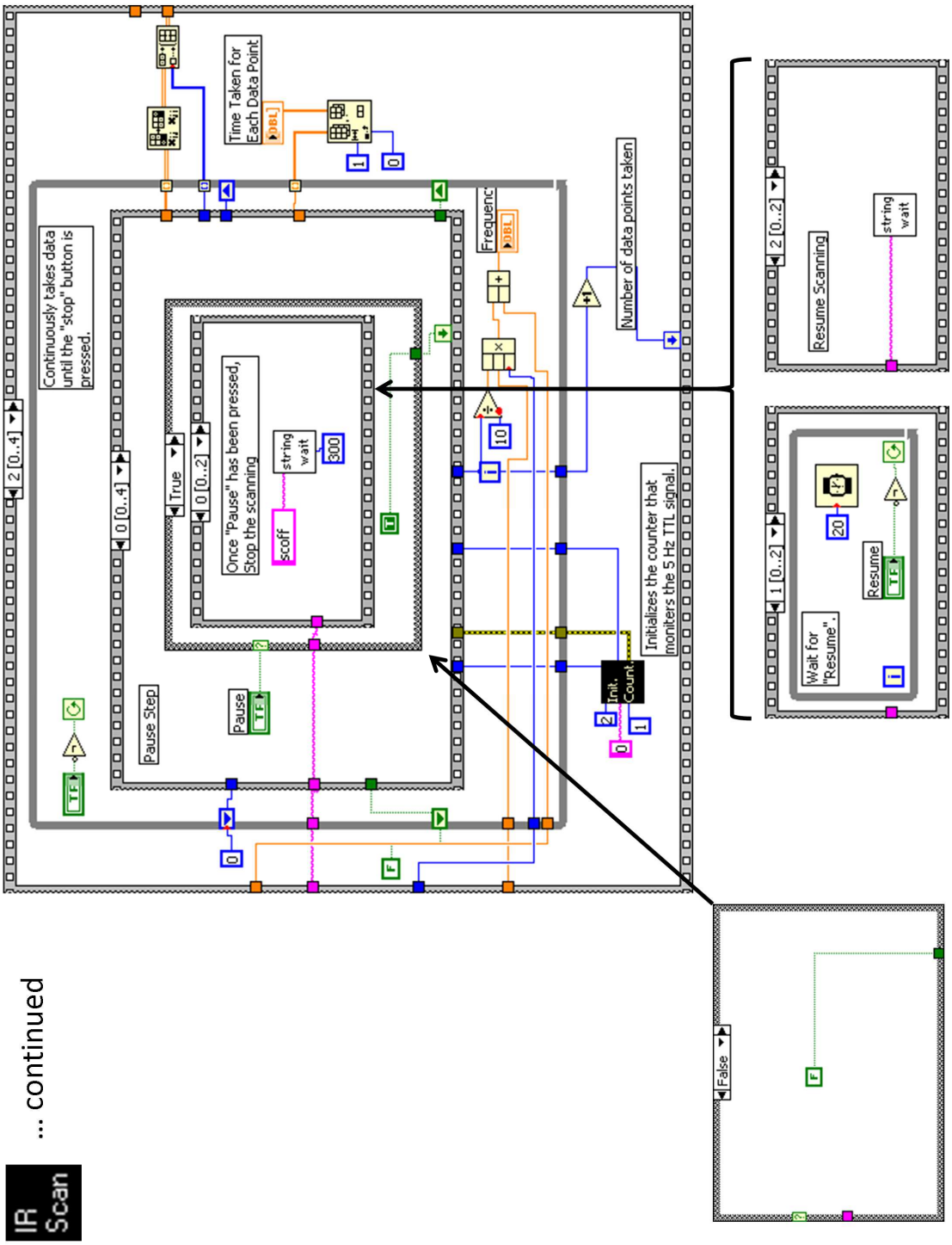

IR Scan ... continued

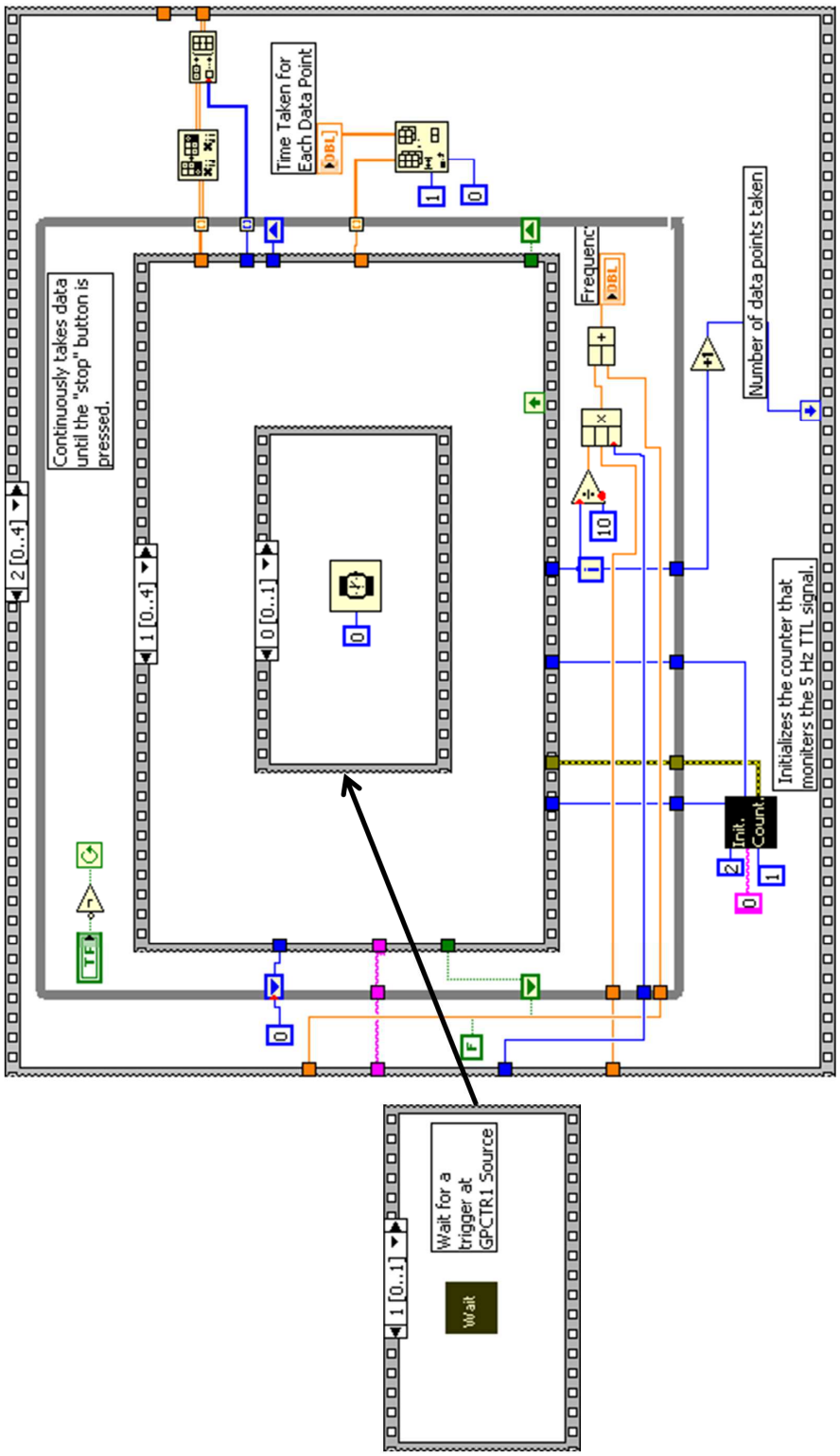

IR Scan

... continued

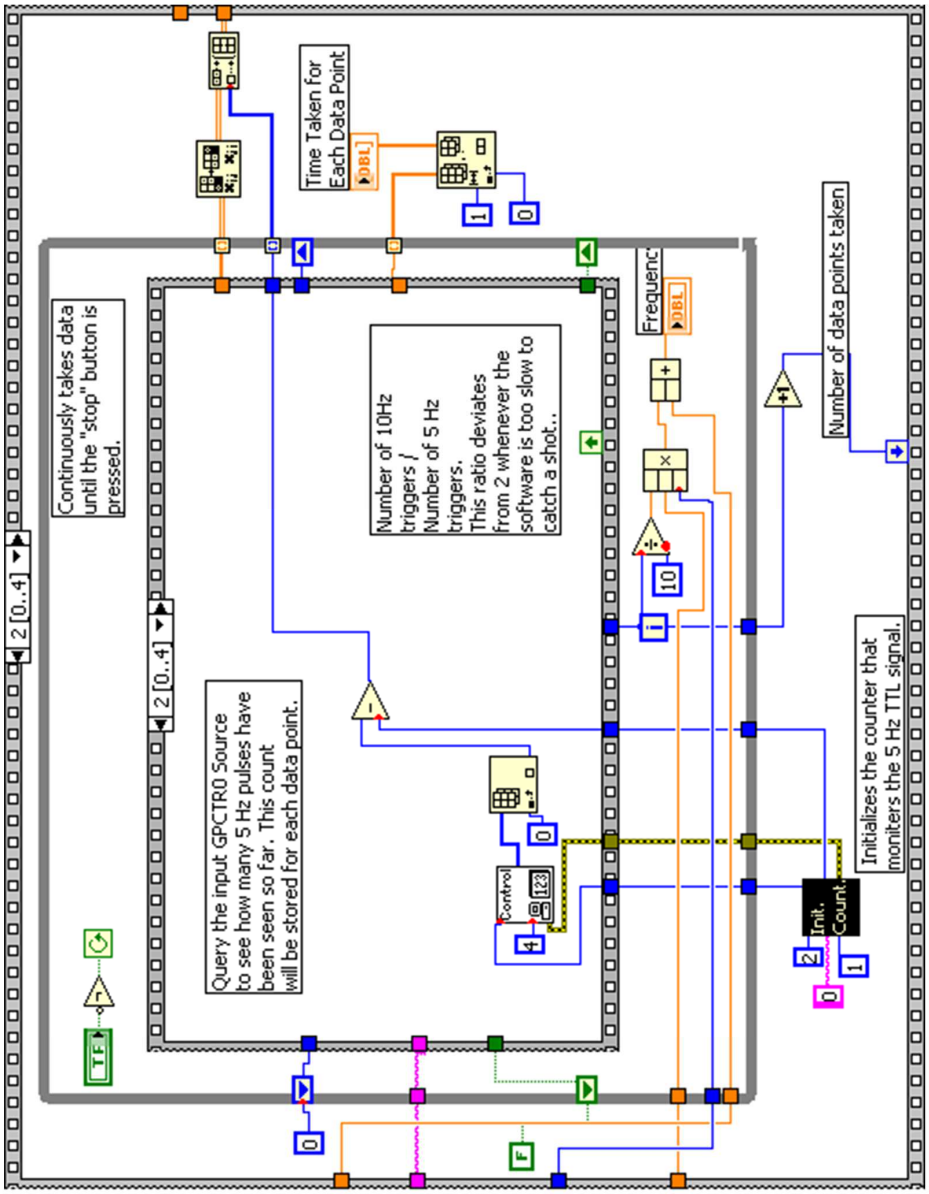

IR Scan ... continued

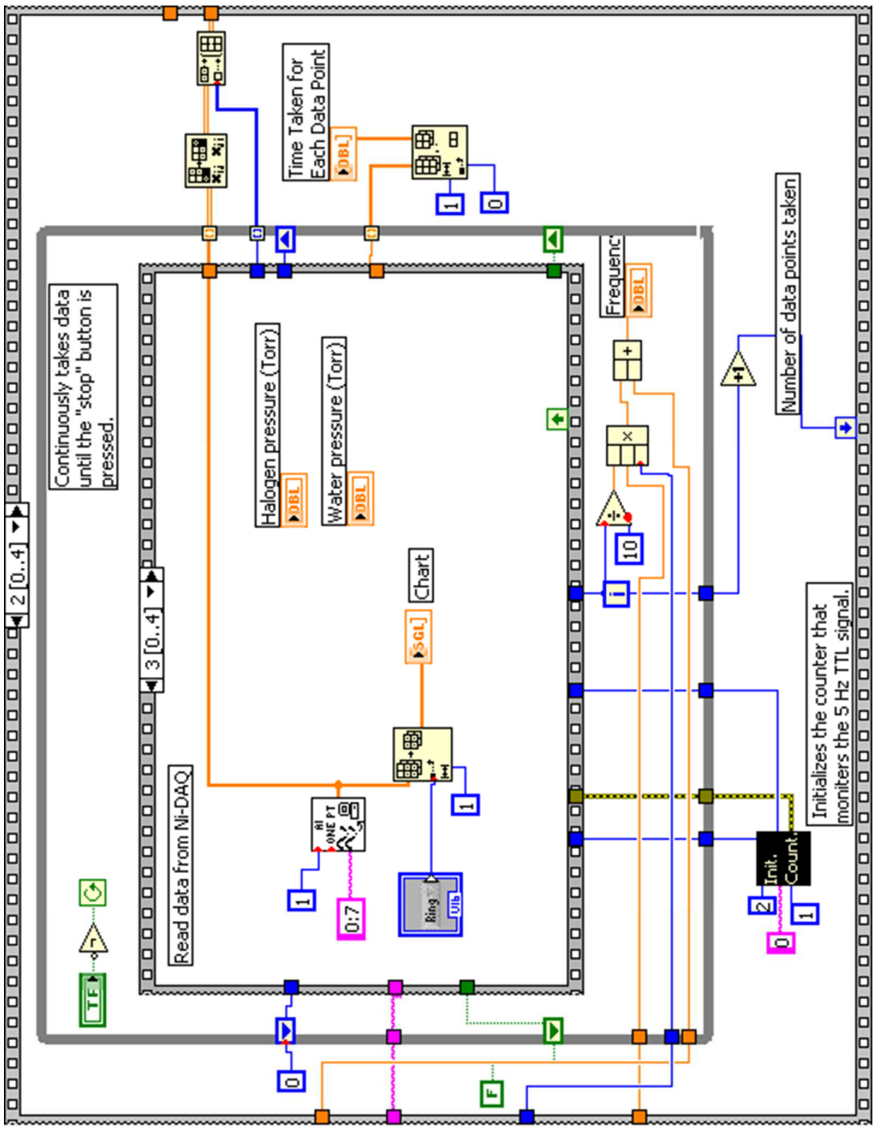

IR Scan

... continued

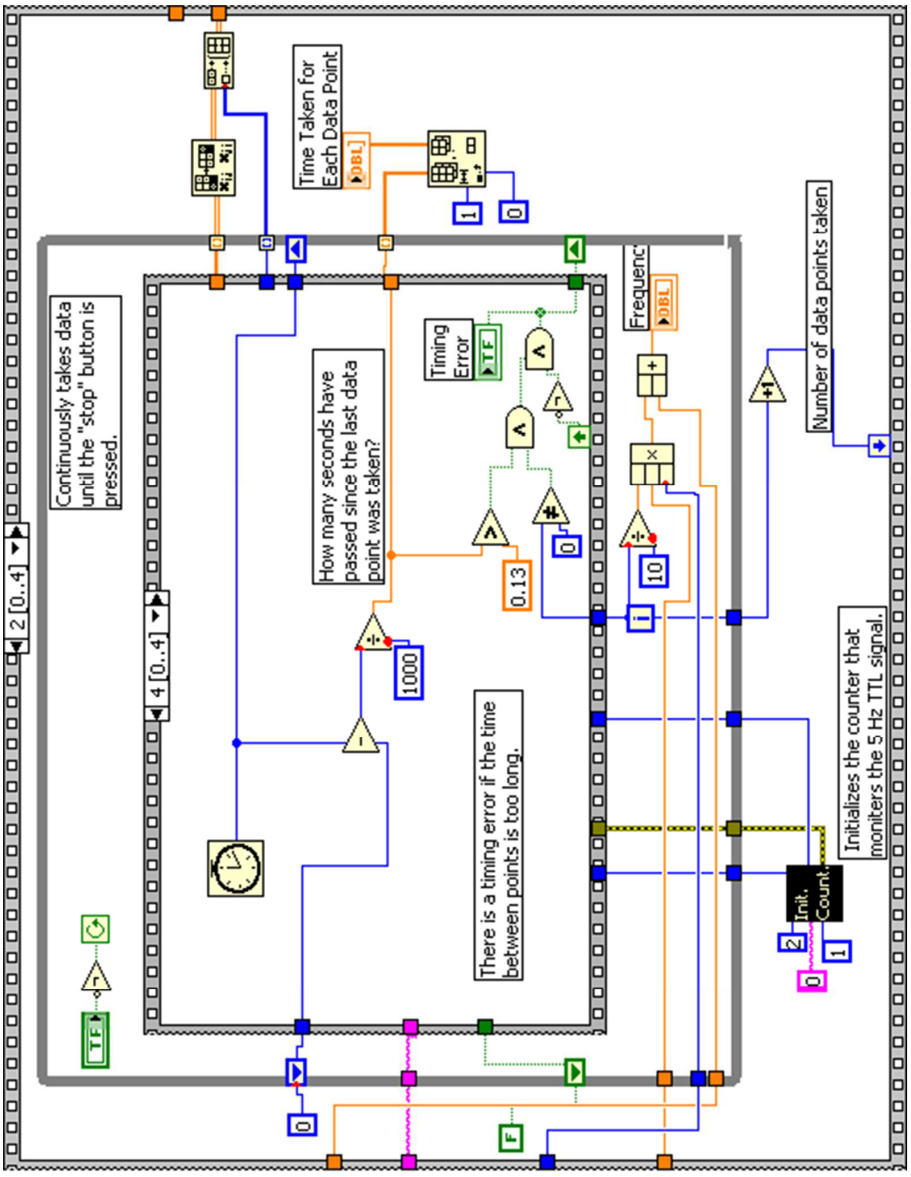

IR Scan

… continued

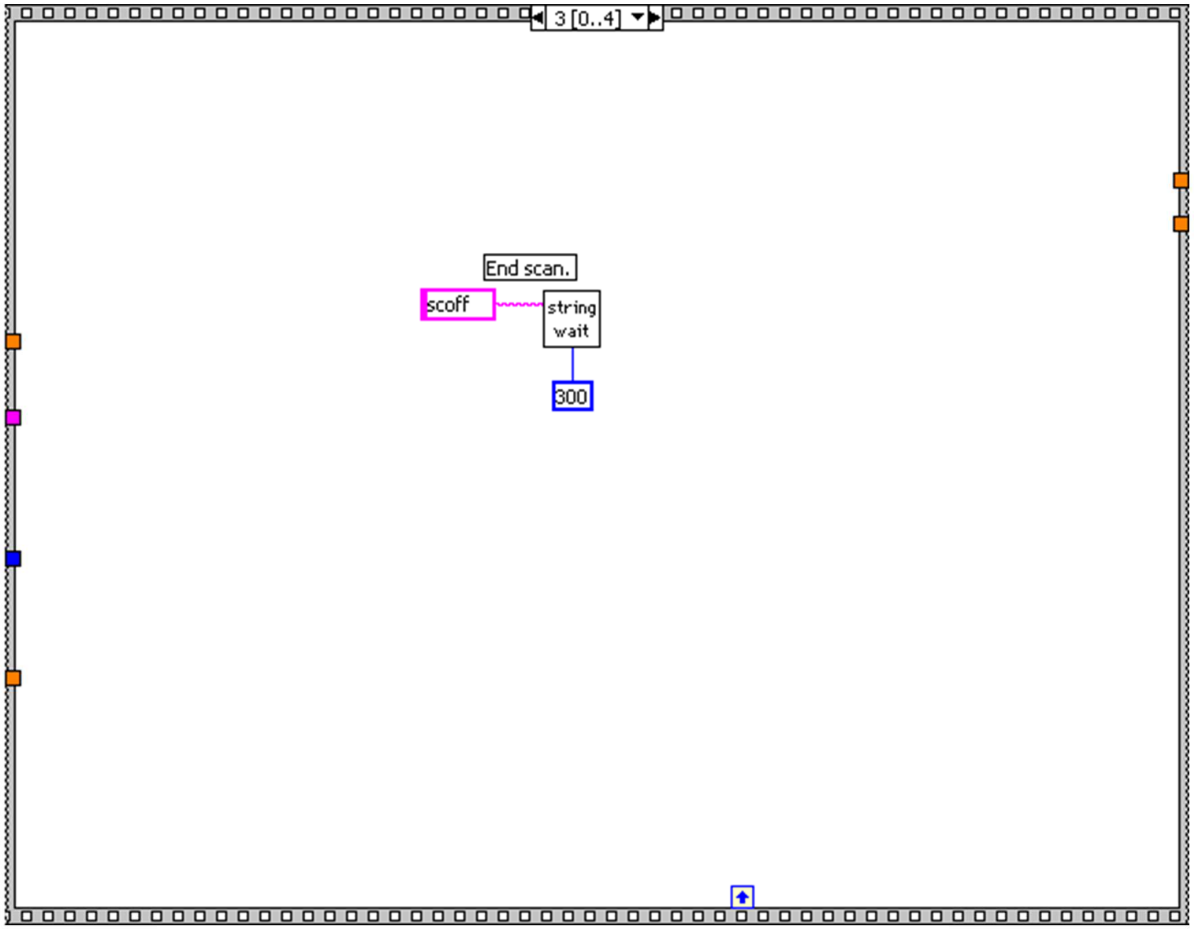

IR Scan ... continued

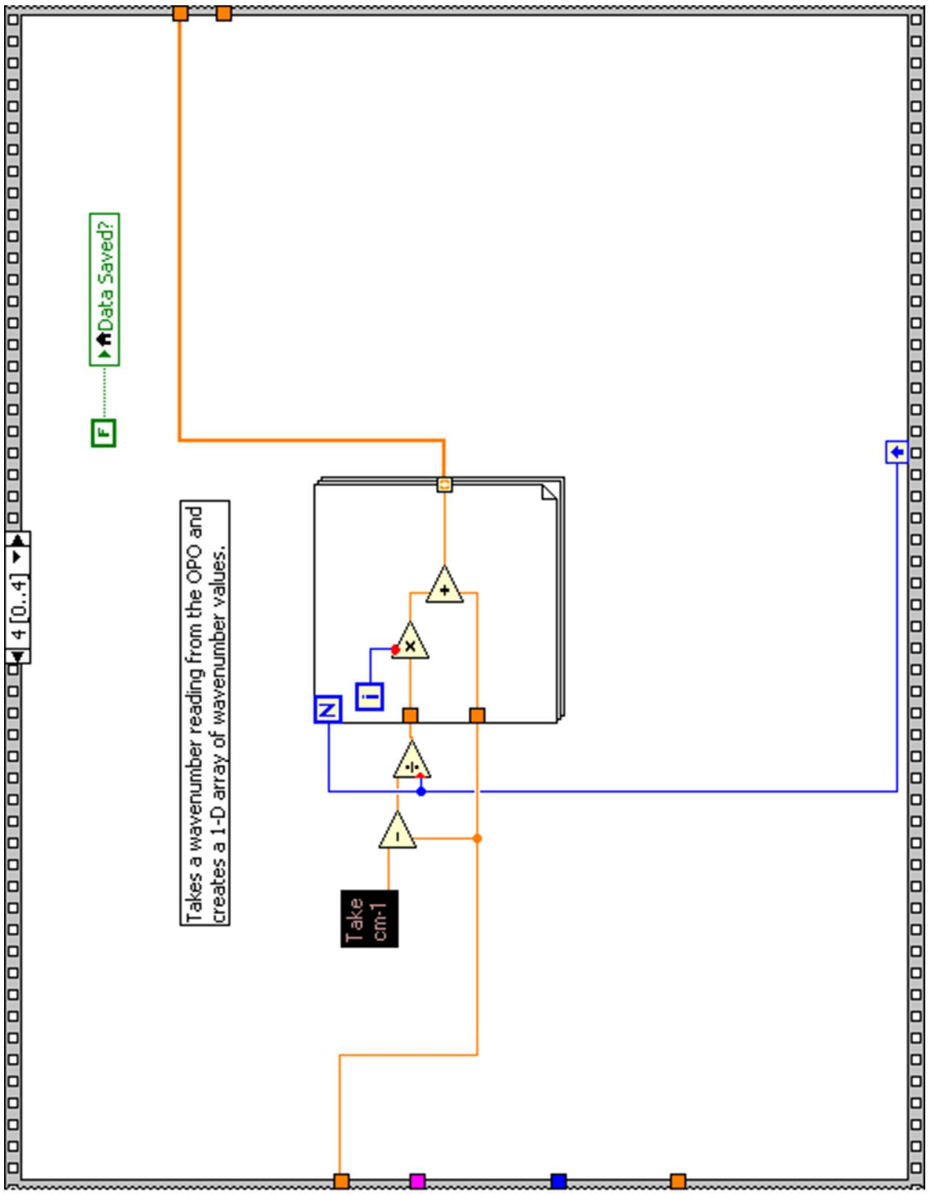

Initialize Counter.vi

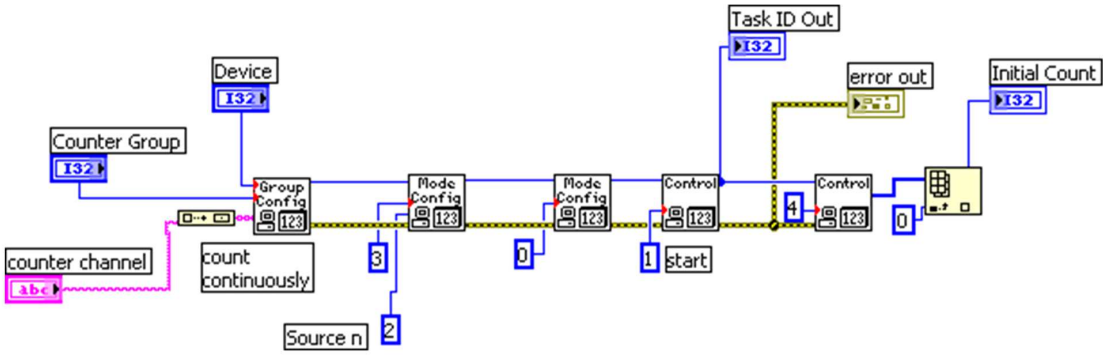

Waiter.vi

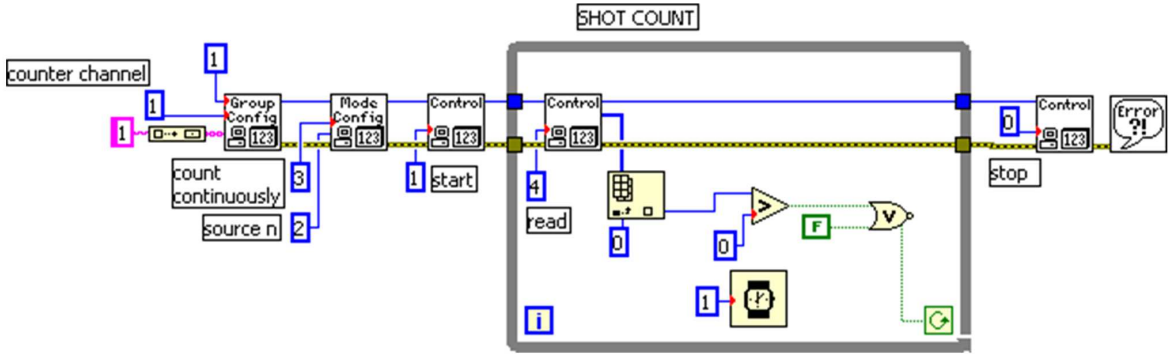

UV Scan

UV scan.vi

Front panel

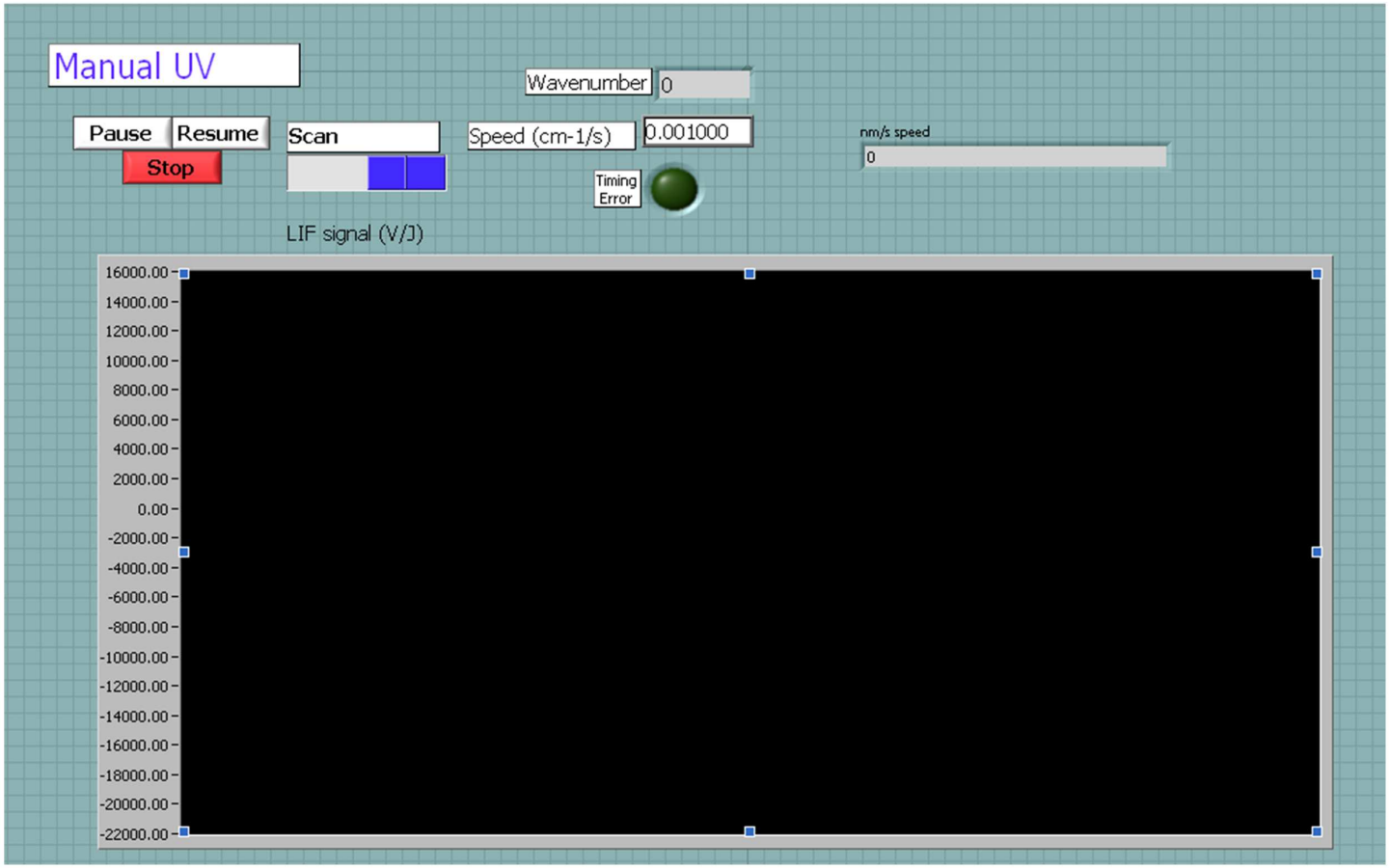

UV scan.vi

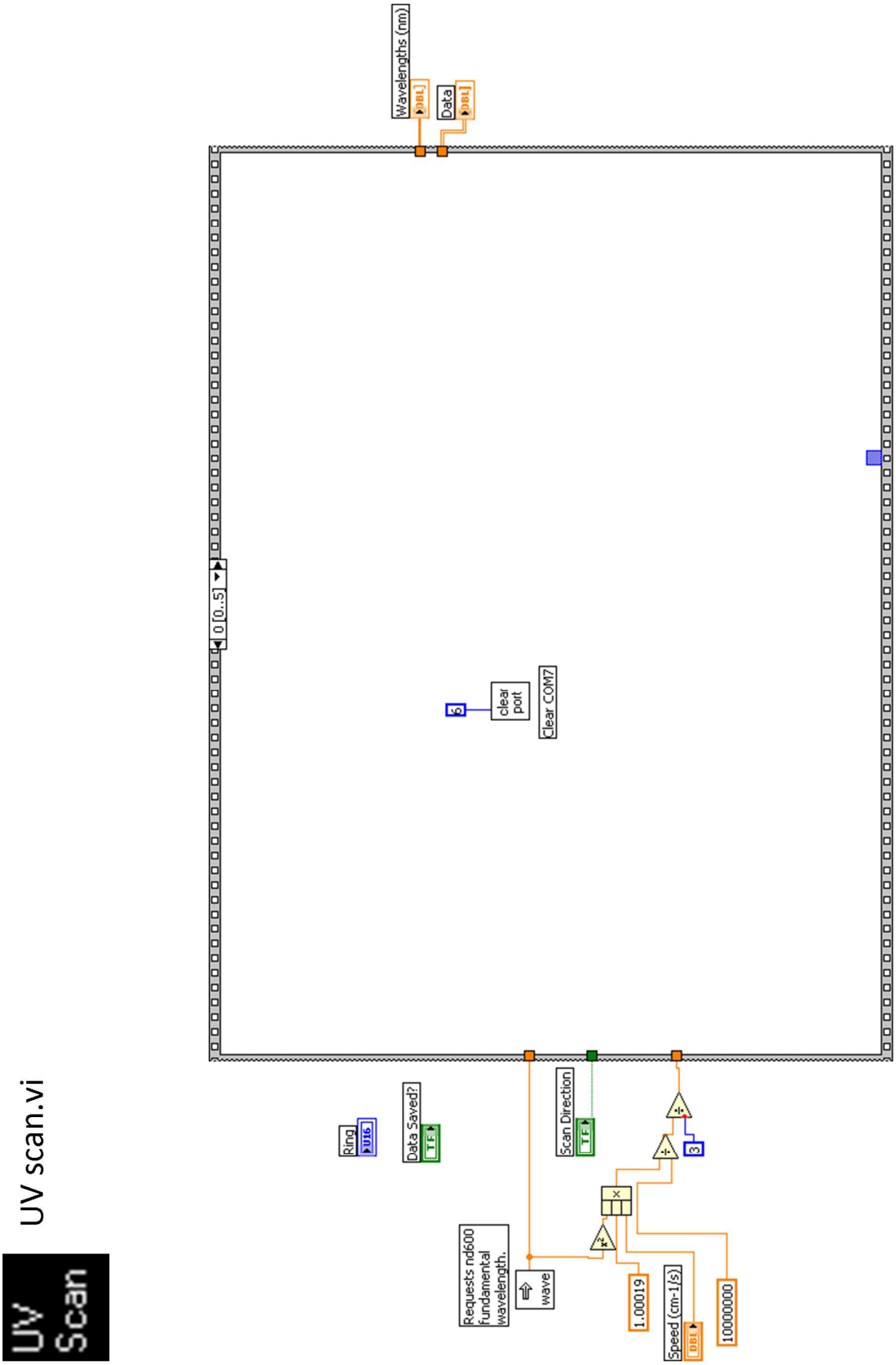
UV Scan
Wavelengths (nm)
Data
0 [0..5]
6
clear port
Clear COM7
Ring
Data Saved?
Scan Direction
Requests nd600 fundamental wavelength.
wave
1.00019
Speed (cm-1/s)
10000000
3

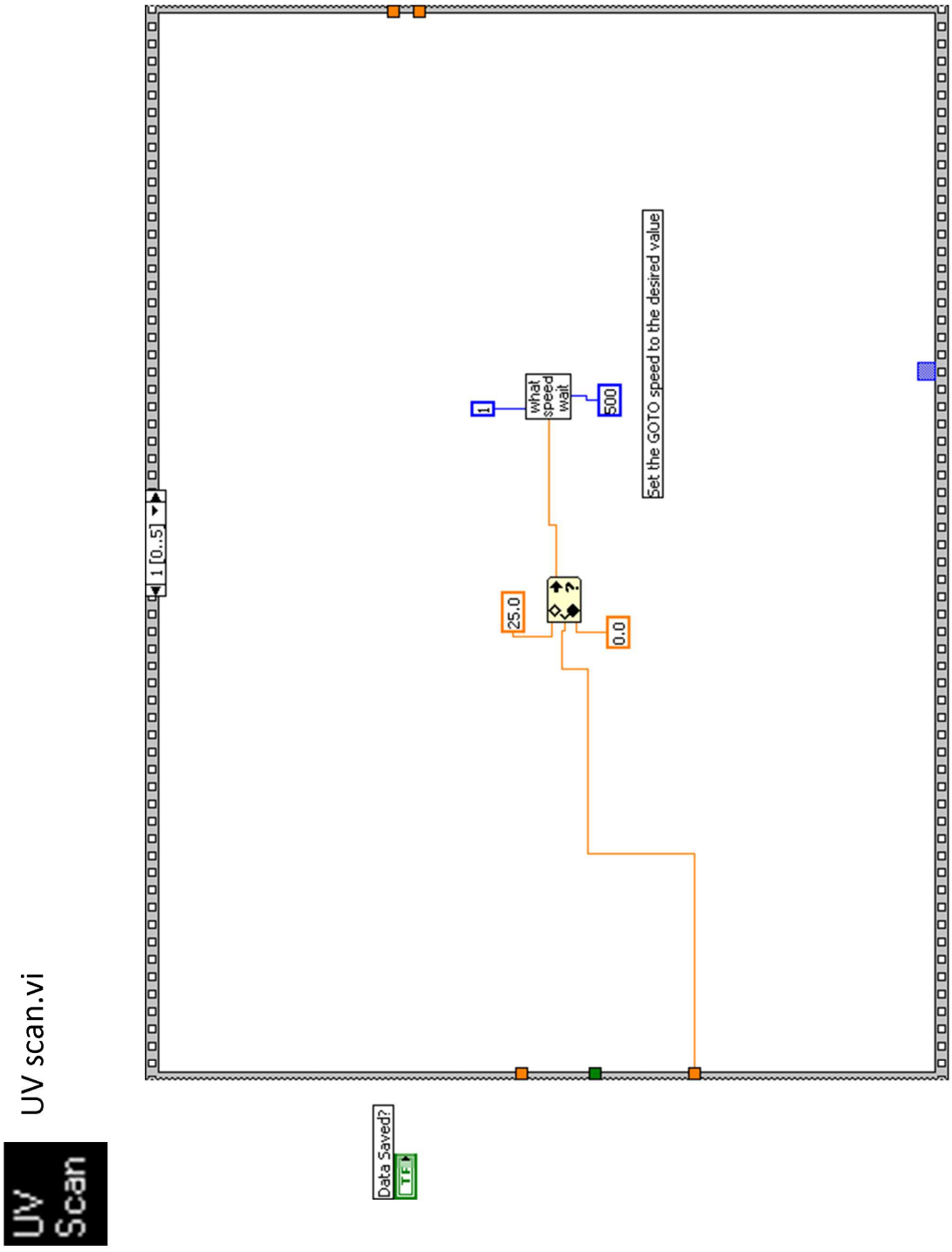
UV Scan
UV scan.vi
Data Saved?
TF
1 [0..5]
Set the GOTO speed to the desired value
what speed wait
1
500
25.0
0.0

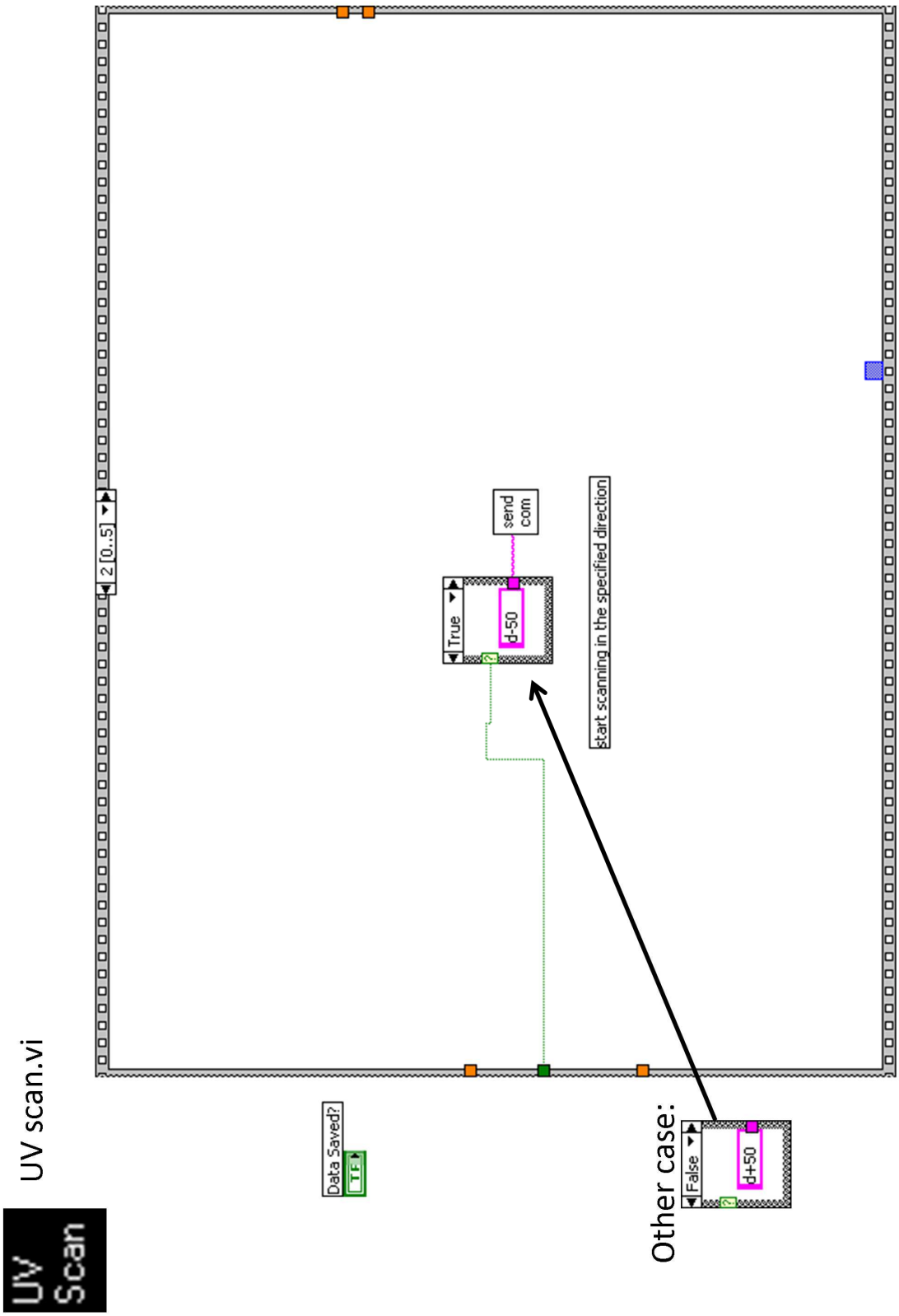
UV Scan
UV scan.vi
2 [0..5]
send com
True
d-50
start scanning in the specified direction
Data Saved?
TF
Other case:
False
d+50

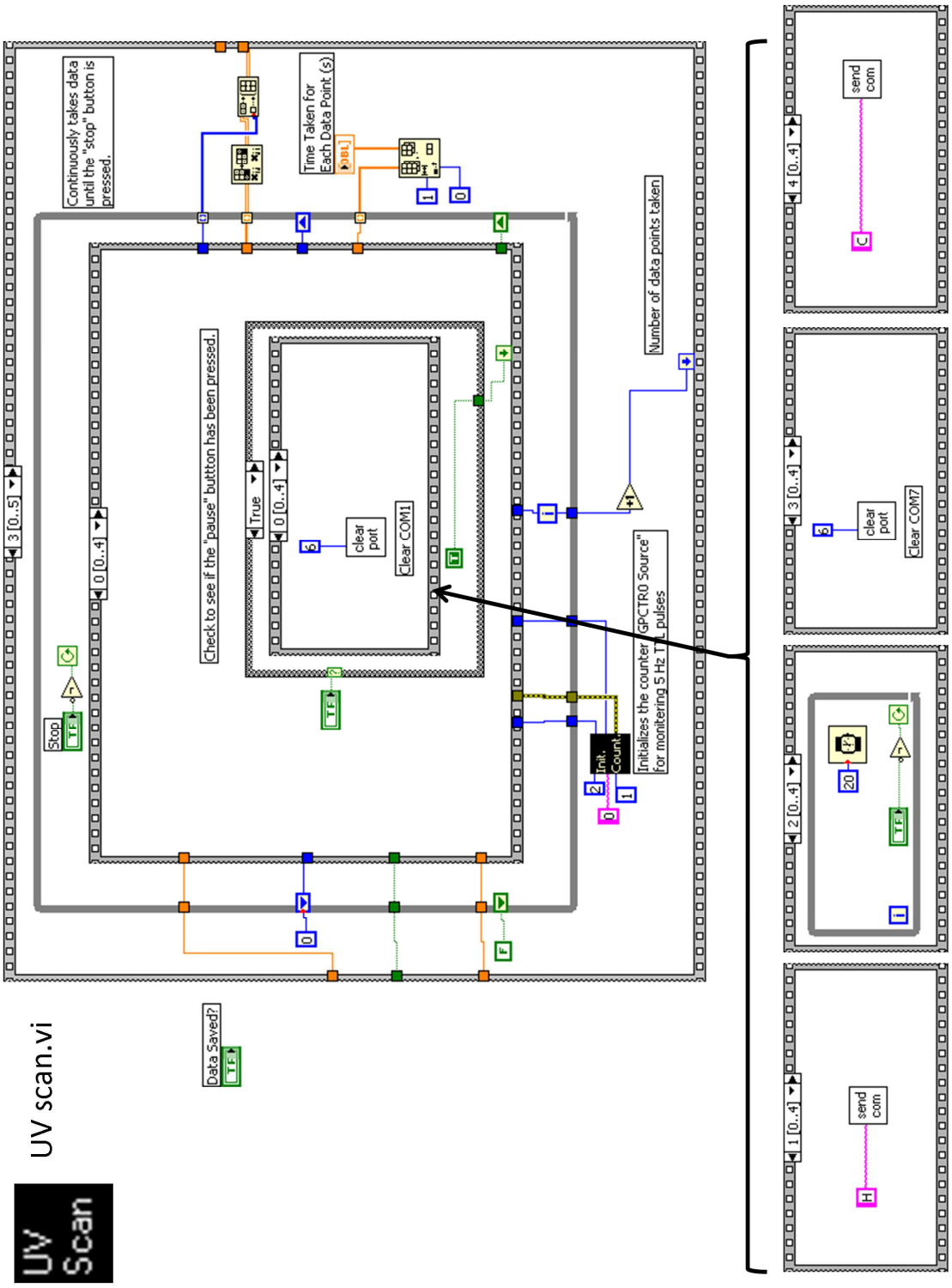
UV Scan
UV scan.vi
Continuously takes data until the "stop" button is pressed.
Time Taken for Each Data Point (s)
Check to see if the "pause" button has been pressed.
True
clear port
Clear COM1
Number of data points taken
Initializes the counter "GPCTR0 Source" for monitering 5 Hz TTL pulses
Init. Count
Stop
Data Saved?
send com
clear port
Clear COM7
20

UV scan.vi

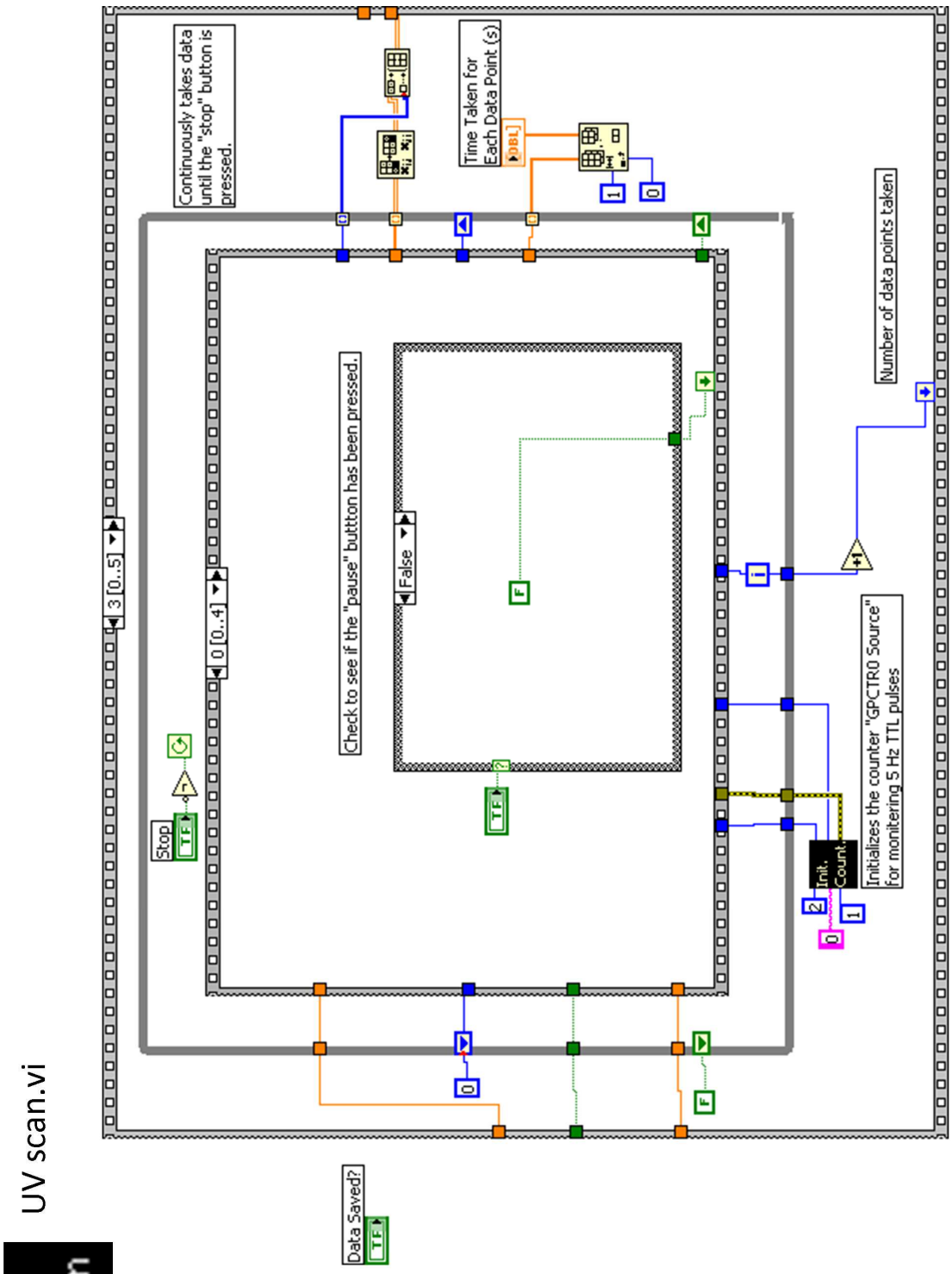
UV Scan
Continuously takes data until the "stop" button is pressed.
Time Taken for Each Data Point (s)
DBL
Number of data points taken
Check to see if the "pause" buttton has been pressed.
False
Stop
TF
Initializes the counter "GPCTR0 Source" for monitering 5 Hz TTL pulses
Init.
Count
Data Saved?
3 [0..5]
0 [0..4]

UV scan.vi

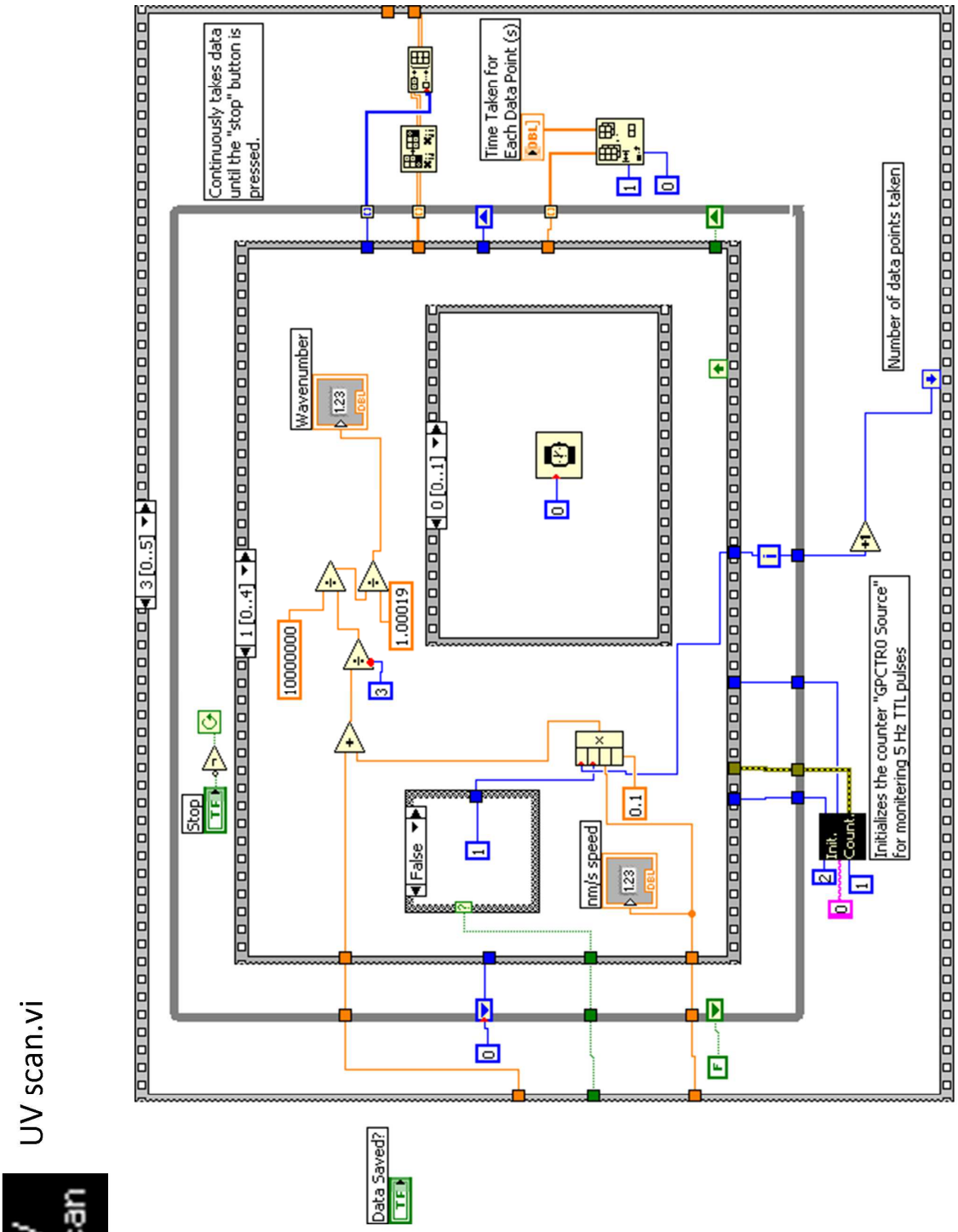
UV Scan
Continuously takes data until the "stop" button is pressed.
Time Taken for Each Data Point (s)
Number of data points taken
Wavenumber
Stop
10000000
1.00019
0.1
nm/s speed
False
Init. Count
Initializes the counter "GPCTR0 Source" for monitering 5 Hz TTL pulses
Data Saved?

UV scan.vi

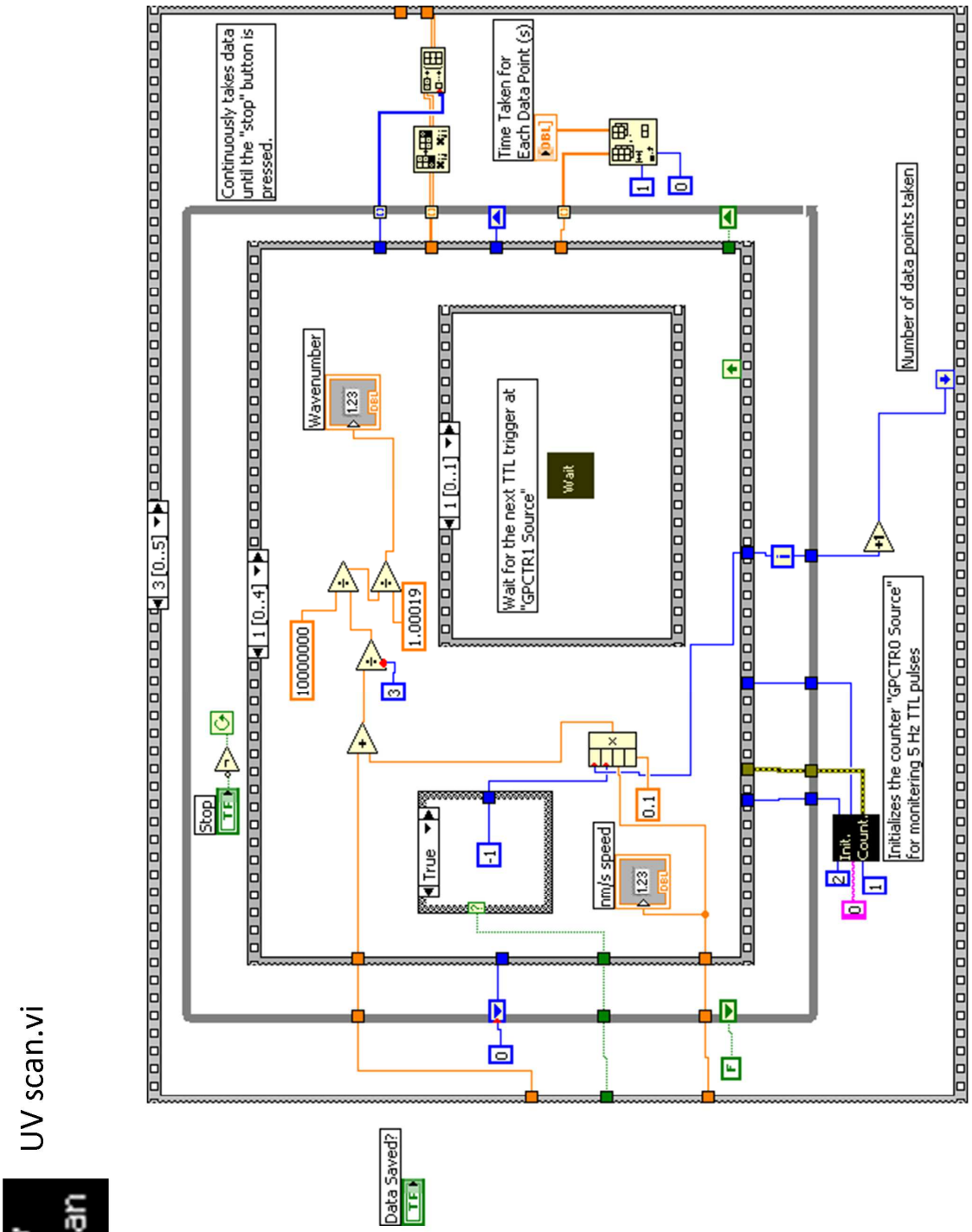
UV Scan
Continuously takes data until the "stop" button is pressed.
Time Taken for Each Data Point (s)
Number of data points taken
Wavenumber
Wait for the next TTL trigger at "GPCTR1 Source"
Wait
Stop
True
nm/s speed
Init. Count
Initializes the counter "GPCTR0 Source" for monitering 5 Hz TTL pulses
Data Saved?
10000000
1.00019
0.1

UV Scan

UV scan.vi

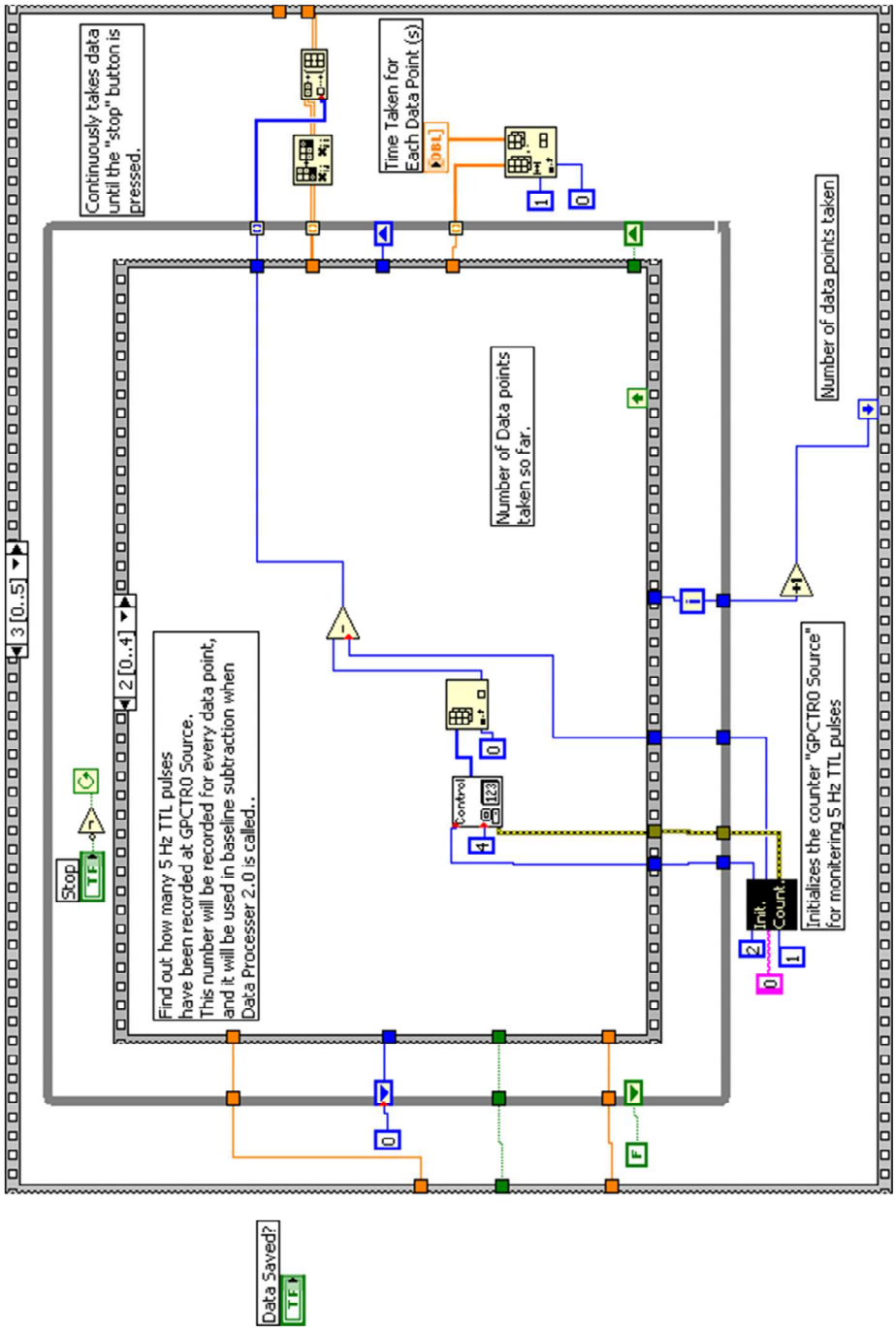

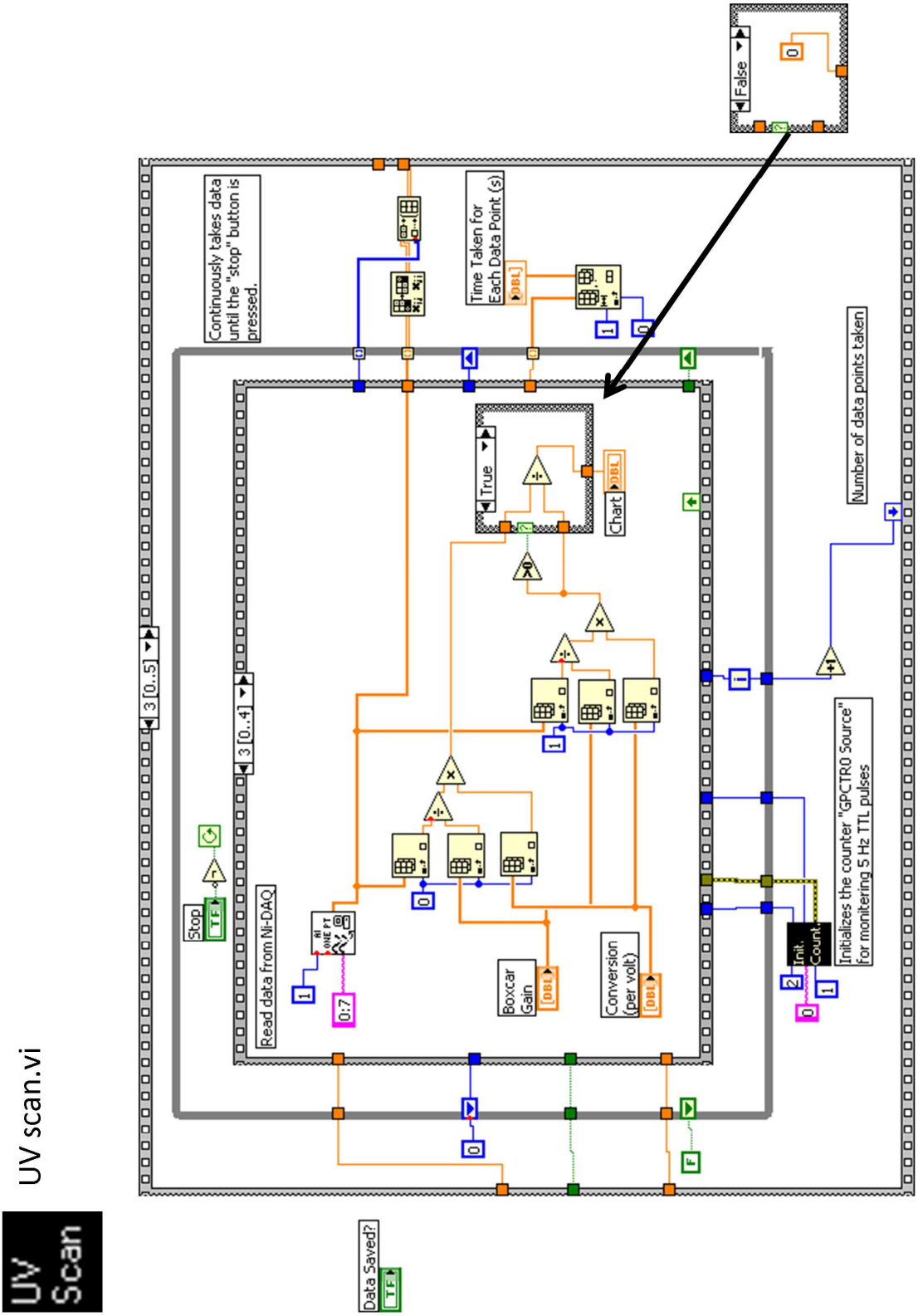
UV Scan
UV scan.vi
Continuously takes data until the "stop" button is pressed.
Time Taken for Each Data Point (s)
Number of data points taken
Stop
Read data from NI-DAQ
Boxcar Gain
Conversion (per volt)
Chart
Initializes the counter "GPCTR0 Source" for monitering 5 Hz TTL pulses
Init. Count
Data Saved?
True
False

UV Scan

UV scan.vi

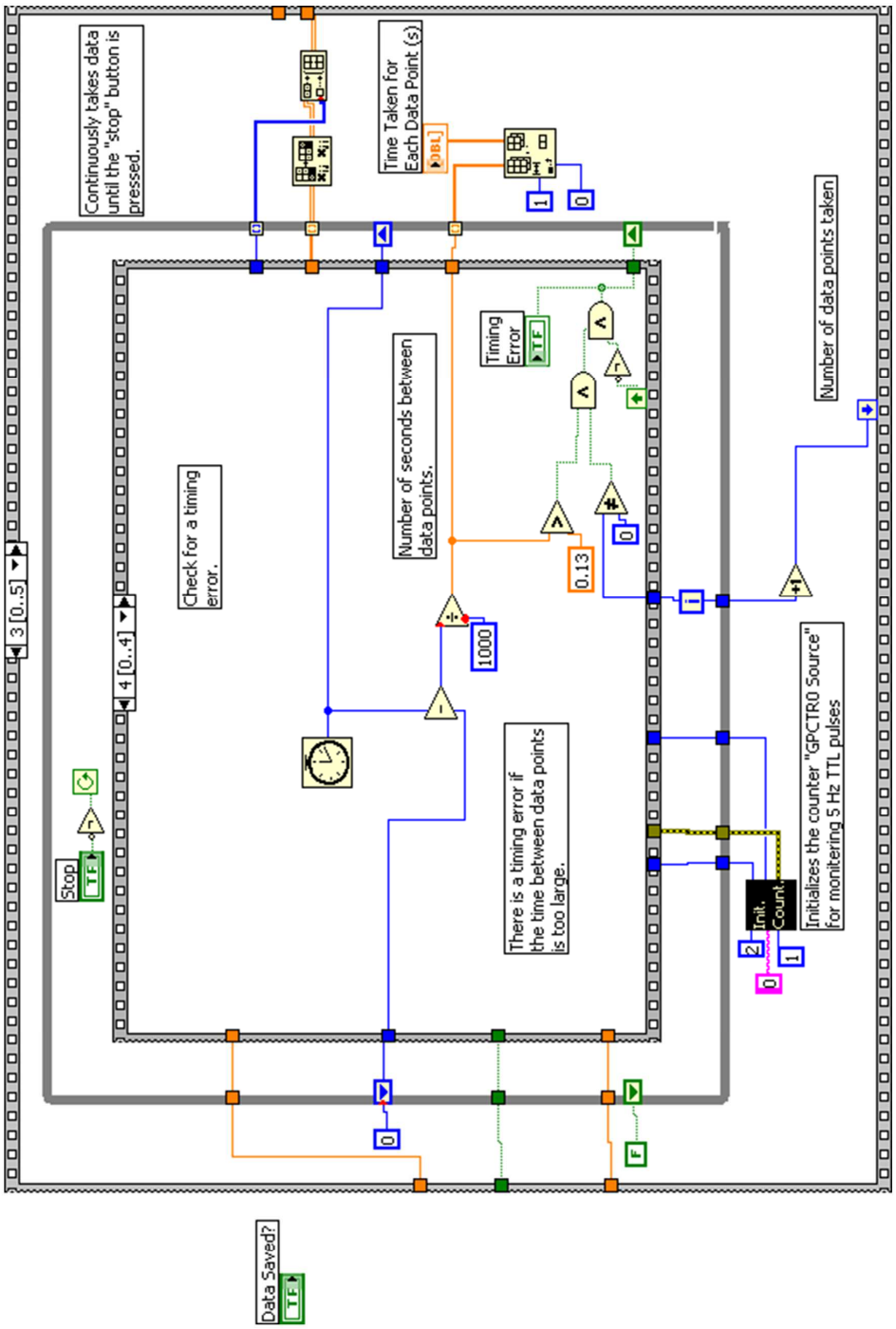

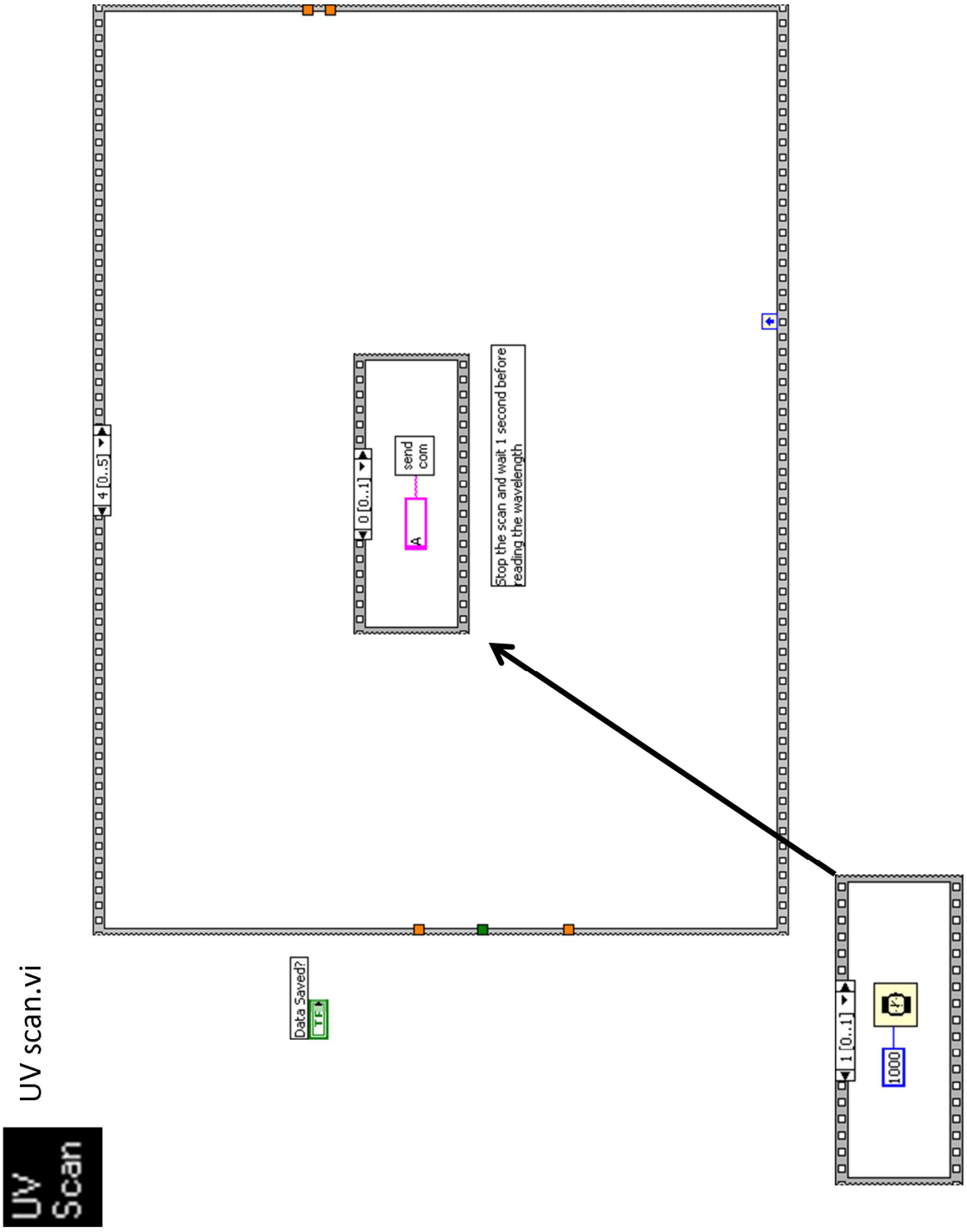
UV Scan
UV scan.vi
Data Saved?
TF
4 [0..5]
0 [0..1]
send com
A
Stop the scan and wait 1 second before reading the wavelength
1 [0..1]
1000

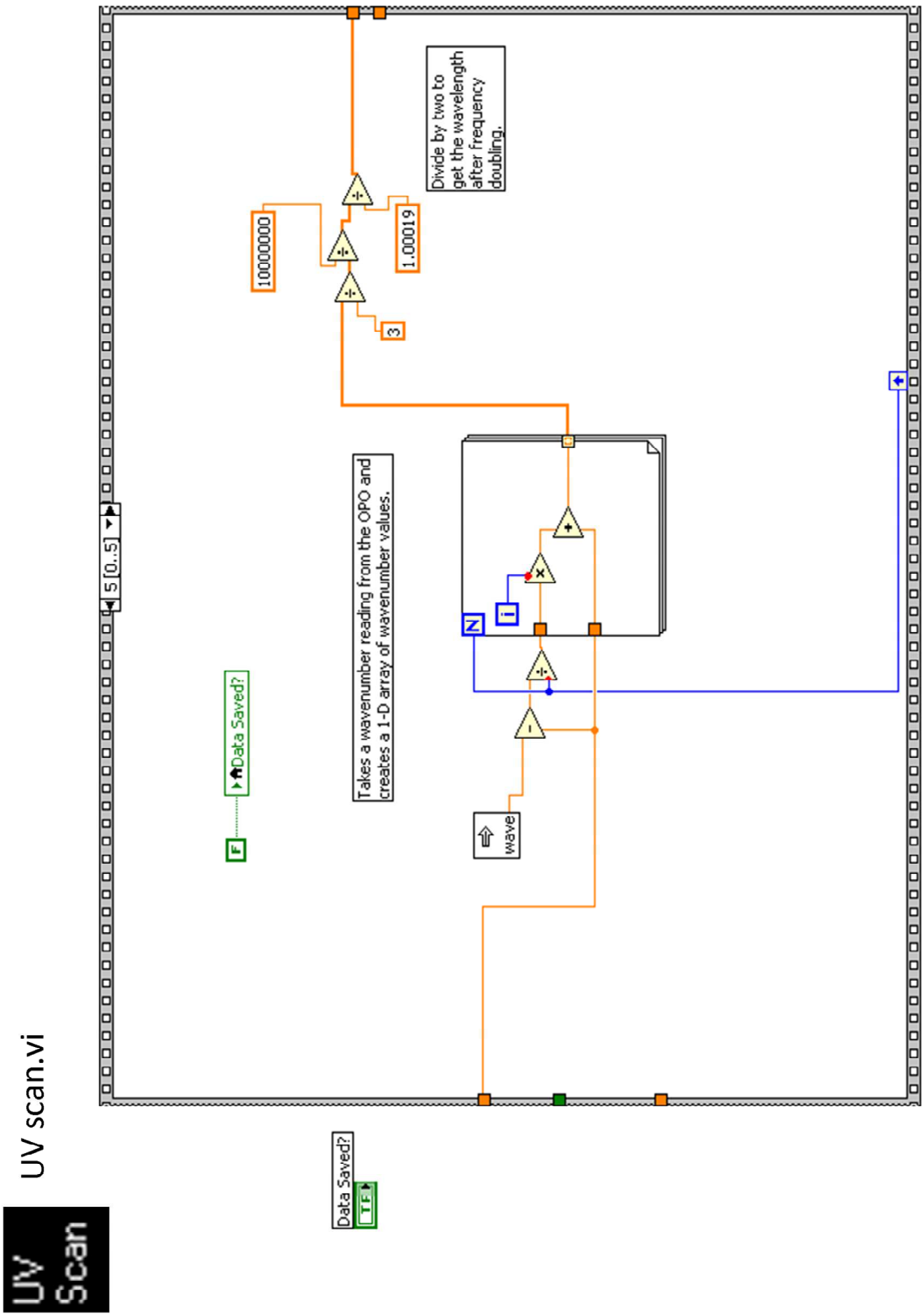
UV Scan
UV scan.vi
Data Saved?
TF
S [0..5]
Data Saved?
F
Takes a wavenumber reading from the OPO and creates a 1-D array of wavenumber values.
wave
N
i
Divide by two to get the wavelength after frequency doubling.
10000000
1.00019
3

Auto Delay

Delay Scan.vi

Front panel

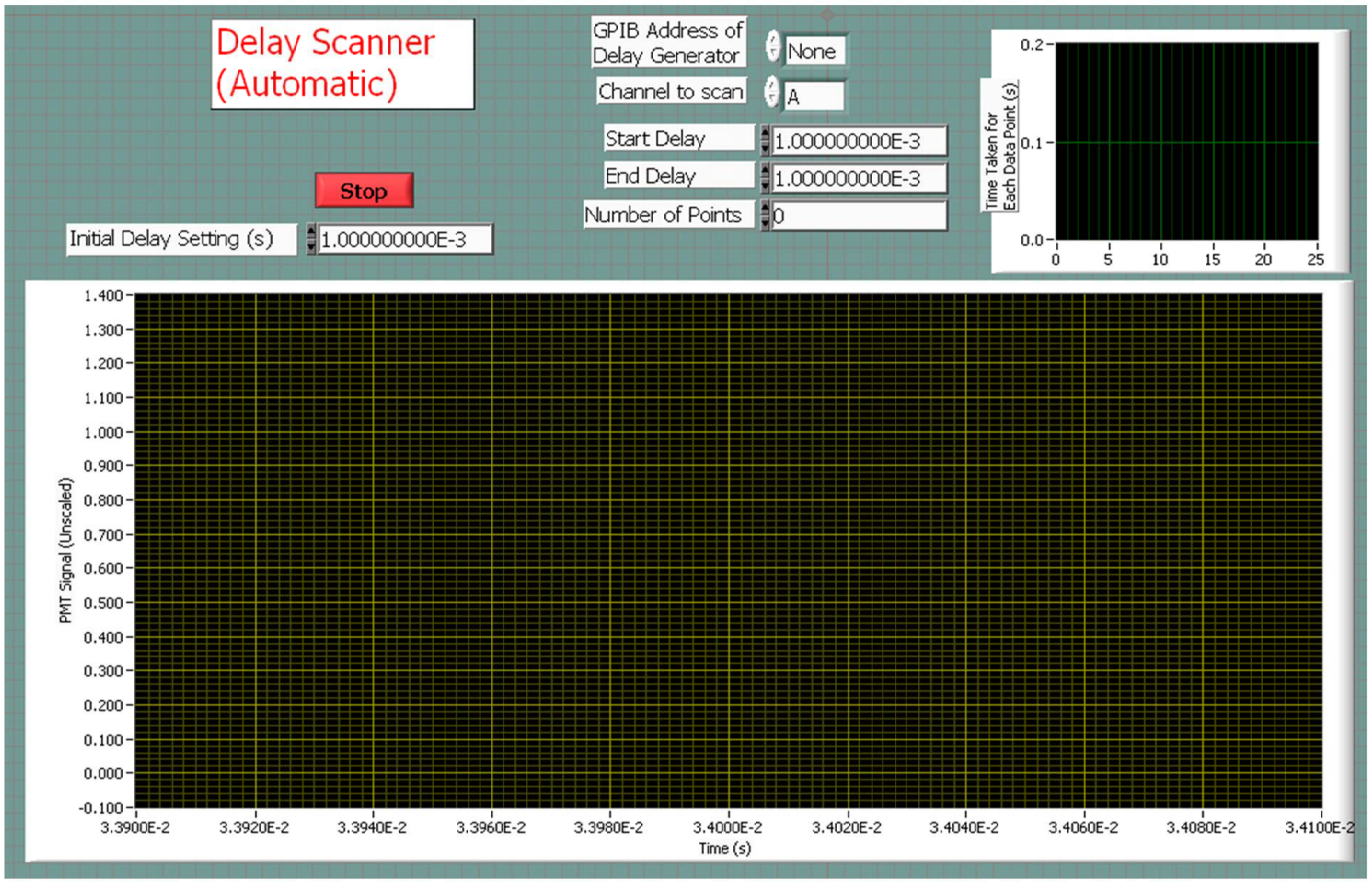

Auto Delay

Delay Scan.vi

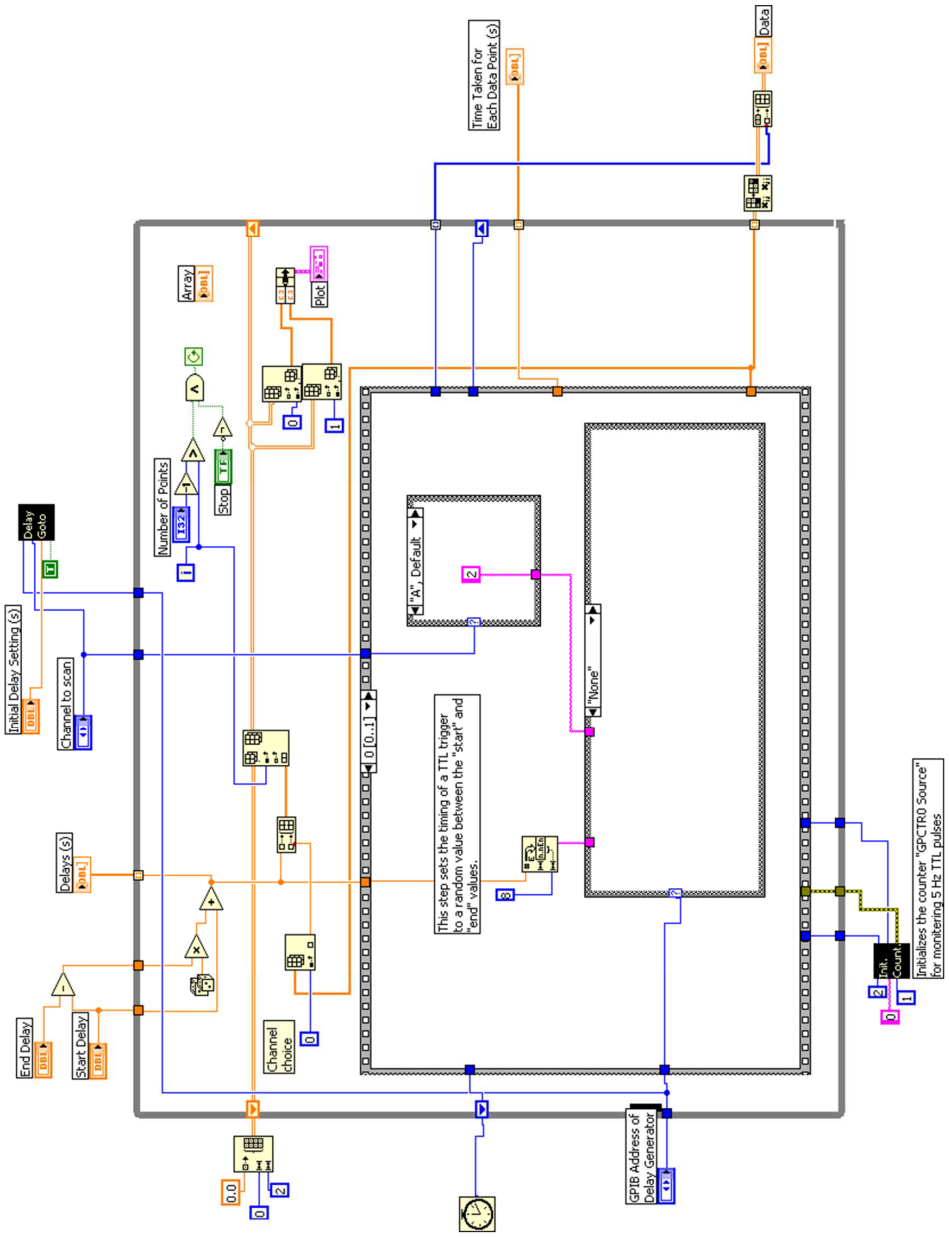

Auto Delay

Delay Scan.vi

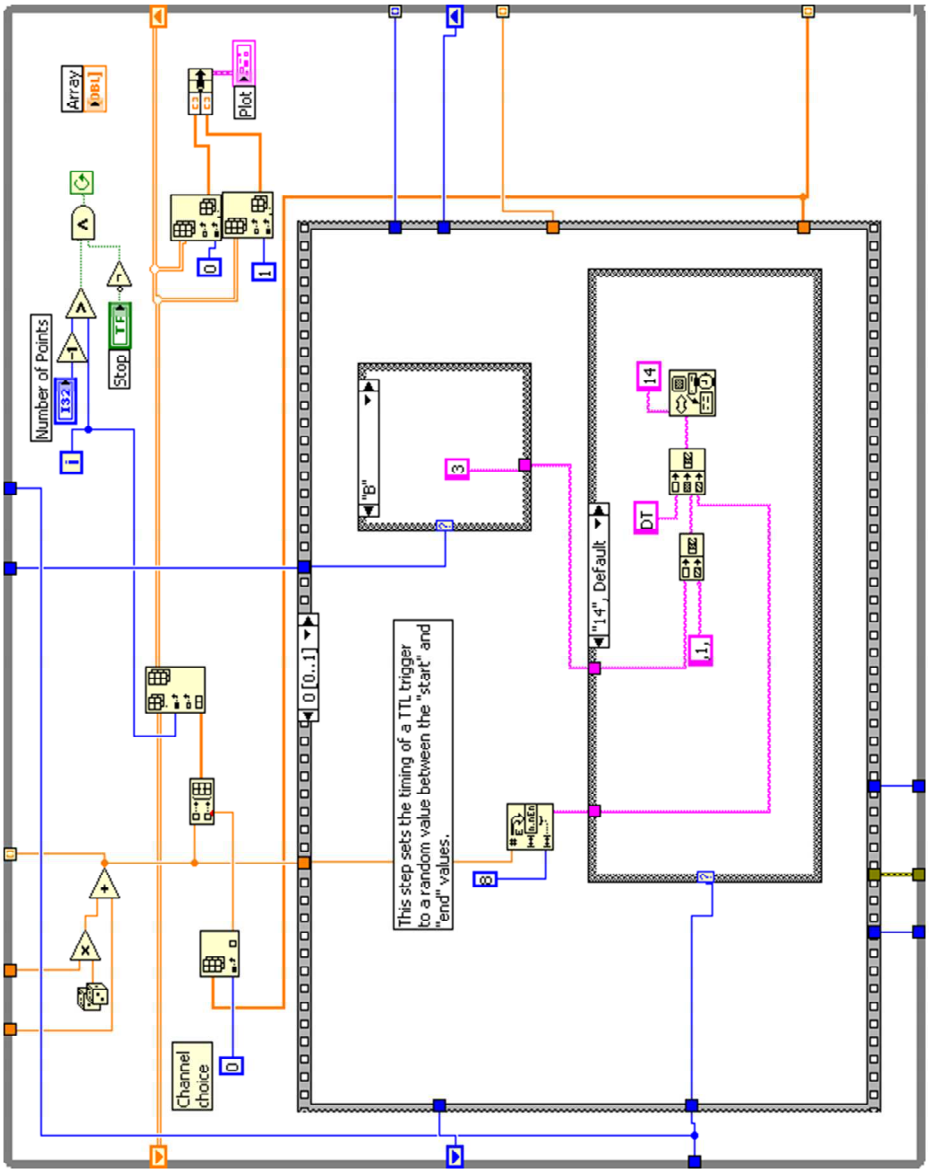

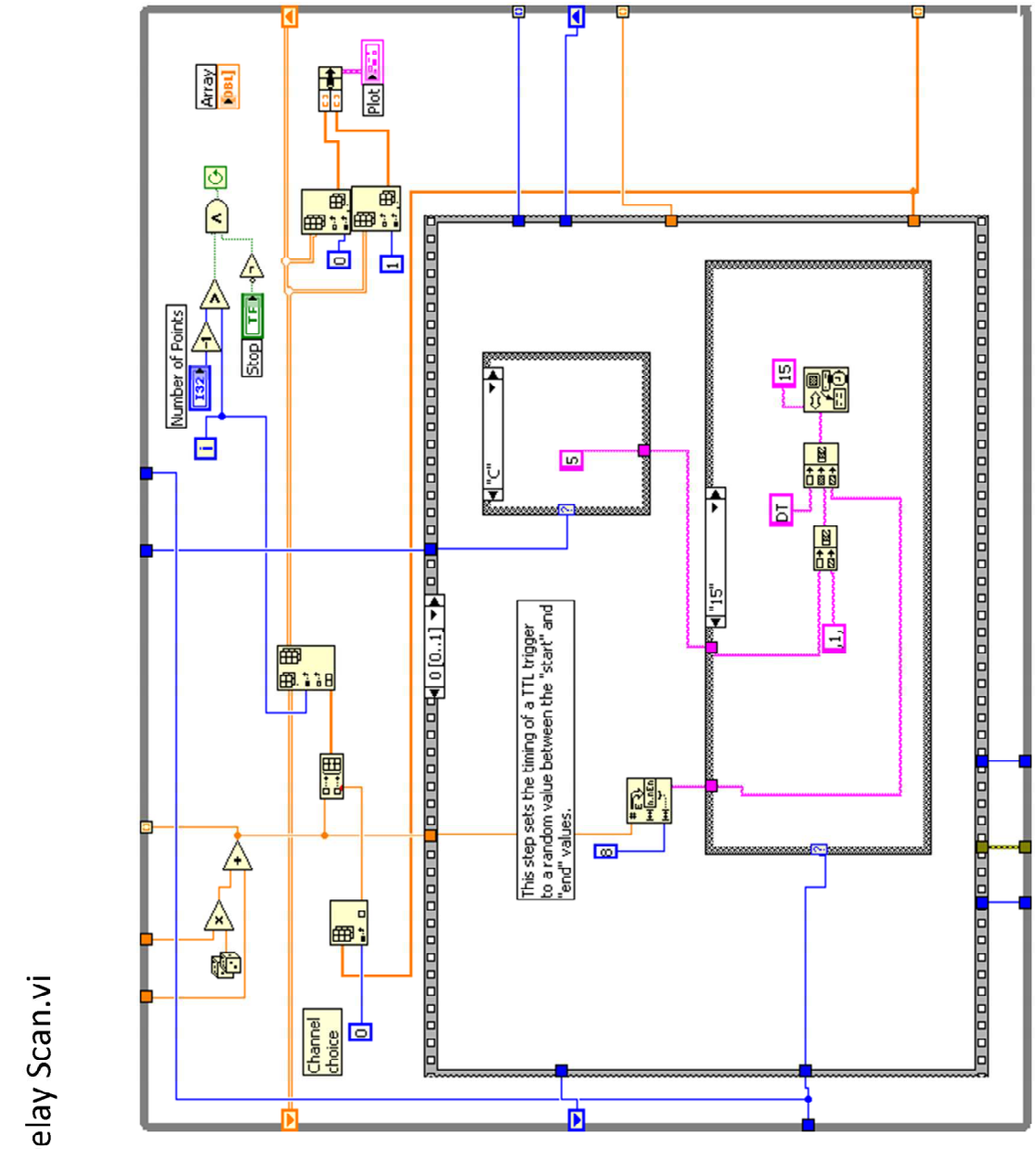
Auto Delay
Delay Scan.vi
Array
Plot
Number of Points
Stop
Channel choice
This step sets the timing of a TTL trigger to a random value between the "start" and "end" values.
"C"
"15"
DT
15
5
0 [0..1]

Auto Delay

Delay Scan.vi

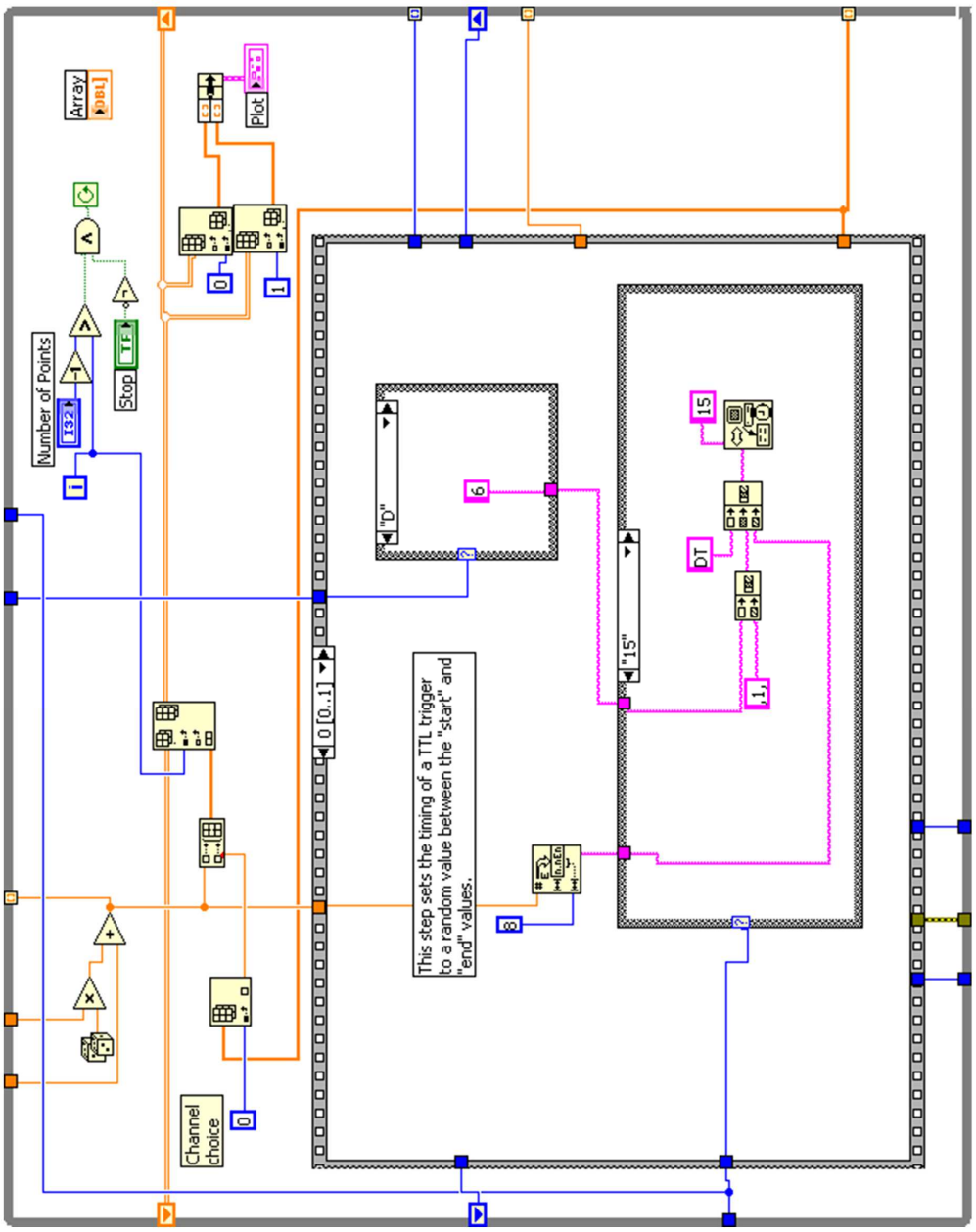

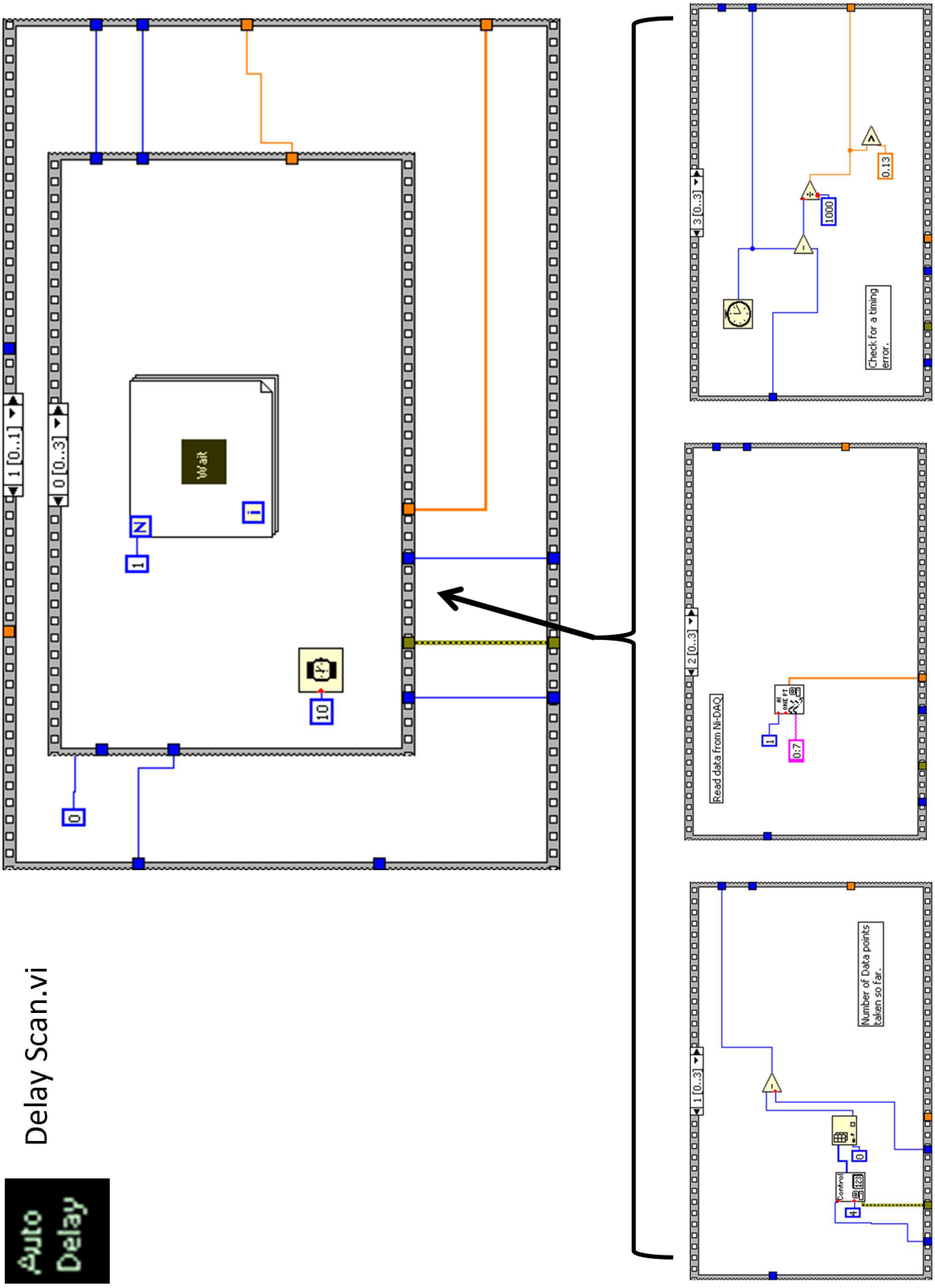
Auto Delay
Delay Scan.vi
Wait
Read data from NI-DAQ
Number of Data points taken so far.
Check for a timing error.

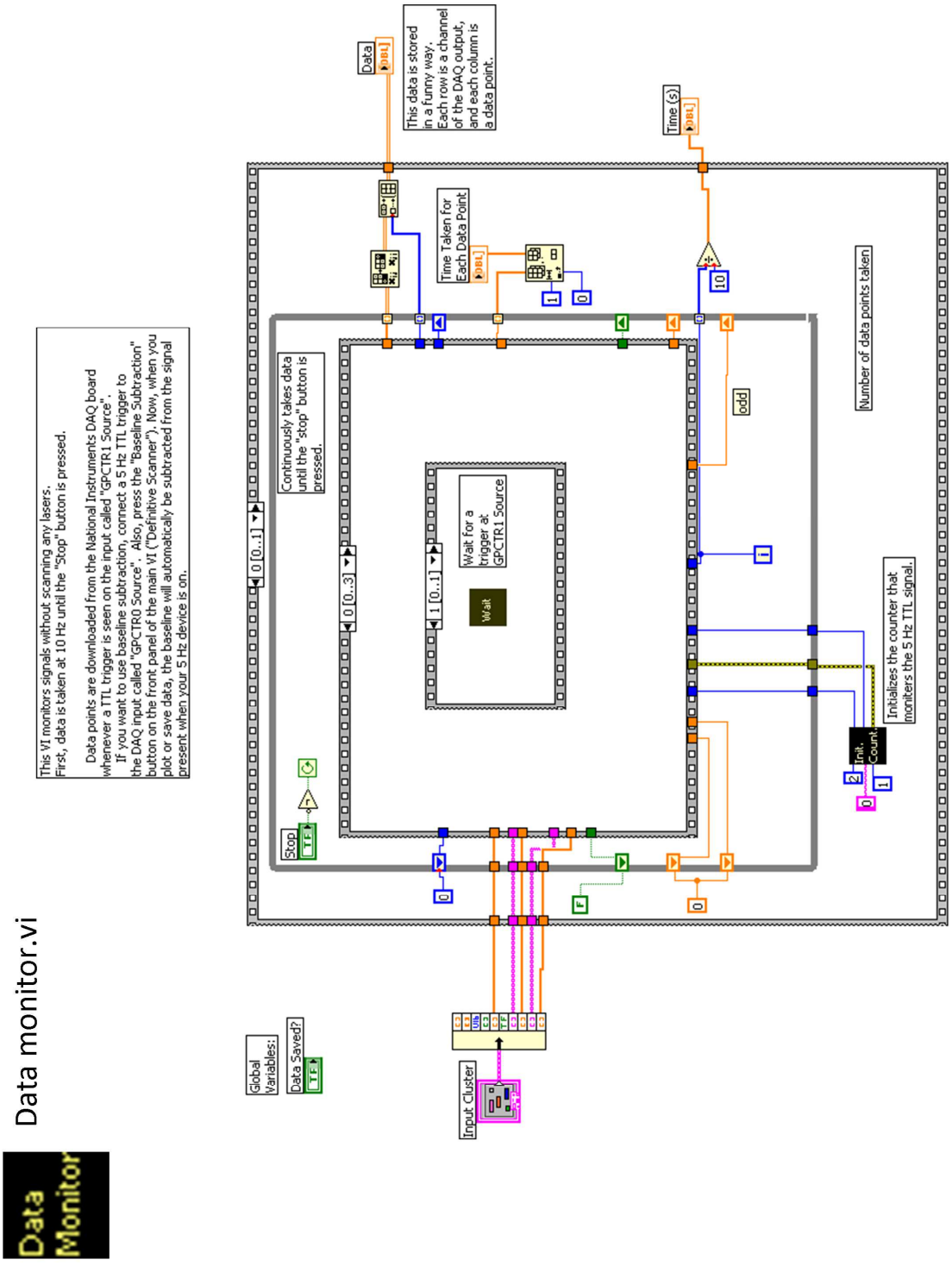
Data Monitor
Data monitor.vi
This VI monitors signals without scanning any lasers.
First, data is taken at 10 Hz until the "Stop" button is pressed.
Data points are downloaded from the National Instruments DAQ board whenever a TTL trigger is seen on the input called "GPCTR1 Source".
If you want to use baseline subtraction, connect a 5 Hz TTL trigger to the DAQ input called "GPCTR0 Source". Also, press the "Baseline Subtraction" button on the front panel of the main VI ("Definitive Scanner"). Now, when you plot or save data, the baseline will automatically be subtracted from the signal present when your 5 Hz device is on.
Data
This data is stored in a funny way. Each row is a channel of the DAQ output, and each column is a data point.
Time (s)
Time Taken for Each Data Point
Continuously takes data until the "stop" button is pressed.
Wait for a trigger at GPCTR1 Source
Wait
odd
Number of data points taken
Initializes the counter that moniters the 5 Hz TTL signal.
Init. Count
Stop
Global Variables:
Data Saved?
Input Cluster

Data monitor.vi inner sequence

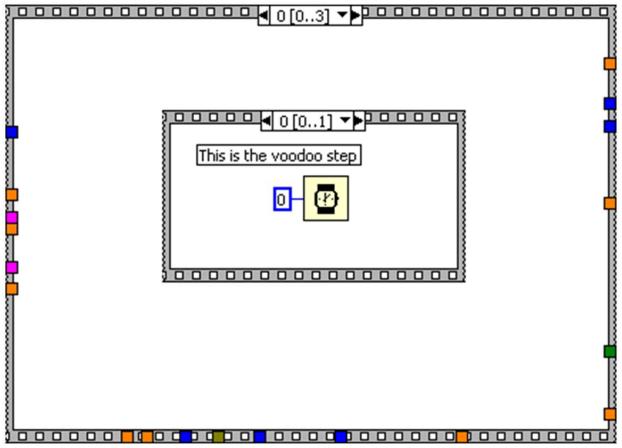

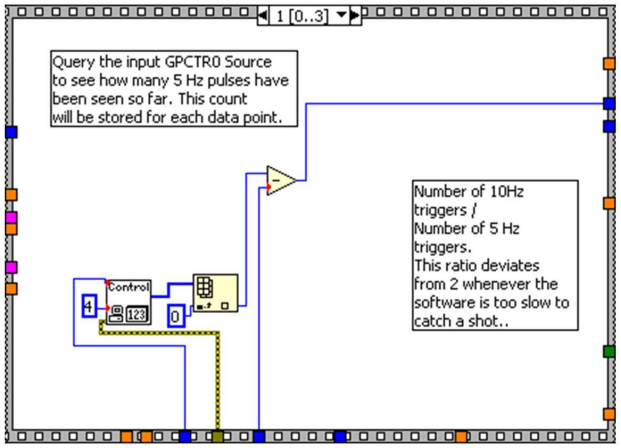

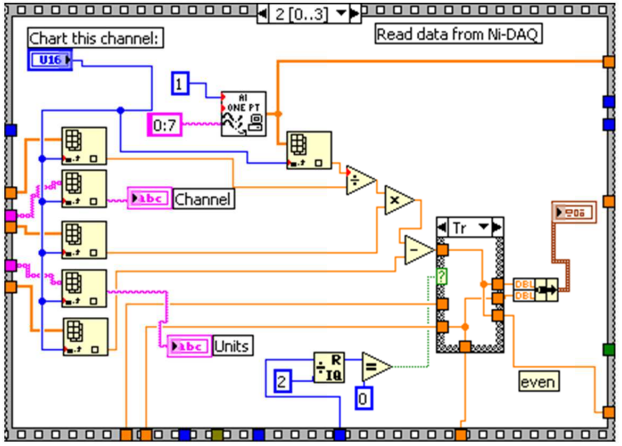

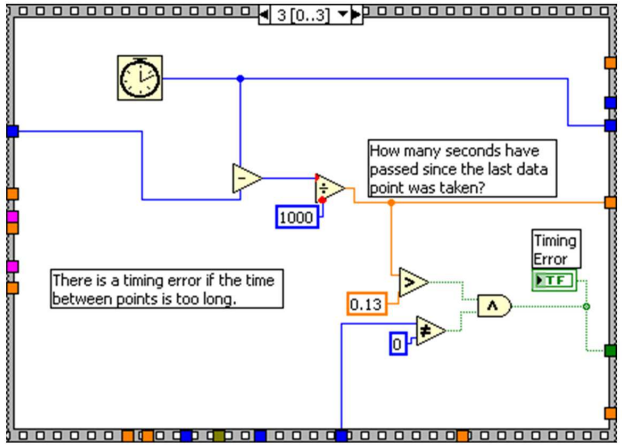

Data monitor.vi

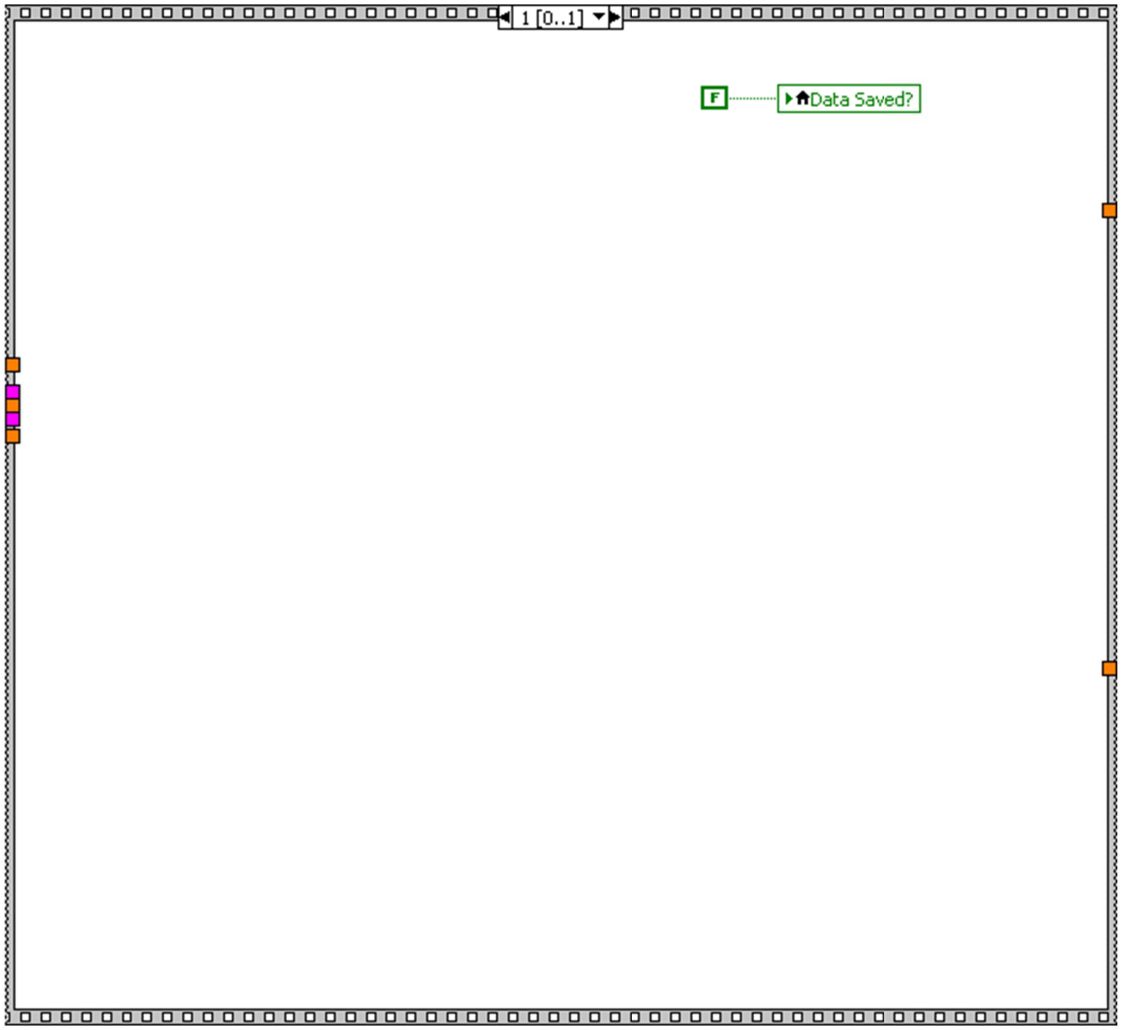

Statistics.vi

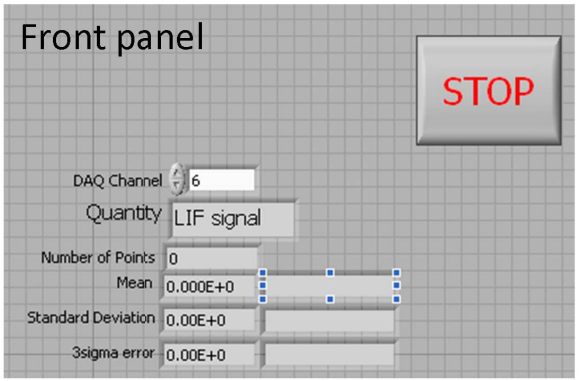

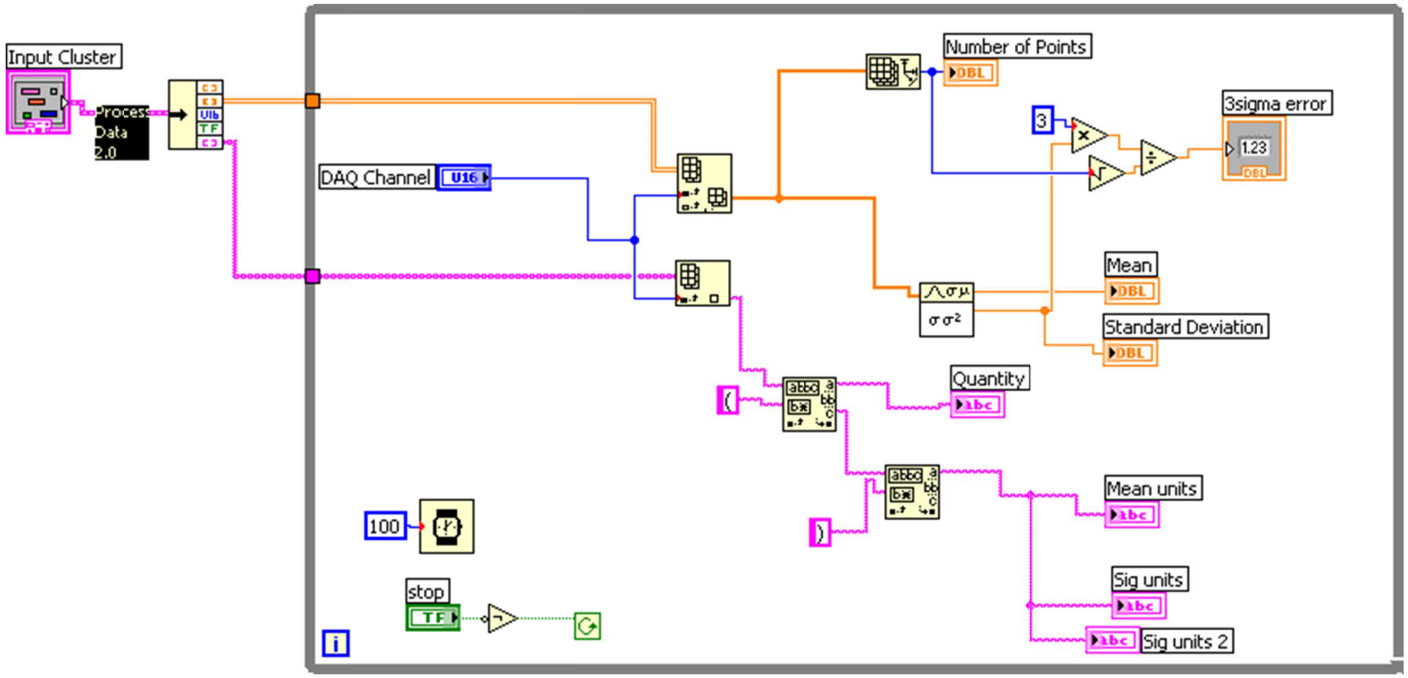

Process LIF data 2.0.vi (Truncated on the right)

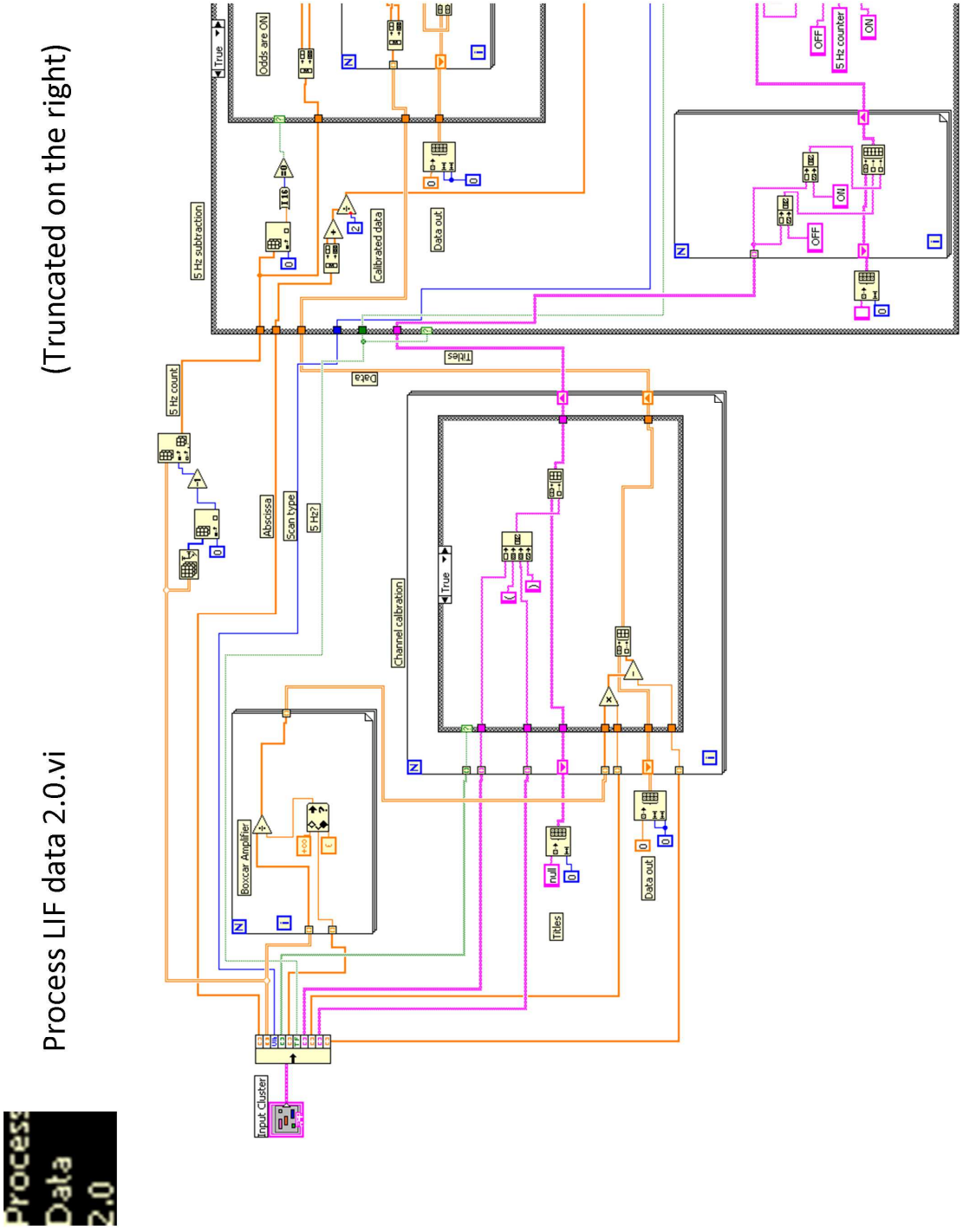

Process LIF data 2.0.vi (Truncated on the left)

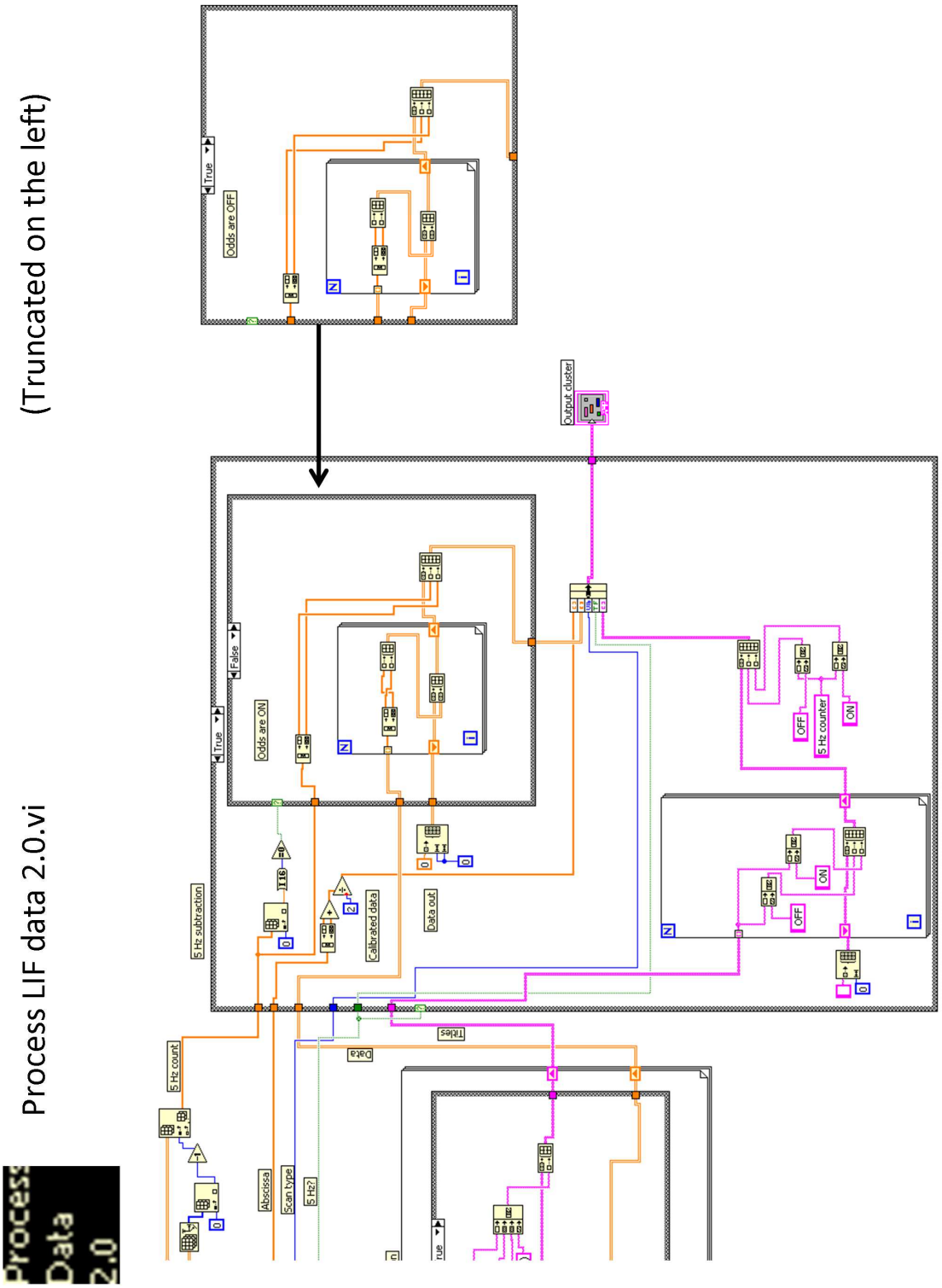

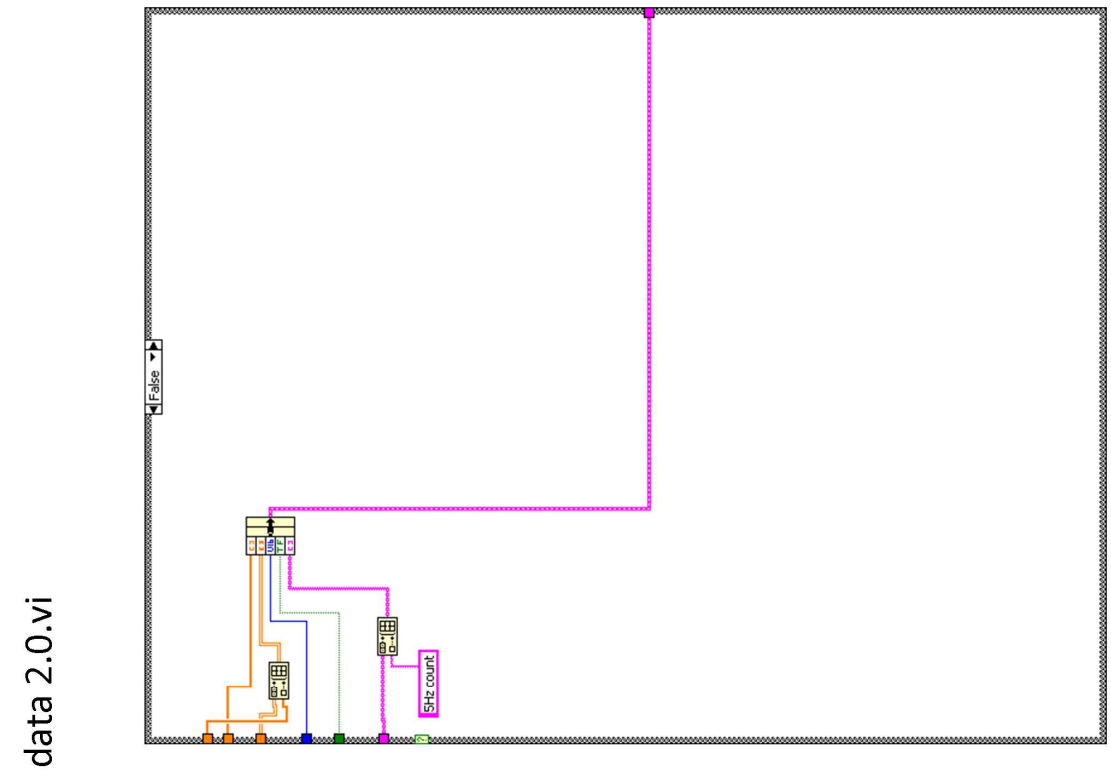

Process LIF data 2.0.vi

Save Data

Save data from OPO scan.vi

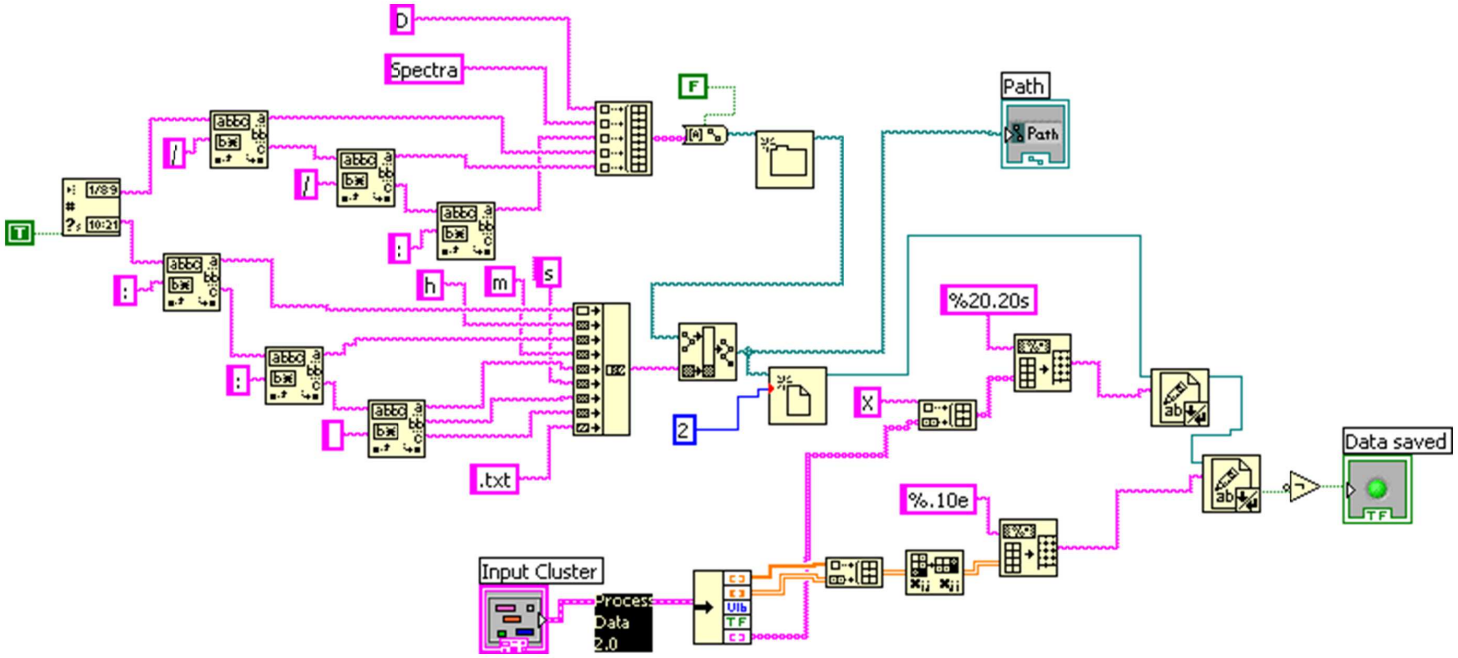

Note that despite its name, this program saves data from any type of scan.

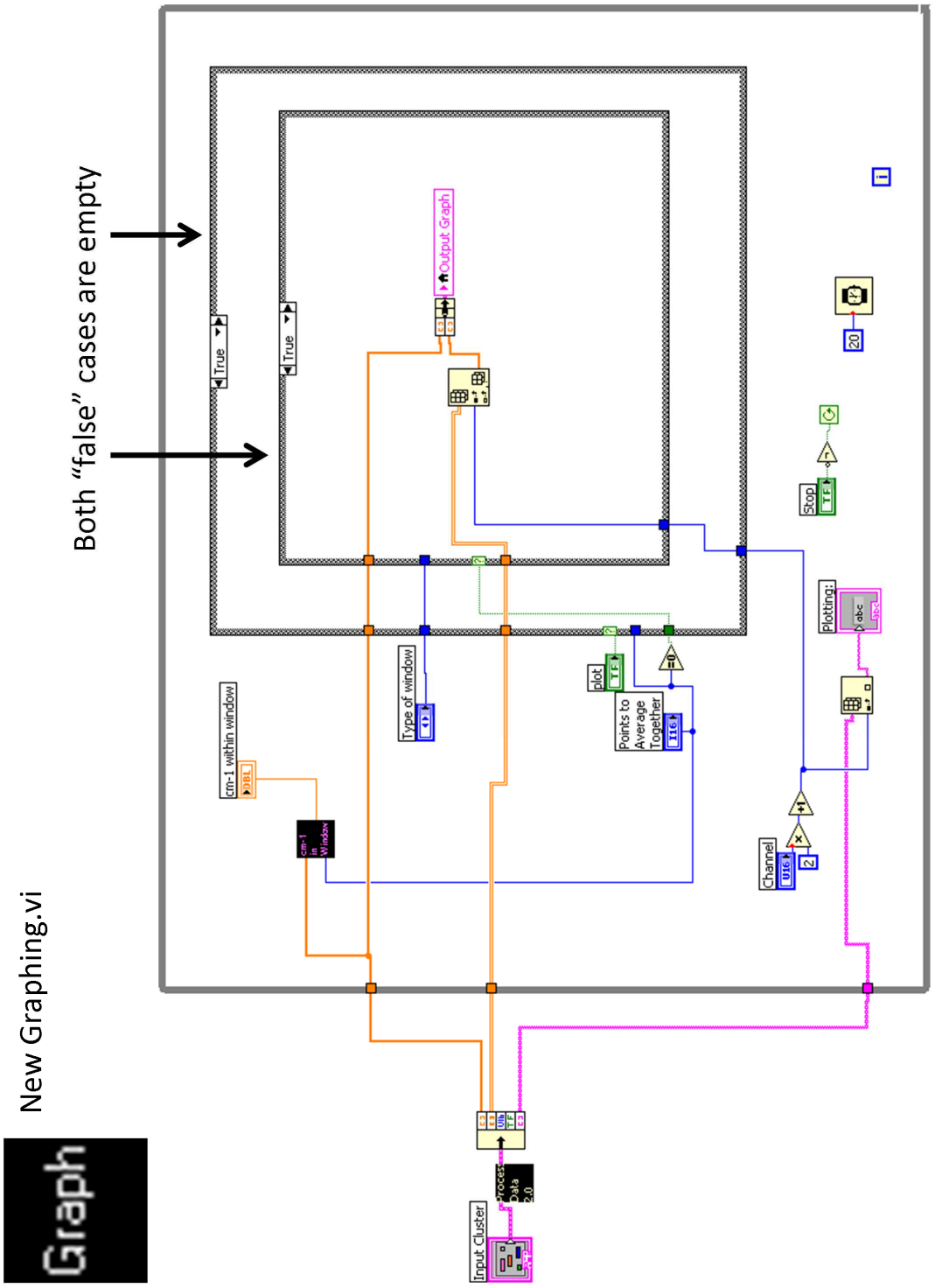
Graph
New Graphing.vi
Both "false" cases are empty
True
True
Output Graph
Type of window
cm-1 within window
plot
Points to Average Together
Stop
Plotting:
Channel
20
2
Input Cluster

cm-1 in window.vi

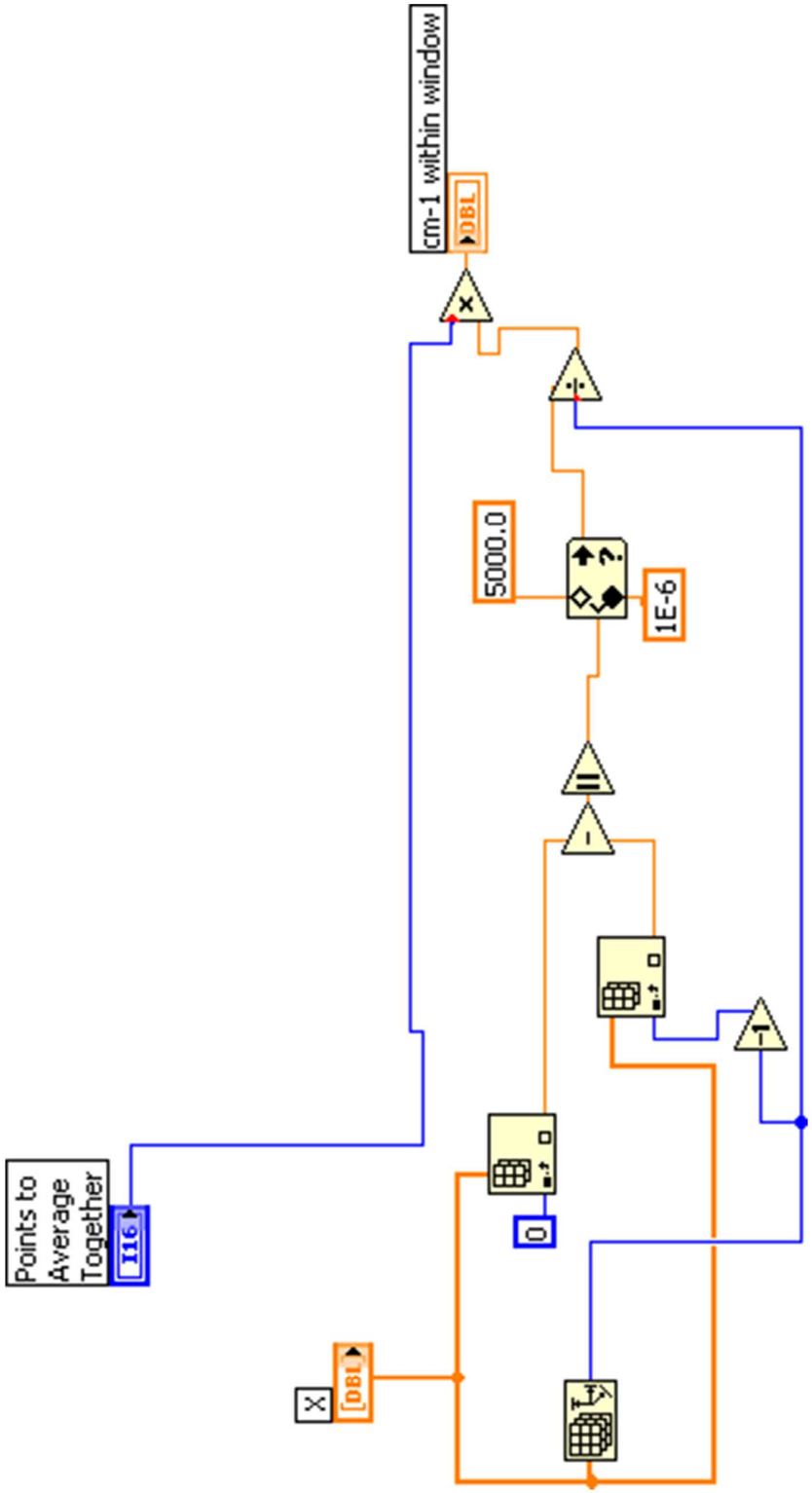

B.2 Frequency Calibration Program

This LabView program uses known line positions to remove frequency drift from LIF spectra. The user fits spectral segments to a thermal simulation to find a frequency offset as well as a linear correction.

Frequency_Calibration_2010.vi

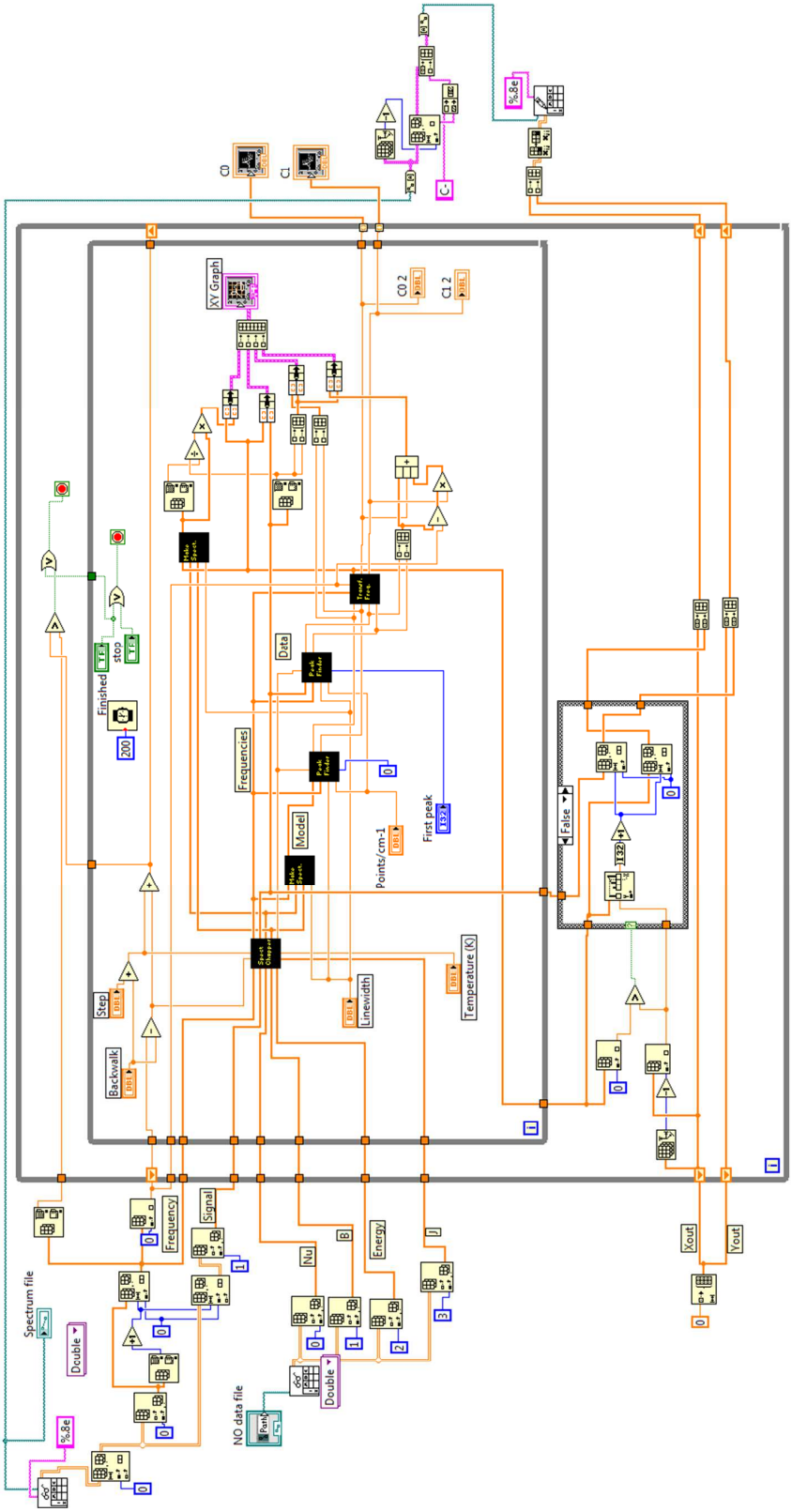

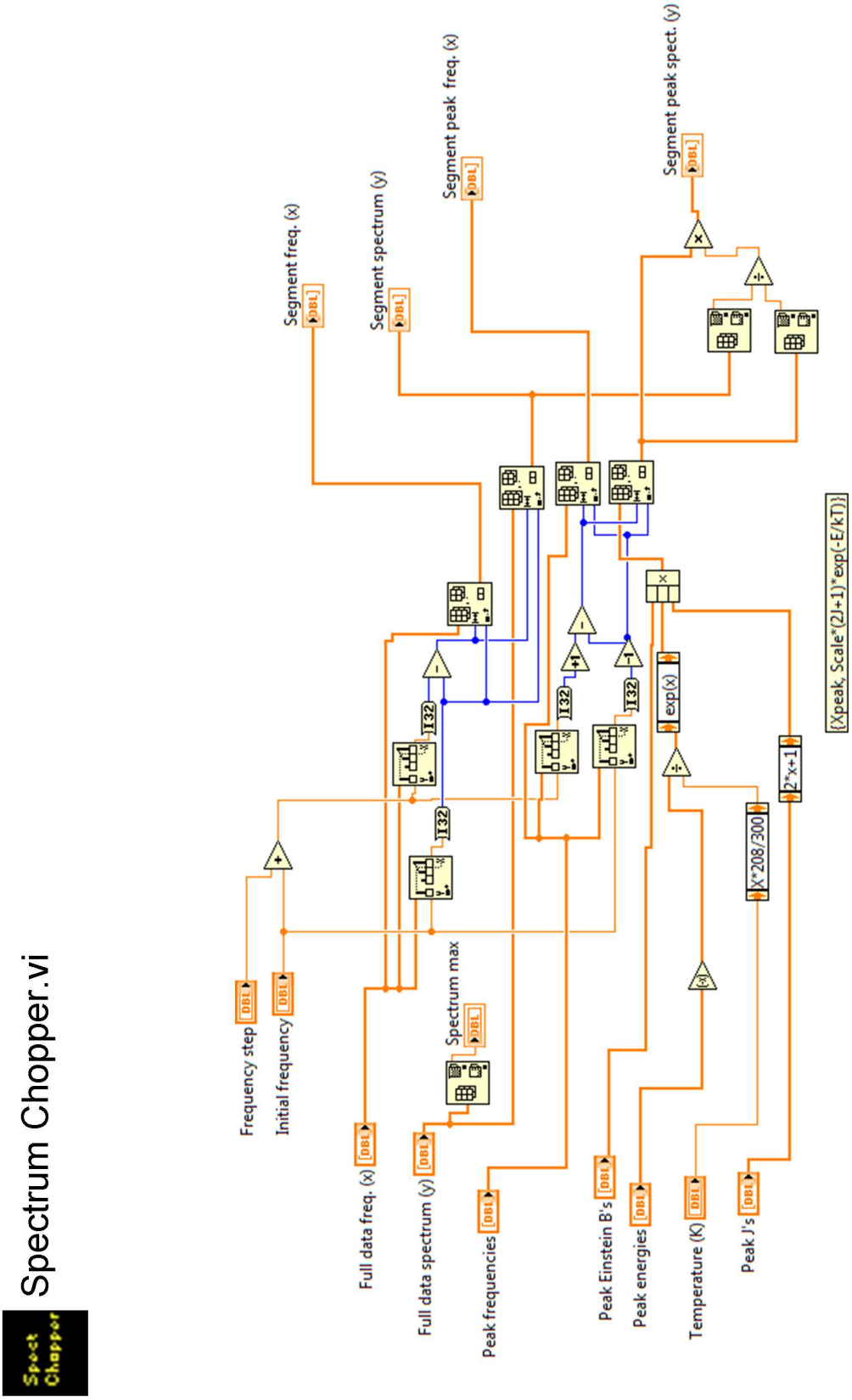
Spect Chopper
Spectrum Chopper.vi
Segment freq. (x)
Segment spectrum (y)
Segment peak freq. (x)
Segment peak spect. (y)
Frequency step
Initial frequency
Spectrum max
Full data freq. (x)
Full data spectrum (y)
Peak frequencies
Peak Einstein B's
Peak energies
Temperature (K)
Peak J's
I32
exp(x)
2*x+1
X*208/300
{Xpeak, Scale*(2J+1)*exp(-E/kT)}

Model for LSF.vi

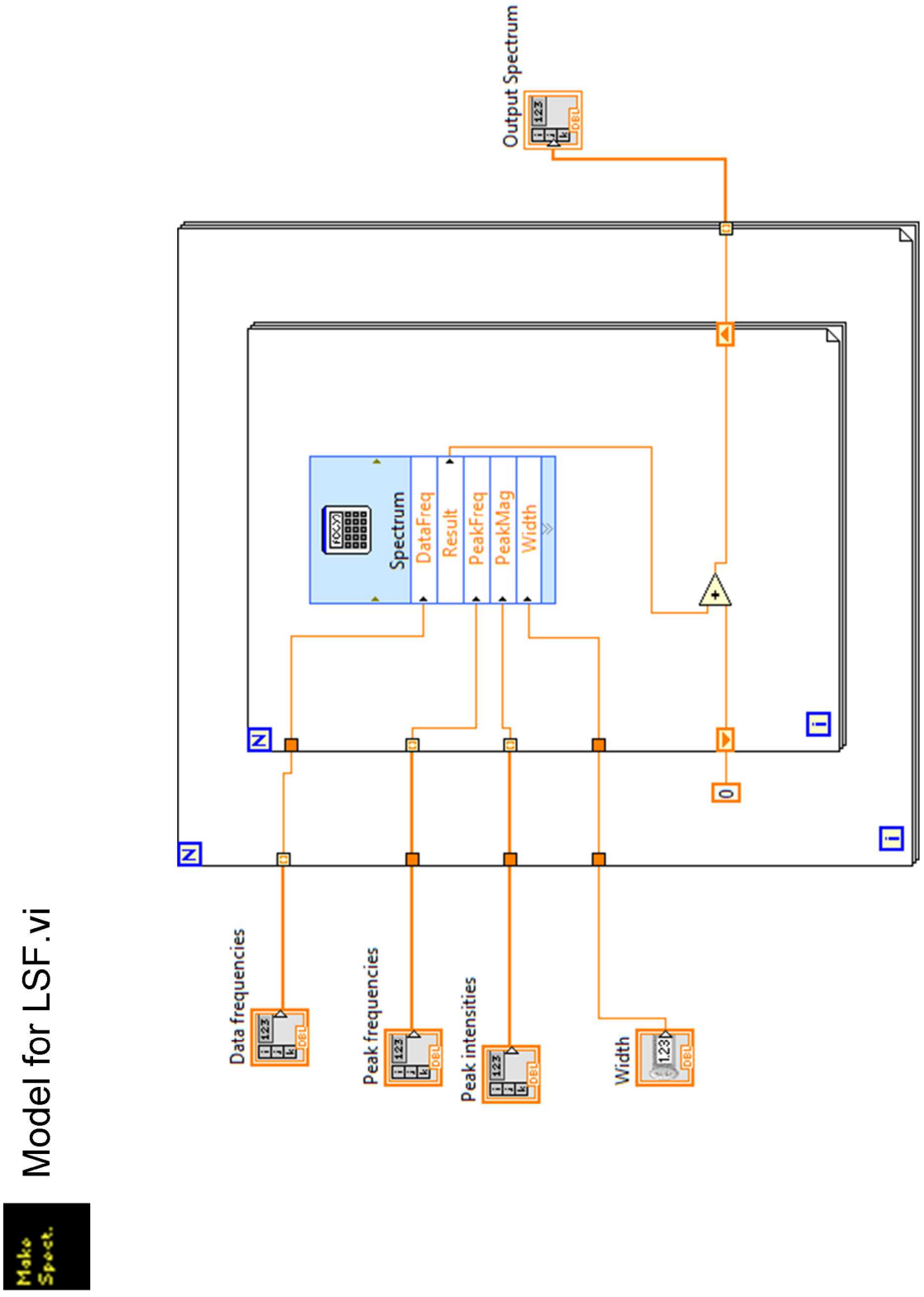

Peak finder.vi

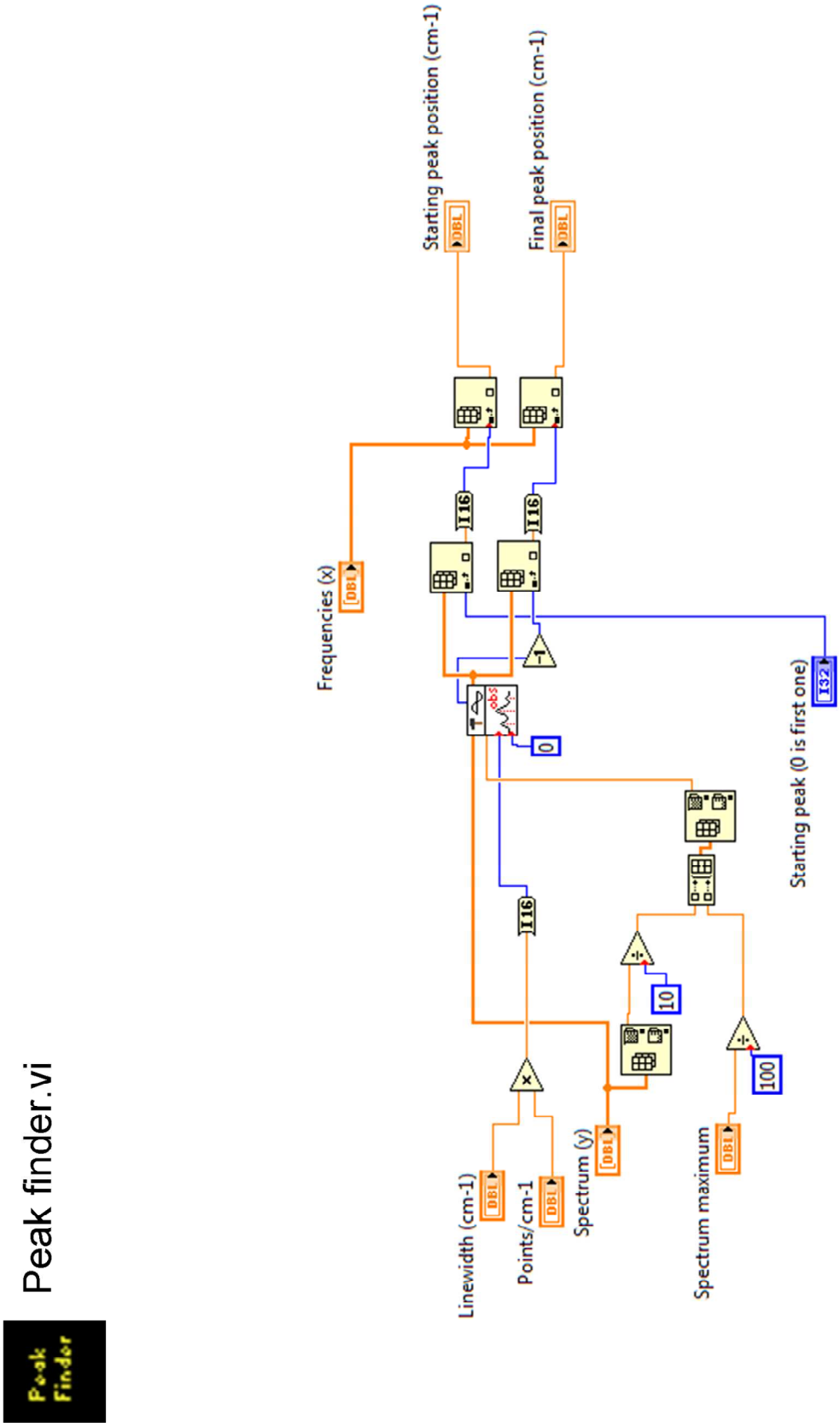

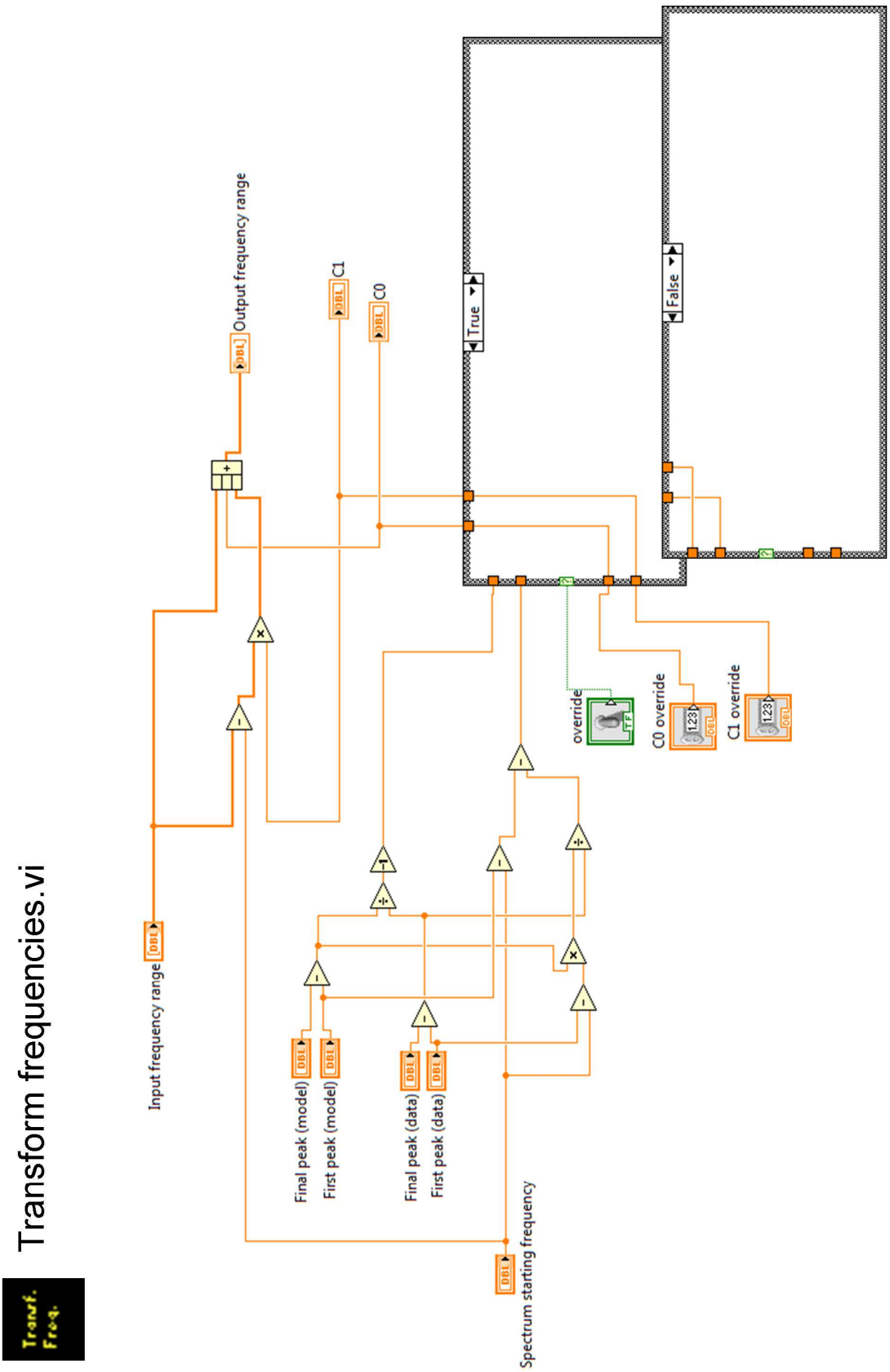
Transf. Freq.
Transform frequencies.vi
Input frequency range
Output frequency range
C1
C0
True
False
override
C0 override
C1 override
Final peak (model)
First peak (model)
Final peak (data)
First peak (data)
Spectrum starting frequency

B.3 LIF Spectrum Fitter

This FORTRAN program takes an input LIF spectrum and extracts ground state populations using a STARPAC least squares fitting subroutine. Before entering this program, the LIF intensity plot should be scaled to probe energy on a shot to shot basis in order to eliminate errors from drifting laser power. In addition, the user must input a file containing information on peaks (name, frequency, Einstein B factor, tumbling angular momentum (N), electronic level index, and total angular momentum (J)). Another input file contains information on the ground states of relevance to the spectrum. Its columns are N, J, electronic index, and energy (cm-1). Control of the program is achieved using a final file called "par.dat" which contains various fit parameters including the name of the data file to be considered, frequency range to examine, the maximum J value included, peak width, and the names of the files containing molecular info. There are some parameters which are not currently implemented in the program. Here and in the "par.dat" file for other programs which will be discussed below, each parameter is treated as a possible fit variable. The first column contains its guess value, the second is a boolean which determines whether or not it will be floated in the STARPAC fit, and the final column contains the parameter name. Outputs from this analysis include a best fit spectrum whose name is that of the original data file with an "m" appended to the beginning, and a formatted file containing populations and distinguished by a "p" appended to the beginning. The convention for naming electronic manifolds is as follows: "1" is $^2\Pi^e_{3/2}$, "2" is $^2\Pi^e_{1/2}$, "3" is $^2\Pi^f_{1/2}$, and "4" is $^2\Pi^f_{3/2}$.

```
c LIFfit2010
c LIF spectrum fitter with weighted data points.
c Updated March 2010
c compile with this command:
c       f90 LIFfit2010.f -L/central/lib -lstar64
```

```
c The program currently reads in a LIF spectrum covering
c  one or more diatomic radical bands.

c It then extracts population data from the spectrum
c  and writes the populations to a file.

c Each band's populations are stored in a seperate file.
c  Populations are labelled by N(rotational quantum number + 1)
c  and omega(electronic quantum number). rms variance is also
c  stored for later use in error bars.

c The variance-covariance matrix is stored in a separate file,
c  as is the original data with best fit simulation.

c The y-axis should already be
c   scaled to probe energy on a shot-to-shot basis.

c 2010 changes: added option to fit the entire spectrum to a
c  single temperature rather than floating all populations
c  seperately.

************************************************************
      program LIFfits2008
      implicit real*8 (a-h, o-z)

c File containing the spectrum to be fit. Will be used to derive
c  names of output files.
      character*100 Cpathname,Cdatafile

c Multiple bands can be fit at once. Information is extracted from
c  two data files for each band, one for peaks and the other for term
c  values. NPeaks(I) is the number of available peaks for band I, and
c  NStates(I) is the number of energy levels.
      dimension NPeaks(100),NStates(100)


c Experimental spectrum to be analyzed:
      dimension Y(1e5),XM(1e5,1)


c Weighting factor for each data point:
      dimension WT(1e5)


c STARPAC fit outputs: PV is the best-fit model; RES is residuals.
c  The others are probably uncertainties.
      dimension RES(1e5),PV(1e5),SDPV(1e5),SDRES(1e5)


c Vital statistics for each peak in the spectrum: Wavenumber(cm-1),
c  Einstein B(cm^3*cm-1)/(Js), Total angular momentum J (excluding
c  nuclear spin).  "Level" refers to lower-state electronic
c  subbands, and "N" is an integer index for lower-state angular
c  momentum in each subband: N is always 1 for the first level
c  Level 1 is 2P3/2e
```

```
c  Level 2 is 2P1/2e
c  Level 3 is 2P1/2f
c  Level 4 is 2P3/2f



      dimension PeakWvn(5000),PeakB(5000),PeakJ(5000)
      dimension IPeakLevel(5000),IPeakN(5000)


c IpeakPARprobed is a lookup table. It tells which entry of the PAR()
c  array corresponds to each peak. Since most entries of PAR() are
c  quantum state populations, this array really tells which state
c  is probed by a particular peak.
      dimension IPeakPARprobed(5000)


c Information about the 2Pi lower states.  Energy, J, and "Level" and
c  "N" are used the same way they were to label peaks.
      dimension StateEnergy(500),StateJ(500)
      dimension IstateLevel(500),IstateN(500)

c Fit parameters: PAR() is the array of actual parameters to be fit.
c  IFIXED() determines which of them will be floated or fixed.
c  PAREnergy() and PARJ() are angular momentum and energy for the
parameters
c   that correspond to quantum state populations.
c  Cparname() gives a name for each parameter.
c  VCV(()) is the variance-covariance matrix
c  STP() and SCALE() are needed by STARPAC, but I don't know what
information
c   they contain.  However, STP(1) must be negative.
      dimension PAR(500)
      dimension IFIXED(500)
      dimension PAREnergy(500),PARJ(500)
      character*100 Cparname(500)
      dimension VCV(500,500)
      dimension STP(500), SCALE(500)



c DSTAK() is the workspace for STARPAC. Varying its length can be
c  disastrous.
      dimension DSTAK(1e7)


c LIFspec is the function that returns a spectral simulation based on
c  a set of populations and other parameters.
      external LIFspec

c DSTAK must be put in a common block so STARPAC can access it.
      common /errchk/Ierr
      common /cstak/dstak

c These common blocks are the best way to pass essential information
c  to the model function.  Since STARPAC imposes strict rules
c  on it, it's not possible to pass these arrays directly.
```

```
      common /Data/       NallowedPeaks
      common /PeakInfo/ PeakWvn,PeakB,IPeakPARprobed,PeakJ,
     .                  IpeakLevel
      common /LevelInfo/ PARJ,PARenergy,NxtraPAR
      common /Qinfo/ StateEnergy,StateJ,IStateLevel,IStateN,
     .               NStates

************************************************************
c  Important!
c  The program only accepts data sets with fewer than 1e5
c  points. If you want to fit more points, this must be
c  changed in several places.



c  This program will use a starpac nonlinear least-squares
c  fitting subroutine to fit a data set to a model.
c  The current model is a set of Gaussian peaks.

c  These are all parameters that are required by the Starpac
c   function NLSC.
      STP(1) = -2.0
      MIT = -2.0
      STOPSS = 2.1
      STOPP = 2.0
      SCALE(1) = -2.
      DELTA = -2.0
      IVAPRX = 1
      NPRT = 0
      LDSTAK = 10000000
      IVCV=500

c  DataReader does four things. It reads in the data to be
c  analyzed, it reads in relevant information about
c  the bands that are covered by the spectrum, it reads in
c  the user-defined parameters (Jmax,Width), and
c  it reads in term values from a separate file.

      WRITE(*,*) 'Calling DataReader'
      CALL DataReader(Cpathname,CdataFile,
     .                N,XM,Y,
     .                PAR,IFIXED,CParname,NPAR,Nbands,
     .                NPeaks,
     .                IPeakN,NStates,
     .                IstateN,StateJ,IstateLevel,StateEnergy)

      WRITE(*,*) 'Finished with Data Reader'
      WRITE(*,*) 'File: ',TRIM(Cpathname)//Cdatafile
      WRITE(*,100) 'N=',N
      WRITE(*,110) 'Jmax=',PAR(1)
      WRITE(*,110) 'Sigma=',PAR(2)
      WRITE(*,100) 'NPAR=',NPAR
      WRITE(*,110) 'PeakWvn(1)=',PeakWvn(1)
      WRITE(*,100) 'Nstates(1)=',Nstates(1)

 100  FORMAT(A15,I10)
 110  FORMAT(A15,F10.2)
```

```
 120  FORMAT(A15,E10.2)

c  MakeArrays initializes the arrays XM(),PAR(),IFIXED(),and WT()

      WRITE(*,*) 'Calling MakeArrays'
      CALL MakeArrays(N,XM,Y,WT,Nbands,
     .    NPeaks,IPeakN,
     .    Nstates,IstateLevel,IstateN,StateJ,StateEnergy,
     .    NPAR,Nxtrapar,CParname,PAREnergy,PARJ,PAR,IFIXED)

      WRITE(*,*) "Finished with MakeArrays"
      WRITE(*,*) "NPAR=",NPAR

      IXM = N
      M = 1

      WRITE(*,*) 'Calling Starpac'



      CALL NLSWS (Y,WT,XM,N,M,IXM,LIFspec,PAR,NPAR,RES,LDSTAK,
     .   IFIXED,STP,MIT,STOPSS,STOPP,SCALE,DELTA,IVAPRX,NPRT,
     .   NNZW,NPARE,RSD,PV,SDPV,SDRES,VCV,IVCV)

      IF(Ierr.NE.0) THEN
       WRITE(*,*)
       WRITE(*,*)
       WRITE(*,*) "WARNING!!!!!!!!!"
       WRITE(*,*) "An error has been detected in the fit."
       WRITE(*,*) "Error #",Ierr
       WRITE(*,*)
       WRITE(*,*)
      END IF

      WRITE(*,*) "Calling the data writer"
      CALL Writer(Cpathname,CDatafile,
     .             N,XM,Y,M,IXM,NPAR,PAR,Nxtrapar,
     .            VCV,IFIXED,RES,CParname,PAREnergy,PARJ)
      WRITE(*,*) "Finished with the data writer"

      end program


*************************************************************
      SUBROUTINE DataReader(Cpathname,CdataFile,
     .                N,XM,Y,
     .                PAR,IFIXED,CParname,NPAR,Nbands,
     .                NPeaks,IPeakN,
     .                Nstates,IstateN,StateJ,IstateLevel,StateEnergy)

      implicit real*8 (a-h, o-z)
      real*8 xtemp
      character*100 CDataFile
      character*100 Cpathname
      character*100 Cbandfile(100),CStatefile(100)
      character*100 CParname(500)
      character*5 CBranchName(5000)
```

```
      integer N,NPAR,Nbands
      dimension XM(1e5,1),Y(1e5)
      dimension PAR(500),IFIXED(500)
      dimension PeakWvn(5000),PeakB(5000),IPeakLevel(5000),
     .  IPeakN(5000),PeakJ(5000)
      dimension IPeakPARProbed(5000)
      dimension Xlimits(2)
      dimension Npeaks(100),Nlevels(100)
      dimension IstateN(500),StateJ(500),IstateLevel(500),
     .  StateEnergy(500),Nstates(100)

      integer Jmax
      real*8 PeakWidth

      common /PeakInfo/ PeakWvn,PeakB,IPeakPARprobed,PeakJ,
     .                  IpeakLevel



**********************************************************
c This subroutine reads in information from several different files.
c N is the number of data points.
c Nbands is the number of bands in the spectrum
c NPeaks() is an array whose entries are the number of participating
c   peaks in each band
c NWghtRgns is the number of regions where data points will
c  be unweighted.

c Jmax is the maximum value of tumbling angular momentum to be
c  considered in the fit.  Note that even though it's called "J",
c  it is actually an integer label.  For each electronic sub-band,
c  the first rotational level is called "1", and the highest is called
c  "J".
c PeakWidth is the 1/e width of the peaks

c WvlOffset is the shift in the calibration of the LIF laser


c XM() and Y() are the wavelength and intensity values from the raw
data
c  file.
c PeakWvn(),PeakB(),IPeakLevel(),and IPeakN() are the
c  frequency,Einstein B-factor,electronic sublevel probed,
c  and lower-state rotational angular momentum for each peak.

c Sublevel 1 = Doublet Pi 3/2+
c Sublevel 2 = Doublet Pi 1/2+
c Sublevel 3 = Doublet Pi 3/2-
c Sublevel 4 = Doublet Pi 1/2-

c Read the file "par.dat"
      OPEN (1,file='par.dat')

c Read in the name of the file to be analyzed
c  and the wavelength limits you want to use
      READ(1,100) CPathname
      READ(1,100) CDatafile
```

```
      READ(1,*) Xlimits(1)
      READ(1,*) Xlimits(2)
      READ(1,*) NPAR
      READ(1,*)
      WRITE(*,*) TRIM(Cpathname)//CDataFile

 100  FORMAT(A50)

c Read in first parameters
      READ(1,*)

      DO I=1,NPAR
       READ(1,*) PAR(I),IFIXED(I),CParname(I)
       CParname(I)=' '//CParname(I)
      END DO



c Read in the number of bands to be included, and the names of the
files
c   where peak info is stored for each band.
      READ(1,*)
      READ(1,*) Nbands
      DO I=1,Nbands
      READ(1,100) Cbandfile(I)
        READ(1,100) CStatefile(I)
      END DO
      CLOSE (UNIT=1)


c Read in peak positions and transition strengths for each band

      J=1
      DO I=1,Nbands
       OPEN (1,file=Cbandfile(I))
       READ(1,*)
       K=1
       DO
         READ(1,*,END=20)
     .    CBranchName(J),PeakWvn(J),PeakB(J),
     .    IPeakN(J),IPeakLevel(J),PeakJ(J)
         J=J+1
         K=K+1
       END DO
 20    NPeaks(I)=K-1
       CLOSE (UNIT=1)
      END DO

      J=1
      DO I=1,Nbands
       OPEN (1,file=CStatefile(I))
       READ(1,*)
       K=1
       DO
        READ(1,*,END=30)
     .   IStateN(J),StateJ(J),IStateLevel(J),StateEnergy(J)
```

```
        J=J+1
        K=K+1
       END DO
 30    Nstates(I)=K-1
       CLOSE (UNIT=1)
      END DO


c Read in the data to be fit


      OPEN (1,file=TRIM(Cpathname)//CDataFile)
      I=1

      READ(1,*)
      DO
        READ(1,*,END=50) Xtest,Ytest
        IF((Xtest.gt.Xlimits(1)) .and. (Xtest.lt.Xlimits(2))) THEN
         XM(I,1) = Xtest
         Y(I) = Ytest
         I=I+1
        END IF
      END DO
 50   N = I-1

      CLOSE (UNIT=1)

      WRITE(*,*) XM(1,1),XM(N,1)


      Return
      end subroutine DataReader

*************************************************************

      SUBROUTINE MakeArrays(N,XM,Y,WT,Nbands,
     .    NPeaks,IPeakN,
     .    Nstates,IstateLevel,IstateN,StateJ,StateEnergy,
     .    NPAR,Nxtrapar,CParname,PAREnergy,PARJ,PAR,
     .    IFIXED)


      implicit real*8 (a-h,o-z)

c Peaks and states per band:
      dimension Npeaks(100),Nstates(100)

c The spectrum to be fit:
      dimension XM(1e5,1),Y(1e5)

c Fit weights:
      dimension WT(1e5)

c STARPAC fit outputs:
      dimension RES(1e5),PV(1e5),SDPV(1e5),SDRES(1e5)
```

```
c Peak info
      dimension PeakWvn(5000),PeakB(5000),PeakJ(5000)
      dimension IPeakLevel(5000),IPeakN(5000)

c Peak-state lookup table
      dimension IPeakPARprobed(5000)

c Lower-state info
      dimension StateEnergy(500),StateJ(500)
      dimension IStateLevel(500),IstateN(500)

c Parameter arrays
      dimension PAR(500)
      dimension IFIXED(500)
      dimension PAREnergy(500),PARJ(500)
      character*100 Cparname(500)
      dimension VCV(500,500)
      dimension STP(500),SCALE(500)

c STARPAC workspace
      dimension DSTAK(10000000)

c Character variables for naming parameters.
      character*3 CJ,CK,CL,CM

c Will need to sort peaks by frequency in order to self-calibrate.
      dimension SortedPeakWvn(5000)


      external LIFspec
      external IPRINT
      common /cstak/dstak

      common /Data/ NallowedPeaks
      common /PeakInfo/ PeakWvn,PeakB,IPeakPARprobed,PeakJ,
     .                  IpeakLevel



**********************************************************

      OPEN(9,FILE='Starpacerrors')

      WRITE(*,*) 'Nstates(1)=', Nstates(1)
      Jmax=PAR(1)
      Sigma=PAR(2)
      Nxtrapar=NPAR

      NPAR = NPAR + Jmax*4*Nbands

c Initialize IFIXED() (Make all populations fixed)

      DO I=Nxtrapar+1,NPAR
         IFIXED(I)=1
      END DO
c Initialize PAR() (Make all populations negative)
      DO I=Nxtrapar+1,NPAR
```

```
       PAR(I)=-2000.0
      END DO
c Initialize CParname()
      I=Nxtrapar+1
      DO J=1,Nbands
       DO K=1,4
        DO L=1,Jmax
         WRITE(Unit=CJ,fmt='(I3)') J
         WRITE(Unit=CK,fmt='(I3)') K
         WRITE(Unit=CL,fmt='(I3)') L

         CParname(I)='  Bnd'//CJ//'  Ele'//
     .              CK//'  Rot'//CL
         I=I+1
        END DO
       END DO
      END DO


c Now find out which levels are covered in the spectrum.
c If the level corresponds to a peak that is covered in the data,
c  then IFIXED will be set to 0 for that peak, and it will be varied
c  by STARPAC

      M=0
      Iallowedpeak=1
      Ipeak=1
      DO J=1,Nbands
      DO K=1,NPeaks(J)

      IParIndex=Nxtrapar+(J-1)*4*Jmax+
     .  (IPeakLevel(Ipeak)-1)*Jmax+IPeakN(Ipeak)

       DO I=1,N
        IF( (ABS(PeakWvn(Ipeak)-XM(I,1)).lt.Sigma).
     .        AND.(IPeakN(Ipeak).le.Jmax) )THEN

           Wvntst=PeakWvn(IPeak)
           Btst=PeakB(IPeak)
           Ntst=IPeakN(IPeak)
           Leveltst=IPeakLevel(IPeak)
           PeakJtst=PeakJ(IPeak)

           PeakWvn(IPeak)=0.0
           PeakB(IPeak)=0.0
           IPeakN(IPeak)=0
           IPeakLevel(IPeak)=0
           PeakJ(IPeak)=0

           PeakWvn(Iallowedpeak)=Wvntst
           PeakB(Iallowedpeak)=Btst
           IPeakN(Iallowedpeak)=Ntst
           IPeakLevel(Iallowedpeak)=Leveltst
           PeakJ(Iallowedpeak)=PeakJtst
           IPeakPARprobed(Iallowedpeak)=IParIndex

           IF(PAR(3).lt.0.1) THEN
```

```
            IFIXED(IParIndex)=0
           END IF

           PAR(IParIndex)=1.0e-4
           PARenergy(IParIndex)=0.0
           PARJ(IParIndex)=0.0

           DO L=1,NStates(J)
            IF((IPeakN(Iallowedpeak).eq.IstateN(M+L)).and.
     .       (IStateLevel(M+L).eq.IPeakLevel(Iallowedpeak))) THEN
              PARenergy(IParIndex)=StateEnergy(M+L)
              PARJ(IParIndex)=StateJ(M+L)
            END IF
            IF((IPeakN(Iallowedpeak).eq.IstateN(M+L)).and.
     .       (IStateLevel(M+L).eq.IPeakLevel(Iallowedpeak))) EXIT
           END DO

           Iallowedpeak=Iallowedpeak+1
         END IF
         IF( (ABS(PeakWvn(Ipeak)-XM(I,1)).lt.Sigma).
     .        AND.(IPeakN(Ipeak).le.Jmax) ) EXIT
        END DO
        Ipeak=Ipeak+1

       END DO
c       M=NStates(J)
       END DO
       NallowedPeaks=Iallowedpeak-1


c Create the weight array
       DO I=1,N
          WT(I)=1.0
       END DO


       WRITE(*,*) "XM(N,1)=",XM(N,1)

       RETURN

       END SUBROUTINE MakeArrays


*************************************************************
       subroutine Writer(Cpathname,CDataFile,
      .           N,XM,Y,M,IXM,NPAR,PAR,
      .           Nxtrapar,VCV,IFIXED,RES,CParname,
      .           PAREnergy,PARJ)
       implicit real*8 (a-h, o-z)
       character*100 Cpathname,Cdatafile,
      .      Cmodfile,Cpopfile,Ccovarfile,Creportfile
       character*100 Cparamfile,Crawpopfile,Ccalerrfile
       character*100 CParname(500)
       dimension Y(1E5),XM(1E5,1),PV(1E5),RES(1e5)
       dimension PAR(500),PARerror(500),IFIXED(500),VCV(500,500)
       dimension PAREnergy(500),PARJ(500)
       dimension A(10),T(10)
```

```
**********************************************************
c Sends the populations and the best-fit model to output files.

      Jmax=PAR(1)

      Cmodfile = TRIM(Cpathname)//'m'//Cdatafile
      Cpopfile = TRIM(Cpathname)//'p'//Cdatafile
      Ccovarfile = TRIM(Cpathname)//'covar'//Cdatafile
      Cparamfile = TRIM(Cpathname)//'param'//Cdatafile
      Crawpopfile=TRIM(Cpathname)//'praw'//Cdatafile
      Ccalerrfile=TRIM(Cpathname)//'Calerr'//Cdatafile
      Creportfile=TRIM(Cpathname)//'report'//Cdatafile

      WRITE(*,*) "original file: ",Cdatafile
      WRITE(*,*) "model file: ",Cmodfile
      WRITE(*,*) "population file: ",Cpopfile
      WRITE(*,*) "covariance file: ",Ccovarfile
      WRITE(*,*) "other parameters file: ",Cparamfile
      WRITE(*,*) "raw populations: ",Crawpopfile
      WRITE(*,*) "Calibration errors: ",Ccalerrfile
      WRITE(*,*) "1 temperature report: ",Creportfile

      M=1
      DO J=1,NPAR
       IF(IFIXED(J).eq.0) THEN
        PARerror(J) = SQRT(VCV(M,M))
        M=M+1
       ELSE
        PARerror(J) = 0.0
       END IF
      END DO



      OPEN (4,file=Cmodfile)
      CALL LIFspec(PAR, NPAR, XM, N, M, IXM, PV)
      WRITE(4,70) "Wvn(cm-1)", "Data",
     .        "Model","Residual"
      DO ipoint=1,N
            WRITE(4, 80) XM(ipoint,1),
     .        Y(ipoint), PV(ipoint),RES(Ipoint)
      END DO
      CLOSE (UNIT=4)

c      OPEN (4,file=Ccovarfile)
c      M=1
c      K=1
c      DO I=1,NPAR
c       IF(IFIXED(I).lt.1) THEN
c        DO J=1,NPAR
c         IF(IFIXED(J).lt.1) THEN
c          WRITE(4,110) VCV(M,K),Cparname(I),Cparname(J)
c          K=K+1
c         END IF
c        END DO
c        M=M+1
c       END IF
```

```
c      END DO
c      CLOSE (UNIT=4)

       IF(Nxtrapar.gt.0) THEN
        OPEN (4,file=Cparamfile)
        M=1
        DO I=1,Nxtrapar
         Error=0.0
         IF(IFIXED(I).lt.1) THEN
          Error = sqrt(VCV(M,M))
          M=M+1
         END IF
         WRITE(4,120) Cparname(I),IFIXED(I),PAR(I),Error
        END DO
        CLOSE (UNIT=4)
        END IF

       OPEN (4,file=Cpopfile)
       WRITE(4,90)  "2Pi3/2eJ","E","Pop","error",
      .             "2Pi1/2eJ","E","Pop","error",
      .             "2Pi1/2fJ","E","Pop","error",
      .             "2Pi3/2fJ","E","Pop","error"

       L=Nxtrapar
       DO K=1,Jmax
        WRITE(4,100) PARJ(L+K),PARenergy(L+K),
      .              PAR(L+K),PARerror(L+K),
      .              PARJ(L+K+Jmax),PARenergy(L+K+Jmax),
      .              PAR(L+K+Jmax),PARerror(L+K+Jmax),
      .              PARJ(L+K+2*Jmax),PARenergy(L+K+2*Jmax),
      .              PAR(L+K+2*Jmax),PARerror(L+K+2*Jmax),
      .              PARJ(L+K+3*Jmax),PARenergy(L+K+3*Jmax),
      .              PAR(L+K+3*Jmax),PARerror(L+K+3*Jmax)
       END DO
       CLOSE (UNIT=4)


       OPEN(4,file=Crawpopfile)
       M=1
       Write(4,130) "J","Value","Uncertainty","Energy",
      .             "Boltz","Boltzerror","Name"
       DO I=NxtraPAR+1,NPAR
        Boltz=0.0
        BoltzError=0.0
        IF(PAR(I).gt.0.0) THEN
         Boltz=log(PAR(I)/(2*PARJ(I)+1))
         Boltzerror=abs(Parerror(I)/PAR(I))
        END IF
        WRITE(4,140) PARJ(I),PAR(I),Parerror(I),
      .      PARenergy(I),Boltz,Boltzerror,Cparname(I)
       END DO
       CLOSE (UNIT=4)


c Calculate average rotational/electronic temperatures
c  and print a simple output file.
```

```
      Itempfit=PAR(3)
      IF(Itempfit.gt.0.1) THEN
       A(1)=PAR(4)
       T(1)=PAR(5)
       A(2)=PAR(6)
       T(2)=PAR(7)
       A(3)=PAR(8)
       T(3)=PAR(9)
       A(4)=PAR(10)
       T(4)=PAR(11)

       Trot=(T(1)+T(2)+T(3)+T(4))/4
       Telec=119.82*298/207.119/
     .           log((A(2)+A(3))/(A(1)+A(4)))

       WRITE(*,*) Trot,Telec
       OPEN (4,FILE=Creportfile)
       WRITE(4,150) "Trot","Telec"
       WRITE(4,160) Trot,Telec
       WRITE(4,*)
       WRITE(4,70) "T1","T2","T3","T4"
       WRITE(4,80) T(1),T(2),T(3),T(4)
       WRITE(4,*)
       WRITE(4,70) "Pop1","Pop2","Pop3","Pop4"
       WRITE(4,80) A(1),A(2),A(3),A(4)
       CLOSE(UNIT=4)

      END IF


 70   FORMAT (4A25)
 80   FORMAT (4e25.8)
 90   FORMAT (16A25)
 100  FORMAT (16E25.8)
 110  FORMAT (e25.8,2A50)
 120  FORMAT (A50,I10,2e25.8)
 130  FORMAT (7A25)
 140  FORMAT (6e25.8,A25)
 150  FORMAT (2A20)
 160  FORMAT (2E20.8)


      RETURN
      END


*************************************************************
      subroutine LIFspec(PAR, NPAR, XM, N, M, IXM, PV)
      implicit real*8 (a-h, o-z)
      real*8 E,B,Pop,g,c,DelWvn,S
      integer I,J,ILvlProbed,Itempfit,NxtraPAR
      dimension PAR(NPAR), XM(IXM,M), PV(N)
      dimension T(10), A(10), Q(10)
      dimension PeakWvn(5000),PeakB(5000),IPeakPARprobed(5000)
      dimension PeakJ(5000),IPeakLevel(5000)
      dimension PARJ(500),PARenergy(500)
      dimension StateEnergy(500),StateJ(500)
```

```
      dimension IStateLevel(500),IStateN(500),NStates(100)
      common /cstak/dstak

      common /Data/       NallowedPeaks
      common /PeakInfo/ PeakWvn,PeakB,IPeakPARprobed,PeakJ,
     .                  IPeakLevel
      common /LevelInfo/ PARJ,PARenergy,NxtraPAR
      common /Qinfo/ StateEnergy,StateJ,IStateLevel,IStateN,
     .               NStates

************************************************************

c Each peak is modeled as a gaussian with the same width.
c The heights of these peaks are taken to be proportional B
      pi = 3.14159265

c For direct temperature fitting, "T" contains the temperature
c  for each electronic manifold and "A" contains the population
c  for each manifold.  "Q" is the partition function for each
c  manifold.

c Speed of light in cm/s
      c = 2.99792458E10

      Jmax=PAR(1)
      Sigma=PAR(2)
      Itempfit = PAR(3)


      IF(Itempfit.gt.0.1) THEN

c read in temperatures and populations
       A(1)=PAR(4)
       T(1)=PAR(5)
       A(2)=PAR(6)
       T(2)=PAR(7)
       A(3)=PAR(8)
       T(3)=PAR(9)
       A(4)=PAR(10)
       T(4)=PAR(11)

c       WRITE(*,*) T(1)
c       READ(*,*)

c construct partition functions
       DO I=1,4
        Q(I)=0.0
       END DO

       DO K=1,NStates(1)
         degen=2*StateJ(K)+1
c kT in wavenumbers, T in Kelvin
         Ielec=IStateLevel(K)
         xkT=T(Ielec)*207.119/298
         Energ=StateEnergy(K)
         Q(Ielec)=Q(Ielec)+degen*exp(-Energ/xkT)
       END DO
```

```
      END IF



      DO I=1,N
        PV(I)=0.0
        DO J=1,NallowedPeaks
          freq=XM(I,1)
          DelWvn=abs(freq-PeakWvn(J))
          IF (DelWvn.lt.(50*Sigma)) THEN
           ILvlProbed=IPeakPARprobed(J)
           Pop = PAR(ILvlProbed)

           IF(Itempfit.gt.0.1) THEN
            Ielec=IPeakLevel(J)
            degen=2*PeakJ(J)+1
            xkT=T(Ielec)*207.119/298
            Energ=PAREnergy(ILvlProbed)
            Amp=A(Ielec)
            Pop=Amp*degen*exp(-Energ/xkT)/Q(Ielec)
           END IF

           B = PeakB(J)
c  Lorentzian:
c           g=1/(1+ (DelWvn)**2/Sigma**2)/(pi*Sigma)

c  Gaussian:
           g=(1/sqrt(pi)/Sigma)*exp(-((Delwvn/Sigma)**2))

c  Hybrid:
c           g=Sigma**2/2/((DelWvn**2+Sigma**2)**(3/2))
           PV(I) = PV(I) + Pop*B*g
          END IF

        END DO
      END DO
      RETURN
      END



      Subroutine IPRINT(IPRT)
      IPRT=9
      RETURN
      END SUBROUTINE IPRINT
```

B.4 Double Exponential Fits

This program takes as an input the "p-" output of the LIFfits routine. It separately fits each electronic sub-band to a two component model featuring a low temperature (T1) a high temperature (T2), and a branching probability into the low temperature channel (alpha). The program outputs the best fit value of each quantity as well as an estimated error as long as the variable has not been fixed (using the same input format as discussed in section B.1). In addition, the program reports the summed population in each channel for the purposes of calculating a spin-orbit temperature. As before, the labeling of the states is as follows: "1" is $^2\Pi^e_{3/2}$, "2" is $^2\Pi^e_{1/2}$, "3" is $^2\Pi^f_{1/2}$, and "4" is $^2\Pi^f_{3/2}$.

```
c Double_Exp_fit_2009 (6-2009)
c Weighted fit for a double-exponential data set
c compile with this command:
c    ifort Double_Exp_fit.f -L/central/lib -lstar

c First, initial fit parameters are read from the file
c  "par.dat"

c Also, fitting weights are read from a file called
"NOstateweights.txt"

c Next, the data set is read in from a file named in par.dat.

c Two output files are generated. "mod_xxxx_K" contains the fit
c   and data for manifold "K", and "val_xxxx" contains the
c   best-fit parameters
c   and the variance-covariance matrix. Here, "xxxx" refers to the
c   name of the original data file.

c All four electronic manifolds will be fit simultaneously.
c There will be four sets of four input columns (16 total)
c  column a: Angular momentum
c  column b: Term values
c  column c: Population
c  column d: Sigma error (will be squared for weighting)


************************************************************
```

```
      program Double_Exp_fit
      implicit real*8 (a-h, o-z)

c File containing the data to be fit. Will be used to derive
c  names of output files.
      character*100 Cpathname,Cdatafile

c Inputs from the data file:
      dimension AngMom2D(1e5,4),Energy2D(1e5,4)
      dimension Pops2D(1e5,4),Error2D(1e5,4)
      dimension Weights2D(1e5,4)

c Intermediate arrays for each eletronic manifold
      dimension AngMom(1e5),XM(1e5,1),Y(1e5),Error(1e5)

c Number of states for each manifold
      dimension Nlev(4)


c Weighting factor for each data point:
      dimension WT(1e5)

c Collected results: fits and parameters
      dimension Report(4,8), Fits(1e5,13,4)


c STARPAC fit outputs. PV is the best-fit model; RES is residuals.
c  The others are probably uncertainties.
      dimension RES(1e5),PV(1e5),SDPV(1e5),SDRES(1e5)
      dimension Chan1(1e5),Chan2(1e5)

c Fit parameters: PAR() is the array of actual parameters to be fit.
c  IFIXED() determines which of them will be floated or fixed.
c  Cparname() gives a name for each parameter.
c  VCV(()) is the variance-covariance matrix
c  STP() and SCALE() are needed by STARPAC, but I don't know what
information
c   they contain.  However, STP(1) must be negative.
      dimension PAR(500)
      dimension IFIXED(500)
      character*100 Cparname(500)
      dimension VCV(500,500)
      dimension STP(500), SCALE(500)

c DSTAK() is the workspace for STARPAC. Varying its length can be
c  disastrous.
      dimension DSTAK(1e7)

c Model is the function that returns a simulation based on
c  a set of parameters.
c Current model: double exponential.
c  Y = C*( (alpha)*exp(-X/E1) + (1-alpha)*exp(-X/E2) )

      external Model

c DSTAK must be put in a common block so STARPAC can access it.
      common /cstak/dstak
```

```
      common /data/AngMom, Chan1, Chan2

c  Important!
c  The program only accepts data sets with fewer than 1e5
c  points. If you want to fit more points, this must be
c  changed in several places.


c  These are all parameters that are required by the Starpac
c   function NLSC.
      STP(1) = -2.0
      MIT = -2.0
      STOPSS = 2.1
      STOPP = 2.0
      SCALE(1) = -2.
      DELTA = -2.0
      IVAPRX = 1
      NPRT = 0
      LDSTAK = 10000000
      IVCV=500

c  DataReader first reads par.dat to find the name of the data
c   file and initial values for the fit parameters.  Next, it
c   reads the data file.

      WRITE(*,*) 'Calling DataReader'
      CALL DataReader(Cpathname,CdataFile,Emin,Emax,
     .                Nlines,AngMom2D,Energy2D,Pops2D,Error2D,
     .                PAR,IFIXED,CParname,NPAR,Weights2D)

      WRITE(*,*) 'Finished with Data Reader'
      WRITE(*,*) 'File: ',TRIM(Cpathname)//Cdatafile
      WRITE(*,100) 'Nlines=',Nlines
      WRITE(*,110) Cparname(1),PAR(1)
      WRITE(*,110) Cparname(2),PAR(2)
      WRITE(*,110) Cparname(3),PAR(3)
      WRITE(*,100) 'NPAR=',NPAR

 100  FORMAT(A15,I10)
 110  FORMAT(A15,F10.2)


      DO I=1,4


       AngMom(:) = AngMom2D(:,I)
       XM(:,1) = Energy2D(:,I)
       Y(:) = Pops2D(:,I)
       Error(:) = Error2D(:,I)

c Set weights, normalize Y, count valid states, and record
c overall population
       BranchSum = 0.0

       J = 1
       DO K=1,Nlines
        IF ((Y(K).gt.-1000).and.
```

```
     .     ((XM(K,1).gt.Emin).and.(XM(K,1).le.Emax))) THEN
           AngMom2D(J,I) = AngMom(K)
           Energy2D(J,I) = XM(K,1)
           Pops2D(J,I) = Y(K)
           Error2D(J,I) = Error(K)
           WT(J)=Weights2D(K,I)
           BranchSum = BranchSum+Y(K)
           J = J+1
          END IF
         END DO
         Nlev(I) = J-1

         Report(I,1) = I
         Report(I,2) = BranchSum

         DO L=1,Nlev(I)
          Pops2D(L,I) = Pops2D(L,I)/BranchSum
          Error2D(L,I) = Error2D(L,I)/BranchSum
         END DO

         AngMom(:) = AngMom2D(:,I)
         XM(:,1) = Energy2D(:,I)
         Y(:) = Pops2D(:,I)
         Error(:) = Error2D(:,I)

         N = Nlev(I)
         IXM = Nlev(I)
         M = 1

         WRITE(*,*) 'Calling Starpac'

         CALL NLSWS (Y,WT,XM,N,M,IXM,Model,PAR,NPAR,RES,LDSTAK,
     .    IFIXED,STP,MIT,STOPSS,STOPP,SCALE,DELTA,IVAPRX,NPRT,
     .    NNZW,NPARE,RSD,PV,SDPV,SDRES,VCV,IVCV)

c Make the "report" matrix (fit parameters)

         Report(I,3) = PAR(1)
         Report(I,5) = PAR(2)*298/207.1206178
         Report(I,7) = PAR(3)*298/207.1206178

         J=1
         Scaler = 1.0
         DO K=1,NPAR
          IF (K.gt.1) Scaler = 298/207.1206178
          Report(I,2*K+2)=0.0
          IF (IFIXED(K).lt.1) THEN
           Report(I,2*K+2)=sqrt(VCV(J,J))*Scaler
           J=J+1
          END IF
         END DO

c Make the "fits" matrix (models and raw data)

        Fits(1:Nlev(I),1,I) = XM(1:Nlev(I),1)
        Fits(1:Nlev(I),2,I) = WT(1:Nlev(I))
        Fits(1:Nlev(I),3,I) = Y(1:Nlev(I))
```

```
      Fits(1:Nlev(I),4,I) = Error(1:Nlev(I))
      Fits(1:Nlev(I),5,I) = PV(1:Nlev(I))
      Fits(1:Nlev(I),6,I) = Chan1(1:Nlev(I))
      Fits(1:Nlev(I),7,I) = Chan2(1:Nlev(I))
      Fits(1:Nlev(I),8,I) = AngMom(1:Nlev(I))

c Perform a Boltzmann analysis

      DO J=1,Nlev(I)
       Fits(J,9,I) = log(Y(J)/(2*AngMom(J)+1))
       Fits(J,10,I) = Error(J)/Y(J)
       Fits(J,11,I) = log(PV(J)/(2*AngMom(J)+1))
       Fits(J,12,I) = log(Chan1(J)/(2*AngMom(J)+1))
       Fits(J,13,I) = log(Chan2(J)/(2*AngMom(J)+1))
      END DO



      END DO

      WRITE(*,*) "Calling the data writer"
      CALL Writer(Cpathname,CDatafile,Cparname,
     .            Nlev,Report,Fits)
      WRITE(*,*) "Finished with the data writer"

      end program


************************************************************
      SUBROUTINE DataReader(Cpathname,CdataFile,Emin,Emax,
     .                Nlines,AngMom2D,Energy2D,Pops2D,Error2D,
     .                PAR,IFIXED,CParname,NPAR,Weights2D)

      implicit real*8 (a-h, o-z)
      real*8 xtemp,Emin,Emax,am
      character*100 CDataFile
      character*100 Cpathname
      character*100 CParname(500)
      integer NPAR, Nlines, N, Nstate
      dimension AngMom2D(1e5,4),Energy2D(1e5,4)
      dimension Pops2D(1e5,4),Error2D(1e5,4)
      dimension Weights2D(1e5,4)
      dimension PAR(500),IFIXED(500)
      dimension Testline(100),Weightline(100)

************************************************************
      OPEN (1,file='par.dat')

c Read in the name of the file to be analyzed
c  and the x-axis limits you want to use
      READ(1,100) CPathname
      READ(1,100) CDatafile
      READ(1,*) Emin
      READ(1,*) Emax
      READ(1,*) NPAR
      READ(1,*)
      WRITE(*,*) TRIM(Cpathname)//CDataFile
```

```
 100  FORMAT(A50)

c Read in first parameters
      READ(1,*)
      DO I=1,NPAR
       READ(1,*) PAR(I),IFIXED(I),CParname(I)
       CParname(I)=' '//CParname(I)
      END DO

c Read in the data to be fit
      OPEN (1,file=TRIM(Cpathname)//CDataFile)
      I=1
      READ(1,*)
      DO
        READ(1,*,END=50) Testline(1:16)
        DO L=1,4
         AngMom2D(I,L) = Testline(4*(L-1)+1)
         Energy2D(I,L) = Testline(4*(L-1)+2)
         Pops2D(I,L) = Testline(4*(L-1)+3)
         Error2D(I,L) = Testline(4*(L-1)+4)
        END DO
        I=I+1
      END DO
 50   Nlines = I-1
      CLOSE (UNIT=1)

c Read in the weights for each rovibronic state
      OPEN (1,file="NOstateweights.txt")
      READ(1,*)
      I=1
      DO
        READ(1,*,END=51) Weightline(1:5)
        N = INT(Weightline(1))
        Nstate = INT(Weightline(3))
        Weights2D(N,Nstate) = Weightline(5)
      END DO
 51   CLOSE (UNIT=1)


      Return
      end subroutine DataReader


*********************************************************
      subroutine Writer(Cpathname,CDataFile,Cparname,
     .           Nlev,Report,Fits)
      implicit real*8 (a-h, o-z)
      character*100 Cpathname,Cdatafile,CFitBase,
     .      CFitfile,CReportFile
      character*100 CParname(500)
      character*1 iteration
      dimension Nlev(4)
      dimension Report(4,8), Fits(1e5,13,4)
*********************************************************
c Sends the populations and the best-fit model to output files.
```

```
      CFitBase ='fit_'//Cdatafile
      CReportFile = TRIM(Cpathname)//'rep_'//Cdatafile

      WRITE(*,*) "original file: ",Cdatafile
      WRITE(*,*) "Report file: ",CReportFile

      DO I=1,4
       WRITE(UNIT=iteration,FMT='(I1)') I
       CFitFile = TRIM(Cpathname)//iteration//"_"//CFitBase
       Write(*,*) "Fits file: ",CFitfile
       OPEN (4,file=CFitFile)
       WRITE(4,70) "Energy","Weight","Data","Error",
     .  "Model","Chan1","Chan2","J","Boltzdata",
     .  "Boltzerror","BoltzMod","Boltz1","Boltz2"
       DO J=1,Nlev(I)
        WRITE(4,80) Fits(J,1:13,I)
       END DO
       CLOSE (UNIT=4)
      END DO


      WRITE(*,*)
      WRITE(*,*)
      OPEN (4,file=CReportFile)
      Write(4,90) "State","Summed_Pop","Alpha","Alpha_Error",
     .            "T1","T1_Error","T2","T2_Error"

      Write(*,110) "State","Summed_Pop","Alpha","Alpha_Error",
     .            "T1","T1_Error","T2","T2_Error"


      DO I=1,4
       WRITE(4,100) Report(I,1:8)
       WRITE(*,120) Report(I,1:8)
      END DO




 70   FORMAT (12A25)
 80   FORMAT (13e25.8)
 90   FORMAT (8A25)
 100  FORMAT (8e25.5)
 110  FORMAT (8A15)
 120  FORMAT (f15.0,e15.3,6f15.2)


      RETURN
      END


*************************************************************
      subroutine Model(PAR, NPAR, XM, N, M, IXM, PV)
      implicit real*8 (a-h, o-z)
      dimension PAR(NPAR), XM(IXM,M), PV(N)
      dimension AngMom(1e5), Chan1(1e5), Chan2(1e5)
```

```
      common /cstak/dstak
      common /data/ AngMom, Chan1, Chan2

*************************************************************

c Double exponential decay.  "E1" is the sticking componant.

      Alpha=PAR(1)
      E1=PAR(2)
      E2=PAR(3)

      Q1=0.0
      Q2=0.0

      DO I=1,N
       Q1=Q1+(2*AngMom(I)+1)*exp(-XM(I,1)/E1)
       Q2=Q2+(2*AngMom(I)+1)*exp(-XM(I,1)/E2)
      END DO

      DO I=1,N
       Chan1(I)=(2*Angmom(I)+1)*
     .           Alpha*exp(-XM(I,1)/E1)/Q1
       Chan2(I)=(2*Angmom(I)+1)*
     .           (1-Alpha)*exp(-XM(I,1)/E2)/Q2
       PV(I)=Chan1(I)+Chan2(I)
      END DO

      RETURN
      END
```